ADVANCES IN
QUANTUM CHEMISTRY

DV-Xα FOR ADVANCED NANO MATERIALS AND OTHER INTERESTING TOPICS IN MATERIALS SCIENCE

EDITORS

JOHN R. SABIN
QUANTUM THEORY PROJECT
UNIVERSITY OF FLORIDA
GAINESVILLE, FLORIDA

ERKKI BRÄNDAS
DEPARTMENT OF QUANTUM CHEMISTRY
UPPSALA UNIVERSITY
UPPSALA, SWEDEN

FOUNDING EDITOR

PER-OLOV LÖWDIN†

GUEST EDITORS

ERKKI J. BRÄNDAS
DEPARTMENT OF QUANTUM CHEMISTRY
UPPSALA UNIVERSITY
UPPSALA, SWEDEN

HIOROHIKO ADACHI
KYOTO UNIVERSITY
DEPARTMENT OF MATERIALS
SCIENCE AND ENGINEERING
KYOTO, JAPAN

MASAYUKI UDA
WASEDA UNIVERSITY
DEPARTMENT OF MATERIALS
SCIENCE AND ENGINEERING
TOKYO, JAPAN

RIKA SEKINE
DEPARTMENT OF CHEMISTRY
SHIZUOKA UNIVERSITY
SHIZUOKA, JAPAN

VOLUME 42

ACADEMIC PRESS
An imprint of Elsevier Science

Amsterdam · Boston · London · New York · Oxford · Paris
San Diego · San Francisco · Singapore · Sydney · Tokyo

Contributors

Numbers in parentheses indicate the pages on which the authors' contributions begin.

Hirohiko Adachi (1, 67, 145, 175), Department of Materials Science and Engineering, Kyoto University, Sakyo, Kyoto 606-8501, Japan

Matti Alatalo (127), Laboratory of Physics, Helsinki University of Technology, P. O. Box 1100, 02015 HUT, Finland

Hideki Araki (109), Department of Materials Science and Engineering, Osaka University, 2-1 Yamada-oka, Suita, Osaka, 565-0871, Japan

Erkki J. Brändas (383), Department of Quantum Chemistry, Uppsala University, Box 518, S-751 20 Uppsala, Sweden

Mads Brandbyge (299), Mikroelektronik Centret (MIC), Technical University of Denmark, Bldg. 345E, DK-2800 Lyngby, Denmark

Hyunju Chang (163), Advanced Materials Division, Korea Research Institute of Chemical Technology, Taejon, 305-600, Korea

Youngmin Choi (163), Advanced Materials Division, Korea Research Institute of Chemical Technology, Taejon, 305-600, Korea

Don Ellis (35), Department of Physics & Astronomy and Institute of Environmental Catalysis, Northwestern University, Evanston IL 60208

Noboru Esashi (439), School of Science, Kwansei Gakuin University 2-1 Gakuen, Sanda, Hyogo 669-1337, Japan

Kimichika Fukushima (223), Advanced Energy System Design and Engineering Department, Isogo Engineering Center, Toshiba Corporation, 8, Shinsugita-cho, Isogo-ku, Yokohama, 235-8523, Japan

Tatsuya Hagiwara (187), Department of Environmental Chemistry and Materials, Okayama University, 3-1-1 Tsushima-Naka, Okayama 700-8530, Japan

Yoshinori Hayafuji (239, 439), School of Science, Kwansei Gakuin University 2-1 Gakuen, Sanda, Hyogo 669-1337, Japan

M. Hoshino (399), The Institute of Physical and Chemical Research 2-1, Hirosawa, Wako, Saitama 351-0198, Japan

E. Iguchi (215), Division of Materials Science and Engineering, Graduate School of Engineering, Yokohama National University, Tokiwadai, Hodogaya-ku, Yokohama 240-8501, Japan

Takugo Ishii (67), Department of Materials Science and Engineering, Osaka University, 2-1 Yamada-oka, Suita, Osaka, 565-0871, Japan

Takamasa Isobe (465), Department of Materials Science, Shonan Institue of Technology, 1-1-25 Tsujido-nishikaigan, Fujisawa, 251-8511 Japan

Shigeyuki Ito (263), Department of Materials Science and Engineering, Graduate School of Engineering, Nagoya University, Furo-cho, Chikusa-ku, Nagoya 464-8603, Japan

Shinichi Itoh (209), Kyoto University of Education, Fukakusa Fujimori-cho 1, Fushimi, Kyoto, 612-8522, Japan

Tomoko Jimbo (453), Hitachi, Ltd., Device Development Center, 16-3, Shinmachi 6-chome, Ome-shi, Tokyo 198-8512, Japan

László Kövér (331), Institute of Nuclear Research of the Hungarian Academy of Sciences P.O. Box 51, H-4001 Debrecen, Hungary

Yukinori Koyama (145), Department of Materials Science and Engineering, Kyoto University, Sakyo, Kyoto 606-8501, Japan

J. Kuriplach (77), Department of Low Temperature Physics, Charles University, V Holešovičkách 2, CZ-180 00 Prague 8, Czech Republic

Jae Do Lee (163), Advanced Materials Division, Korea Research Institute of Chemical Technology, Taejon, 305-600, Korea

Yi Liu (315), Department of Materials Science and Engineering, Graduate School of Engineering, Nagoya University, Furo-cho, Chikusa-ku, Nagoya 464-8603, Japan

Hiroshi Maeda (275), Department of Manufacturing Science, Osaka University, 2-1, Yamada-oka, Suita, Osaka 565-0871, Japan

Shuji Matsuo (407), Department of Chemistry, Faculty of Science, Fukuoka University, Nanakuma, Jonan-ku, Fukuoka 814-0180, Japan

Fumiyoshi Minami (275), Department of Manufacturing Science, Osaka University, 2-1, Yamada-oka, Suita, Osaka 565-0871, Japan

Yoshinari Miura (187), Department of Environmental Chemistry and Materials, Okayama University, 3-1-1 Tsushima-Naka, Okayama 700-8530, Japan

Masataka Mizuno (109), Department of Materials Science and Engineering, Osaka University, 2-1 Yamada-oka, Suita, Osaka, 565-0871, Japan

Masahiko Morinaga (263, 315), Department of Materials Science and Engineering, Graduate School of Engineering, Nagoya University, Furo-cho, Chikusa-ku, Nagoya 464-8603, Japan

José Luis Mozos (299), Instituto de Ciencia de Materiales de Barcelona - CSIC, 08193 Bellaterra, Barcelona, Spain

Takeshi Mukoyama (283), Kansai Gaidai University, Hirakata, Osaka, 573-1001 Japan

Yasuji Muramatsu (353), Kansai Research Establishment, Japan Atomic Energy Research Institute (JAERI) Kouto, Mikazuki, Sayo-gun, Hyogo 679-5148, Japan

Ágnes Nagy (363), Department of Theoretical Physics, University of Debrecen, H4010 Debrecen, Hungary

Yoshiyuki Nakajima (399, 419), Riken Keiki Co. Ltd., Research Department 2-7-6, Azusawa, Itabashi-ku, Tokyo 174-8744, Japan

Hirohide Nakamatsu (419), Institute for Chemical Research, Kyoto University, Gokasho, Uji, Kyoto 611-0011, Japan

Hiroshi Nakatsugawa (215), Division of Materials Science and Engineering, Graduate School of Engineering, Yokohama National University, Tokiwadai, Hodogaya-ku, Yokohama 240-8501, Japan

Tokuro Nanba (187), Department of Environmental Chemistry and Materials, Okayama University, 3-1-1 Tsushima-Naka, Okayama 700-8530, Japan

Fumiyasu Oba (175), Department of Materials Science and Engineering, Case Western Reserve University, 302 White Bldg., 10900 Euclid Avenue, Cleveland, Ohio 44106-7204, USA (from September 2002)

Kazuyoshi Ogasawara (1, 67), Department of Materials Science and Engineering, Kyoto University, Sakyo, Kyoto 606-8501, Japan

Yasuhiko Ohama (439), Neutron Scattering Laboratory, Institute for Solid State Physics, University of Tokyo, Shirakata 106-1, Tokai 319-1106, Japan

Yasuaki Oohara (215), Neutron Scattering Laboratory, Institute for Solid State Physics, University of Tokyo, Shirakata 106-1, Tokai 319-1106, Japan

Pablo Ordejón (299), Instituto de Ciencia de Matariales de Barcelona - CSIC, 08193 Bellaterra, Barcelona, Spain

M.J. Puska (127), Laboratory of Physics, Helsinki University of Technology, P. O. Box 1100, 02015 HUT, Finland

Yoshiyuki Sakai (429), Department of Industrial Education, Ashiya University, 13-22, Rokurokuso-cho, Ashiya, Hyogo, Japan

Taketo Sakuma (23), Department of Advanced Materials Science, Graduate School of Frontier Science, The University of Tokyo 7-3-1 Hongo, Bunkyo-ku, Tokyo 113-8656, Japan

Masayoshi Seike (239), School of Science, Kwansei Gakuin University 2-1 Gakuen, Sanda, Hyogo 669-1337, Japan

Yasuharu Shirai (109), Department of Materials Science and Engineering, Osaka University, 2-1 Yamada-oka, Suita, Osaka, 565-0871, Japan

Kaori Shirozu (407), Department of Chemistry, Faculty of Science, Fukuoka University, Nanakuma, Jonan-ku, Fukuoka 814-0180, Japan

Mojimir Šob (77), Institute of Physics of Materials, Academy of Sciences of the Czech Republic, Žižkova 22, CZ-616 62 Brno, Czech Republic

H. Sormann (77), Institut für Theoretische Physik, Technische Universität Graz, Petersgasse 16, A-8010 Graz, Austria

Kurt Stokbro (299), Mikroelektronik Centret (MIC), Technical University of Denmark, Bldg. 345E, DK-2800 Lyngby, Denmark

Sunao Sugihara (465), Department of Materials Science, Shonan Institue of Technology, 1-1-25 Tsujido-nishikaigan, Fujisawa, 251-8511 Japan

Wataru Takahara (275), Department of Manufacturing Science, Osaka University, 2-1, Yamada-oka, Suita, Osaka 565-0871, Japan

Ken-ichi Takai (239), School of Science, Kwansei Gakuin University 2-1 Gakuen, Sanda, Hyogo 669-1337, Japan

Isao Tanaka (145, 175), Department of Materials Science and Engineering, Kyoto University, Sakyo, Kyoto 606-8501, Japan

K. Tanaka (239), School of Science, Kwansei Gakuin University 2-1 Gakuen, Sanda, Hyogo 669-1337, Japan

Yuichi Tateishi (407), Department of Chemistry, Faculty of Science, Fukuoka University, Nanakuma, Jonan-ku, Fukuoka 814-0180, Japan

Jeremy Taylor (299), Mikroelektronik Centret (MIC), Technical University of Denmark, Bldg. 345E, DK-2800 Lyngby, Denmark

Yoko Uchida (453), Hitachi, Ltd., Semiconductor & Integrated Circuits, 16-3, Shinmachi 6-chome, Ome-shi, Tokyo 198-8512, Japan

Masayuki Uda (283, 399, 419, 453), Department of Materials Science and Engineering, Waseda University, Shinjuku, Tokyo, 169-8555 Japan and Laboratory for Materials Science and Technology, Waseda University, Shinjuku, Tokyo, 169-0051 Japan

Hisanobu Wakita (407), Department of Chemistry, Faculty of Science, Fukuoka University, Nanakuma, Jonan-ku, Fukuoka 814-0180, Japan

O. Warschkow (35), Dept. of Physics & Astronomy and Institute of Environmental Catalysis Northwestern University, Evanston IL 60208

Masahiro Yamamoto (465), Department of Materials Science, Shonan Institue of Technology, 1-1-25 Tsujido-nishikaigan, Fujisawa, 251-8511 Japan

Tomoyuki Yamamoto (199), Computational Science Division, RIKEN, 2-1 Hirosawa, Wako-shi, Saitama 351-0198, Japan

Daisuke Yamashita(1) (263), Department of Materials Science and Engineering, Graduate School of Engineering, Nagoya University, Furo-cho, Chikusa-ku, Nagoya 464-8603, Japan

Daisuke Yamashita(2) (399, 419, 453), Department of Materials Science and Engineering, Waseda University, Shinjuku, Tokyo, 169-8555 Japan

Takushi Yokoyama (407), Department of Chemistry, Faculty of Science, Kyushu University, Ropponmatsu, Chuo-ku, Fukuoka 810-8560, Japan

Hiroshi Yukawa (263, 315), Department of Materials Science and Engineering, Graduate School of Engineering, Nagoya University, Furo-cho, Chikusa-ku, Nagoya 464-8603, Japan

Yukio Yutoh (465), Department of Materials Science, Shonan Institute of Technology, 1-1-25 Tsujido-nishikaigan, Fujisawa, 251-8511 Japan

Preface

The Discrete Variational Xα (DV-Xα) molecular orbital calculation method is one of the most versatile methods for estimating the electronic structures of atom-aggregates or clusters at both ground and excited states. Also, the DV-Xα method has been extensively used for solid-state chemistry and physics, materials science, and electron- and X-ray spectroscopy with great success.

This is the third volume in a series of DV-Xα activities and includes a selection of papers presented at the third international workshop and at the fourteenth annual meeting of "DV-Xα" held at RIKEN, Wako, Japan, from July 31 to August 3, 2001. The first and second volumes on DV-Xα activities were published in 1997 in *Advances in Quantum Chemistry* (Vol. 29) with the subtitle *Electronic Structure of Clusters,* and in 2000 in *Advances in Quantum Chemistry* (Vol. 37) with the subtitle *DV-Xα for Atomic Spectroscopy and Materials Science.*

The third international workshop on the DV-Xα method was devoted to discussions of (1) Present and Future Applications, (2) Atomic Spectroscopy, (3) Materials Science and (4) Future Development, in which 23 invited papers were presented. The fourteenth annual meeting had 52 poster papers, which were presented in 8 Sessions, i.e. Materials Science (1,2,3), Surfaces, Boundaries and Defects (1,2), Organic and Inorganic Compounds (1) and Spectroscopy (1,2). Fruitful discussions were held and the marvelous results shown in the workshop and the annual meeting are summarized in this volume.

Finally, special thanks should be expressed to Drs. T. Ebisuzaki, J. Onoe and T. Yamamoto (RIKEN) for providing a guesthouse for the guest speakers, a lecture hall and the necessary facilities in RIKEN. The financial support of RIKEN, National Institute for Materials Science, TDK, Toshiba, Kobe Steel, Riken Keiki, Hitachi and Sankyou Publishing is also much appreciated, and made it possible to invite ten excellent scientists from abroad. The great success of this meeting was in great part due to the self-sacrificing effort of Dr. T. Ishii.

Tokyo, August 20, 2002

H. Adachi, M. Uda and H. Wakita
Chairpersons
The Third International Workshop on DV-Xα
and The Fourteenth Annual Meeting on DV-Xα

Many-electron theory for electronic transition process - Its importance in materials science -

Hirohiko Adachi and Kazuyoshi Ogasawara
Department of Materials Science and Engineering, Kyoto University

(Received June 6, 2002; in final form June 18, 2002)

The newly developed discrete variational multi-electron(DV-ME) method has been applied to the problem of electronic transition process where the many-electron theory is indispensable. The computational procedure of DV-ME method has been described in some details. The application of the method to the analysis of x-ray absorption near edge structure (XANES) from transition metal oxides has been made. We have also performed theoretical analysis for ultraviolet absorption spectrum from lanthanide doped metal fluoride crystal. The multiplet splitting and configuration interaction are substantial in calculating the theoretical spectrum. The importance of configuration interaction has been manifested in reproducing the 3d transition metal $L_{2,3}$ XANES. For the analysis of charge-transfer type compound, multiexcitation due to the transition from ligand to metal orbitals has effectively been taken into account in the calculation to give the satellite peak observed in the experimental spectrum. The optical absorption spectra of lanthanide ion caused by 4f-5d transition have been calculated to demonstrate a good agreement with the experiment, indicating the effectiveness of the present method for new materials design and development.

KEYWORDS: many-electron theory, relativistic DV-ME method, CI calculation, x-ray absorption, UV absorption, relativistic DV-Xα method

e-mail: adachi@cms.mtl.kyoto-u.ac.jp

ADVANCES IN QUANTUM CHEMISTRY, VOLUME 42

0065-3276/03 $35.00

I. Introduction

In the field of materials science, the quantum mechanical calculation of electronic states has gained increased importance, since it is helpful not only for deep understanding of various basic properties of materials, but also for design and development of many kinds of new materials. For the electronic state calculation, the molecular orbital method like discrete variational Xα(DV-Xα) method[1] and band structure calculation methods such as plane-wave-basis pseudopotential (PWPP) method[2], full potential linearized augmented plane wave (FLAPW) method[3] and orthogonalized linear combination of atomic orbitals (OLCAO) method[4] have been proved to be very efficient to provide accurate electronic structure and chemical bonding. These approaches have been employed to solve various problems of materials science.

In the study of the properties of practical materials, it is very important to understand "localized quantum structure", that is, the local atomic arrangement and the localized electronic state and chemical bonding at very small space around surface, interface and lattice defects such as atomic vacancy and impurity. For this problem, recently developed experimental techniques such as high-resolution electron microscope and various electron and x-ray spectroscopies are efficient. In order to analyze these experiments correctly, accurate information on electronic state and chemical bonding is necessary. The first-principles electronic state calculations by the molecular orbital method and the band theory above described have been proved to be very useful for these purposes. However, there are some difficult problems, which cannot be solved by the above theoretical approaches of the one-electron model, and a more precise and detailed analysis is required to understand the experimental results. Therefore, the first-principles calculation of many-electron theory like configuration interaction (CI) method should be employed to solve the problems.

We have recently developed a new theoretical method of the first-principles CI type of calculation for many-electron systems, which we call discrete variational multi-electron (DV-ME) method[5,6]. In the present paper, we have applied it to the theoretical analyses of x-ray absorption near edge structure (XANES) for transition metal oxides[7], including the charge-transfer type oxides. The importance of many-electron theory and the effectiveness of DV-ME method are demonstrated. The many-electron theory is

also substantial for the study of optical spectrum in UV/visible region. The theoretical analysis of the optical absorption spectra for laser materials has been made by DV-ME method. The ultraviolet absorption spectra due to f-d transitions of lanthanide ions have been calculated and discussed.

2. Computational method

Usually the first principles calculation of electronic structure is made within the one-electron theory of self-consistent-field approximation by Hatree-Fock model or density functional theory. However, these approaches are generally insufficient to represent accurate electronic states for many-electron systems. Then more accurate theoretical approach like configuration interaction type of calculation is necessary.

For many-electron theory, some semiempirical methods such as crystal-field theory and ligand-field theory have already been established. These theories are useful for theoretical analysis of well-known materials, but are not very efficient for unknown materials because some empirical parameters from experiment are necessary in the calculation. Therefore, a first-principles method is indispensable for new materials design and development.

As the eigenfunction of many-electron Hamiltonian for open shell configuration,

$$H = \sum_{i}^{n} \left\{ -\frac{1}{2}\nabla_i^2 - \sum_{v} \frac{Z_v}{r_{iv}} + \sum_{j>i}^{n} \frac{1}{|\mathbf{r}_i - \mathbf{r}_j|} \right\}, \qquad (1)$$

the wave function Ψ can be expressed not by a single Slater determinant as in the one-electron model, but by a linear combination of Slater determinants written by

$$\Psi_a(\mathbf{r}_1, \mathbf{r}_2, \cdots\cdots, \mathbf{r}_n) = \sum_{\ell} W_{\ell a} \Phi_\ell(\mathbf{r}_1, \mathbf{r}_2, \cdots\cdots, \mathbf{r}_n), \qquad (2)$$

where Φ_ℓ is the Slater determinant. Then, the Slater determinant is the basis in this case. The Slater determinant is formed by a combination of products of molecular orbitals and written as

$$\Phi_\ell = \begin{vmatrix} \phi_{\ell 1}(\mathbf{r}_1)\,\phi_{\ell 1}(\mathbf{r}_2) \cdots\cdots \phi_{\ell 1}(\mathbf{r}_n) \\ \phi_{\ell 2}(\mathbf{r}_1)\,\phi_{\ell 2}(\mathbf{r}_2) \cdots\cdots \phi_{\ell 2}(\mathbf{r}_n) \\ \cdots\cdots \\ \phi_{\ell n}(\mathbf{r}_1)\,\phi_{\ell n}(\mathbf{r}_2) \cdots\cdots \phi_{\ell n}(\mathbf{r}_n) \end{vmatrix} . \qquad (3)$$

The molecular orbital function ϕ_i is obtained by usual DV-Xα molecular orbital calculation in DV-ME method. The secular equation is constructed by Slater determinants as the basis functions and is given by

$$\left.\begin{aligned} &\tilde{\mathbf{H}}\,\tilde{\mathbf{W}} = \tilde{\mathbf{E}}\,\tilde{\mathbf{S}}\,\tilde{\mathbf{W}} \\ &H_{ab} = \int \Psi^*_a H \Psi_b \, d\tau \ , \end{aligned}\right\} \tag{4}$$

contrary to that of one-electron molecular orbital theory where the secular equation is made by atomic orbitals as the basis.

In some cases where the system contains heavy elements and the process concerns inner shells, a relativistic calculation is necessary. In such cases, we utilize the relativistic molecular orbitals which can be obtained by relativistic DV-Xα molecular orbital calculation for Dirac Hamiltonian

$$H = c\,\boldsymbol{\alpha}\mathbf{p} + \beta c^2 + V_{eff}\,. \tag{5}$$

In the calculation, the two-electron interaction term in the Hamiltonian is most serious problem to evaluate, because of the computational difficulty of the multicenter double integral. In DV-ME method, however, the evaluation of this term is feasible by DV numerical integration technique without any mathematical limitation. For a practical use of this method, whole electronic system is divided into two parts, one of which is that of closed shells and the other of open shells. We consider that the secular equation can be constructed by Slater determinants only containing open shell molecular orbitals.

This method is often used for problems concerning the electronic transition. The transition energy is calculated as the energy difference between the initial and final electronic states, while the probability of dipole transition can be estimated by oscillator strength

$$P_{ab} = \frac{2}{3}\left(E_a - E_b\right)\int \Psi^*_a \mathbf{r} \Psi_b \, d\tau\,, \tag{6}$$

calculated by directly using the many-electron wave functions. The DV-ME method makes it possible to treat many of too complicated problems for the one-electron model, so-called many-electron effect.

In DV-Xα calculation of one-electron molecular orbital theory, the transition energy is estimated by the energy difference between the initial and final orbitals for Slater's transition state[8], where a half electron is removed from the intial orbital and is

put in the final orbital. The transition probability is evaluated by the element of dipole matrix between the initial and final orbitals. The application of DV-Xα method to the analysis for various electron and x-ray spectroscopies has thoroughly been described elsewhere[9].

3. Results and discussion

3.1 Effects of configuration interactions on 3d transition metal $L_{2,3}$ XANES

The x-ray absorption near edge structure (XANES) is often used for chemical state analysis, because it reflects the electronic state of unoccupied orbitals. The spectrum is caused by the x-ray absorption accompanying the electronic transition from 2p core levels to mainly 3d levels according to the dipole selection rule. Figure 1

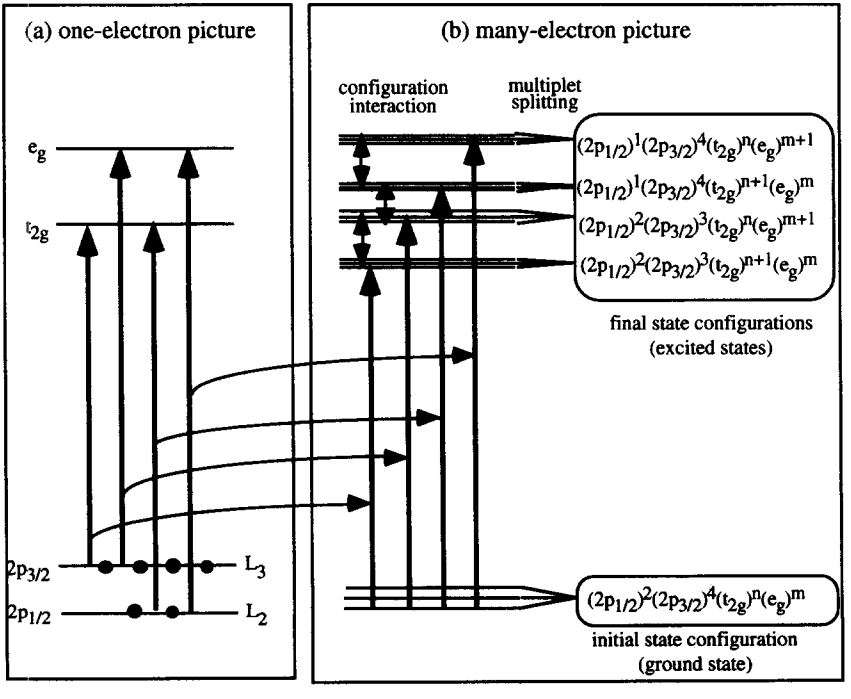

Fig. 1 Schematic diagram of electronic transition due to x-ray absorption.

demonstrates the schematic diagram for x-ray absorption process. We consider the case of 3d transition metal $L_{2,3}$ XANES from metal oxide, for example, from $SrTiO_3$. In this compound, 3d level is considered to split into two levels, namely, t_{2g} and e_g, since the Ti^{4+} ion is situated at the octahedral site. The 2p level is split into $2p_{1/2}$ and $2p_{3/2}$, or L_2 and L_3, by spin-orbit coupling. Then, the absorptions from both of these 2p levels to two of these 3d levels take place and four absorption peaks can be observed in the absorption spectrum. In the 2p shell, two electrons occupy L_2 and four electrons occupy L_3 state, then the intensity of L_3 absorption is expected to be two times of that of L_2 from the one-electron model. Among these absorptions for Ti^{4+} ion with d^0 configuration, intensity ratio of two peaks, one of which corresponds to the transition to t_{2g}, and the other to e_g state, is 3/2, because the t_{2g} and e_g are triply and doubly degenerate states, respectively. Therefore, the relative intensities of the four peaks are 6 and 4 for L_3 absorption, and 3 and 2 for L_2 absorption.

The experimental Ti $L_{2,3}$ XANES spectrum[10] is shown in Fig.2(a). The spectrum shows four peaks indeed, but the intensity ratio does not agree with the one-electron model. Therefore, more accurate theoretical approach seems to be necessary. In many-electron theory, the initial state of the x-ray absorption process is the ground state whose configuration is generally expressed by $(2p_{1/2})^2(2p_{3/2})^4(t_{2g})^n(e_g)^m$ for the 3d transition metal compound, as shown in Fig.1(b). In the present case, both of n and m are zero, since Ti^{4+} ion takes d^0 configuration. The final state is the excited state where one of 2p electrons is transferred to the 3d level, and is expressed by one of $(2p_{1/2})^2(2p_{3/2})^3(t_{2g})^1$, $(2p_{1/2})^2(2p_{3/2})^3(e_g)^1$, $(2p_{1/2})^1(2p_{3/2})^4(t_{2g})^1$ or $(2p_{1/2})^1(2p_{3/2})^4(e_g)^1$ configuration. Each of these initial and final electronic states is generally split into multiplet levels by electron-electron interactions. In addition, the interactions among these configurations should be taken into account to obtain the accurate electronic states for the many-electron system. In this case, fully relativistic calculation is required since the interactions with inner-shell electrons should explicitly be considered. This relativistic many-electron calculation can be executed by relativistic DV-ME method. Here, the expression $2p_{1/2}$, $2p_{3/2}$, t_{2g} and e_g are not suitable for rigorous explanation of relativistic theory. Instead the representations of the double group such as γ_{6u}, γ_{8u}, γ_{7g} and γ_{8g}, respectively corresponding to them should be employed. However, the relativistic effects for 3d states, namely t_{2g} and e_g, are very small, then more familiar expressions are used in the present paper.

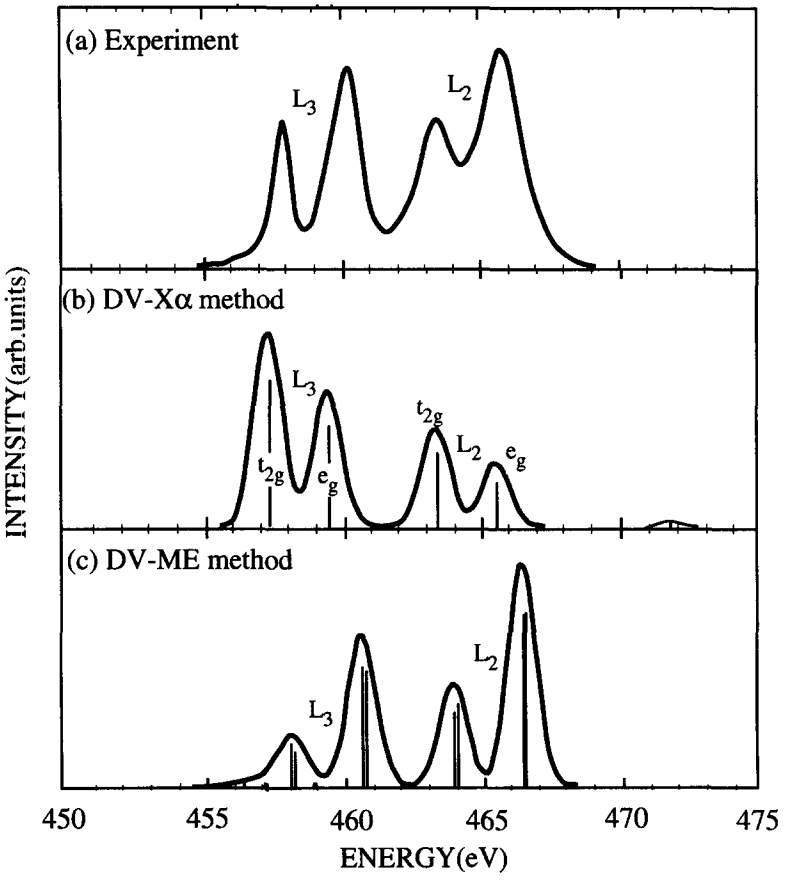

Fig.2 Comparison of experimental and calculated Ti $L_{2,3}$ XANES spectra from $SrTiO_3$ with d^0 configuration.

Figure 2(b) shows the theoretical spectrum calculated by the relativistic DV-Xα method of one-electron model, by the use of TiO_6^{8-} cluster. The peak energy is evaluated from Slater's transition state calculation, and the peak level is replaced by a Gaussian with FWHM of 0.5 eV to obtain the theoretical spectrum. The result shows the four absorption peaks whose energies agree well with the experiment shown in Fig.2(a). However, the relative intensities of these peaks in the experimental spectrum are completely different from those expected from one-electron picture, but are almost inverted. Figure 1(c) demonstrates the calculated result by relativistic DV-ME method

of many-electron theory. We use the relativistic molecular orbitals calculated above DV-Xα method to make the Slater determinants. It is clear that the intensity ratio has drastically been improved by taking account of the multiplet splittings and the configuration interactions, showing very good agreement with the experiment.

Next, we made various types of calculations to investigate the effects of configuration interactions on the intensity ratio. In the present case, the initial state is singlet and we consider four configurations as the final states, namely, configuration A which corresponds to transition from $2p_{3/2}$ to t_{2g}, B from $2p_{3/2}$to e_g, C from $2p_{1/2}$ to t_{2g} and D from $2p_{1/2}$ to e_g as shown in Fig. 3. These configurations A, B, C and D contain 24, 16, 12 and 8 electronic microstates, respectively, to each of which one Slater determinant corresponds. Thus, for example, the multiplet levels in the configuration A are comprised of 24 Slater determinants.

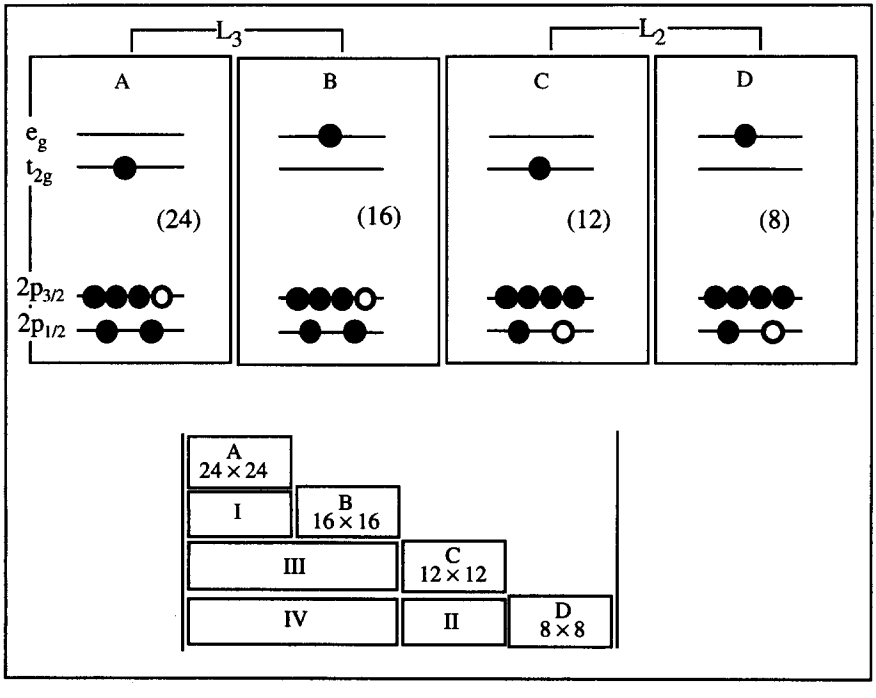

Fig.3 Schematic diagram for final state configurations. A:$(2p_{1/2})^2(2p_{3/2})^3(t_{2g})^1(eg)^0$, B:$(2p_{1/2})^2(2p_{3/2})^3(t_{2g})^0(eg)^1$, C:$(2p_{1/2})^1(2p_{3/2})^4(t_{2g})^1(eg)^0$, D:$(2p_{1/2})^1(2p_{3/2})^4(t_{2g})^0(eg)^1$ Number in parenthesis denotes that of micro states in the configuration.

Consequently, we consider total 61 Slater determinants from the ground state and excited states configurations to construct the secular equation. For the final state calculation, the secular matrix comprises four matrices as shown in Fig.3, namely, 24 × 24 for configuration A, 16 × 16 for B, 12 × 12 for C and 8 × 8 for D. The multiplet splittings are caused by the interactions within these configurations to produce 24, 16, 12, and 8 multiplet levels, respectively. Furthermore, the interactions among these configurations indicated I, II, III and IV in Fig.3, take place to provide the correct electronic states for many-electron system. We define that the configuration interaction is the interaction among these configurations in the present paper.

We have made four types calculations to examine the interactions among these configurations. In the first calculation, we only consider the multiplet splittings within the four configurations, but no configuration interaction among them. The result calculated is displayed in Fig.4(a).

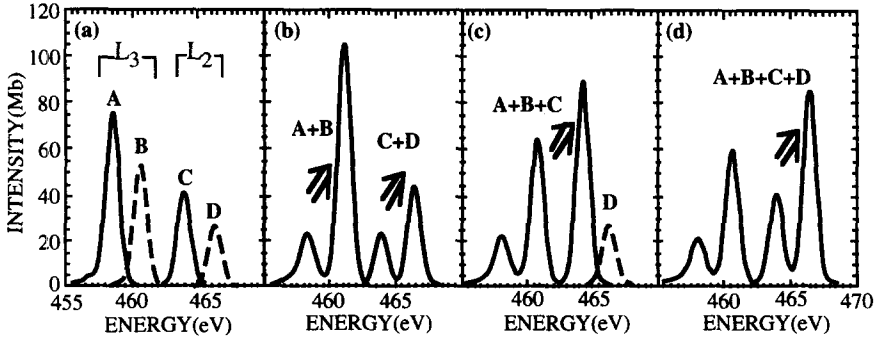

Fig.4 Effects of configuration interactions on Ti $L_{2,3}$ XANES from $SrTiO_3$

The spectrum is composed of four peaks A, B, C and D corresponding to the four configurations. Each peak contains many levels to give a multiplet structure. Although each peak shows a fine structure due to the multiplet splittings, we do not discuss about it since the level separations are so small that the structure is not clear in this case. The relative peak intensities are 24, 16, 12 and 8, attributed to the numbers of the microstates in the configurations and are the same to the one-electron model. In the second calculation, we include the configuration interactions partly, which are indicated by I and II in Fig.3, namely, those between A and B, and between C and D. Thus, the

configuration interactions within the L_2 and L_3 excitations are separately taken into account in this case. The result is shown in Fig.4(b). It can be seen that the intensity ratios within the L_2 and L_3 are largely modified. However, the intensity ratio of L_3 to L_2, which is sometimes called as branching ratio, does not change. A further calculation is made including the configuration interactions III in addition to I and II, that is among A, B and C configurations, but separating the configuration D. This calculation brings about a drastic change of the intensity ratio of L_3 to L_2 as shown in Fig.4(c). Finally, all interactions among the four configurations including IV are taken into account in the calculation. Figure 4(d) demonstrates the result thus obtained, and is the same to Fig.3(c). The spectrum reproduces very well the experiment. These examinations clarifies that the configuration interactions are essential for the correct analysis of the Ti $L_{2,3}$ XANES spectrum.

3.2 Analysis of 3d transition metal $L_{2,3}$ edge XANES from various metal oxides

The DV-ME method can be applied to general transition metal compounds with d^n configurations. The theoretical M $L_{2,3}$ XANES spectra from V_2O_3, Cr_2O_3, Fe_2O_3 and CoO with d^2, d^3, d^5 and d^7 configurations, respectively, have been calculated by DV-Xα and DV-ME methods, and are compared with experiments. In all of these oxides, transition metal ions occupy the octahedral sites. The cluster models used are $(MO_6)^{q-}$, similar to the case of TiO_6^{8-}, but the lattice distortions are taken into account according to the crystal structures of above metal oxides. The initial- and final-state configurations and numbers of the Slater determinants utilized in the DV-ME calculations are listed in Table 1. In the case of Fe^{3+} ion (Fe_2O_3) with d^5, for instance, five intial- and ten final-state configurations are considered, and total 1512 Slater determinants are employed in the calculation.

The comparisons between theoretical and experimental $L_{2,3}$ XANES spectra for these oxides are demonstrated in Figs.5~8. Figure 5 indicates the V $L_{2,3}$ XANES spectra from V_2O_3 with d^2 configuration. The result calculated by DV-Xα method shows the spectrum of four peaks, where both of L_2 and L_3 peaks are split into t_{2g} and e_g, as deduced from the one-electron model. However, the experimental spectrum[11] shows more complicated structure, that is, with peaks labeled by a~f. This structure is well reproduced by DV-ME calculation as exhibited in Fig.5(c), though the structure at higher energy O K edge seen in the experimental spectrum has not been dealt with in

Table 1 Occupation numbers in each levels for initial and final state configurations and numbers of Slater determinants

	$2p_{1/2}$	$2p_{3/2}$	t_{2g}	e_g	NS	total
	2	4	0	0	1	
	2	3	1	0	24	
(d^0)	2	3	0	1	16	61
	1	4	1	0	12	
	1	4	0	1	8	
	2	4	2	0	15	
	2	4	1	1	24	
	2	4	0	2	6	
	2	3	3	0	80	
	2	3	2	1	240	
(d^2)	2	3	1	2	144	765
	2	3	0	3	16	
	1	4	3	0	40	
	1	4	2	1	120	
	1	4	2	1	72	
	1	4	0	3	8	
	2	4	3	0	20	
	2	4	2	1	60	
	2	4	1	2	36	
	2	4	0	3	4	
	2	3	4	0	60	
	2	3	3	1	320	
(d^3)	2	3	2	2	360	1380
	2	3	1	3	96	
	2	3	0	4	4	
	1	4	4	0	30	
	1	4	3	1	160	
	1	4	2	2	180	
	1	4	1	3	48	
	1	4	0	4	2	

	$2p_{1/2}$	$2p_{3/2}$	t_{2g}	e_g	NS	total
	2	4	5	0	6	
	2	4	4	1	60	
	2	4	3	2	120	
	2	4	2	3	60	
	2	4	1	4	6	
	2	3	6	0	4	
	2	3	5	1	96	
(d^5)	2	3	4	2	360	1512
	2	3	3	3	320	
	2	3	2	4	60	
	1	4	6	0	2	
	1	4	5	1	48	
	1	4	4	2	180	
	1	4	3	3	160	
	1	4	2	4	30	
	2	4	6	1	4	
	2	4	5	2	36	
	2	4	4	3	60	
	2	4	3	4	20	
	2	3	6	2	24	
(d^7)	2	3	5	3	96	390
	2	3	4	4	60	
	1	4	6	2	12	
	1	4	5	3	48	
	1	4	4	4	30	
	2	4	6	2	6	
	2	4	5	3	24	
	2	4	4	4	15	
(d^8)	2	3	6	3	8	105
	2	3	5	4	12	
	1	4	6	3	16	
	1	4	5	4	24	

NS denotes the number of Slater determinants in each configuration

this calculation. The result by DV-ME calculation indicates that the multiplet splittings are so large that the definite structure can be seen in the $L_{2,3}$ XANES.

In the experimental Cr $L_{2,3}$ XANES spectrum from Cr_2O_3[12] shown in Fig. 6(a), the structure characterized by labels a~g is observed. The DV-Xα calculation does not reproduce it, while the DV-ME result shows very good agreement with the experiment. The level spreadings by multiplet splittings as well as the configuration interactions are considerably large also in this case.

Figure 7 displays the Fe $L_{2,3}$ XANES spectra from Fe_2O_3. The peak separation between L_2 and L_3 becomes larger than the former oxides, since the 2p level splitting by

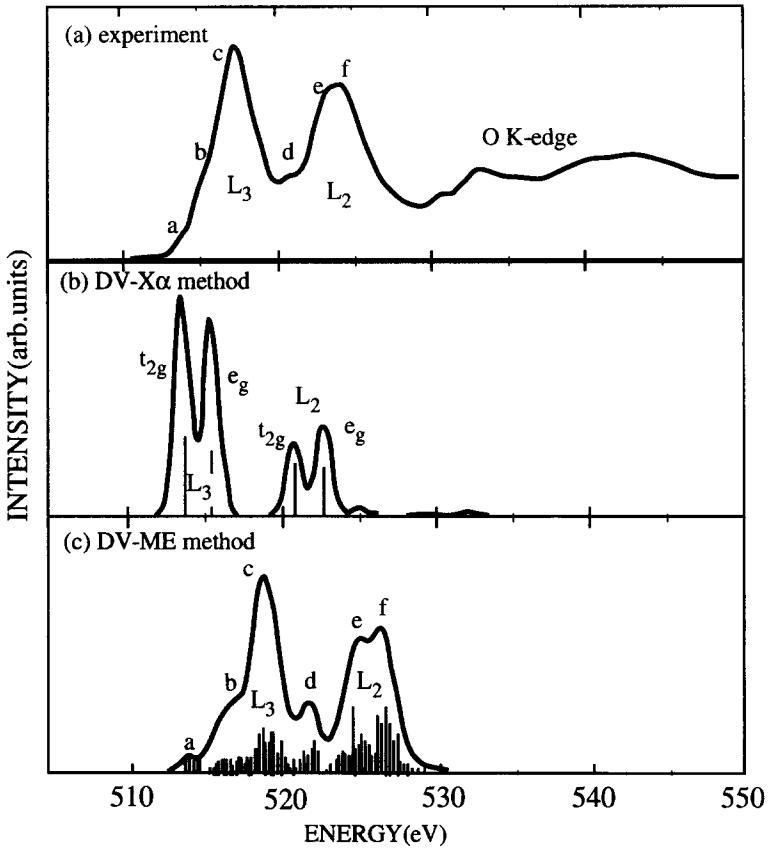

Fig. 5 Comparison of theoretical and experimental V $L_{2,3}$ XANES from V_2O_3 with d^2 configuration

spin-orbit coupling increases with atomic number. This leads the configuration interactions between L_2 and L_3 excitations to be weakened, and then the effect on the intensity ratio between them, namely branching ratio is decreased. In the experimental spectrum[12], peaks a~f are seen, though they are not very clear. The DV-ME calculation provides these peaks as shown in Fig.7(c), but the agreement is not very good. The peak a is largely separated from peak b in the theoretical spectrum calculated by DV-ME method, while it appears as only a shoulder of the L_3 peak in the experimental spectrum. The reason of this discrepancy is not clear at this moment.

For Co $L_{2,3}$ XANES from CoO, the comparison is given in Fig.8, where the

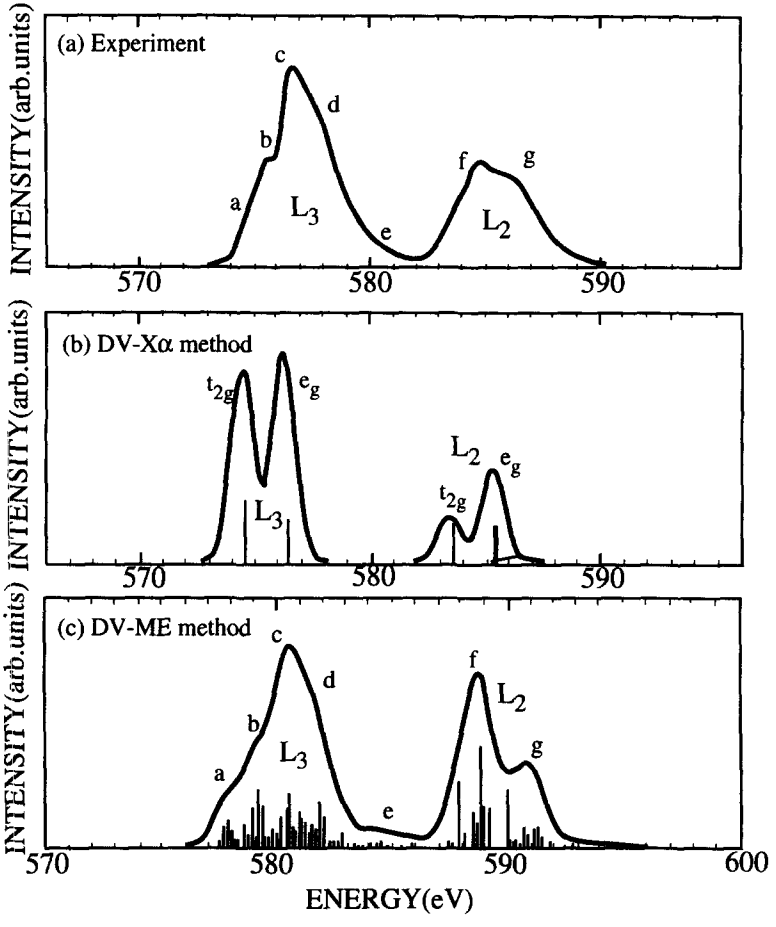

Fig. 6 Comparison of theoretical and experimental Cr $L_{2,3}$ XANES from Cr_2O_3 with d^3 configuration

experimental spectrum[13] is composed of the peaks a~g. The DV-ME calculation provides theoretical spectrum well corresponding with the experiment, though the structure of L_2 peak is not very clear compared with the DV-ME result.

For the theoretical analysis of the 3d transition metal $L_{2,3}$ XANES, the semiempirical calculations has previously been reported by van der Laan et al.[14] They used several empirical parameters of two-electron coulomb and exchange interactions

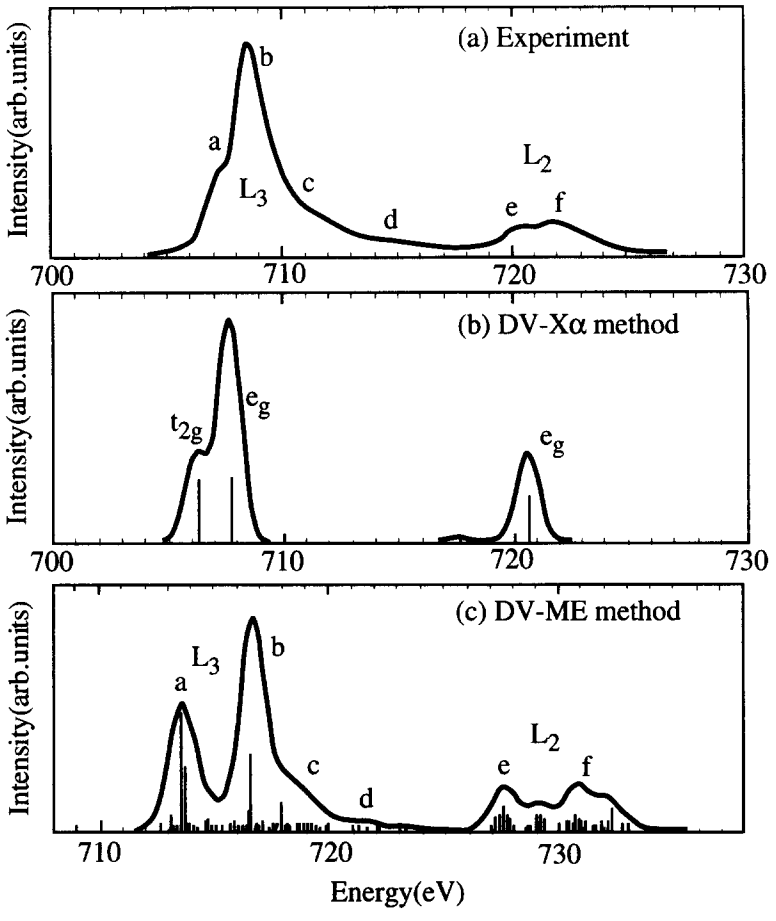

Fig. 7 Comparison of theoretical and experimental Fe $L_{2,3}$ XANES from Fe_2O_3 with d^5 configuration

and spin-orbit interactions as well as crystal field splitting to fit the experiment. On the other hand, DV-ME method does not require any empirical parameter in the calculation, then is also efficient for theoretical prediction of the XANES spectrum from unknown materials. Furthermore, the first-principles calculation reproduces well the fine structure in the spectrum such as a weak peak and a peak shoulder, which are considerably difficult to be provided correctly by the semiempirical method.

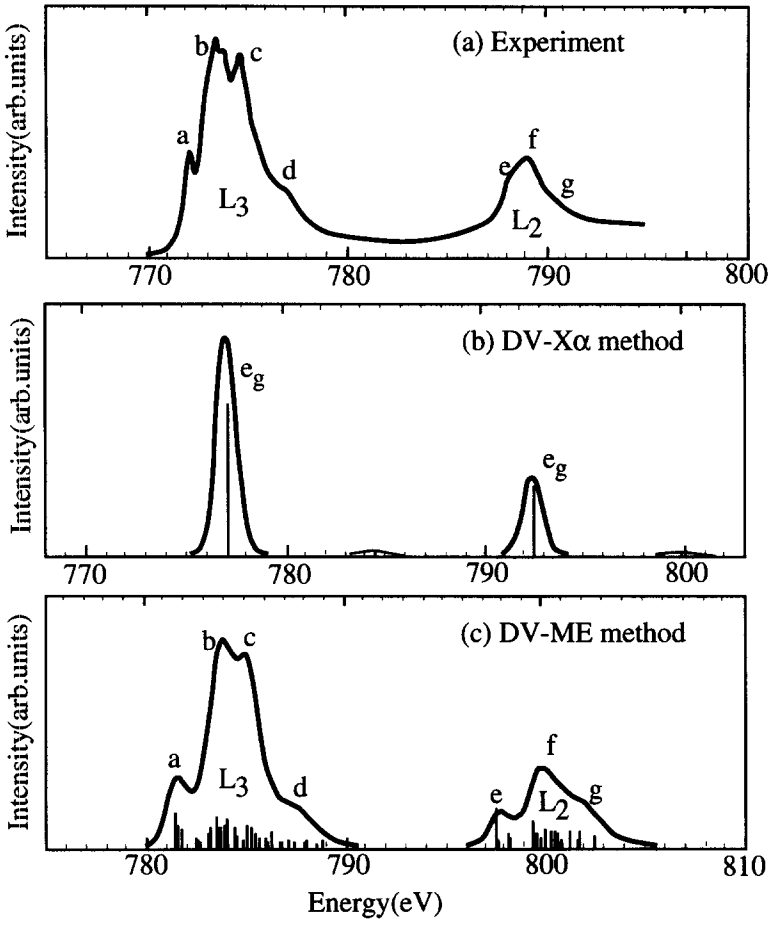

Fig. 8 Comparison of theoretical and experimental Co $L_{2,3}$ XANES from CoO with d^7 configuration

3.3 XANES spectrum from charge-transfer type compound

The valence electronic state of 3d transition metal compound is simply described by the 2p band of ligand X and the transition metal 3d band situated above it as shown in Fig.9. The energy gap between these two bands is decreased with the atomic number and also with oxidation state of the metal element. The energy gap becomes so small that they overlap to some extent, and then the interaction between them becomes very large in some compounds of later transition element with high valence. Among them,

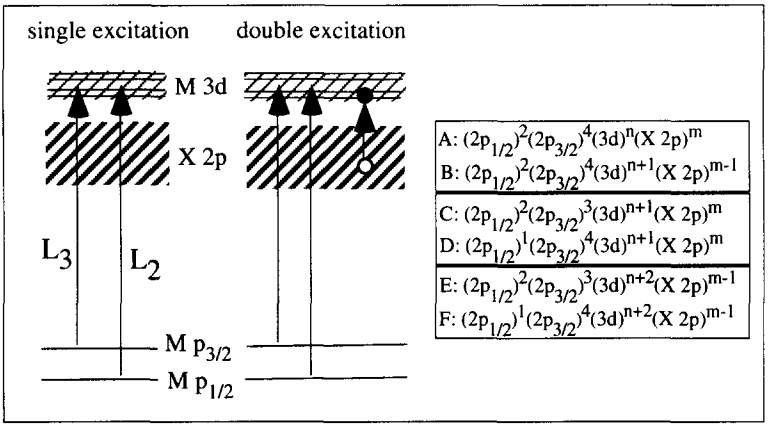

Fig.9 Schematic diagram for level structure of charge-transfer compound and transition process of single and double excitaions. Configurations A and B correspond to ground states, C and D to single excitaions and E and F to double excitations.

there are some compounds, which are called as charge-transfer type compound. In the x-ray and electron spectra of these compounds, the peaks deduced from multiexcitation process are often observed. Then, for the spectral analysis of these compounds, we should consider the multiexcitations, including the transition from valence state of ligand orbitals to metal d band, in addition to the excitation from the core levels to 3d levels. Thus, we should include configurations from these ground states, single excitations and double excitations given in Fig.9 in the DV-ME calculation.

Figure 10 demonstrates the experimental and theoretical spectra of Ni $L_{2,3}$ XANES from NiO. In the experimental spectrum[15], the peaks a~h can be distinguished, though the structure is not very clear. The DV-ME calculation shown in Fig 10(c) gives these peaks except the small peaks d and e. The peak d has been considered to be caused by the charge transfer from O 2p to Ni 3d. For this problem, the semiempirical calculations for various nickel compounds have been made by van der Laan et al.[16] to produce this peak. The first-principles DV-ME calculation including the double excitations given in Fig.9 has been performed to obtain the theoretical spectrum exhibited in Fig.10(d). The result manifests the peak d, while the weak peak e seen in the measured spectrum could not be obtained by this calculation. This can be ascribed to the transition to continuum state[17].

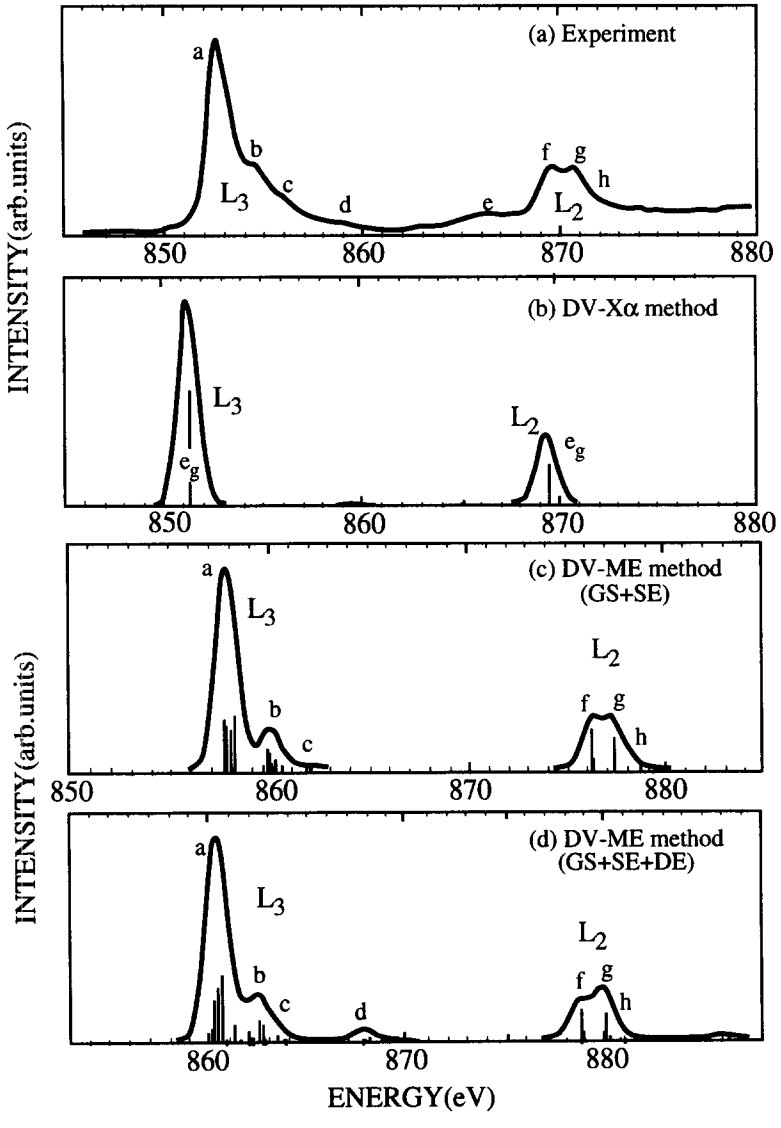

Fig.10 Comparison of theoretical and experimental Ni $L_{2,3}$ XANES from NiO with d^8 configuration.

3.4 Theoretical analysis of f-d transition for lanthanide compounds

In the materials science, the development of optical materials like laser crystal is one of most interesting topics. For such a problem, the theoretical analysis of multiplet

structure is essential. For example, d-d transition for transition metal ion, and f-d transition as well as f-f transition for lanthanide ion in crystal are important. For d-d transition, the ligand-field theory has been successfully applied for various problems since a large quantity of the experimental data is available to provide the empirical parameters for the practical calculation, though this approach is considered to be inadequate for new materials design. The application of DV-ME method to the search of new optical materials containing Cr^{3+}, Cr^{4+} and Cr^{5+} ions have recently been made[5,18,19,20].

Among various electronic transition, d-f transition of lanthanide ion has attracted attention because of a great possibility for ultraviolet laser materials. For f-f transition of lanthanide ions, the extension of atomic structure theory is effective since the 4f orbital of lanthanide is well localized and the chemical effects of ligands is insignificant. However, the 5d orbital of lanthanide is widely spread and the interaction with ligand orbitals is expected to be considerably strong. Therefore, the first-principles calculation should be employed for the f-d transition. We have carried out calculations of relativistic DV-ME method for trivalent lanthanide ions (Ln) such as Ce^{3+}, Pr^{3+} and Nd^{3+} doped in $LiYF_4$ crystal[21,22]. We assume that Ln ion is substituted for Lu ion of eight-fold coordination, then LnF_8^{5-} cluster is mainly used as the model. In the case of Ce^{3+} doped, larger cluster $CeLi_8Y_4F_{48}^{25-}$ is also calculated to examine the long-range interactions with the second and third neighbors. Figure 11 shows the molecular orbital levels calculated by the relativistic DV-Xα method for CeF_8^{5-} with f^1, PrF_8^{5-} with f^2 and NdF_8^{5-} with f^3 configuration. It is seen that the level splittings of Ln 4f by the interactions of ligand orbitals are very small, though the level splittings by spin-orbit coupling are appreciable. On the contrary, the Ln 5d bands are widely spread to imply the strong interactions with ligands. The energy separations between 4f and 5d are several eV, and then the 4f-5d transition corresponds to ultraviolet absorption.

Figure 12 displays the comparison of ultraviolet absorption spectra between theory and experiment for Ln doped $LiYF_4$ crystals. Generally, the agreement between theory and experiment is rather good, while the discrepancy in the absolute energy is not small. The reason has not been clarified yet, though a consideration of the lattice relaxation due to the substitution of absorbing lanthanide ion and extension of basis are possible to reduce the discrepancy. For the case of Ce ion with f^1 configuration, the one-

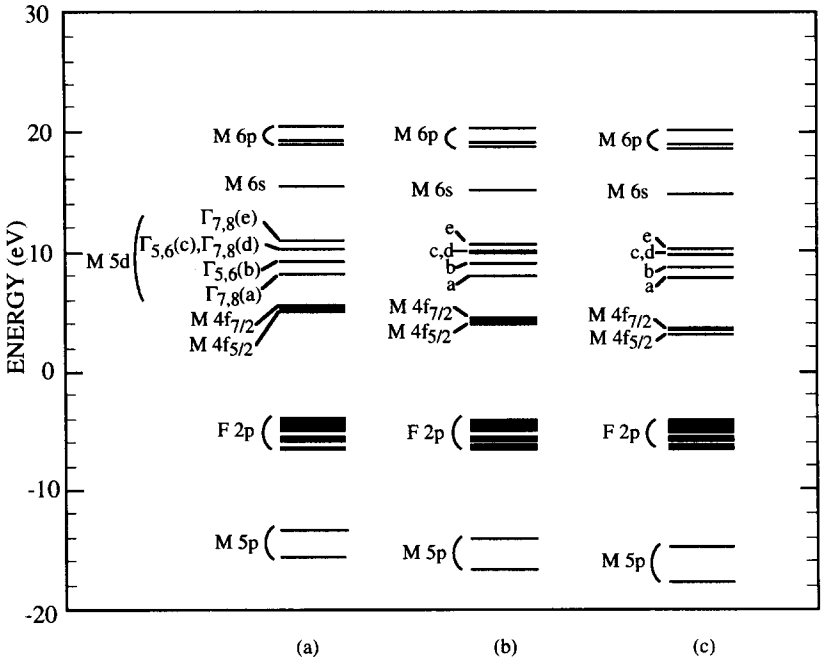

Fig.11 Level structures of LnF_8^{5-} clusters. (a) Ce^{3+}, (b) Pr^{3+} and (c) Nd^{3+}

electron calculation is valid, then the result by DV-Xα calculation for $CeLi_8Y_4F_{48}^{25-}$ cluster is used for the theoretical spectrum. In the theoretical spectrum, the peak E is seen. It is found that the peak E is not caused by Ce 4f-5d transition, but by Ce 4f-Y 4d transition, from the Mulliken population analysis. This peak has not been observed in the experimental absorption spectrum[23], while the excitation spectra recently measured using synchrotron radiation has clearly shown this peak[24].

In the case of Pr^{3+} with f^2 configuration, we employed total 231 Slater determinants, namely, 140 Slater determinants from final state $4f^15d^1$ configuration in addition to 91 Slater determinants from the initial state $4f^2$ configuration. In the initial states, low lying excited state $\Gamma_{3,4}$ above the ground state Γ_2 by only 0.0098 eV exists, then the spectrum from $\Gamma_{3,4}$ is also indicated overlying that from the ground state Γ_2 in the theoretical spectra. From the calculation, we have also obtained the f-f transition at lower energies below 4 eV, but is not shown in the figure. In the theoretical spectra, the weak peaks A_2 and B_2 are indicated. These peaks have been observed in the excitation

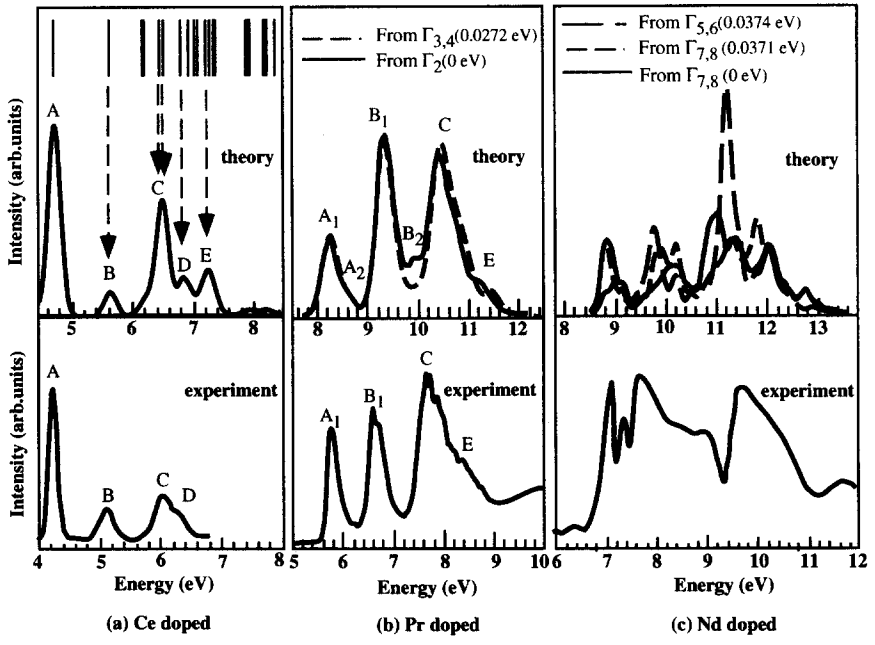

Fig.12 Comparison between theoretical and experimental ultraviolet absorption spectra for Ln ion doped $LiYF_4$ crystals. Upper figures denote theoretical and lower experimental.

spectra[24], though it was not seen in the absorption spectrum shown in Fig.12(b).

For f^3 configuration of Nd^{3+} ion, the agreement between theory and experiment[25] seems not very good. In this case, total 1274 Slater determinants are taken into account in the calculation, containing 364 for intial state f^3 configuration. In the initial states, some excited terms such as $\Gamma_{7,8}$ and $\Gamma_{5,6}$ lie slightly above the ground state $\Gamma_{7,8}$. The calculated spectra from these terms are considerably different from each other and the contributions from these terms to the measured spectrum are considered to be appreciable even at room temperature, then the spectral analysis involves rather complicated problems in this case.

4. Conclusion

In the materials science, accurate and detailed theoretical analysis for various spectroscopies are very important. For such purpose, DV-ME method newly developed

is very powerful and has been applied to some problems such as the 3d transition metal $L_{2,3}$ XANES and the ultraviolet absorption due to the f-d transition of lanthanide ions. In the case of $L_{2,3}$ XANES, theoretical spectra obtained by relativistic DV-ME method generally shows very good agreement with experiment. The importance of configuration interactions has been clarified by demonstrating their effects on the peak intensities. For the charge-transfer type oxide, the satellite peak in XANES has been attributed to the transition from ligand orbitals to metal 3d orbital, by calculation including the double excitation process.

The DV-ME calculation is also effective for analysis of optical absorption spectrum. The ultraviolet absorption spectra from lanthanide doped $LiYF_4$ crystals has been calculated by DV-ME method and compared with the measured spectra. The theoretical spectra show reasonable agreement with the experiments indicating the effectiveness for prediction of the spectrum from unknown materials. In conclusion, DV-ME method can be considered as a very powerful tool in future study of new materials design and development.

Acknowledgement

The author would like to acknowledge Mr.H.Ikeno for his assistance of numerical computations. The present work was supported by a Grant-in-Aid for Science Research on Priority Areas (No.751) from the Ministry of Education, Science, Sports and Culture of Japan.

References

1) H.Adachi, M.Tsukada and C.Satoko, J.Phys.Soc.Jpn **45**(1978) 875
2) CASTEP Program on Cerius 4.2, Molecular Simulations Inc., San Diego, CA
3) P.Blaha, K.Schwarz and J.Luitz, WIEN97, A Full Potential Linearized Augmented Plane Wave Package for Calculating Crystal Properties, Technical University of Vienna, Austria(1999)
4) W.Y.Ching, J.Amer.Ceram.Soc., **73**(1990) 3135
5) K.Ogasawara, T.Ishi, I.Tanaka and H.Adachi, Phys. Rev. **B61**(2000) 143
6) K.Ogasawara, T.Iwata, Y.Koyama, T.Ishii, I.Tanaka and H.Adachi,

Phys.Rev.**B64**(2001) 115413K

7) T.Iwata, Master thesis, School of Engineering, Kyoto University, 2001

8) J.C.Slater,"Quantum Theory of Molecules and Solids", vol.4, McGraw-Hill, 1974

9) H.Adachi, Advances in Quantum Chemistry **37**(2001) 1

10) G.van der Laan, Phys.Rev. **B41**(1990) 41

11) R.Zimmermann, R.Claessen, F.Reinert, P.Steiner and S.Hufner, J.Phys.:Condens.Matter **10**(1998) 5697

12) L.Krivaneka and H.Paterson, Ultramicroscopy **32**(1990) 313

13) F.M.F.de Groot, M.Abbate, J.van Elp, G.A.Sawatzky, Y.J.Ma, C.T.Chen and F.Sette, J.Phys.:Condens.Matter **5**(1993) 2277

14) G.van der Laan and I.W.Kirkman, J. Phys.:Condens. Matter **4**(1992) 4189

15) L.A.Montoro, M.Abbate, E.C.Almeida and J.M.Rosolen, Chem.Phys.Lett. **309**(1990) 14

16) G.van der Laan, J.Zaanen, A.Sawatzky, R.Karnatak and J.M.Esteva, Phys.Rev. **B33**(1986) 4253

17) H.Ikeno, T.Miyamae, K.Ogasawara, I.Tanaka and H.Adachi, in preparation for publication

18) T.Ishii, K.Ogasawara, H.Adachi and I.Tanaka, J.Chem.Phys. **115**(2001) 492

19) T.Ishii, K.Fujimura, K.Ogasawara, H.Adachi and I.Tanaka, J.Phys.Condens.Matter, **13**(2001) 5757

20) T.Ishii, K.Ogasawara, H.Adachi and I.Tanaka, Appl.Phys.letters **78**(2001) 2154

21) K.Fujimura, T.Tohei, T.Ishii, K.Ogasawara, H.Adachi and I.Tanaka, The Fourth International Conference on Advanced Materials and Proceeding(PRICM4), The Japan Institute of Metals,(2001) 583

22) K.Fujimura, Master thesis, School of Engineering, Kyoto University, 2002

23) D.J.Ehrlich, P.F.Moulton and R.M.Osgood Jr, Opt.Lett. **4**(1979) 184

24) M.F.Reid, L.van Pieterson, R.T.Wegh and A.Meijerink, Phys.Rev.**B62**(2000) 14744

25) Z.Kollia, E.Sarantopoulou, A.C.Cefalas, C.A.Nicolaides, A.K.Naumov, V.V.Semashko, R.Y.Abdulsabirov, S.L.Korableva and M.A.Dubinskii, J.Opt.Soc.Am. **B12**(1995) 782

Grain Boundary Plasticity and Failure in Oxide Ceramics at High Temperatures

Taketo Sakuma
Department of Advanced Materials Science, Graduate School of Frontier Science, The University of Tokyo
7-3-1 Hongo, Bunkyo-ku, Tokyo 113-8656, Japan

(Received January 18, 2002; accepted January 30, 2002)

Abstract

High-temperature mechanical properties in materials have long been studied from their macroscopic stress-strain behavior. However, there are limitations in such a macroscopic approach to identify an atomistic process to control the mechanical characteristics. A trial to break through the limitations are introduced in this paper, which demonstrates the importance of the knowledge of atomic bonding state or quantum chemistry.

CONTENTS

1. INTRODUCTION

Plastic flow in materials at high temperatures, typically above about 0.5 of the homologous temperature of T / T_m (T_m the absolute melting temperature), has been analyzed mainly from their stress-stain behavior, in particular, from the relation between stain rate $(\dot{\varepsilon})$ and steady-state flow stress (σ) using a phenomenological constitutive equation as follows,

ADVANCES IN QUANTUM CHEMISTRY, VOLUME 42

0065-3276/03 $35.00

$$\dot{\varepsilon} = A\left(\frac{\sigma^n}{d^p}\right)\exp\left(-\frac{Q}{RT}\right) \quad (1)$$

where A is the material constant, d is the grain size, n and p are the stress and grain size exponents, Q is the activation energy for plastic flow and RT is the gas constant times absolute temperature [1,2]. On the basis of eq. (1), the flow mechanism has been discussed from the three major parameters of stress exponent (inverse strain rate sensitivity), grain size exponent and activation energy. This type of approach is effective to speculate the rate-controlling mechanism and to understand the overall stress-strain behavior, but we have often met difficulties to identify the mechanism because the different phenomenological models sometimes predict a very similar strain rate against flow stress relationship. In addition, this approach is not sufficient to find an atomistic process to control the high-temperature plastic flow. This situation is the same in the cavitation and failure in polycrystalline materials at high temperatures. It is highly requested to establish a more microscopic approach to elucidate high temperature mechanical properties in materials [3]. The present paper aims to show that an analysis from quantum chemistry is one of the useful approaches to describe an grain boundary sliding or intergranular failure in fine-grained ceramics at high temperatures and to break through the limitation of the phenomenological analysis.

2. TENSILE DUCTILITY IN SUPERPLASTIC TZP

Superplastic flow in ceramic materials has extensively been examined since 1986 [4]. A typical ceramic to exhibit a large tensile elongation in excess of about 100% is tetragonal zirconia polycrystal (TZP), which is zirconia base ceramics containing a suitable amount of cubic-stabilizing oxides such as CaO, MgO, Y_2O_3, etc. TZP has a very stable, fine-grained structure, and hence exhibits extensive ductility at high temperatures [5]. The previous data of superplastic TZP were compiled by the Domínguez-Rodríguez group and analyzed using the basic relationship of eq. (1) [6]. According to their analysis, all data can reasonably be described as a single relationship by assuming a threshold stress for plastic flow and the probable values of n=2, p=2 and Q=460 kJ/mol. This conclusion is essentially similar to that deduced for superplastic metals [7]. It has also been clarified that the microstructural requirements for micrograin superplasticity are the same for metals and ceramics [8]. The next step

must be a microscopic analysis to find a physics base of grain boundary sliding and also of the threshold stress.

In contrast, a new approach has recently been made to find an origin of tensile ductility in superplastic ceramics. Formerly, it was pointed that the elongation to failure in superplastic ceramics can be described as a function of the Zener-Hollomon parameter of $\dot{\varepsilon}\exp(Q/RT)$ [9]. Since this parameter corresponds to high-temperature flow stress under a constant grain size, the rule says that the elongation becomes larger with a decrease in flow stress. However, many exceptions have later been found in superplastic ceramics [10-15]. The present author's group reported that the elongation to failure in TZP is very sensitive to the cation's segregation in grain boundaries [16], i.e. the grain boundary chemistry plays a critical role in the tensile elongation.

The most typical result obtained in glass-doped TZP is shown in Fig. 1, which is a comparison of the elongation to failure in five glass-doped TZP at 1400°C and an initial strain rate of 1.3×10^{-4} s^{-1}. The glass content in TZP is 5wt%, and the glass compositions are SiO_2- 2wt% Li_2O, SiO_2- 2wt% MgO, SiO_2- 2wt% Al_2O_3, SiO_2- 2wt% TiO_2 and pure SiO_2 glass [17]. The dopant content is not so large, 2wt% in glass phase which is 1000ppm in each sample, but the elongation is very much affected by the type of doped cation, e.g., the elongation is reduced from 1100% in TZP-5wt%SiO_2 to only 38% in TZP-5wt%(SiO_2-2wt%Li_2O).

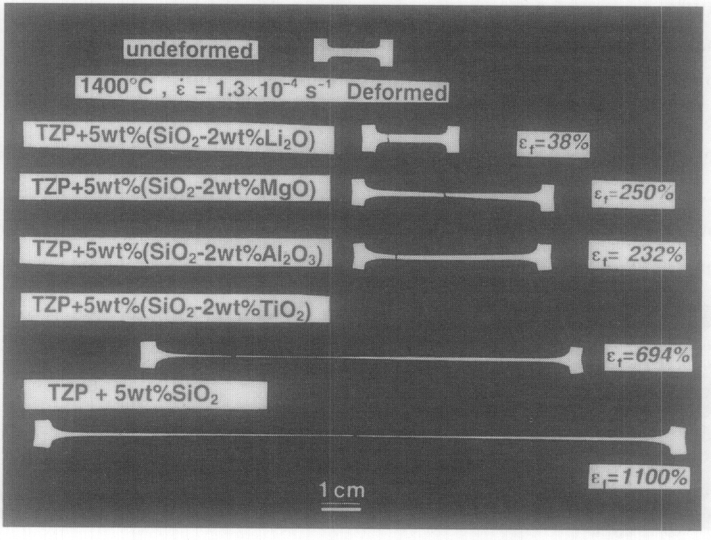

Fig. 1 A comparison of elongation to failure in five glass-doped TZP at 1400°C and an initial strain rate of $1.3\times10^{-4}s^{-1}$ [17].

It is necessary to note that zirconia grains are not wetted by glass phase at conventional sintering temperatures, and that two grain junctions are essentially solid-solid boundaries. The doped cations tend to segregate in the solid-solid grain boundaries, and affect very seriously the tensile elongation [15,16]. One of the striking results obtained in Fig. 1 is such that the valency of doped cation is of a primary importance to determine the tensile elongation. The monovalent Li ion reduces most drastically the elongation while tetravalent Ti ion has a much smaller effect on the reduction in tensile elongation. In ionic crystals, vacancies are introduced to maintain local electrical neutrality by an addition of aliovalent dopant. In zirconia ceramics, oxygen vacancies are formed by an addition of cations whose valency is lower than Zr ions. Since both Zr and Si ions are tetravalent, no vacancies will be introduced by the presence of Ti ions near grain boundaries, if trivalent Ti ions are not generated. In contrast, the doping of Li, Mg or Al ions will result in the generation of oxygen vacancies. The number of vacancies must increase with a doping of lower valency cation for the same dopant content. In other words, Fig.1 demonstrates that the elongation becomes smaller with an increase of oxygen vacancies formed near grain boundaries by the segregation of low valency cations, i.e., with an increment of dangling bond. This is probably the clear evidence showing the importance of local ionic bonding state near grain boundaries on the intergranular failure at high temperatures.

We made a molecular orbital calculation using a DV-Xα method [18] to find a factor to determine the high-temperature intergranular failure and the elongation in TZP. Fig.2 shows the examples of TZP clusters used for our calculation [19], which are based on zirconia crystals with a tetragonal symmetry and not on the grain boundary structure. This is a very preliminary level in the sense of quantum structure analysis in grain boundaries but we can get the useful information to understand the origin of intergranular failure as follows.

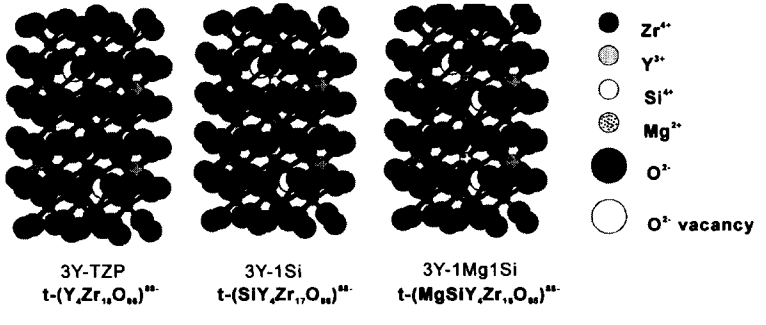

Fig. 2 The clusters for 3Y-TZP and 3Y-TZP with Si and/or Mg ions [19].

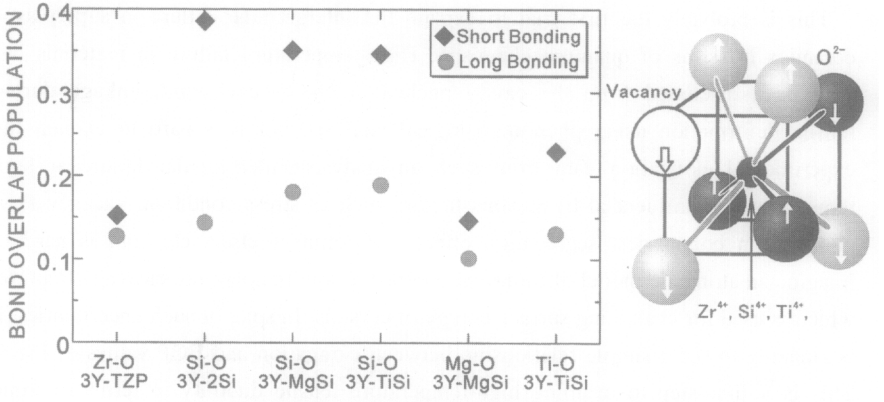

Fig. 3 Calculated BOP between dopant and O^{2-} in each cluster.

Fig.3 shows a plot of bond overlap population (BOP) of several cation-to-oxygen bonds in various clusters estimated by the calculation. There are two types of cation-to-oxygen bonds in tetragonal ZrO_2, the short and long bonds, which are depicted as gray and black bars in Fig.3. The short Si-O bonds have much higher BOP values that other bonds. This fact means that strong covalent bonds will be formed by the segregation of Si ions near grain boundaries. Enhancement of tensile ductility by the segregation of Si ions in grain boundaries may be caused by the generation of strong covalent bonds. In fact, the elongation to failure in various glass doped TZP is correlated well with their BOP values as shown in Fig.4.

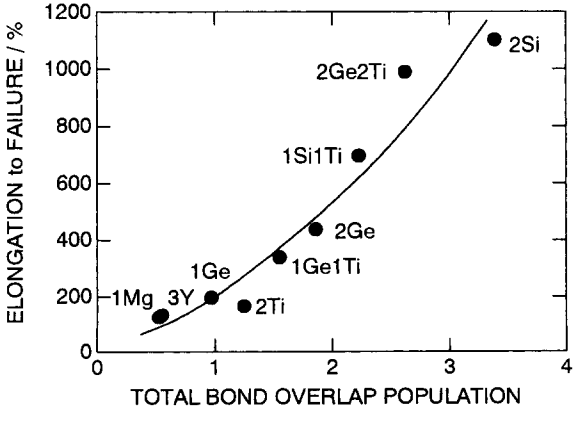

Fig. 4 Elongation to failure in 3Y-TZP and small amount of cation-doped 3Y-TZP at 1400℃ under the initial strain rate of 1.3×10^{-4} s^{-1} against total bond overlap population.

This is probably the first trial to explain the intergranular failure in superplastic ceramics in terms of quantum chemistry. High-temperature failure in materials has long been discussed from the cavity nucleation and/or cavity interlinkage during tensile deformation using phenomenological analysis, but it is hard to explain the experimental elongation data from such an analysis. Intergranular failure at high temperatures is influenced by various factors such as stress condition, vacancy flow along grain boundaries, segregation effect, environment effect etc. and is hard to imagine an atomistic model of failure in contrast to low-temperature cleavage fracture, which is used for evaluating surface energy of crystals. In spite of such uncertainties, it is amazing to see a simple relationship between elongation and BOP values of Fig.4. This is a first step to examine high-temperature tensile ductility in terms of ionic bonding state or quantum chemistry in grain boundaries in oxides. We will have to analyze more carefully the result of Fig.2 to further discuss the intergranular failure from local bonding state.

3. HIGH-TEMPERATURE CREEP IN POLYCRYSTALLINE Al_2O_3

Creep strain rate in high-purity, polycrystalline Al_2O_3 is very sensitive to a small cation doping in a certain high temperature range [20]. Fig.5 is a plot of creep strain against time in polycrystalline Al_2O_3 doped with various trivalent cations at 1250°C and an applied stress of 50MPa [21]. The grain size is controlled to be about 1μm in all materials. The dopant content is only 0.05 mol% in each sample but the creep strain rate is reduced drastically by the doping, in particular, by the addition of

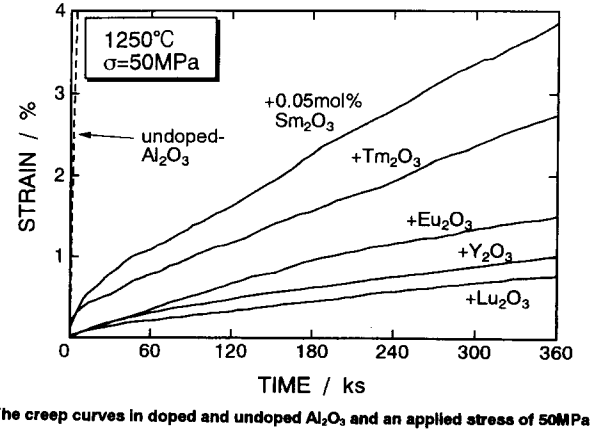

Fig. 5 The creep curves in doped and undoped Al_2O_3 and an applied stress of 50MPa [21].

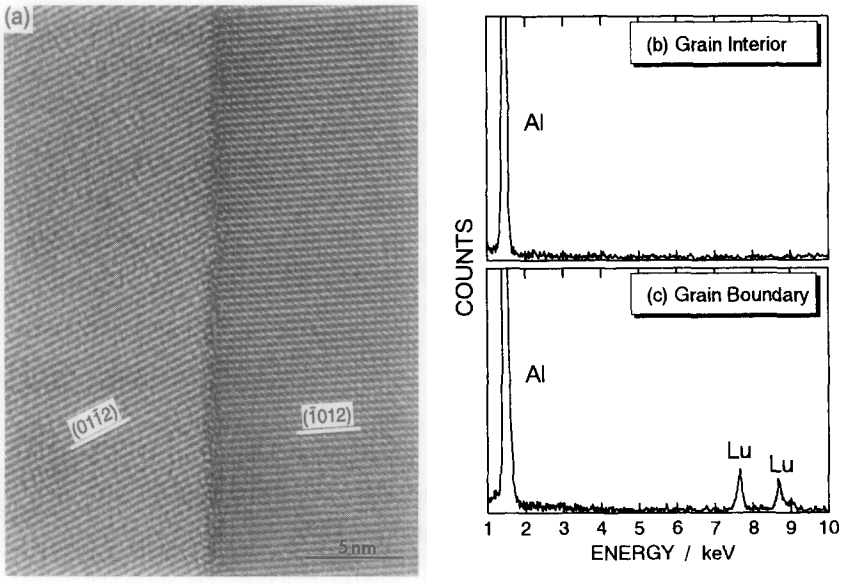

Fig. 6 **HREM image of as-sintered 0.05 mol% Lu_2O_3-doped Al_2O_3 (a), and the EDS spectra taken with a probe size of about 1 nm from (b) the matrix and (c) the grain boundary [25].**

either Y_2O_3 or Lu_2O_3. The steady-state creep rate in Y_2O_3 or Lu_2O_3-doped Al_2O_3 is reduced in a factor of about 200 in comparison with undoped Al_2O_3 at the same testing condition.

According to the phenomenological analysis of the creep strain rate on the basis of eq (1), the stress exponent is about 2, and the activation energy is about 800 kJ/mol in doped Al_2O_3, which is about twice as large as that in undoped one [22]. The activation energy value of doped Al_2O_3 is even larger that the reported activation energy of lattice diffusion of Al^{3+} or O^{2-} ions [23,24]. This behavior appears at temperatures where grain boundary diffusion or sliding plays a key role in creep deformation.

Fig.6 is an electron micrograph in Lu_2O_3-doped Al_2O_3 (a) and the TEM-EDS data obtained from a grain interior (b) and the grain boundary (c) [25]. No second phase is formed is this material, and Lu^{3+} ions are present only in grain boundaries as shown in the spectra of Fig.6. The reduction in creep strain rate with cation doping is caused by its segregation in grain boundaries and probably by the suppression of grain boundary diffusion. To discuss the small dopant effect more clearly, it is necessary to examine the change in ionic bounding state in or near grain boundaries by cation's segregation.

One of the effective ways to detect experimentally the ionic bonding state is to

examine the TEM-EELS spectra as demonstrated in Fig.7, which shows the spectra obtained from grain interior or grain boundary in undoped and Lu_2O_3-doped Al_2O_3 [26]. We examined the O-K edge, Al-L_1 edge and Al-$L_{2,3}$ edge ELNES using FE-TEM with a probe size of 0.7 nm, and found a change in Al-L_1 edge ELNES between the spectra from grain interior and grain boundary in cation-doped Al_2O_3. The grain boundary spectrum of ② in undoped Al_2O_3 is not so different from the spectrum from grain interior of ①, while the grain boundary spectrum in Lu_2O_3-doped Al_2O_3 exhibits a little bit broader profile than the grain interior spectrum, particularly at an energy level of 95-100 eV. The spectra may be not so sensitive to grain boundary structure rather than chemistry. A similar trend can be seen in the EELS data obtained from iron with and without phosphorus, in which the difference in the intensity between matrix and grain boundary is large in a phosphorus-containing iron but is much smaller in phosphorus-free iron [27].

To understand the change in the Al-L_1 edge ELNES with Lu^{3+} ion's segregation in grain boundaries, the molecular orbital calculation was made to evaluate the density of state (DOS) [28]. The DOS obtained for the $[Al_5O_{21}]^{27-}$ and $[Al_2Lu_3O_{21}]^{27-}$ clusters are

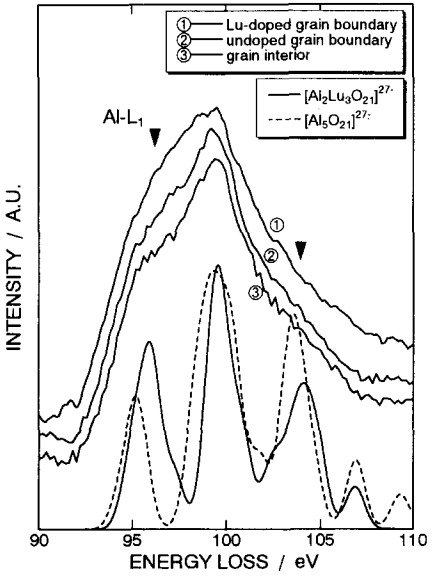

Fig. 7 **Energy loss near edge shape (ELNES) spectrum of Al-L_1 edge taken from Lu^{3+} doped grain boundary, undoped grain boundary and grain interior in Al_2O_3. Calculated unoccupied density of states of conduction band (DOS) for $[Al_5O_{21}]^{27-}$ and $[Al_2Lu_3O_{21}]^{27-}$ clusters are also plotted for comparison [26].**

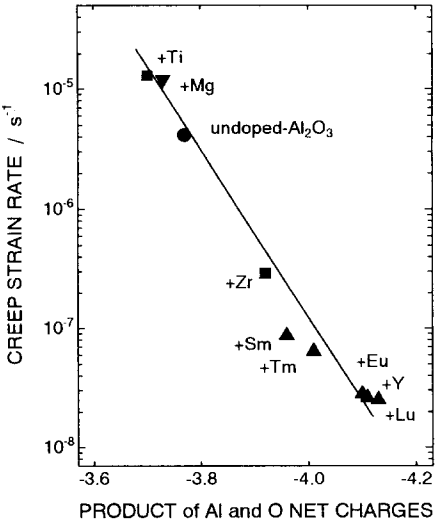

Fig.8 **A plot of the creep strain rate under an applied stress of 50 MPa at 1250℃ against product of Al and O net charges. The creep strain is correlated well with the product of net charges [29].**

shown in Fig. 7. The profile for the $[Al_2Lu_3O_{21}]^{12-}$ cluster predicts a little higher intensity than that for the $[Al_5O_{21}]^{27-}$ cluster at an energy level of 95-100eV. This may correspond to a broadness of the experimental Al-L_1 edge ELNES obtained from the grain boundary in Lu_2O_3-doped Al_2O_3.

A more precise argument can be made from the relationship between observed creep rate and the net charge values estimated from the molecular orbital calculation as shown in Fig. 8 [29]. The produce of Al and O net charges has a better correlation with the experimental creep rate rather than bond overlap population. Fig. 8 shows that the creep rate is reduced with larger negative values of net charges. It is possible to speculate that the net charge values are the parameter to describe grain boundary diffusivity in Al_2O_3 as well as creep strain rate. For instance, MgO is a well-known sintering aid in Al_2O_3 to promote densification during sintering. The enhanced densification is believed to be an acceleration of grain boundary diffusion by the presence of Mg^{2+} ion. It was also pointed out that TiO_2 is effective to promote the densification of Al_2O_3 probably due to the acceleration of grain boundary diffusion [30]. There results correspond to the smaller negative values of the product of net charges in Ti- or Mg-containing clusters rather than pure Al_2O_3 cluster as demonstrated in Fig. 8.

It is not easy to get experimentally grain boundary diffusivity data in Al_2O_3 as well

as in other ceramic materials. If a parameter to describe grain boundary diffusivity in ceramics such as product of net charges is obtained from the molecular orbital calculation, it will be highly useful to find a suitable dopant to design ceramic materials. At present, such a trial is very limited, and the effectiveness of molecular orbital calculation is not firmly established. However, the present author believes that the theoretical calculations will be more popular in the near future to design modern high-performance ceramics.

4. CONCLUDING REMARKS

Grain boundary-related plastic flow or failure in oxide ceramics at high temperatures is often very sensitive to a small doping of cation, which segregates in grain boundaries. This behavior is caused by the change in ionic bonding state in or near grain boundaries with dopant segregation. Two examples discussed in this paper are summarized as follows,

(1) The elongation to failure in superplastic TZP with a glass phase depends sensitively on the segregation of cation in grain boundaries. Especially, the generation of oxygen vacancies, i.e. of dangling bonds, by the segregation of cations in or near grain boundaries deteriorates very much the tensile elongation. In addition, the tensile elongation is correlated well with the values of bond overlap population estimated from a molecular orbital calculation. Intergranular failure in superplastic TZP can be understood from the strength of covalency in grain boundaries.

(2) High-temperature creep strain rate in polycrystalline Al_2O_3 is suppressed very much by a doping of cation in the level of 0.05 mol%. This is caused by its grain boundary segregation, and is likely to result from the suppression of grain boundary diffusion. The net charge values estimated from the molecular orbital calculation are the useful parameter to describe the creep strain rate and grain boundary diffusivity in Al_2O_3.

Acknowledgements

The present author wishes to express the gratitude to the Ministry of Education, Science, Culture Sports, Science and Technology Japan and Japan Society for the Promotion of Science for the financial support by a Grant-in-Aid for Scientific Research (A)(2)-10450254, (2)-12130202 and Grant-in-Aid for Scientific Research on Priority Areas (B)(2)-12130202.

References

1. M.F. Ashby and H.J. Frost, Deformation Mechanism Maps, Pergamon Press (1982).
2. A.K. Mukherjee, J.E. Bird and J.E. Dorn, Trans. ASM, **62** 155 (1969).
3. T. Sakuma, Current Opinion in Solid State & Materials Science, **2** 296 (1997).
4. F. Wakai, S. Sakaguchi and Y. Matsuno, Adv. Ceram. Mater., **1** 259 (1986).
5. Y. Yoshizawa and T. Sakuma, Acta Metall. Mater., **40** 2943 (1992).
6. M. Jimenez-Melendo, A. Dominguez-Rodriguez and A. Bravo-Leon, J. Am. Ceram. Soc. **81** 2761 (1998).
7. T.G. Langdon, Acta Metall. Mater., **42** 2437 (1994).
8. A.K. Mukherjee, Mater. Sci. Tech., Vol. 6, Plastic Deformation and Fracture of Materials, Ed. by H. Mughrabi, Weinheim, VCH p. 407 (1993).
9. W.-J. Kim, J. Wolfensteine and O.D. Sherby, Acta Metall. Mater., **39** 199 (1991).
10. T. Sakuma and Y. Yoshizawa, Mater. Sci. Forum, **170-172** 369 (1994).
11. P.Thavorniti and T. Sakuma, Mater. Sci. Eng., **A202** 249 (1995).
12. K. Tsurui and T. Sakuma, Scripta Mater., **34** 443 (1996).
13. T. Kondo, Y. Takigawa and T. Sakuma, Mater. Sci. Eng., **A231** 163 (1997).
14. T. Kondo, Y. Takigawa, Y. Ikuhara and T. Sakuma, Mater. Trans. JIM, **39** 1108 (1998).
15. P. Thavorniti, Y. Ikuhara and T. Sakuma, J. Am. Ceram. Soc., **81** 2927 (1998).
16. Y. Ikuhara, P. Thavorniti and T. Sakuma, Acta Mater., **45** 5275 (1997).
17. T. Sakuma, Y. Ikuhara, T. Yamamoto and H. Yoshida, to be published.
18. H. Adachi, M. Tsukada and C. Satoko, J. Phys. Soc. Jpn., **45** 875 (1978).
19. A. Kuwabara, S. Yokota, Y. Ikuhara and T. Sakuma, Mater. Sci. Forum, **357-359** 399 (2001).
20. H. Yoshida, Y. Ikuhara and T. Sakuma, Phil. Mag. Lett., **76** 9 (1997).
21. H. Yoshida, Y. Ikuhara and T. Sakuma, Phil. Mag. Lett., **79** 249 (1999).
22. H. Yoshida, Y. Ikuhara and T. Sakuma, J. Mater. Res., **13** 2597 (1998).
23. M.L. Gall, B. Lesage and J. Bernardini, Phil. Mag., **A70** 761 (1994).
24. D. Prot and C. Monty, Phil. Mag., **A73** 899 (1996).
25. H. Yoshida, Y. Ikuhara and T. Sakuma, J. Inorg. Mater., **1** 229 (1999).
26. Y. Ikuhara, H. Yoshida and T. Sakuma, Mater. Sci. Eng., **A319-321** 24 (2001).
27. D. Ozkaya, J. Yuan, L.M. Brown and P.E. Flewitt, J. Microscopy, **180** 300 (1995).
28. I. Tanaka, J. Kawai and H. Adachi, Solid State Commun. **93** 533 (1995).
29. H. Yoshida, Y. Ikuhara and T. Sakuma, Phil. Mag., in press.
30. J.D. Powers and A.M. Glaeser, J. Am. Ceram. Soc., **76** 2225 (1993).

TOWARD STRUCTURE-FUNCTION RELATIONS - A HYBRID QUANTUM/CLASSICAL APPROACH

D. E. Ellis, O. Warschkow

Dept. of Physics & Astronomy
and
Institute of Environmental Catalysis
Northwestern University, Evanston IL 60208
(Received February 26 2002; in final form 26 June 2002)

Abstract

The calculation of electronic structure of materials by first principles quantum methods is now essentially routine, thanks to development of Density Functional approaches. However, the electronic structure depends in detail upon the nuclear positions, which are not generally known in advance. The prediction and verification of atomic positions- the geometrical configuration- of a complex molecule like a protein, or of a chemically reactive surface, or of a doped solid interface, for example, begins to yield to atomistic simulations based upon classical or semiclassical force-fields. A significant remaining problem is to couple together quantum and classical methodologies on several length- and time-scales which would be capable of carrying information forward into the continuum regime of materials modelling. We describe a particular approach to the so-called multiscale modelling problem spanning the range 1 -1000 _ and 1 - 10^7 femtosec and its intended applications to predicting structure-function relationships required for materials analysis and design. Principles are illustrated by three examples: an isolated protein, a defective oxide surface, and a bioceramic analog.

CONTENTS

ADVANCES IN QUANTUM CHEMISTRY, VOLUME 42

0065-3276/03 $35.00

I. Introduction

One of the great dreams and principal goals of materials theorists has been to develop the science of computation and the art of modeling to a point where the relationships between structure and function are made evident. To make clear the scope and meaning of the words 'structure' and 'function' used here, we may cite some examples such as

(1)the combined selectivity and reactivity of a catalytically active surface, operating in the automotive exhaust stream

(2)the ability of a macromolecule to 'chaperone' a metal ion on its journey through blood and cells to the target site

(3)the time- , field-, and temperature- dependent response of multilayer composites found in electronic and optical computing and communications components.

Frequently we have seen visionary statements about 'materials by design', 'rational design of drugs', and have heard calls for Great Leaps Forward based upon a combination of ultrahigh spatial- and time- resolution experimental techniques and advances in theoretical modeling. This optimism is probably well founded; however, a considerable amount of work has to be done before the components of such a marvelous mechanism work well together. This article to dedicated to the examination of some steps being taken toward the 'small' end of the relevant scales- namely, the range 1 -1000 _ and 1 - 10^7 femtosec. This is the area where interatomic interactions demand a first-principles quantum mechanical description, with consequences for microscopic dynamics which underly all coarser scale simulations.

We begin by describing developments in Density Functional (DF) theory [1-5] which have made it possible to expand the range of electronic structure analyses from that of moderate size (N < 100 atoms) molecules and periodic solids to that of macromolecules and defected/interfaced solids with thousands of atoms.[6-10] The reader will have noticed that the 'typical examples' cited above all involve finite times 't' and temperatures 'T'; thus, t and T are key variables. This implies that the standard static quantum chemical methodologies with T=0 have to be bridged somehow into the realm of dynamics. One successful approach makes use of atomistic simulations in which classical interatomic potentials are coupled to or partially derived from static quantum models. We take up this theme in Sec. III, sketching in some details of one of the many viable implementations of so-called QM/MM (Quantum Mechanics / Molecular Mechanics) schemes[11-15]. Even though the basic ideas and algorithms are extremely simple, they already permit extraction of thermodynamic properties, diffusion rates, and micro-mechanical properties which can be compared with suitably constructed

experiments. In addition, the MM schemes provide a natural bridge to the still-larger scales of modeling of macroscopic structures which may be based upon time- and space-adaptive finite element methodologies[16-20].

A second approach which shows great promise is so-called 'First Principles Molecular Dynamics', in which a time dependent Schrödinger equation is used in the framework of DF theory to couple electronic and nuclear motion. The best known example of this methodology is that of Parinello and Car, in which an effective mass is assigned to the electron to bring electronic and nuclear time scales closer together[21,22]. Successful applications have been reported for molecules, liquids, solids, and reconstructed surfaces[23-26]. One particularly nice recent example traces the dynamics of NO attached to the heme group of nitroxyhemoglobin, revealing some details of the complex energy surface and coupling between admolecule rotations and subtrate flexure[25]. The implementation of First Principles MD is generally dependent upon development of a plane-wave based pseudopotential (PP), permitting rapid computation per unit time step. The viability of the PP approach has been well demonstrated; however, it is not a panacea and would in fact require very heavy computational resources for the systems which we are typically studying.

A third promising methodology deserves mention- that is Tight Binding Molecular Dynamics, which has a mixture of first-principles and semiempirical character. Tight Binding (TB) schemes have a long and illustrious history in electronic structure theory, based initially upon the ideas of Linear Combination of Atomic Orbitals (LCAO) expansions in a minimal basis. Slater and Koster popularized TB-LCAO as a compact method for fitting first-principles band structures and adapting empirical band structures to experimental data[27]. On a more fundamental level, the fact that the Hermitian Hamiltonian matrix can be reduced to tridiagonal form leads to the idea of an optimal localized basis set with interaction of limited range. The resulting introduction and use of partial fraction expansions for quantities such as partial densities of states made the method both flexible and powerful[28,29]. More recently it was realized that with parametrized TB matrix elements representing electronic structure, time dependent problems could be solved for systems with thousands or millions of atoms with reasonable computation time[30,31]. Some very nice recent examples include relations between magnetism and local order[32] and manifold thermo-mechanical properties of porous, amorphous, liquid, and solid Si[33-36].

In the following Sections we briefly discuss some recent applications which illustrate the principles and practices advocated here. In treating a 'simple' protein we explore the power of linear, or 'Order(N)' , DF approaches which break a large system into multiple interacting fragments. We emphasize the need to develop feasible response functions such as the density derivatives $d\rho/dN$ as a tool in

rapidly and semiautomatically screening molecular properties. Our second example concerns the role of defects in transport and chemical properties of an Fe_2O_3 hematite surface. Here the interplay between first-principles DF analysis of electronic density and atomistic simulations is made evident, and a certain degree of internal consistency can be demonstrated. The final case study, that of metal substitutions in the bone-analog hydroxyapatite, is chosen to indicate one of the favorable directions for development of viable methodologies for describing and designing biomaterials.

II. Embedded Clusters and Order (N) Density Functional Methodology

Density Functional theory provides a comprehensive first-principles quantum mechanical approach to the electron density and derived properties. In its most common form, a self-consistent procedure is developed which ultimately determines the ground state charge and spin densities, through solution of the single particle Kohn-Sham equations[37,38]. In practice, the resulting one-electron wavefunctions and eigenvalues have been extensively used to interpret both ground state and excited state properties. Rigorous prescriptions for the treatment of excitations have now appeared, and this remains an active area of development
[39-43].

While the formal content of DF theory continues to evolve, an equally important and concurrent development of practical computational algorithms can be observed. We focus here on the utility of Embedded Cluster (EC) approaches, and their use in realizing algorithms showing essentially linear growth in computational effort with system size. Here N can be taken either as the number of electrons or as the number of atoms to be considered. There are a considerable number of ways to decompose a multi-atomic system to achieve order(N) analysis times, dating back to the earliest days of computational physics and chemistry[44-46]. For example, the idea of partitioning the Hamiltonian matrix, given in a basis of atomic orbitals, appeals to basic ideas of chemical bonding and the limited range of interatomic interactions. Placing the resulting coupled equations in the language of Green's functions leads naturally to the concepts of embedding fields and accompanying boundary conditions, all of which can be subjected to reasonable approximations. In an embedded cluster approach one chooses a finite localized fragment of the larger system, and solves the DF problem self-consistently in the density-dependent potential and boundary conditions derived from the host[47-50]. By moving around the 'window' which defines the local cluster, one obtains a sequence of views of the system, which can be patched together to represent the whole. The so-called Divide & Conquer (DAC) scheme

places these ideas on a rigorous footing, and through the mechanism of a common Fermi energy (chemical potential) provides a key for establishing equilibrium among the various clusters[6-10]. The electronic density of each cluster 'k' is determined by Fermi-Dirac statistics as

$$\rho_k(\mathbf{r}) = \sum n_{ik} |\psi_{ik}|^2 \qquad (1)$$

with occupation numbers 'n' and single particle wavefunctions 'ψ' determined by the global self-consistent potential. The interior region of each cluster is projected onto an atomic-like density representation, which is used to synthesize the global density, and from it, the potential.

The rest is 'mere detail', but nonetheless important for obtaining quantitatively useful models of interesting molecular and solid systems. We now sketch out a few more details of implementation of the Embedded Cluster Density Functional (ECDF) scheme and its performance. Given an entity like a protein, the first step is to decompose the atom set into chemically meaningful and overlapping fragments. The interior region of each fragment will be used to extract electronic structure parameters for propagation onto chemically equivalent regions; the overlap of fragments provides a 'buffer zone' of atoms which participate in the quantum mechanical solutions for each cluster but have a less accurate representation than the interior. A measure of convergence can be obtained by generating a series of models, in which the fragments are defined as groups of atoms lying within successively larger radii R_B , and comparing output properties such as partial densities of states.

Basis functions are chosen in order to generate variational solutions of the DF single particle equations; these functions may be analytical (Gaussian, Slater-exponential, polynomial) or purely numerical solutions for atoms in a potential well. Matrix elements of the Hamiltonian and Overlap operators are calculated numerically to the desired order of precision, using a mixture of atom-centered Gauss-quadrature and random sampling strategies. Standard secular matrix equation solvers are used to find single-particle energy eigenvalues and eigenvectors for every fragment. At each stage of self-consistent iterations the total charge and spin densities are assembled from the designated interior atoms, and used to generate the Coulomb and exchange and correlation potentials needed by each cluster in the following step. The assembly process is typically mediated by either using analytical Mulliken population analysis of eigenvectors, or by a least-squares fit to the fragment densities. When every cluster has its potential and density converged to the desired criterion, iterations are halted and property analysis begins.

How is order(N) behavior of computation time achieved? As is well known, standard matrix diagonalization procedures such as are applied to a cluster of size M (measured by number of basis functions, ~ number of atoms) have a M^3

characteristic resolution time. There are furthermore terms linear in M (generation of functions) and quadratric in M (assembly of potentials and matrices), so that time required for a single cluster behaves like $t_M = (a_1 M^1 + a_2 M^2 + a_3 M^3)$ with prefactors a_i that can turn out to be quite important. If the number of fragments is P= N/M, the computational time will be roughly P t_M ; i.e., linear in N, and strongly dependent upon strategies for minimizing the typical fragment size M and efficiently passing data between parallel solutions of the fragment. Experience shows that this is indeed obtainable, even with the use of rather simple algorithms on loosely coupled multiprocessor networks.

Although we emphasize here the use of atomistic simulations as a 'search engine' for finding minimum- energy structures and mapping portions of the potential energy surface, the ECDF scheme can also be used for this purpose. This is most effective when a rather small (< 20) number of free structural parameters are to be varied, and we use atomic force algorithms already well-developed and tested for free molecules[51-53]. A few special precautions have to be taken to distinguish and utilize forces on well-described interior atoms, as opposed to those sensed by the overlapping buffer atoms.

III. Atomistic Simulations and Interatomic Potentials

Simulation methods using classical equations of motion have turned out to be highly effective in addressing questions of dynamics and thermodynamics[54-61]. While fundamental electronic processes may occur in the femtosec (10^{-15} s) range, molecular vibrations are typically three orders of magnitude slower. The picosec (10^{-12} s) range sets the time scale for atomistic simulations and molecular mechanics (MM) in general. The good news is that simple interatomic potentials can be found which adequately reproduce observed geometrical configurations, can be used to search for equilibrium structures, and are useful in describing transport and energy transfer over short time intervals[58-60]. The bad news is that with today's computers and straightforward algorithms, the available simulation time for a significant macromolecular or solid system is of the order of 10-100 nsec. This is far less than required for study of diffusion processes and kinetics of many important reactions. Clever schemes have been developed to treat special problems, such as searching for the transition-state barrier height and position along a reaction path. MM methods in general involve solution of Newton's force-momentum equations

$$\mathbf{dp}_i/dt = -\mathbf{grad}_i(U) \qquad (2)$$

with discrete time-steps of the order of femtosec, with some kind of 'thermostat' to control the sample temperature[43]. In the end, it becomes necessary to move to a coarser-grained model of the structure, which can in turn merge into finite-

element and continuum modeling.

It is appropriate to mention here the important role played by stochastic sampling or Monte Carlo (MC) procedures, which do not explicitly involve the time variable. MC and Generalized Simulated Annealing (GSA) schemes with a variable effective temperature T are found to be highly efficient at surveying large regions of configuration space, which may have numerous local energy minima[62-65]. The key step in MC/GSA sampling is the generation of sequential random states of the system, with a selected probability distribution

$$P(X_1, X_2,...X_N)= G(E,T) \quad (3)$$

where 'G' may represent Maxwell-Boltzmann statistics, or a more sophisticated rule optimized for the specific system. Sequential or cyclic application of MC/GSA and MM techniques based upon a given interatomic potential proves to be very effective in mapping regions of the energy surface, which is in turn critical for understanding dynamics.

In the present context we are most interested in the overlap and feedback between quantum mechanics (e.g.,as represented by the ECDF scheme) and atomistic simulations. Consider the following scheme:

(1)Generate a simple interatomic potential with parameters (U_1, U_2,...U_M) optimized to fit some observed data- say lattice parameters, bond lengths, cohesive energy, and dielectric and elastic constants of a bulk crystal.

(2) Create an (hkl) surface by cleavage of the ideal crystal, and 'decorate' with defects such as vacancies. Using the bulk-derived potential and MM, relax the surface structure to obtain coordinates (X_1, X_2, ...X_L).

(3) Using the derived geometry, carry out DF analyses of surface and bulk regions. Extract charge densities, local atomic charges, bond orders, binding energies and spectroscopic profiles.

(4) Compare computed electronic properties with available data, and with theoretical data bases on related systems. Use these comparisons to improve the potential parameters (U_1, U_2,...U_M) and repeat steps 2-4 until convergence in potential is achieved.

(5) Use the optimized potential in simulations to predict diffusion and reactivity of the surface with incoming molecules, over the computationally available time interval.Pass this information on to the next coarser level of simulation, and back to DF procedures dedicated to description of the electronic structure associated with basic processes (adsorption, dissociation, recombination) of surface-molecule
reactions.

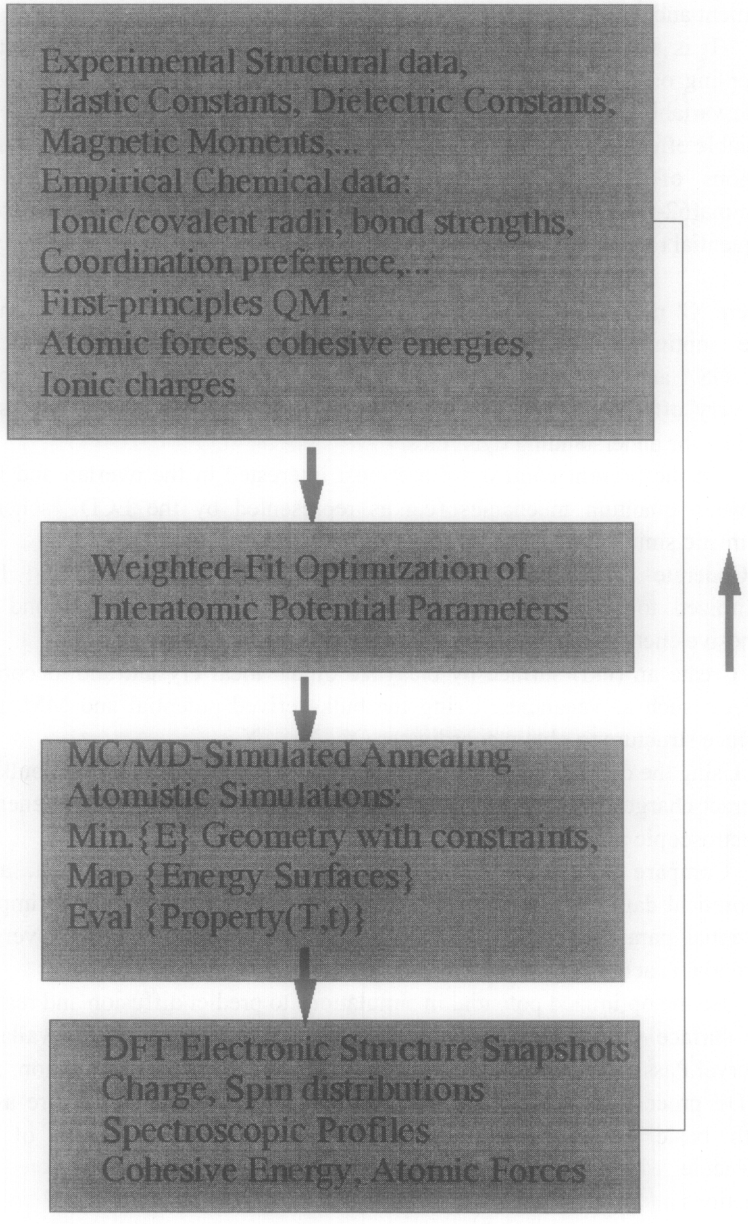

Fig.1. Schematic of Data Flow and Interface Between Quantum Mechanical, Atomistic Simulation, and Experimental Components.

In favorable cases, where there are few degrees of freedom the DF/classical interface can be organized to directly recover an effective interatomic potential[66-68]. In our first example, we consider the case where adequate atomic structural data are available, and first-principles DF calculations can be effectively used to seek properties that can be fed back into atomistic models. The number of degrees of freedom is , however, too great to permit direct 'inversion' to obtain potential parameters. In addition we consider the value of projection techniques on electrostatic potential and charge distributions as a rapid-scan means of surveying interesting portions of the extended system. The second and third examples represent cases in which there exist some data (e.g., ideal bulk, impurity-free crystal) suitable for initial potential generation, but in which atomistic simulations play an essential role in determining local structures whose electronic properties are to be analyzed.

IV. Example 1: Electronic Structure of Two Simple Proteins

With accomplishment of the first mapping of the human genome and that of numerous microorganisms, attention has already turned to the 'grand challenge' of understanding protein structure- proteomics is a new catchword[69]. In the recent past a great deal of attention has been given to the so-called 'protein folding' problem, which is in principle amenable to large scale MM and MC searchs using empirical potentials[70,71]. The relatively long time scales (msec or more) and numerous local minima on the potential energy surface make this a far from trivial problem. How does a protein determine its conformation, and how is it affected by the environment? From the electronic structure perspective, proteins offer a rich field of study due to their key role in cell regulation and metabolism. Seen from a distance, a protein appears as a macromolecule with characteristic shape, and ionic and electronic affinities associated with both local and global conformation. Theoretical techniques developed for analysis of surfaces and interfaces can be adapated for the study of 'superficial' protein properties. Due to the generally low symmetry, we expect to make topographical surveys of properties, focusing upon regions which show especially interesting reactivity or shape-function relations. The response of the protein to external fields and to the addition/ subtraction of charge can be visualized on a supra-atomic scale by mapping changes in properties. In particular the changes $(d\rho/dN)_+$ and $(d\rho/dN)_-$ associated with electron transfer from/to the molecule can be associated directly with the chemical concepts of soft-soft interactions, which are complementary to the soft-hard interactions characteristic of the Coulomb field[72]. Density response analysis has been further emphasized by Fukui and others as a powerful way to estimate reactive regions within/on the macromolecular framework [73,74].

The scheme used to break up a given protein structure into DAC fragments of 'buffer radius' R_B is as follows: Each carbon atom is described in a separate DAC fragment. N, O and S atoms are described in the same fragment as the nearest carbon atom, and lastly, hydrogen atoms are described in the same fragment as the nearest non-H atoms. This partition scheme is appealing. since it has the tendency to keep functional groups (like _COOH, $-NH_2$, $-CONH_2$ or the peptide bridge _CONH-) together in the same fragment. Since our calculations did not employ a solvent model it was necessary to "de-ionize" the protein side chains; i.e., all carboxylate anions ($-COO^-$) and ammonium cations ($-NH_3^+$) were changed to neutral carboxylic acids and amino groups, respectively. Similarly, other, formally charged protein residues were converted into their neutral acid/base counterparts.

All calculations in this work - be they of the divide-and-conquer or the traditional (single fragment) Kohn-Sham variety - were performed in the framework of the discrete variational (DV) method of solving the DF equations using our own DV, and DACDV codes [10,75]. Specifically, molecular orbitals were expanded in LCAO fashion in terms of a valence double numerical orbital basis set, all molecular integrals were evaluated over a numerical grid, the Coulomb problem was solved by using a "model" -density, least-squares fitted to the eigenvector-derived density of each SCF cycle and expressed in terms of an auxiliary "fit-function" basis set. A simple well-known exhange and correlation potential was employed [76].

We first consider a synthetic deca-peptide, stored in the Brookhaven Protein Data Base under the entry 1TOR [77,78], consisting of 153 atoms in 10 residues. It is thus small enough that the effects of DAC buffer radius R_B on various properties can be studied and also directly compared with the results of full (i.e., non-divide-and-conquer) DF calculations. This comparison allows an assessment of the accuracy of the method. The reactive properties we will be looking at in particular are: Partial atomic charges and densities of states (DOS) as well as Fukui-type differentials of these with respect to change of the total number of electrons in the system. Calculations on this protein where performed using DAC buffer radii R_B = 6.0, 7.5, 9.0 and 10.0 au, which results in these fragments containing in addition to the reference atoms, an average of 30-50 buffer atoms. These DAC calculations are then compared in Table 1 with the results of a traditionally performed "all-in-one" calculation which in every respect represents the DAC $R_B \rightarrow \infty$ limit.

		$R_B = 6.0\ a_0$	$R_B = 7.5\ a_0$	$R_B = 9.0\ a_0$	$R_B = 10.0\ a_0$	$R_B \rightarrow \infty$
Avg. Number of Fragment Atoms		16	25	37	46	153
$-CONH_2$	C	+0.597	+0.571	+0.587	+0.582	+0.603
	O	-0.447	-0.444	-0.458	-0.451	-0.449
	N	-0.776	-0.779	-0.778	-0.777	-0.780
	H	+0.384	+0.386	+0.388	+0.388	+0.391
	H	+0.354	+0.351	+0.357	+0.357	+0.358
$-NH_2$	N	-0.793	-0.794	-0.801	-0.799	-0.801
	H	+0.322	+0.332	+0.333	+0.335	+0.335
	H	+0.338	+0.332	+0.325	+0.326	+0.327
Standard Deviation w.r.t. $R_B \rightarrow \infty$		+0.022	+0.010	+0.007	+0.003	--

Table 1: Comparison of Mulliken partial atomic charges calculated for the 1TOR protein using four O(N)-scaling DAC models of increasing buffer size R_B with those obtained using a traditional, $O(N^3)$-scaling single-fragment calculation , denoted here as $R_B \rightarrow \infty$.

The calculated Mulliken partial atomic charges Q_A , as well as their standard-deviations, show convergence with increasing fragment size, toward the single-fragment reference model. A more detailed verification is obtained by examining the potential field throughout the molecule, as synthesized from its component fragments, as shown in Fig. 2.

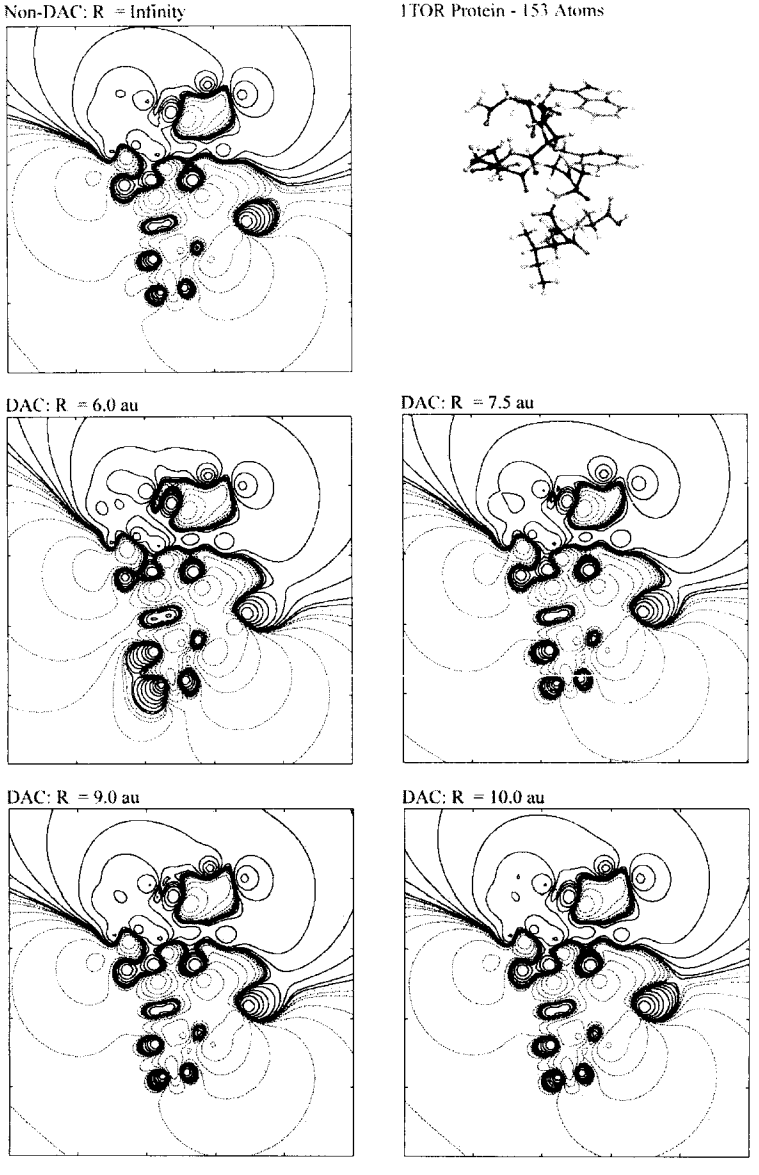

Fig. 2. Equal-interval contours of electrostatic potential in a plane through the center of mass for the 1TOR protein, with varying DAC fragment size.

Figure 3 shows the same convergence effect for the calculated total density of states (TDOS). This convergence is also observed locally as is evident in the local density of states (LDOS) for the -$CONH_2$ functional group of the single asparagine residue which is displayed in the same figure.

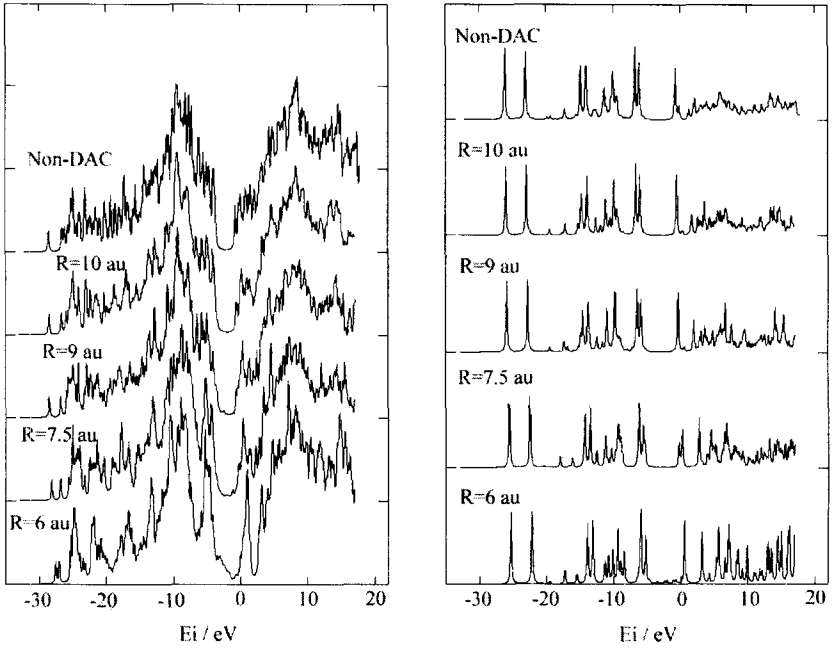

Fig. 3. Electronic (a) total and (b) partial (-$CONH_2$) densities of states for the 1TOR protein, with varying DAC fragment size. The zero of energy is the Fermi level.

Let us now explore how these models perform with respect to response properties, in particular those which measure changes in the electronic structure upon removal or addition of electrons to the system. We will be looking for small changes in the electronic structure and the question is whether these changes will still be visible within the errors associated with the DAC fragment truncation. Here, we answer the question empirically using the 1TOR protein as a test case. Table 2 lists atomic Fukui indices f(-), approximated here as the difference $Q_A(+1)$-$Q_A(0)$ of Mulliken charges Q_A obtained in two calculations on the neutral and single positively charged protein.

Site	Group	R_B = 6.0 a_0	R_B = 7.5 a_0	R_B = 9.0 a_0	R_B = 10.0 a_0	$R_B \rightarrow \infty$
N13	$-NH_2$	0.008 (57)	0.030 (5)	0.038 (3)	0.049 (2)	0.066 (1)
O13	-CONH-	0.024 (4)	0.034 (4)	0.037 (4)	0.040 (5)	0.058 (2)
O12	-CONH-	0.034 (1)	0.038 (2)	0.043 (2)	0.049 (3)	0.057 (3)
O11	-CONH-	0.021 (8)	0.037 (3)	0.033 (5)	0.048 (4)	0.043 (4)
C5	Trp-Aromatic	0.034 (2)	0.062 (1)	0.072 (1)	0.058 (1)	0.043 (5)

Table 2: Comparison of selected Fukui indices $f(-)^-$ calculated for selected sites of the 1TOR protein using four O(N)-scaling DAC models of increasing buffer size R_B with those obtained using a traditional, $O(N^3)$-scaling single-fragment calculation (denoted here as $R_B \rightarrow \infty$) . Listed are those 5 sites that show the largest response in the 'exact' single-fragment calculation; the rank of the response is given in parentheses.

The agreement of these indices in comparison to those obtained by the non-DAC calculation is numerically not very impressive, which can be attributed in part to the fact that the magnitude of the calculated indices is not much larger than the error in the charges from which they are calculated (Table 1). Yet, as can be seen from the ranking given with the indices, all but the smallest model (R_B=6.0 a_0) manage to correctly predict which are the five sites of largest index and hence largest predicted reactivity; even the smallest model identifies four of the five correctly. In this way, we arrive at some measure of the size of fragment needed to extract a particular type of information and the data illustrate two points which believe are important:

(a) Convergence of charge-projections does occur and a desired level of accuracy can be achieved by using a sufficiently large cut-off.

(b) Most, if not all, of the qualitative charge distribution and differential response information is already contained in the smaller cut-off models.

The mean-square error of 0.022 in the partial atomic charges of the smallest model (R_B=6.0 a_0) may seem large. However, seeking high accuracy in atomic charges and Fukui-indices, being as they are of a somewhat arbitrarily defined nature and certainly of relative rather than absolute value, seems to us to be a bit of a misplaced effort. We argue that for most purposes the two smalles models are

quite adequate. In any case, we envisage a typical application to employ a smaller cut-off model in a survey-type calculation to identify potential areas of interest and then, in a follow-up, use of a locally increased cutoff in those areas.

Having now established the type of data that can be obtained using the various DAC cut-off models and having confirmed its accuracy by comparison with a traditionally performed DF free-molecule calculation, we can now proceed to calculate those same properties for a considerably larger system; a system that is clearly beyond the reach of traditional methods and for which a linear-scaling _ or O(N) _ approach, such as DAC, is of the essence. We now consider the functionally interesting 1AAG protein, known as Carcinogenic Embryo Antigen Antibody [79], which contains 3365 atoms. As was the case for the 1TOR example, functional groups were charge neutralized. The division of this protein into DAC fragments was performed using the same partitioning strategy as described above, which leads to a total of 1381 fragments, with on average ~3 reference atoms per fragment. Initial calculations were made with a buffer cut-off R_B=6.0 au to establish general trends ; final calculations were made with a cut-off of 7.5 au. With this choice, the average fragment size (reference and buffer atoms) was 20 atoms and 40 atoms, respectively. The calculations were performed in parallel on 16 processors of an 8 node Linux cluster on which each SCF cycle took approximately one hour. Starting with the superposed atomic densities, convergence proceeded steadily with SCF iterations. Our convergence criterion (change in all density fit-expansion coefficients smaller than 10^{-4}) was accomplished in 42 cycles.

In order to make some simple predictions about electrophilic and nucleophilic sites on the protein surface, we again resort to electrostatic potential maps and to differential electron densities. In Fig. 4 we present a composite in which the Coulomb potential (reconstructed from partial charges) is projected onto the van der Waals surface of 1AAG. Two perpindicular views are given, so that some hint of the three-dimensional structure can be seen.

In Figure 5 is displayed the total DOS for the 1AAG protein which is qualitatively very similar to that of the smaller 1TOR protein (cf. Figure 2). A fragment characterization of the most prominent peaks was accomplished using level-by-level population analysis.

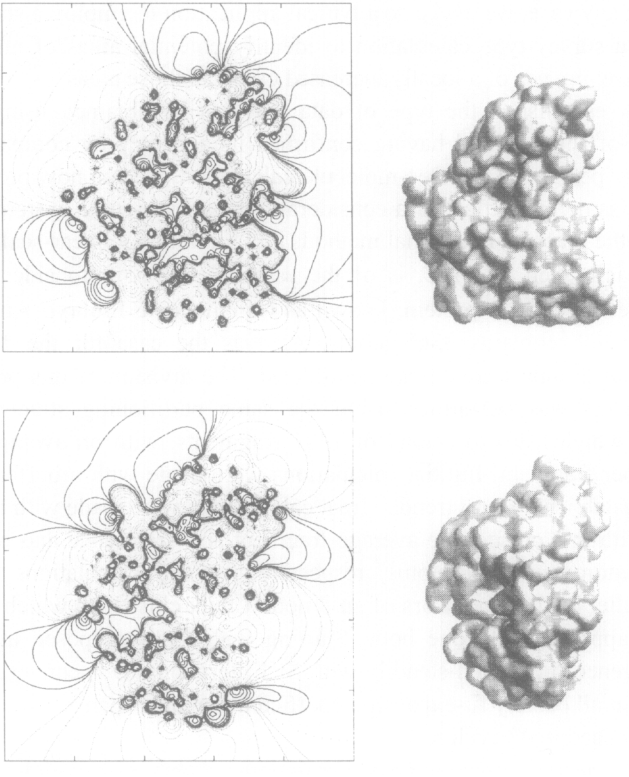

Fig. 4. Electrostatic potential of 1AAG projected upon its van der Waals surface, given in two orthogonal views (x,z) and (y,z) planes through the center of mass. In the inset is a magnified view of atomic positions, Coulomb potential, and local electron excess.

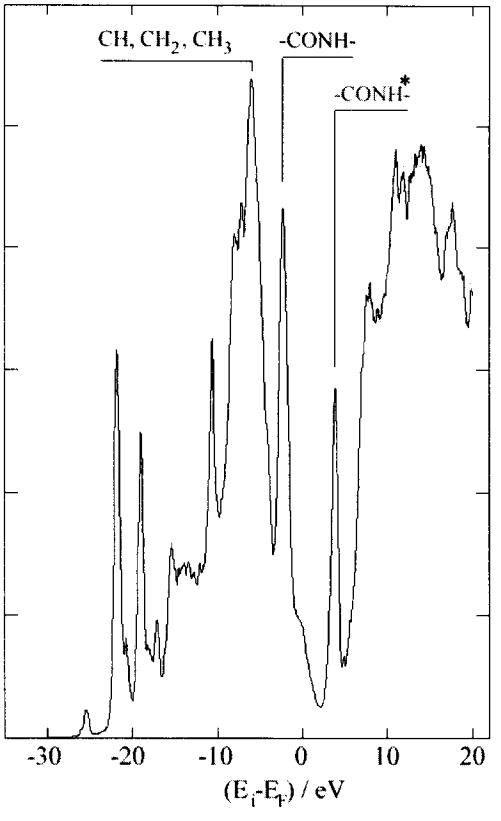

Fig.5. Total density of states for 1AAG protein; the zero of energy is the Fermi level. Functional group origin of prominent peaks is indicated.

The Fukui response function $(d\rho/dN)_-$, approximated here as the difference ρ (0)- ρ (+1) of electron densities $\rho(\mathbf{r})$, was obtained in two calculations on the neutral and single positively charged protein and is shown in Fig. 6, projected upon the molecular Van der Waals surface. A magnification of the interesting 'knob' region is given in the inset, showing both local atomic structure, electrostatic potential, and the local electron excess.

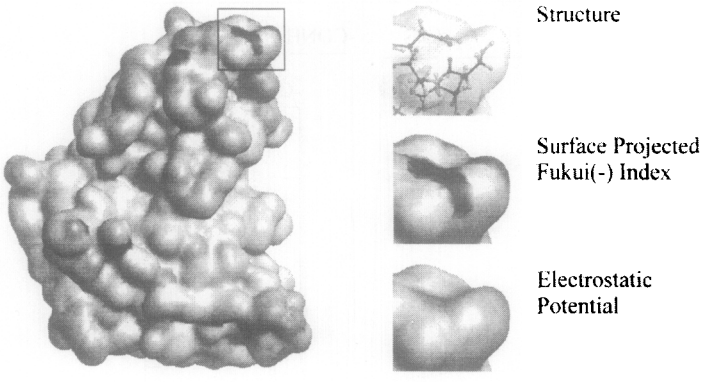

Fig. 6. Response functions of 1AAG protein: $(d\rho/dN)_-$ is projected upon the Van der Waals surface of the molecule. Features around the 'knob' region shown in the insets include local atomic structure, electrostatic potential difference, and local electron excess.

We could think of automated 'docking' type calculations that would use these data to find binding sites for inhibitor molecules. The electron density defines the electrostatics of the system, and protein docking models based on electrostatics are already in quite common use. We think such techniques could conceivably be augmented by taking the Fukui response functions of the protein and the inhibitor into consideration. Because Fukui-functions are related to the important soft-soft type or orbital-controlled inter-molecular interactions, not covered by the electrostatics, they would provide an alternative criterion that could guide a molecule to a potential binding site; for example, we have proposed the overlap of Fukui-functions of the two reactants could as such a criterion for it would be largest when electron accepting regions of the protein are matched with electron-donating areas of the inhibitor and visa versa[74].

The technical details of using this data whether by mere visual inspection

and human interpretation or automated procedures remain to be substantiated in due course; the main point that we wish to illustrate here is that calculation by first-principles methods of the electrostatics and response properties that are driving such models is becoming increasingly routine. The main challenge now is to make full use of the results of such calculations.

V. Example 2: Defect Structure and Vacancy Diffusion near a Hematite Surface

Metal oxide surfaces are ubiquitous, due to the action of the atmosphere on structural materials, and an understanding of their formation, growth, and stability is obviously critical for control of corrosion and wear processes. They are also of great utility as catalytic supports, substrates for electronic components, magnetic microstructures for data recording, etc. The chemical and geometrical structure such surfaces is challenging from both experimental and theoretical points of view. Even the 'simple' cases like nearly ideal (hkl) surfaces of MgO and NiO present intriguing difficulties. Hematite, α-Fe_2O_3, has been extensively studied with respect to bulk properties, as fine particles, and for its surfaces[80-83], so that a general picture is now available. The experimental magnetic structure is that of a canted antiferromagnet, with a Curie temperature of 675 C, and a small remnant magnetization. Recent experimental interest has focused upon nanoparticles, revealing superparamagnetic character and strong surface-related anisotropy. The ion transport properties, due to flux of both cations and oxygen vacancies, need to be understood in detail in order to interpret and predict reactive processes at and near the surfaces. The α-Fe_2O_3 (0001) surface is perhaps the best characterized, with DF band-structure, atomistic simulations, and experiment generally in accord on the relaxation of surface layers which are nominally composed of alternating Fe^{+3} and O^{-2} layers in the sequence Fe-O-Fe-Fe-O-Fe-Fe... [84,85].

Here we present a brief outline of recent studies [86] on defect structure and vacancy diffusion the the (0001) surface, using the hybrid schemes discussed above. Let us examine first the predictions of atomistic simulations concerning type and relative energy ordering of oxygen vacancy sites:

The frequency of jumps from one vacancy site to another depends upon the available pathways, and in particular upon the height of the barrier along the minimum-energy trajectory. The transition state corresponding to the peak of the 'mountain pass' connecting the valleys representing two sites was searched for by a process of constrained variation. Among the most interesting results, we see that the second layer vacancy has the lowest formation energy, that the near-surface region is predicted to have a highly vacancy diffusion rate than bulk, and that the

diffusion takes place preferentially by 'surfing' between adjacent layers.

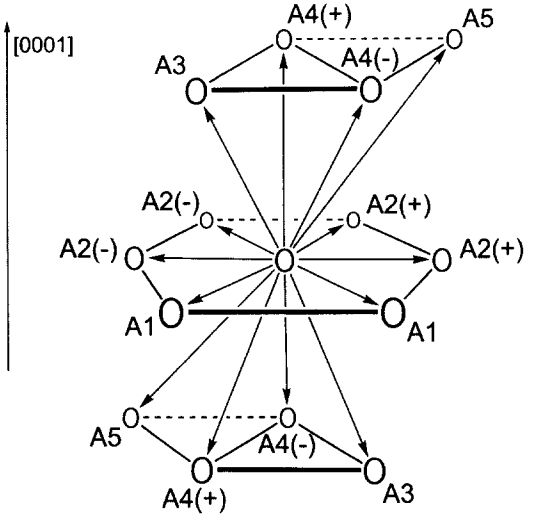

Fig.7. Distinct oxygen vacancy sites in near-surface layers of hematite, showing connection paths for possible diffusion jumps.

Given the vacancy-site geometries determined by atomistic energy minimization, we next consider the resulting electronic properties. Comparison of the relative vacancy energies suggests that the most important surface-related regions for chemical reactivity would be associated with the depression of the surface around the second-layer vacancies. Among the simplest outputs, which are nevertheless of importance in verifying the interatomic potentials and predicting reactivity, are the self-consistent atomic configurations associated with the vicinity of defect sites. Recalling that the initial potential parametrization is based upon an idealized model of the bulk crystal with ions of nominal valency, we will be most interested in local deviations from this reference state. The nominal high spin cation configuration Fe^{+3} $(3d\uparrow)^5(3d\downarrow)^0 4s^0 4p^0$ is somewhat modified by covalency effects in the bulk, principally through mixing of ~0.5e of $(3d\downarrow)$ character into the "oxygen 2p" valence band, with lesser occupancy (<0.1 e) of 4s and 4p orbitals. The average configuration in bulk, as given by Mulliken atomic orbital populations is $Fe^{+2.36}$ with a spin moment of ~4.5 μ_B arranged in an

approximately antiferromagnetic structure. Not surprisingly, we fing surface- and vacancy-related modifications to charge and spin distributions. In general, both ionic charge and magnetic moments are reduced near the surface, and close to the O-vacancy in particular. The average cation charge is reduced to ~2.15-2.20 close to a near-surface vacancy, which is not a big change in comparison to bulk, but worth considering in refined interatomic potential models. As shown in Fig. 8, the overall charge distribution is little modified in the vicinity of a vacancy- charge compensation is accomplished over the distance of several shells of neighbors, consistent with the population analysis.

Layer:		O(1)	O(2)	O(3)	O(4)	O(5)	O(6)	Bulk
Relative Defect Energy: (eV)		+0.15	-0.05	+0.57	+0.37	+0.28	+0.26	0.00
Transition		Energy	(eV)					
A1		1.66	0.71	0.58	0.63	0.63	0.62	0.63
A2	+	0.99	2.47	2.57	2.76	2.62	2.66	2.66
	-	2.03	1.36	2.66	2.69	2.67	2.65	
A3	↑	---	2.40	1.23	1.83	1.78	1.73	1.73
	↓	2.31	1.76	1.64	1.71	1.72	1.72	
A4	↑ +	---	2.64	1.22	1.23	1.07	1.09	1.11
	↑ -	---	0.89	1.44	1.14	1.06	1.11	
	↓ +	2.55	1.75	1.04	1.00	1.08	1.12	
	↓ -	0.80	1.97	0.95	0.99	1.10	1.12	
A5	↑	---	5.22	5.30	5.65	5.38	5.43	5.44
	↓	5.13	5.83	5.46	5.31	5.42	5.45	

Table 3. Calculated defect relative formation and migration energies for oxygen vacancies in the vicinity of the Fe_2O_3 (0001) surface. O(1) is top layer, O(2) is second oxygen layer, etc. For pathway notation A1, A2,... refer to Fig. 5.

The cation spins near the surface and vacancies suffer some net reduction in moment, and become highly 'confused' in orientation. This is evidenced by instabilities in the SCF convergence procedure and indications of multiple metastable states, and is at least compatible with reported surface anisotropy and sensitivity to surface treatment and environment in nanoparticles. However, as

shown in Fig. 9, the gross picture of highly localized Fe d-moments on cation sites is well preserved.

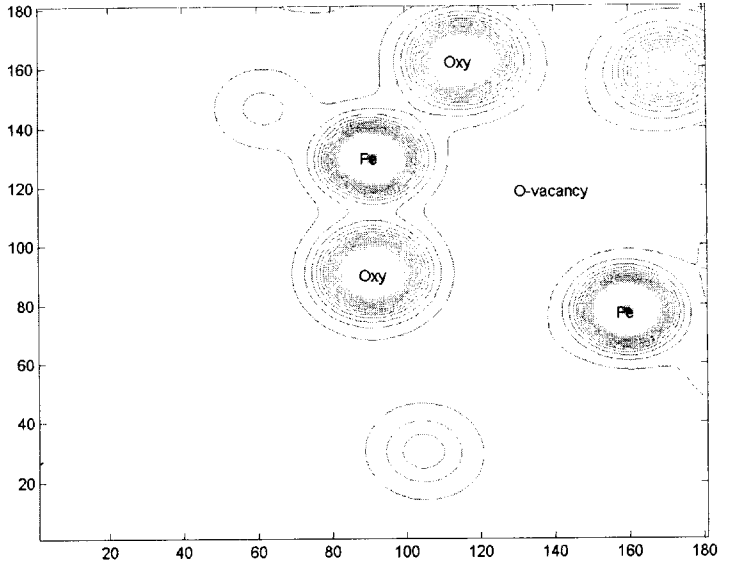

Fig. 8. Equal-interval contour map of charge density in an Fe –O- O' plane closest to the lowest energy (Layer 2) oxygen vacancy.

From these and more detailed electronic structure analyses, we can understand why the bulk-based semiempirical interatomic potential works fairly well for surface structure, and by implication, for near-surface oxygen vacancies- the local ionic configurations suffer only ~10% changes. Nevertheless, it will be worthwhile to introduce surface-related and magnetic interaction terms in future simulations.

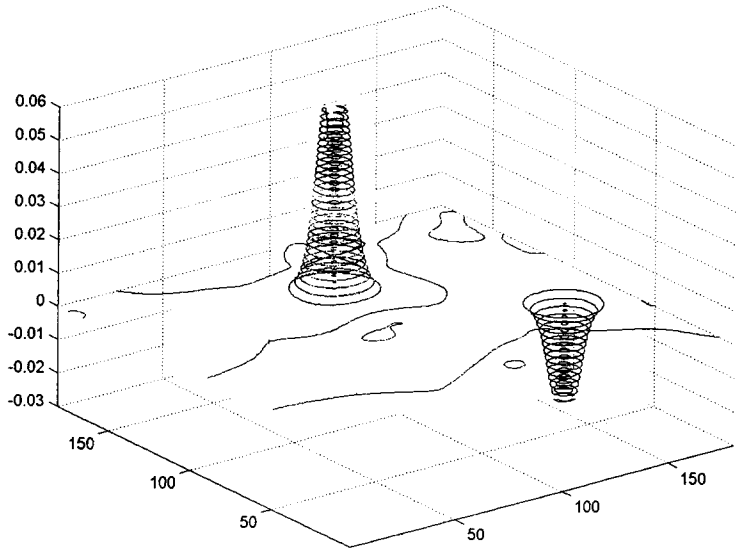

Fig. 9. Equal-interval contour map of spin density in an Fe –O- O' plane closest to the lowest energy (Layer 2) oxygen vacancy.

VI. Example 3: Metal Substitutions in the Bone Analog Hydroxyapatite

Hydroxyapatite (HAP) provides a starting point for the understanding of formation and regeneration of bone and tooth and, in various modifications, has wide medical applications. With chemical formula $Ca_{10}(PO_4)_6(OH)_2$ it can be visualized as a layered structure with two Ca sites, Ca(I) and Ca(II) bound to oxygen ligands in a distorted octahedral arrangement. The structure is knitted together by interlinked phosphate groups, while the hydroxyl radicals are rather free to move along a channel parallel to the c-axis. In bone (OH) is partially substituted by carbonate groups, and several metals substitute readily, presumably on the Ca^{+2} sites. One of the important substituents is zinc, taken up and released as part of the dynamic circulation of the element in the body metabolism. A second important substituent is lead, which is readily absorbed from the environment and is known as a cause of neurological and growth problems in affected children[87,88].

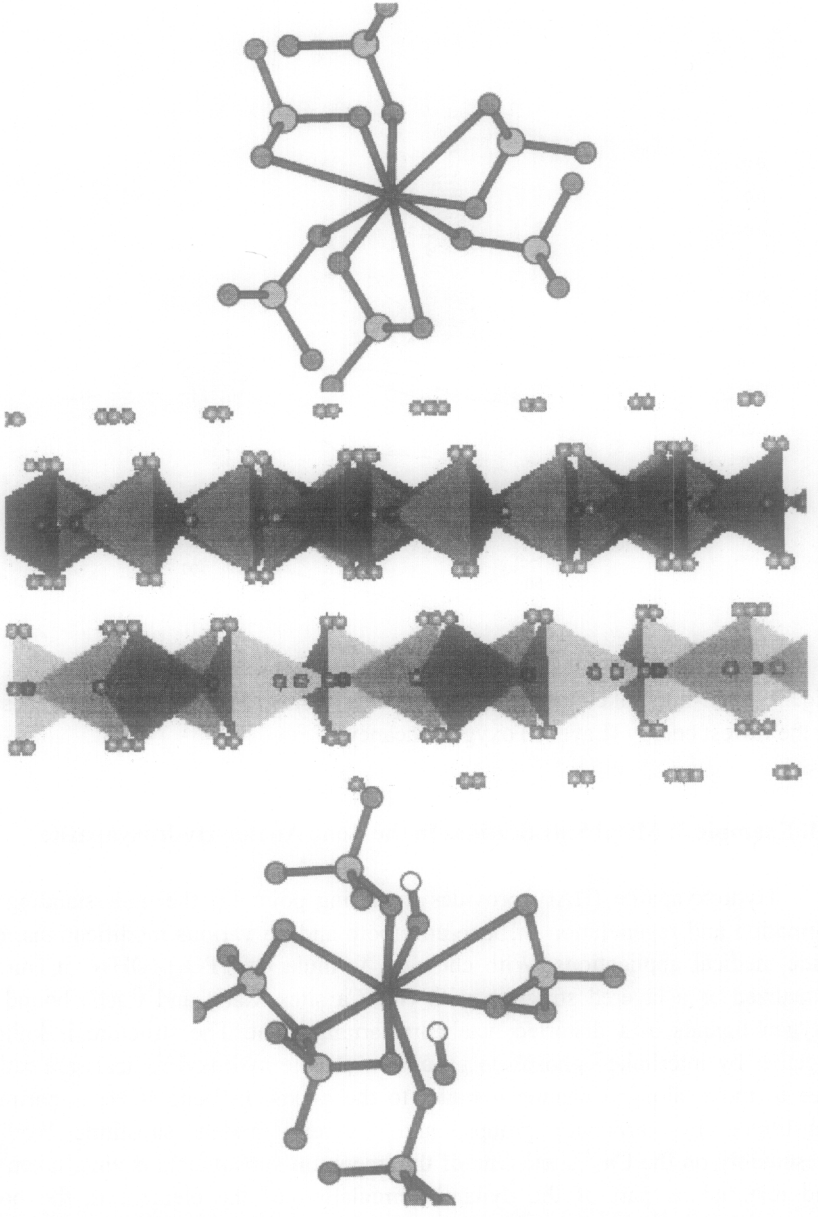

Fig. 10. Schematic of hydroxyapatite crystal structure. Top: Local geometry about Ca(I) and Bottom: about Ca(II) sites.

Here we briefly review some recent work on Zn substitution in HAP which exemplifies part of an extensive multilaboratory effort on related systems[89,90].Given the experimental lattice parameters and atomic positions of HAP obtained by X-ray and neutron diffraction, it is straightforward to calculate the electronic structure of the 'host' compound. With Ca-O distances ranging over $2.36 < R < 2.51$ _ the calcium ions are found to be close to the nominal divalent structure, while the tightly bound PO_4 groups exhibit strong covalent interactions. Some authors have preferred to describe Ca(I) and Ca(II) as 9- and 7-fold coordinated, respectively due to nearby secondary oxygen neighbors. The OH group is coordinated to Ca(II), and exhibits a mixture of ionic and covalent character. A Partial Densities of States diagram is given in Fig. 7 to show the overlapping energy bands due to the different chemical components. ECDF calculations were made with a near-minimal numerical basis set, and ~100 atoms in the variational space.

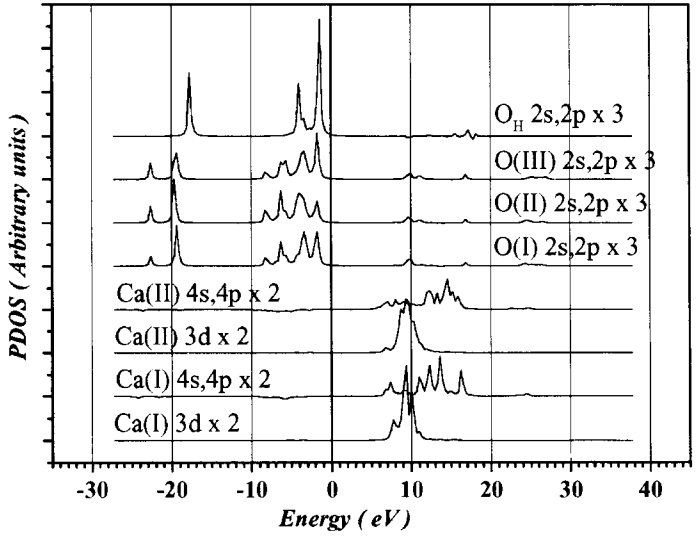

Fig.11. Partial densities of states for selected sites in HAP

In order to study relaxation of the HAP lattice around an impurity, an interatomic potential was constructed by fitting parameters to best reproduce lattice constants, atomic positions, and dielectric constant. The program GULP [61] was used to search for the best fit structure, using Buckingham-type pairwise interactions among the atoms of the form

$$\mathbf{V_{ij} = q_i q_j / r + A\, e^{-r/\lambda} - B / r^6} \qquad (4)$$

and a simple harmonic spring for OH. This kind of potential has proved quite effective in modeling oxide ceramics, and when lattice elastic constants are available they can be usefully included in the fit.

Since we are interested here in isoelectronic substitution of Ca^{+2} by Zn^{+2} and Pb^{+2} the main relaxation effects are expected to be mostly due to differences in ionic radii: Zn(0.74) < Ca (0.99) < Pb(1.19) _, at least from the atomistic point of view. However, zinc has a complex chemistry with significant 4-, 5-, and 6-fold coordination geometries which can not be simply dismissed. Therefore, the Zn-O or Pb-O nearest neighbor interactions were modeled by a Lennard-Jones potential

$$V_{LJ} = C_{12} / r^{12} - C_6 / r^6 \qquad (5)$$

so that the local parameters could be 'tuned' to produce the desired coordination and
bond lengths consistent with ionic radii in that coordination. The GSA procedure was used to relax a volume of several hundred atoms around the impurity, and the different sites were ranked by energy. The (admittedly crude) interatomic potential predicts the Ca(II) 6- fold site to be most stable, as has been proposed by other workers. For Zn, the Ca(II) 4-fold site is next most stable and energetically available, followed by Ca(I) 6-fold.

Given the relaxed impurity geometry we may now carry out DF studies of embedded clusters. The resulting charge densities and spectral properties then can be used to predict and help interpret experimental results. As an example, we consider the X-ray Absorption Near Edge Structures (XANES) and the closely-related Spatially Resolved Electron Energy Loss Spectra (SREELS) of the impurity atoms. One of the great advantages of XANES and SREELS is that very low element concentrations, say 50 ppm, can be readily detected using synchrotron sources, with absorption/loss profiles which reveal both chemical state of the metal ion and influence of the near neighbor environment. Higher energy Extended X-ray Absorption Fine Structure (EXAFS) and Diffraction Anomalous Fine Structure (DAFS) can also be analyzed for neighbor composition and coordination number[91-97].

For Zn^{+2} , the K-edge absorption starting ~ 9660 eV is dominated by 1s-->4p transitions, with the ionic 4p level broadened into a band of states with mixed ligand character, followed by undulations in cross-section caused by backscattering from the first few neighbor shells. As might be expected, 6-, 5-, and 4-fold sites with varying degrees of distortion show considerably different profiles, making a kind of 'fingerprint' identification possible. In the approximation that the transition oscillator strength is slowly varying in energy, the XANES/EELS profile can be represented by the appropriate partial densities of states curve. In order to treat the sizable excited state shifts due to the core hole, it is often convenient to generate an excited state potential with the constraint of a vacancy in the core level. Using these approximations we here show spectra calculated for the Ca(II) site in relaxed 6- and 4-fold geometries.[90] It is expected that experimental XANES data will be shortly available.

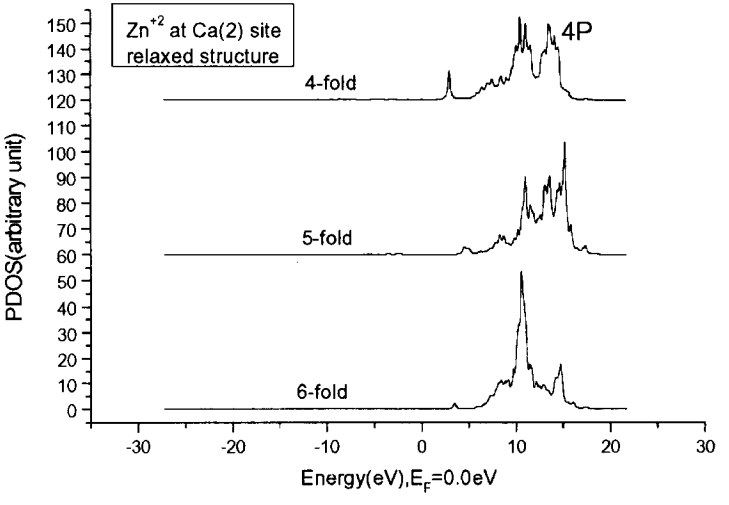

Fig.12. Zinc K-edge absorption spectra predicted for Ca(II) substitution sites, (a) in six-fold and (b) in four-fold relaxed geometry.

For Pb^{+2} the most convenient transitions arise from the L-edges, corresponding to 2s -->X (L_1), $2p_{1/2}$ -->X (L_2), and $2p_{3/2}$ -->X (L_3) electronic excitations. Due to dipole selection rules the L_1 and $L_{2,3}$ edges reveal distinctly different features of the unoccupied states (p-like for L_1, and s,d for $L_{2,3}$). With relativistically calculated electronic wavefunctions it is further possible to exploit the different content of the L_2 and L_3 edges. We report spectra obtained with a fully relativistic embedded cluster model elsewhere, and compare them with experimental data currently available on 100% substituted Pb-HAP [98]

VII. Conclusions

We have argued that a hybrid combination of classical atomistic simulations and first-principles Density Functional analyses of electronic structure is a powerful and appropriate tool to bridge the gap between traditional (t=0, T=0) quantum chemical analyses of electronic structure and finite-t, finite-T properties of real materials of interest. There now exist linear-scaling DF algorithms capable of revealing electronic energy levels and density distributions of systems containing thousands of atoms and little or no symmetry, with reasonable computer resources. Flexible atomistic procedures with simplified interatomic potentials are also highly developed, permitting finite temperature simulations extending up to nanoseconds of 'real' time on samples of many thousands, or millions, of atoms. Progress has been made on developing feedback mechansims to include both experiment, analogy, and DF data in a process of iterative refinement of effective potentials; this remains an area of active research. As we move toward the goals of describing, understanding, and controlling structure-function relations, increasing attention is being paid to improving the interfaces between atomistic processes, multiscale models, and continuum descriptions. The three examples we have chosen- a model protein, a surface defect structure, and a bioceramic- give a snapshot of current directions and capabilities, which we hope will stimulate others to join the exciting world-wide effort in materials theory and simulation.

VIII. Acknowledgments

This research was supported by the U.S. Department of Energy under Grant No. FG02 84ER45097. This work was also supported in part by the EMSI program of the National Science Foundation and the U.S. Department of Energy Office of Science (CHE-9810378) at the Northwestern University Institute for Environmental Catalysis. On the occasion of the fourteenth anniversary of the

DV-Xα Society of Japan, it is also appropriate to acknowledge the inspiration and example of Prof. Hirohiko Adachi in advancing materials theory throughout many years.

IX. References

1. J.C. Slater, "The Self-Consistent Field for Molecules and Solids" , Vol. 4, McGraw-Hill, New York (1974).
2. J. Callaway and N.H. March, in "Solid State Physics" , eds. H. Ehrenreich and D. Turnbull, Academic Press, New York (1984).
3. R. G. Parr and W. Yang, "Density Functional Theory of Atoms and Molecules" ,Oxford University Press, New York (1989).
4. E.S. Kryachko and E. Ludena, "Density Functional Theory of Many-Electron Systems" , Kluwer Academic, Dordrecht (1990).
5. "Density Functional Theory of Molecules, Clusters and Solids" , ed. D.E. Ellis, Kluwer Academic, Dordrecht (1995).
6. W. Yang, Phys. Rev. Lett. **66**, 1438 (1991)
7. W. Yang, J. Mol. Struct. **255**, 461 (1992)
8. W. Wang and Z. Zhou, in "Density Functional Theory of Molecules, Clusters, and Solids", ed. D.E. Ellis, (Kluwer Academic, Dordrecht, 1995) p.177
9. Q. Zhao and W. Yang, J. Chem. Phys. **102**,9598 (1995).
10. O. Warschkow, D.E. Ellis, and J.M.Dyke, J. Comp. Phys. **143**, 70(1998).
11. B. R. Brooks, R. E. Bruccoleri, B. D. Olafson, D. J. States, S. Swaminathan, and M. Karplus, J. Comp. Chem. **4**, 187 (1983).
12. A. D. Mackerell, Jr., B. Brooks, C. L. Brooks, III, L. Nilsson, B. Roux, Y. Won, and M. Karplus, in "The Encyclopedia of Computational Chemistry", Vol. 1, eds. P. v. R. Schleyer *et al.* (John Wiley & Sons, Chichester, 1998) p 271.
13. T. L. Windus, M. W. Schmidt, and M. S. Gordon, in "Toward Teraflop Computing and New Grand Challenge Applications", eds. R. J. Kalia and P. Vashishta, (Nova Science Publisher, New York, 1995) p 189.
14. M. S. Gordon, M. A. Freitag, P. Bandyopadhyay, V. Kairys, J. H. Jensen, and W. J. Stevens, J. Phys. Chem. **105**, 293 (2001).
"Combined Quantum Mechanical and Molecular Mechanical Methods", Vol. 712, ACS Sympos. Series, eds. J. Gao and M. A. Thompson, (ACS, Washington, D.C.,1998).
15. K.C. Mundim and D.E. Ellis, Brazil. J. of Physics **29**, 199 (1999).
D.E. Ellis, K.Mundim, V.P. Dravid, and J.W. Rylander, in "Computer Aided Design of High Temperature Materials" , eds. A. Pechenik, R.K.Kalia, and P. Vashishta, (Oxford University Press, Oxford, 1999)p350.
16. W. K. Liu, S. Jun, and Y. F. Zhang, Int. J. Num. Meth. Fluids **20**, 1081 (1995).
17. T. Belytschko, Y. Kronganz, D. Organ, M. Fleming, and P. Krysl, Comp. Meth. in Appl. Mech. and Eng. **139**, 3 (1996).
18. M. Fleming, Y. A. Chu, B. Moran, and T. Belytschko, Int. J. Num. Meth. Engr.

40, 1 (1997)
19. W. K. Liu, S. Hao, T. Belytschko, S. F. Liu, and C. T. Chang, Int. J. Num. Meth. Engr. **47**, 1343 (2000).
20. G. J. Wagner and W. K. Liu, Int. J. Num. Meth. Engr. **50**, 507 (2000).
21. R. Car and M. Parinello, Phys. Rev. Lett. **55**, 2471 (1985).
22. Q. M. Zhang, G. Chiarotti, A. Sellini, R. Car, and M. Parinello, Phys. Rev. **B42**, 5071 (1990).
23. I. Stich, D. Marx, M. Parinello, and K. Terakura, Phys. Rev. Lett. **78**, 3669 (1997); *ibid,* J. Chem. Phys. **107**, 9482 (1997).
24. G. Stapper, M. Bernasconi, N. Nicoloso, and M. Parinello, Phys. Rev. **B59**, 797 (1999).
25. C. Rovira and M. Parinello, Intern. J. Quantum Chem. **80**, 1172 (2000).
26. I. Stich, M. Parinello, and J. M. Holender, Phys. Rev. Lett. **76**, 2077 (1996).
27. J. C. Slater and G. F. Koster, Phys. Rev. **94**, 1498 (1954).
28. D. W. Bullett and M. L. Cohen, Sol. Sta. Commun. **21**, 157 (1977).
29. D. W. Bullett, Solid State Phys. **35**, 129 (1980) p1.
30. T. N. Todorov, J. Phys: Condens. Mat. **13**, 10125 (2001).
31. J. Purton, D. W. Bullett, P. M. Oliver, and S. C. Parker, Surf. Sci. **336**, 166 (1995).
32. L. Feng, M. R. Press, S. N. Khanna, and P. Jena, Phys. Rev. **B39**, 6914 (1989).
33. H. Cruz, D. Luis, N. E. Capuj, and L. Pavesi, J. Apply. Phys. **83**, 7693 (1998).
34. F. F. Abraham, Computer Modeling in Engr. & Sci. **1**, 63 (2000).
35. V. Rosato and M. Celino, J. Appl. Phys. **86**, 6826 (1999).
36. N. Bernstein, M. J. Aziz, and E. Kaxiras, Phys. Rev. **B58**, 4579 (1998).
37. P. Hohenberg and W. Kohn, Phys. Rev. **136**, B864 (1964).
38. W. Kohn and L.J. Sham, Phys. Rev. **140**, A1133 (1965).
39. M. Levy and 'A. Nagy, Phys. Rev. Lett. **83**, 4361 (1991).
40. 'A. Nagy, Physics Reports **298**, 1 (1998)
41. 'A. Nagy and K. D. Sen, J. Chem. Phys. **115**, 6300 (2001).
42. 'A. Nagy and M. Levy, Phys. Rev. **A6305**:2502 (2001).
43. S. J. A. Gisbergen, C. Fonseca Guerra and E. J. Baerends, J. Comput. Chem. **21**, 1511 (2000).
44. P.-O. Löwdin, Theor. Chim. Acta **89**, 277 (1994); Phys. Scripta **32**, 261 (1985)
45. B. N. Figgis and M. A. Hitchman, "Ligand Field Theory and Its Applications", (Wiley, New York, 1999).
46. F. A. Cotton, in "Chemical Applications of Group Theory", 3rd Edn, (Wiley, New York, 1990) p 287.
47. D.E. Ellis, G.A. Benesh and E. Byrom, Phys. Rev. B 20, 1198 (1979).
48. D.E. Ellis, J. Guo and H.P. Cheng, J. Phys. Chem., 92, 3024 (1988).
49. D.E. Ellis, J. Guo, and D.J. Lam , J.Am.Cer.Soc. 73, 3231 (1990).
50. D.E. Ellis and J.Guo, in "Electronic Density Functional Theory of Molecules, Clusters, and Solids", ed. D.E. Ellis, (Kluwer, Dordrecht, 1995)p263.
51. C. Satoko, Chem. Phys. Lett. **83**, 111 (1981).

52. A. Berces and T. Ziegler, Top. Curr. Chem. **182**, 41 (1996).
53. L. Y. Fan, L. Versluis, T. Ziegler, E. J. Baerends, and W. Ravenek, Intern. J Quantum Chem., Suppl. **22**, 173 (1988).
54. A. Rahman, Phys. Rev. **136**, A405 (1964).
55. M.L. Allinger, J.A. Hirsch, M.A. Miller, I.J.Tyminski, and F.A. Van-Catledge, J. Am. Chem. Soc. **90**, 1199 (1968).
56. S. Nose, J. Chem. Phys. **81**, 511 (1984).
57. S. J. Weiner, P. A. Kollman, D. A. Case, U. C. Singh, C. Ghio, G. Alagona, S. Profeta, Jr., and P. Weiner, J. Amer. Chem. Soc. **106**, 765 (1984).
58. G. Ciccotti, D. Frenkel, and I. R. McDonald, (eds), "Simulation of Liquids and Solids" , (North-Holland, Amsterdam, 1987)
59. M. P. Allen and D.J. Tildesley, "Computer Simulation of Liquids", (Clarendon Press, Oxford, 1987).
60. F. Yonesawa (ed) " Molecular Dynamics Simulations" , (Springer-Verlag, Berlin, 1992)
61. J.D. Gale, J. Chem. Soc., Faraday Trans. **93**, 629 (1997).
62. N. Metropolis, A.W. Rosenbluth, A.H. Teller, and E. Teller, J. Chem. Phys. **21**,1087 (1953).
63. K. Binder and D. E. Heermann, "Monte Carlo Simulation in Statistical Physics" , Springer-Verlag, Berlin, 1988)
64. E. P. G. Areas, P. G. Pascotti, S. Schreier, K.C. Mundim, and P. M. Bisch, J. Phys. Chem. **99**, 14882 (1995).
65. K. C. Mundim and C. Tsallis, Int. J. Quant. Chem., **58**, 373 (1996)
66. M. Z. Bazant and E. Kaxiras, Phys. Rev. Lett. **77**, 4370 (1996).
67. M. Z. Bazant and E. Kaxiras, in E. Kaxiras, J. Joannopoulas, P. Vashishta, and R. Kalia (eds.) "Materials Theory, Simulations, and Parallel Algorithms", MRS Proceedings Vol. **48**, (Mater. Res. Soc., Pittsburgh, 1996).
68. K. C. Mundim, L.A.C. Malbouisson, S. Dorfman, D. Fuks, J. Van Humbeeck, and V. Liubich, J. Molec. Struc. (Theochem) **539**, 191 (2001).
69. C. H. Arrowsmith, A. M. Edwards, and B. desPallieres, Modern Drug Discovery **5**, 41 (2000).
70. Y. Duan, W. Wang, and P. A. Kollman, Proc. Natl. Acad. Sci. **95**, 9897 (1998).
71. T. Dandekar and P. Argos, J. Mol. Biol. **236**, 844 (1994).
72. R. G. Parr and W. Yang, J. Am. Chem. Soc. **106**, 4049 (1984).
73. K. Fukui, T. Yonezawa, and H.Shingu, J. Chem. Phys. **20**, 722 (1952).
74. L.A. Clark, D.E. Ellis and R.Q. Snurr, J. Chem. Phys. **114**, 2580 (2001).
75. D. E. Ellis, in "Density Functional Theory of Molecules, Clusters and Solids" , ed. D.E. Ellis, Kluwer Academic, Dordrecht (1995) p168.
76. S. H. Vosko, L. Wilk, and M. Nusair, Can. J. Phys. **58**, 1200 (1980).
77. F. C. Bernstein, T. F. Koetzle, G. J. B. Williams, E. F. Meyer, Jr., M. D. Brice, J. R. Rodgers, O. Kennard, T. Shimanouchi, and M. Tasumi, J. Mol. Biol. **112**, 535 (1977).
78. P. Orlewski, M. Marraud, M.T. Cung, V. Tsikaris, M. Sakarellos-Daitsiotis, C. Sakarellos, E. Vatzaki, and S.J. Tzartos, Biopolymers **40**, 419 (1996).

79. M. T. Mas, K. C. Smith, D. L. Yarmush, K. Aisaka, and R. M. Fine, Protein Struct. Funct. **14**, 483 (1992).
80. R. Dieckmann, Phil. Mag. A **68**, 725 (1993).
81. F. J. Morin, Phys. Rev., **83**, 1005 (1951); *Ibid.,* **93**, 1195 (1954); Bell Sys. Tech. J., **37**, 1047 (1958).
82. S. A. Chambers and S. I. Yi, Surf. Sci. **425**, 276 (1999); Surf. Sci. **439**, L785 (1999).
83. M. F. Hansen, C. B. Koch, and S. Morup, Phys. Rev. **B62**, 1124 (2000).
84. X. G. Wang, W. Weiss, Sh. K. Shaikhutdinov, M. Ritter, M. Peterson, F. Wagner, R. Schlögl and M. Scheffler, Phys. Rev. Lett. **81**, 1038 (1998).
85. C. R. A. Catlow, J. Corish, J. Hennessey and W. C. Mackrodt, J. Am. Ceram. Soc. **71**, 42-49 (1988).
86. O. Warschkow, D. E. Ellis, J._H. Hwang, N. Mansourian-Hadavi and T. O. Mason, J. Am. Ceram. Soc. (to be published).
87. T. S. B. Narasaraju and D. E. Phebe, J. Mater. Sci. **31**, 1 (1996).
88. B. D. Ratner, A. S. Hoffman, F. J. Schoen and J. E. Lemons (eds.) "Biomaterials Science" (Academic Press, San Diego, 1996).
89. D.U. Schramm, J. Terra, A.M. Rossi, and D.E. Ellis, Phys. Rev. **B63**, 24107 (2000).
90. J. Terra, M. Jiang, and D.E. Ellis, Philos. Mag. A (to be published).
91. "X-Ray Absorption: Principles, Applications, Techniques of EXAFS, SEXAFS and XANES", eds. R. Prins and D. Koningsberger (Wiley, New York, 1988).
92. J. Stöhr, "NEXAFS Spectroscopy", (Springer-Verlay, Berlin, 1992).
93. J. J. Rehr, R. C. Albers, and S. I. Zabinsky, Phys. Rev. Lett. **69**, 3397 (1992).
94. "Resonant Anomalous X-Ray Scattering: Theory and Applications", eds. G. Materlik, C. J. Sparks, and K. Fischer, (North Holland, Amsterdam, 1994).
95. P. D. Nellist and S. J. Pennycook, Microscopy and Microanalysis **3**, (suppl. 2), Proc. Microscopy and Microsnalysis '97 Cleveland, OH, eds. G. W. Bailey *et al.*, (Springer, New York, 1997) p 1149.
96. M. F. Chisholm, A. Maiti, S. J. Pennycook, and S. T. Pantelides, Phys. Rev. Lett. **81**, 132 (1998).
97. M. Kim, G. Duscher, N. D. Browning, K. Sohlberg, S. T. Pantelides, and S. J. Pennycook, Phys. Rev. Lett. **86**, 4056 (2001).
98. M. Jiang, D. E. Ellis, and J. Terra (unpublished).

Many-electron calculation for the analysis of optical absorption spectra in Cr^{4+}-doped solid-state laser crystals

Takugo Ishii*, Kazuyoshi Ogasawara, and Hirohiko Adachi
Department of Materials Science and Engineering, Kyoto University, Sakyo, Kyoto 606-8501, Japan

(Received February 12, 2002; in final form March 13, 2002)

The multiplet energies and absorption spectra of Cr^{4+}-doped $Y_3Al_5O_{12}$ (YAG), Mg_2SiO_4 (forsterite), and $Ca_2MgSi_2O_7$ (åkermanite) were calculated by a nonempirical many-electron electronic-structure calculation method. The cluster models having the atoms outside the central CrO_4 tetrahedron were used, $(CrY_6Al_4O_{44})^{54-}$ for Cr^{4+}:YAG, $(CrMg_9Si_2O_{37})^{44-}$ for Cr^{4+}:forsterite, and $(CrCa_6Mg_2SiO_{38})^{52-}$ for Cr^{4+}:åkermanite. In Cr^{4+}:YAG, both the near-infrared and visible bands originated from the transitions to the states originating from the same $^3T_1(et_2)$ parent term. In Cr^{4+}:forsterite and Cr^{4+}:åkermanite, the different polarization dependence was observed, although the CrO_4 structures were similar to each other. The contribution of the atomic orbitals of atoms outside the CrO_4 tetrahedra affected the transition probability.

KEYWORDS: multiplet structure, impurity center, Cr^{4+} solid-state lasers

*Corresponding author: itack@mac.com

CONTENTS

ADVANCES IN QUANTUM CHEMISTRY, VOLUME 42

0065-3276/03 $35.00

1. INTRODUCTION

The tetrahedrally coordinated Cr^{4+} is the impurity center of the Cr^{4+} solid-state laser crystals. The absorption and the emission in the near-infrared (NIR) region are responsible for the transitions related to the lasing. The theoretical understanding of the basic absorption spectra has been based on the ligand field theory [1]. Since the analysis based on the ligand field theory involves some empirical parameters, the determination of the parameters has made it difficult to understand straightforwardly the spectra. Although ab initio calculation methods under a one-electron approximation became popular, they are still unable to apply to the problems of impurity-metal centers which has an open-shell electron configuration producing multiplet structure.

Recently, the discrete variational multielectron (DVME) method was developed by Ogasawara et al. [2]. It is the first ab initio method that handles directly the multiplet structure, independent of the traditional ligand field theory. The latest systematic study on the multiplet structures of transition metals by the DVME method was done by Ishii et al. [3]. The method was also applied widely to the analyses of x-ray absorption spectra involving multiplet structures [4] and the magnetism of transition-metal ion pair system involving superexchange interaction [5]. The aim of this work is performing the DVME calculations for the analysis of optical absorption spectra in Cr^{4+}-doped $Y_3Al_5O_{12}$ (YAG), Mg_2SiO_4 (forsterite), and $Ca_2MgSi_2O_7$ (åkermanite).

2. METHOD

2.1. The computational procedure of multiplet calculation

The details of the DVME method were written in Ref. [2]. Only the outlines and needed explanations for the present study are written in the following.

First, a one-electron molecular orbital (MO) calculation by the SCAT code [6] is conducted. The method is based on the density functional theory, and the exchange potential $X\alpha$ is set at 0.7. The self-consistent calculation is conducted with the use of a cluster model. The atomic orbitals as the basis functions of the one-electron calculation were 1s–4p for chromium (Cr) and calcium (Ca), 1s–2p for oxygen (O), 1s–3d for magnesium (Mg), aluminum (Al), and silicon (Si), and 1s–5p for yttrium (Y). From the one-electron calculation, one-electron MO energies and MOs are numerically obtained.

Next, the one-electron MOs directly related to the multiplet structure are taken to construct many-electron wave functions in the form of linear combination of Slater determinants. In the case of the multiplet structure derived from the d–d transition of Cr^{4+} state (d^2 electron configuration), the five MOs having the main component of

Cr 3d orbital are the components of Slater determinants. The number of Slater determinants as the basis functions of many-electron system is 45. Since the components of Slater determinants are MOs, covalency is included in the many-electron wave functions. In the effective many-electron Hamiltonian, the one-electron operator part which represents the interaction between the d-electrons and the other electrons plus nuclei is expressed as average potentials. On the other hand, the two-electron operator part which represents the Coulomb repulsion between d-electrons is calculated explicitly. For the calculation of matrix elements, two-electron integrals are calculated. The integrals are numerically obtained. Although the DVME method is an ab initio method in principle, two reduction factors were introduced to obtain the results with a good accuracy in multiplet energy. One was applied to the matrix elements of one-electron operator term, and the values were 0.8 for YAG and 0.65 for forsterite and åkermanite. The main cause for the overestimation was the neglect of lattice relaxation around Cr atom, and the reduction factor will be removed when the calculation is combined with a geometry optimization one in the future. The other reduction factor was applied to the two-electron operator term, and the values were determined by fixing the related spin-flip transition energy at an average 0.93 eV. The reduction factor will be removed in the future when much larger number of Slater determinants involving valence MOs are involved to sufficiently include electron correlation. Finally, multiplet energies and many-electron wave functions are obtained by diagonalizing the effective many-electron Hamiltonian. A theoretical absorption spectrum is obtained by applying the oscillator strength of the electric-dipole transition from ground state to the Lorentz resonance curve with a full width at half maximum of 325 cm^{-1}.

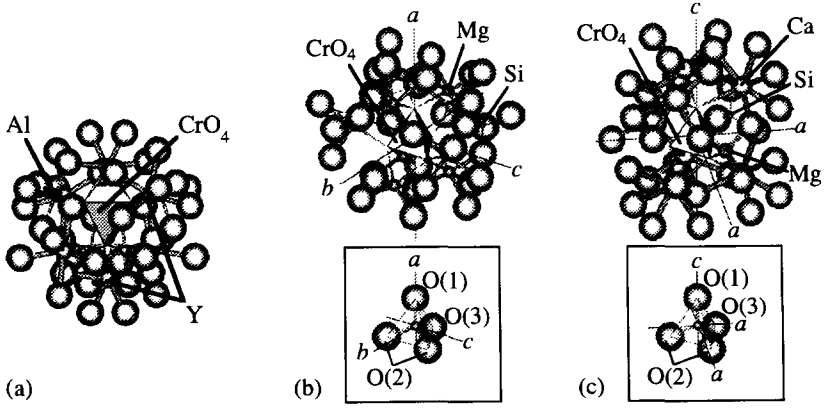

Fig. 1. Cluster models (a) $(CrY_6Al_4O_{44})^{54-}$ for Cr^{4+}:YAG, (b) $(CrMg_9Si_2O_{37})^{44-}$ for Cr^{4+}:forsterite, and (c) $(CrCa_6Mg_2SiO_{38})^{52-}$ for Cr^{4+}:åkermanite. The inset in (b) and (c) shows the labels of ligand O atoms in CrO_4 tetrahedron referred in Tables 2 and 3.

2.2. Cluster models

The impurity Cr^{4+} ion is substituted for tetrahedrally coordinated Al site in YAG, or Si site in forsterite and åkermanite. The cluster models are $(CrY_6Al_4O_{44})^{54-}$ for Cr^{4+}:YAG, $(CrMg_9Si_2O_{37})^{44-}$ for Cr^{4+}:forsterite, and $(CrCa_6Mg_2SiO_{38})^{52-}$ for Cr^{4+}:åkermanite, shown in Fig. 1. The models were cut out from the host lattices, and the site symmetries at the central Cr atom are S_4 for YAG [7], and C_s for forsterite [8] and åkermanite [9]. In every model, point charges with formal valences were placed at the atomic sites outside the cluster to reproduce the effective Madelung potential. The four ligand O atoms around a Cr atom were completely shared by the coordination polyhedra of host lattice, YO_8 and AlO_6 in YAG, MgO_6 and SiO_4 in forsterite, and CaO_8, MgO_4, and SiO_4 in åkermanite. Among the polyhedra, only the SiO_4 tetrahedron in forsterite model did not share the ligand O atoms. The CrO_4 tetrahedra of forsterite and åkermanite have the same structural features: the Cr–O separation decreased in the order Cr–O(3) > Cr–O(2) > Cr–O(1).

3. RESULTS AND DISCUSSION

3.1. One-electron calculation

The calculated one-electron MO energies by Cr^{4+}:YAG, Cr^{4+}:forsterite, and Cr^{4+}:åkermanite models are shown in Fig. 2. The valence bands were composed of O 2p orbitals, and the unoccupied bands (conduction band) were composed of the atomic orbitals of host cations. In the band gap, the Cr-3d impurity levels were

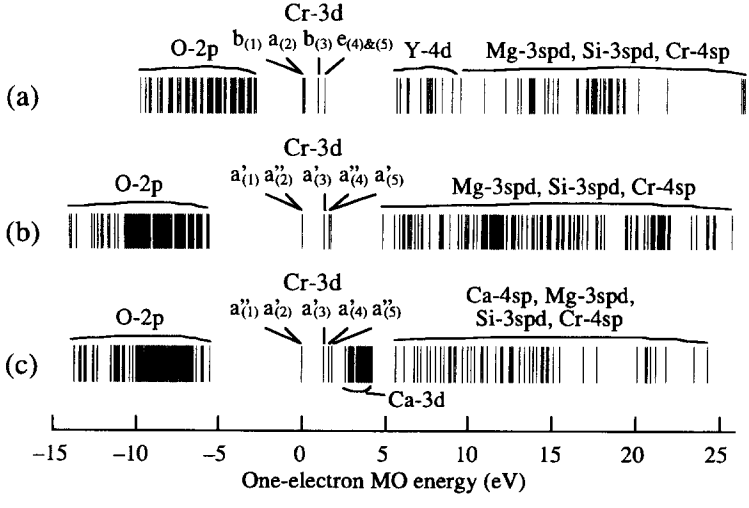

Fig. 2. One-electron MO energies by (a) Cr^{4+}:YAG, (b) Cr^{4+}:forsterite, and (c) Cr^{4+}:åkermanite models.

Table 1. Composition of impurity-level MOs in Cr^{4+}:YAG.

	Cr		Ligand O		Y		Al
MO	3d	4s+4p	2s	2p	4d	4p+5s+5p	3s+3p+3d
$b_{(1)}(e)$	0.84	0.00	0.00	0.13	0.01	0.00	0.01
$a_{(2)}(e)$	0.80	0.00	0.00	0.17	0.01	0.00	0.01
$b_{(3)}(t_2)$	0.73	0.04	0.01	0.19	0.02	0.00	0.01
$e_{(4)\&(5)}(t_2)$	0.71	0.05	0.01	0.19	0.01	0.00	0.02

Table 2. Composition of impurity-level MOs in Cr^{4+}:forsterite.

			Ligand O						
	Cr			2p				Mg	Si
MO	3d	4s+4p	2s	O(1)	O(2)	O(3)	Total	3s+3p+3d	3s+3p+3d
$a'_{(1)}(e)$	0.82	0.00	0.00	0.03	0.08	0.03	0.14	0.04	0.00
$a''_{(2)}(e)$	0.82	0.00	0.00	0.02	0.08	0.05	0.15	0.03	0.00
$a'_{(3)}(t_2)$	0.67	0.06	0.01	0.08	0.08	0.03	0.19	0.07	0.00
$a''_{(4)}(t_2)$	0.67	0.07	0.01	0.03	0.15	0.01	0.19	0.05	0.00
$a'_{(5)}(t_2)$	0.69	0.06	0.01	0.02	0.08	0.09	0.20	0.04	0.00

Table 3. Composition of impurity-level MOs in Cr^{4+}:åkermanite.

			Ligand O							
	Cr			2p				Ca	Mg	Si
MO	3d	4s+4p	2s	O(1)	O(2)	O(3)	Total	3d+4s,p	3s,p,d	3s,p,d
$a''_{(1)}(e)$	0.82	0.00	0.00	0.03	0.08	0.03	0.14	0.02	0.01	0.01
$a'_{(2)}(e)$	0.81	0.00	0.00	0.04	0.08	0.02	0.14	0.03	0.01	0.01
$a'_{(3)}(t_2)$	0.65	0.08	0.02	0.04	0.07	0.06	0.16	0.06	0.01	0.02
$a'_{(4)}(t_2)$	0.62	0.07	0.00	0.09	0.09	0.02	0.19	0.09	0.01	0.01
$a''_{(5)}(t_2)$	0.63	0.08	0.01	0.06	0.14	0.01	0.20	0.05	0.03	0.00

located, split into four or five levels by ligand field. Two electrons occupied the lowest impurity level. In every result, the ideal ligand-field splitting of parent T_d symmetry was approximately kept: the impurity levels can be classified into e-symmetry originating levels and t_2-symmetry originating ones. The five impurity-level MOs were taken as the components of Slater determinants in multiplet calculation.

The estimation of covalency has been a great matter to determine the magnitude of empirical parameters in the traditional ligand-field analysis. The analyzed results of impurity-level MO composition by Mulliken's scheme are shown in Table 1–3 for Cr^{4+}:YAG, Cr^{4+}:forsterite, and Cr^{4+}:åkermanite. The contribution of Cr 3d orbitals were largely reduced by the mixing of O 2p orbitals, which produced covalency. The proportion of Cr 3d orbitals were about 0.8 for e-symmetry originating MOs, and 0.7 for t_2-symmetry originating ones. Considering the corresponding magnitude

0.8–0.9 in the case of octahedrally coordinated Cr^{3+}, we can say that the results in the tetrahedrally coordinated system showed large covalency. In each crystal, the result showed the presence of the significant contribution of cations composing host lattice. In the case of forsterite model, the contribution of Si orbitals was negligible. Those results indicate that the coordination polyhedra surrounding completely the ligand O atoms should be included in the models, but the other coordination polyhedra outside the cluster do not affect the impurity Cr states. This result is new for the traditional ligand field theory, because it typically handled only the environment within the ligand O atoms. The different contribution of ligand O atoms between forsterite and åkermanite indicates the importance of the atoms outside the CrO_4 tetrahedra, which had a similar structure.

3.2. Multiplet calculation

3.2.1. Cr^{4+}:YAG

The calculated multiplet energies and absorption spectrum of Cr^{4+}:YAG are shown in Fig. 3(a). The multiplet states are presented by the multiplet-term symbols in the parent T_d symmetry, classified into singlet states (^1E, $^1A_1$, $^1T_2$, $^1T_1$) and triplet states ($^3A_2$, $^3T_2$, $^3T_1$). The focused states in this work are triplet states, to which the multiplet-term symbols in the exact S_4 symmetry are also attached. For comparison, an experimentally obtained absorption spectrum after Kück et al. [10] is shown in Fig. 3(b). The spectrum has two major bands: the near-infrared band at around 10

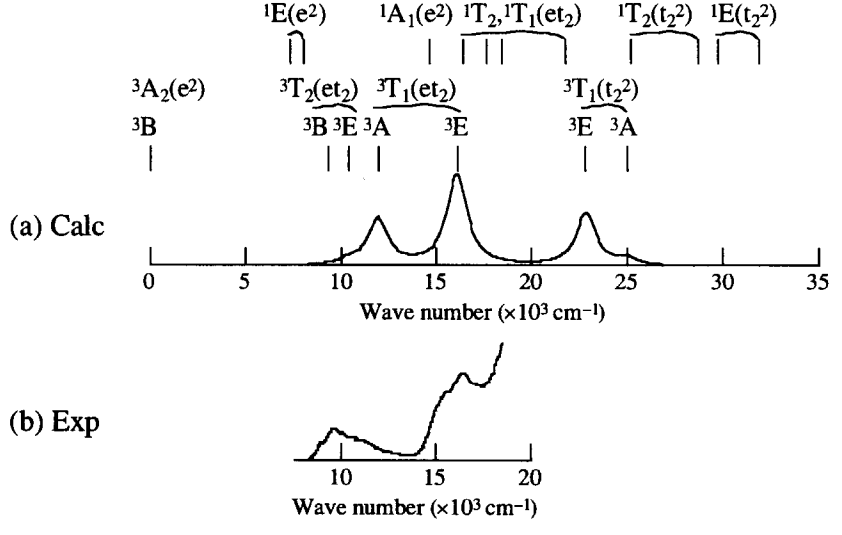

Fig. 3. (a) The calculated multiplet energy and absorption spectrum by the Cr^{4+}:YAG model. (b) The experimentally obtained absorption spectrum after Kück et al. [7].

000 cm^{-1} and visible band at about 15 400 cm^{-1}. In the early years, the NIR and visible bands were considered to originate from the transitions to the $^3T_2(et_2)$ and $^3T_1(et_2)$ states, respectively, based on a simple and popular analysis under the ideal parent T_d symmetry. Controversal discussion was left on the oscillator strength of the transition to the NIR band, because the transition to the $^3T_2(et_2)$ state is originally forbidden. Eilers et al. proposed a different understanding which suggested that the two bands appeared by the transitions to the states originating from the same $^3T_1(et_2)$ parent term which is originally allowed [11].

The calculated absorption spectrum showed the two-band structure corresponding to the experimentally obtained spectrum. The NIR band originated from $^3B[^3A_2(e^2)] \rightarrow {}^3A[^3T_1(et_2)]$ transition, and the visible band originated from $^3B[^3A_2(e^2)] \rightarrow {}^3E[^3T_1(et_2)]$ transition. This result showed that the ligand-field energy splitting of the $^3T_1(et_2)$ parent term should be large enough to create the NIR and visible bands. The agreement in the absolute energy of NIR band may not perfect, but the existence of the large energy splitting was confirmed by theoretical calculation for the first time. By the traditional ligand field theory, the magnitude always depended on the empirical parameters, and no straightforward confirmation has been done. The negligibly small oscillator strength of the transitions to the two states originating from $^3T_2(et_2)$ term also showed that the NIR band should not originate from the transitions to the states of $^3T_2(et_2)$ term. From those results by the theoretical calculation without using any empirical parameters to adjust the magnitude of the concerning ligand-field splitting, Eilers' suggestion was justified to be valid.

3.2.2. Cr^{4+}:forsterite and Cr^{4+}:åkermanite

The calculated multiplet energies and absorption spectra of Cr^{4+}:forsterite and Cr^{4+}:åkermanite are shown in Figs. 4(a) and 5(a), respectively. The corresponding experimentally obtained spectra are shown in Figs. 4(b) and 5(b) after Verdún et al. [12] and Garrett et al. [13], respectively. The absorption spectra show the polarization dependence of the electric vector of incident light on crystallographic axes.

The calculated absorption spectra reproduced the obvious structures in the experimentally obtained spectra: three strong peaks for different polarizations in visible region, and weak NIR bands. The three peaks in visible region were attributed to the transitions to the different states originating from the $^3T_1(et_2)$ parent term split largely by the ligand field in C_s symmetry. On the other hand, the NIR band was attributed to the transitions to the states originating from the $T_2(et_2)$ term. The small oscillator strength originated from the forbidden character of the $^3A_2(e^2) \rightarrow {}^3T_2(et_2)$ transition in the parent T_d symmetry. Thus, the origin of the NIR band in Cr^{4+}:forsterite and Cr^{4+}:åkermanite is different from Cr^{4+}:YAG.

In Cr^{4+}:forsterite, the strongest peaks in visible and NIR regions were observed differently for **E**//a and **E**//c polarizations, respectively. On the other hand, in

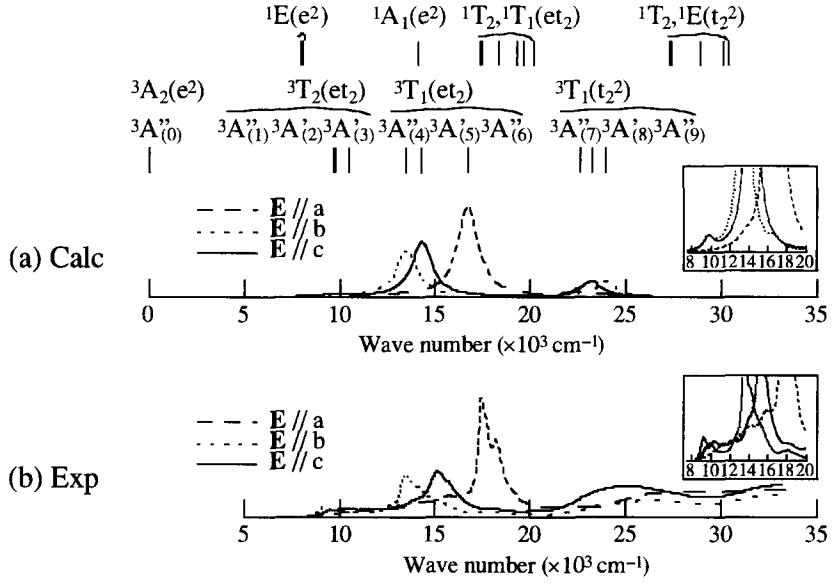

Fig. 4. (a) The calculated multiplet energy and absorption spectrum by the Cr^{4+}:forsterite model. (b) The experimentally obtained absorption spectrum by Verdún et al. [9]. Details are in the inset.

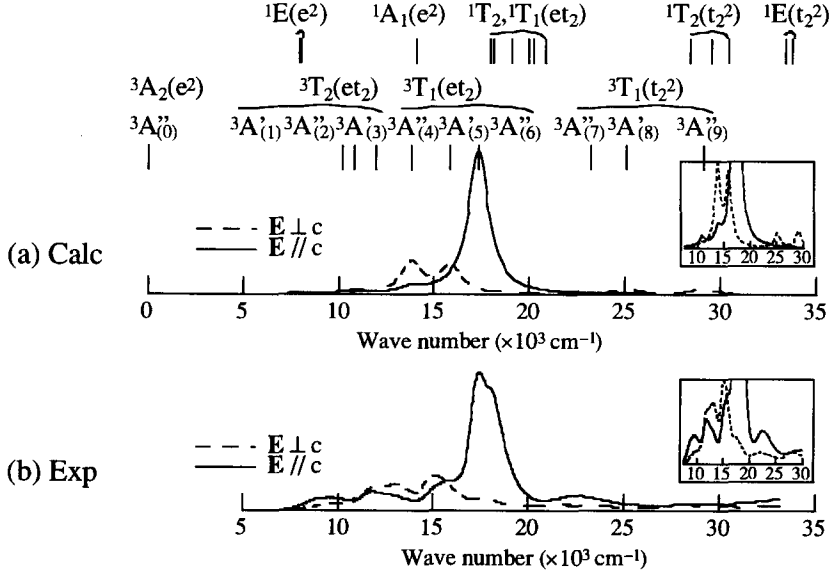

Fig. 5. (a) The calculated multiplet energy and absorption spectrum by the Cr^{4+}:åkermanite model. (b) The experimentally obtained absorption spectrum by Garrett et al. [10].

Cr^{4+}:åkermanite, the strongest peaks in visible and NIR regions were for the same **E**//c polarization. Thus, the polarization dependence was differently obtained between forsterite and åkermanite, although the CrO_4 tetrahedra had a similar structure. As indicated by the analysed results of impurity-level MOs, the atoms outside the CrO_4 tetrahedra should have to do with the polarization dependence. Actually, it was already confirmed by another calculation by a $(CrO_4)^{4-}$ åkermanite model that the polarization of the strongest peak in NIR region was **E**⊥c, which corresponds to (**E**//a + **E**//b) polarization in Cr^{4+}:forsterite. The results suggested that the traditional CrO_4 model is not appropriate to discuss polarization dependence. To handle explicitly many-electron wave functions is needed when the discussion is on transition probability.

4. SUMMARY

Multiplet-structure calculations for the analysis of the optical absorption spectra in Cr^{4+}:YAG, Cr^{4+}:forsterite, and Cr^{4+}:åkermanite were performed by a nonempirical method, independent of the traditional ligand field theory. In Cr^{4+}:YAG, both the NIR and visible bands were attributed to the transitions to the states originating from the same $^3T_1(et_2)$ parent term with a large ligand-field splitting. In Cr^{4+}:forsterite and Cr^{4+}:åkermanite, the different polarization dependence was observed. It indicated that the atoms outside the CrO_4 circumstance should be included in the model when we want to discuss not only peak position but also the transition probability.

ACKNOWLEDGEMENT

This study was supported by a Grant-in-Aid for Scientific Research from the Ministry of Education, Sports, and Culture. Author T. Ishii is the Postdoctoral Research Fellow of Japan Society for the Promotion of Science.

REFERENCES

(1) S. Sugano, Y. Tanabe, and H. Kamimura, *Multiplets of Transition-Metal Ions in Crystals* (Academic, New York, 1970).
(2) K. Ogasawara, T. Ishii, I. Tanaka, and H. Adachi, Phys. Rev. B **61,** 143 (2000).
(3) T. Ishii, K. Ogasawara, and H. Adachi, J. Chem. Phys. **116,** 471 (2002).
(4) K. Ogasawara, T. Iwata, Y. Koyama, T. Ishii, I. Tanaka, and H. Adachi, Phys. Rev. B **64,** 115413 (2001).
(5) T. Ishii, K. Ogasawara, I. Tanaka, and H. Adachi, Mat. Trans., JIM, **40,** 416 (1999).
(6) C. Satoko, M. Tsukada, and H. Adachi, J. Phys. Soc. Jpn. **45,** 1333 (1978).
(7) F. Euler and J. A. Bruce, Acta Crystallogr. **19,** 971 (1965).
(8) J. R. Smyth and R. M. Hazen, Am. Mineral. **58,** 588 (1973).
(9) Y. A. Malinovskii and Z. V. Panina, Kristallografiya **42,** 1022 (1997) [Crystallogr. Rep.

42, 946 (1997)].
(10) S. Kück, K. Petermann, U. Pohlmann, and G. Huber, J. Lumin. **68**, 1 (1996).
(11) H. Eilers, U. Hömmerich, S. M. Jacobsen, W. M. Yen, K. R. Hoffman, and W. Jia, Phys. Rev. B **49,** 15505 (1994).
(12) Verdún, L. M. Thomas, D. M. Andrauskas, and A. Pinto, in *OSA Proceedings on Tunable Solid State Lasers, Vol. 5,* 1989, edited by M. L. Shand and H. P. Jenssen (Optical Society of America, Washington, DC, 1989), p. 85.
(13) M. H. Garrett, V. H. Chan, H. P. Jenssen, M. H. Whitmore, A. Sacra, D. J. Singel, and D. J. Simkin, in *OSA Proceedings on Advanced Solid-State Lasers, Vol. 10, 1991*, edited by G. Dubé and L. Chase (Optical Society of America, Washington, DC, 1991), p. 76.

Theoretical Calculations of Positron Annihilation Characteristics in Inorganic Solids – Recent Advances and Problems

M. Šob[1], H. Sormann[2], J. Kuriplach[3]
[1] *Institute of Physics of Materials, Academy of Sciences of the Czech Republic, Žižkova 22, CZ-616 62 Brno, Czech Republic*
[2] *Institut für Theoretische Physik, Technische Universität Graz, Petersgasse 16, A-8010 Graz, Austria*
[3] *Department of Low Temperature Physics, Charles University, V Holešovičkách 2, CZ-180 00 Prague 8, Czech Republic*

(Received December 19, 2001; accepted December 28, 2001)

Abstract
Principles and applications of positron annihilation spectroscopy to electronic structure and defect studies are briefly reviewed and some recent advances and pending problems are illustrated by specific examples. In particular, it turns out that the sensitivity of calculated momentum densities of electron-positron annihilation pairs (MDAP) to the choice of electron crystal potential is higher or comparable to its sensitivity with respect to the choice of description of the electron-positron interaction. As a result, it is very hard to distinguish between various electron-positron interaction theories on the basis of the comparison of theoretical and experimental MDAPs. Furthermore, the positron affinity is determined theoretically for several systems having a band gap (semiconductors, insulators). It appears that the calculated positron affinities are significantly underestimated when compared to experimental data and, apparently, electron-positron interactions in such systems are not described satisfactorily by contemporary theoretical approaches. The above examples are related rather to electronic structure studies, but positrons are often used to investigate various open-volume defects in solids, which is dealt with in the last illustration. A non-selfconsistent computational technique suitable for the theoretical examination of configurations having large number (thousands) of non-equivalent atoms has been updated recently to treat non-periodic solids. It is based on the superposition of atomic densities in order to approximate the electronic density of the system studied. Though the charge redistribution due to selfconsistency effects is neglected, positron annihilation characteristics are determined quite reasonably. This allows for studying properties of extended defects like grain boundaries (and other interfaces), dislocations, precipitates, etc., which is very helpful when interpreting experimental positron annihilation data. Our technique is demonstrated for the case of nanocrystalline Ni where realistic atomic configurations are taken from large-scale molecular dynamics simulations.

ADVANCES IN QUANTUM CHEMISTRY, VOLUME 42

0065-3276/03 $35.00

CONTENTS

1. INTRODUCTION

Positron annihilation spectroscopy (PAS) is one of the experimental methods enabling us to probe the microstructure and electronic structure of matter up to atomic dimensions. Its applications extend from advanced problems of solid state physics and materials science to industrial use. The PAS is applied to the studies of electron characteristics and magnetic structure of solids, defects in materials, plastic deformation at low and high temperatures, phase tranformations in alloys, etc. (the recent development of PAS is documented in the Proceedings of the latest positron annihilation conferences [1–4] and in the Proceedings of the Enrico Fermi Summer Schools [5, 6]). During the last two decades, PAS became a standard tool in solid state physics and materials science. It is also widely used in chemistry, biology and medicine (e.g., for location of tumors). The process of measurement does not influence the properties of the investigated sample; therefore, the PAS is a non-destructive testing approach which does not exclude a study of the same sample by another methods. Experimental equipment for many applications is commercially produced and is relatively cheap. This is the reason why more and more research laboratories use the PAS not only for basic research, but also, e.g., for diagnostics of machine parts working in hard conditions and for characterisation of high-tech materials.

In electronic structure studies, strong electron-positron (e-p) interaction is an unwelcome complication. It deforms the electron wave functions and, therefore, the information on electronic structure is somewhat encoded. However, it is this interaction which makes the PAS so sensitive to open-volume crystal lattice defects. It turns out that for a thorough interpretation of positron annihilation data, a theoretical analysis supported by ab initio electronic structure calculations is indispensable to determine how the various features of electron density and defect configuration are reflected by positron annihilation signal and to draw some quantitative conclusions. The usefulness of information recovered from experimental data is therefore crucially dependent on the accuracy of the description of electronic structure itself and of e-p interaction.

The purpose of the present work is to discuss some recent advances and pending problems in applications of modern PAS. In Section 2, principles and methods of PAS are briefly summarized. Section 3 deals with the sensitivity of calculated MDAPs to electron crystal potential and to e-p interaction; quantitative illustrative examples are given. In Section 4, recent problems in calculations of positron affinities in semiconductors and insulators are discussed. Section 5 shows some possibilities of PAS in studying defect configurations at nanoscale; grain boundaries in nanocrystalline Ni are employed as an example. Section 6 summarizes our conclusions and gives some outlooks for future work.

2. PRINCIPLES AND APPLICATIONS OF THE POSITRON ANNIHILATION SPECTROSCOPY

Positron is an antiparticle of an electron. It was theoretically predicted by P. Dirac in 1928 and experimentally discovered by C. Anderson in 1932. Positrons, as antimatter counterparts of electrons, have the same mass and the same lifespan as electrons (they are stable, do not decay), but opposite electric charge. If a positron meets an electron, the annihilation process takes place; in most cases, two γ-quanta arise according to the equations

$$e^+ + e^- \rightarrow 2\,\gamma, \tag{1}$$

$$E_{2\gamma} = 2\,m_0\,c^2 + E_{e+} + E_{e-}, \tag{2}$$

$$m_0\,c^2 = 0.511\,\mathrm{MeV}, \tag{3}$$

where $E_{2\gamma}$, E_{e-} and E_{e+} are the energies of the resulting γ-quanta pair and of annihilating electron and positron, respectively, m_0 is the rest mass of the electron (and also of the positron) and c is the velocity of light. On the Earth, there is a lot of electrons attracted to a positron by strong Coulomb interaction (Fig. 1); therefore, the typical positron lifetime (till annihilation) is about 100–1000 ps.

Fig. 2 shows a positron sitting in a vacancy in some crystalline material. While the positron is gathering information about its neighborhood (its wavefunction is,

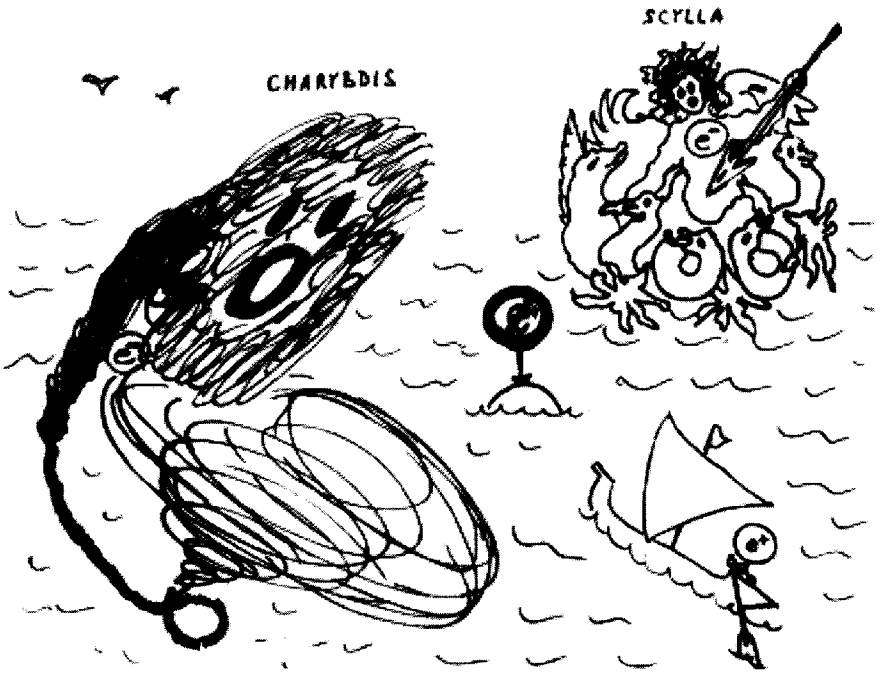

Fig. 1. The challenges a positron must face in our (non-anti)material world. For a positron, electrons constitute the same danger as Scylla and Charybdis for mythological Ulysses.

roughly speaking, adjusted to its environment), the electron counter intelligence service is hunting for it. The electrons feel the positron electrostatic field and, sooner or later, one of the electrons will get the positron (Fig. 3), either as a young man aged around 100 ps, or as an old greybeard of 500 ps (these positron lifetimes are typical for metals).

However, the information positron gathered about its neighborhood during its lifetime is not lost. It is contained in the characteristics of the γ-quanta which advise us about the annihilation event. Today, using modern electronic equipment, we are able to decode this information and to learn more about the surroundings of positron before the annihilation.

In a more scientific language the process of positron annihilation may be described as follows (Fig. 4). A positron generated in some source (usually a radioactive nucleus, such as ^{22}Na, ^{44}Ti, ^{64}Cu, ^{58}Co or ^{68}Ge) penetrates into a sample and reduces its energy from several MeV to the level of $\sim kT \approx 0.03$ eV by ionization collisions and electron and plasmon excitations within about 5 ps (k is the Boltzmann constant,

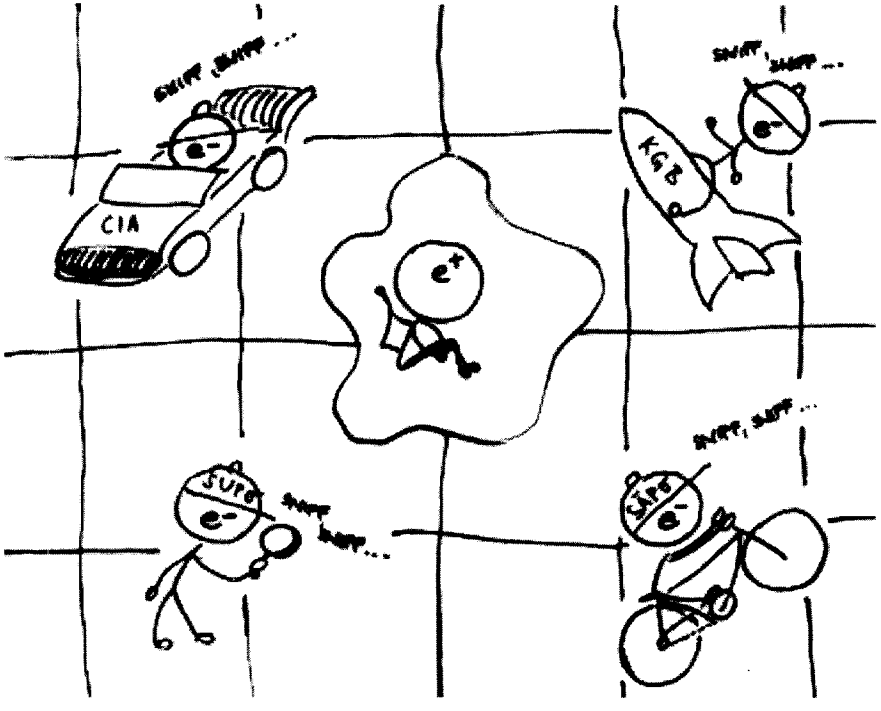

Fig. 2. A positron gathering information about its environment. The electron counter intelligence service is searching for it. Due to the strong Coulomb attraction, an electron screening cloud is formed around the positron. The positron's picoseconds are numbered.

T is the absolute temperature). In the case of ^{22}Na, the birth of a positron is indicated by the emission of a γ-quantum of energy of 1.28 MeV. During the subsequent time interval τ (typically 100–500 ps, depending on the material and its structure) this thermalized positron annihilates with an electron, the energy of which is of the order of 1–10 eV. In most cases, two γ-quanta with energy of 511 keV $\pm\Delta E$ arise (the probability of creation of more photons is quite low). They propagate in the directions deviating from 180° by the angle Θ (Fig. 4). The energy of 511 keV is equivalent to the rest mass of an electron or a positron. As the energy and momentum of the thermalized positron is negligible with respect to the energy and momentum of a typical electron, the ΔE and Θ correspond to the energy and momentum of annihilated electron. Angular correlation positron annihilation spectrometers measure the lateral component of the photon-pair momentum, which is proportional to the deviation Θ of the γ-quanta from the straight direction. In a Doppler-broadening experiment, the longitudinal component of the photon-pair momentum is recorded, proportional to

Fig. 3. The positron annihilation event. The information the positron has gathered is taken away by the pair of annihilation photons to our fast-electronics γ-ray detectors, where it is decoded and analyzed.

the deviation ΔE of photon energy from the rest mass of the electron (or positron). The positron lifetime is registered as the time difference between the emission of the γ-quantum generated almost simultaneously with the positron and one of the 511-keV annihilation γ-quanta. The lifetime τ of a positron in the material is inversely proportional to the electron density at the site where positron was annihilated. Measurement of angular correlation, Doppler broadening and positron lifetime represent three basic techniques of PAS. Let us note that there are also other positron techniques as low-energy positron diffraction, positron-annihilation-induced Auger electron spectroscopy, positron re-emission spectroscopy and age-momentum correlation [4, 6]. Recent developments include also slow-positron beam techniques where monoenergetic positrons of energy of 1–40 keV are used for investigations of structure of surface layers and yield depth-resolved information on open-volume defects like vacancies, vacancy clusters, voids, etc., up to the depth of 4000 nm [4, 6–8].

The main areas of applications of PAS in solid state physics and materials science today are:

1. **Electronic structure of metallic and superconducting materials.** Here PAS yields important information on electron momentum distribution

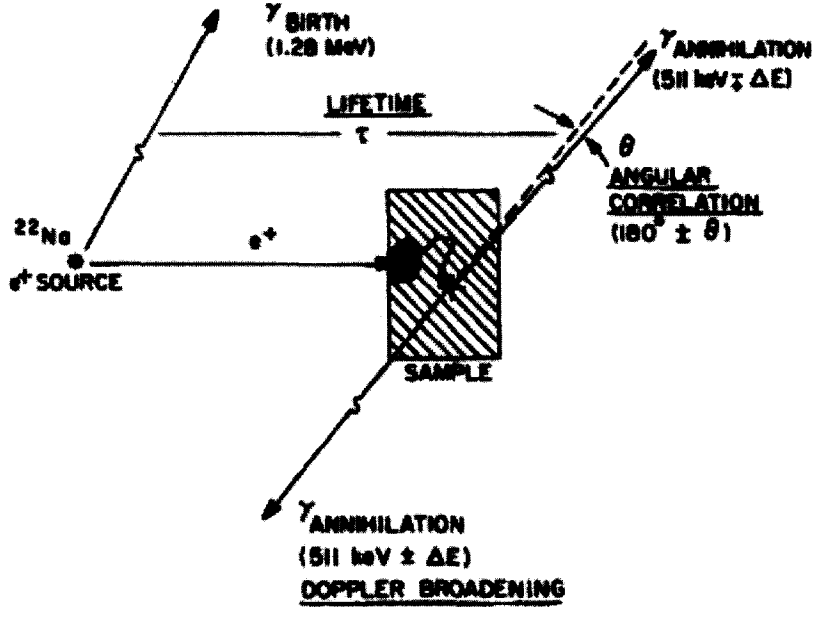

Fig. 4. Positron annihilation in a solid sample and basic positron annihilation experiments [9, 10].

and on topology of Fermi surface. In comparison with the other methods of Fermi surface investigations, the PAS does not require low temperatures, strong magnetic fields and high purity of the samples and, therefore, we can study, for example, the Fermi surface geometry of concentrated alloys, changes of electronic structure at phase transitions, etc.

2. **Defects in solids.** Positrons are preferably localized at the open-volume defects such as vacancies, vacancy clusters, dislocation cores, voids, etc. For example, PAS belongs to the most accurate methods for determination of vacancy formation enthalpies. It also yields useful information on distribution and type of open-volume defects. The latest development of the Doppler broadening (DB) technique has led to an essential improvement of defect recognition possibilities by PAS. In particular, the significant reduction of the background in the high-momentum regions of DB spectra allows for the identification of the atomic environment of positron trapping sites [11–13].

3. SENSITIVITY OF CALCULATED MOMENTUM DENSITIES TO CRYSTAL POTENTIAL AND ELECTRON-POSITRON INTERACTION

A very important feature of positron annihilation is a strong Coulomb e-p interaction. As mentioned in the introduction, it may be considered as a blessing in defect studies as it greatly enhances the sensitivity of positrons to open-volume defects (see, e.g., [5, 6, 14]). On the other hand, it is taken as a curse in electronic structure investigations. Namely, it is many-body and long-range, which is hard for a thorough theoretical description. It deforms electron and positron wavefunctions and, in this way, it changes information on electronic structure we get from PAS (see, e.g., [5, 6, 15, 16]). In the last decades, there were a lot of various theories of e-p interaction in solids. Some of them are quite sophisticated, but it seems that none of them is able to explain fully all aspects of e-p interaction. And there is one important question we want to address in this contribution: How much we are able, on the basis of comparison of theoretical and experimental results, to distinguish (or to quantify) various e-p interaction theories? Can we decide which one is better or more realistic?

For this purpose, we have undertaken several "sensitivity studies" to see how the momentum densities of annihilation pairs (MDAP) are sensitive to (i) various crystal potentials and (ii) various e-p interaction theories [17–20]. Here we would like to summarize briefly the most important results of these studies and draw some major conclusions.

3.1. The effect of crystal potential

Let us suppose that we calculate the MDAP for some material from first principles, i.e., from the fundamental quantum theory. The MDAP $\rho(\mathbf{p})$ within the local-density approximation is given by

$$\rho(\mathbf{p}) = \sum_{n\mathbf{k}} f(n,\mathbf{k})\,\delta(\mathbf{p}-\mathbf{k}-\mathbf{K}) \left| \int_{\Omega} d^3r\, \exp(-i\mathbf{p}\cdot\mathbf{r}) \times \sqrt{g_{\mathrm{ep}}(\mathbf{r};n\mathbf{k})}\,\psi_{n\mathbf{k}}(\mathbf{r})\psi_{+}(\mathbf{r}) \right|^2 , \tag{4}$$

where $\hbar\mathbf{p}$ represents the electron-positron pair momentum and $f(n,\mathbf{k})$ denotes the Fermi-Dirac distribution function for an electron state of band index n and (reduced) Bloch vector $\mathbf{k}$. The functions $\psi_{n\mathbf{k}}$ and ψ_{+} are the wave functions of an electron in the state $|n\mathbf{k}\rangle$ and of a thermalized positron, both normalized to unity in the volume of the Wigner-Seitz cell Ω. Further, $\mathbf{K}$ denotes a reciprocal-lattice vector such that $\mathbf{p}-\mathbf{K}$ lies in the first Brillouin zone. The two-particle e-p correlation function $g_{\mathrm{ep}}(\mathbf{r};n\mathbf{k})$ is, in general, dependent both on the positron position $\mathbf{r}$ and

electron state $|n\mathbf{k}\rangle$. It describes the formation of a screening electron cloud and the enhancement of the electron density around the positron (Fig. 2). Eq. (4) gives the MDAP *per spin direction*, i.e., without a factor 2 for the spin degeneracy.

To get the electron and positron wavefunctions, we must calculate the electron and positron crystal potential. For the calculation of MDAP according to Eq. (4), we must also adopt some e-p interaction theory to obtain the e-p correlation function g_{ep}.

Most electronic structure calculations determining the electron and positron crystal potential are performed within the density functional theory. They may differ in the choice of exchange-correlation energy (usually, in the local-density approximation, formulas of von Barth-Hedin [21], of Perdew and Zunger [22] and of Vosko-Wilk-Nusair [23] are used, the last two parametrizing the electron-gas data of Ceperley and Alder [24], in generalized-gradient approximation one often adopts the formulas of Perdew et al. [25] or of Perdew, Burke, and Ernzerhof [26]). In most cases, the calculations are converged to self-consistency, i.e., the electron density obtained from the electron crystal potential V_{e} generates, within some tolerance, the same electron crystal potential.

Let us suppose that we will employ some electron crystal potential $V_{\mathrm{e}}^{(\alpha)}$ and get some MDAP $\rho^{(\alpha)}$ and, when using some another potential $V_{\mathrm{e}}^{(\beta)}$, we arrive at the MDAP $\rho^{(\beta)}$ (applying the same e-p interaction theory in both cases). The sensitivity s_V of the MDAP with respect to the electron crystal potential may be defined as [17–20]

$$s_V = \frac{\Delta\rho_j^{(\alpha,\beta)}}{\Delta V_{\mathrm{e}}^{(\alpha,\beta)}}, \tag{5}$$

where the *relative deviation in the potential* is given by

$$\Delta V_{\mathrm{e}}^{(\alpha,\beta)} \equiv \frac{\int_\Omega d^3r\, |V_{\mathrm{e}}^{(\alpha)}(\mathbf{r}) - V_{\mathrm{e}}^{(\beta)}(\mathbf{r})|}{\int_\Omega d^3r\, |V_{\mathrm{e}}^{(\alpha)}(\mathbf{r})|} \tag{6}$$

and the *relative deviation in the momentum densities* is defined by

$$\Delta\rho_j^{(\alpha,\beta)} \equiv \frac{\int d^3k\, |\rho^{(\alpha)}(\mathbf{k}+\mathbf{G}_j) - \rho^{(\beta)}(\mathbf{k}+\mathbf{G}_j)|}{\int d^3k\, \rho^{(\alpha)}(\mathbf{k}+\mathbf{G}_j)} \tag{7}$$

with the integration in k space going over the first Brillouin zone and $\mathbf{G}_j$ indicating whether the calculation of $\Delta\rho$ is performed within the central momentum region [$\mathbf{G}_0 = (000)$] or within some Umklapp region [the nearest Umklapp regions correspond to $\mathbf{G}_1 = (2\pi/a)(110)$ for bcc metals and $\mathbf{G}_1 = (2\pi/a)(111)$ for fcc metals (a is the lattice constant)].

3.2. The effect of electron-positron interaction

Alternatively, we could define the sensitivity s_T of MDAP with respect to various e-p interaction theories (for a fixed electron crystal potential V_e) as

$$s_T = \frac{\Delta\rho}{\Delta T}. \tag{8}$$

However, it is difficult to quantify the difference ΔT between different e-p interaction theories; we do not know how to do that. Therefore, the sensitivity of MDAP to these theories may be estimated only by comparison of the resulting MDAPs.

An important problem consists in the fact that the sensitivity of MDAP with respect to various crystal potentials is too high, whereas it is too low with respect to various e-p interaction theories. It may happen that $\Delta\rho$ due to uncertainties in the crystal potential (e.g., in the exchange-correlation potential) may be comparable or even higher than $\Delta\rho$ due to different e-p interaction theories. For example, let us suppose that the Vosko-Wilk-Nusair formula for the exchange-correlation energy [23] is the best choice in the crystal potential. In this case, a certain e-p interaction theory, say theory A, will give the best agreement with the experimental MDAP. However, when we suppose that possibly the von Barth-Hedin exchange-correlation energy [21] is the best choice, it may happen that some another e-p interaction theory, say theory B, yields the best agreement with experiment. Then the question is: How to decide which e-p interaction theory is better?

3.3. Illustrative examples

Let us illustrate this situation on the series of 4*sp* and 3*d* metals with atomic numbers from 19 (K) to 30 (Zn). Most of these metals have the body-centered cubic (bcc) or face-centered cubic (fcc) crystal structure; Sc, Ti, Co, and Zn, with their hexagonal close-packed (hcp) structure, are also treated as fcc metals with the same atomic volume as in the hcp case. For comparison, the results for alkali metals are also presented.

To see the sensitivity of MDAP with respect to various crystal potentials, we employed the following ones:

$V_e^{(M)}$: Non-selfconsistent muffin-tin potentials based on Mattheiss' construction scheme [27], i.e., on a superposition of atomic electron densities. The exchange-correlation part of the potentials has been approximated according to Slater formula. For all *d*-band metals investigated in the present study, the atomic configuration $3d^{n-1}\,4s^1$ has been used as it turned out that this configuration is closer to the atom state in a solid than is the configuration $3d^{n-2}\,4s^2$ (see Refs. [28] and [29]). Also the non-selfconsistent calculations with these configurations and full Slater exchange

are, as a rule, in a good accordance with the self-consistent calculations using a better treatment of the exchange-correlation potential [30, 31].

$V_e^{(CA)}$: Selfconsistent muffin-tin potentials, obtained by the conventional non-relativistic augmented-plane-wave method. For the exchange-correlation part of the potentials, we used a local-density approximation based on correlation energy calculations by Ceperley and Alder [24] (CA) in the parametrized form of Vosko *et al.* [23].

$V_e^{(S)}$: Self-consistent muffin-tin potentials, where only the exchange part of the electron-electron interaction according to Slater formula is taken into account, and correlation effects are completely neglected.

The positron potentials $V_p^{(M)}$, $V_p^{(CA)}$, and $V_p^{(S)}$ have been obtained by taking the corresponding electron potentials without the exchange-correlation terms and by using the opposite sign compared to that for the electrons.

We would like to stress here that we have chosen these three potentials as *examples* to investigate the influence of various approximations to crystal potentials frequently used in MDAP calculations, e. g. employing various electron exchange-correlation potentials.

Now, we may compare all pairs of potentials. (CA,S) represents the comparison of two selfconsistent potentials with different choices of the exchange-correlation (xc) part. (M,S) corresponds to the comparison of potentials including the same approximation of the xc part of the potentials (namely, simply Slater exchange), but without or including selfconsistency. Consequently, the comparison of (CA,M) demonstrates the combined influence of these two effects.

The muffin-tin type potentials are spherically symmetric inside the muffin-tin spheres with the radius r_{MT} and constant in the interstitial region Ω_{out}; this constant is given by the average value of the crystal potential in the interstitial region. As the crystal potential is determined up to an additive constant, we may shift it such that its constant value in Ω_{out} is equal to zero; this is the reason why it is also called the muffin-tin zero. However, if we compare two muffin-tin potentials, their shape may be quite different and their average values in the interstitial space do not have to be the same. In addition to that, there is no absolute scale for the crystal potentials [32] so that we do not know *a priori* how to adjust the compared potentials with respect to each other. Therefore, we better define the relative deviation of both potentials as a function of the parameter η

$$\Delta V_e^{(\alpha,\beta)}(\eta) \equiv \frac{4\pi \int_0^{r_{MT}} dr\, r^2 |V_e^{(\alpha)}(r) - V_e^{(\beta)}(r) + \eta| + \Omega_{out}|\eta|}{4\pi \int_0^{r_{MT}} dr\, r^2 |V_e^{(\alpha)}(r)|}, \qquad (9)$$

where η means the difference between the constant parts of the two potentials within Ω_{out}, the volume between the surface of the muffin-tin sphere and the boundary of the Wigner-Seitz cell. We choose η such that ΔV_e becomes a minimum; such a

comparison seems to be more appropriate than just to set the averages of both crystal potentials in the interstitial space to the same value, i.e., to put $\eta = 0$ in Eq. (9). All values of ΔV_e used in this work are based on this method. It turns out, *a posteriori*, that the physical conclusions are not dependent on the fact whether Eq. (9) is evaluated using $\eta = 0$ or whether the minimum values of ΔV_e are used. The integral in the denominator of the expression (9) is evaluated setting the value of $V_e^{r(\alpha)}$ in the interstitial region to zero.

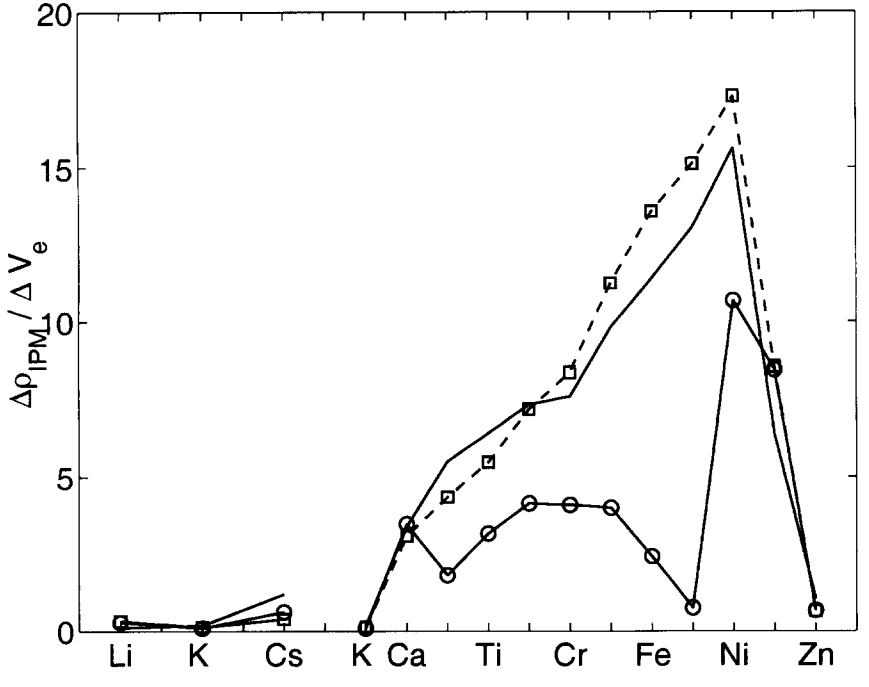

Fig. 5. Valence sensitivities s_V of the MDAPs in the central momentum region [G_j=(000)] calculated within the IPM in alkali metals (Li, K, Cs), calcium, and the series of metals from scandium to zinc. The values of η in Eq. (9) are chosen such that the ΔV_e are minimum – see the discussion in the text. For clarity of the figure, only every second name of the series Ca→Sc→Ti→V→ Cr→Mn→Fe→Co→Ni →Cu→Zn is indicated along the horizontal axis. Solid lines with circles: comparison of potentials (CA,M); dashed lines with squares: comparison of potentials (CA,S); solid lines: comparison of potentials (M,S).

As an illustration, let us show here (Fig. 5) the sensitivities s_V [Eq. (5)] of the MDAP due to the valence electrons (further called valence sensitivities) calculated within the central momentum region for alkali metals, calcium, and the series of

metals from Sc to Zn within the independent particle model (IPM), i.e., using $g_{ep}(\mathbf{r}; n\mathbf{k}) \equiv 1$ in Eq. (4); a detailed discussion of sensitivities of MDAP due to valence and core electrons both in central momentum regions and in Umklapp regions may be found in [19] together with the analysis of sensitivities of electron momentum densities; there we can see the net effect of the changes in electronic structure (without the positron).

It may be seen from Fig. 5 that for the alkali metals and for all cases investigated [(CA,M), (CA,S), and (M,S)], s_V exhibits relatively small values (an extended discussion of these results is given in Ref. [17]). Generally, for the 3*d* metals, the valence sensitivities are significantly higher than for the alkali metals, and a detailed interpretation of the sensitivity profiles is quite complicated. In order to discuss these results properly, it is necessary to remember that – in contrast to the alkali metals – more than one valence band contributes to the momentum density. If we investigate separately the MDAP values due to the *first* (energetically lowest) valence band and due to the *higher* valence bands, we learn that the individual contributions to $\Delta\rho$ are quantitatively similar and of the opposite sign. For these reasons, we should expect a cancellation of the potential-caused deviations for the *first* and the *higher* bands resulting in small sensitivities of the MDAP for the whole *d*-band region. However, this expectation is not fulfilled by the results for the pairs (CA,S) and (M,S). On the contrary, we observe a monotonous increase of these quantities from K over Ca and all 3*d* metals up to nickel where remarkable values of s_V of 15 and more are reached, indicating that the MDAP of the 3*d* metals is very sensitively influenced both by the xc part of the crystal potential and by the fact whether the potential is selfconsistent or not. The reason for this increase is that the *first* valence band is always completely occupied whereas – for most of the 3*d* metals – some of the higher bands intersect the Fermi level and are therefore only partially occupied. Consequently, the cancellation effect mentioned above is *incomplete* for all metals from Sc to Ni; only for the last two metals investigated, copper and zinc, with their completely filled 3*d* shells, this compensation effect is *nearly* (Cu) or *completely* (Zn) perfect which explains the abrupt decrease of the sensitivity curves in Fig. 5 for these metals.

On the basis of the similarity of the curves (CA,S) and (M,S), it may be concluded that the sensitivity of MDAP to various xc terms is roughly the same as the sensitivity due to the fact whether the potentials are selfconsistent or not.

Until now, we have not discussed the curve for (CA,M) in Fig. 5 with its relatively complicated shape. At first, we observe that for all 3*d* bands (except for Cu and Zn), the sensitivity for (CA,M) is smaller than both the sensitivities for (CA,S) and (M,S). This indicates a further compensation process, namely, between the effects of different xc potentials and of selfconsistency. Another strange feature of this curve is its decrease for Mn $\rightarrow$ Fe $\rightarrow$ Co, followed by a steep increase to Ni and Cu. As a result of numerous calculations, we got out that this behavior is due

Table I. Atomic and metallic electron configurations for K, Ca, and the $3d$ transition metals. E_0 and E_F mean the valence electron bottom energy and the Fermi energy in Ry, calculated by using the $V_e^{(CA)}$ electron crystal potentials. The definition of the energy E_1 and the meaning of the terms *first* band and *higher* bands are given in the text.

	atomic configuration of valence electrons:						metallic configuration of valence electrons:	
	total	3d	4s	E_0	E_1	E_F	first band	higher bands
K	1		1	0.0003		0.1614		
Ca	2		2	–0.0101		0.2729		
Sc	3	2	1	0.0662	0.3889	0.4340	1.964	1.036
Ti	4	3	1	0.1391	0.4645	0.5677	1.920	2.080
V	5	4	1	0.2169	0.5248	0.6765	1.745	3.275
Cr	6	5	1	0.2231	0.5309	0.7695	1.648	4.352
Mn	7	6	1	0.1096	0.4498	0.6564	1.921	5.079
Fe	8	7	1	0.0905	0.4326	0.6744	1.751	6.249
Co	9	8	1	0.0423	0.4111	0.6576	1.927	7.073
Ni	10	9	1	–0.0005	0.3816	0.6245	1.919	8.081
Cu	11	10	1	–0.0752	0.2832	0.5975	1.893	9.107
Zn	12	10	2	–0.2028	–0.0694	0.5467	1.541	10.459

to a change of the sign of the differences between $\rho^{(CA)}$ and $\rho^{(M)}$: $\rho^{(CA)} < \rho^{(M)}$ for all metals before Co and $\rho^{(CA)} > \rho^{(M)}$ for Ni and Cu (after Co) nearly everywhere in the central momentum zone, leading to the very small value of $s_V^{(val)} \approx 0.76$ for the sensitivity of valence MDAP in Co.

To make the interpretation of the above results more transparent, let us divide the k space integral in the numerator of the expression (7) into two parts: for the first valence band and for the other valence bands. For this purpose, we define for each metal the energy E_1 which separates the first band from the higher bands. This definition is illustrated by Figs. 6 and 7, where we show the eigenvalues of valence electrons in fcc scandium (Fig. 6) and copper (Fig. 7) as a function of $|\mathbf{k}|$, i.e., without taking into account the direction of the Bloch vector. The energy E_1 is represented by the mean value of the maximum energy of the lowest band and the minimum energy of the second-lowest band.

The results of this procedure for the electron bands obtained by using self-consistent crystal potentials $V_e^{(CA)}$ is given in Table I where we show the values of the bottom valence energy E_0, the above defined energy E_1, and the Fermi energy E_F for the metals investigated, together with the numbers of electrons per unit cell which belong to the *first* band and to the *higher* bands. We may see that the number of electrons in the *first* band is always higher than the number of $4s$ electrons in the

corresponding atomic configuration: this is obvious because the *first* band is in all cases more or less hybridized by the $3d$ bands and contains therefore both *sp*- and *d*-like electrons. Of course, for our purpose, the above procedure of getting E_1 is only useful for *d*-band metals and not for the alkali metals and calcium.

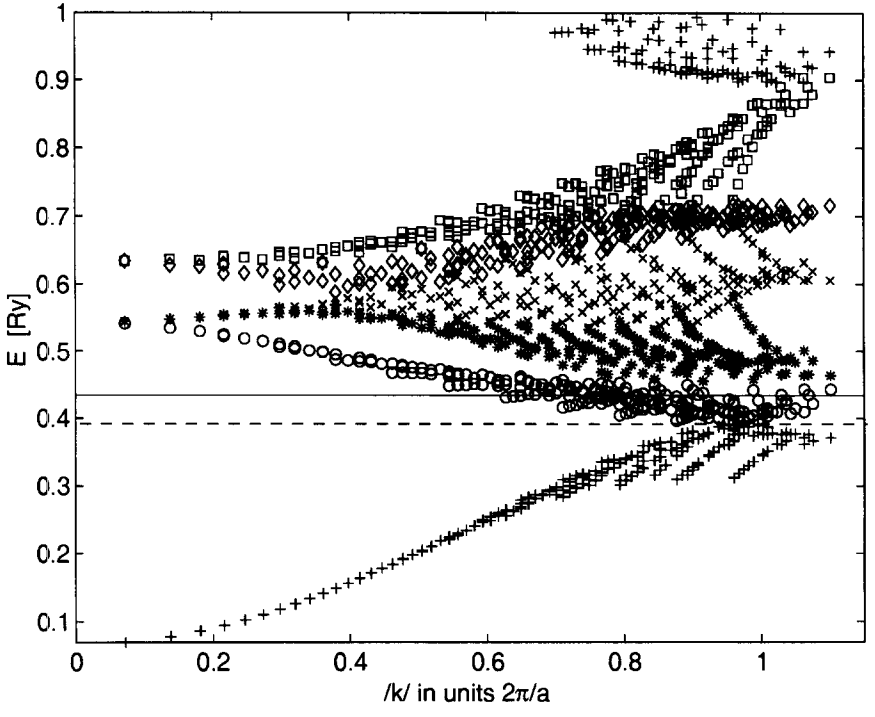

Fig. 6. Energy eigenvalues for valence electrons in fcc scandium as a function of |k| (given in units of $2\pi/a$, where a is the lattice constant of the metal). The horizontal lines indicate the Fermi energy (solid line) and the energy E_1 defined in the text (dashed line).

Let us perform now a more detailed analysis of valence sensitivities s_V for the potentials (CA,M) [solid line with circles in Fig. 5]. First, let us define a "modified" sensitivity $\bar{s}_V$ by the equation

$$\bar{s}_V = \frac{\delta\rho_j^{(\alpha,\beta)}}{\Delta V_e^{(\alpha,\beta)}} \tag{10}$$

with $\Delta V_e^{(\alpha,\beta)}$ given by Eq. (6) and

$$\delta\rho_j^{(\alpha,\beta)} \equiv \frac{\int d^3k\,(\rho^{(\alpha)}(\mathbf{k}+\mathbf{G}_j) - \rho^{(\beta)}(\mathbf{k}+\mathbf{G}_j))}{\int d^3k\,\rho^{(\alpha)}(\mathbf{k}+\mathbf{G}_j)}, \tag{11}$$

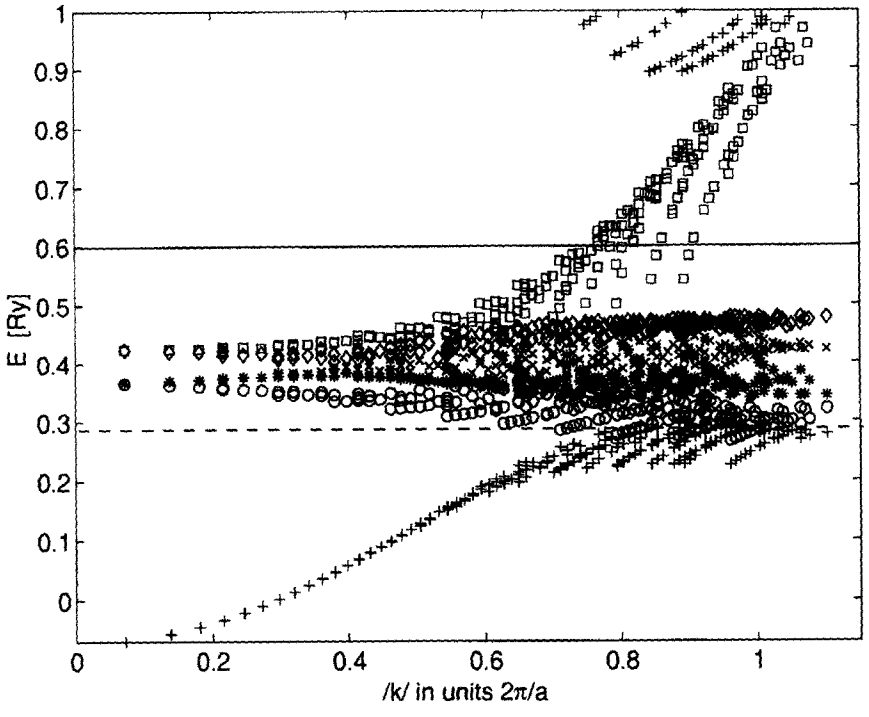

Fig. 7. Energy eigenvalues for valence electrons in fcc copper as a function of $|\mathbf{k}|$ (given in units of $2\pi/a$, where a is the lattice constant of the metal). The horizontal lines indicate the Fermi energy (solid line) and the energy E_1 defined in the text (dashed line).

i.e., similarly as in Eq. (7), but without absolute values in the numerator. Fig. 8 shows the behavior of $\bar{s}_V$ not only for the *whole energy region* $E_0 \leq E \leq E_F$, but also for the energy regions of the *first* band ($E_0 \leq E \leq E_1$) and of the *higher* bands ($E_1 \leq E \leq E_F$); the latter two will be denoted in the following as $\bar{s}_V^l$ and $\bar{s}_V^h$, respectiveiy.

Comparing the solid curve with circles in Fig. 5 with the results shown in Fig. 8, we may conclude that a relation $s_V = -\bar{s}_V = -\bar{s}_V^l - \bar{s}_V^h$ should hold for all metals from Sc to Fe, whereas for Co, Ni, Cu and Zn, a relation $s_V = \bar{s}_V = \bar{s}_V^l + \bar{s}_V^h$ should be valid. A carefull analysis of our numerical results shows that, indeed, these relations are almost perfectly fulfilled by all metals from Sc to Fe and by Ni, and quite satisfactorily by Co, Cu, and Zn. Therefore, on the basis of the behavior of $\bar{s}_V$ and its components, we can explain the behavior of s_V. It turns out that, for the greatest part of the *d*-band metals, the sensitivity s_V of MDAP due to the valence electrons

in the central momentum region with respect to the potentials (CA,M) is dominated by the contribution of electrons from the first band where the (integrated) difference $\delta\rho$ between $\rho^{(\mathrm{CA})}$ and $\rho^{(\mathrm{M})}$ within the central momentum region is negative for all metals from Sc to Fe. In all these cases, the higher bands play only a subordinate role for the s_V, but it is worth mentioning that the corresponding differences between $\rho^{(\mathrm{CA})}$ and $\rho^{(\mathrm{M})}$ are positive.

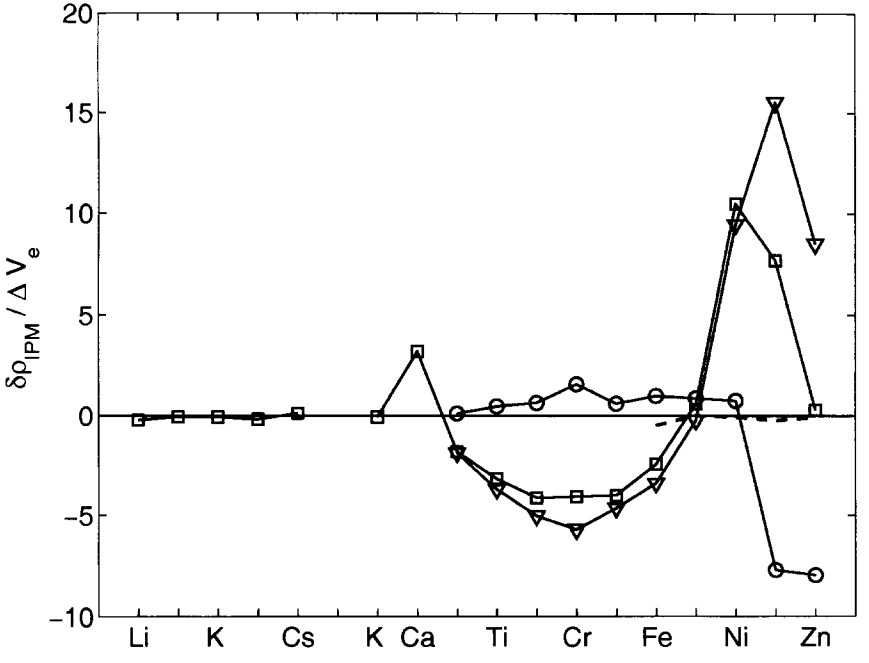

Fig. 8. The "modified" sensitivity $\bar{s}_V$ for MDAPs due to valence electrons in the central momentum region calculated for the potentials (CA, M). The curve with squares: $\bar{s}_V$ for the whole energy region, $E_0 \leq E \leq E_F$; the curve with triangles: $\bar{s}_V^l$ for the energy region of the *first* band, $E_0 \leq E \leq E_1$; the curve with circles: $\bar{s}_V^h$ for the energy region of the *higher* bands, $E_1 \leq E \leq E_F$. The energy E_1 is defined in the text and given in Table I. The dashed line from Fe to Zn shows the values of $\bar{s}_V$ for the whole energy region (i.e., a hypothetical branch of the curve with squares) under the assumption that all $3d$ bands of these metals are fully occupied.

Let us note that the behavior of $\bar{s}_V^l$ and $\bar{s}_V^h$ along the series Fe $\rightarrow$ Co $\rightarrow$ Ni $\rightarrow$ Cu $\rightarrow$ Zn is very interesting (Fig. 8). Here we observe a change of the sign of the differences $\delta\rho$ between $\rho^{(\mathrm{CA})}$ and $\rho^{(\mathrm{M})}$ (from negative to positive values for the first band, and vice versa for the higher bands), with the consequence that, for cobalt,

both the first and the higher bands show a very small sensitivity with respect to V_e. The reason for this special situation of Co cannot be understood on the basis of the present investigation. For Cu and Zn, both the first band and the higher bands show marked values (up to 16) of $\bar{s}_V^1$ and $\bar{s}_V^h$ with different signs, positive for the first and negative for the higher bands.

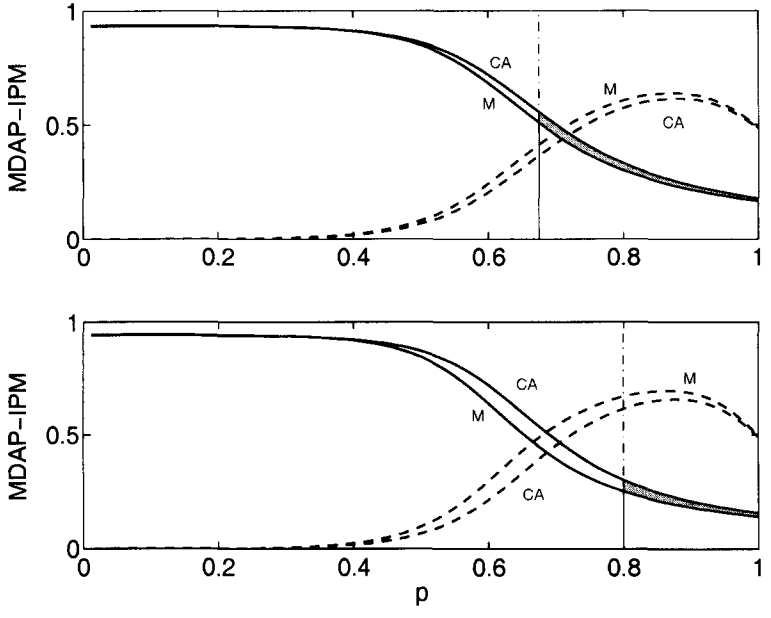

Fig. 9. The valence MDAP profiles for nickel (the upper part) and copper (the lower part) along the [100] direction in the momentum space for the *first* band (full lines) and the *higher* bands (dashed lines). The momentum p is given in units of $2\pi/a$ with a being the lattice constant. The letters CA and M refer to the corresponding crystal potentials (see the text), and the dashed-dotted lines denote the Fermi momenta. The shaded areas indicate the regions of momenta where the (integrated) differences $\delta\rho$ between $\rho^{\mathrm{M}}(\mathbf{p})$ and $\rho^{\mathrm{CA}}(\mathbf{p})$ belonging to the *first* band are not cancelled by the differences between $\rho^{\mathrm{M}}(\mathbf{p})$ and $\rho^{\mathrm{CA}}(\mathbf{p})$ belonging to the *higher* bands because the higher bands are only partially occupied. Note: despite the fact that the individual deviations between $\rho^{\mathrm{M}}(\mathbf{p})$ and $\rho^{\mathrm{CA}}(\mathbf{p})$ are significantly larger for Cu than for Ni, due to the more effective cancellation effect in copper, the sensitivity s_V for this metal is much smaller than for nickel.

Therefore, the sensitivity s_V with respect to the whole energy region is determined by a more or less pronounced cancellation of $\bar{s}_V^1$ and $\bar{s}_V^h$. This cancellation is almost perfect for zinc, leading to small values of s_V for this metal (see Fig. 8)

but only incomplete in the case of Ni and Cu which is illustrated in Fig. 9 where the shaded region indicates the contribution of the *first* valence band which has no counterpart in the *higher* valence bands. This clarifies the abrupt decrease of the s_V and $\bar{s}_V$ curves in Figs. 5 and 8, respectively, for these metals. Similar analysis may be performed also for the pairs of potentials (CA,S) and (M,S), explaining the behavior of corresponding curves in Fig. 5.

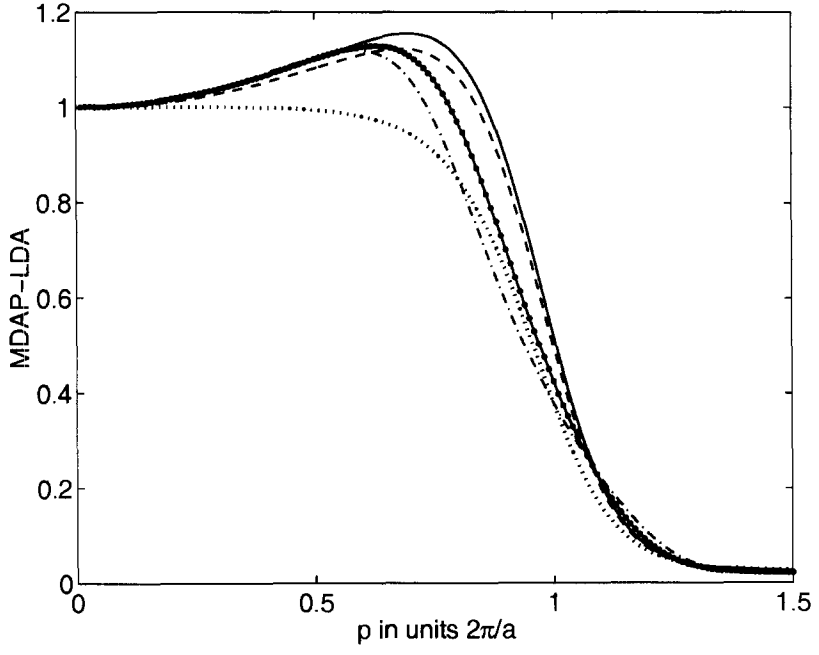

Fig. 10. Normalized MDAPs $\rho(\mathbf{p})$ in calcium along the [100] direction in the momentum space. The enhancement effects are described by the local-density approximation. Solid line: (CA) electron and positron crystal potentials, enhancement according to [41]; dashed line: (CA) potentials, enhancement according to [33, 34]; dashed-dotted line: (M) potentials, full line with dots: (S) potentials, enhancement for both curves according to [41]; dotted line: (CA) potentials, enhancement according to [44].

Now, let us discuss the sensitivity of the MDAP with respect to various e-p interaction theories. We remain in the range of local-density approximation [Eq. (4)]. According to the proposal of Daniuk *et al.* [33, 34], the e-p correlation function g_{ep} can be taken from the enhancement theory of thermalized positrons within a homogeneous electron gas (see, e.g., Refs. [35] and [36]), namely

$$g_{\mathrm{ep}}(\mathbf{r}; n\mathbf{k}) = \epsilon_{\mathrm{hom}}\left[r_{\mathrm{s}}(\mathbf{r}); \chi_{n\mathbf{k}}\right]; \quad r_{\mathrm{s}}(\mathbf{r}) = \left[4\pi n(\mathbf{r})/3\right]^{-1/3}, \tag{12}$$

with $n(\mathbf{r})$ being the total *local* density of the electron gas.

Following the ideas of Šob [37–39] and, independently, of Mijnarends and Singru [40], the quantity $\chi_{n\mathbf{k}}$ which describes the momentum-dependence of the enhancement factor can be considered as an energy- and state-dependent function. However, despite the impressing success of the local-density approximation, the physically most convincing form of $\chi_{n\mathbf{k}}$ is not clear.

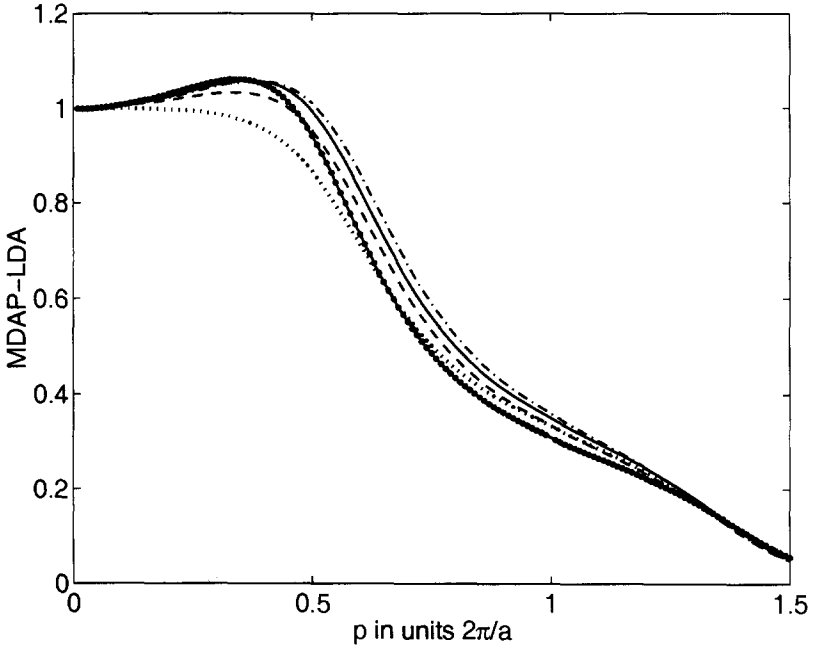

Fig. 11. Normalized MDAPs $\rho(\mathbf{p})$ in vanadium along the [100] direction in the momentum space. The description of the curves is the same as in Fig. 10.

Let us discuss here three approaches to the e-p correlation function g_{ep}:

Theory A [37–41]: Eq. (12) with

$$\chi_{n\mathbf{k}} = \begin{cases} \sqrt{(E_{n\mathbf{k}} - E_0)/(E_\mathrm{F} - E_0)} & E_{n\mathbf{k}} - E_0 \geq 0 \\ 0 & E_{n\mathbf{k}} - E_0 < 0. \end{cases} \tag{13}$$

Here E_0 is the bottom energy of the electron conduction bands and E_F is the Fermi energy.

Theory B [33, 34, 42, 43]: Eq. (12) with

$$\chi_{n\mathbf{k}}(\mathbf{r}) = \begin{cases} \sqrt{(E_{n\mathbf{k}} - V_\mathrm{e}(\mathbf{r}))/(E_\mathrm{F} - V_\mathrm{e}(\mathbf{r}))} & E_{n\mathbf{k}} - V_\mathrm{e}(\mathbf{r}) \geq 0 \\ 0 & E_{n\mathbf{k}} - V_\mathrm{e}(\mathbf{r}) < 0. \end{cases} \tag{14}$$

The values of $\chi_{n\mathbf{k}}$ according to Eqs. (13) and (14) differ considerably for the valence electrons and are quite similar (namely, small or zero) for the core electrons.

Theory C: g_{ep} according to Boroński and Nieminen [44]; it is given by

$$g_{\mathrm{ep}}(\mathbf{r}; n\mathbf{k}) = 1 + 1.23r_s + 0.8295r_s^{3/2} - 1.26r_s^2 + 0.3286r_s^{5/2} + r_s^3/6. \qquad (15)$$

Here the position dependence is included by means of $r_s(\mathbf{r})$ given in Eq. (12). No momentum dependence of the enhancement is included.

Let us assume now that we want to compare the calculated positron annihilation profiles with experimental data to get out which of these three approaches to e-p interaction is the most appropriate one.

Figs. 10 and 11 demonstrate the differences of the MDAPs calculated with various crystal potentials and e-p interaction theories in Ca and V. The solid line, solid line with dots and dash-dotted line show the effect of using various crystal potentials ($V_{\mathrm{e}}^{(\mathrm{CA})}$, $V_{\mathrm{e}}^{(\mathrm{S})}$, and $V_{\mathrm{e}}^{(\mathrm{M})}$, respectively) with the fixed e-p interaction theory (theory A), whereas the solid, dashed and dotted line exhibit the impact of employing various e-p interaction theories (A, B, and C, respectively) with the fixed crystal potential ($V_{\mathrm{e}}^{(\mathrm{CA})}$). It may be seen that the differences due to various e-p interaction theories (between the curves in the second set) are comparable and in some regions even smaller than the differences due to various crystal potentials (between the curves in the first set). This makes it very difficult or even impossible to decide, on the basis of comparison of theoretical and experimental MDAPs, which of the e-p interaction theories is better as the variations of the MDAP are masked by the effects of crystal potentials. It seems to us that a unified description of both electron-electron and electron-positron interaction in solids could solve, at least partly, this problem and would be highly desirable.

4. POSITRON AFFINITIES IN METALS, SEMICONDUCTORS AND INSULATORS

Another positron quantity related to electronic structure is the positron affinity (A_+) [45]. It can be calculated as a sum of the electron (μ_{e}) and positron (μ_p) chemical potentials, i.e.,

$$A_+ = \mu_{\mathrm{e}} + \mu_{\mathrm{p}}. \qquad (16)$$

The electron chemical potential is considered here to be the energy of the highest occupied electron state at zero temperature. The positron chemical potential is identified with the lowest positron energy. Of course, both quantities (μ_{e} and μ_{p}) have to be defined with respect to the same reference level. Alternatively, the positron affinity can be determined as a negative of the sum of electron (Φ_{e}) and positron (Φ_{p}) work functions:

$$A_+ = -(\Phi_{\mathrm{e}} + \Phi_{\mathrm{p}}). \qquad (17)$$

The positron affinity is a bulk property and does not depend on the surface characteristics of the studied material. However, when doing practical measurements of A_+, surface effects have to be carefully treated [46]. The equivalent definitions (16) and (17) are, respectively, suitable for obtaining the A_+ from theory and experiment. A necessary prerequisite to measure A_+ is that the positron work function is a negative number. Namely, it is usually measured by means of so-called positron re-emission spectroscopy [47], and if no positrons are spontaneously re-emitted from the sample (after they thermalize), the positron work function cannot be determined. To be complete, A_+ can also be obtained by measuring the formation potential of positronium atoms [48].

The practical importance of A_+ is apparent in cases when two different materials have a common interface. The most frequent case is a matrix with some embedded precipitates. Then, the difference in A_+ between the host and precipitate determines the positron potential step at the interface. For a positron, a precipitate may represent both a potential well or a barrier. In the first case, the positrons can, in principle, be trapped in the precipitate. On the basis of ab initio electronic structure calculations, it is possible to determine the height of the potential step and thereby to predict whether the positrons will be trapped or repelled by the precipitates. For instance, trapping of positrons in nano-sized lithium precipitates embedded in MgO matrix was independently verified by performing such calculations [49]. Another aspect of positron affinity is that the calculated value of A_+ can be used to estimate the positron work function (without actually measuring it) using Eq. (17) as Φ_e is known for many materials. Therefore, knowledge of positron affinity is very important in number of interesting situations.

Table II. Theoretical and experimental values of the positron affinity for selected materials.

material	type	structure	positron affinity (eV) theory	experiment
tungsten (W)	metal	bcc	-1.5[a]	-1.5[b]
diamond (C)	semiconductor	diamond	-3.0[c]	-1.2[c]
silicon carbide (3C-SiC)	semiconductor	zinc blende	-5.5[c]	-3.8[c]
magnesium oxide (MgO)	insulator	rock salt	-6.0[d]	-2.3; -4.2[d]

[a] this work, [b] [53], [c] [50] and references therein, [d] [49] and references therein.

However, the application of positron affinity is not quite free from problems. It turns out that, using the state-of-the-art approaches, the calculated positron affinity is underestimated (its magnitude is overestimated) in materials with a band gap [46, 49, 50]. Table II contains the calculated positron affinities of selected materials together with their experimental counterparts (see [46, 50] for more examples). The linear-muffin-tin-orbital (LMTO) method within the atomic sphere approximation

(ASA) [51] was employed in calculations (computational details are given in [46]). For the sake of comparison, we include also tungsten, which is a metallic system. One can see that an excellent agreement between theory and experiment was achieved in this case and a similar conclusion has been found for other studied metals [52]. On the contrary, the calculated affinities for semiconductors and insulators turn out to be too low (their magnitudes are too large) when compared to experiment.

A detailed analysis of this effect was done in Ref. [46], where three distinct polytypes of SiC were examined. Actually, both electron and positron parts of the problem were found to contribute to the deficiency presented above. As for positrons, it should be taken into account that they are not completely screened in systems having a band gap. All calculated values in Table II were obtained using the so-called semiconductor model [54] for electron-positron correlations (except for W where the correction due to incomplete positron screening has no meaning).

Of course, the calculated values of A_+ are, to some extent, sensitive to the choice of the exchange-correlation potential for electrons. To be more specific, the above values were obtained using the scheme of Ceperley and Alder [24] as parametrized by Perdew and Zunger [22]. If the potential of von Barth and Hedin [21] would be employed, the values of A_+ would be by about 0.5 eV lower (i.e., larger in magnitude). This means that one has to be careful when comparing numbers obtained using different exchange-correlation potentials. The values of μ_p (and thereby A_+) can slightly be increased (i.e., decreased in magnitude) by using another approaches to the electron-positron correlation potential [54, 55]. On the other hand, it is well known that the local density approximation (LDA) does not work satisfactorily when calculating electronic structure of semiconductors and insulators [56]. Even if this fact and its influence on the value of μ_e is considered, one can hardly get the values of A_+ which would match the experimental ones. As also concluded by Panda et al. [50], contemporary approaches to electron-positron interactions in systems having a band gap require a revision.

5. POSITRON DEFECT STUDIES IN POLYCRYSTALLINE METALS AT NANOSCALE

Positrons are used to investigate so-called open-volume defects in solids, such as vacancies and their clusters, dislocations, grain boundaries, etc., where the electron density is "less-than-average". Such defects are attractive for positrons as the repulsion of the atomic nuclei is weaker there and the positron can relax into the additional volume due to the defect with considerable energy advantage. In this way, positron samples the "free volume" in the solid and its wavefunction is usually strongly localized in the region of the defect [5, 6, 10]. It turns out that the response of the positron is defect specific and, therefore, different types of defects can be distinguished.

Probably the most common positron annihilation technique used in defect studies is the positron lifetime spectroscopy (PLS). In open-volume defects, the positron lifetime increases considerably (for example, in monovacancies it is about 1.6× higher than in the defect-free bulk material). To associate measured lifetimes with particular defects, positron lifetime calculations are often indispensable. At present, reliable models of many types of defects based on atomistic simulation are available. It is therefore advisable to investigate positron trapping at defects with realistic atomic configurations which may appear in real materials, rather than at elementary defects with simplified geometry as has been done frequently so far.

In this section we demonstrate a suitable computational technique applied to a model sample of nanocrystalline Ni (the details will be published elsewhere [57]). The formula to calculate the positron lifetime τ reads [52]

$$1/\tau = \pi r_0^2 c \int n_e(\mathbf{r}) n_p(\mathbf{r}) \gamma[n_e(\mathbf{r})] d^3\mathbf{r}, \tag{18}$$

where r_0 is the classical electron radius, c is the velocity of light, n_e and n_p are, respectively, electron and positron densities, and γ stands for the so-called enhancement factor which describes the pileup of electrons around positrons. The enhancement factor is closely connected with the e-p correlation function g_{ep} introduced in Eq. (4) and increases with decreasing electron density. The positron lifetime also increases with decreasing electron density and saturates at a value of 500 ps. This fact somewhat limits the possibilities of PLS in the case of large vacancy clusters (voids) because the lifetime corresponding to positrons trapped at such clusters almost does not change with their size. Nevertheless, there are many defects where this limitation does not apply.

5.1. Atomic superposition method

The electron density to be used in Eq. (18) and the positron crystal potential is usually obtained from ab initio electronic structure calculations. However, for systems having large number (thousands) of non-equivalent atoms, this procedure is unmanageable. A method devised to perform positron calculations in such systems is the atomic superposition technique (ATSUP) [58]. It is a non-selfconsistent technique which makes use of the atomic densities and electron Coulomb potentials of all atomic species in the system considered in order to approximate the electron density and Coulomb potential in the defect region by numerical superposition on a three dimensional (3D) mesh according to the atomic configuration of the system supposing its periodicity. The positron potential is constructed as a sum of two parts: $V_p = -V_e^{Coul} + V^{corr}$, where V_e^{Coul} is the electron Coulomb potential originating from the superposition of Coulomb atomic potentials (the negative sign is due to the opposite charge of positrons) and V^{corr} is the positron correlation potential which

depends on the electron density n_e. The Schrödinger equation for positrons is then solved numerically on the 3D-mesh using the conjugate gradient method [58]. As an output of the calculations, we get the positron wavefunction and energy as well as the positron lifetime and momentum distribution of annihilation photons characteristic for the defect studied. The calculated positron lifetime may be compared with experimental results. A great advantage of the ATSUP technique consists in its high computational speed; therefore, quite large atomic configurations may be treated.

Some model (virtual) samples of materials may contain excessive number of atoms (even hundreds of thousands or more). Such samples are too large to be considered as one cell for positron calculations and smaller parts ('cuts') containing regions of interest have to be examined. However, such cuts (generally parallelepipeds) are not periodic and the ATSUP technique has to be modified. Explanations of needed changes are given in [59]. Here we mention the basic points only.

First, a shallow potential well is created for positrons by adjusting the positron potential at the sides of the cut and, in this way, physically reasonable behavior of the positron wave function in this region is achieved. Second, as the cut may contain more positron traps, we extend the procedure for solving the Schrödinger equation so that it is possible to look for more positron states. We also employ a multigrid approach to speed up the calculations.

5.2. Defects in nanocrystalline Ni

In this study, we investigated nanocrystalline sample of Ni described in detail by Van Swygenhoven et al. [60]. It was constructed as follows: First, the simulation cell volume was filled with nanograins (seeds) with random location and crystallographic orientation. Subsequently, the grains were allowed to grow until they touched each other. The sample was then relaxed for 50-100 ps at 300 K using molecular dynamics with second-moment (tight-binding) potentials according to Cleri and Rosato [61]. As a result, a computer sample of nanocrystalline Ni was obtained. It contained about 1.2 million of atoms and 15 grains, the average grain size being 12 nm. Its average density amounted to 96 % of that of the perfect bulk Ni. A lot of high-angle grain boundaries were present. However, the sample did not contain any large vacancy clusters and only small free volumes (up to size of one vacancy) associated with grain boundaries (GBs) were found.

So far, we have examined only several GBs and one triple junction (a common point of three or more GBs). Table III contains the results of our lifetime calculations for several positron lowest states at selected GBs (they are identified by the grain numbers of adjacent grains). Most calculated lifetimes are in the interval of 117–126 ps except for the GB 13-14. This GB exhibits slightly lower lifetimes (110–118 ps) than the triple junction and other GBs as it is close to a twin GB and has a little bit

denser atomic arrangement and, therefore, smaller amount of free volume (Figs. 12 and 13). All these values exceed the calculated bulk positron lifetime in Ni (100 ps) only slightly and correspond to rather shallow positron traps. The sites of positron localization (maxima of the positron density) are marked by large spheres in Figs. 12 and 13. In the case of GB 1-14, we have found a vacancy (with a positron lifetime of 162 ps) close to the GB (Fig. 12).

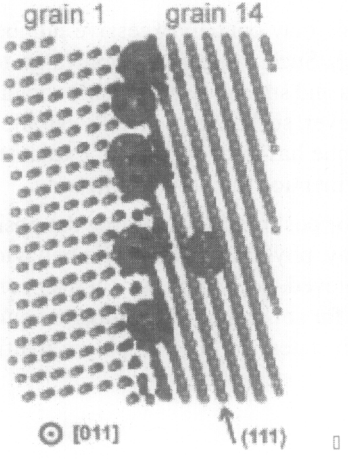

Fig. 12. A part of the grain boundary 1-14. The sites of positron localization are marked by large spheres. The vacancy is located a little bit aside from the GB. The orientation of some atomic planes is also indicated.

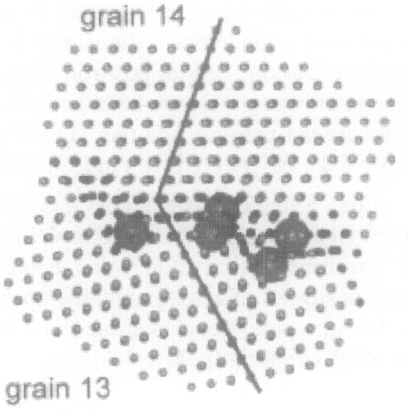

Fig. 13. A part of the grain boundary between the grains 13 and 14 together with the sites of positron localization. A pair of two twin atomic planes is indicated by solid lines.

Till now, we have analyzed a small fraction of GBs existing in the sample and found one vacancy only (see Table III). This would correspond to a vacancy concentration of about 1 ppm which may not be too far from reality. Currently, a computer code for a geometrical analysis of free volumes in simulated samples is being developed. This will allow us to perform positron lifetime calculations for regions indicated by that code (without looking for them 'manually') and, consequently, to determine the concentration of vacancies with a higher precision.

Table III: Calculated positron lifetimes for selected grain boundaries and triple junction (last column) in the computer sample of nanocrystalline Ni.

grain boundary	1-7	1-14	13-14	3-7-15
lifetimes (ps)	118-126	117-123, 162	110-118	119-125

The experimental lifetime spectra on nanocrystaline Ni [62] exhibit two components. Depending on the sample preparation procedure the first one ranges from 156 to 187 ps and its intensity varies from 43 to 80 %. This component is attributed to vacancy-like defects which are supposed to be associated with grain boundaries [63]. It seems, therefore, that in the measured samples positrons are trapped predominantly by defects having a size of about one vacancy.

The longer lifetime component found in measured samples varies from 300 to 400 ps. It corresponds to larger vacancy agglomerates, which do not appear in the computer sample due to the way of its construction (see above and [60]), and we do not discuss it here in detail. Other examples of positron calculations and experiments in nanocrystalline materials may be found, e.g., in [59, 64].

As for the comparison of theoretical calculations with experimental data, we concluded that the measured samples contain vacancies and vacancy clusters whereas the computer sample seems to be rather dominated by shallow traps (that have not been yet observed experimentally) though vacancy-like defects are also present. The real nanocrystalline samples certainly contain many shallow positron traps as there is a large volume fraction of GBs in such samples. From the point of view of PAS the comparison of theory and experiment is complicated by the fact that the trapping efficiency for these shallow traps is not known; it seems that it is quite low (compared, e.g., to that for vacancies), which prevents these traps from being observed by PAS.

It would be desirable, of course, to construct a computer sample which would be closer to the measured samples. At least a realistic description of larger vacancy agglomerates is needed. Furthermore, the influence of different preparation conditions on the structure of GBs would also be worth of studying. For these purposes, our sample may be considered as a good start. It may be expected that, changing the conditions of computer simulations and improving the description of interatomic interactions, we will arrive, by trial and error, to more and more realistic computer samples.

6. CONCLUSIONS

In this paper we have discussed some recent advances and pending problems in application of positron annihilation spectroscopy (PAS) to solid state physics and materials science. It turns out that PAS may be very helpful in variety of issues, but it also has some serious limitations. Very often careful theoretical calculations have to be performed in order to understand properly the positron annihilation signal.

In Secs. 3 and 4 of this paper, we discussed the reliability and accuracy of first-principles electronic structure calculations in PAS. We can believe that, probably, the computational tools we have are good enough to find electronic structure and

positron states with sufficient accuracy. These tools include, among others, the Kohn-Sham equations based on density functional theory and the numerical methods for their solution. However, the main difficulty seems then to consist in the fact that we do not have the input which is sufficiently accurate. In the electron crystal potential, there are several approximative descriptions for exchange-correlation energy and we do not know which one is the best one. Regrettably (or fortunately?), using different formulas yields somewhat different electronic structures and electronic wavefunctions. To include positron properly, we need a reliable description of electron-positron interaction. There are also several different approaches for that. Most of them have a local-density nature. However, recently it was demonstrated that non-local effects in e-p correlations are of substantial importance for d-electrons in transition metals and for core electrons [65]. Now, one of the problems we discussed here is that the sensitivity of the calculated momentum densities of annihilation pairs (MDAP) with respect to different electron-positron interaction theories is smaller or comparable with their sensitivity with respect to different crystal potentials. We have shown that this fact may have far reaching consequences. Specifically, in this contribution, we have demonstrated that, at present, a high sensitivity of MDAP to crystal potentials makes it difficult to apply the comparison of theoretical and experimental MDAPs as a criterion to decide which electron-positron interaction theory is better. This is not very good news for theorists working in the field. Also the calculated values of positron affinities A_+ are influenced by the choice of electron potential and electron-positron interaction theory quite strongly and, in semiconductors and insulators they are quite different from the experimental data. It seems to us that, to solve these problems, we will have to change the present paradigm and to try to describe the electron-electron and electron-positron interaction in solids on equal footing, in some very unifying and compact way, including properly all interactions and not having to resort to some serious approximations. A theory like that would be very desirable.

In Sec. 5, we have shown that the present atomistic simulation techniques enable us to generate quite realistic computer samples and to calculate the corresponding positron signals which may be then compared with those obtained in experiment. Due to the speed and capacity of present-day computers, we may investigate positron states at defects with realistic atomic configurations which may appear in real materials. In this way, theoretical PAS investigations have achieved a qualitatively higher level where the results of a positron experiment performed on a complex system can be simulated before actually performing the experiment itself. Of course, the goal of such simulations is not to obtain numbers, but insights. The results include electron and positron wavefunctions, charge densities, trapping coefficients, positron-defect binding energies, formation and migration enthalpies, etc. Comparing the calculated positron annihilation characteristics with experimental results yields also significant information about the adequacy of defect configuration. In this manner, there is a feedback between the structural models and reality which brings us to more and

more complete description of the underlying structures and atomic configurations of material defects – we can somehow 'tune' the computer sample to reproduce as much experimental results as possible. This also requires better and better description of interatomic interactions. We expect that in future the first-principles methods will allow to simulate larger and larger atomic configurations and will contribute most significantly to studies of electronic structure and atomic configuration of extended defects such as grain boundaries, interfaces, dislocation cores, etc., especially in systems with covalent bonds, such as non-close-packed metals, non-cubic intermetallics, metal-ceramic interfaces, semiconductor systems, etc. Notwithstanding, simpler methods, such as atomic superposition method [58], embedded atom method [66] and N-body central force [67] or second-moment [61] potentials, will remain essential for studies of very large systems. To proceed further, it is necessary to combine simpler methods with the first-principles approaches on one hand and experiment on the other.

Therefore, in understanding properties of defects in materials, our task is twofold: First, we should have reliable description of interatomic interactions and relevant numerical methods to be able to create realistic atomic configurations (e.g., a computer sample of nanocrystalline Ni analyzed in this paper). Second, we need a code which, taking the computer-generated sample as input, will give us the defect characterization and distribution and, for the purpose of PAS, for example, the positron lifetime distribution or some other annihilation characteristics. Here we face a problem of defect trapping efficiency which is different for different types of defects and it is quite hard to compute. Nevertheless, some advancement in this direction have already been recorded and further work is in progress.

7. ACKNOWLEDGEMENTS

This research was supported by the Grant Agency of the Czech Republic (Projects No. 106/99/1178 and 106/02/0877), by the Grant Agency of the Academy of Sciences of the Czech Republic (Project No. A1010817), by the Research Project Z2041904 of the Academy of Sciences of the Czech Republic and by the Ministry of Education of the Czech Republic (Project No. LB98202). A part of this study has been performed in the framework of the COST Action P3 (Projects No. OC P3.10 and OC P3.150) and of the COST Project No. OC 523.90; here we acknowledge the organisational and partial financial support of the Ministry of Education of the Czech Republic. Thanks are due to O.K. Andersen and O. Jepsen for permitting the use of their LMTO-ASA package. We also thank M.J. Puska and T. Korhonen for providing us with their ATSUP and LMTO positron codes which served as a basis for further developments. Last, but not least, we are grateful to H. Van Swygenhoven for the computer sample of nanocrystalline Ni and Z. Beneš for drawing Figs. 1–3.

8. REFERENCES

[1] Positron Annihilation (Proc. 9th Int. Conf. on Positron Annihilation, Szombathely, Hungary, 1991), edited by Z. Kajcsos and C. Szeles (Trans Tech Publ., Aedermannsdorf, 1992). Appeared as Mater. Sci. Forum **105-110**, (1992).

[2] Positron Annihilation (Proc. 10th Int. Conf. on Positron Annihilation, Beijing, China, 1994), edited by Y.J. He, B.S. Cao, and Y.C. Jean (Trans Tech Publ., Aedermannsdorf, 1995). Appeared as Mater. Sci. Forum **175-178**, (1995).

[3] Positron Annihilation (Proc. 11th Int. Conf. on Positron Annihilation, Kansas City, USA, 1997), edited by Y.C. Jean, M. Eldrup, D.M. Schrader, and R.N. West (Trans Tech Publ., Aedermannsdorf, 1997). Appeared as Mater. Sci. Forum **255-257**, (1997).

[4] Positron Annihilation (Proc. 12th Int. Conf. on Positron Annihilation, Munich, Germany, 2000), edited by W. Triftshäuser, G. Kögel, and P. Sperr (Trans Tech Publ., Uetikon-Zürich, 2001). Appeared as Mater. Sci. Forum **363-365**, (2001).

[5] Positron Solid State Physics, edited by W. Brandt and A. Dupasquier (North Holland, Amsterdam, 1983).

[6] Positron Spectroscopy of Solids, edited by A. Dupasquier and A.P. Mills, Jr. (IOS Press, Amsterdam, 1995).

[7] Proc. of the 8th Int. Conf. on Slow-Positron Beam Techniques for Solids and Surfaces (SLOPOS-8), Cape Town, South Africa, 1998, edited by D.T. Britton and M. Härting (Elsevier, Amsterdam, 1999). Appeared as Applied Surface Science **149**, (1999).

[8] Proc. of the 9th Int. Conf. on Slow-Positron Beam Techniques for Solids and Surfaces (SLOPOS-9), Dresden, Germany, September 16-22, 2001, to be published. It will appear in Applied Surface Science (2002).

[9] R.W. Siegel, Ann. Rev. Mater. Sci. **10**, 393 (1980)

[10] H. Krause-Rehberg and H.S. Leipner, Positron Annihilation in Semiconductors: Defect Studies (Springer Verlag, Berlin-Heidelberg, 1999).

[11] K.G. Lynn, J.R. MacDonald, R.A. Boie, L.C. Feldman, J.D. Gabbe, M.F. Robbins, E. Bonderup and J. Golevchenko, Phys. Rev. Lett. **38**, 241 (1977).

[12] M. Alatalo, H. Kauppinen, K. Saarinen, M.J. Puska, J. Mäkinen, P. Hautojärvi and R.M. Nieminen, Phys. Rev. B **51**, 4176 (1995).

[13] J. Kuriplach, A.L. Morales, C. Dauwe, D. Segers and M. Šob, Phys. Rev. B **58** 10475 (1998).

[14] M.J. Puska and R.M. Nieminen, Rev. Mod. Phys. **66**, 841 (1994); M. Mizuno, H. Arai, and Y. Shirai, this volume.

[15] M. Šob, in Proc. sub [2], p. 855.

[16] M. Alatalo and M.J. Puska, this volume.

[17] H. Sormann and M. Šob, Phys. Rev. B **41**, 10529 (1990).

[18] H. Sormann and M. Šob, in Proc. sub [1], p. 841.

[19] H. Sormann and M. Šob, Phys. Rev. B **64**, 045102 (2001).

[20] H. Sormann and M. Šob, in Proc. sub [4], p. 612.
[21] U. von Barth and L. Hedin, J. Phys. C: Solid St. Phys. **5**, 1629 (1972).
[22] J.P. Perdew and A. Zunger, Phys. Rev. B **23**, 5048 (1981).
[23] S.H. Vosko, L. Wilk, and M. Nusair, Can. J. Phys. **58**, 1200 (1980).
[24] D.M. Ceperley and B.J. Alder, Phys. Rev. Lett. **45**, 566 (1980).
[25] J.P. Perdew, J.A. Chevary, S.H. Vosko, K.A. Jackson, M.R. Pederson, D.J. Singh, and C. Fiolhais, Phys. Rev. B **46**, 6671 (1992).
[26] J.P. Perdew, S. Burke, and M. Ernzerhof, Phys. Rev. Lett. **77**, 3865 (1996).
[27] L.F. Mattheiss, Phys. Rev. **134**, A970 (1964).
[28] E.C. Snow and J.T. Waber, Acta Metall. **17**, 623 (1969)
[29] P. Ziesche, H. Wonn, C. Müller, V.V. Nemoshkalenko, and V.P. Krivitskii, phys. stat. sol. (b) **87**, 129 (1978).
[30] V.L. Moruzzi, A.R. Williams, J.F. Janak, and C. Sofes, Phys. Rev. B **9**, 3316 (1974).
[31] C. Müller, H. Wonn, W. Blau, P. Ziesche, and V.P. Krivitskii, phys. stat. sol. (b) **95**, 215 (1979).
[32] W.R.L. Lambrecht, B. Segall, and O.K. Andersen, Phys. Rev. B **24**, 7412 (1981).
[33] S. Daniuk, G. Kontrym-Sznajd, J. Mayers, A. Rubaszek, H. Stachowiak, P. A. Walters, and R. N. West, in Positron Annihilation, edited by P. C. Jain, R. M. Singru, and K. P. Gopinathan (World Scientific, Singapore, 1985), p. 43; *ibid.*, p. 279.
[34] S. Daniuk, G. Kontrym-Sznajd, A. Rubaszek, H. Stachowiak, J. Mayers, P. A. Walters, and R. N. West, J. Phys. F: Metal Phys. **17**, 1365 (1987).
[35] A. Rubaszek and H. Stachowiak, Phys. Status Solidi B **124**, 159 (1984).
[36] A. Rubaszek and H. Stachowiak, Phys. Rev. B **38**, 3846 (1988).
[37] M. Šob, in Proceedings of the 8th Annual International Symposium on the Electronic Structure of Metals and Alloys, edited by P. Ziesche (Technische Universität Dresden, Dresden, 1978), p. 170.
[38] M. Šob, in Positron Annihilation, edited by R. R. Hasiguti and K. Fujiwara (The Japanese Institute of Metals, Sendai, 1979), p. 309.
[39] M. Šob, J. Phys. F: Metal Phys. **12**, 571 (1982).
[40] P. E. Mijnarends and R. M. Singru, Phys. Rev. B **19**, 6038 (1979).
[41] S. Daniuk, M. Šob, and A. Rubaszek, Phys. Rev. B **43**, 2580 (1991).
[42] S. Daniuk, G. Kontrym-Sznajd, J. Majsnerowski, M. Šob, and H. Stachowiak, J. Phys.: Condens. Matter **1**, 6321 (1989).
[43] G. Kontrym-Sznajd and J. Majsnerowski, J. Phys.: Condens. Matter **2**, 9927 (1990).
[44] E. Boroński and R. Nieminen, Phys. Rev. B **34**, 3820 (1986).
[45] M.J. Puska, P. Lanki, and R.M. Nieminen, J. Phys.: Condens. Matter. **1**, 6081 (1989).
[46] J. Kuriplach, M. Šob, G. Brauer, W. Anwand, E.-M. Nicht, P.G. Coleman, and

N. Wagner, Phys. Rev. B **59**, 1948 (1999).
[47] D.W. Gidley and W.E. Frieze, Phys. Rev. Lett. **60**, 1193 (1988).
[48] P. J. Schultz and K. G. Lynn, Rev. Mod. Phys. **60**, 701 (1988).
[49] M.A. van Huis, A. van Veen, H. Schut, C.V. Falub, S.W.H. Eijt, P.E. Mijnarends, and J. Kuriplach, Phys. Rev. B (2002), in press.
[50] B.K. Panda, G. Brauer, and W. Skorupa, and J. Kuriplach, Phys. Rev. B **61**, 15848 (2000).
[51] For a review see, O.K. Andersen, O. Jepsen, and M. Šob, in Electronic Band Structure and Its Applications, edited by M. Yussouff (Springer-Verlag, Heidelberg, 1987), p.1.
[52] M.J. Puska and R.M. Nieminen, Rev. Mod. Phys. **66**, 841 (1994).
[53] G. Brauer, W. Anwand, E.-M. Nicht, P.G. Coleman, A.P. Knights, H. Schut, G. Kögel, and N. Wagner, J. Phys.: Condens. Matter. **7**, 9091 (1995).
[54] M.J. Puska, S. Mäkinen, M. Manninen, and R.M. Nieminen, Phys. Rev. B **39**, 7666 (1989).
[55] B. Barbiellini, M.J. Puska, T. Korhonen, A. Harju, T. Torsti, and R.M. Nieminen, Phys. Rev. B **53**, 16201 (1996).
[56] R.O. Jones and O. Gunnarson, Rev. Mod. Phys. **61**, 689 (1989).
[57] J. Kuriplach, S. Van Petegem, H. Van Swygenhoven, and P. Derlet, to be published.
[58] M.J. Puska and R.M. Nieminen, J. Phys. F: Metal Phys. **13**, 333 (1983); A.P. Seitsonen, M.J. Puska and R.M. Nieminen, Phys. Rev. B **51** 14057 (1995).
[59] J. Kuriplach, S. Van Petegem, D. Segers, C. Dauwe, M. Hou, E.E. Zhurkin, H. Van Swygenhoven, and A.L. Morales, in Structure and Mechanical Properties of Nanophase Materials – Theory and Computer Simulations vs. Experiment, edited by D. Farkas, H. Kung, M. Mayo, H. Van Swygenhoven, and J. Weertman, Mat. Res. Soc. Symp. **634** (Materials Research Society, Warrendale, PA, 2001), paper B3.8.
[60] H. Van Swygenhoven, D. Farkas, and A. Caro, Phys. Rev. B **62**, 831 (2000); H. Van Swygenhoven and P. Derlet, to be published.
[61] F. Cleri and V. Rosato, Phys. Rev. B **48**, 22 (1993).
[62] F. Dalla Torre, S. Van Petegem, and H. Van Swygenhoven, to be published.
[63] H.E. Schaefer and R. Würschum, Phys. Lett. A **119**, 370 (1987).
[64] J. Kuriplach, S. Van Petegem, M. Hou, E.E. Zhurkin, H. Van Swygenhoven, F. Dalla Torre, G. Van Tendeloo, M. Yandouzi, D. Schryvers, D. Segers, A.L. Morales, S. Ettaoussi, and C. Dauwe, Proc. sub [4], p. 94.
[65] A. Rubaszek, Z. Szotek, and W.M. Temmerman, Phys. Rev. B **63**, (2001) 165115; *ibid.* **61**, 10100 (2000); *ibid.* **58**, 11285 (1998).
[66] A.F. Voter: in Intermetallic Compounds, vol. 1, edited by J.H. Westbrook and R.L. Fleischer (Wiley, Chichester-New York 1995), p. 77.
[67] M.W. Finnis and J.E. Sinclair: Phil. Mag. A **50**, 45 (1984).

Theoretical calculation of positron lifetimes for defects in solids

Masataka Mizuno, Hideki Araki, and Yasuharu Shirai
Department of Materials Science and Engineering, Osaka University
2-1 Yamada-oka, Suita, Osaka, 565-0871, Japan

(Received February 15, 2002; in final form May 1, 2002)

Abstract

Theoretical calculations of positron lifetimes for vacancy defects in B2-type intermetallic compounds (FeTi, CoTi and NiTi) and MgO have been performed using DV-Xα method. In B2-type intermetallic compounds, the charge transfer from Ti to Fe/Co/Ni induces the difference of the positron localization between the Ti vacancy and Fe/Co/Ni vacancy. At the Fe/Co/Ni vacancy surrounded by the positively charged Ti atoms, the positron is not well localized and yields a shorter positron lifetime than at the Ti vacancy. Our recent positron lifetime measurement for MgO reveals that the bulk positron lifetime of MgO is about 30 ps shorter than the previously reported value. The experimental positron lifetime for the bulk state is well reproduced by the semiconductor model. The comparison of calculated and experimental positron lifetimes for the Mg vacancy suggests that the inward relaxation occurs around the Mg vacancy trapping the positron.

CONTENTS

ADVANCES IN QUANTUM CHEMISTRY, VOLUME 42

0065-3276/03 $35.00

1. INTRODUCTION

Positron lifetime spectroscopy is a powerful tool for the study of vacancy-type defects in solids. In a perfect crystal lattice, the positron is delocalized in the interstitial regions because of the repulsion from the ion cores. The vacancy-type defects in solids trap the positron due to the missing of the ion cores. The localization of the positron at the defect leads to the increase of the positron lifetime compared to the bulk lifetime due to the decrease of the electron-positron overlap. In compounds, several types of defects may exist and it is more difficult to characterize the measured positron lifetime than in elemental solids. In particular, the charge transfer between constituent atoms affects the positron distribution. This indicates that the atomic superposition method [1] in which the positron wavefunction is solved under atomic charge densities can not be applied for the positron in compounds. In this case, a theoretical calculation including electronic structure calculations is indispensable in order to interpret the measured positron lifetime. In the present work, we have performed theoretical calculations of positron lifetimes of the bulk and the mono-vacancy for B2 type intermetallic compounds TMTi (TM=Fe, Co and Ni) and MgO based on first-principles electronic structure calculation. We also present the experimental results for CoTi and MgO. The accuracy of the calculation and properties of defects in these solids are discussed by the comparison of the calculated positron lifetimes and the experimental values.

2. METHOD

2.1 Electronic structure calculation

In order to obtain the electron density and potential for the calculation of the positron wavefunction, the DV-Xα cluster method using a program code SCAT [2,3] is employed. In this method, the exchange-correlation potential is given by

$$V_{xc}(r) = -3\alpha\left[\frac{3}{8\pi}\rho(r)\right]^{\frac{1}{3}}, \qquad (1)$$

where $\rho(r)$ is the electron density and α is the scaling parameter, fixed at 0.7. The molecular orbital wave function is expressed by a linear-combination of atomic orbitals (LCAO) and may be written as

$$\phi_l = \sum_i C_{il}\chi_i , \qquad (2)$$

where C_{il} 's are coefficients. As the basis function χ_i we use the numerical atomic orbitals obtained by solving the radial part of the Schrödinger equation for each atom in a given environment. In order to obtain the orbital populations and the net charges, the Mulliken population analysis [4] is performed. The orbital population, $Q_i(l)$, and the overlap population, $Q_{ij}(l)$, of the l-th molecular orbital between χ_i and χ_j are defined by

$$Q_i(l) = \sum_l \sum_j f_l C_{il} C_{jl} \sum_k \omega(r_k)\chi_i(r_k)\chi_j(r_k), \qquad (3)$$

$$Q_{ij}(l) = \sum_l f_l C_{il} C_{jl} \sum_k \omega(r_k)\chi_i(r_k)\chi_j(r_k), \qquad (4)$$

where f_l is the occupation number of the l-th molecular orbital, r_k is one of the sample points and $\omega(r_k)$ is the integration weight of the sample point. 500 sample points per atom are used for the numerical integration. The orbital population is useful to determine the effective atomic charge. The bond overlap population between A and B atoms is given by

$$Q_{AB} = \sum_{i\in A}\sum_{j\in B}\sum_l Q_{ij}(l). \qquad (5)$$

The overlap population can be used as a measure of strength of the covalent bonding. The net charge of each atom ΔQ_A is obtained by

$$\Delta Q_A = Z_A - \sum_{i\in A} Q_i , \qquad (6)$$

where Z_A is the atomic number of atom A.

The model clusters composed of 113 atoms are used for the bulk state of FeTi, CoTi and NiTi. In the case of MgO, the model cluster is composed of 43 Mg atoms and O atoms surrounding each Mg atom. The Madelung potential generated by point charges is employed in the calculation of MgO. For the calculation of the vacancy state, the central atom of the model cluster for the bulk state is extracted. The lattice relaxation around the vacancy is not taken into account for FeTi, CoTi and NiTi. In order to estimate the effect of the lattice relaxation, the first-nearest neighbor O atoms are relaxed by –10 to 10 % of the bond length for the calculation of the Mg vacancy in MgO.

2.2 Positron state calculation

The three-dimensional potential $V_+(r)$ experienced by a positron is constructed as a sum of the electrostatic potential $V_C(r)$ due to the nuclei and the electrons, and a correlation potential $V_{corr}(n_-(r))$ describing the electron-positron correlation:

$$V_+(r) = V_C(r) + V_{corr}(n_-(r)), \qquad (7)$$

where $n_-(r)$ is the electron density. For the density dependence of $V_{corr}(n_-(r))$ we have used the interpolation formula of Boroński and Nieminen [5] based on the result of many-body calculation by Arponen and Pajanne [6] The Schrödinger equation for the positron is solved by the finite-difference method [7] employing the periodic boundary conditions for delocalized positron wave function in the bulk state. In the case of the localized positron at the vacancy, the boundary condition is the vanishing of the positron wave function on the surface of a large polyhedron.

The positron lifetime τ is calculated as the reciprocal value of the positron annihilation rate λ given by

$$\lambda = \pi r_0^2 c \int n_+(r) n_-(r) \gamma(r) dr\,, \qquad (8)$$

where r_0 is the classical electron radius, c is the speed of light, $n_+(r)$ is the positron density and $\gamma(r)$ is the enhancement factor describing the short-range pileup of the electron at the positron. For the enhancement factor, we have used the interpolation formula by Puska *et al.* [8] based on Lantto's data [9] quoted by Boroński and Nieminen [5]. This parameterization is called BN model here. Partial annihilation rates are obtained using the results of the Mulliken population analysis.

In insulators and semiconductors, the band-gap affects the enhancement effect. The band gap is considered to reduce the enhancement because of an imperfect screening of electrons. Two models are proposed by Puska *et al.* for the enhancement in compounds having the band gap [10]. One is called semiconductor model using the dielectric constant. The other is called insulator model based on atomic polarizability. The calculated positron lifetimes for bulk state in MgO reported by Puska *et al.* are 119 ps within the semiconductor model and 167 ps within the insulator model. In the insulator model, adjustable parameters are included and determined in order to reproduce the experimental lifetime of several insulators including MgO. However, experimental results recently measured in our group indicate the positron lifetime of bulk component is much shorter than

previously reported value of 166 ps. It is suggested that this longer positron lifetime may reflect the defect component introduced by impurities as discussed below. Therefore the insulator model is not appropriate. In this work, the conventional enhancement factor, the BN model, mentioned above and the semiconductor model are employed for MgO.

3. Positron lifetimes in TMTi compounds (TM=Fe, Co and Ni).

3.1 Defects in intermetallic compounds

In intermetallic compounds having a wide range of concentrations around the stoichiometry, structural defects are introduced in order to compensate deviations from the stoichiometry and have influence on several properties. Main structural defects are vacancies on the sublattice or antisite atoms occupying the other sublattice. If the vacancies are mainly responsible for the deviation from the stoichiometry, longer positron lifetimes should be measured compared to the bulk lifetime. The measured and calculated positron lifetimes for both the bulk and the monovacancy in most of elemental metals were reported. However, it is difficult to estimate the positron lifetime in intermetallic compounds using the reported values for the constituent elemental metals. In intermetallic compounds, the charge transfer occurs between the constituent atoms and affects the localization of the positron at the vacancy.

3.2 Bulk state in TMTi

The total and partial densities of states for FeTi, CoTi and NiTi are shown in Fig. 1. The DOS curves are obtained by broadening the discrete energy levels by Gaussian function with full width at half-maximum (FWHM) equal to 0.5 eV. They are shifted so as to set the Fermi level (E_F) at zero. There have been several theoretical studies for the series of Ti-based intermetallic compounds, FeTi, CoTi and NiTi [11-13]. The basic features of our DOS agree with those in previous works. The TM 3d band is located just below the E_F and interacts mainly with the Ti 3d orbitals. Going from FeTi to NiTi, the TM 3d band is shifted downwards and the separation between the Ti and TM 3d band increases. Figure 2 shows the net charges calculated from the Mulliken population analysis. The electron transfer occurs from the Ti to TM atoms and its amount increases from FeTi to NiTi. The increasing electron transfer causes the increasing downward shift of the TM 3d band.

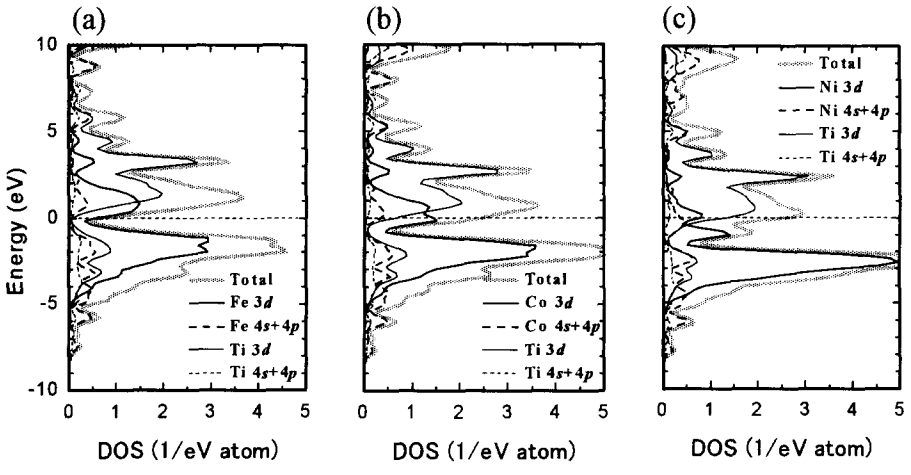

Fig.1 Total and partial of states for (a) FeTi, (b) CoTi and (c) NiTi.

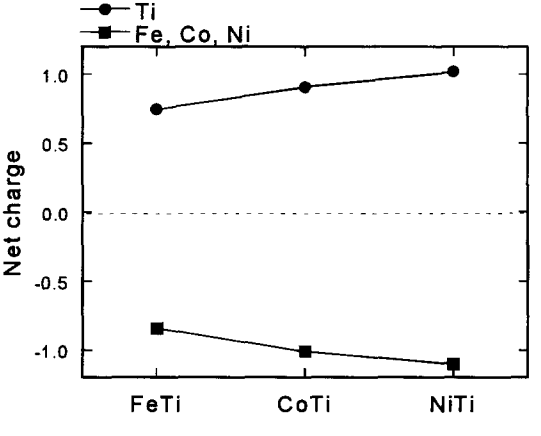

Fig. 2 Net charge in FeTi, CoTi and NiTi.

The positron lifetimes, annihilation rates and positron distributions for bulk state are presented in Table 1. The λ_{core} represents the sum of annihilation rate from 1s to 3p orbitals. Although all the three compounds have almost the same positron lifetime, the annihilation rates and positron distribution show different character. The largest contribution to the positron annihilation is the TM 3d orbital. Judging from the atomic radius, the Ti atom is expected to have a larger contribution to the positron annihilation rate. However the positron distribution in Table 1 shows that the positron resides more around the TM atom and the preference becomes stronger with the increase of the atomic number. Figure 3 shows the positron and electron density along the [111] direction (containing both the Ti and TM atom sites). The distance in the figure represents the length from the center between the Ti and TM nuclei. Whereas the positron density is peaked around the interstitial regions because of the repulsion from the nuclei, the peak is slightly shifted to the TM site and the positron overlaps with the electron of the TM atom more than the Ti atom. This indicates that the positron density around the TM atom is higher and the annihilation occurs preferably around the TM atom rather than around the Ti atom. As seen in Fig. 2, the electron transfer occurs from Ti to TM atom. The Ti atom is positively charged and the region around the Ti atom turns into positive environments for the positron.

Table 1 Positron lifetime, annihilation rate and positron distribution for bulk state in FeTi, CoTi and NiTi.

	Lifetime(ps)	Annihilation rate (ns^{-1})				Positron distribution
	τ_{theo}	λ_{core}	λ_{3d}	λ_{4s}	λ_{4p}	
FeTi	115					
Fe		0.859	2.082	0.846	1.451	0.600
Ti		1.370	0.846	0.438	0.797	0.400
CoTi	117					
Co		0.757	2.216	0.928	1.450	0.619
Ti		1.279	0.769	0.415	0.729	0.381
NiTi	120					
Ni		0.652	2.169	0.990	1.567	0.636
Ti		1.206	0.706	0.395	0.670	0.364

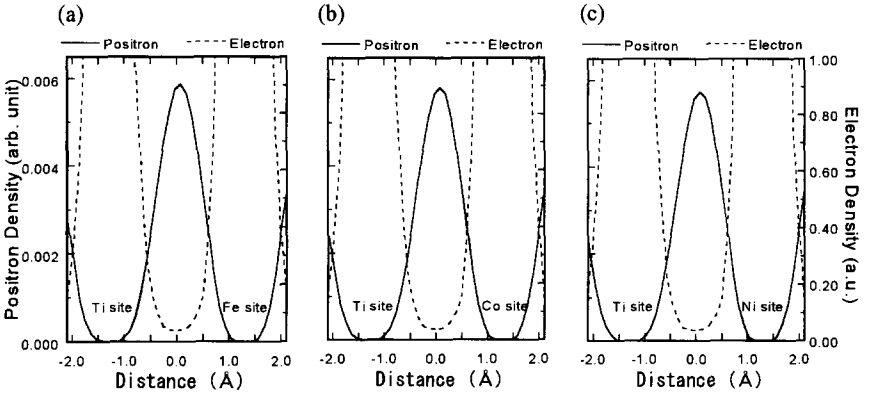

Fig. 3 Positron and electron density around the interstitial region between the Ti and TM site in (a) FeTi, (b) CoTi and (c) NiTi. The densities are shown along the [111] direction containing both the Ti and TM site.

3.2 Vacancy state in TMTi

The positron lifetimes, annihilation rates and positron distributions for vacancy state are given in Table 2. In all the three compounds, the positron lifetime of the Ti vacancy is longer than that of the TM vacancy. The difference in the positron lifetime between the Ti vacancy and the TM vacancy increases in the order of FeTi, CoTi and NiTi. The large values of positron density at the TM atoms around the Ti vacancy indicate that the positron wave function is mainly distributed at the TM atoms surrounding the Ti vacancy. Therefore, the positron is well localized at the Ti vacancy and the localization leads to a longer positron lifetime. In comparison with the bulk state, the decrease of the core annihilation rate also indicates the localization of the positron wave function at the Ti vacancy. On the contrary, the positron distribution at the TM atoms around the TM vacancy is comparable to that of the Ti atoms although the TM atoms are not located near the TM vacancy. The large contribution of the TM atoms to the positron annihilation rate indicates that the positron wave function is not well localized at the TM atom vacancy. Figure 4 shows the positron density near the vacancy along the [110] direction. It is clearly seen that the positron density at the Ti vacancy is higher than that at the TM atom vacancy. Is may be also seen that the difference of the positron density between the Ti vacancy and the TM vacancy increases when going from FeTi to NiTi. This

difference is due to an increasing electron transfer. Figure 5 shows the potential $V_+(r)$ experienced by a positron which is a sum of the electrostatic potential $V_C(r)$ due to the nuclei and the electrons, and a correlation potential $V_{corr}(n(r))$ describing the electron-positron correlation. Because of the electron transfer from the Ti to the TM atoms, the TM atoms are negatively charged and the potential around the Ti vacancy surrounded by the TM atoms is lower than the in other regions. On the other hand, the potential around the TM vacancy is also negative; at the center of the TM vacancy, it is slightly higher than the interstitial regions 2.5 Å away from the center. This is because the potential at the interstitial region is lowered by the negatively charged TM atoms. As a result, the positron is more scattered throughout the interstitial region and is not well localized at the TM vacancy.

Table 2 Positron lifetime, annihilation rate and positron distribution at vacancies in FeTi, CoTi and NiTi.

	Lifetime(ps)	Annihilation rate (ns^{-1})				Positron distribution
	τ_{theo}	λ_{core}	λ_{3d}	λ_{4s}	λ_{4p}	
FeTi						
Fe Vac.	144					
Fe		0.503	1.288	0.592	1.035	0.451
Ti		1.109	0.814	0.545	1.037	0.549
Ti Vac.	197					
Fe		0.357	1.276	0.822	1.600	0.820
Ti		0.245	0.211	0.177	0.387	0.180
CoTi	135					
Co Vac.						
Co		0.547	1.633	0.732	1.136	0.509
Ti		1.125	0.768	0.525	0.925	0.491
Ti Vac.	201					
Co		0.301	1.282	0.857	1.600	0.828
Ti		0.221	0.189	0.171	0.356	0.172
NiTi						
Ni Vac.	134					
Ni		0.513	1.740	0.811	1.247	0.541
Ti		1.093	0.727	0.502	0.848	0.459
Ti Vac.	205					
Ni		0.254	1.258	0.899	1.595	0.836
Ti		0.203	0.169	0.166	0.340	0.164

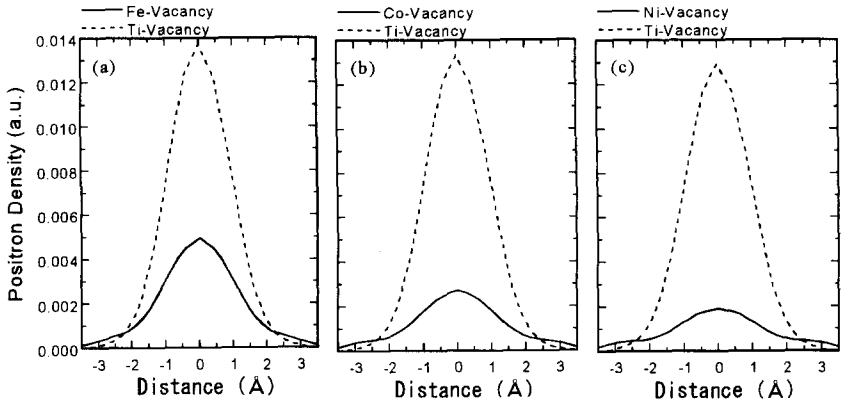

Fig. 4 Positron density around the vacancy in (a) FeTi, (b) CoTi and (c) NiTi. The densities are shown along the [110] direction.

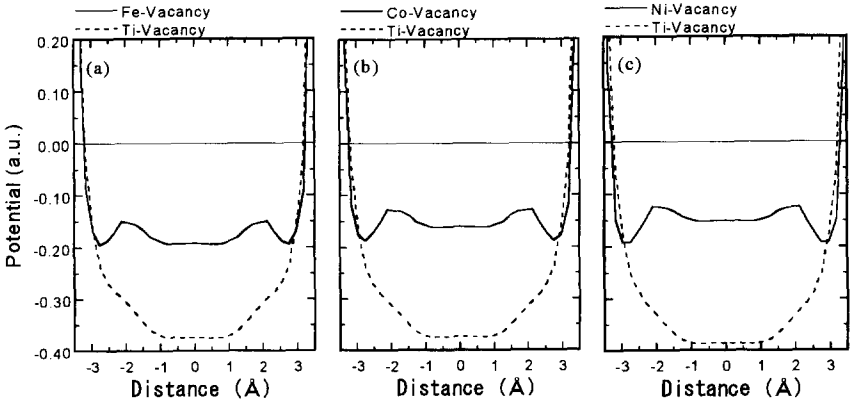

Fig. 5 Potential experienced by the positron ($V_+(r)$ in Eq.7) around the vacancy in (a) FeTi, (b) CoTi and (c) NiTi. The profiles are shown along the [110] direction.

3.4 Comparison with experimental values

The experimental positron lifetimes in CoTi are presented in Fig. 6 [14]. Positron lifetime spectra were measured at room temperature using a fast-fast timing coincidence system with a time resolution (FWHM) of 190 ps. A 30 μCi positron source of ^{22}NaCl was sandwiched between two identical sample plates. The source contribution and the resolution functions were evaluated by using the code RESOLUTION [15]. The lifetime spectra were analyzed by means of the POSITRONFIT EXTENDED program [16,17]. Irrespective of the kind of the defects introduced for the deviation from the stoichiometry, the thermal vacancies still remain in water-quenched specimens. If structural vacancies are induced due to the deviation from stoichiometry, the positron lifetime of the vacancy state, which is longer than that of the bulk state, is detected even at room temperature both in water-quenched and in furnace-cooled specimens. On the other hand, if antisite atoms are introduced due to the deviation from the stoichiometry, the longer positron lifetime is not observed in furnace-cooled specimens where thermal vacancies disappear. The positron lifetime in the furnace-cooled specimen near the stoichiometry can be considered as the bulk positron lifetime. Our calculated

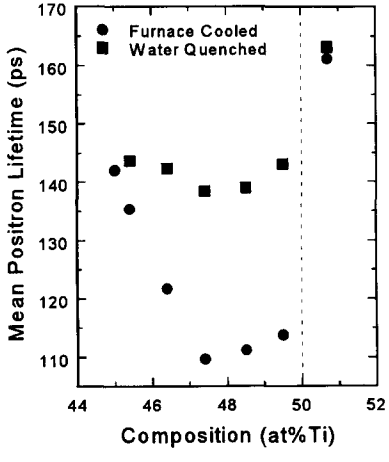

Fig. 6 Mean positron lifetime for CoTi.
Solid circles: furnace cooled after anneals at 1323K
Solid squares; water quenched after anneals at 1323K

positron lifetime of the bulk state in CoTi, 117 ps, is in a good agreement with the experimental value. The slight decrease of positron lifetime in the furnace-cooled specimens going from the stoichiometry to 47% Ti is due to the increase of the composition of the Co atom having a larger annihilation rate as seen in Table 2.

In comparison with the positron lifetime of furnace-cooled specimen, it seems reasonable to suppose that the positron lifetime of 143 ps in water-quenched $Co_{50.5}Ti_{49.5}$ at the Ti-poor side is associated with the annihilation at the Ti vacancy. On the other hand, the positron lifetimes both of the water-quenched and of the furnace-cooled specimens in $Co_{49.5}Ti_{50.5}$ exhibit almost the same value of about 163 ps which is longer than the bulk positron lifetime. This suggests that the structural vacancies are mainly responsible for the deviation from the stoichiometry on the Co-poor side in CoTi and the positron lifetime of about 163 ps originates from the positron annihilation at the Co vacancy.

The calculated positron lifetime of the bulk state of CoTi is good agreement with the experimental data, whereas the calculated positron lifetimes of the vacancy state show the opposite trend to the experimental values. As mentioned above for the calculated results, the electron transfer from the Ti to TM atom in TMTi causes a longer positron lifetime of the Ti vacancy compared to that of the Co vacancy. On the contrary, the experimental results show that the positron lifetime of the Co vacancy is longer than that of the Ti vacancy. One of the reasons may be that the lattice relaxation around the vacancy is neglected in our calculation. Generally, the inward relaxation around a vacancy reduces the positron lifetime due to the decrease of the open space. However, the difference between the calculated and experimental lifetime for the Ti vacancy is too large to be compensated by the lattice relaxation. Another reason consists in the fact that impurities such as oxygen trapped at the vacancy may reduce the positron lifetime. In the case of the Co vacancy, the experimental positron lifetime may reflect another type of vacancies which have a larger size than a monovacancy. In B2-type FeAl, the divacancy and triple defects, i.e. two vacancies and one antisite atoms were observed using positron annihilation methods, Mössbauer spectroscopy and X-ray diffraction [18]. We will calculate the positron lifetimes for the Co divacancies and triple defects composed of two Co vacancies and one antisite Co atoms in near future.

The accuracy of the theoretical calculation of the positron lifetime also needs further consideration. The difficulty of the positron calculation for TiTM compounds arises from their crystal structure and the charge transfer. The interstitial regions in the B2 structure are slightly larger than in other structures such as $L1_0$ and $L1_2$, since the B2 structure is not the close-packed. In comparison with a vacancy, the size of the interstitial regions in the B2 structure is not large enough to trap the positron, whereas the charge transfer between the constituent atoms complicates the situation as it affects the Coulomb potential around the

interstitial regions. In metals, the Coulomb potential at a vacancy is always lower than in the other regions and the positron is trapped at a vacancy. However, in intermetallic compounds where the charge transfer occurs, it is possible that the Coulomb potential at the interstitial regions near negatively charged atoms is comparable to that at the vacancies surrounded by positively charged atoms as seen in Fig. 5. The positron distribution around the vacancy in these intermetallic compounds is very sensitive to the amount of the charge transfer. Therefore, high accuracy electronic structure calculation is required for the determination of the positron state in these intermetallic compounds. In this work, we employed model clusters composed of 113 atoms. This cluster size is large enough to calculate the positron state at a vacancy in metals, whereas it is possible that the potential experienced by a positron is not well reproduced by the cluster size in intermetallic compounds such as CoTi. For further considerations, larger model clusters should be used or band-structure calculations with large supercells should be performed which can reproduce the potential around the vacancy more accurately.

4. Positron lifetimes in MgO

In MgO, impurity atoms having a different charge from Mg atom induce Mg vacancies for the charge neutrality [19]. In the case of Al^{3+} impurity, two Al^{3+} atoms give rise to one Mg vacancy in order to cancel out excess of charge by two Al^{3+} atoms. Figure 7 shows the change in mean-positron lifetimes of MgO with addition of aluminium recently measured in our group using sintered specimens made of ultra-high purity MgO powder in which the amount of the impurities is under 30 ppm. Positron lifetime measurement and analysis for MgO were made in the same way as for CoTi. Mean-positron lifetime increases linearly with the addition of Al. The increase of the mean-positron lifetime can be ascribed to the formation of Mg vacancies, since the positron in ionic compounds such as MgO is not localized at the anion vacancy due to the Coulomb repulsion from the surrounding cation atoms. We can determine the type and amount of defects employing two-component analysis for positron lifetime spectra. According to the trapping model [20-22], the positron lifetime spectrum, $T(t)$, may be approximated by to two discrete components:

$$T(t) = \left(\frac{I_0}{\tau_0}\right)\exp\left(-\frac{t}{\tau_0}\right) + \left(\frac{I_d}{\tau_d}\right)\exp\left(-\frac{t}{\tau_d}\right). \qquad (9)$$

The second term represents the defect component. The decay constant τ_d is the positron lifetime in the defect. The relative intensity of the defect component, I_d, increases with the defect concentration (I_0+I_d=1). The first decay constant τ_0 is always shorter than the bulk positron lifetime τ_b [23,24] because the trapping rate κ is included in τ_0 as

$$\tau_0 = \frac{1}{\lambda_b + \kappa}. \tag{10}$$

The relative intensity I_0 and I_d can be written as

$$I_0 = \frac{\lambda_b - \lambda_d}{\lambda_b + \kappa - \lambda_d}, \quad I_d = \frac{\kappa}{\lambda_b + \kappa - \lambda_d}. \tag{11}$$

The bulk positron lifetime τ_b can be derived from the decay constants τ_0 and τ_d and the relative intensity according to

$$\tau_b = \frac{1}{I_0/\tau_0 + I_d/\tau_d}. \tag{12}$$

The results of the two-component analysis are shown in Fig. 8. The bulk lifetime τ_b

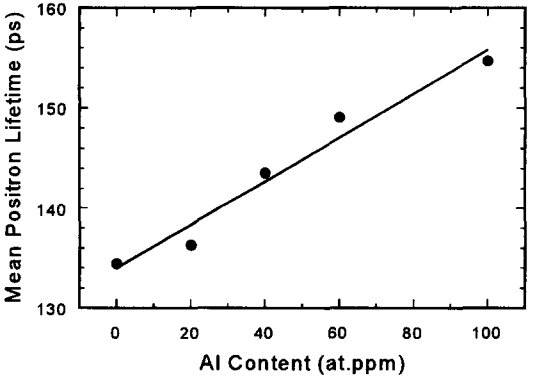

Fig. 7 Changes in mean positron lifetimes of MgO with addition of aluminum.

=135-140 ps is much shorter than the previously reported bulk lifetime of 166 ps [15] which seems to reflect not the bulk but the defect state arising from impurities. The relative intensity of defect component I_d increases with the increase of the Al content. This is the evidence for the Mg vacancy formation by the addition of Al.

The calculated positron lifetimes for the bulk state and at the Mg vacancy in MgO are listed in Table 3. In both cases, the positron lifetime obtained within the semiconductor model is longer than that evaluated within the BN model since the reduction of the screening of the positron by electrons is taken into account in the semiconductor model. The experimental bulk lifetime of 135-140 ps is well reproduced by the calculation using the semiconductor model. On the other hand, in the case of the Mg vacancy, the calculated positron lifetime within the BN model is in a better agreement with the experimental lifetime of 180 ps than within the semiconductor model. The reason for this contradiction is that the lattice relaxation around the vacancy, which affects the positron lifetime, was not taken into account.

In order to estimate the effect of the lattice relaxation, the first nearest oxygen atoms around the Mg vacancy are relaxed and the electronic structure and positron

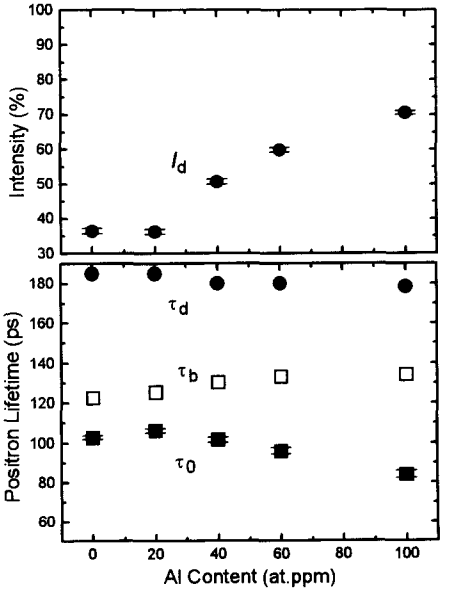

Fig.8 Results of the two-component analysis of the lifetime spectra for MgO with addition of Al.

lifetime calculations are performed. The results are shown in Fig. 9. For the agreement with the experimental value, about 5 % inward relaxation is required within the semiconductor model. However, about 6 % outward relaxation around the Mg vacancy is expected using first-principles calculation, CASTEP [26]. The outward relaxation arises from the Coulomb repulsion between the oxygen atoms. In the case of MgO including the positron, the positron localized at the Mg vacancy can be considered to reduce the Coulomb repulsion, which leads to the inward relaxation. In order to discuss the absolute value of lattice relaxation, further calculations including the relaxation effect by the positron are needed.

Table 3 The calculated positron lifetimes in MgO. τ^{BN} and τ^{SM} are the calculated positron lifetimes within BN model and semiconductor model, respectively.

	τ^{BN} (ps)	τ^{SM} (ps)
bulk	121	131
Mg vacancy	180	202

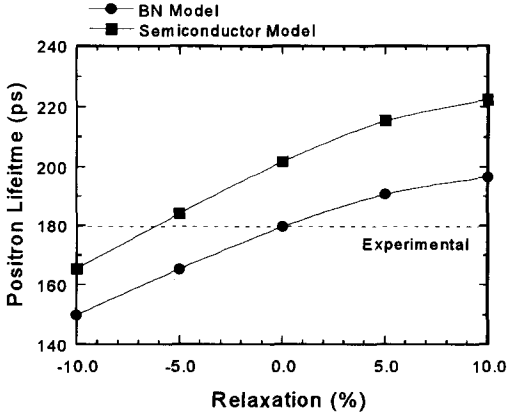

Fig. 9 Effect of lattice relaxation on positron lifetime for Mg vacancy in MgO.

5. Conclusion

We have performed theoretical calculations of positron lifetimes for the bulk and the vacancy in B2-type intermetallic compounds (TMTi: TM=Fe, Co and Ni) and MgO using the electronic structure obtained by DV-Xα method.

In the TMTi intermetallic compounds, the electron transfer occurs from the Ti to the TM atoms and its amount increases in the series of FeTi, CoTi and NiTi. The charge transfer induces the difference of the potential experienced by the positron at the Ti and TM vacancy. The positron lifetime for the Ti vacancy is longer than that for the TM vacancy since the Ti vacancy is surrounded by the negatively charged TM atoms. However, the experimental results for CoTi show opposite trends. It is suggested that the experimental positron lifetimes reflect another types of vacancies or vacancies trapping impurities. Further, it turns out that the potential seen by the positron at the vacancy in intermetallic compounds is sensitive to the amount of the charge transfer. Electronic structure calculations with larger model clusters or band calculations with large supercells are desirable for further consideration.

Our recent positron lifetime measurement reveals that the positron lifetime of bulk MgO is shorter than that previously reported. The bulk positron lifetime can be well reproduced using the semiconductor model. With respect to the defect component, the measured positron lifetime for the Mg vacancy is shorter than that expected from our theoretical calculation within the semiconductor model. This result suggests that the inward relaxation around the Mg vacancy occurs because of the decrease of the Coulomb repulsion between oxygen atoms surrounding the Mg vacancy at which the positron is localized.

6. References

[1] M. J. Puska and R. M. Nieminen, J. Phys. F: Met. Phys. **13**, 333 (1983).
[2] H. Adachi, M. Tsukada and C. Satoko, J. Phys. Soc. Jpn. **45**, 875 (1978).
[3] D. E. Ellis and G. S. Painter, Phys. Rev. B **2**, 2887 (1970).
[4] R. S. Mulliken, J. Chem. Phys. **23**, 1833 (1955).
[5] E. Boroński and R. M. Nieminen, Phys. Rev. B **34**, 3820 (1986).
[6] J. Arponen and E. Pajanne, Ann Phys. (N.Y.) **121**, 343 (1979); J. Phys. F **9**, 2359 (1979).
[7] G. E. Kimball and G. H. Shortley, Phys. Rev. B **45**, 815 (1934).
[8] M. J. Puska, A. P. Seitsonen, and R. M. Nieminen, Phys. Rev. B **52**, 10 947 (1995).

[9] L. Lantto, Phys. Rev. B **36**, 5160 (1987).
[10] M. J. Puska, S. Mäkinen, M. Manninen and R. M. Nieminen, Phys. Rev. B **39**, 7666 (1989).
[11] R. Eibler, J. Redinger and A. Neckel, J. Phys. F: Met. Phys. **17**, 1533 (1987).
[12] J. M. Zhang and G. Y. Guo, J. Phys.: Condens. Matter **7**, 6001 (1995).
[13] J. Y. Rhee, B. N. Harmon and D. W. Lynch, Phys. Rev. B **54**, 17385 (1996).
[14] S. Aono, H. Araki and Y. Shirai, (*unpublished*).
[15] P. Kirkegaard, M. Eldrup, O. E. Mogensen and N. Pederson, Computer Phys. Commun., **23**, 307 (1981).
[16] P. Kirkegaard and M. Eldrup, Computer Phys. Commun., **3**, 240 (1972).
[17] P. Kirkegaard and M. Eldrup, Computer Phys. Commun., **7**, 401 (1974).
[18] S. Gialanella, R. S. Brusa, W. Deng, F. Marino, T. Spataru and G. Principi, J. Alloys Comp. **317-318**, 485 (2001).
[19] Y. Chen and M. M. Abraham, J. Phys. Chem. Solids **51**, 747 (1990).
[20] W. Brandt, in *Positron Annihilation*, edited by A. T. Stewart and L. O. Roellig, (Academic Press, New York, 1967), p.155.
[21] B. Bergersen, M. J. Stott, Solid State Commun. **7**, 1203 (1969).
[22] D. C. Connors, R. N. West, Phys. Lett. **A30**, 24 (1969).
[23] M. Doyama, J. Phys. Soc. Jpn. **33**, 1495 (1972).
[24] A. Seeger, Appl. Phys. **4**, 183 (1974).
[25] R. Pareja, M. A. Pedrosa and R. Gonzáles, in *Positron Annihilation*, edited by P. C. Jain, R. M. Singru and K. P. Gopinathan (World Scientific, Singapore, 1985), p. 708.
[26] F. Oba, I. Tanaka and H. Adachi, (*private communication*).

Recent advances in the calculations for momentum distributions of annihilating electron–positron pairs in solids

M. Alatalo and M. J. Puska
Laboratory of Physics, Helsinki University of Technology
P.O. Box 1100, 02015 HUT, Finland

(Received August 3, 2001; accepted January 16, 2002)

Abstract

We discuss the recent advances in the theoretical and experimental studies for the momentum distributions of annihilating electron–positron pairs in solids. First, we briefly review the experimental setup and, on the other hand, the theoretical background starting from the two–component density–functional theory. We then move on to describing the recent work on this field, especially the comparison between the calculations and experiments performed in order to understand defects and defect complexes in solids. The high-momentum region of the spectra are fingerprints of the chemical environment of the annihilation. Simple models based on the superposition of free atom densities can model this momentum region. Moreover, we show that using self-consistent calculations for the valence electron densities, momentum distributions that are in quantitative agreement with the experiments for the whole momentum region can be obtained. This further raises the potential of the experiment-theory comparison in defect identification.

Contents

ADVANCES IN QUANTUM CHEMISTRY, VOLUME 42

0065-3276/03 $35.00

1 Introduction

Positron annihilation spectroscopy has during the recent decades become an important and versatile tool for studying defects in solids [1, 2, 3, 4]. In contrast to the delocalised nature of the positron wave functions in perfect bulk, open-volume defects are known to *trap* positrons. This leads to different annihilation characteristics and allows one both to distinguish between perfect and defected samples and even between different defects species. The characteristics to be measured include the positron lifetime and the momentum (or angular) distribution of the annihilation radiation. The lifetime, which is discussed in more detail elsewhere in this volume, is a useful quantity for determining the open volumes and concentrations of vacancy type defects. However, it is an integrated quantity which means that part of the information obtained on the annihilation events has been lost, making it less straightforward to obtain any *chemical* information from the lifetime only.

The momentum distribution, on the other hand, can be used to extract information on the chemical surroundings where the annihilation took place. The annihilations with the low momentum valence electrons produce the high peak around 511 keV whereas the high momentum tail arises from the annihilations with the tightly bound core electrons (See Fig. 3 below). The wave functions of the core electrons are localized and resemble those in free atoms. Therefore, the high momentum part of the momentum distribution is characteristic to the chemical environment of the annihilation event. It was realized for a long time ago already [5], that it is possible to determine this high momentum part accurately by measuring the Doppler broadened momentum spectrum by using a two-detector system. In the conventional Doppler–broadening method, only one of the annihilation quanta is detected which leads to a high number of background events which tend to dominate at the low amplitude high momentum region. If, however, both quanta are detected simultaneously, one can exclude the background almost completely. In the original work of Lynn and Goland, a NaI detector was used in coincidence with a Ge detector in order to provide the synchronization needed for the recording of the γ quanta arising from the annihilation events only. Little later it was realized [6] that the background can be lowered by another four orders of magnitude by detecting the *energies* of both γ:s using two Ge detectors in coincidence. This technique has been revived twenty years later by Asoka–Kumar *et al.* [7] who showed that, especially combined with theoretical calculations, it can be used to achieve elemental specificity in the positron measurements.

Soon after the double–detector method was published, it was applied to the study of vacancies in Al and Cu [8]. Apart from this, the method was not much applied till 1995 when Alatalo *et al.* used it for detecting vacancy–

impurity complexes in InP [9]. They also introduced a simple method for the calculation of the core part of the momentum distribution. The calculations for the electron–positron momentum distribution have later been extended to include the valence electrons, the wave functions of which have been calculated self-consistently [10, 11, 12, 13]. The purpose of this paper is to review these methods and describe the physics obtained using them. The rest of the paper is organized as follows. In Sec. 2, we briefly review the two-component density–functional theory on which many of the calculations for positrons in solids are based on and, on the other hand, provide some recent results that support the use of the simpler 'conventional' scheme. In Sec. 3 we describe the methods for calculating the electron–positron momentum distributions and discuss the results of these calculations and their relationship to the recent experiments in Sec. 4. Finally, we provide some conclusions and speculations on the future directions.

2 Two–component density–functional theory

Suppose we have a system consisting of negatively and positively charged fermions with densities n_- and n_+, respectively. In principle, the positive particles need not to be positrons, and the below scheme can be also applied to the electron–hole liquid, liquid hydrogen etc. Here we assume the positive particles to be positrons and that both the electrons and positrons are moving in an external potential $V_{ext}(\mathbf{r})$. According to the density–functional theory (DFT) [14] the total energy of such a system can be written as [15]

$$E[n_-, n_+] = F[n_-] + F[n_+] - \int d\mathbf{r} V_{ext}(\mathbf{r})[n_-(\mathbf{r}) - n_+(\mathbf{r})] \\ - \int d\mathbf{r} \int d\mathbf{r}' \frac{n_-(\mathbf{r}) n_+(\mathbf{r}')}{|\mathbf{r} - \mathbf{r}'|} + E_c^{e-p}[n_-, n_+], \tag{1}$$

where $E_c^{e-p}[n_-, n_+]$ is the electron–positron correlation energy functional and the functional $F[n]$ reads as

$$F[n] = T[n] + \frac{1}{2} \int d\mathbf{r} \int d\mathbf{r}' \frac{n(\mathbf{r}) n(\mathbf{r}')}{|\mathbf{r} - \mathbf{r}'|} + E_{xc}[n]. \tag{2}$$

Above, $T[n]$ is the kinetic energy of noninteracting electrons or positrons, $E_{xc}[n]$ is the exchange–correlation energy between indistinguishable particles and $E_c^{e-p}[n_-, n_+]$ is the electron–positron correlation energy functional. The most commonly used approximation for $E_{xc}[n]$ is the local density approximation (LDA) where the exchange–correlation energy is approximated as

$$E_{xc}[n] = \int n(\mathbf{r}) \epsilon_{xc}(n(\mathbf{r})) d\mathbf{r}, \tag{3}$$

where $\epsilon_{xc}(n(\mathbf{r}))$ is the exchange–correlation energy per particle in a *homogeneous* one-component electron gas. Several improvements over the LDA nowadays exist but they are beyond the scope of this paper. The electron–positron correlation energy at the limit of vanishing positron density was first calculated by Arponen and Pajanne [16]. At finite positron densities, the correlation energy functional was first parametrized by Boroński and Nieminen [15] and later on by Puska, Seitsonen and Nieminen [17]. Both parametrizations are based on the hypernetted chain calculation by Lantto [18], which can be considered highly accurate. The electron–positron correlation is usually also treated within the LDA. Only for the limit of vanishing positron density schemes beyond the LDA, such as the generalized gradient approximation (GGA) [26] or the weighted density approximation (WDA) [27, 28], have been constructed.

From the above total energy functional, one can derive the two-component Kohn-Sham equations for the electrons and positrons, respectively (in atomic units):

$$-\frac{1}{2}\nabla_i^2\psi_i(\mathbf{r}) + \left[\frac{\delta E_{xc}[n]}{\delta n_-(\mathbf{r})} - \phi(\mathbf{r}) + \frac{\delta E_c^{e-p}[n]}{\delta n_-(\mathbf{r})}\right]\psi_i(\mathbf{r}) = \epsilon_i\psi_i(\mathbf{r}) \tag{4}$$

$$-\frac{1}{2}\nabla_i^2\psi_i^+(\mathbf{r}) + \left[\frac{\delta E_{xc}[n]}{\delta n_+(\mathbf{r})} + \phi(\mathbf{r}) + \frac{\delta E_c^{e-p}[n]}{\delta n_+(\mathbf{r})}\right]\psi_i^+(\mathbf{r}) = \epsilon_i^+\psi_i^+(\mathbf{r}), \tag{5}$$

where

$$\phi(\mathbf{r}) = \int d\mathbf{r}' \frac{-n_-(\mathbf{r}') + n_+(\mathbf{r}') + n_0(\mathbf{r}')}{|\mathbf{r} - \mathbf{r}'|} \tag{6}$$

is the total Coulomb potential. Here, $n_0(\mathbf{r})$ denotes the positive ionic or nuclear charge density providing the external potential $V_{ext}(\mathbf{r})$. Because in the positron spectroscopy measurements there is only one positron in the solid sample at a time, one makes a self-interaction correction when calculating positron states [15, 17] by dropping out the self-Coulomb and self-exchange terms from Eq. (5). It has been suggested [20] that the self-interaction correction should be extented by using the limit of vanishing positron density for the electron-positron correlation. However, using this correction in the two-component scheme has been shown to yield results which contradict the experiments [17, 20]. The electron and positron densities are obtained by

$$n_-(\mathbf{r}) = \sum_{\epsilon_i \le \epsilon_F} |\psi_i(\mathbf{r})|^2 \tag{7}$$

$$n_+(\mathbf{r}) = \sum_i^{N_+} |\psi_i^+(\mathbf{r})|^2, \tag{8}$$

where ϵ_F is the electron Fermi energy, N_+ is the number of positrons, and $\psi_i(\mathbf{r})$ ($\psi_i^+(\mathbf{r})$) are the Kohn–Sham single particle eigenstates for electrons (positrons). Solving Eqs. (4)-(8) self-consistently yields the electron and positron densities and allows one to calculate e.g. the positron annihilation rate λ which, in the LDA, can be written in terms of these densities as

$$\lambda = \pi r_0^2 c \int d\mathbf{r} n_+(\mathbf{r}) n_-(\mathbf{r}) g(0; n_+, n_-), \tag{9}$$

where $g(0; n_+, n_-)$ is the electron–positron pair correlation function evaluated at the positron in a homogeneous two–component plasma with positron density n_+ and electron density n_-, r_0 is the classical electron radius and c is the speed of light. The inverse of the annihilation rate is the positron lifetime which is one of the important measurable quantities in positron annihilation spectroscopy.

In the limit of vanishing positron density the above equations simplify considerably. This situation is encountered when the positron resides in a perfect bulk lattice, i.e. its wave function is completely delocalized. Therefore, the positron cannot affect the electronic structure which can be solved self–consistently by setting the electron–positron correlation potential $\frac{\delta E_c^{e-p}[n]}{\delta n_-(\mathbf{r})}$ and the positron density to zero. Using the result of the electronic structure calculation, one can solve the positron state from the Kohn–Sham equation where in this case the potential sensed by the positron reads as

$$V_+(\mathbf{r}) = \phi(\mathbf{r}) + V_{corr}(n_-(\mathbf{r})), \tag{10}$$

where $\phi(\mathbf{r})$ is the Coulomb potential, obtained from the electronic structure calculation and V_{corr} is the zero–positron–density limit of the electron–positron correlation potential. A commonly used form for this potential is the parametrization by Boroński and Nieminen [15] who used the data of Arponen and Pajanne [16].

In the case of positrons localized into defects, the positron density does not vanish and the above approximation is in principle invalid. Nevertheless, it has been widely applied since the calculations performed using the full two–component formalism tend to be overly time consuming. The ensuing scheme is called as the 'conventional' scheme. It should not be confused with the above-mentioned self-interaction correction scheme using the limit of vanishing positron density for the electron-positron correlation. It requires the simultaneous self-consistent solution of the electron and positron densities whereas in the conventional scheme the electron density is first solved without the effect of the positron and then the positron state is calculated without any self-consistency iterations. The use of the conventional scheme can be justified by noticing that the positron and the electron screening cloud around it form a neutral quasiparticle which does not affect the average electron density of the

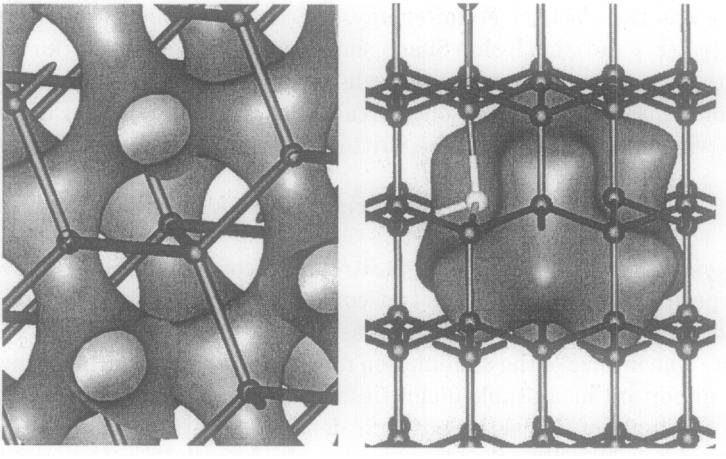

(a) (b)

Figure 1: (a) An isosurface of the positron wave function in a perfect Si lattice. The positions of the Si atoms are denoted by spheres, and the electronic interatomic bonds as sticks. The positron lifetime in this state is according to experiments and theory about 220 ps. (b) An isosurface of the positron wave function at a vacancy surrounded by one Sb impurity. The Sb atom is denoted by a light sphere. The positron lifetime in this state is according to theory about 230 ps [From Ref. [22]].

system. Moreover, the results of the conventional scheme have been shown to be in agreement with those obtained by the two-component density-functional calculations [15, 17].

Within the conventional scheme the practical calculations can be further simplified by noting that the positron annihilation characteristics can often be estimated using non-self-consistent electron densities. This is because the corresponding calculated positron density has a tendency to follow the details of the electron density so that the electron-positron overlap remains unchanged. These ideas are benefitted in the so-called atomic superposition method [21] in which the electron density and the positron potential are obtained by overlapping neutral atom charge densities, and the positron wave function is calculated without geometrical approximation in a three-dimensional point grid. As an example of the use of the atomic superposition method, Fig. 1 shows the density of a positron delocalized in a perfect Si-lattice as well as that for a positron trapped by a vacancy defect in Si.

Using the two-component DFT (or the conventional scheme) one can also compute the Hellman–Feynman forces, caused by the electrons and positrons, acting on the *ions* and move the ions accordingly. It has been shown [19, 20] that the positron induced relaxations around, say, vacancies in semiconductors can be considerably large and affect also the annihilation characteristics. The positron induced Hellman–Feynman force within the conventional scheme can be obtained as follows. In this case the total energy reads as

$$E_{tot}\left[n_{-}(\mathbf{r}), n_{+}(\mathbf{r})\right] = E_{tot}\left[n_{-}(\mathbf{r})\right] + \epsilon_p, \tag{11}$$

where ϵ_p is the positron energy eigenvalue. The positron induced force can then be obtained from

$$\mathbf{F}_p(\mathbf{R}) = -\int \frac{\partial \epsilon_p}{\partial \mathbf{R}} |\psi^{+}(\mathbf{r})|^2 d\mathbf{r}. \tag{12}$$

Above, $\mathbf{R}$ denote the ionic positions and the integration is over the three-dimensional coordinate space. In the atomic superposition one obtains further

$$\frac{\partial \epsilon_p}{\partial \mathbf{R}} = \tag{13}$$
$$\left[\frac{\partial V_{Coul}^{atom}(r')}{\partial r'}|_{r'=|\mathbf{r}-\mathbf{R}|} + \frac{\partial V_{corr}(n)}{\partial n}|_{n=n(\mathbf{r})} \frac{\partial n_{-}^{atom}(r')}{\partial r'}|_{r'=|\mathbf{r}-\mathbf{R}|}\right] \frac{\mathbf{r}-\mathbf{R}}{|\mathbf{r}-\mathbf{R}|},$$

where $V_{Coul}^{atom}(r)$ and $n_{-}^{atom}(r)$ are the spherical Coulomb potential and electron density for a neutral atom at $\mathbf{R}$.

As an example of the force calculations Fig. 2 shows the forces acting on a nearest-neighbor ion surrounding a vacancy in Si trapping a positron[22]. In the calculation the T_d symmetry of the perfect lattice point is assumed. The force due to the electronic structure is calculated using the pseudopotential-plane-wave method. This force tends to relax the ions inwards toward the center of the vacancy. The positron indused force, calculated using the atomic superposition method, naturally points outwards. At the equilibrium these forces are equal resulting in an outward relaxation of the ions surrounding the vacancy. The ensuing positron lifetime is roughly 260 ps, close to the reported experimental values [23] that are around 270 ps, whereas the value obtained with a zero relaxation is clearly smaller.

3 Calculations for the electron–positron momentum distribution

The momentum distribution of the annihilating electron–positron pairs can be written as

$$\rho(\mathbf{p}) = \pi r_0^2 c \sum_i |\int d\mathbf{r} e^{-i\mathbf{p}\cdot\mathbf{r}} \psi_i^{ep}(\mathbf{r}, \mathbf{r})|^2, \tag{14}$$

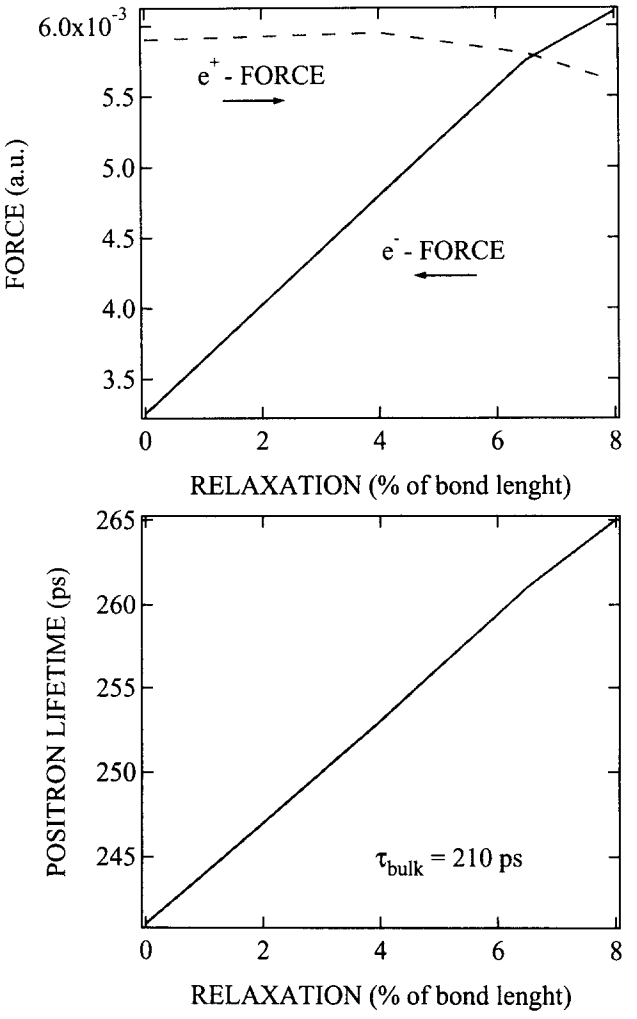

Figure 2: (a) Forces acting on the atoms neighboring a vacancy in Si as a function of the atomic relaxation. The force caused by the electrons is obtained by a pseudopotential plane wave calculation and the positron incuded forces by the atomic superposition method. (b) The positron lifetime at a vacancy in Si vs. the relaxation [From Ref. [22]].

where $\mathbf{p}$ is the total momentum of the annihilating pair and $\psi_i^{\mathrm{ep}}(\mathbf{r},\mathbf{r})$ is the two–particle wave function when the positron and electron reside at the same point. The two–particle wave function is in principle difficult to calculate and therefore it is usually written in terms of the positron and electron single–particle wave functions $\psi_+(\mathbf{r})$ and $\psi_i(\mathbf{r})$, respectively. We assume here that there is only one positron in the system and have therefore dropped the index i present in the positron wave functions in Eqs. (5) and (8). The two–particle wave function then reads as

$$\psi_i^{\mathrm{ep}}(\mathbf{r},\mathbf{r}) = \psi_+(\mathbf{r})\psi_i(\mathbf{r})\sqrt{\gamma_i(\mathbf{r})}, \tag{15}$$

where all the many–body effects have been buried into the enhancement factor $\gamma_i(\mathbf{r})$. Setting the enhancement factor to unity yields the independent particle model (IPM), which is known to be a reasonable approximation at the high momentum region [6]. As discussed below, it can also be utilized in more precise calculations for a wider momentum region.

Eq. (15) would suggest that the momentum distribution should be calculated from

$$\rho(\mathbf{p}) = \pi r_e^2 c \sum_i |\int d\mathbf{r} e^{-\mathbf{i}\mathbf{p}\cdot\mathbf{r}} \psi_+(\mathbf{r})\psi_i(\mathbf{r})\sqrt{\gamma_i(\mathbf{r})}|^2. \tag{16}$$

This form has been used succesfully for the calculation of the low–momentum region of the distribution, which is dominated by the annihilation with valence electrons [25]. However, it has been shown [24] that it might yield spurious effects at the high momentum region. Instead, Alatalo *et al.* [24] ended up using the so–called state-dependent enhancement factors

$$u_j^2(0) = \lambda_j/\lambda_j^{\mathrm{IPM}}, \tag{17}$$

where $\lambda_j^{\mathrm{IPM}} = \pi r_e^2 c \int d\mathbf{r} \psi_+^2(\mathbf{r})\psi_j^2(\mathbf{r})$ is the annihilation rate calculated using the IPM and λ_j is the annihilation rate obtained by a calculation utilizing the LDA or the GGA [26]. Using these enhancement factors, Eq. (14) can be written in the form

$$\rho(\mathbf{p}) = \pi r_e^2 c \sum_i u_j^2(0) |\int d\mathbf{r} e^{-\mathbf{i}\mathbf{p}\cdot\mathbf{r}} \psi_+(\mathbf{r})\psi_i(\mathbf{r})|^2. \tag{18}$$

In Ref. [24], positron wave functions obtained from a linear-muffin-tin-orbital (LMTO) calculation were used in a parametrized form, assuming an isotropic form around each nucleus. This enables a quick calculation and is shown to be a reasonable approximation for perfect bulk systems [24, 29]. As an example, Fig. 3 shows momentum distribution of the Al core electrons in comparison with the measured Doppler spectrum. The theoretical distributions have been convoluted by a Gaussian function corresponding to the experimental resolution. For vacancy type defects where the wave function

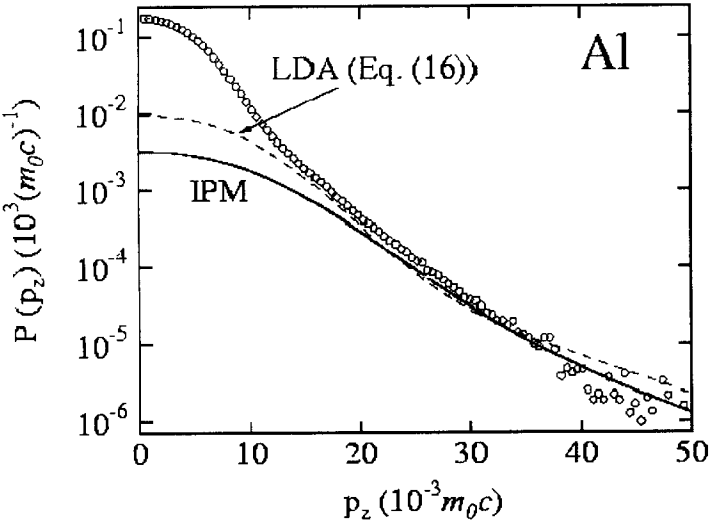

Figure 3: Positron annihilation probability density $P(p_z)$ for bulk Al. The experimental data (circles) are shown together with two different theoretical approximations: IPM (solid line) and the state-independent LDA scheme of Eq. (16) (dashed line) [From Ref. [24]].

of the localized positron is rather unisotropic, some improvements have been considered. Ghosh *et al.* [30] performed calculations utilizing the positron wave functions, obtained with the method of superimposed atomic densities, which were used for the calculation of the annihilation rates and thus the state dependent enhancement factors, also in the calculation of the momentum distribution. Some improvement was found for bulk Al and vacancies in Al [30]. Tang *et al.* [31] used an *ab initio* approach to the problem, by using the full-potential linearized augmented plane wave (FLAPW) all–electron method [32] for the calculation of the electronic states and a full potential plane wave method for the positrons. They obtained a good agreement with the experiment for bulk Si and oxygen–vacancy complexes in Si. The FLAPW method was also used by Baruah *et al.* [33] for the calculation of the electron momentum density in Li; the data obtained with the FLAPW was then used in the construction of the one- and two–dimensional angular distribution of the positron annihilation radiation. Instead of the schemes of Eqs. (16) and (17) Rubaszek *et al.* ended up with a state-selective electron-positron correlation functions which depend on the momentum of the annihilating electron.

4 Theoretical and experimental results

In the first application of the double–detector Doppler broadening method to defects in semiconductors, Alatalo *et al.* considered impurity–vacancy complexes in InP [9]. A Zn decorated phosphorous vacancy (V_P) serves as a good test case for the method, since the Zn 3*d* electrons produce a clearly wider momentum distribution than the less localized In 4*d* electrons. Indeed, the native vacancy in Zn–doped InP was identified to be V_P decorated with Zn, although the exact atomic configuration of this defect remained somewhat unclear. Another early experimental application to defects was made by Szpala *et al.* [35] who studied defects in Si, showing that the vacancy–Sb pair was responsible for the saturation of the electrical activity in highly Sb doped Si. The method has also been tested with extensive experiments [36] and calculations combined with experimental data [29] for elemental bulk materials. Moreover, the chemical specificity was demonstrated by Myler *et al.* [37] by measuring the fingerprints of implanted ions in Si and comparing them with the corresponding bulk materials. The two–detector Doppler measurements, combined with calculations using the KKR method, have also been used to assess the validity of different enhancement schemes [38], although this kind of approach has been recently criticized [39] on the basis that the effect of the crystal potential chosen in any particular calculation is larger than that of the different enhancements.

Several other applications of the double detector Doppler broadening method to defects in solids have been published during the recent years [40, 41, 42, 43, 44, 45, 46, 47, 48]. Here, we concentrate on the works where calculations have been used to support the experiments, especially those where theoretical improvements have been presented. In a theoretical paper, Hakala *et al.* [12] used the method of Ref. [24], extended to include the self–consistently calculated valence electron states [11] to study vacancy clusters in Si. The agreement with the experiments [24, 49] was good in the cases where experimental data is available. The authors also pointed out that, with a computational method at hand that can reproduce both the high *and* low momentum region, the comparison of the whole spectrum with the experiments is more meaningful than to compare the integrated S and W parameters only.

The same method, combined with experiments, was used by Saarinen *et al.* [45] to identify vacancy–impurity complexes in *n*-type Si (See Fig. 4). It was shown that the native vacancy defects in highly As–doped Si are monovacancies surrounded by three As atoms ($V–As_3$), confirming earlier theoretical predictions [50] on the As diffusion mechanism in Si. In contrast to the earlier works where the theoretical spectra were convoluted with the experimental resolution, Saarinen *et al.* [45] used a *deconvoluted* experimental spectra to

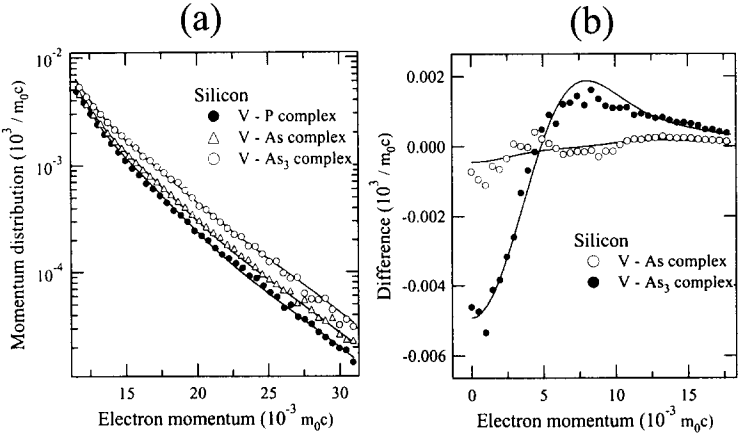

Figure 4: (a) High-momentum parts of the positron-electron momentum distributions. Measured results for positrons trapped in electron-irradiated P-doped (filled circles), electron-irradiated As-doped (open circles), and as-grown As-doped Si (triangles) samples as well as calculated distributions (solid lines) for vacancy-P, vacancy-As, and vacancy-As_3 complexes are shown. (b) Momentum differences of vacancy-As and vacancy-As_3 complexes with respect to the momentum distribution at the vacancy-P complex. The measured and calculated results are given by markers and solid lines, respectively [From Ref. [45]].

compare directly with the calculations. This resulted in a remarkably good agreement between the theory and experiment, also in the case of vacancy–P and vacancy–As complexes that were identified in addition to the V–As_3 complex. Indeed, as pointed out by Ghosh *et al.*, [51] the effect of the detector resolution is important and should be taken into account in comparing the theory with the experiments.

Apart from defects in semiconductors, other interesting applications of the double detector Doppler broadening technique include a study of nanosize Cu particles in an Fe–Cu alloy [52, 53] and a measurement of the electron momentum using in–flight annihilation [54].

5 Conclusion

In this brief review we have discussed results extracted from the electron–positron momentum distributions in solids. The present status of the cal-

culations for the momentum distributions enables a quantitative comparison with the experiments, although full self–consistent calculations are naturally quite time consuming. On the other hand, simple model calculations utilizing e.g. the method of superimposed atoms and including only the atomic like core electron states as a first approximation can be used in a 'quick and dirty' interpretation of the experiments. Here we have tacitly assumed that the problems related to the electron–positron correlations can be solved and proceeded in describing the practical calculations and their results, although this field is still under active study [55].

Naturally, there is still room for improvement, especially in the speed of the computations. An interesting line of development during the recent years has been the use of real space methods in the calculation of the electronic structure [56, 57] and also the positron states [58, 59, 60]. Work is in progress to utilize these methods also in the calculation of the momentum distributions.

Acknowledgements

The authors wish to thank Kimmo Saarinen and Mikko Hakala for many useful discussions and providing some unpublished material for our disposal.

References

[1] R. Krause-Rehberg and H. S. Leipner, *Positron Annihilation in Semiconductors*, (Springer, Heidelberg, 1999).

[2] K. Saarinen, P. Hautojärvi, and C. Corbel, in *Identification of Defects in Semiconductors*, edited by M. Stavola (Academic, New York, 1998).

[3] A. Dupasquier and A. P. Mills Jr. (Eds.) *Positron Spectroscopy of Solids*, (IOS Press, Amsterdam, 1995).

[4] M. J. Puska and R. M. Nieminen, Rev. Mod. Phys, **66**, 841 (1994).

[5] K. G. Lynn and A. N. Goland, Solid State Commun. **18**, 1549 (1975).

[6] K. G. Lynn, J. R. MacDonald, R. A. Boie, L. C. Feldman, J. D. Gabbe, M. F. Robbins, E. Bonderup, and J. Golovchenko, Phys. Rev. Lett. **38**, 241 (1977); J. R. MacDonald, K.G. Lynn, R.A. Boie, and M.F. Robbins, Nucl. Instr. Meth. **153**, 189 (1978).

[7] P. Asoka-Kumar, M. Alatalo, V. J. Ghosh, A.C. Kruseman, B. Nielsen, and K. G. Lynn, Phys. Rev. Lett. **77**, 2097 (1996).

[8] K. G. Lynn, J. E. Dickman, W. L. Brown, M. F. Robbins, and E. Bonderup, Phys. Rev. B **20** (1979).

[9] M. Alatalo, H. Kauppinen, K. Saarinen, M. J. Puska, J. Mäkinen, P. Hautojärvi, and R. M. Nieminen, Phys. Rev. B **51**, 4176 (1995).

[10] B. K. Panda, S. Fung, and C. D. Beling, Phys. Rev. B **53**, 1251 (1996); B. K. Panda, W. LiMing, S. Fung, and C. D. Beling, Phys. Rev. B **56**, 7356 (1997).

[11] B. Barbiellini, M. Hakala, M. J. Puska, R. M. Nieminen, and A. A. Manuel, Phys. Rev. B **56**, 7136 (1997).

[12] M. Hakala, M. J. Puska, and R. M. Nieminen, Phys. Rev. B **57**, 7621 (1998).

[13] Z. Tang, M. Hasegawa, T. Chiba, H. Sumiya, Y. Kawazoe, and S. Yamaguchi, Phys. Rev. B **57**, 12 219 (1998).

[14] P. Hohenberg and W. Kohn, Phys. Rev. **136**, B864 (1964); W. Kohn and L. J. Sham, Phys. Rev. **140**, A1133 (1965).

[15] E. Boroński and R. M. Nieminen, Phys. Rev. B **34**, 3280 (1986); R. M. Nieminen, E. Boroński, and L. J. Lantto, Phys. Rev. B **32**, 1377 (1985).

[16] J. Arponen and E. Pajanne, Ann. Phys. (N.Y.) **121**, 343 (1979).

[17] M. J. Puska, A. P. Seitsonen, and R. M. Nieminen, Phys. Rev. B **52**, 10 947 (1995).

[18] L. J. Lantto, Phys. Rev. B **36**, 5160 (1987).

[19] K. Laasonen, M. Alatalo, M. J. Puska, and R. M. Nieminen, J. Phys.: Condens. Matter **3**, 7217 (1991).

[20] L. Gilgien, G. Galli, F. Gygi, and R. Car, Phys. Rev. Lett. **72**, 3214 (1994).

[21] M. J. Puska, and R. M. Nieminen, J. Phys. F **13**, 2695 (1983); A. P. Seitsonen, M. J. Puska, and R. M. Nieminen, Phys. Rev. B **51**, 14 057 (1995).

[22] M. Hakala and M. J. Puska, unpublished.

[23] S. Dannefaer, in *Proceedings of Defect Control in Semiconductors*, edited by K. Sumino (North–Holland, Amsterdam, 1989) p. 1561.

[24] M. Alatalo, B. Barbiellini, M. Hakala, H. Kauppinen, T. Korhonen, M. J. Puska, K. Saarinen, P. Hautojärvi, and R. M. Nieminen, Phys. Rev. B **54**, 2397 (1996).

[25] M. Šob, in *Positron annihilation*, edited by Yuan–Jin He, Bi–Song Cao, and Y. C. Jean, Mater. Sci. Forum **175–178**, 855 (1995).

[26] B. Barbiellini, M.J. Puska, T. Torsti and R.M. Nieminen, Phys. Rev. B **51**, 7341 (1995); B. Barbiellini, M.J. Puska, T. Korhonen, A. Harju, T. Torsti and R.M. Nieminen, Phys. Rev. B **53**, 16 201 (1996).

[27] K. Jensen and A. B. Walker, J. Phys. F **18**, L277 (1988).

[28] A. Rubaszek, Z. Szotek, and W. Temmerman, Phys. Rev. B **58**, 11 285 (1998).

[29] V. J. Ghosh, M. Alatalo, P. Asoka-Kumar, B. Nielsen, K. G. Lynn, A. C. Kruseman, and P. E. Mijnarends, Phys. Rev. B **61**, 10 092 (2000).

[30] V. J. Ghosh, M. Alatalo, P. Asoka-Kumar, K. G. Lynn, and A. C. Kruseman, Appl. Surf. Sci. **116**, 278 (1997).

[31] Z. Tang, T. Nonaka, Y. Nagai, and M. Hasegawa, Mater. Sci. Forum **363–365**, 67 (2001).

[32] M. Weinert, E. Wimmer, and A. J. Freeman, Phys. Rev. B **26**, 4571 (1982).

[33] T. Baruah, R. R. Zope, and A. Kshirsagar, Phys. Rev. B **60**, 10770 (1999).

[34] A. Rubaszek, Z. Szotek, and W. M. Temmerman, Phys. Rev. B **61**, 10100 (2000).

[35] S. Szpala, P. Asoka–Kumar, B. Nielsen, J. P. Peng, S. Hayakawa, K. G. Lynn, and H.–J. Gossman, Phys. Rev. B **54**, 4722 (1996).

[36] U. Myler and P. J. Simpson, Phys. Rev. B **56**, 14 303 (1997).

[37] U. Myler, R. D. Goldberg, A. P. Knights, D. W. Lawther, and P. J. Simpson, Appl. Phys. Lett. **69**, 3333 (1996).

[38] P. E. Mijnarends, A. C. Kruseman, A. van Veen, H. Schut, and A. Bansil, J. Phys.: Condens. Matter **10**, 10 3838 (1998).

[39] H. Sormann and M. Šob, Mat. Sci. Forum **363–365**, 612 (2001).

[40] J. Mäkinen, T. Laine, J. Partanen, K. Saarinen, P. Hautojärvi, K. Tappura, T. Hakkarainen, H. Asonen, M. Pessa, J. P. Kauppinen, K. Vänttinen, M. A. Paalanen, and J. Likonen, Phys. Rev. B **53**, 7851 (1996).

[41] K. Saarinen, T. Laine, K. Skog, J. Mäkinen, P. Hautojärvi, K. Rakennus, P. Uusimaa, A. Salokatve, and M. Pessa, Phys. Rev. Lett. **77**, 3407 (1996).

[42] K. Saarinen, T. Laine, S. Kuisma, J. Nissilä, P. Hautojärvi, L. Dobrzynski, J. M. Baranowski, K. Pakula, R. Stepniewski, M. Wojdak, A. Wysmolek, T. Suski, M. Leszczynski, I. Grzegory, and S. Porowski, Phys. Rev. Lett. **79**, 3030 (1997).

[43] Y. Y. Shan, K. G. Lynn, Cs. Szeles, P. Asoka-Kumar, T. Thio, J. W. Bennett, C. B. Beling, S. Fung, and P. Becla, Phys. Rev. Lett. **79**, 4473 (1997).

[44] J. Kuriplach, A. L. Morales, C. Dauwe, D. Segers, and M. Šob, Phys. Rev. B **58**, 10 475 (1998).

[45] K. Saarinen, J. Nissilä H. Kauppinen, M. Hakala, M. J. Puska, P. Hautojärvi, and C. Corbel, Phys. Rev. Lett. **82**, 1883 (1999).

[46] M. P. Petkov, M. H. Weber, K. G. Lynn, R. S. Crandall, and V. J. Ghosh, Phys. Rev. Lett. **82**, 3819 (1999).

[47] V. J. Ghosh, B. Nielsen, and T. Friesnegg, Phys. Rev. B **61**, 207 (2000).

[48] J. Gebauer, R. Krause-Rehberg, C. Domke, Ph. Ebert, K. Urban, and T. E. M. Staab, Phys. Rev. B **63**, 045203 (2001).

[49] H. Kauppinen, C. Corbel, K. Skog, K. Saarinen, T. Laine, P. Hautojärvi, P. Descardin, and E. Ntsoenzok, Phys. Rev. B **55**, 9598 (1997).

[50] M. Ramamoorthy and S. T. Pantelides, Phys. Rev. Lett. **76**, 4753 (1996).

[51] V. J. Ghosh, B. Nielsen, A. C. Kruseman, P. E. Mijnarends, A. van Veen, and K. G. Lynn, Appl. Surf. Sci. **149**, 234 (1999).

[52] Y. Nagai, M. Hasegawa, Z. Tang, A. Hempel, K. Yubuta, T. Shimamura, Y. Kawazoe, A. Kawai, and F. Kano, Phys. Rev. B **61**, 6574 (2000).

[53] Y. Nagai, Z. Tang, M. Hasegawa, T. Kanai, and M. Sanayasu, Phys. Rev. B **63**, 134110 (2001).

[54] A. W. Hunt, D. B. Cassidy, P. A. Sterne, T. E. Cowan, R. H. Howell, K. G. Lynn, and J. A. Golovchenko, Phys. Rev. Lett. **86**, 5612 (2001).

[55] For the recent advances in the study of electron–positron correlations and enhancement, see e.g. E. Boroński and H. Stachowiak, Phys. Rev. B **57**, 6215 (1998); A. Rubaszek, Z. Szotek, and W. M. Temmerman, Phys. Rev. B **63**, 165115 (2001); H. Sormann, G. Kontrym-Sznajd, and R. N. West, Mater. Sci. Forum **363–365**, 609 (2001); H. Stachowiak, E. Boroński, and G. Banach, Phys. Rev. B **62**, 4431 (2000).

[56] For a review, see T. L. Beck, Rev. Mod. Phys. **72**, 1041 (2000).

[57] M. Heiskanen, T. Torsti, M.J. Puska, and R.M. Nieminen, Phys. Rev. B **63**, 245106 (2001).

[58] A. P. Seitsonen, M. J. Puska, and R. M. Nieminen, Phys. Rev. B **51**, 14 057 (1995).

[59] J. E. Pask, B. M. Klein, P. A. Sterne, and C. Y. Fong, Comp. Phys. Comm. **135**, 1 (2001).

[60] T. Torsti *et al.* unpublished.

Electronic Structures and Electrode Potentials of Layered Lithium Insertion Electrodes by the First Principles Calculation

Yukinori Koyama[z], Isao Tanaka and Hirohiko Adachi
Department of Materials Science and Engineering, Kyoto University Sakyo, Kyoto 606-8501, Japan

(Received February 7, 2002; in final form March 7, 2002)

Abstract

In order to evaluate intercalation voltage of $LiMO_2$ and to understand the electronic mechanism determining the voltage, two kinds of first principles calculations are combined. The voltage is quantitatively evaluated by total energy calculations using the full-potential linearized augmented plane wave method. The electronic structures are analyzed by molecular orbital calculations on model clusters using the discrete variational Xα method. Two factors determining the voltage are estimated separately: 1) the effective electrostatic potential at the Li position, and 2) the energy of the highest occupied molecular orbital. They are related to the energies required to remove a Li ion and an electron from $LiMO_2$, respectively. The sum of these two factors reproduces well the theoretical voltage. Moreover, it agrees well with experimental voltage.

CONTENTS

[z] E-mail: koyama@cms.MTL.kyoto-u.ac.jp

ADVANCES IN QUANTUM CHEMISTRY, VOLUME 42

0065-3276/03 $35.00

KEYWORDS

lithium battery, voltage, oxide, first principles calculation

INTRODUCTION

A number of materials with the ability of insertion and/or extraction of lithium have been investigated for application to electrode materials of primary and/or secondary lithium batteries. In 1970s, transition-metal chalcogenides, e.g., TiS_2 and MoS_2, attracted attention as the positive electrode materials. In 1980, Mizushima *et al.* first reported $LiCoO_2$ as the positive electrode material of rechargeable lithium battery [1]. Its voltage is as high as approximately 4 V against metallic lithium, though the voltages of the many chalcogenides are approximately 2 V. Since then, numerous investigations on the 3*d* transition-metal oxides as the electrode materials have been performed [2-4].

Layered $LiMO_2$ (M = 3*d* transition-metal element) with α-$NaFeO_2$-structural type is a series that has been widely investigated [4]. For it, the redox reaction of M(III)/M(IV) can be used. Its crystal structure is of an ordered rock-salt type such that Li and M occupy alternate (111) layers, as shown Fig. 1. Among the layered oxides, $LiCoO_2$ was first investigated as electrode material and has been used as the positive electrode material of commercial lithium-ion battery. It has good electrochemical properties [1, 5-7], namely, high intercalation voltage, large reversible capacity, high energy density and excellent cyclic durability. Three other oxides, $LiVO_2$, $LiCrO_2$ and $LiNiO_2$, also have the isomorphic crystal structure as $LiCoO_2$. $LiNiO_2$ has somehow lower voltage and larger reversible capacity than $LiCoO_2$ [8, 9]. In contrast, $LiVO_2$ and $LiCrO_2$ have less reversible capacities [10-12]. Crystal structures of $LiTiO_2$, $LiMnO_2$ and $LiFeO_2$ are related to the rock-salt type, but they are not really isostructural to α-$NaFeO_2$ [13-15]. Although $LiFeO_2$ and $LiMnO_2$ would obviously be of great interest, the structures conventionally prepared do not allow Li to be intercalated reversibly to any significant degree. Several different approaches [16-20] have been attempted to prepare $LiMnO_2$ and $LiFeO_2$ with the α-$NaFeO_2$-structural type. However, those with good reversibility of Li intercalation have not been prepared yet.

For electrode materials of rechargeable lithium battery, examinations for many properties such as intercalation voltage, reversible capacity, cyclic durability, chemical stability and conductivity of Li ion, are very important. While many studies on the electrochemical and physical properties of the materials have been

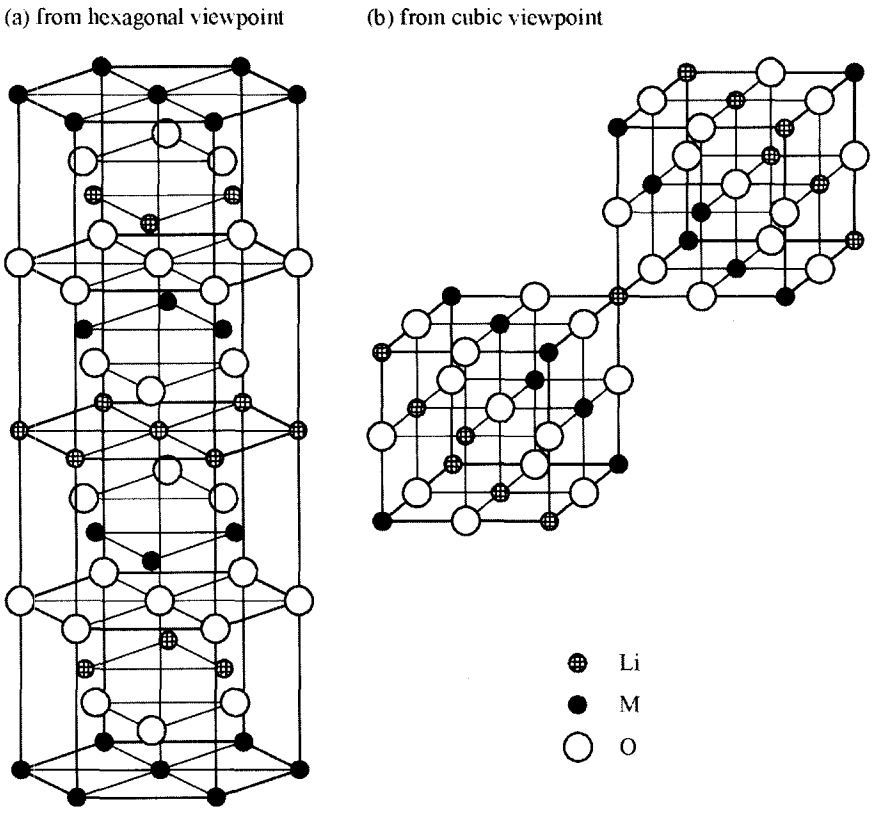

Fig 1. Crystal structure of layered $LiMO_2$ with α-$NaFeO_2$-structural type (a) from the hexagonal viewpoint and (b) from the cubic viewpoint. Li, M and O atoms are denoted by crossed-patterned, filled and open circles, respectively.

performed, the mechanism on Li intercalation process has not been clear. In order to design and to develop advanced electrode materials rationally, the electronic mechanism behind the intercalation process should be thoroughly understood. Theoretical calculations are indispensable for such a purpose.

In the present study, our attention is directed to understanding of the electronic mechanism that determines the intercalation voltage of lithium transition-metal oxide. The voltage of lithium transition-metal oxide is examined in detail by experiment [2]. Roughly speaking, the voltage increases with rising atomic number of transition-metal element in each period in the Periodic table. For example, $LiVO_2$ shows a voltage of approximately 3 V against metallic

lithium although only about one-third of Li can be extracted [10, 11]. On the other hand, $LiCoO_2$ and $LiNiO_2$ can be used at approximately 4 V [1, 5-9]. The voltage should be related to sum of energy required to remove a Li ion from $LiMO_2$ and that to remove an electron. The former is related to the electrostatic potential at the Li position. The latter is analogous to the work function of the system, although these two factors are dependent on each other.

Some theoretical studies showed the voltages by first principles calculations. Miura *et al.* were the first who attempt to correlate the voltage of spinel-type $Li_xMn_2O_4$ ($0 \leq x \leq 2$) using first principles calculations by the discrete variational (DV)-Xα method on model clusters [21]. They discussed the voltage from the viewpoint of the difference in work function, but they did not take account of the chemical potential of Li ion. Moreover, they performed calculations only for spinel-type $LiMn_2O_4$. Aydinol *et al.* made a systematic theoretical study [22, 23] on the voltage of $LiMO_2$ (M = Ti, V, Mn, Co, Ni, Cu, Zn and Al) using the first principles plane-wave pseudopotential method. Although the work truly contributed to gaining an insight into the problem, it cannot be fully sure of their results. The reason is that they did not include spin polarization into their calculations, which may be essential for the discussion of certain transition-metal oxides. Wolverton and Zunger [24-26] studied Li/Co and Li-vacancy/Co orderings associated with the intercalation process of $LiCoO_2$ using a combination of first principles total energy calculations by the full-potential linearized augmented plane wave (FLAPW) method, a cluster expansion technique and Monte Carlo simulations. Its voltage was also discussed in detail.

Despite these elaborate studies and successes, the important question from the viewpoint of the design and development of electrode materials has not been answered: What is the factor determining the voltage? In the present study, two kinds of first principles calculations are combined in order to evaluate the voltage of layered $LiMO_2$ (M = Ti - Ni) and to understand the electronic mechanism determining the voltage. The electronic structures of layered $LiMO_2$ are analyzed using first principles molecular orbital calculations by the DV-Xα method in order to discuss the electronic mechanism determining the voltage. This is followed by first principles total energy calculations using the FLAPW method in order to allow for a quantitative discussion of the voltage.

COMPUTATIONAL PROCEDURE

Molecular orbital (MO) calculations were performed using model clusters for layered $LiMO_2$ employing the computer code called SCAT [27], which is a

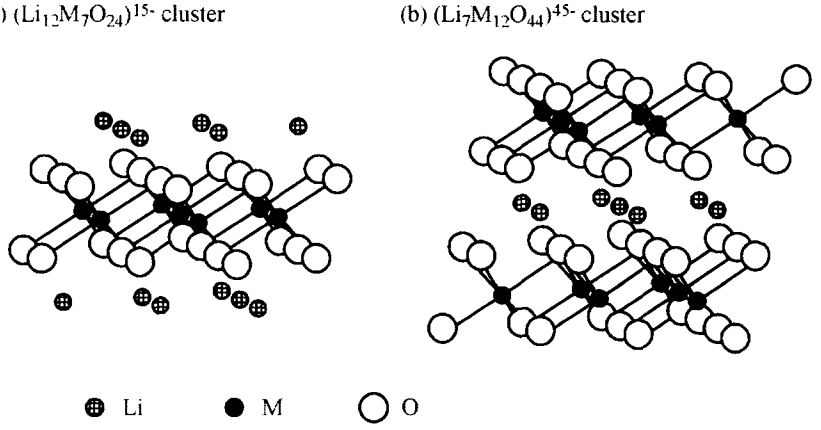

Fig 2. Model clusters for layered $LiMO_2$ (M = Ti - Ni), (a) $(Li_{12}M_7O_{24})^{15-}$ and (b) $(Li_7M_{12}O_{44})^{45-}$. Li, M and O atoms are denoted by crossed-patterned, filled and open circles, respectively.

modified version of the original DV-Xα program [28, 29]. Spin polarization was taken into account using the exchange and correlation term by Slater with $\alpha = 0.7$. Numerical atomic orbitals, which are generated flexibly by solving the radial part of the Schrödinger equation for a given environment, were used as basis functions. Minimal basis sets were used in order to understand the phenomena simply from the viewpoint of chemical bondings. Basis sets were 1*s*, 2*s* and 2*p* for Li and O, and 1*s*, 2*s*, 2*p*, 3*s*, 3*p*, 3*d*, 4*s* and 4*p* for 3*d* transition-metal elements. Integrations to obtain energy eigenvalues and eigenfunctions were made numerically.

Two kinds of model clusters as shown in Fig. 2 were chosen for layered $LiMO_2$ (M = Ti - Ni). One is centered by transition-metal ion. Li ions are located on the surface of the clusters. On the other hand, Li ion is located at the center of the other set of clusters. As will be seen later, the results of the two kinds of clusters are the same except for a small difference in absolute energy level. The model clusters were embedded in electrostatic potential generated by approximately 10,000 point charges of formal values. The values of Li, M and O were +1, +3 and –2, respectively.

Although $LiTiO_2$, $LiMnO_2$ and $LiFeO_2$ with α-$NaFeO_2$-structural type are metastable or not yet synthesized, all lithium 3*d* transition-metal oxides of $LiTiO_2$ to $LiNiO_2$ were chosen in the present study. Lattice parameters were adopted from the experimental data for $LiMO_2$ (M = V, Cr, Co and Ni). Metastable layered $LiFeO_2$ was synthesized by hydrothermal and ionic exchange method [18, 19].

Lattice parameters for layered $LiFeO_2$ were adopted from the experimental data reported by Ado *et al* [19]. The structure of layered $LiMnO_2$ [16, 17] was a distorted α-$NaFeO_2$-type due to the strong cooperative Jahn-Teller effect of high-spin Mn^{3+} ion. In the present study, the distortion was ignored and the structure was considered as a regular α-$NaFeO_2$-type, keeping the same volume and interlayer distances as the experimental data reported by Capitaine *et al* [16]. Experimental synthesis of $LiTiO_2$ with α-$NaFeO_2$-structural type has not been reported yet. The lattice parameters reported by Aydinol *et al* [22], which were optimized using the first principles plane-wave pseudopotential method, were adopted.

Spin polarization was allowed in all of the present calculations. Low-spin states were used for $LiCoO_2$ and $LiNiO_2$ as initial states of the calculation, whereas high-spin states for $LiTiO_2$ to $LiFeO_2$. In the present study, the spin state was not constrained during self-consistent calculations. In other words, the resultant spin configuration is an energetically favorable one, at least in the sense of local minimum. As for the magnetic structure, all of $LiMO_2$ were assumed to exhibit ferromagnetic ordering, since detailed magnetic structures were unknown. Singh reported that the difference in the total energy obtained by first principles band-structure calculations for ferromagnetic and antiferromagnetic $LiMnO_2$ is 0.173 eV [30]. The assumption of ferromagnetic ordering does not affect the discussion in the present study significantly.

Total energy band-structure calculations were made by the FLAPW method using the program code WIEN97 [31], developed by Blaha *et al.* The sphere radius was chosen to be 0.85 Å for all atoms. The exchange and correlation term under the generalized gradient approximation (GGA) of Perdew *et al.* [32] was employed. The number of basis functions was determined by an energy cutoff of 340 eV. Li-1*s* and M-3*s* and 3*p* orbitals were treated as semicore states. Reciprocal space integration was carried out using 5×5×5 mesh points in the first Brillouin zone. Convergence tests of the energy differences with respect to the basis-function cutoff, the number of mesh-points for the integration in reciprocal space and the sphere radii were carefully checked. The primitive cell of α-$NaFeO_2$-structural type is a rhombohedral one that contains only one chemical formula unit. The lattice parameters were the same as those used in the cluster calculations. Spin polarization was taken into account, assuming a ferromagnetic structure.

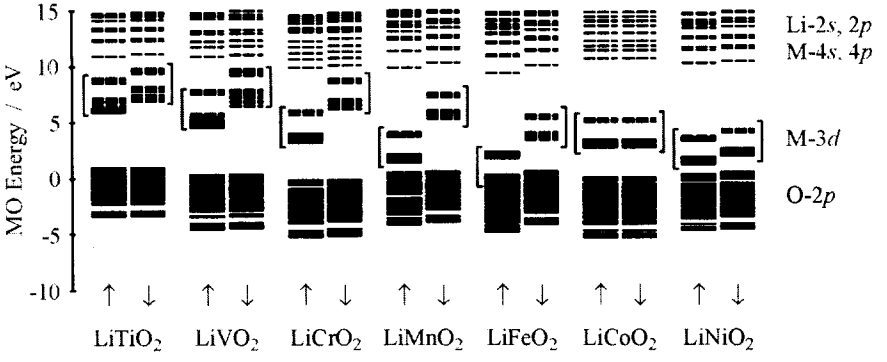

Fig 3. Energy level diagrams of the M-centered clusters, $(Li_{12}M_7O_{24})^{15-}$, obtained by DV-Xα calculation. ↑ and ↓ denote majority (up) and minority (down) spin states, respectively.

RESULTS AND DISCUSSION

Molecular orbital calculation using model clusters

Figure 3 shows MO energy level diagrams of all $LiMO_2$ by cluster calculations using the M-centered clusters, $(Li_{12}M_7O_{24})^{15-}$. With the increase in atomic number of M from Ti to Fe, the M-3*d* levels of majority spin (up spin) decrease in energy and the energy separation between majority and minority (down) spins increases. This behavior is quite natural for transition-metal oxides, leading to a high-spin electronic configuration of Mn^{3+} and Fe^{3+}. Conversely, $LiCoO_2$ and $LiNiO_2$ exhibit a low-spin configuration. This agrees well with experimental data [33]. The results of a series of Li-centered clusters, $(Li_7M_{12}O_{44})^{45-}$ are not greatly different except for absolute energy levels, which will be explained later.

The open-circuit voltage, $V_{OCV}(x)$, is given by the difference in the chemical potential of Li in the positive electrode material of Li_xMO_2, $\mu_{Li}^{positive}(x)$, and that in negative electrode material of metallic lithium, $\mu_{Li}^{negative}$.

$$V_{OCV}(x) = -\left(\mu_{Li}^{positive}(x) - \mu_{Li}^{negative} \right) / zF, \qquad (1)$$

where F is the Faraday constant and z is the charge transported by Li in the electrolyte. In most nonelectrically conducting electrolytes, $z = 1$. $\mu_{Li}^{positive}(x)$ may be related to sum of energies required to remove a Li ion and an electron from

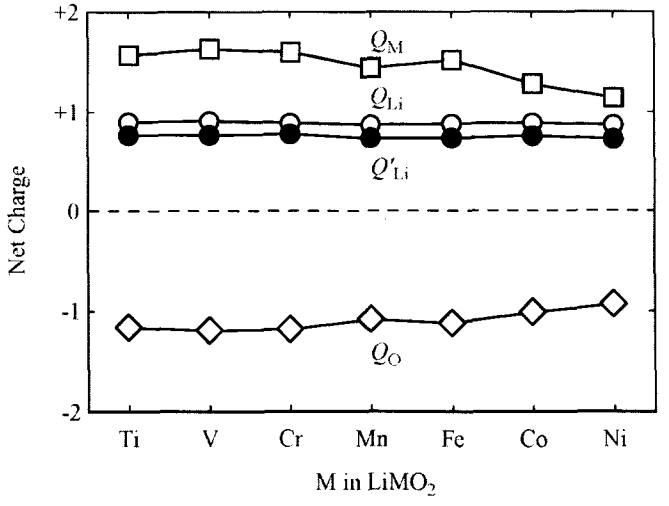

Fig 4. Net charges of Li, M and O, and modified charge of Li given by Eq. (2) in the M-centered clusters obtained by DV-Xα calculation.

Li_xMO_2. The former is related to the electrostatic potential at the Li position in Li_xMO_2. The latter is analogous to the work function of the system. These two factors in layered $LiMO_2$ will be evaluated on the basis of cluster calculations. Figure 4 shows net charges of Li, M and O ions obtained by Mulliken's population analysis [34] at the central part of the M-centered clusters. Regarding charges of Li, two values are shown. One is the net charge of Li, Q_{Li}, directly obtained by standard Mulliken's population analysis and the other is the modified net charge of Li, Q'_{Li}, determined by

$$Q'_{Li} = -(Q_M + 2Q_O), \qquad (2)$$

where Q_M and Q_O are the net charges of M and O obtained by standard Mulliken's population analysis. Because of the use of clusters that are different from the formal stoichiometry of the corresponding compounds, charge neutrality is not strictly satisfied. In order to discuss the electrostatic potential, a modified value, as given by Eq. (2), is practically useful. Q_{Li} may be better evaluated in the Li-centered cluster. It is approximately +0.7, which is almost independent of the transition-metal species. It is not significantly different from Q'_{Li} in the M-centered cluster, which is approximately +0.75. On the other hand, net charges of M and O are almost half of formal charges. This provides the evidence for the

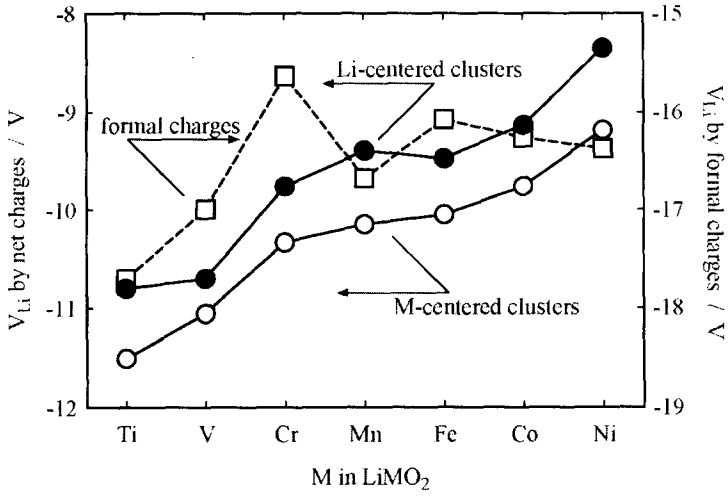

Fig 5. Electrostatic potential at the Li position deduced by the formal and net charges.

strong covalent bonding between M and O [35]. The values and their dependence on the transition-metal species are almost the same when a series of Li-centered clusters are used.

The electrostatic potential (Madelung potential) at the Li position, V_{Li}, is then computed using the net charges and the modified one. Calculations were made by the Ewald summation technique employing the program code GULP [36]. In this program, the acceleration parameter, η, was optimized in order to have an optimum convergence with respect to distance. The potential deduced by a set of formal charges is compared with that by net charges in Fig. 5. The potential deduced from the net charges is smaller by approximately 7 V than that from the formal charges, because of their smaller ionicity. Besides the absolute value, the dependence on the transition-metal species is different. It exhibits a maximum at $LiCrO_2$ when the formal charges are used, whereas it increases almost monotonically when the net charges are used. This could be explained by the trade-off between interatomic distances and net charges. The potential by formal charges is overly sensitive to the variation of the interatomic distance. The difference of about 1 V in the effective potentials evaluated using the two types of clusters is found. The dependence of the potential on transition-metal element by the two types of clusters is almost the same.

The energy required to remove an electron from the system may be correlated

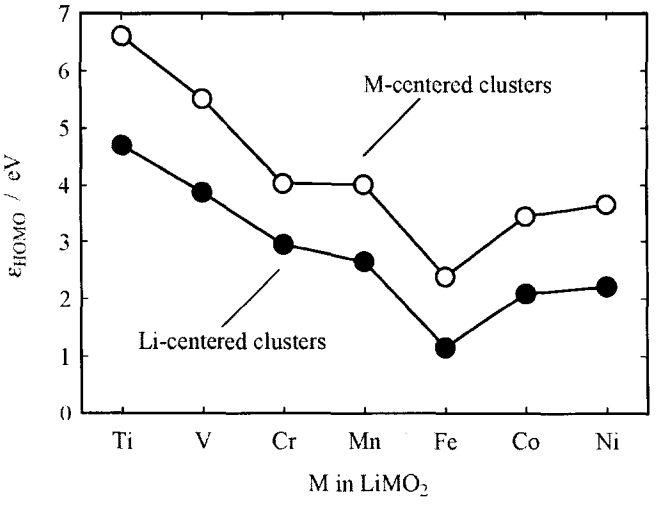

Fig 6. Energy of the HOMO in the two kinds of model clusters obtained by DV-Xα calculation.

with the energy of the highest occupied molecular orbital (HOMO), ε_{HOMO}. It is true that some ambiguity is always present for absolute energy levels. However, relative values may be reliable among a series of isostructural compounds. Figure 6 displays the energy of the HOMO. Results of the two types of clusters are almost the same except for the difference in absolute energy of about 1 eV. It is interesting that the energy of the HOMO does not decrease monotonically with increasing atomic number of transition-metal element; it shows a minimum at $LiFeO_2$ and then increases. In the case of isolated transition-metal ion of a fixed valence, the energy of *3d* orbital decreases with the increase in its atomic number when spin polarization is not allowed, because of the increase in the nuclear potential. In the present case, however, spin configuration is changed from high-spin state to low-spin one at $LiCoO_2$. This leads to the minimum of the energy of the HOMO at $LiFeO_2$, as shown in Fig. 6.

The sum of energies required to remove a Li ion and an electron from $LiMO_2$ can be expressed as

$$-(e V_{Li} + \varepsilon_{HOMO}), \qquad (3)$$

which is shown in Fig. 7. Comparison of this quantity with experimental and theoretical voltages will be made in the following section.

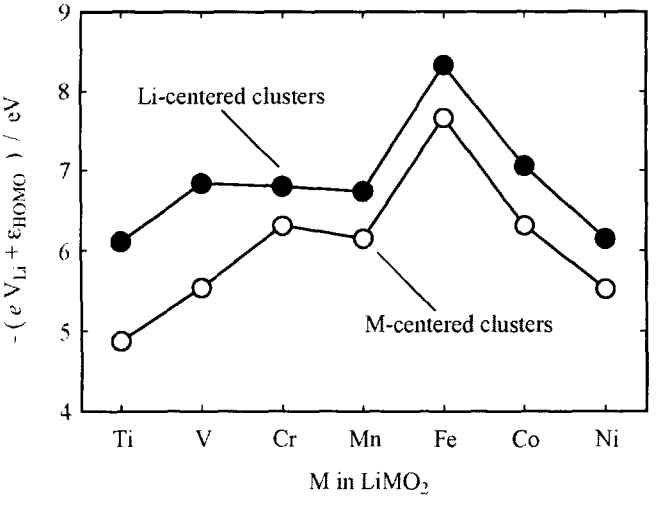

Fig 7. Sum of energies required to remove a Li ion and an electron from $LiMO_2$ given by Eq. (3).

Band-structure calculation for $LiMO_2$ and MO_2

Band-structures of layered $LiMO_2$ and MO_2 were systematically reported by Aydinol *et al.* [22] using the plane-wave pseudopotential method. As described above, they did not include spin polarization. Figure 8 compares density of states (DOS) of $LiCoO_2$ obtained 1) by the present FLAPW calculation, 2) by the present cluster calculation using the Co-centered cluster, 3) by Aydinol *et al.* using the pseudopotential method, and 4) by Czyżyk *et al.* [37] using the localized spherical waves (LSW) method. They are aligned so as to make the highest occupied energy zero. The cluster result was broadened by Gaussian functions with a full width at half maximum (FWHM) of 0.5 eV. As can be seen in Fig. 8, the DOS of up and down spins are the same. In other words, the net magnetic moment is zero. Therefore, inclusion of spin polarization does not change the electronic structure in this case. The DOS of the present FLAPW calculation using the tetrahedron method looks almost the same as that reported by Czyżyk *et al.* The O-2*p* band by Czyżyk *et al.* is composed of three major peaks. A gap can be seen between the O-2*p* and the Co-3*d* (t_{2g}-like) bands. The result of the present cluster calculation agrees well with those of the band-structure calculations except for the larger band gap. Contrary to them, the DOS reported by the pseudopotential calculation did not reproduce these features, particularly

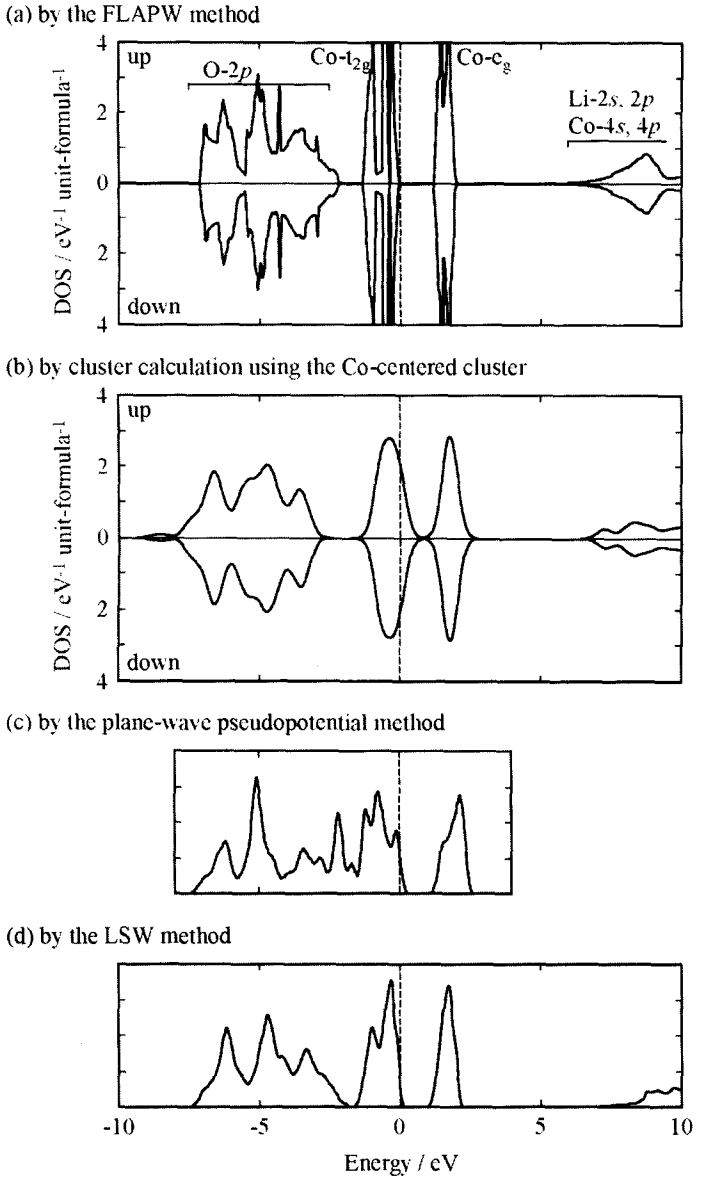

Fig 8. Density of states of $LiCoO_2$ obtained (a) by the FLAPW calculation, (b) by the cluster calculation using the Co-centered cluster, (c) by the plane-wave pseudopotential method (Ref. 22) and (d) by the LSW method (Ref. 37).

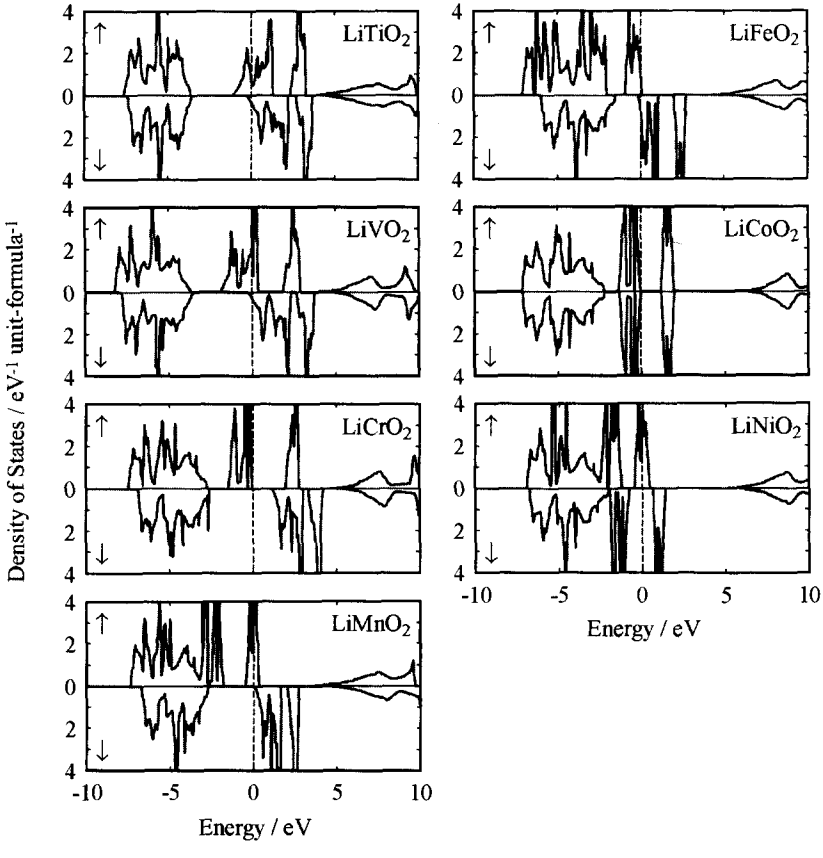

Fig 9. Density of states of layered $LiMO_2$ (M = Ti - Ni) obtained by the FLAPW calculations. They are aligned so as to make the highest occupied energy zero.

around the band gap. Aydinol *et al.* [22] pointed out that the choice of computational method does not affect the voltage. However, the claim may not always be valid. The DOS of the layered $LiMO_2$ (M = Ti - Ni) by the FLAPW calculations are compared in Fig. 9. No contradictory results are found with the cluster results, which confirms the validity of each computational result.

The average voltage of $LiMO_2$ is given by

$$V_{AVE} = \int_0^1 V_{OCV}(x)dx \ , \qquad (4)$$

using $V_{OCV}(x)$ defined by Eq. (1). The following quantity V^*_{AVE} is often used [22-25, 38, 39] as an approximated average voltage by the band-structure calculation.

$$V^*_{AVE} = - \{ E_T[LiMO_2] - E_T[MO_2] - E_T[Li] \} / F , \qquad (5)$$

where E_T is the total energy of the system. V^*_{AVE} is equal to V_{AVE} when both entropy and volume-change terms are negligible in free-energy difference between $LiMO_2$ and MO_2. The latter term is known to be on the order of 10^{-5} V [22]. In the present study, the total energies per unit formula for $LiMO_2$, MO_2 and metallic lithium with the body centered cubic (BCC) structure were computed independently, and then V^*_{AVE} was obtained. The same lattice parameters of $LiMO_2$ as those for cluster calculations were used. As experimental data of MO_2 are not known for most of the cases, the same lattice parameters as those for $LiMO_2$ were used for MO_2. In other words, structural optimization was not carried out. Wolverton and Zunger [24] reported that lattice constants are reduced by 1.1 % for a and 10.8 % for c in the extraction of Li from layered $LiCoO_2$ by FLAPW calculation. However, their V^*_{AVE} for $LiCoO_2$ is 3.78 V, which is only 0.32 V higher than the present FLAPW result. The present V^*_{AVE} values are displayed in Fig. 10, together with those reported by the pseudopotential calculations [22]. Experimental voltages are shown for comparison. The values of V^*_{AVE} calculated by the two methods are not significantly different. This is a surprising result because the magnitude of the voltage is only about 10^{-4} of the total energies of $LiMO_2$ and MO_2.

The tendency of V^*_{AVE} by the FLAPW calculation and that of the quantity shown in Fig. 7 agree well for M = Ti, V, Cr, Mn and Co. The FLAPW result is approximately 1 V smaller for $LiFeO_2$, and is approximately 1 V larger for $LiNiO_2$ when values in Figs. 7 and 10 are aligned to meet the best agreement. Since two calculations were conducted for the same pair of $LiMO_2$ and MO_2 structures, excluding the lattice relaxation associated with the extraction of Li, the discrepancy cannot be attributed to the structural relaxation. However, the value shown in Fig. 10 includes both the total energies of $LiMO_2$ and MO_2, whereas only the response of $LiMO_2$ to the extraction of Li is taken into account in the case of Fig. 7. The differences of $LiFeO_2$ and $LiNiO_2$ may be explained by the differences in the relative stability of MO_2.

Unfortunately, experimental data of $LiMO_2$ (M = Ti, Cr, Mn and Fe) are not available. In addition, experimental data of layered $LiVO_2$ is obtained in the range of $0 \le x \le 1/3$ in $Li_{1-x}VO_2$ [10, 11], whereas a whole range of x from 0 to 1 is used to obtain the experimental voltages for $Li_{1-x}CoO_2$ and $Li_{1-x}NiO_2$. They may not be comparable. Nevertheless, the experimental voltage agrees with the calculated

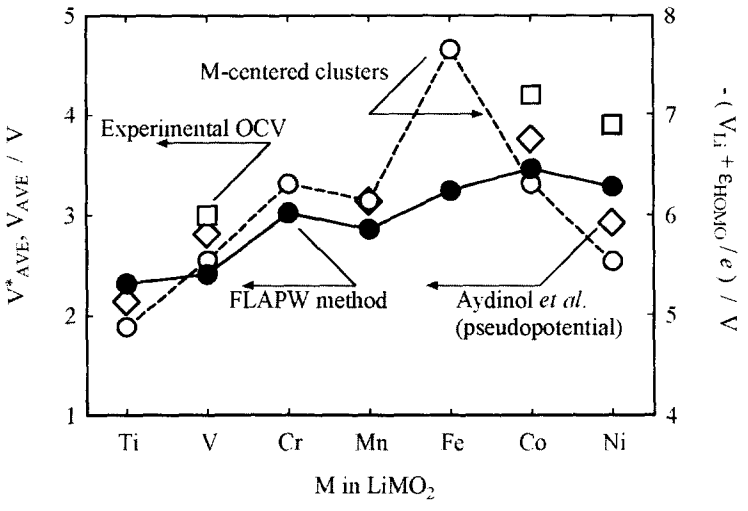

Fig 10. Average voltages obtained by the present FLAPW calculation and by the plane-wave pseudopotential calculation (Ref. 22). Value defined in Fig. 7 is shown for comparison.

V^*_{AVE} within an error of 1 V.

CONCLUSION

Two kinds of first principles calculations, i.e., molecular orbital calculation using model clusters by the DV-Xα method and total energy band-structure calculation by the FLAPW method, are combined in order to evaluate the voltage of layered $LiMO_2$ (M = Ti - Ni) and to understand the electronic mechanism determining the voltage. The voltage is quantitatively evaluated using the FLAPW method. The electronic structure is then analyzed using molecular orbital calculation. Effective electrostatic potential at the Li position is estimated using the net charges by the Ewald summation technique. The effective electrostatic potential should be related to the energy required to remove a Li ion from $LiMO_2$. It is smaller by approximately 7 V than the electrostatic potential deduced by the formal charges because of the smaller ionicity. Besides the absolute value, the dependence on the transition-metal species is different. The effective electrostatic potential monotonically increases with the increase in the atomic number of transition-

metal element. The potential deduced by formal charges should be overly sensitive to the variation of the interatomic distances. The energy required to remove an electron from the system is estimated from the energy of the HOMO. It shows a minimum value at $LiFeO_2$, which can be explained by the balance of two factors: 1) the decrease in energy of the M-3*d* band with the increase in the atomic number of transition-metal element, and 2) the spin configuration of the M-3*d* band. The approximated average voltage, V^*_{AVE}, obtained by the FLAPW calculation reproduces experimental average voltage within an error of 1 V. The sum of the two factors as described above is found to explain the experimental dependence of the voltage on the transition-metal element. The sum also agrees well with the theoretical average voltage except for $LiFeO_2$ and $LiNiO_2$, which show discrepancies of about 1 V.

REFERENCES

(1) K. Mizushima, P. C. Jones, P. J. Wiseman and J. B. Goodenough, Mater. Res. Bull., 15, 783 (1980).
(2) T. Ohzuku and A. Ueda, Solid State Ionics, 69, 201 (1994).
(3) E. Ferg, R. J. Gummow, A. de Kock and M. M. Thackeray, J. Electrochem. Soc., 141, L147 (1994).
(4) R. Koksbang, J. Barker, H. Shi and M. Y. Saïdi, Solid State Ionics, 84, 1 (1996).
(5) J. N. Reimers and J. R. Dahn, J. Electrochem. Soc., 139, 2091 (1992).
(6) T. Ohzuku and A. Ueda, J. Electrochem. Soc., 141, 2972 (1994).
(7) G. G. Amatucci, J. M. Tarascon and L. C. Klein, J. Electrochem. Soc., 143, 1114 (1996).
(8) T. Ohzuku, A. Ueda, M. Nagayama, Y. Iwakoshi and H. Komori, Electrochim. Acta, 38, 1159 (1993).
(9) A. Hirano, R. Kanno, Y. Kawamoto, Y. Takeda, K. Yamaura, M. Takano, K. Ohyama, M. Ohashi and Y. Yamaguchi, Solid State Ionics, 78, 123 (1995).
(10) L. A. de Picciotto, M. M. Thackeray, W. I. F. David, P. G. Bruce and J. B. Goodenough, Mater. Res. Bull., 19, 1497 (1984).
(11) L. A. de Picciotto and M. M. Thackeray, Mater. Res. Bull., 20, 1409 (1985).
(12) C. D. W. Jones, E. Rossen and J. R. Dahn, Solid State Ionics, 68, 65 (1994).
(13) T. A. Hewston and B. L. Chamberland, J. Phys. Chem. Solids, 48, 97 (1987).
(14) J. N. Reimers, E. W. Fuller, E. Rossen and J. R. Dahn, J. Electrochem. Soc., 140, 3396 (1993).
(15) I. Koetschau, M. N. Richard, J. R. Dahn, J. B. Soupart and J. C. Rousche, J.

Electrochem. Soc., 142, 2906 (1995).
(16) F. Capitaine, P. Gravereau and C. Delmas, Solid State Ionics, 89, 197 (1996).
(17) Y.-I. Jang, B. Huang, Y.-M. Chiang and D. R. Sadoway, Electrochem. Solid-State Lett., 1, 13 (1998).
(18) B. Ammundsen, J. Desilvestro, T. Groutso, D. Hassell, J. B. Metson, E. Regan, R. Steiner and P. J. Pickering, J. Electrochem. Soc., 147, 4078 (2000).
(19) K. Ado, M. Tabuchi, H. Kobayashi, H. Kageyama, O. Nakamura, Y. Inaba, R. Kanno, M. Takagi and Y. Takeda, J. Electrochem. Soc., 144, L177 (1997).
(20) R. Kanno, T. Shirane, Y. Inaba and Y. Kawamoto, J. Power Sources, 68, 145 (1997).
(21) K. Miura, A. Yamada and M. Tanaka, Electrochim. Acta, 41, 249 (1996).
(22) M. K. Aydinol, A. F. Kohan, G. Ceder, K. Cho and J. Joannopoulos, Phys. Rev. B, 56, 1354 (1997).
(23) G. Ceder, M. K. Aydinol and A. F. Kohan, Comp. Mater. Sci., 8, 161 (1997).
(24) C. Wolverton and A. Zunger, Phys. Rev. B, 57, 2242 (1998).
(25) C. Wolverton and A. Zunger, J. Electrochem. Soc., 145, 2424 (1998).
(26) C. Wolverton and A. Zunger, Phys. Rev. Lett., 20, 606 (1998).
(27) H. Adachi, M. Tsukada and C. Satoko, J. Phys. Soc. Jpn., 45, 875 (1978).
(28) F. W. Averill and D. E. Ellis, J. Chem. Phys., 59, 6412 (1973).
(29) D. E. Ellis, H. Adachi and F. W. Averill, Surf. Sci., 58, 497 (1976).
(30) D. J. Singh, Phys. Rev. B, 55, 309 (1997).
(31) P. Blaha, K. Schwarz and J. Luitz, "WIEN97, A Full Potential Linearized Augmented Plane Wave Package for Calculating Crystal Properties", Karlheinz Schwarz, Techn. Univ. Wien, Vienna (1999).
(32) J. P. Perdew, K. Burke and M. Ernzerhof, Phys. Rev. Lett., 77, 3865 (1996).
(33) Experiments for $LiCoO_2$ can be found in J. van Elp, J. L. Wieland, H. Eskes, P. Kuiper, G. A. Sawatzky, F. M. F. de Groot and T. S. Turner, Phys. Rev. B, 44, 6090 (1991).
(34) R. S. Mulliken, J. Chem. Phys., 23, 1833 (1955).
(35) Y. Koyama, Y.-S. Kim, I. Tanaka and H. Adachi, Jpn. J. Appl. Phys., 38, 2024 (1999).
(36) J. D. Gale, J. Chem. Soc. Faraday Trans., 93, 629 (1997).
(37) M. T. Czyżyk, R. Potze and G. A. Sawatzky, Phys. Rev. B, 46, 3729 (1992).
(38) E. Deiss, A. Wokaun, J. L. Barras, C. Daul and P. Dufek, J. Electrochem. Soc., 144, 3877 (1997).
(39) S. K. Mishra and G. Ceder, Phys. Rev. B, 59, 6120 (1999).

Electronic Structure of Chromium Aluminum Oxide

Hyunju Chang, Youngmin Choi, and Jae Do Lee

Advanced Materials Division, Korea Research Institute of Chemical Technology Taejon, 305-600, Korea

(Received February 6, 2002; in final form April 19, 2002)

Chromium aluminum oxide compounds have received attention recently, because of their potential application as a phase shift mask material for deep UV microlithography in semiconductor industry. Their performance as a mask material seems to strongly depend on their electronic structure. It motivated us to investigate the electronic structure of chromium aluminum oxide via the first principle calculation method and X-ray photoelectron spectroscopy (XPS). The atomistic simulation is used to determine their atomic structures of different concentrations of Al in Cr_2O_3. Then the embedded cluster method within the framework of discrete variational (DV)-Xα method is employed to investigate the electronic structure of their optimized structures. The density of states (DOS) for several model clusters are calculated and discussed with experimental XPS, conjunction with their atomic structures.

CONTENTS

KEYWORDS

Phase shift mask; XPS; cluster method; density of states

ADVANCES IN QUANTUM CHEMISTRY, VOLUME 42

0065-3276/03 $35.00

1. INTRODUCTION

In past several years, chromium aluminum oxide (Cr-Al-O) compounds have got increasing attention due to their application to attenuated-phase shift mask for deep-UV microlithography in semiconductor fabrication process[1]. The prior requirements of mask material are proper optical band gap and chemical stability at the exposure wavelength. Cr-Al-O-based mask materials have been studied for application of microlithography using 193 nm wavelength of ArF laser [2]. First, Cr-based materials have been developed for the mask materials at 248 nm exposure wavelength due to its optical band gap of 4.25 eV (about 290 nm) and its chemical stability during etching process. For the mask material of 193 nm (6.42 eV) exposure wavelength, Al was introduced to Cr_2O_3, because the optical band gap of Al_2O_3 is much larger than the exposure wavelength. However, the semiconductor industry requests more fine microlithography technique with shorter wavelength of 157 nm F_2 laser. For further development of new mask material, full understanding of the present material is needed. Previously Z. Jiang et al. [3,4] calculated the band gap of chromium aluminum oxide theoretically by the Discrete Variational (DV)-Xα method with the cluster model of crystalline phase. However, the electronic structure of Cr-Al-O system has not been discussed with experimental spectroscopy yet. In this report, we show X-ray photoelectron spectroscopy (XPS) spectra and discuss the calculated atomic structures and the density of states from the model clusters conjunction with XPS results.

2. EXPERIMENTS

Chromium aluminum oxide (Cr-Al-O) films were deposited using a planner circular type DC magnetron reactive sputtering system with a disc-shaped 4 inch Cr-Al target [2]. The Ar, N_2, and O_2 gas mixture was injected as a reaction gas into the chamber. The films were deposited under the conditions of substrate temperature of 573K, power of 40W and total chamber pressure of 4.7×10^{-3} Torr. The target to substrate distance was fixed to be 132.4mm. Films were deposited on quartz and Si substrates simultaneously. The Composition of film was analyzed by a wavelength dispersive spectrometer (WDS). The photoemission spectra were measured by an ESCALAB MKII (VG Scientific) spectrometer. The exciting beams were Mg Kα radiation ($h\nu$=1253.6eV) for X-ray photoelectron spectroscopy. Binding energy was referred to the C 1s peak at 284.6eV from adventitious hydrocarbon contaminant.

3. COMPUTATIONAL METHODOLOGY

3.1 Atomistic Simulation

The atomistic simulation method, which is implanted in GULP (General Utility Lattice Program)[5], is employed to determine the atomic structures of several combinations of Cr-Al-O system, such as Cr_4O_6, $Cr_3Al_1O_6$, $Cr_2Al_2O_6$, $Cr_1Al_3O_6$, and Al_4O_6. The details of the atomistic simulation technique have been described elsewhere [6] and we will give a short review here. The atomistic calculations are based on Born model, in which potential energy is partitioned into long range Coulombic term and short range pair potential of Buckingham form,

$$V_{ij}(r_{ij}) = A_{ij} \exp(\frac{-r_{ij}}{\rho_{ij}}) - \frac{C_{ij}}{r_{ij}^6} \quad (1)$$

where r_{ij} is interatomic distance, and A_{ij}, ρ_{ij}, and C_{ij} are parameters assigned to each ion-ion interaction [7], listed in Table 1. The ionic polarizibility was incorporated into the potential model via shell model. The shell model describes ionic polarization by treating each ion in terms of core (representing the nucleus and core electrons) connected via a harmonic spring to a shell (representing the valence electron) [8]. The shell model has been proven to simulate effectively both dielectric and elastic properties for many ceramic oxides. The spring constant of the shell model is also listed in Table 1.

Table 1
Interatomic potential parameters used for Cr-Al-O system

Interaction	A(eV)	ρ (Å)	C (eV•Å^6)
Cr^{3+} - O^{2-}	9547.96	0.2192	32.0
Al^{3+} - O^{2-}	1725.20	0.28971	0.0
O^{2-} - O^{2-}	1204.18	0.3165	0.0
Spring constant	O core - O shell	6.3	

Cr_2O_3 and Al_2O_3 have rhombohedral structures, as shown in Fig. 1-(a) and they form a completely solid solution at whole composition. It is reported that lattice parameters of solid solution change linearly with a concentration ratio of Cr and Al [9]. Therefore, we took lattice parameters by interpolation between lattice parameters of Cr_2O_3 and Al_2O_3 for $Cr_3Al_1O_6$, $Cr_2Al_2O_6$, and $Cr_1Al_3O_6$. However there are four possibilities even when one Cr ion is replaced by Al in $Cr_3Al_1O_6$, for example. To determine the structure of the lowest energy, the electrostatic energies were calculated for all the possible combinations of Cr and Al. Figure 1-(b) shows the configurations of cations in a unit cell, which have the lowest energies. The individual atomic positions were also relaxed keeping the lattice parameters fixed. It was found that the atomic positions hardly changed after relaxation.

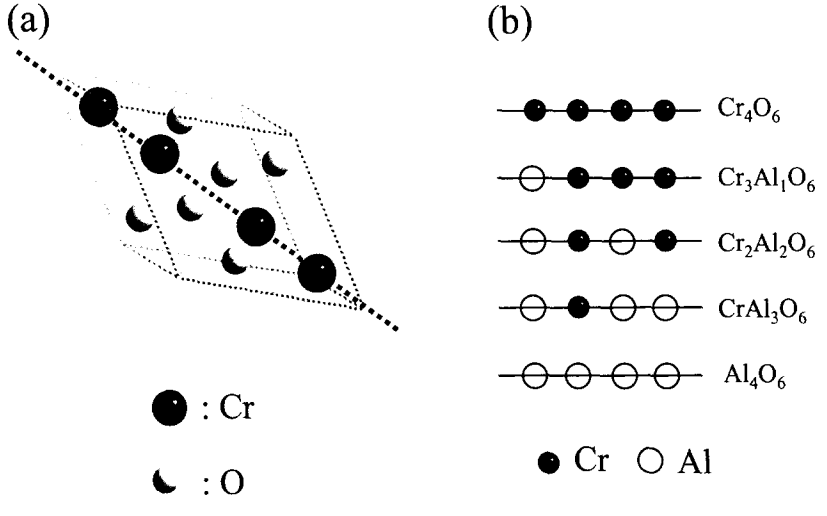

Fig. 1 (a) Unit cell of Cr_2O_3 rhombohedral structure, which consists of 4 Cr atoms along the dotted line. (b) Schematic diagrams of cation (Cr and Al) configuration in a unit cell, which give the lowest energies by the atomistic simulation.

3.2 Embedded Cluster Method

The first-principles method employed for embedded cluster calculations is the Discrete Variational (DV)-Xα method, which is described in detail elsewhere [10,11]. The DV-Xα method is based on density functional theory, in which the Coulomb and exchange potential energy is a functional of the electronic density. The exchange potential for DV-Xα method is represented as

$$V_{X\alpha}(\vec{r}) = -3\alpha\left[\left(\frac{3}{8\pi}\right)\rho(\vec{r})\right]^{\frac{1}{3}}, \qquad (2)$$

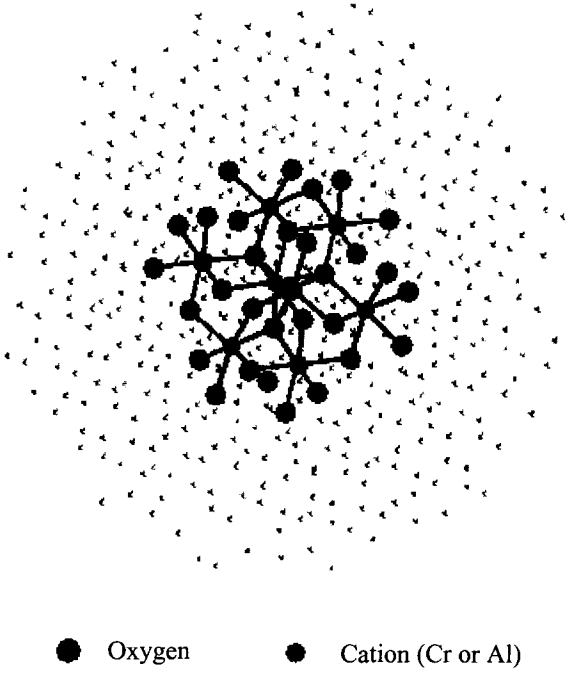

Fig. 2 A model cluster of 38 atoms, M_8O_{30} (M=Cr or Al) embedded in crystal environment: Dark big circles are oxygens and gray small circles are cations. The small dots are atomic positions of environment, which are treated as ionic potentials.

where the value of 0.7 for α has been known to be optimal in reproducing experimental ionization energies and used through our calculations.
In the present cluster calculations, we have used a frozen core approximation. Details of it can be obtained from Ref.[10]. Atomic-centered core orbitals are obtained from appropriate atomic/ionic configurations, and are held fixed through the SCF iteration process within the frozen core approximation. Here we include *(3d4s4p)* orbitals of Cr, *(2s2p)* orbitals of O, and *(2s2p3s3p)* orbitals of Al in the variational procedure.
Figure 2 shows one of the model clusters that we took for Cr-Al-O system. 38 atoms of M_8O_{30}(M=Cr,Al) are included in each cluster, in which each cation is fully coordinated with 6 oxygens. We have carried out calculations for five model clusters of Cr_8O_{30}, $Cr_6Al_2O_{30}$, $Cr_4Al_4O_{30}$, $Cr_2Al_6O_{30}$, and Al_8O_{30} representing Cr_2O_3, $Cr_3Al_1O_6$, $Cr_2Al_2O_6$, $Cr_1Al_3O_6$, and Al_2O_3, respectively. The center of the cluster was taken between the central two cations. The atoms in a cluster were grouped as 2M-3O-6O-6M-3O-6O-6O-6O (M=Cr or Al) according to their distance from the center. Each cluster was embedded in about 450 atom environment within a sphere of radius 10 Å. The atoms in the environment are represented as ionic potentials obtained from the cluster calculations self-consistently.
The coordinates of the each ion in the cluster and the environment were taken from the optimized structure by atomistic simulation. When Cr is replaced by Al, the positions of the ions deviate a little from those of the crystalline Cr_2O_3. Therefore, no symmetry was assumed for the present cluster calculations.
Partial density of states (PDOS) of the central cations and the nearby oxygens are calculated using Mulliken charge analysis of the molecular orbitals with Lorentzian broadening, as described in Ref. [12].

4. RESULTS AND DISCUSSIONS

Figure 3 shows the X-ray photoelectron spectroscopy (XPS) spectra of the various samples of Cr-Al-O system. Cr component of the sample increases from (a) to (g), where (a) is close to Al_2O_3 while (g) is close to Cr_2O_3. However, it should be noted that any samples are not exactly Al_2O_3 nor Cr_2O_3, since it is difficult to obtain the stoichiometric sample with DC magnetron reactive sputtering. Therefore, we have to limit our discussion to the trend of change as the ratio of Cr and Al changes. In Fig. 3-(I), there are two major peaks shown. The first peak, in the range of 20 eV and 25 eV, and the broad second peak, near 5 eV, can be assigned to O 2s band and O 2p band, respectively. The O 2s peak seems hardly influenced by the ratio of Cr and Al in Cr-Al-O compounds. Figure 3-(II) shows XPS spectra measured under 16 eV for the information of the valence band in detail. The O 2p peak near 5 eV is getting broader as Al component increases, and it develops into two peaks at the sample (a). The third peak near 1 eV is found in

the sample (g) of Fig. 3-(II), as pointed by an arrow. There is also a shoulder peak near 1 eV in the samples of (e) and (f). This third peak near 1eV seems to belong to Cr 3d valence band, since this peak is clearly shown as Cr component increases.

The calculated PDOS is shown in Fig. 4. The first peak of Fig. 3-(I), between 20 eV and 25 eV of binding energy, is confirmed as O 2s peak by PDOS calculation. The PDOS peak of Cr 3d below 0 eV, which is pointed by an arrow, is the valence band of partially occupied Cr 3d. This Cr 3d peak agrees with the third peak of Fig. 3-(II), which is shown in Cr- rich compounds only. The PDOS of O 2p locates in the range of 5 eV and 12 eV below Fermi energy. The O 2p PDOS does not show any big change from Al_2O_3 to Cr_2O_3. The O 2p PDOS of Al_2O_3 is little broader than the others. The O 2p valence band seems hardly changed, when Cr is replaced by Al.

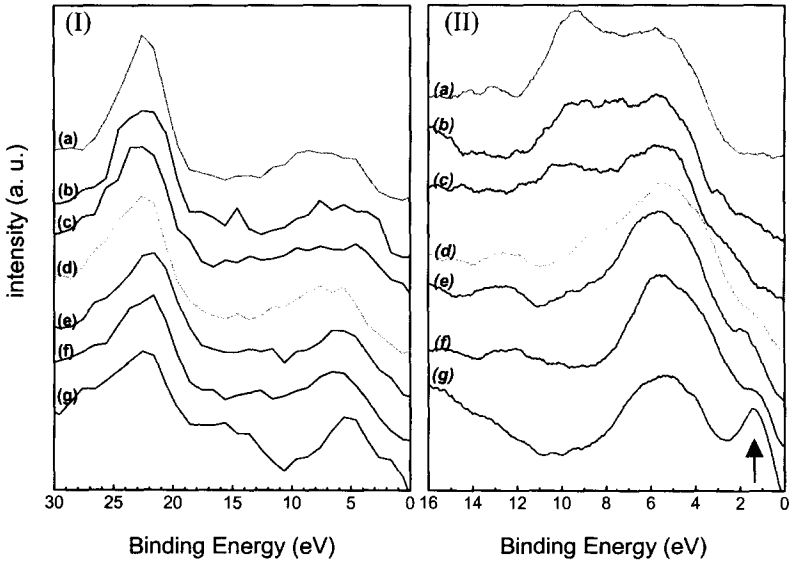

Fig. 3 X-ray photoelectron spectroscopy (XPS) spectra of the various samples of Cr-Al-O system; (I) shows XPS spectra under 30 eV, while (II) shows more detailed XPS spectra under 16 eV. Cr component of the sample increases from (a) to (g), where Cr/Al/O atomic ratios are (a)(0.00/0.28/0.72), (b)(0.08/0.33/0.59)), (c)(0.13/0.26/0.61), (d)(0.16/0.20/0.64)), (e)(0.29/0.12/0.59)), (f)(0.40/0.05/0.55), (g)(0.61/0.01/0.38), respectively.

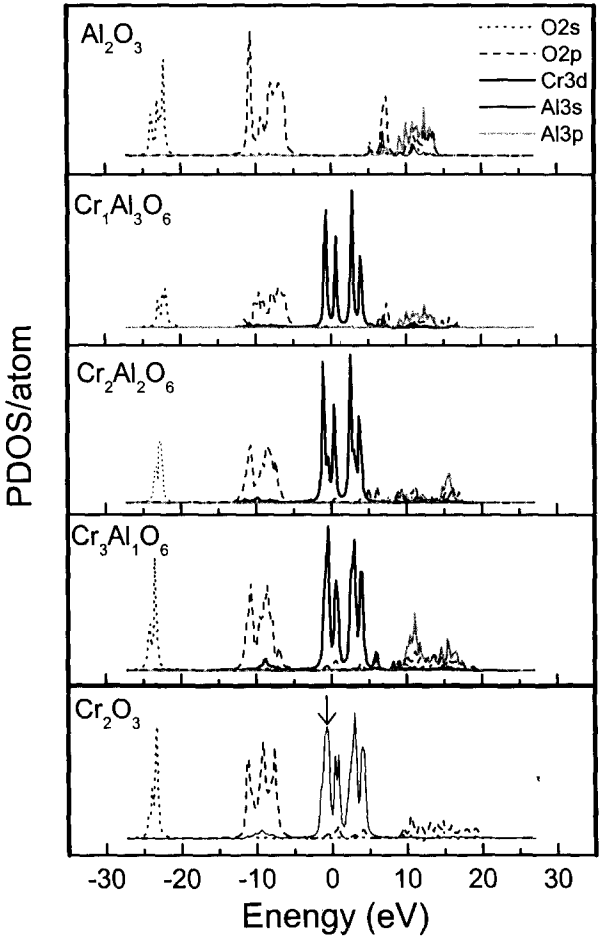

Fig. 4 Partial density of states of the central cations and the nearest neighboring oxygens from the model cluster calculations of Cr-Al-O system. Fermi energy of the system is taken as 0 eV.

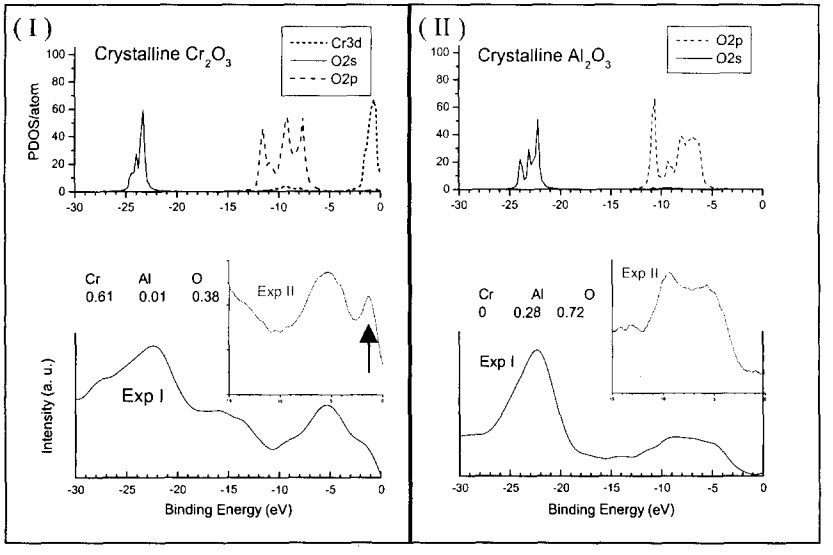

Fig. 5 Comparison of PDOS and XPS spectra; (I) The PDOS is calculated from the cluster taken from crystalline Cr_2O_3, and the XPS spectra are obtained from the Cr-rich compound of sample (g). (II) The PDOS is calculated from the cluster taken from crystalline Al_2O_3, and the XPS spectra are obtained from the Al-rich compound of sample (a).

Figure 5 shows comparison of XPS spectra of sample (a) and (g), and the PDOS of valence band of Cr_2O_3 and Al_2O_3 in detail. In Fig. 5-(I), the PDOS of O 2s and Cr 3d of Cr_2O_3 agrees well with the XPS spectra, while the PDOS of O 2p does not. The calculated O 2p PDOS of Cr_2O_3 is much broader than XPS O 2p band of sample (g). In Fig. 5-(II), an overall shape of PDOS of O 2s and O 2p of Al_2O_3 agrees well with XPS spectra. The main reasons for disagreement of O 2p PDOS with XPS in Cr-rich compound can be two aspects. All the measured samples are off the stoichiometry of M_2O_3(M=Cr or Al). It means coordination of O near a cation can be much different from the coordination of O in rhombohedral structure. Usually O 2p PDOS is very sensitive to the coordination of O with the nearby cations. The disagreement in the Cr-rich compounds infers that local oxygen coordination is much different from that in rhombohedral structure. The mixed structure of crystalline and amorphous structures of Cr_2O_3 film was reported when it was prepared by DC magnetron sputtering method [13]. Another

possible reason is a limitation of frozen core approximation in our calculations. The effect of Cr 3p should be checked in the further investigation.

5. SUMMARY

We have investigated the local electronic structure of the Cr-Al-O system using XPS and atomistic simulations and model cluster calculations. Our atomistic simulations show that no drastic change in atomic structure when Cr is replaced by Al. It is expected from that the ionic radius of Al^{3+}(0.054 nm) is similar to that of Cr^{3+} (0.062 nm) in the coordination number 6 environment. Therefore our cluster calculations, based on the structure obtained from atomistic simulation, reveal the characteristics of crystalline Cr_2O_3 and Al_2O_3 only. Unfortunately, our Cr-rich compounds are much out of stoichiometry of Cr_2O_3, rather close to Cr_3O_2. Thus we cannot expect 6-fold coordination of oxygens around Cr. Moreover, the discrepancy between O 2p PDOS and XPS results demonstrates that its local structure is much different from the crystalline structure of Cr_2O_3. On the contrary to Cr-rich compounds, the calculated O PDOS agrees well with XPS spectra of Al-rich compounds. It infers that the structure of Al-rich compounds seems to keep 6-fold coordination. Even the Al-excess compound of the sample (a) seems to keep 6-fold coordination locally. From our calculations and XPS results, we can conclude that the amorphous structure can be expected in Cr-rich compounds, while the crystalline structure is kept locally in Al-rich compounds.

6. ACKNOWLEDGMENTS

Financial support of the Ministry of Science and Technology of Korea is gratefully acknowledged.

7. REFERENCES

[1] M. D. Levenson, N. S. Viswanathan, and R. A. Simpson, IEEE Trans. Electron Devices ED-29, 1828 (1982).
[2] E. Kim, S. Hong, S. Lim, Y. Kim, D. Kim, and K. No, Appl. Opt., **37**(19), 4254 (1998)
[3] Z. Jiang, T. Yamaguchi, E. Kim, S. Hong, K. No, Y. Kang, S. Park, and Y. Koh, Bulletin of the Society for Discrete Variational Xa, **10**(2), 22 (1997)
[4] Z. Jiang, K. Ohshimo, M. Aoyama, and T. Yamaguchi, Jpn. J. Appl. Phys., **37**, 4008 (1998)
[5] J. D. Gale, J. Chem. Soc., Faraday Trans., **93**(4), 629 (1997)
[6] C. R. A. Catlow: *Solid State Chemistry : Techniques,* A. K. Cheetham and P. Day Ed. (Clarendon Press, Oxford, 1987)

[7] L. Minervini, M. O. Zacate, and R. W. Grimes, Solid State Ionics., **116,** 333 (1996)
[8] B. G. Dick and A. W. Overhauser, Phys. Rev., **112,** 90 (1958)
[9] M. Watanabe, T. Hirayama, M. Yoshinaka, K. Hirota, and O Yamaguchi, Mat. Res. Bull., **31**(7), 861 (1996)
[10] E. J. Baerends, D. E. Ellis, and P. Ros: Chem. Phys. **2,** 41 (1973)
[11] A. Rosen, D. E. Ellis, H. Adachi, and F. W. Averill: J. Chem. Phys., **65,** 3629 (1976)
[12] D. E. Ellis, G. A. Benesh, and E. Byrom, *Phys. Rev. B,* **16,** 3308 (1977)
[13] E. Kim, Z. Jiang, and K. No, Jpn. J. Appl. Phys., **39**(8), Part 1, 4820 (2000)

Electronic States Associated with Bond Disorder at ZnO Grain Boundaries

Fumiyasu Oba*
Engineering Research Institute, The University of Tokyo, Bunkyo, Tokyo 113-8656, Japan

Isao Tanaka and Hirohiko Adachi
Department of Materials Science and Engineering, Kyoto University, Sakyo, Kyoto 606-8501, Japan

(Received January 15, 2002; in final form February 6, 2002)

Abstract
Symmetric tilt boundaries in ZnO have been investigated by a first-principles molecular orbital method to elucidate the effects of bond disorder on the electronic structure. Equilibrium geometries with and without dangling bonds, which are obtained within a Σ=7 misorientation by empirical lattice statics calculations, are employed. For the configuration without dangling bonds, the electronic structure is similar to that of the bulk despite the presence of bond distortion. The configuration with dangling bonds exhibits localized electronic states near the conduction band edge, which are not deep in the band gap. The interaction of atomic orbitals that constructs the valence and conduction band is examined to understand this behavior. The results suggest that bond disorder has a tendency to generate specific electronic states within the valence and conduction band owing to the band structure intrinsic to ZnO. Bond disorder is therefore unlikely to form deep electronic states in general at ZnO grain boundaries.

Keywords: ZnO, Grain boundary, Molecular orbital method, Electronic structure, Dangling bond

CONTENTS

* JSPS Research Fellow; e-mail: oba@sigma.t.u-tokyo.ac.jp

ADVANCES IN QUANTUM CHEMISTRY, VOLUME 42

0065-3276/03 $35.00

1. INTRODUCTION

Grain boundaries often generate specific properties in polycrystalline materials. Nonlinear current-voltage characteristics of ZnO ceramics, which are utilized as varistors, are one of good examples of the boundary-induced electrical properties. [1-3] The appearance of the characteristics is attributed to the double Schottky barrier originating from deep interfacial electronic states in the band gap. [4-8] A number of reports suggest that the formation of the interfacial states is related to the presence of some impurities and/or native defects associated with oxygen excess at boundary regions. [9-14] Deformed atomic arrangements or bond disorder such as distorted and dangling bonds at boundary regions likewise has a potential to generate specific electronic states in the band gap. However, this fundamental effect has not been clarified. Recently, the electronic structure of some tilt and twist grain boundaries has been investigated using first-principles calculations for covalent materials such as Si [15], Ge [16], and SiC [16], and metal oxides such as Al_2O_3 [18], TiO_2 [19], $SrTiO_3$ [20], and ZnO [21-24]. According to these reports, bond disorder at boundary regions generally induces localized electronic states near the valence and/or conduction band edges. Furthermore, for the boundaries with dangling and/or largely distorted bonds in Si and Ge, such electronic states can be deep in the band gap. [15, 16] It should be significant to understand the electronic structure originating from bond disorder in ZnO as well, differentiating from the extrinsic effects by impurities and native defects.

In the present study, stoichiometric configurations of symmetric tilt boundaries with a Σ=7 misorientation in ZnO have been investigated by a first-principles molecular orbital method to elucidate the effects of bond disorder on the electronic structure. Two types of equilibrium geometries previously obtained by empirical lattice statics calculations [21] are employed: one configuration shows a reconstructed atomic arrangement without dangling bonds, whereas the other has some dangling bonds at the boundary core. The electronic structure particular to these geometries is investigated in comparison with the bulk and $(10\bar{1}0)$ surface of ZnO. The effects of bond disorder are discussed form the viewpoint of the interaction of atomic orbitals that constructs the band structure of ZnO.

2. COMPUTATIONAL PROCEDURE

The molecular orbital calculations were conducted using SCAT program code [25] based on the discrete variational (DV) -Xα method [26]. In this method, one-electron Schrödinger equations are iteratively solved to achieve the self-consistent electronic structure of model clusters. Molecular orbitals (MOs) are represented by the linear combination of the atomic orbitals that are numerically obtained by solving Schrödinger equations for constituent atoms. At respective iterations for the self-consistent field, the charge densities of the atoms are renewed using atomic orbital populations calculated using Mulliken's scheme

[27]. Thus, the atomic basis functions are generated under given chemical environments, which enables fairly accurate MO calculations using only a nearly minimal number of basis functions. 1*s*-2*p* for O and 1*s*-4*p* for Zn are sufficient to reproduce the core and valence states of ZnO. In the present calculation, however, Zn-4*d* and -5*sp* orbitals were added for better reproduction of the conduction band.

The structures of the grain boundary model clusters used in the calculations are shown in Fig. 1.These were constructed on the basis of the atomic structures of an [0001] /$(\bar{1}\,\bar{2}30)\Sigma$=7 symmetric tilt boundary that were previously determined by lattice statics calculations using empirical interatomic potentials. [21] The translation states as well as the atomic positions were optimized so as to minimize the total lattice energy. As a consequence, two types of equilibrium geometries, A and B shown in Fig. 1, were obtained with similar boundary energies of approximately 1.4 Jm^{-2}. For the boundary A, the atomic arrangement is largely reconstructed to vanish dangling bonds, although the boundary core shows relatively open structure. For the boundary B, larger open channels are present and some atoms adjacent to the channels have lost one of the first nearest neighbors. In other words, these atoms have dangling bonds. For respective geometries, the model clusters were constructed on the basis of the connection of ZnO_4 tetrahedral units to include four O- and three Zn-basal planes. The compositions and charges of the clusters are $[Zn_{36}O_{70}]^{68-}$ and $[Zn_{42}O_{77}]^{70-}$ for the boundaries A and B, respectively. The Zn and O atoms in the columns marked with asterisks in Fig. 1 will be focused because of the most remarkable characters: for the boundary A, these atoms are located at the middle of the open core structure and show large bond distortion, while these have dangling bonds for the boundary B.

The sizes of model clusters are chosen according to our previous study on the ZnO $(10\bar{1}0)$ surface; the electronic structures for atoms below the third $(10\bar{1}0)$ layer from the surface are not significantly influenced by the presence of the surface. [28] Therefore, we believe the present grain boundary clusters including three or four $(10\bar{1}0)$ layers from the channels are sufficient in size to reproduce electronic structure particular to the geometries. To take electrostatic potential into account and minimize the termination effects of the finite-sized clusters, about 10 000 point charges with the charges of ±2 were located at external atomic sites.

For comparative discussion, calculations for ZnO bulk and the $(10\bar{1}0)$ surface were conducted using $[Zn_{57}O_{96}]^{78-}$ and $[Zn_{36}O_{58}]^{44-}$ model clusters, respectively, and point charges. The structures are shown in Fig. 2. Similarly to the boundaries', these clusters were constructed on the basis of the connection of ZnO_4 tetrahedral units to include up to the fifth nearest neighbors of the Zn atoms located at the center of the clusters; for the surface cluster, atoms above the surface plane were then removed. Atomic coordinates calculated by lattice statics calculations [21] were also used. The errors of +0.5% and -2.5% for the lattice constants *a* and *c*, and +2.4% for the internal parameter were confirmed not to affect the electronic structure significantly. [21] The atomic positions at the surface were relaxed to

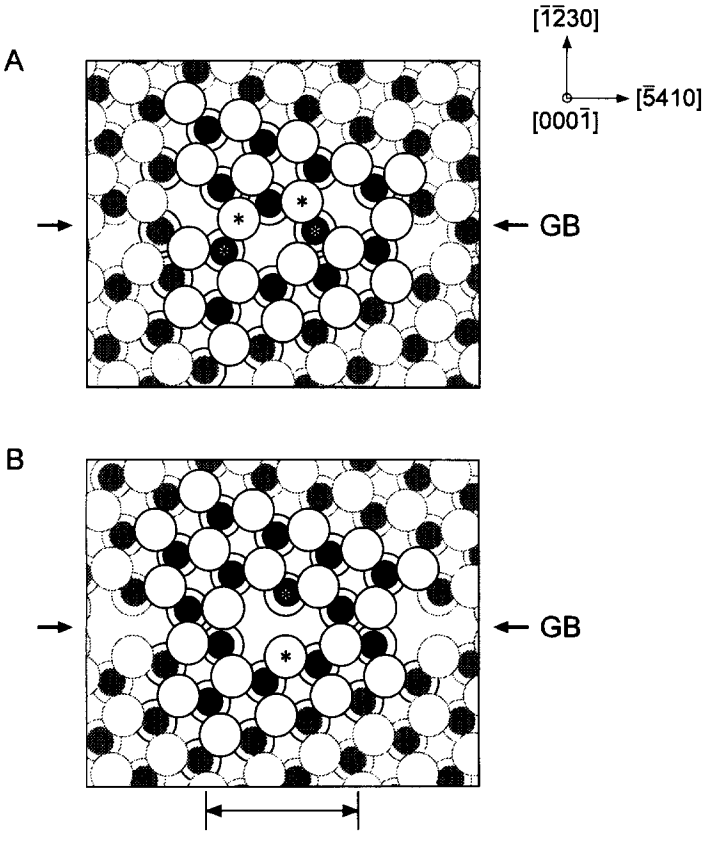

Fig. 1 View of the grain boundary geometries and model clusters from the [000$\bar{1}$] direction. The boundaries are indicated by arrows and the scale corresponds to the periodicity unit of the Σ=7 misorientation. Filled and open circles denote Zn and O atoms, respectively. Atoms in the clusters are shown with black circles. Atomic columns most characteristic of respective geometries are marked with asterisks.

achieve optimum geometry. The most remarkable feature is that Zn atoms on the surface are relaxed more inwardly by 0.16 Å. Such a feature has also been recognized by some researchers and the amount of relaxation is within a reported range: 0.03 Å - 0.4 Å [29, 30].

To discuss one-electron structure and the interactions of atomic orbitals, we use

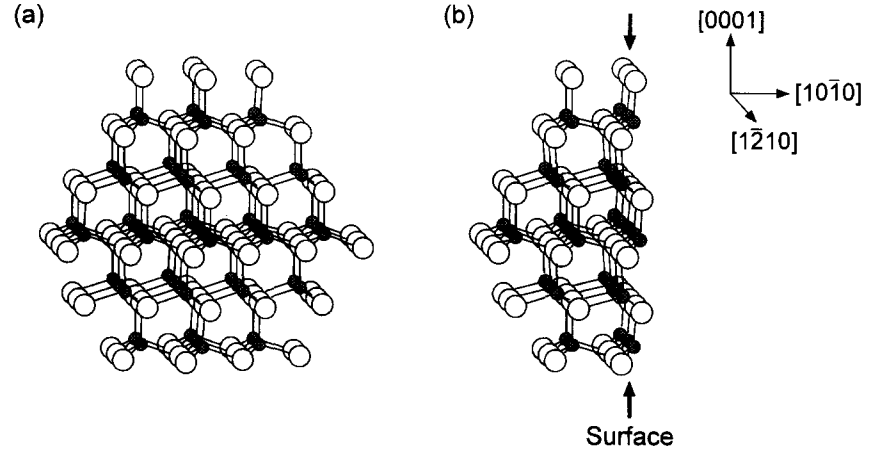

Fig. 2 Structures of (a) the bulk and (b) the $(10\bar{1}0)$ surface model clusters. Filled and open circles denote Zn and O atoms, respectively. Zn atoms located at the center in the bulk or on the surface are shown with black circles.

partial density of states (PDOS) and overlap populations for each atom. For the calculations of PDOSs, atomic orbital populations were obtained at discrete MOs on the basis of Mulliken's scheme. [27] They were then substituted by Gaussian functions of 0.7 eV full width at half maximum (FWHM) to form PDOS curves. The overlapping parts of the orbital populations for neighboring atoms, which are called overlap populations, can be used as a measure of the strength of the interactions of atomic orbitals or covalent bonding. To facilitate understanding, these quantities will be used with a Gaussian substitution as in the case of the PDOSs.

3. RESULTS AND DISCUSSION

The calculated PDOS for the bulk model cluster is shown in Fig. 3(a). To reproduce the electronic structure of the bulk ZnO as appropriately as possible, the results for the Zn atom located at the center of the cluster and its first nearest neighboring O atoms were used per atom.

Concerning the occupied states, two bands are recognized within the energy range taken in the figure. The lower one located at about –17 eV consists of O-2*s*. The upper one located between –7 eV and 1 eV is mainly constructed by Zn-3*d* and O-2*p*, and electrons are occupied up to this valence band. Such twofold band

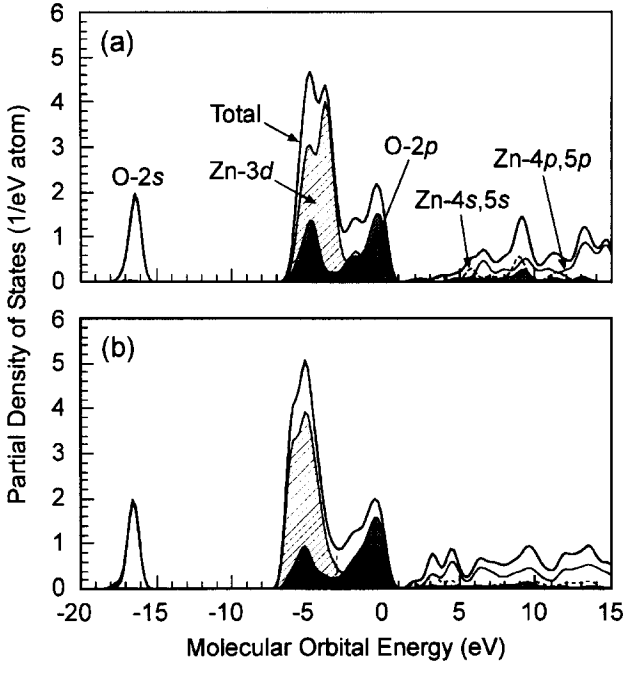

Fig. 3 Partial density of states for the selected atoms in (a) the bulk and (b) the surface model clusters. Zn atoms located at the center in the bulk or on the surface and their first nearest neighboring O atoms are employed. (See Fig. 2)

structure composed of O-2*s* and -2*p* is typical to metal oxides, while the significant admixture of Zn-3*d* with O-2*p* is characteristic of ZnO. Above the valence band, the band gap and the unoccupied conduction band are located. The conduction band is composed mainly of Zn-4*sp* and -5*sp*. The lower part shows very small DOS owing to large Zn-Zn interactions, as will be discussed later. The band gap, i.e., the gap between the highest occupied molecular orbital (HOMO) at the valence band top and the lowest unoccupied molecular orbital (LUMO) at the conduction band bottom, is calculated to be 1.8 eV, although this gap is hardly recognized in the figure owing to the Gaussian substitution. The shape of the total DOS, which was obtained as a sum of PDOSs, is very similar to the reported results of first-principles band structure calculations based on the local-density approximation. [22, 31, 32] However, there are two remarkable discrepancies with experimental reports. First, the position of Zn-3*d* band is about 2.5 eV higher in energy than that observed by x-ray photoelectron spectroscopy. [33] Second, an

experimental band gap is reported to be 3.30 eV [34], which is much larger than the gaps in the present result and the reported results of LDA-based band structure calculations. [22, 31, 32] These discrepancies are attributed to the LDA. [31, 35] Vogel *et al.* have made LDA calculations including the self-interaction and electronic relaxation corrections, and found that the position of the Zn-3*d* band and the band gap become much closer to the experimental ones. [35] However, the character of the electronic states near the band edges seems not to be affected significantly by the corrections. Therefore, we believe that the effects of bond disorder on the electronic structure, which are expected to appear mainly near band edges or in the band gap, can be discussed within the present approximation.

Figure 3(b) shows the PDOS for the central Zn atom and its neighboring O atom on the surface layer in the surface model cluster. The shape of the valence band is not so much different from that of the bulk. On the other hand, a remarkable feature is recognized in the conduction band: sharp peaks are present near the band edge, in contrast to the very small density of states for the bulk cluster. These are associated with dangling bonds at the surface, which are therefore not observed in the PDOSs for the atoms located below the surface layer. The states are present at more than 1.9 eV above the HOMO of the surface cluster. Considering the band gap of 1.8 eV for the bulk cluster, these states should be present in the conduction band.

The PDOSs for the selected atoms in the boundary A and B model clusters, which are marked with asterisks in Fig. 1, are shown in Fig. 4(a) and (b). For the boundary A, all the atoms exhibit PDOSs similar to that of the bulk, as in the case of the PDOS for the selected atoms shown in Fig. 4(a). This is presumably due to the complete fourfold coordination, although there is large bond distortion. On the other hand, a feature similar to the surface appears in the PDOS for the boundary B, as shown in Fig. 4(b). There are sharp states associated with dangling bonds near the conduction band edge. These states are located at more than 1.8 eV above the HOMO of the boundary B cluster and therefore within the conduction band. The other atoms in this geometry have complete fourfold coordination and do not show obvious features in their PDOSs. Thus, deep states are not recognized in the band gap even for the boundary with dangling bonds.

Recently, we have also investigated these boundaries using first-principles plane-wave pseudopotential calculations within the local-density approximation and obtained similar results; the most localized electronic states specific to the boundary geometries appear within the valence and conduction band. [22] Likewise, it has been reported that deep states are not formed in the band gap for an [0001] Σ=7 twist boundary [23] and the $(10\bar{1}0)$ surface [30].

To understand why electronic states associated with bond disorder do not clearly appear in the band gap in ZnO, the interaction of atomic orbitals was investigated on the basis Mulliken's scheme. Figure 5 shows the distribution of overlap populations for the bulk model cluster in comparison with its PDOS. The populations were obtained with respected to the Zn atom located at the center of the cluster. The values with its first nearest neighboring O atoms, O_4 (four atoms), or second nearest neighboring Zn atoms, Zn_{12} (12 atoms), were summed up for

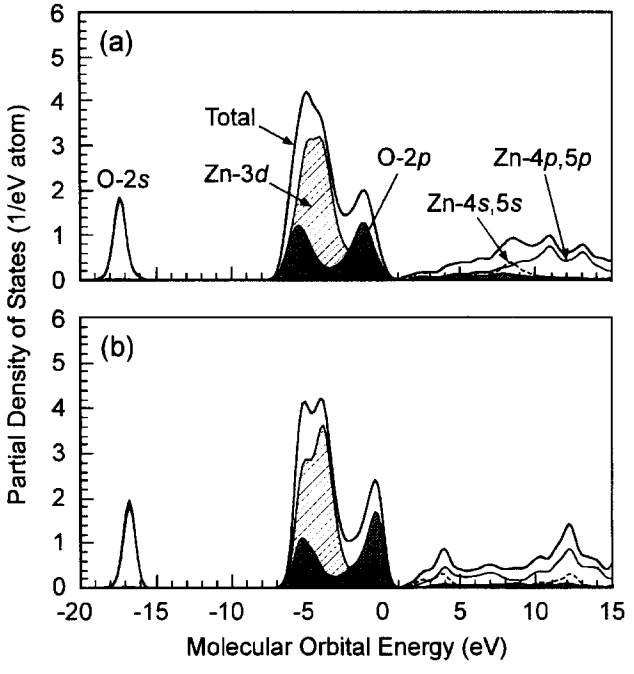

Fig. 4 Partial density of states for the selected atoms in (a) the boundary A and (b) the boundary B model clusters. Atoms that are located on the columns marked with asterisks in Fig. 1 are employed.

respective molecular orbitals. These were then substituted by Gaussian functions of 0.7 eV FWHM. The plus and minus values denote bonding and antibonding interactions, respectively.

The overlap populations indicate that the valence band is constructed mainly by the bonding interactions between Zn-O. In detail, the bonding interactions between Zn-3*d* and O-2*p* are dominant at the lower part of the valence band, while the upper part consists of their antibonding interactions along with the bonding interactions between Zn-*sp* and O-2*p*.

The conduction band is composed mainly of Zn-O antibonding interactions as well as Zn-Zn bonding/antibonding interactions. Especially, near the conduction band edge, the Zn-Zn bonding component is somewhat larger than the Zn-O antibonding one. These bonding interactions are mainly made by Zn-4*s*, and spread the conduction band to the lower energy side. This should be an origin of large electron mobility in *n*-type ZnO. [36].

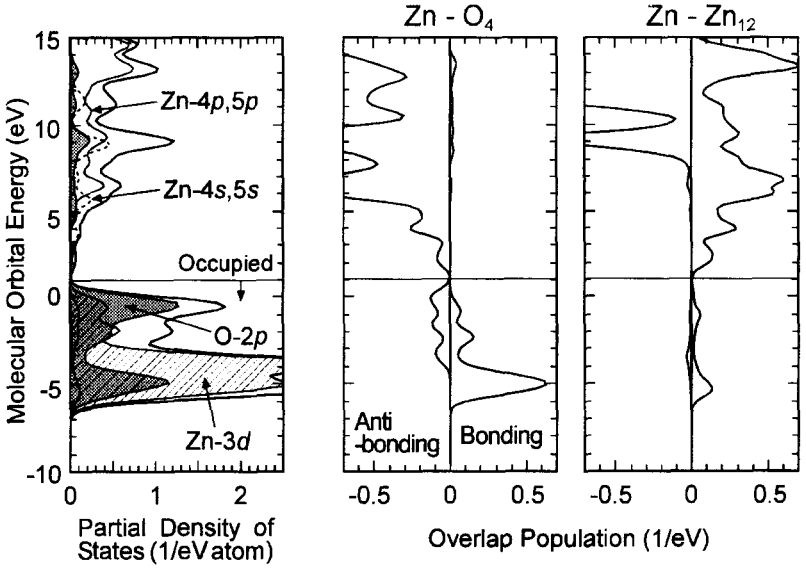

Fig. 5 Overlap populations with respect to the central Zn atom in the bulk model cluster in comparison with its partial density of states. The populations with four O atoms at the first nearest neighbor sites (O_4) and 12 Zn atoms at the second nearest neighbor sites (Zn_{12}) are shown. Plus and minus values denote bonding and antibonding interactions, respectively.

In Fig. 6, the band structure is schematically drawn in comparison with that of a covalent material. Considering simple covalent interactions, the valence band is constructed mainly by bonding interactions between adjacent atoms, while the conduction band by antibonding interactions, as shown on the left side of Fig. 6. In this case, distorted/dangling bonds are expected to generate electronic states within the band gap because these effects tend to diminish or vanish the splitting between the bonding and antibonding states. In practice, it has been reported that bond disorder induces highly localized electronic states near the valence and conduction band edges for tilt and twist boundaries in Si, Ge and SiC. [15-17] In addition, such electronic states can be deep in the band gap when bond distortion is large and/or dangling bonds are present. [15,16]

For ZnO dealt with in the present study, the lower part of the conduction band consists of the Zn-Zn bonding interactions in addition to the Zn-O antibonding interactions, as shown in Fig. 5 and 6. These features should be attributed partly to some ionicity that is expected to diminish Zn-O covalent interactions. Owing to

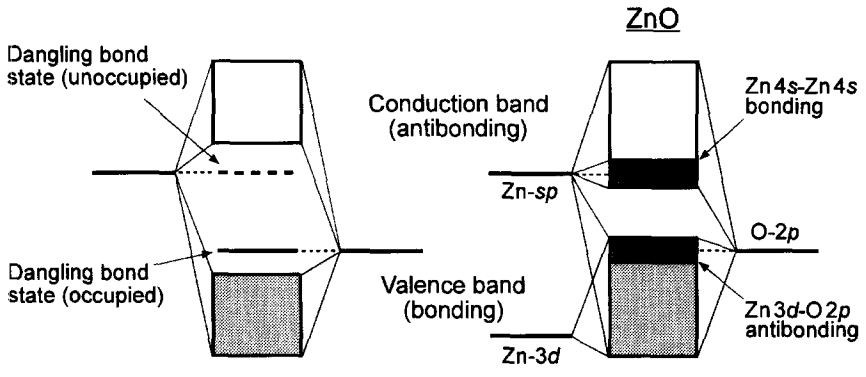

Fig. 6 Schematics of band structure for a covalent material (left) and ZnO (right).

the large bonding interactions between Zn-4*s* to spread the conduction band to the lower energy side, localized electronic states associated with bond disorder on Zn-*sp* should have a tendency to appear in the conduction band rather than in the band gap.

In addition, the antibonding interactions between Zn-3*d* and O-2*p* exist near the top of the valence band in ZnO. This character indicates that the electronic states associated with distorted/dangling bonds on O-2*p* tend to appear within the valance band, as in the case of the conduction band.

For the grain boundaries in other metal oxides such as Al_2O_3, TiO_2, and $SrTiO_3$, it has been reported that deep electronic states are not formed either, although localized states are recognized at the valence and/or conduction band edges for the boundaries of Al_2O_3 and TiO_2. [18-20] This behavior may also be attributed to the band structure with some ionicity. For the grain boundaries of ZnO, the effects of bond disorder on the conduction band bottom are much smaller. This is presumably due to much higher delocalization of the conduction band associated with Zn-Zn bonding interactions. Thus, the small effects of the bond disorder in the vicinity of the band gap can be generally explained by the band structure intrinsic to ZnO. Deep electronic states are unlikely to be generated solely by bond disorder even if other boundaries are investigated. In ZnO varistors, interfacial electronic states have been observed at 0.6 - 1.0 eV below the bottom of the conduction band. [6-8] The present results suggest that such deep states should be attributed not to bond disorder but to native defects and/or impurities at boundary regions.

4. CONCLUSION

Two types of stoichiometric configurations of symmetric tilt boundaries with a Σ=7 misorientation in ZnO have been investigated by a first-principles molecular orbital method in comparison with its bulk and $(10\bar{1}0)$ surface. For the configuration without dangling bonds, the electronic structure resembles that of the bulk despite the presence of bond distortion. On the other hand, the configuration with dangling bonds exhibits localized electronic states near the conduction band edge. However, these states are not deep in the band gap. The analysis of the interactions of atomic orbitals for the bulk model cluster suggests that this behavior results from the band structure intrinsic to ZnO. The formation of deep electronic states should therefore not be attributed to bond disorder at grain boundaries in ZnO.

5. ACKNOWLEDGMENTS

The authors would like to thank S. R. Nishitani, B. Slater, and D. H. Gay for helpful discussions. This work was supported by a Grant-in-Aid for Scientific Research on Priority Areas (No. 751) and for JSPS Fellows from the Ministry of Education, Culture, Sports, Science and Technology of Japan.

6. REFERENCES

(1) D. R. Clarke, J. Am. Ceram. Soc., **82**, 485 (1999).
(2) M. Matsuoka, Jpn. J. Appl. Phys., **10**, 736 (1971).
(3) K. Mukae, K. Tsuda, and I. Nagasawa, Jpn. J. Appl. Phys., **16**, 1361 (1977).
(4) G. E. Pike, S. R. Kurtz, P. L. Gourley, H. R. Philipp, and L. M. Levinson, J. Appl. Phys., **57**, 5512 (1985).
(5) F. Greuter, G. Blatter, M. Rossinelli, and F. Stucki, in "Advances in Varistor Technology", edited by L. M. Levinson, American Ceramic Society, Westerville, 1989), p. 31.
(6) J. P. Gambino, W. D. Kingery, G. E. Pike, H. R. Philipp, and L. M. Levinson, J. Appl. Phys., **61**, 2571 (1987).
(7) R. A. Winston and J. F. Cordaro, J.Appl. Phys., **68**, 6495 (1990).
(8) K. Tsuda and K. Mukae, J. Ceram. Soc. Jpn., **100**, 1239 (1992).
(9) Y. Yano, Y. Takai, and H. Morooka, J. Mater. Res., **9**, 112 (1994).
(10) M. Yodogawa, Y. Ikuhara, F. Oba, and I. Tanaka, Key Eng. Mater., **157-158**, 249 (1999).
(11) E. Sonder, M. M. Austin, and D. L. Kinser, J. Appl. Phys., **54**, 3566 (1983).
(12) S. Fujitsu, H. Toyoda, and H. Yanagida, J. Am. Ceram. Soc., **70**, C71 (1987).
(13) K. Tsuda and K. Mukae, J. Ceram. Soc. Jpn., **97**, 1211 (1989).
(14) F. Stucki and F. Greuter, Appl. Phys. Lett., **57**, 446 (1990).

(15) M. Kohyama and R. Yamamoto, Phys. Rev. B, **50**, 8502 (1994).
(16) E. Tarnow, P. Dallot, P. D. Bristowe, J. D. Joannopoulos, G. P. Francis, and M. C. Payne, Phys. Rev. B, **42**, 3644 (1990).
(17) M. Kohyama, Phil. Mag. Lett., **79**, 659 (1999).
(18) S. D. Mo, W. Y. Ching, and R. H. French, J. Am. Ceram. Soc., **79**, 627 (1996).
(19) I. Dawson, P. D. Bristowe, M. H. Lee, M. C. Payne, M. D. Segall, and J. A. White, Phys. Rev. B, **54**, 13727 (1996).
(20) S. D. Mo, W. Y. Ching, M. F. Chisholm, and G. Duscher, Phys. Rev. B, **60**, 2416 (1999).
(21) F. Oba, I. Tanaka, S. R. Nishitani, H. Adachi, B. Slater, and D. H. Gay, Philos. Mag. A, **80**, 1567 (2000).
(22) F. Oba, S. R. Nishitani, H. Adachi, I. Tanaka, M. Kohyama, and S. Tanaka, Phys. Rev. B, **63**, 045410 (2001).
(23) H. S. Domingos and P. D. Bristowe, Comp. Mater. Sci., **22**, 38 (2001).
(24) J. M. Carlsson, B. Hellsing, H. S. Domingos, and P. D. Bristowe, J. Phys: Condens. Mater., **13**, 9937 (2001).
(25) H. Adachi, M. Tsukada, and C. Satoko, J. Phys. Soc. Jpn., **45**, 875 (1978).
(26) D. E. Ellis, H. Adachi, and F. W. Averill, Surf. Sci., **58**, 497 (1976).
(27) R. S. Mulliken, J. Chem. Phys., **23**, 1833 (1955).
(28) K. Matsunaga, F. Oba, I. Tanaka, and H. Adachi, J. Electroceram., **4**, 69 (1999).
(29) J. E. Jaffe, N. M. Harrison, and A. C. Hess, Phys. Rev. B., **49**, 11153 (1994).
(30) P. Schröer, P. Krüger, and J. Pollmann, Phys. Rev. B, **49**, 17092 (1994).
(31) P. Schröer, P. Krüger, and J. Pollmann, Phys. Rev. B, **47**, 6971 (1993).
(32) Y. N. Xu and W. Y. Ching, Phys. Rev. B, **48**, 4335 (1993).
(33) W. Göpel, J. Pollmann, I. Ivanov, and B. Reihl, Phys. Rev. B, **26**, 3144 (1982).
(34) V. Srikant and D. R. Clarke, J. Appl. Phys. **83**, 5447 (1998).
(35) D. Vogel, P. Krüger, and J. Pollmann, Phys. Rev. B, **54**, 5495 (1996).
(36) K. I. Hagemark and L. C. Chacka, J. Solid. Stat. Chem., **15**, 261 (1975).

Chemical bonding state of sodium silicates

Tokuro Nanba*, Tatsuya Hagiwara, Yoshinari Miura
Department of Environmental Chemistry and Materials, Okayama University
3-1-1 Tsushima-Naka, Okayama 700-8530, Japan

(Received December 31, 2001; in final form May 10, 2002)

Abstract

The chemical bonding state of sodium silicates was estimated by a DV-Xα cluster MO method and a population analysis. Cluster models were constructed from the silicate crystals, pure silica, sodium disilicate and sodium metasilicate. The MO calculations successfully reproduced the experimental observations in XPS valence band spectra and core-orbital energies. According to the overlap population, covalent character increased with increasing Na_2O content, and it was also the case for Na ions. The exceptional change was found in bridging oxygen (BO), where anti-bonding overlap between Si and BO was clearly seen around the top of the occupied levels and its contribution increased with increasing Na_2O content. Correlations between the experimental core-orbital energies and the theoretical electronic populations were also examined, where the best correlation was found in the case of using a total atomic population given by the sum of the net atomic population and the overlap population.

Contents

Keywords: silicate, DV-Xα, XPS, chemical shift, bonding state
*Corresponding author: tokuro_n@cc.okayama-u.ac.jp

ADVANCES IN QUANTUM CHEMISTRY, VOLUME 42

0065-3276/03 $35.00

1. Introduction

It is well known that core-orbital signals in X-ray photoelectron spectra (XPS) shift chemically according to the electronic state of a material. The reason for the chemical shift is commonly understood as a change in the chemical bonding character, that is, ionicity or covalency of a chemical bond. Charge potential model (1) is the most famous theoretical model, from which we can obtain a simplified equation (2), indicating that the chemical shift is proportional to the charge on an atom. According to the theories, O1s shift in oxide materials is interpreted as follows. When ionicity in the bonding character increases, it leads to an increase in the electronic density of oxide ions, resulting in lower binding energy shift of the O1s signal. In the case of alkali silicate glasses (3), O1s signals move to lower binding energy side with increasing the amount of alkali oxides, which is interpreted as an increase in the negative charge on oxide ions due to the increase of ionicity in the chemical bonding character.

Point charge model (4) is often used in the estimation of atomic charges, where it is assumed that charge is localized on atoms and electrons are transferred in a chemical bond according to the difference in electronegativity. When an oxygen gets electrons from a neighboring silicon, the neighboring silicon is sure to lose electrons due to charge neutrality. In this case, electronic density of the oxygen increases and that of the silicon decreases. It is consequently expected in XPS measurement that O1s and Si2p signals shift to the opposite direction. Contrary to the expectation, all the XPS signals in alkali silicate glasses move to the lower binding energy side with increasing the alkali oxide content, not excepting the alkali ions (3). The experiments suggest that electronic density of all the glass constituents increases along with the addition of alkali oxides. It is not explainable from the standpoint of ionicity such as the point charge model.

Charge sharing model on the basis of covalency seems to be required to explain the concurrent increase or decrease in electronic density of all the glass constituents. According to the concept, the chemical shift of the XPS signals is associated with the change in the amount of electrons shared between cation and anion in a chemical bond, that is, a chemical shift to the lower binding energy side is interpreted as an increase in the shared electrons due to an increase in covalent character of the chemical bond. According to the interpretation, however, the experimental chemical shift indicates that the covalency of R–O bonds also increases with increasing an alkali oxide (R_2O) content, which seems to be in conflict with the general understanding that R_2O is more ionic than SiO_2.

Neither ionicity nor covalency explains the experimental chemical shifts. Then, what is the appropriate model to explain the chemical shifts, and how does the chemical bonding character in alkali silicate system change along with the composition? In the present paper, chemical bonding state in the sodium silicate

system is investigated on the basis of theoretical MO calculations to interpret the experimental observations.

2. Investigation Procedures

Three compositions were chosen to the investigation, that is, SiO_2, $Na_2O{\cdot}2SiO_2$ and $Na_2O{\cdot}SiO_2$. The binary glasses were prepared by a conventional melt-quenching method, and the binary crystals were also obtained by heat-treatment of the glasses. As for SiO_2, commercial products both in vitreous and crystalline states were used as specimens.

XPS measurements were carried out using a monochromatic Al-Kα radiation ($h\nu$ = 1486.6 eV). Fresh surfaces of the rod-shaped specimens were analyzed just after being fractured in a high vacuum ($\approx 7\times10^{-8}$ Pa). Neutralization of the surface charge was performed by both an electrically grounded Ni-mesh screen and a low energy flood gun (5). Binding energy was corrected by referencing the C1s signal for an adventitious hydrocarbon accumulated in the vacuum as 284.6 eV (5).

The discrete variational Xα (DV-Xα) method (6) was used to examine the chemical bonding states of the sodium silicates, where Mulliken population analysis (7) was adopted for the evaluation of net charge and bond overlap population. Cluster models shown in Fig. 1 were constructed from the respective crystal structures (8–10). The basis atomic orbitals used in the MO calculations are O = 1s–2p, Si = 1s–3d and Na = 1s–3d. The population analyses were done only for the atoms around the center of the clusters in order to reduce the effects of bond termination. The cluster size, that is, the number of atoms in a cluster was chosen as an objective atom was surrounded by at least two layers of SiO_4 tetrahedra. The cluster was also embedded in the Madelung potential to reduce the termination effects.

According to the Mulliken population analysis (7), ionicity and covalency of a chemical bond A–B are evaluated by net charge ΔQ_A and bond overlap population Q_{AB}, respectively given in Eqs. 1 and 2, where both quantities are commonly obtained from the sums of overlap population Q_{ij}^l given in Eq. 3.

$$\Delta Q_A = Z_A - Q_A,\ Q_A = \sum_{i\in A} Q_i,\ Q_i = \sum_l Q_i^l,\ Q_i^l = \sum_j Q_{ij}^l \tag{1}$$

$$Q_{AB} = 2\sum_{i\in A,\, j\in B} Q_{ij},\ Q_{ij} = \sum_l Q_{ij}^l \tag{2}$$

$$Q_{ij}^l = n_l c_{il} c_{jl} S_{ij} \tag{3}$$

Q_{ij}^l is the partial overlap population, that is, electronic population of the overlapped region between the atomic orbitals χ_i and χ_j in the molecular orbital ϕ_l,

which is the product of n_l: the number of electrons in MO ϕ_l (usually $n_l = 2$), c_{il} and c_{jl}: the contribution of AOs χ_i and χ_j in MO ϕ_l, and S_{ij}: the overlap integral between AOs χ_i and χ_j. In Eq. 1, Q_A is the gross atomic population or gross atomic charge on atom A, which is given by the sum of atomic orbital population Q_i. Subtracting Q_A from atomic number Z_A, that is, the number of electrons in the neutral state, the net charge ΔQ_A is obtained. It is also noted in the Mulliken population analysis (7) that the gross atomic population Q_A is given by the sum of

(a) $(Si_{17}O_{52})^{36-}$ cluster

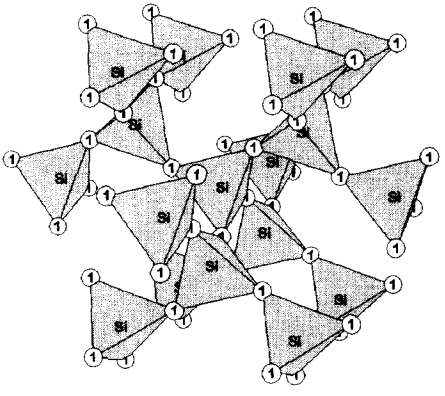

(b) $(Na_{26}Si_{22}O_{69})^{24-}$ cluster

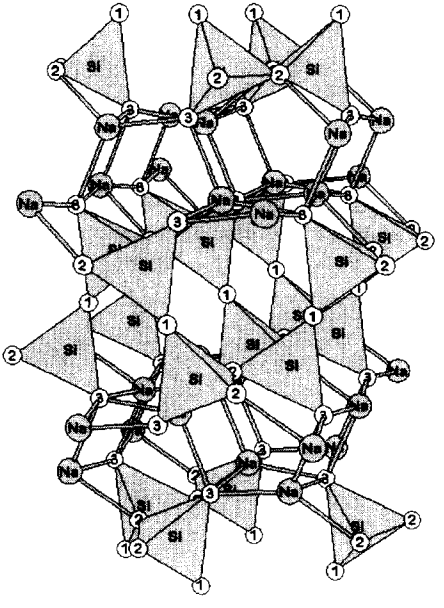

(c) $(Na_{36}Si_{17}O_{58})^{4-}$ cluster

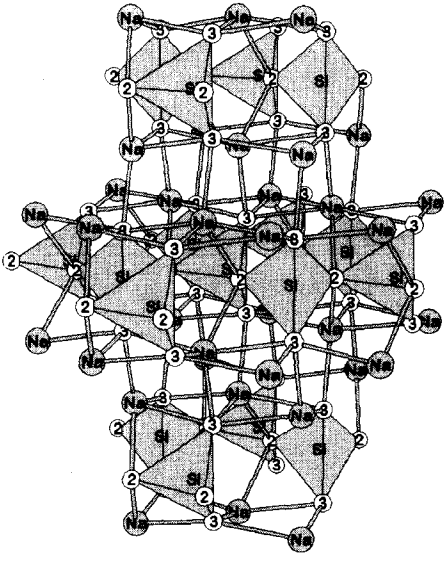

Fig. 1. Cluster models used in the MO calculations prepared from (a) α–cristobalite SiO_2 (7), (b) α–$Na_2Si_2O_5$ (8) and (c) Na_2SiO_3 (9) crystals, respectively. The numbered spheres represent oxygen atoms, 1: bridging oxygen surrounded by no Na (BO1), 2: bridging oxygen also coordinated by Na (BO2) and 3: non-bridging oxygen (NBO). The numbers of sample points are 34500, 93600 and 88800 for the respective clusters (a), (b) and (c).

net atomic population (Q_{AA}) and half of total overlap population ($\frac{1}{2}\Sigma Q_{AB}$), that is, $Q_A = Q_{AA} + \frac{1}{2}\Sigma Q_{AB}$, where Q_{AA} is given by the summation for $j \in$ A in Eq. 1,

$$Q_{AA} = \sum_{i \in A} \sum_{l} \sum_{j \in A} n_l c_{il} c_{jl} S_{ij} \tag{4}$$

and $\frac{1}{2}\Sigma Q_{AB}$ is equivalent to the summation for $j \notin$ A in Eq. 1.

Theoretical intensity of the X-ray photoelectron peak for an MO ϕ_l is estimated from Eq. 5 (11).

$$I_l \propto \sum_i Q_i^l \sigma_i \tag{5}$$

where Q_i^l is the partial AO population given in Eq. 1 and σ_i is the photoionization cross-section of AO χ_i (12). X-ray photoelectron spectra were simulated by assuming a Gaussian lineshape, in which σ_is for the AOs, Si3d, Na3p and Na3d were assumed as zero because σ_is for the AOs vacant in the ground state were expected to be negligibly small compared with those of the occupied AOs. Density of states (DOS) and overlap population diagrams were also obtained from the AO and overlap populations, respectively.

3. Results and Discussion

3.1. Validity of MO calculation

The experimental valence band (VB) spectra of the sodium silicates are shown in Fig. 2. It is seen from Fig. 2 that the crystalline silicates show almost the same spectra with the vitreous ones, and it is also the case for core-orbital spectra, indicating the similarity in electronic states between the crystalline and vitreous silicates. It is probably due to the analogy in local structure, and it is hence deduced that the evaluation with the cluster models based on the structure of silicate crystals is valid also for the silicate glasses.

The simulated VB spectra are also shown in Fig. 2, where energy was corrected to agree with the experimental ones on the peak positions. As shown in Fig. 2, the relative intensity of the peaks is also in good agreement, indicating that the simulation satisfactorily reproduces the electronic states of the silicates. Two main peaks are seen at 5–10 and 10–15 eV, and the low binding energy (BE) peak increases in both relative intensity and width with increasing Na_2O content. Contribution of AOs to the XPS spectra is estimated by comparing the XPS spectra with DOS shown in Fig. 3. The low BE peak consists mostly of O2p, in which the higher BE component is assigned to BO2p and the lower BE component is associated with NBO2p. Relative amount of the NBO2p component increases with increasing Na_2O content, resulting in the increase of relative

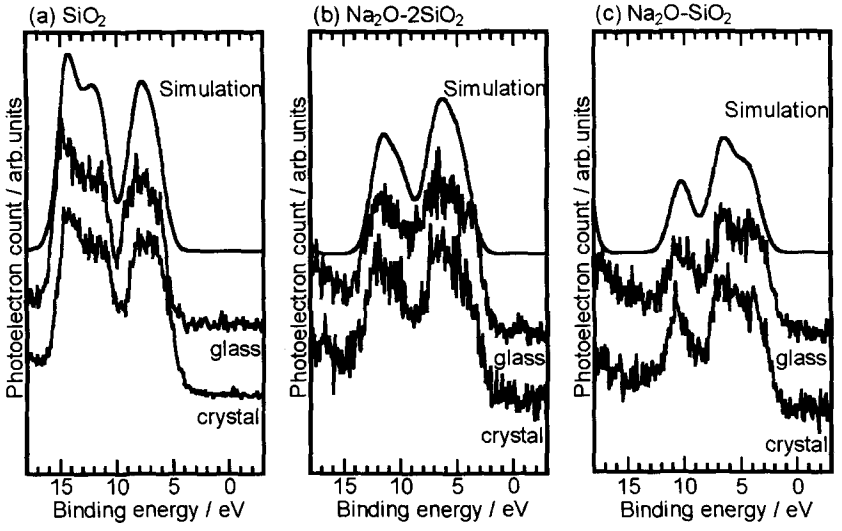

Fig. 2. Experimental valence band XPS spectra for the vitreous and crystalline silicates, and the theoretical spectra simulated from the cluster models.

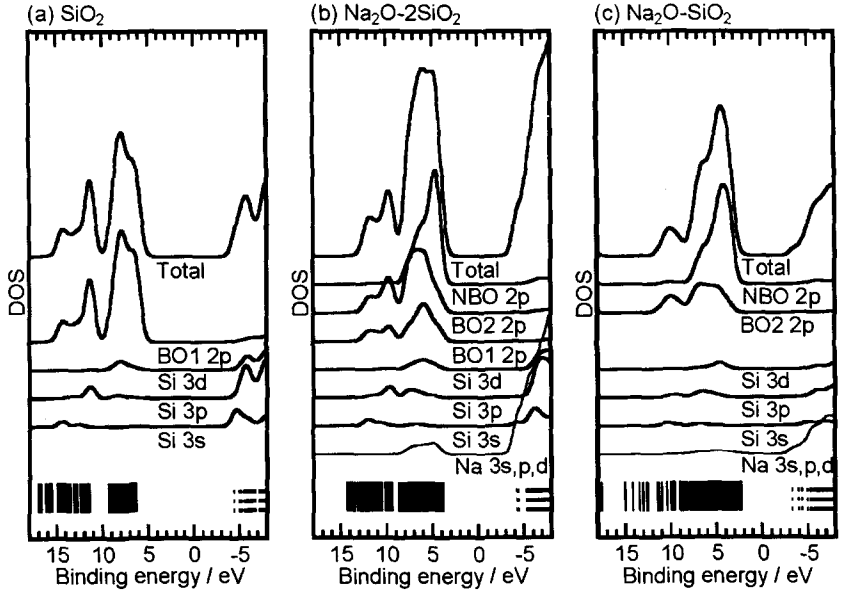

Fig. 3. Density of states (DOS) calculated from the cluster models. Continuous and broken vertical lines indicate occupied and unoccupied levels, respectively.

intensity and width for the low BE peak.

As shown in Fig. 2, the MO calculations successfully reproduce the electronic states of valence shell region. Then, how is the core-orbital region? Fig. 4 shows the correlation in core-orbital energy between the experiments and simulations, where the theoretical energies are corrected for the same quantity as in the case of the valence shell region. The experimental binding energies for the crystalline silicates are shown in Fig. 4, and it is also the case in the subsequent figures. It is seen a good correlation between the experiments and the simulations. In particular, the plot for O1s binding energy shows an almost straight line. It should be noted, however, that the theoretical energy is corrected according to the experiments and the uncorrected energy is not valid for the comparison. In other words, MO calculation does not predict the chemical shift of XPS signals without experiments. As predicted in the theories (1,2), if the chemical shift is proportional to the atomic charge, MO calculation will be useful also in the prediction of the chemical shift.

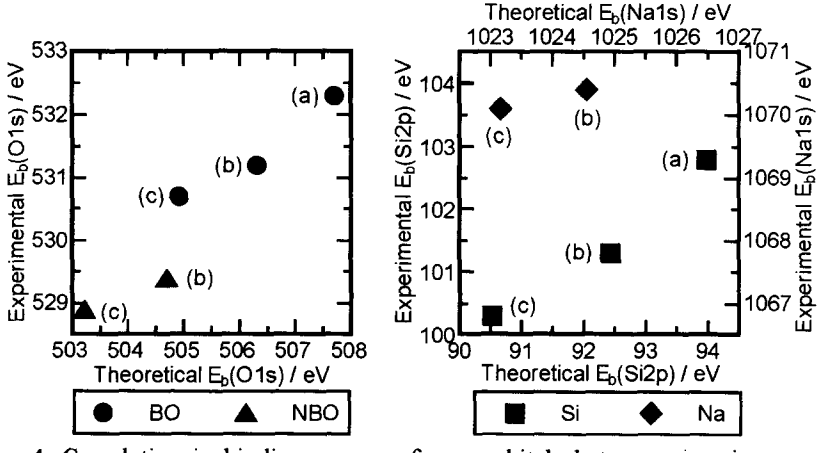

Fig. 4. Correlation in binding energy of core-orbitals between experiments and simulations for the silicates, (a) SiO_2, (b) $Na_2O{\cdot}2SiO_2$ and (c) $Na_2O{\cdot}SiO_2$. Experimental data for the crystalline silicates are shown here.

3.2. Chemical bonding character

Chemical bonding character was evaluated with net charge ΔQ_A and bond overlap population Q_{AB}. Fig. 5 shows the correlation between theoretical ΔQ_A and experimental binding energy E_b of core-orbital levels. It is seen a common trend in BO, Si and Na that E_b decreases and ΔQ_A also decreases with increasing Na_2O content. However, NBO shows the opposite change. It has been generally

convinced in R_2O–SiO_2 system that ionicity of the system increases with increasing R_2O content. In such case, both the negative charge on oxygen and positive charge on Si and Na should increase with increasing R_2O content. Only BO follows the expectation.

On the other hand, all the constituents, O, Si and Na commonly show the lower binding energy shift with increasing Na_2O content in both the experiment and simulation (Fig. 4). If chemical shift is ruled by atomic charge as expected from the theories (1,2), NBO is exception. In Fig. 5, if $\Delta Q_{NBO}(c)$ were smaller than $\Delta Q_{NBO}(b)$ and the plots for BO and NBO lay on a straight line, the experimental XPS chemical shift would be explained by atomic population.

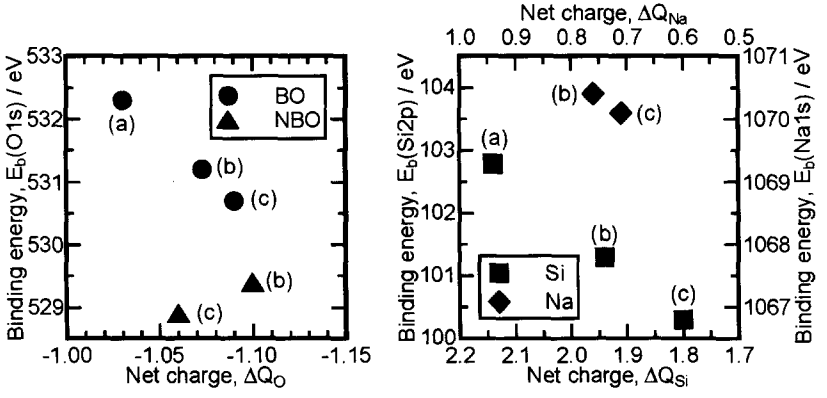

Fig. 5. Correlation between net charge and binding energy of core-level XPS signals for the silicates, (a) SiO_2, (b) $Na_2O{\cdot}2SiO_2$ and (c) $Na_2O{\cdot}SiO_2$.

When it is assumed as another case that the XPS chemical shift is ruled by overlap population, bond overlap population Q_{AB} should increases with increasing Na_2O content. In Fig. 6, E_b is plotted against the sum of Q_{AB}, that is, total overlap population which is obtained by summing Q_{AB} over the neighbors of an atom A. In obtaining ΣQ_{AB}, the interacting atoms B were chosen assuming two cases. In the case given by the open markers in Fig. 6, all the atoms in a cluster excepting atom A were chosen for B, and in another case given by the filled markers, only the neighboring bonding atoms were chosen for B. For example in the latter case, bridging oxygen BO2 in sodium disilicate (b) is surrounded by two Si and one Na, and hence the total overlap population ΣQ_{AB} for BO2 is obtained by $2{\times}Q_{Si\,BO2} + 1{\times}Q_{Na\,BO2}$. As expected, ΣQ_{AB} for A = NBO, Si and Na increases with increasing Na_2O content in the both cases, indicating the increase in the valence shell population. BO is however exceptional. As shown in Fig. 5, negative charge on

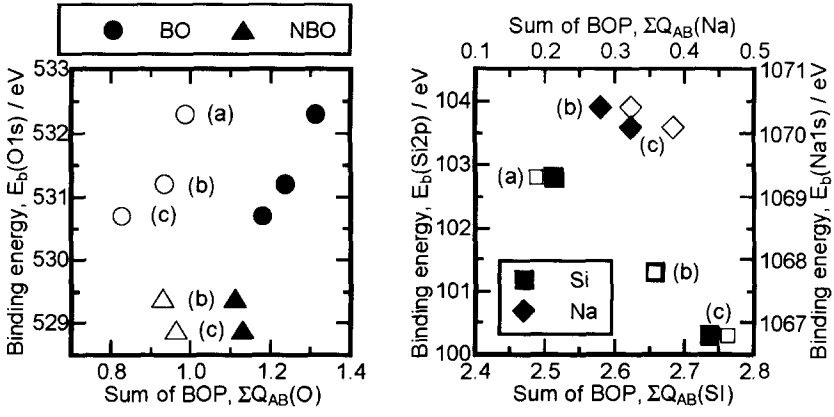

Fig. 6. Correlation between sum of bond overlap population (BOP) and binding energy of core-level XPS signals for the silicates, (a) SiO_2, (b) $Na_2O{\cdot}2SiO_2$ and (c) $Na_2O{\cdot}SiO_2$. Open and filled markers represent sum of BOP for all the atoms in the cluster and for the neighboring bonding atoms, respectively.

BO increases with increasing Na_2O content, suggesting the increase in ionic character, that is, the decrease in overlap population of BO. Hence, the change in ΣQ_{AB}(BO) shown in Fig. 6 seems consistent with the change in atomic charge on BO seen in Fig. 5. It is also seen a large difference in ΣQ_{AB}(BO) between the two cases, which is due to a large anti-bonding interaction between the neighboring O–O pairs. The change in ΣQ_{AB}(BO) against the composition is also interpreted by the chemical bonding state of BO.

Overlap population diagrams are shown in Fig. 7, in which bond overlap populations Q_{AB} are also indicated. All the bonds, except Si–BO1 and Si–BO2, increase in Q_{AB} with increasing Na_2O content. Comparing Q_{AB} for the Si–O bonds, Si–BO2, Si–BO1 and Si–NBO, Q_{AB} increases in this order. Anti-bonding overlap is clearly seen in Si–BO bonds around the top of the occupied levels even in the pure silica (a). In particular, the decrease in $Q_{Si\,BO2}$ is remarkable, which leads to the decrease in ΣQ_{AB}(BO) shown in Fig. 6. The structural change in the silicates is also interpreted on the basis of bond overlap population. When Na_2O is added to a silicate, electrons are introduced into the MO levels around the top of the occupied levels. Then, Si–BO bonds decrease in overlap population due to the increase in anti-bonding overlap, resulting in the elongation and dissociation in Si–BO bonds. Covalency in Si–NBO bonds seems much higher than Si–BO bonds, which is probably due to the higher π-bonding character of Si–NBO bonds (13). As shown in DOS (Fig. 3), Si3d and NBO2p orbital populations overlap each other, resulting in the formation of π-bonding.

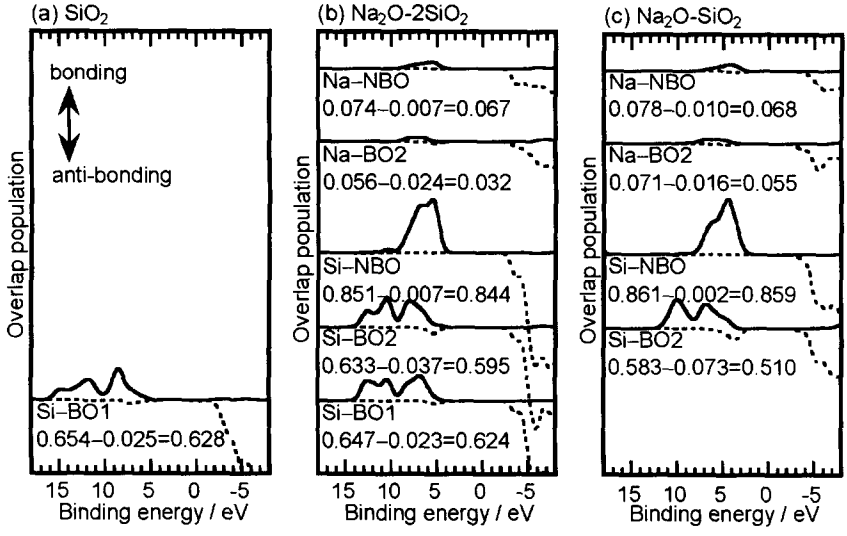

Fig. 7. Overlap population diagrams calculated from the cluster models. The continuous and broken lines indicate bonding and anti-binding overlap, respectively. The numerical values shown indicate bond overlap population, Q_{AB}.

3.3. Chemical shift of core-level XPS signals

In the Mulliken population analysis (7), gross atomic population Q_A is given by $Q_{AA} + \frac{1}{2}\Sigma Q_{AB}$, where Q_{AA} is the net atomic population and ΣQ_{AB} is the total overlap population. Large negative charge on oxygen means high gross atomic population. The negative charge on NBO in metasilicate (c) is much smaller than disilicate (b) (Fig. 5), while the total overlap population of NBO is slightly larger (Fig. 6). The small negative charge on NBO(c) is, therefore, due to low net atomic population, that is, small amount of electrons localized on NBO. It is said in general that NBO carries much lone pair electrons than BO, suggesting the higher net atomic population of NBO. As opposed to the expectation, NBO in metasilicate has lower net atomic population than BO. Overlap population also contributes to gross atomic population, where total overlap population is divided into halves to conserve the total amount of electrons. Evaluating the contribution of overlap population to the XPS chemical shift not in half but in full, the total atomic population of NBO in metasilicate becomes higher than that of BO. The total atomic population (AP) of an atom A is given by $Q_{AA} + \Sigma Q_{AB}$. Fig. 8 shows the correlation between the total AP so determined and the experimental XPS chemical shift. Except for oxygen in metasilicate (c), a linear correlation (dotted line in Fig. 8) is seen for oxygen in pure silica (a) and disilicate (b). Si2p also

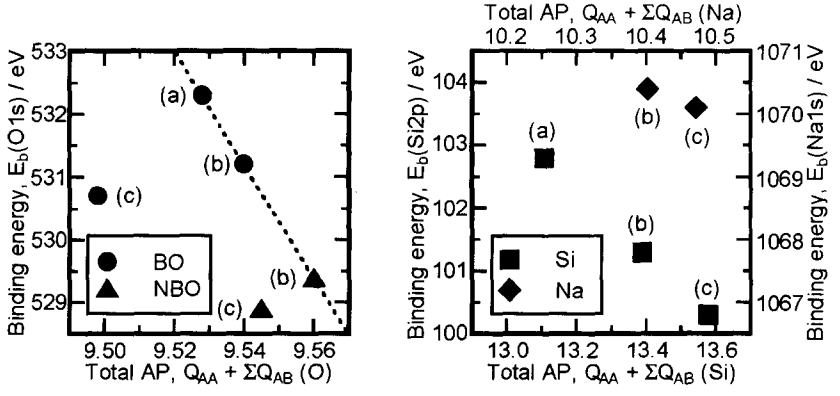

Fig. 8. Correlation between total atomic population (AP) $Q_{AA} + \Sigma Q_{AB}$ and binding energy of core-level XPS signals for the silicates, (a) SiO_2, (b) $Na_2O{\cdot}2SiO_2$ and (c) $Na_2O{\cdot}SiO_2$.

shifts linearly against the total AP.

As mentioned, the results shown in the figures are only for the atoms around the center of the clusters because it was expected that the outer atoms received much bond termination effect than the inner atoms. Actually, oxygen atoms have larger negative charge as they separate from the center, indicating that the results are strongly dependent on the size and shape of the clusters. If different atomistic configuration were used for the cluster model for sodium metasilicate (c), the better correlation might be achieved. Even in the case, it should be kept in mind that the present model for the sodium metasilicate (Fig. 1) gave good agreements both in the valence and core-orbital regions (Figs. 2 and 3). In the original theoretical model (1), the XPS chemical shift is given by a change in electrostatic potential q/r, where q is charge and r is radius. In the approximation (2), however, r is treated as constant. In the present study, only the q dependence has been investigated. The results obtained may suggest that the r dependence is not negligible.

4. Conclusion

The chemical bonding states of sodium silicates, pure silica, disilicate and metasilicate were investigated on the basis of theoretical MO calculations. The theoretical expectations were compared with the experimental observations in XPS. The simulations were in good agreement with the experiments both in the valence band spectra and the atomic core-orbital energies of all the constituents.

Except for NBO, the net charge of BO, Si and Na decreased and the gross atomic population increased with increasing Na_2O content, which was opposed to the general empirical knowledge that ionic character would increase along with the addition of alkali oxides. In the case of covalency, however, an exceptional change in the overlap population was found not in NBO but in BO, that is, the overlap population of BO decreased with increasing Na_2O content, which was due to the increase in anti-bonding contribution in Si–BO bonds. The structural change in silicate was, however, consistent with the theoretical estimation in the chemical bonding character, that is, Si–BO bonds have longer bond distance than Si–NBO bonds and they grow in bond distance with increasing Na_2O content. The chemical shift of core-orbital binding energies was also discussed on the basis of atomic and overlap populations. In the Mulliken population analysis of gross atomic population, half of the overlap population is added to the net atomic population. Assuming full contribution of the overlap population, the best correlation was obtained between the experimental chemical shift and the theoretical total atomic population.

5. References

(1) K. Siegbahn, C. Nordling, G. Johansson, J. Hedman, P.F. Hedén, K. Hamrin, U. Gelius, T. Bergmark, L.O. Werme, R. Manne, Y. Baer, "ESCA applied to free molecules", North-Holland Publ. Co., New York (1969) p. 104.
(2) U. Gelius, P.F. Hedén, J. Hedman, B.J. Lindberg, R. Manne, R. Nordberg, C. Nordling, K. Siegbahn, Physica Scripta, 2, 70 (1970).
(3) S. Matsumoto, T. Nanba, Y. Miura, J. Ceram. Soc. Japan, 106, 415 (1998) (in Japanese), J. Ceram. Soc. Jpn. Int. Ed., 106, 439 (1998) (in English).
(4) R. Nordeberg, R.G. Albridge, T. Bergmark, U. Ericson, J. Hedman, C. Nordling, K. Siegbahn, B.J. Lindberg, Arkiv för Kemi, 28, 257 (1967).
(5) S. Matsumoto, T. Nanba, Y. Miura, J. Sur. Sci. Soc. Japan, 18, 466 (1997) (in Japanese).
(6) H. Adachi, M. Tsukada, C. Satoko, J. Phys. Soc. Japan, 45, 875 (1978).
(7) R.S. Mulliken, J. Chem. Phys., 23, 1833, 1841, 2338 and 2343 (1955).
(8) R.W.G. Wyckoff, "Crystal Structures", Interscience Publishers, New York, vol. 1, (1965) p. 316.
(9) A.K. Pant, D.W.J. Cruickshank, Acta Cryst., B24, 13 (1968).
(10) P.A. Grund, M.M. Pizy, Acta Cryst., 5, 837 (1952).
(11) T. Sasaki, H. Adachi, J. Electron Spectrosc. Relat. Phenom., 19, 261 (1980).
(12) J.J. Yeh, I. Lindau, "Atomic Data and Nuclear Data Tables", Academic Press, New York, vol. 32 (1985) p. 1.
(13) T. Uchino, M. Iwasaki, T. Sakka, Y. Ogata, J. Phys. Chem., 95, 5455 (1991).

First principles calculations of pressure-induced structural phase transition of Co

Tomoyuki Yamamoto*

Computational Science Division, RIKEN,
2-1 Hirosawa, Wako-shi, Saitama 351-0198, Japan

(Received February 15, 2002; in final form April 4, 2002)

Abstract

First-principles calculations of cobalt with hcp and fcc structures are performed to investigate the compression mechanism of cobalt and to know a theoretical transition pressure from hcp to fcc phases under high-pressure condition. Here the Full-Potential Linearized Augmented Plane Wave (FP-LAPW) method is employed within the Generalized Gradient Approximation (GGA). Calculated transition pressure from hcp to fcc estimated by the free energy calculations is 128.3 GPa, which agrees well with experiment. The magnetic properties for both hcp and fcc phases at high pressures are also studied.

Contents

Keywords : Co, First principles calculation, Pressure-induced phase transition, magnetic property

*Corresponding author
Tomoyuki Yamamoto
tyama@atlas.riken.go.jp

ADVANCES IN QUANTUM CHEMISTRY, VOLUME 42

0065-3276/03 $35.00

Introduction

The structural and elastic properties of materials at high pressure and/or temperature have been extensively studied both experimentally and theoretically, because these kinds of studies have provided us fundamental knowledge on the Earth's interior. It has been widely accepted that the Earth's core is mainly composed of iron dominated alloys, in which nickel and/or cobalt are possible solutions as minor components. The structural properties of iron have been widely investigated experimentally (1-5) by the use of the synchrotron radiation for some phases at both high pressure and temperature up to the inner-core condition of the Earth, which have also been studied theoretically with the first principles (ab initio) calculations (6-8). On the other hand, these kinds of studies for cobalt have not yet been done actively. Recently new phase, β-cobalt, with fcc structure was found experimentally (9) at pressure beyond 105 GPa under room temperature condition. The structural properties of ε-cobalt with hcp structure have been studied theoretically by the use of some first principles calculational methods (10-13), while only one literature was found for β-cobalt with the Full-Potential Linear Muffin Tin Orbital (FP-LMTO) method (13). Then the structural properties of ε- and β- cobalt are studied here over a wide pressure range with the Full-Potential Linearized Augmented Plane Wave (FP-LAPW) method (14) within both non-spin-polarized and spin-polarized Generalized Gradient Approximation (GGA) (15). Present calculations reproduced the experimental transition pressure from ε- to β- phases very well. Change in magnetic properties of both ε- and β-Co according to an increment of pressure was also studied in this paper.

Computational Details

First principles calculations were carried out for ε- and β- cobalt with hcp and fcc structures, respectively, using the Full-Potential Linearized Augmented Plane Wave (FP-LAPW) package, WIEN97 (16). Both non-magnetic (non-spin-polarized) and magnetic (spin-polarized with ferromagnetic ordering) treatments have been considered for ε- and β-Co. Here the effective exchange-correlation functional GGA-PBE (17) was employed. All electrons up to 2p are treated as core, and 3s, 3p, 3d, 4s and 4p as valence states. The special k-point meshes 15x15x8 for hcp and 15x15x15 for fcc were chosen, which yielded 135 and 200 special k-points, respectively. The muffin-tin radius R_{MT} was set to 2.0 Bohr and the product of the muffin-tin radius and the maximum reciprocal space vector K_{max}, i.e. the plane-wave cutoff, $R_{MT}K_{max}$ is fixed at 9.0 for all calculations. Careful convergence tests were performed with respect to the k-point sampling and the size of basis set, which showed selected k-point meshes and plane wave cut off were appropriate for both ε- and β-Co. Total energy calculations were performed changing the unit cell volumes from $0.65V_0$ to

$1.15V_0$, where V_0 is the experimental volume at zero-pressure. Calculated total energies as a function of volume, E(V), were fitted with the Murnaghan equation of state (18) to obtain the bulk modulus B, its first-order pressure derivative B', the equilibrium volume V_0 and the ground-state total energy E_0, which is expressed by

$$E(V) = E_0 + BV_0\left[\frac{1}{B'(B'-1)}\left(\frac{V_0}{V}\right)^{B'-1} + \frac{1}{B'}\frac{V}{V_0} - \frac{1}{B'-1}\right] \quad (1)$$

where V is the volume. For ε-phase, c/a ratios were optimized changing c/a from -5 to +5% at all volumes. Resulted total energies as a function of c/a were fitted with the third-order polynomial equations, which yield the equilibrium c/a ratio.

Results and Discussions

Calculated total energies for both ε- and β- phases as a function of volume are shown in Fig. 1, together with the fitted curves with the Murnaghan equation of state (eq. (1)).

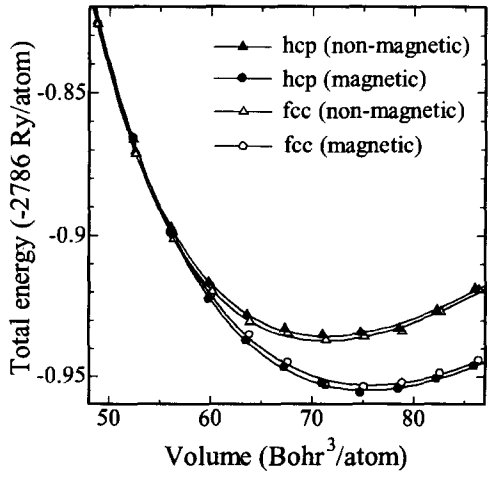

Fig. 1. Calculated total energies for ε- and β-Co as a function of volume. Solid and open symbols are for ε- and β-phases, respectively, and circle and triangle symbols are for spin-polarized and non-spin-polarized results, respectively.

Resulted structural parameters, V_0, B and B', are summarized on Table 1 with the ground state total energies, E_0, in which present results are compared with the experiments (9, 19) and other calculations (10-13). For ε-Co, magnetic treatment is more favorable than non-magnetic one as shown in Fig.1. Then calculated results in magnetic treatment are taken here. Agreement between magnetic calculation and experiment is fairly good, in which difference in the equilibrium volume at zero-pressure is only 1.6 %. Calculated results are slightly different from another calculation with the FP-LAPW (13), though same method as mine was employed. This difference is derived from a way of k-point sampling. Larger set of k-point sampling was employed in my calculations.

Table 1. Comparisons of calculated ground state energy, E_0, equilibrium volume at zero-pressure, V_0, bulk modulus, B, and its first-order pressure derivative, B' between present calculations, other calculations and experiments.

		E_0 (Ry)	V_0 (Bohr^3)	B (GPa)	B'
ε-Co	Experiment[a]		74.9	190	3.6(2)
	Experiment[b]		74.23	199	3.6
	Present calc. fm*	-2786.9549	75.46	210	3.4
	Present calc. nm**	-2786.9355	71.33	219	4.5
	LDA fm*[,c]	-2782.1081	68.0	255	4.0
	GGA fm*[,c]	-2786.7364	73.6	212	4.2
	LCAO GGA[d]		76.2	214	
	LMTO LDA[e]	-2782.173	71.1	276	
	LMTO[f]		73.70	194	4.6
β-Co	Experiment[a]		69.74	224	5.8
	Present calc. fm*	-2786.9532	75.76	209	3.1
	Present calc. nm**	-2786.9372	71.18	220	4.5
	LMTO[f]		69.41	262	4.5

*fm : ferromagnetic ordering
**nm : non-magnetic

a : reference (9)
b : reference (19)
c : reference (10)
d : reference (11)
e : reference (12)
f : reference (13)

Optimized c/a ratios as a function of pressure are plotted for ε-Co in Fig. 2. Here the pressure was obtained with the third-order Birch-Murnaghan equation of state expressed (20) by

$$P = 3Bf(1+2f)^{5/2}(1+af) \tag{2}$$

where

$$f = \frac{1}{2}\left[\left(\frac{V_0}{V}\right)^{2/3} - 1\right]$$

$$a = \frac{3}{2}(B'-4).$$

Experimental c/a ratio (9) remains unchanged at 1.615 to 80GPa, above which pressure it increases continuously. It becomes 1.63 at 110GPa and 1.65 at 150GPa. However, calculated c/a ratio remains unchanged up to about 100GPa and it rather decreases beyond 100 GPa as shown in Fig. 2. Present calculations could not explain the experimental increment of c/a ratio (9) beyond 80 GPa.

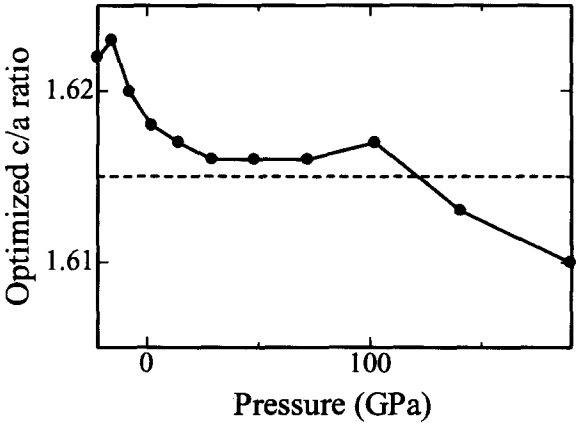

Fig. 2. Optimized c/a ratio for ε-Co as a function of pressure. Pressure was obtained with the third-order Birch-Murnaghan equation of state. Dashed horizontal line at c/a= 1.615 is the experimental c/a ratio at zero-pressure (9).

For β-Co, large discrepancies in the equilibrium volume, the bulk modulus and its first-order pressure derivative appeared between magnetic calculation and experiment as shown in Table 1. Although calculated total energies in magnetic treatment as a function of volume are smaller than those in non-magnetic one at all volumes, as shown in Fig. 1, the non-magnetic calculating results are compared with the experiment, in which good agreement between calculation and experiment was obtained. Another calculation with the FP-LMTO method (13) also suggested β-Co favors magnetic at lower pressure range. However, no detailed calculating condition was written in that paper (13) and no calculation except reference (13) was found for β-Co. Moreover, only one experiment (9) was reported for β-Co under high pressure condition. Further high-pressure experiments and calculations for β-Co are necessary.

The magnetic properties of both ε- and β-Co under high pressure conditions were studied by the use of the results in magnetic treatments, since no experiments on magnetic properties of ε- and β-Co have been reported under high pressure condition. The magnetic moments of these two as a function of pressure were calculated by subtraction of down-spin density by up-spin density inside the muffin-tin sphere, which is shown in Fig. 3. Calculated magnetic moment of ε-Co at zero-pressure was 1.7, which is close to an experimental value (1.6 μ_B) (21).

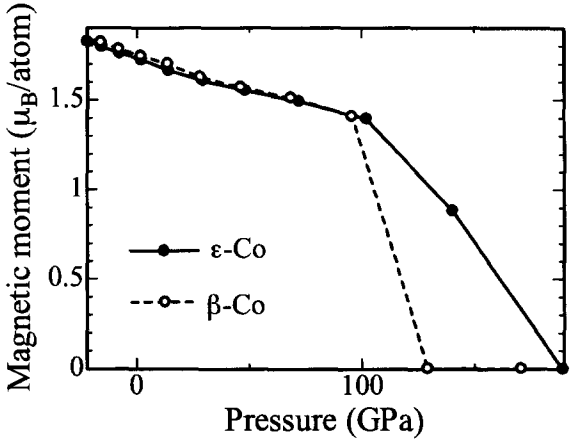

Fig. 3. Calculated magnetic moments for ε- and β-Co as a function of pressure. Solid and open circles denote ε- and β-Co, respectively. Pressure was obtained with the third-order Birch-Murnaghan equation of state.

The magnetic moment of ε-Co decreases gradually up to 100 GPa, above which pressure it decreases steeply and becomes 0 at about 190 GPa as shown in Fig.3. The magnetic moment of β-Co changes almost same manner as ε-Co up to 100GPa, but it suddenly becomes zero beyond 100 GPa.

In order to obtain a theoretical transition pressure from hcp to fcc structures, enthalpies, i.e. Gibbs' free energies at 0 K, for both phases as a function of pressure were calculated. The enthalpy as a function of pressure, H(p), is expressed by (21)

$$H(p) = E_0 + pV = E_0 + \frac{BV_0}{B'-1}\left[\left(\frac{B'}{B}p+1\right)^{1-1/B'} - 1\right] \tag{3}$$

where p is pressure. Calculated enthalpy difference ΔH, i.e. $\Delta H = H_\beta - H_\varepsilon$, between ε- and β-phases is shown in Fig. 4, where H_ε and H_β are enthalpies of ε- and β-phases, respectively. The transition pressure correspond to the point where the enthalpy of β-phase is equal to the corresponding quantity of ε-phase, which is 128.3 GPa for hcp → fcc (magnetic). This theoretical transition pressure falls within the experimental transition pressure range (105-150GPa) (9). ε-phase could coexist with β-phase between 100 and 150 GPa, since the energy difference

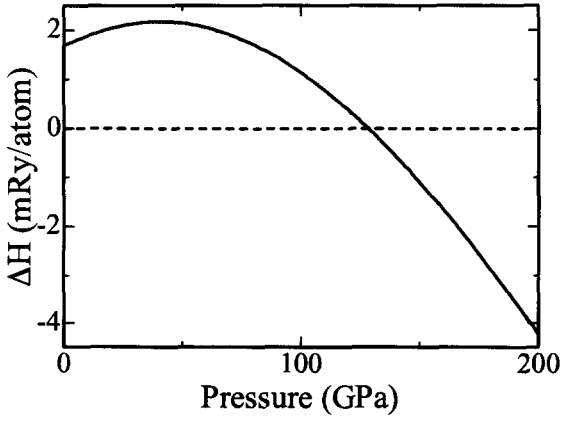

Fig. 4. Calculated enthalpy differences as a function of pressure between ε- and β-phases.

between ε- and β- phases are very small as shown in Fig. 1 and pressure with diamond anvil cell may not be hydrostatic.

Conclusion

First principles calculations were performed to investigate the structural properties of ε- and β- cobalt at high pressures and to know a theoretical transition pressure from ε- to β- phases using the FP-LAPW method within GGA-PBE. Calculated bulk parameters, i.e. the bulk modulus, its pressure derivative and the equilibrium volume, reproduce the observed ones very well for ε-Co. Spin-polarized calculations for β-Co, however, could not reproduce the experimental bulk parameters (9). Good agreement was obtained between non-spin-polarized calculations and experiment (9), though spin-polarized calculations were energetically more favorable than non-spin-polarized one. Only one experiment (9) and one calculation (13) were reported for β-Co and only GGA-PBE exchange correlation functional was examined here. Further high-pressure experiments and first-principles calculations are necessary to understand fully about physical properties of β-Co under high pressure condition.

Acknowledgements

The author acknowledges the Special Postdoctoral Researchers Program in RIKEN.

References

(1) A.P.Jephcoat, H.K.Mao and P.M.Bell, J. Geophys. Res. 91, 4677 (1986).
(2) H.K.Mao, Y.Wu, L.C.Chen and J.F.Shu, J. Geophys. Res. 95, 21737 (1990).
(3) S.K.Saxena, L.S.Dubrovinsky, P.Häggkvist, Y.Cerenius, G.Shen and H.K.Mao, Science 269, 1703 (1995).
(4) C.S.Yoo, J.Akella, A.J.Campbell, H.K.Mao and R.J.Hemley, Science 270, 1473 (1995).
(5) D.Andrault, G.Fiquet, M.Kunz, F.Visocekas and D.Häusermann, Science 278, 831 (1997).
(6) L.Stixrude and R.E.Cohen, Science 267, 1972 (1995).
(7) A.Zupan, P.Blaha, K.Schwarz and J.P.Perdew, Phys. Rev. B58, 11266 (1998).
(8) P.Söderlind, J.A.Moriarty and J.M.Wills, Phys. Rev. B53, 14063 (1996).
(9) C.S. Yoo, H.Cynn, P.Söderlind and V. Iota, Phys. Rev. Lett. 84, 4132 (2000).
(10) G.Steinle-Neumann, L.Stixrude and R.Cohen, Phys. Rev. B60, 791 (1999).
(11) T.C.Leung, C.T.Chan and B.N.Harmon, Phys. Rev. B44, 2923 (1991).

(12) B.I.Min, T.Oguchi and A.J.Freeman, Phys. Rev. B33, 7852 (1986).
(13) C.S.Yoo, P. Söderlind and H.Cynn, J.Phys. Condens. Matter 10, L311 (1998).
(14) D.J.Singh, *Planewaves, Pseudopotentials and the LAPW Method* (Kluwer, Norwell, 1994).
(15) J.P.Perdew and Y.Wang, Phys. Rev. B33, 8800 (1986).
(16) P.Blaha, K.Schwarz and J.Luitz, WIEN97, A Full Potential Linearized Augmented Plane Wave Package for Calculating Crystal Properties (Karlheinz Schwarz, Techn. Universität Wien, Austria), 1999. ISBN 3-9501031-0-4.
(17) J.P.Perdew, S.Burke and M.Ernzerhof, Phys. Rev. Lett. 77, 3865 (1996).
(18) F.D.Murnaghan, Proc. Natl Acad. Sci. USA 30, 244 (1944).
(19) H.R.Schober and H.Dederichs, in *Elastic Piezoelectric Pyroelectric Piezooptic Electrooptic Constants and Nonlinear Dielectric Susceptibilities of Crystals*, edited by K.-H.Hellwege and A.W.Hellwege, Landolt Börnstedt, New Series III, Vol. 11a (Springer, Berlin, 1979).
(20) F.Birch, J. Geophys. Res. 83, 1257 (1978).
(21) H.P.Meyer and W.Sucksmith, Proc. R. Soc. London, Ser. A 207, 427 (1951).
(22) M.P.Habas, R.Dovesi and A.Lichanot, J. Phys. Condens. Matter 10, 6897 (1998).

Electronic structure of Er doped GaAs

Shinichi Itoh

Kyoto University of Education

(Received December 31, 2001; in final form June 10, 2002)

Abstract

Er impurity in GaAs shows strong luminescence due to the 4f intra transition. Relativistic DVXα calculation was performed for Er doped GaAs system in order to investigate the chemical bonding between Er atom and the surrounding As and Ga atoms. The bond overlap populations in the one-electron orbitals between the 4f and the intra or the inter valence orbitals were investigated. Furthermore we calculated for the oxygen co-doping in Er:GaAs system which showed the excellent sharp spectra. The calculated results show the 4f orbitals play an important role to the electronic structure near the Fermi level and the hybridization of the 4f with O 2p orbitals was relatively larger than with As and Ga 4p orbitals in the case of oxygen co-doping. In the obtained molecular orbitals at the Fermi level the 4f character was large. The HOMO-LUMO gap energy was much small ($\sim$ 0.02 eV).

Contents

Keywords Er, GaAs

e-mail: itoh@kyokyo-u.ac.jp

ADVANCES IN QUANTUM CHEMISTRY, VOLUME 42

0065-3276/03 $35.00

1. Introduction

Er doped GaAs has been investigated by many researchers because they appear sharp 1.54 μm luminescence of the 4f electrons and are important for opt-electronic materials [1]. The luminescence is due to the 4f-4f intra-transition in Er3+ ion in GaAs. The excitation energy of the 4f electrons can be considered to being transfered from the host material because the luminescence of the 4f electrons has been observed by the host photo-excitation. Several energy transfer models from the excited carriers in the host GaAs to the 4f electrons can be considered [2]. Therefore it is important to solve the molecular orbitals and their energies of the system in order to consider the mechanism of energy transfer because they are the basic physical quantities which are necessary for the construction of the model. Because it was understood that non-relativistic molecular orbital (MO) calculation has estimated the energy levels of one-electron 4f orbitals artificially, relativistic calculation is need to treat the 4f electrons quantitatively. Thus the relativistic DVX α code is suitable method for the investigation of chemical bonding of the 4f shells. In the present calculation, the cluster models can be said to present well the chemical bonding of the 4f shell of Er in GaAs because the density of Er impurity is low ($\sim$ 10^{17} cm^{-3}) in the host GaAs and the neighbouring atoms to Er center are especially important for the chemical bonding of the inner 4f shell of Er.

2. Method of Calculation

We performed relativistic DVX α calculation for the three cluster models, i.e. $ErAs_4Ga_{12}$, $ErO^{2-}{}_2As_2Ga_{12}$ and ErO_4Ga_{12}. The lattice structure is zinc blende as shown in Fig.1. Here, oxygen co-doping in Er:GaAs is represented as the latter two clusters. Until now, the number of O atoms has not been determined. The spectra reported are complex structures which indicate the simultaneous presence of Er centers with various atomic configurations in the case of oxygen co-doping also. Though it may be said that two O atoms couple with Er frequently on the average number of the ligand atoms with Td symmetry, there is still one possibility of presence of Er-O4 center. The lattice constant is selected to 5.65 Å which is for GaAs. Total charges of the above three clusters are chosen to neutral,

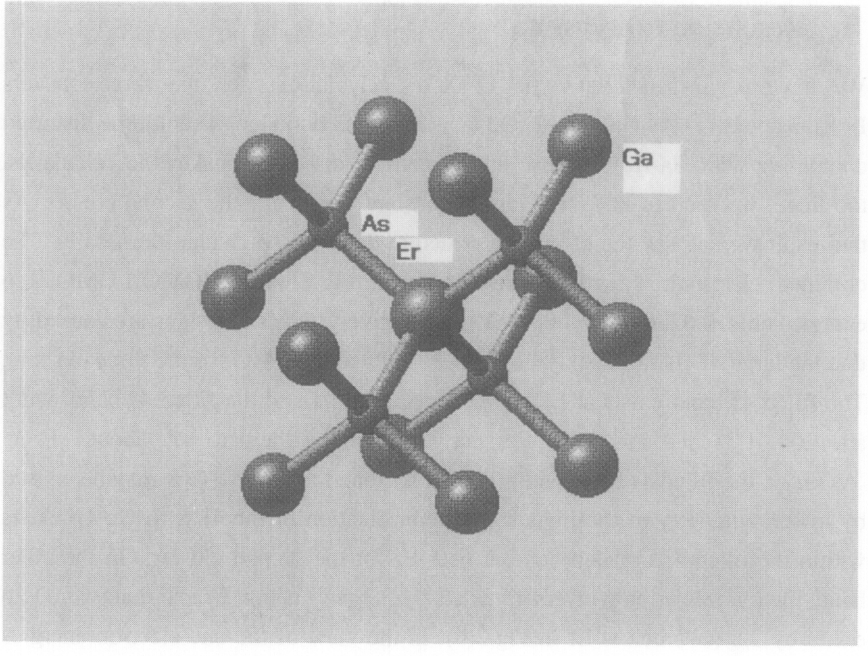

Fig. 1 $ErAs_4Ga_{12}$ cluster. Two or four As atoms are replaced with oxygen in $ErO^{2-}{}_2As_2Ga_{12}$ or ErO_4Ga_{12}, respectively.

-4 and neutral, respectively. Bond overlap populations (BOPs) between the 4f and the inter AOs P(4f,i) are obtained for 4f and i= As(4s, 4p) , Ga(4s, 4p) and O(2p).

$$P(4f,i) = \Sigma k\, C\_\{4f,k\} * C\_\{i,k\}$$

here C_{4f,k} are the coefficients of the 4f AOs in the k-th MO and they are multiplied by the components of being related to the i-th AO(s) of the host atoms in the k-th MO. We get the total bond overlap population between Er and the host atoms As, O and Ga by the sum over all of the AOs of Er and the host atoms.

3. Results and Discussion

We have performed relativistic DVX α calculations for the three clusters $ErAs_4Ga_{12}$, $ErO^{2-}{}_2As_2Ga_{12}$ and ErO_4Ga_{12}. The Er-O bond lengh should be distorted comparing with Ga-As. Because unsymmetrical distortion makes the calculation too huge, we tried to make the lattice constant longer for the second cluster. As the result we can say the electronic structure does not so change drastically. The obtained electronic structures are shown in Fig.2. The HOMO-LUMO gap energies are 0.02, 0.02 and 0.3 (eV), respectively. The small gaps are caused by that the large 4f character exists both in HOMO and LUMO for the three clusters. The filled 4f band exists at Ef for the three clusters and the filled 4f band width are 1.04, 1.78 and 1.12 (eV), respectively. Among them to say about $ErO^{2-}{}_2As_2Ga_{12}$, the filled 4f band width is broader than the others. This may be caused by lower symmetry of the ligand. The hybridization of the 4f with Ga 4p exists within the filled 4f broaden band at near Ef for the second cluster. On the other hand, the hybridization with As 4p exists by 2.3 (eV) below Ef and that with O 2p exists by 2.8 (eV) below Ef in Fig.2(b). In the view of the one-electron energies and MOs, the hybridizations between the 4f and the inter AOs are much smaller than those for intra AOs. Among them, the relative large hybridizations are found in several MOs for between the 4f and As, Ga 4p (Fig.2 (a)) and the 4f and O 2p (Fig.2 (b)). For example, for the one k-th MO which is below Ef by 1.49 (eV) in $ErAs_4Ga_{12}$ the obtained components are C_{4f,k}=0.307, C_{As4p,k}=0.271, C_{Ga4s and 4p,k}=0.421 and below Ef by 2.60 (eV) in $ErO^{2-}{}_2As_2Ga_{12}$ the components are C_{4f,k}=0.296, C_{O2p,k}=0.259, C_{As4p,k}=0.173. On the other hand, for ErO_4Ga_{12} the obtained 4f characters in the MOs are more atomic like and show the less hybridizations in each of the one-electron orbitals than in the case of the two (a), (b) clusters in Fig.2. Next, in order to investigate the hybridizations of the 4f shell, we obtained the bond overlap populations.

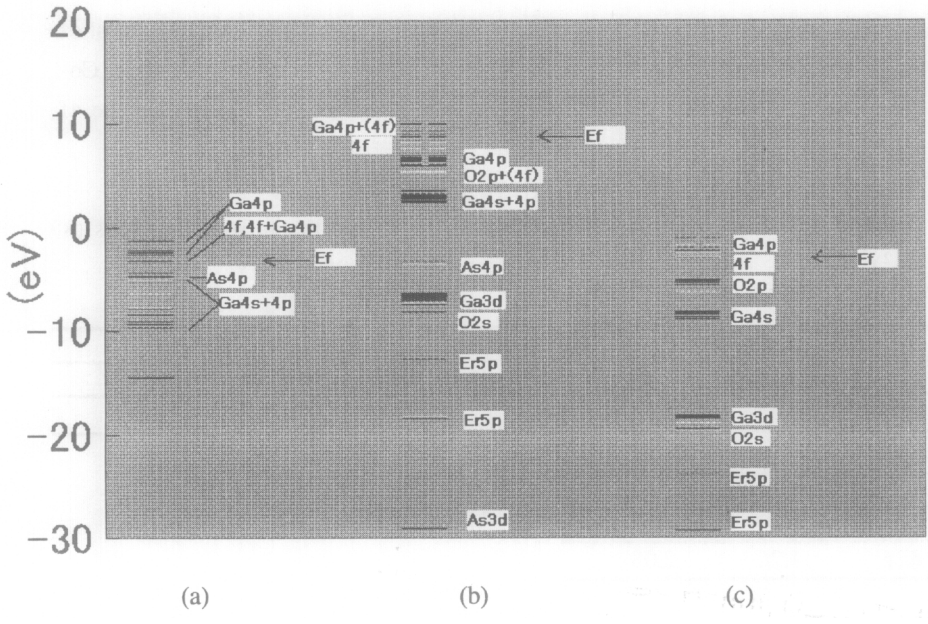

Fig.2 Electronic structure obtained for (a)$ErAs_4Ga_{12}$, (b)$ErO^{2-}{}_2As_2Ga_{12}$ and (c)ErO_4Ga_{12} clusters.

In Table 1 we show the obtained partial bond overlap populations between Er 4f and the surrounding AOs. It is found that the BOPs have the same order both with the nearest and with the second nearest AOs, respectively. This is due to the inner 4f shells which weakly couple with the surrounding AOs. As is expected, the chemical bonding between the 4f and the surrounding AOs is much weaker than the 4f-4f intra coupling. However, the 4f energy levels are also lying among As and Ga 4p levels and it can be said the couplings with As and Ga 4p are necessary to consider the electronic structures. It is noted that Er atom is treated as neutral atom. The obtained 4f electrons are 11.63, 11.26 and 11.62 for the three Fig.2 (a), (b) and (c), respectively, and are consistent with the experimental results. The excess of the charges flows out to the outer Er 5d and 6s orbitals which are important for the charge consistency. Now we can say the conduction band is also

important to discuss the energy transition. Because the obtained LUMO consist of the 4f and Ga 4p, the empty 4f levels seem to couple with surrounding AOs. Co-doped oxygen atoms have a tendency to make a stable band lower than the 4f valence band.

Table.1 Bond overlap populations between Er 4f and the surrounding AOs ($\times 10^{-2}$).

	$ErAs_4Ga_{12}$		$ErO^{2-}{}_2As_2Ga_{12}$		
	As 4p	Ga 4p	O 2p	As 4p	Ga4p
4 f	2.65	3.38	0.104	0.329	0.158

	ErO_4Ga_{12}	
	O 2p	Ga 4p
4 f	1.26	2.08

4. Conclusion

We obtained the one-electron electronic structures and the bond overlap populations for the three Er doped GaAs clusters. The HOHO-LUMO gap energies are much narrow and the 4f impurity levels exist in GaAs band gap. The BOPs between the 4f and As, Ga 4p are small but there are several 4f related one-electron MOs coupled with As or Ga 4p with relatively strong ones. The oxygen co-doped cluster shows the complex hybridizations of the 4f with O 2p, As 4p and Ga 4p.

5. References

[1] K. Takahei et. al., J.Appl.Phys. 76(7), 4332 (1994).

[2]A. Taguchi and K. Takahei, J.Appl.Phys. 83(5), 2800 (1998).

Electronic structures of $Sr_{1-x}La_xRuO_3$

H Nakatsugawa[1], E Iguchi[1], and Y Oohara[2]

[1]*Division of Materials Science and Engineering, Graduate School of Engineering, Yokohama National University, Tokiwadai, Hodogaya-Ku, Yokohama 240-8501, Japan*
[2]*Neutron Scattering Laboratory, Institute for Solid State Physics, University of Tokyo, Shirakata 106-1, Tokai 319-1106, Japan*

(Received December 20, 2001; in final form January 25, 2002)

Abstract

In order to elucidate a suppression of ferromagnetic interactions in $Sr_{1-x}La_xRuO_3$, electronic structures have been investigated by changing x from 0.0 to 0.5, using an XRD and a neutron diffraction study with a Rietveld analysis and a DV-X alpha computational method. In comparison with magnetic properties in $Sr_{1-x}Ca_xRuO_3$, ferromagnetic interactions in $Sr_{1-x}La_xRuO_3$ are found to be suppressed very rapidly against x. Neither structural distortion nor cation-size disorder can account for such rapid suppression. Instead, this may be attributed to the effect of La - O hybridization created by La substitution for Sr. This hybridization-effect weakens the ferromagnetic order around Ru ions and, as a result, the long-range ferromagnetic states are suppressed even if x is small. The DV-X alpha cluster method was employed to estimate an energy difference between up and down spin density of states in $SrRuO_3$ and $Sr_{0.5}La_{0.5}RuO_3$. This calculation predicts that $Sr_{1-x}La_xRuO_3$ contain La - O hybridization which suppresses ferromagnetic interaction even at small x.

CONTENTS

KEYWORDS

suppression of ferromagnetic states; orthorhombic distortion; cation size disorder; density of states; hybridization

ADVANCES IN QUANTUM CHEMISTRY, VOLUME 42

0065-3276/03 $35.00

1. INTRODUCTION

Because of the spin-triplet *p*-wave superconductivity in the copper-free layered perovskite Sr_2RuO_4 [1,2], the anomalous magnetic properties and the transport properties in this material and the related ruthenium oxides have attracted much interest. A series of ruthenium oxides $(Sr,Ca)_{n+1}Ru_nO_{3n+1}$ shows rich properties: a ferromagnetic (FM) metal, an antiferromagnetic (AFM) insulator and a superconductor. In particular, a correct understanding of the magnetic properties in these ruthenates is indispensable so as to gain an insight into the emergence of the spin-triplet superconductivity in Sr_2RuO_4.

$SrRuO_3$ and $CaRuO_3$ have nearly cubic and slightly distorted cubic perovskite structure, respectively. Though both the ruthenates exhibit the metallic behavior [3,4], their magnetic properties differ remarkably: $SrRuO_3$ is a FM metal with the Curie temperature T_C=160 K [5,6] whereas $CaRuO_3$ does not show any magnetic anomalies even at very low temperatures. Such a magnetic difference has been mainly ascribed to the ionic sizes of Sr^{2+} (0.144 nm) and Ca^{2+} (0.134 nm), although there must be various reasons. Because of the ionic radius of Sr^{2+} bigger than Ca^{2+}, $CaRuO_3$ is more distorted [5]. In $Sr_{1-x}Ca_xRuO_3$, each RuO_6 octahedron is tilted slightly and rotated around Ca^{2+} substituted for Sr^{2+} to fill the extra space of Sr-shared positions. The calculated band structures also suggest the importance of the structural distortion. In the band structure constructed by Mazin *et al.* [7], the density of states (DOS) in $SrRuO_3$ has a strong peak at Fermi level, stabilizing FM states; while $CaRuO_3$ is on the border of FM states and paramagnetic (PM) states due to the fact that the more distorted structure of $CaRuO_3$ lowers the DOS at Fermi level [7]. In another calculation by Fukunaga *et al.* [8], FM ground states are formed in both the compounds, but the energies obtained in the calculations, especially for $CaRuO_3$, are very sensitive to the calculational parameters employed. It has been also argued that the larger structural distortion in $CaRuO_3$ would result in larger splitting of Ru t_{2g} orbital, leading to stronger AFM interactions [9]. He *et al.* have recently concluded that $CaRuO_3$ is not a classical AFM, but is rather poised at a critical point between FM and PM ground states [10,11].

There are several literatures studying the properties of $Sr_{1-x}Ca_xRuO_3$ perovskites [9-15]. The variation in properties due to the change in x are now basically understood in terms of the change in magnetic ground state as a function of a Ru - O - Ru bond angle [7], but there must be other parameters to consider. The size-disorder of *A*-site atom must be also an important parameter. In the study of the magnetism and the size-disorder effect on the magnetic properties in *4d*-based ruthenate perovskites, the experiments on $Sr_{1-x}La_xRuO_3$ could provide a very useful knowledge. Referring to the ionic radius of La^{3+} (0.136 nm) with the ionic radii of Sr^{2+} and Ca^{2+}, $Sr_{1-x}La_xRuO_3$ is expected to have the orthorhombic distortion and the size-disorder smaller than $Sr_{1-x}Ca_xRuO_3$. In order to investigate the effects due to the orthorhombic distortion and the cation-size disorder, the elucidation of structural lattice parameters in $Sr_{1-x}La_xRuO_3$ as a function of x is indispensable. Furthermore, there is a high possibility that La^{3+} substituted for Sr^{2+} changes the electronic structures on ions and the chemical bond nature. From these points of view, the structural lattice parameters and

the electronic structures in a series of $Sr_{1-x}La_xRuO_3$ perovskites have been investigated in the present study, using the powder X-ray or neutron diffraction methods with a Rietveld analysis and the discrete variational (DV)-X alpha computational method.

2. EXPERIMENTAL DETAILS

Polycrystalline samples of $Sr_{1-x}La_xRuO_3$ (x= 0.0, 0.1, 0.2, 0.3, 0.4, and 0.5) were synthesized by a conventional solid state reaction method. Stoichiometric mixture of powders of $SrCO_3$ (99.99 %), dried La_2O_3 (99.99 %), and dried RuO_2 (99.95 %) were ground and reacted at 1373 K for 24 h in air. This procedure was repeated several times. The samples were reground, pressed into pellets, and heated again at 1573 K for 24 h in air and cooled to room temperature at the rate of 1 K/min in the last procedure. All of the sintered pellets were analyzed at room temperature, using an X-ray diffractometer with step scanning. The powder XRD patterns show a single-phase compound with the *Pnma* type space symmetry (No.62) for every sample. The sample for x=0.5 also was analyzed at room temperature, using a neutron diffraction study. Neutron scattering measurements were carried out on the ISSP triple-axis spectrometer HQR installed at T_{11} experimental port in JRR-3M in JAERI (Tokai). The structural lattice parameters were refined using a Rietveld analysis program, RIETAN-2000 [16].

3. COMPUTATIONAL PROCEDURES

The interpretation of the experimental results obtained here needs the assist of the theoretical calculations. All computations were performed by means of *ab initio* molecular orbital (MO) method using model clusters. The computer code called SCAT [17], which is a modified version of the original DV-X alpha program [18,19], was employed. The exchange and correlation term by Slater with alpha=0.7 was used, and spin polarizations were taken into account in the calculations [20]. Numerical atomic orbitals (NAOs) were used as basis functions. Basis sets were *1s, 2s, 2p, 3s, 3p, 3d, 4s, 4p,* and *5s* for Sr, *1s, 2s, 2p, 3s, 3p, 3d, 4s, 4p, 4d, 4f, 5s, 5p, 5d, 6s,* and *6p* for La, *1s, 2s, 2p, 3s, 3p, 3d, 4s, 4p, 4d, 5s,* and *5p* for Ru, and *1s, 2s,* and *2p* for O. Integrations to obtain energy eigenvalues and eigenfunctions were made numerically. Population analyses were made in the standard Mulliken's manner [21]. The calculation of the electronic structures has been carried out under the assumption that the electronic structures of $[Sr_{16}Ru_3O_{16}]^{12+}$ and $[Sr_8La_8Ru_3O_{16}]^{18.5+}$ clusters are to be representative of those of $SrRuO_3$ (x=0.0) and $Sr_{0.5}La_{0.5}RuO_3$ (x=0.5), respectively. Figure 1 shows the structure of the $[Sr_8La_8Ru_3O_{16}]^{18.5+}$ cluster employed in the present calculation for x=0.5. The model clusters were embedded in Madelung potential generated by approximately 10,000 point charges of formal values. The values were +2, +4, and -2 for Sr, Ru, and O in $SrRuO_3$. In $Sr_{0.5}La_{0.5}RuO_3$, they were +2, +3, +3.5, and -2 for Sr, La, Ru, and O. Convergence of the electrostatic potential with respect to dipole and quadrupole sums [22] was established within an accuracy of 0.1 %.

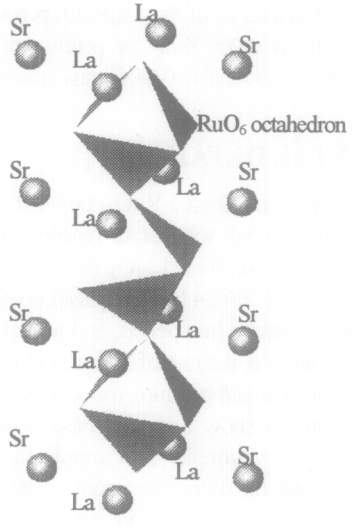

Figure 1. Model cluster used in the DV-X alpha cluster method, i.e., $[Sr_8La_8Ru_3O_{16}]^{18.5+}$ cluster which is employed in the present calculation for $Sr_{0.5}La_{0.5}RuO_3$ (x=0.5).

4. RESULTS AND DISCUSSION

No impurity peak was detected in the present powder XRD or neutron diffraction measurements, and all samples of $Sr_{1-x}La_xRuO_3$ had the $GdFeO_3$ type orthorhombic perovskite structure. Figure 2 shows observed, calculated, and difference intensities in neutron diffraction pattern of $Sr_{0.5}La_{0.5}RuO_3$ (x=0.5). The cubic subcell parameters of $Sr_{1-x}La_xRuO_3$ are shown in Fig.3(a). All three lattice constants, *a*, *b* and *c*, increase with increasing x, although Sr^{2+} (0.144 nm) is replaced with La^{3+} (0.136 nm). There is however an anomaly around x=0.3 in the lattice constant. This must be because electronic structures and magnetic properties change at x=0.3. Furthermore, the Ru - O(1) - Ru and Ru - O(2) - Ru bond angles cross also at x=0.3, as shown in Fig.3(b). The decrease of the Ru - O(1) - Ru bond angle with increasing x suggests the rotation of RuO_6 octahedra around La^{3+} substituted for Sr^{2+} in the similar way to $Sr_{1-x}Ca_xRuO_3$ because of the ionic radius of La^{3+} smaller than Sr^{2+}. The Ru - O - Ru bond angle between RuO_6 octahedra and the Ru - O bond lengths within RuO_6 octahedra change as x increases.

The average net charges evaluated for $[Sr_{16}Ru_3O_{16}]^{12+}$ and $[Sr_8La_8Ru_3O_{16}]^{18.5+}$ clusters at x=0.0 and 0.5 are +2.28*e* and +1.98*e* for Ru, +1.95*e* and +1.97*e* for Sr, and -1.63*e* and -1.43*e* for O, respectively. There must be a small covalent component in the bonding between a cation and an anion. Total DOS and partial DOS of $SrRuO_3$ (x=0.0) and

$Sr_{0.5}La_{0.5}RuO_3$ (x=0.5) are illustrated in Fig.4 together with energy level diagrams. All of the theoretical lines in Fig.4 are the results computed by broadening discrete MO energy eigenvalues, using Gaussian function of 0.5 eV full width at half maximum (FWHM) for easy visualization of the DOS. As shown in Fig.4(a), the filled band located from -10 eV to 0 eV is mainly composed of Ru *4d* and O *2p* orbital at x=0.0. This indicates that the electronic structure around Fermi level consists of Ru *4d* and O *2p* orbital which are hybridized. Figure 4(b) demonstrates the energy levels at x=0.5. The electronic structure around Fermi level consists of Ru *4d*, La *4f*, O *2p* orbital which are also hybridized.

There is an energy difference between up and down spin in Ru *4d* partial DOS which forms FM states. As shown in Fig.5, the energy difference between up and down spin in Ru *4d* partial DOS in $SrRuO_3$ (x=0.0) is larger than that in $Sr_{0.5}La_{0.5}RuO_3$ (x=0.5). This means that FM states are suppressed with increasing x. The unoccupied DOS located above Fermi level is mainly made up of Ru - O and Sr - O hybridization, even though La - O hybridization is included at x=0.5 as shown in Fig.4 (b). The La - O hybridization above Fermi level affects the magnetic local environment around Ru and the local charge state of Ru. Moreover, the local electron densities throughout the Ru - O network and the charge distribution with increasing *x* are likely to fluctuate by this hybridization. Such a fluctuation weakens somewhat the Ru - O hybridization and also the FM interaction between Ru *4d* spins. As a result, FM states in $Sr_{1-x}La_xRuO_3$ are suppressed.

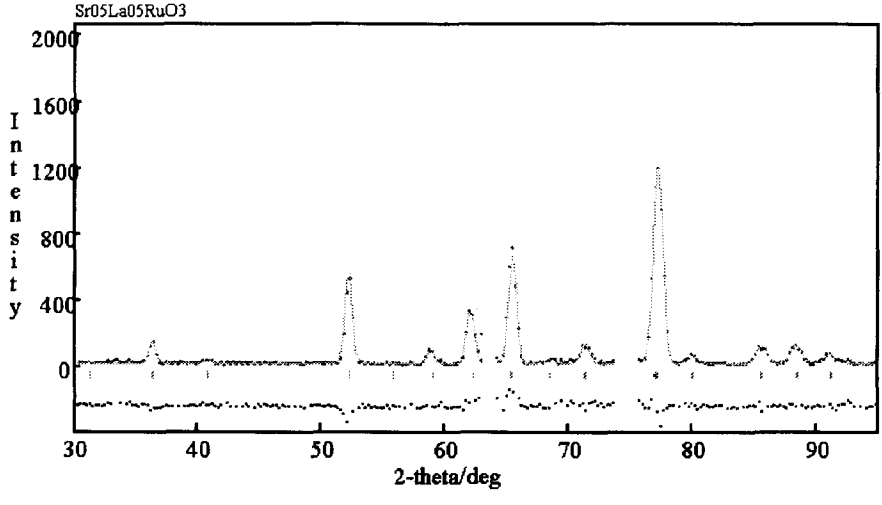

Figure 2. Observed (red dotted line) and calculated (blue line) intensities in powder neutron diffraction of $Sr_{0.5}La_{0.5}RuO_3$ (x=0.5). Tick marks represent the positions of possible Bragg reflections. A blue dotted line at the bottom is the difference between observed and calculated intensities.

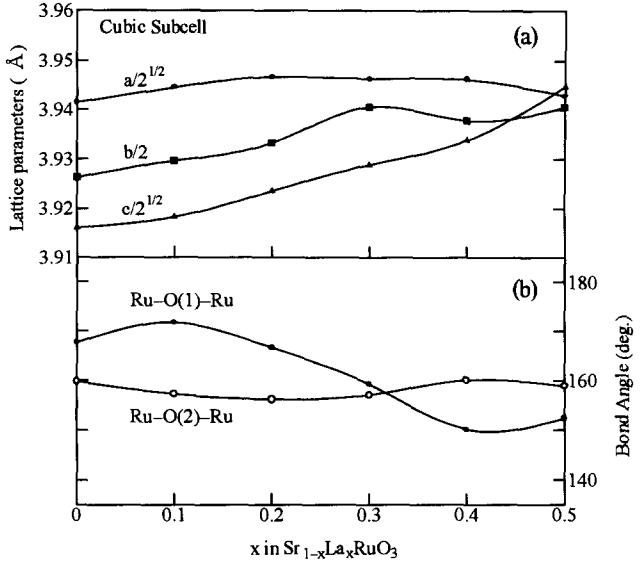

Figure 3. Selected structural data for $Sr_{1-x}La_xRuO_3$. (a) the cubic subcell parameters of $Sr_{1-x}La_xRuO_3$ and (b) the Ru - O(1) - Ru and Ru - O(2) - Ru bond angle. Lines are guides to the eye.

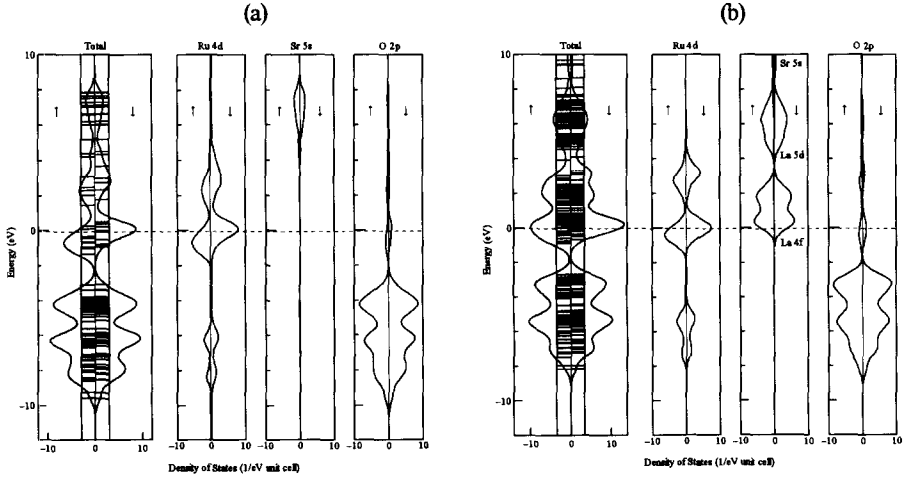

Figure 4. Energy level diagrams and total and partial density of states of (a) $SrRuO_3$ (x=0.0) by $[Sr_{16}Ru_8O_{16}]^{12+}$ cluster and (b) $Sr_{0.5}La_{0.5}RuO_3$ (x=0.5) by $[Sr_9La_8Ru_8O_{16}]^{185+}$ cluster.

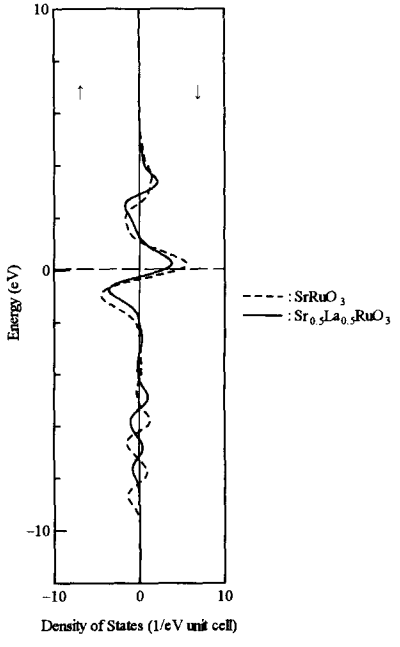

Figure 5. Energy difference between up and down spin density of states, where solid and broken lines indicate that of $SrRuO_3$ (x=0.0) and $Sr_{0.5}La_{0.5}RuO_3$ (x=0.5), respectively.

5. CONCLUSION

The structural lattice parameters and the electronic structures in $Sr_{1-x}La_xRuO_3$ have been investigated using the XRD and the neutron diffraction methods with a Rietveld analysis and the DV-X alpha computational method. The variation of x changes the Ru oxidation so that the Ru - O - Ru bond angle between RuO_6 octahedra and the Ru - O bond lengths within RuO_6 octahedra change as x increases. The ferromagnetism is suppressed very remarkably with increasing x. Since $Sr_{1-x}La_xRuO_3$ contains Ru t_{2g} - O *2p* - Ru t_{2g} interactions, the detailed calculations on the electronic structures in this system are necessary in order to explain the variation of lattice parameters. The energy difference between up and down spin in Ru *4d* partial DOS in $SrRuO_3$ is larger than that in $Sr_{0.5}La_{0.5}RuO_3$. This means that FM states are suppressed with increasing x. In addition, the La - O hybridization above Fermi level affects the magnetic local environment around Ru and the local charge state of Ru. The local electron densities throughout the Ru - O network are likely to fluctuate by the La - O hybridization. Such a fluctuation weakens somewhat the Ru - O hybridization and also the FM interaction between Ru *4d* spins. As a result, FM states in $Sr_{1-x}La_xRuO_3$ are

suppressed.

6. ACKNOWLEDGMENTS

This work was supported by Ogasawara foundation for the promotion of science and engineering and Arai foundation for the promotion of science and engineering.

7. REFERENCES

(1) Y.Maeno, H.Hashimoto, K.Yoshida, S.Nishizaki, T.Fujita, J.B.Bednorz, and F.Lichtenberg, *Nature* (London) **372**, 532 (1994).

(2) K.Ishida, H.Mukuda, Y.Kitaoka, K.Asayama, Z.Q.Mao, Y.Mori, and Y.Maeno, *Nature* (London) **396**, 658 (1998).

(3) H.Kobayashi, M.Nagata, R.Kanno, and Y.Kawamoto, *Mater.Res.Bull.* **29**, 1271 (1994).

(4) G.Gao, S.McCall, M.Shepard J.E.Crow, and R.P.Guertin, *Phys.Rev.* B**56**, 321 (1997).

(5) A.Callaghan, C.W.Moeller, and R.Ward, *Inorg.Chem.* **5**, 1572 (1966).

(6) J.M.Longo, P.M.Raccah, and J.B.Goodenough, *J.Appl.Phys.* **39**, 1327 (1968).

(7) I.Mazin and D.J.Singh, *Phys.Rev.* B**56**, 2556 (1997).

(8) G.Santi and T.Jarlborg, *J.Phys.: Condens. Matter* **9**, 9563 (1997).

(9) F.Fukunaga and N.Tsuda, *J.Phys.Soc.Jpn.* **63**, 3798 (1994).

(10) T.He, Q.Huang, and R.J.Cava, *Phys.Rev.* B**63**, 024402 (2001).

(11) T.He and R.J.Cava, *J.Phys.:Condens.Matter* **13**, 8347 (2001).

(12) K.Yoshimura, T.Imai, T.Kiyama, K.R.Thurber, A.W.Hunt, and K.Kosuge, *Phys.Rev.Lett.* **83**, 4397 (1999).

(13) T.Kiyama, K.Yoshimura, K.Kosuge, H.Michor, and G.Hilscher, *J.Phys.Soc.Jpn.* **67**, 307 (1998).

(14) T.Kiyama, K.Yoshimura, and K.Kosuge, *J.Phys.Soc.Jpn.* **68**, 3372 (1999).

(15) H.Mukuda, K.Ishida, Y.Kitaoka, K.Asayama, R.Kanno, and M.Takano, *Phys.Rev.*B**60**, 12279 (1999).

(16) F.Izumi: *The Rietveld Method* (*Ed.* R.A.Young), *Oxford University Press, Oxford*, Chapter 13 (1993)

(17) H.Adachi, M.Tsukada, and C.Satoko, *J.Phys.Soc.Jpn.* **45**, 875 (1978).

(18) F.W.Averill and D.E.Ellis, *J.Chem.Phys.* **59**, 6412 (1973).

(19) D.E.Ellis, H.Adachi, and F.W.Averill, *Surf.Sci.* **58**, 497 (1976).

(20) H.Nakatsugawa and E.Iguchi, *Jpn.J.Appl.Phys.* **39**, 1186 (2000).

(21) R.S.Mulliken, *J.Chem.Phys.* **23**, 1833 (1955).

(22) H.Coker, *J.Phys.Chem.* **87**, 2512 (1983).

DV-Xα Cluster Calculations of Spin-States in Hydrogen and Cu Oxide Clusters

Kimichika FUKUSHIMA

Advanced Energy System Design and Engineering Department
Isogo Engineering Center, Toshiba Corporation,
8, Shinsugita-cho, Isogo-ku, Yokohama, 235-8523, Japan

(Received December 27, 2001; in final form February 10, 2002)

The molecular orbital method is found to correctly predict the antiferromagnetic state by using localized and unlocalized atomic orbitals within the scheme of the conventional Xα method. In order to investigate the origin of the antiferromagnetic state, we focused on hydrogen clusters with relatively long interatomic distances, and, in particular, examined the dependence of antiferromagnetic properties on the exchange-correlation strength. We also investigated how electronic structure varies with the cluster size. Furthermore, calculations were performed for the spin-states in Cu clusters.

CONTENTS

KEYWORDS: electronic structure, antiferromagnetic state, clusters, molecular orbital theory

*Corresponding author: e-mail kimichika.fukushima@toshiba.co.jp

ADVANCES IN QUANTUM CHEMISTRY, VOLUME 42

0065-3276/03 $35.00

1. INTRODUCTION

Around 1951 [1], an epoch-making neutron diffraction experiment was carried out with MnO, leading to the discovery of the spin structure in antiferromagnetic materials. The description of the antiferromagnetic state was thus rendered one of the most important quests of solid state physics. In 1963, Hubbard first succeeded in formulating a semi-empirical theory to express the antiferromagnetic state accurately based on the band structure model [2]. His theory, now referred to as the Hubbard model, is composed of two terms: a transfer integral term and an on-site Coulomb repulsion term. For a single localized conductive electron per atom, the model predicts that a weak on-site Coulomb repulsion will result in an energy band with no energy gap. A strong on-site Coulomb repulsion, on the other hand, is predicted to prevent two electrons from existing on the same atomic site, rendering the antiferromagnetic state with an energy gap stable.

From the standpoint of first principles, the question of whether or not the antiferromagnetic state may be represented accurately by the molecular orbital method, the local density approximation (LDA) has thus far not been covered extensively in the literature. As for band structure calculations using LDA, there have been some attempts at improvements. One of them is correction by vanishing self-interaction. Another proposal is the so-called LDA+U model [3-5], where U is a strong Coulomb repulsion on atomic site. These methods describe the antiferromagnetic state; however, there still remain problems.

The purpose of the current report is to show that the antiferromagnetic state is predicted by the molecular orbital method with localized atomic orbitals, even by means of the conventional Xα scheme. The origin of the antiferromagnetic state has not yet been fully understood. One of main focuses is to determine how antiferromagnetic properties depend on the exchange-correlation strength. This was done by varying α, the exchange-correlation parameter in the Xα scheme. We also explore the dependence of electronic structure on cluster size, a topic heretofore largely neglected.

Molecular orbital calculations were carried out for the artificial hydrogen clusters H_2, as well as layered H_8 and H_{18} clusters with a relatively long internuclear separation. Calculations were also performed for Cu_2O_{11} clusters, which contain

two octahedra. Hydrogen clusters have localized conductive electrons that occupy the states composed of the 1*s* atomic orbital, and there is a single electron per atom. For transition metal oxides in the antiferromagnetic state, the internuclear separation between metal atoms is large. It is then reasonable to expect that hydrogen clusters having a relatively large internuclear separation would possibly be in the antiferromagnetic state.

The next section will deal with the computational procedure and the model clusters. Section 3 is devoted to a description of the calculated results for hydrogen and Cu-oxide clusters. Section 4 presents the conclusions.

2. COMPUTATIONAL PROCEDURE AND MODEL CLUSTERS

Electronic structure calculations were carried out by the spin-polarized DV-Xα molecular orbital method. The exchange-correlation parameter was set to 0.7, and was varied from this value for the specific cases. The basis functions were numerically calculated atomic orbitals: 1*s* for the H atom, and in Cu oxides, 1*s*, 2*s*, 2*p*, 3*s*, 3*p* and 3*d* for the Cu atom, and 1*s*, 2*s* and 2*p* for the O atom. For the H atom, we added a well potential with a depth of -2.0 a.u., within a radius 0.8 times the internuclear separation. The O^{2-} ion is unstable in a vacuum and becomes stable in a crystal, making it difficult to determine its atomic basis functions. Thus, a basis set consisting of two types of trial functions were adopted for O^{2-}. One of these, hereinafter "the Type I basis function", was calculated using a well potential with a depth of -0.5 a.u., within a radius 0.8 times the internuclear distance between the Cu atoms. The other, hereinafter "the Type II basis function", was derived without a well potential. For this basis function, the number of nodes and the properties near the nucleus and in the region away from the nucleus are the same as the atomic orbital. In this case, the derivative had a discontinuity at the junction between the inner and outer solutions, while the solution interpolated by a polynomial had a smooth derivative. By contrast, the basis functions for Cu^{2+} were easily derived without a well potential. In self-consistent iterations, the initial charges were neutral for the H atoms, and set to +2*e* for the Cu atoms and -2*e* for the O atoms.

For model clusters, the following atomic configurations were presented: Figs. 1

and 2 show the calculated hydrogen clusters H_8 and H_{18}, respectively. The locations of the H atoms for H_2 were ($\pm a_H$, 0, 0) , where a_H was set to 0.126 nm. The H atoms or the layered H_8 were positioned at ($\pm a_H$, $\pm a_H$, $\pm 1.25 a_H$). The H atoms for the layered H_{18} were located at (b_H, b'_H, c_H) where b_H, $b'_H = \pm 2a_H$, 0 and $c_H = \pm 1.25 a_H$. For the H clusters, the symmetry orbitals were not used, but the configuration of electrons for the equivalent H atoms was taken to be identical. The Cu_2O_{11} cluster is shown in Fig. 3. The Cu_2O_{11} cluster was taken to be symmetrical with respect to the xy plane (in this paper, the two independent Cu atoms were not in the z axis, but

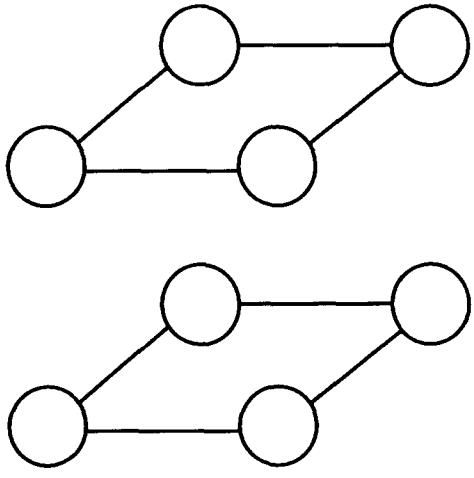

Fig. 1 Model cluster H_8.

rather in the x axis), and the point group adopted was C_s. The O atoms on the symmetry orbital in the xy plane and at the apex were regarded as equivalent. The Cu atoms were cited at ($\pm a_C$, 0, 0), while the O atoms were at ($\pm a_C$, $\pm a_C$, 0), ($\pm 2a_C$, 0, 0), (0, 0, 0) and ($\pm a_C$, 0, $\pm c_C$), where a_C and c_C were taken to be 0.189 nm and 0.243

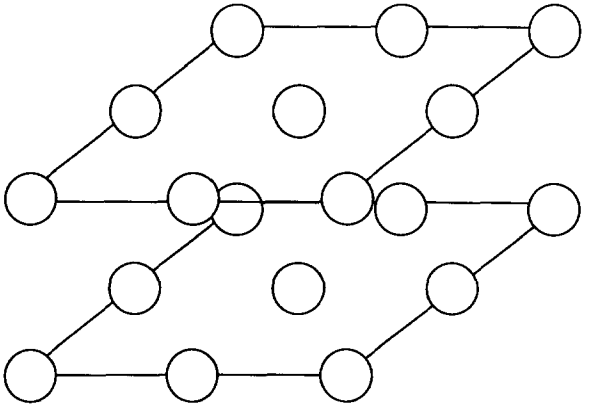

Fig. 2 Model cluster H_{18}.

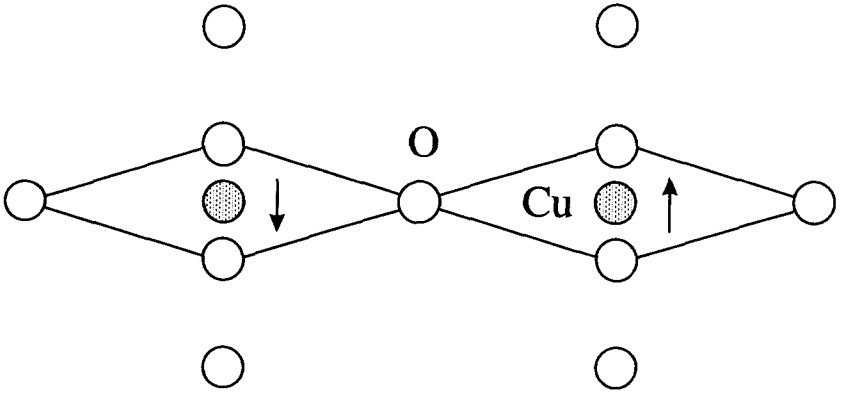

Fig. 3 Model cluster Cu_2O_{11}.

nm, respectively.

500 sampling points were used per atom in the H clusters for the integration of the matrix elements of the Hamiltonian and overlap integrals. Based on the Type I and Type II basis functions, calculations were performed for Cu_2O_{11} using 9,000 and 18,000 sampling points, respectively. The estimated errors in orbital energy were 0.01 eV and 0.04 eV for the former and latter cases, respectively. For Cu_2O_{11}, the Madelung potential from the surrounding ions was factored into the calculations. The ions considered were found in a region $4.02a_K \times 3.02a_K \times 2.74c_K$ along the x, y and z directions in the K_2NiF_4 structure, where a_K and c_K are the unit cell length along the a and c axes, and c_K was 1.33 nm.

3. RESULTS AND DISCUSSION

We first examined the antiferromagnetic state of H_2 in detail. By means of

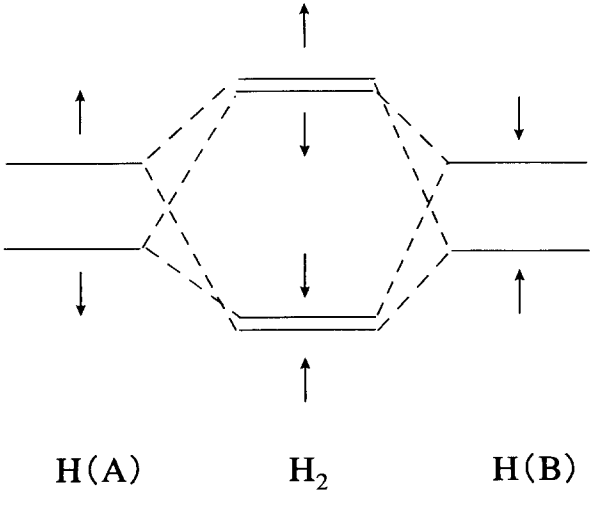

Fig. 4 Antiferromagnetic state for H_2.

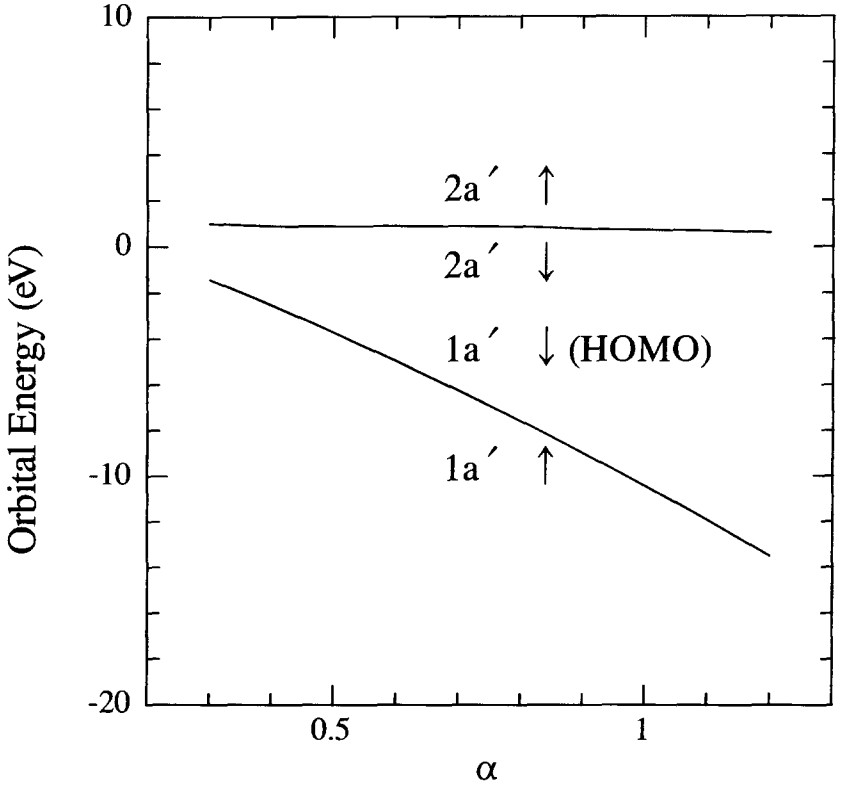

Fig. 5 Orbital energies for H_2 as a function of α.

the spin-polarized molecular orbital method, we derived the antiferromagnetic state as follows: We deal with a system where there is a single localized conductive electron per atom and the energies of atomic orbitals with up and down spins are different from each other, as shown in Fig. 4. Thus, the antibonding molecular orbitals have the possibility of being localized. In the antiferromagnetic state, there are virtually no electrons having down spin at an atomic site adjacent to one without up spin. In order to investigate the origin of the antiferromagnetic state, we examined the dependence of the magnetic moment (at the atomic site in H_2) on α, the exchange-correlation parameter.

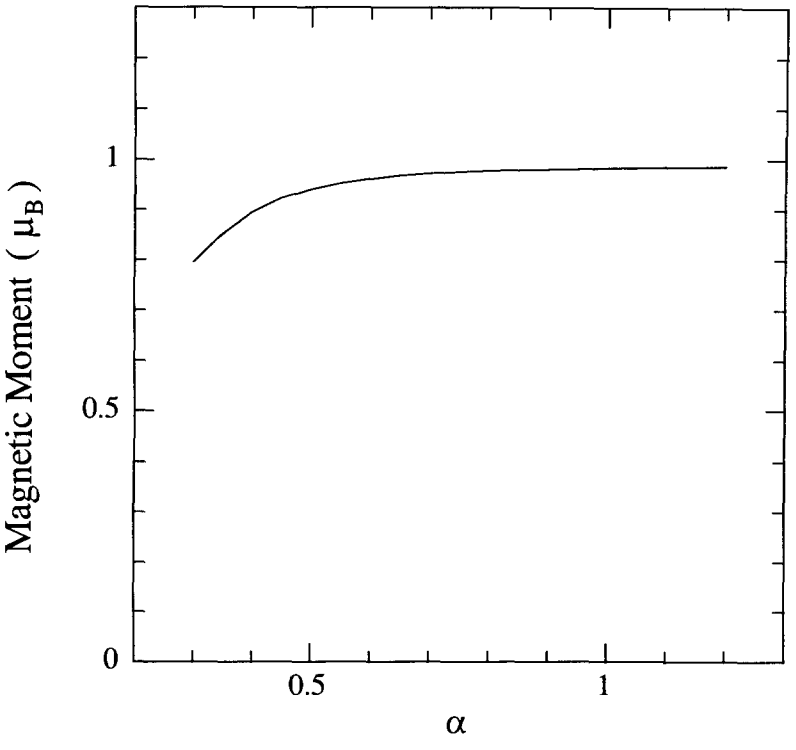

Fig. 6 Magnetic moment for H_2 as a function of α.

Fig. 5 shows orbital energies as a function of α. We can see two energy levels for bonding orbitals with up and down spins occupied by electrons up to the highest occupied molecular orbital (HOMO) and two energy levels for antibonding orbitals with up and down spins unoccupied by electrons above HOMO. The variation in energy for the unoccupied orbitals is small, while a large decrease in energy for occupied orbitals is observed for an increase in α. The energy gap between HOMO and LUMO (lowest unoccupied molecular orbital) increases with α. Figure 6 shows the averaged magnetic moment on the H atomic site. At the present internuclear separation, the magnetic moment increases rapidly for small α and approaches unity. The Hubbard model predicts a different trend. According to the Hubbard

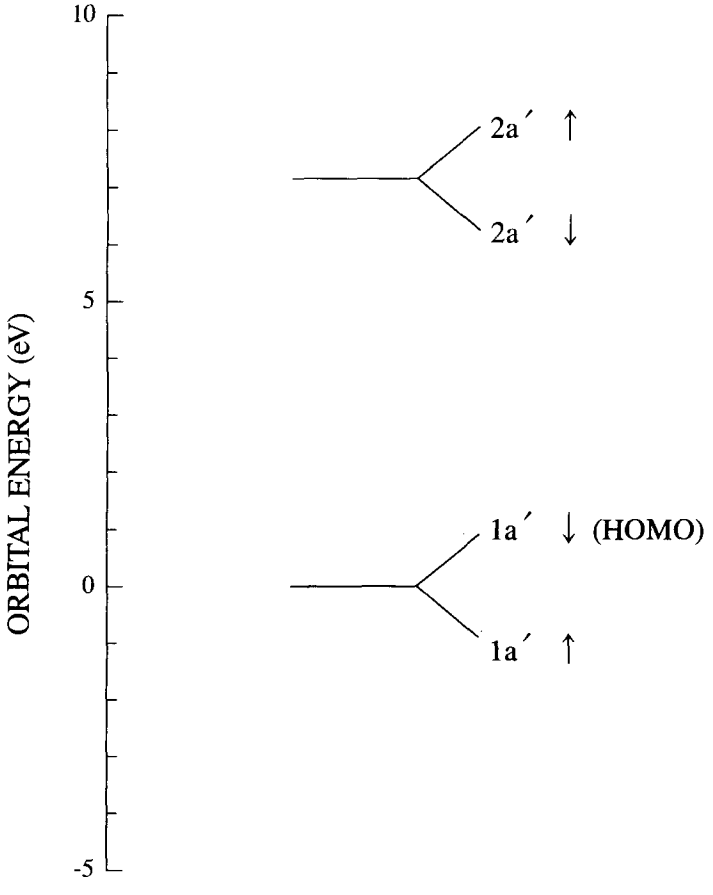

Fig. 7 Energy level diagram for the H_2 cluster.

model, the magnetic moment increases with increasing on-site Coulomb repulsion relative to the band width proportional to the transfer integral. We next investigate the dependence of the energy level structure on cluster size. As shown in Figs. 7 to 9, where the y-axis (i.e., orbital energy) zero represents the HOMO energy, an energy

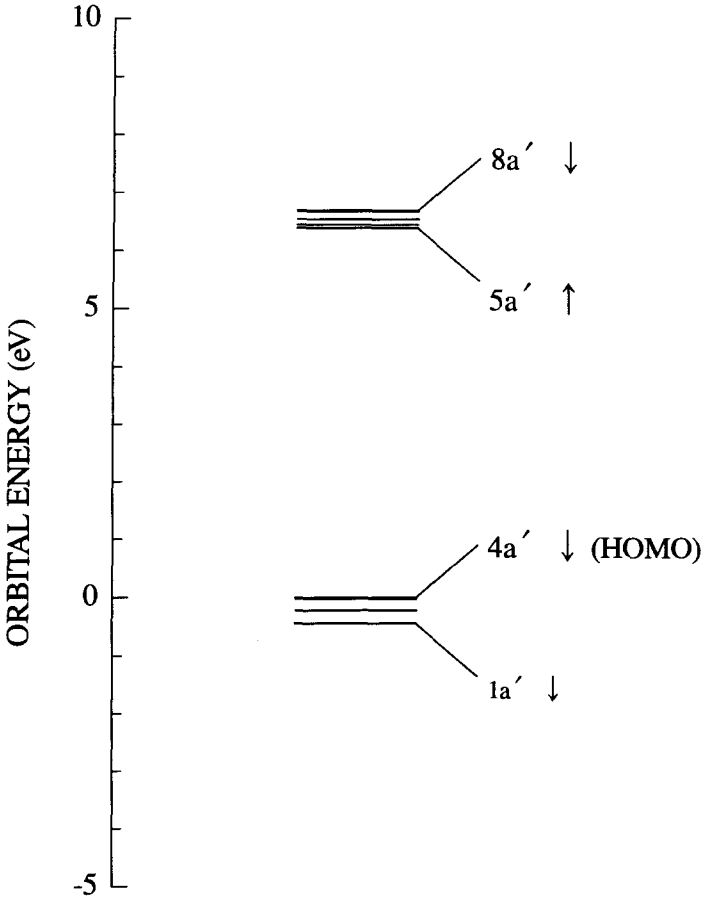

Fig. 8 Energy level diagram for the H_8 cluster.

gap is observed between the occupied and unoccupied states. The band width is not so wide compared to the energy gap. We also investigated the dependence of cluster size on energy gap and magnetic moment. In addition, spin-unpolarized calculations were carried out for the same clusters having the same electronic

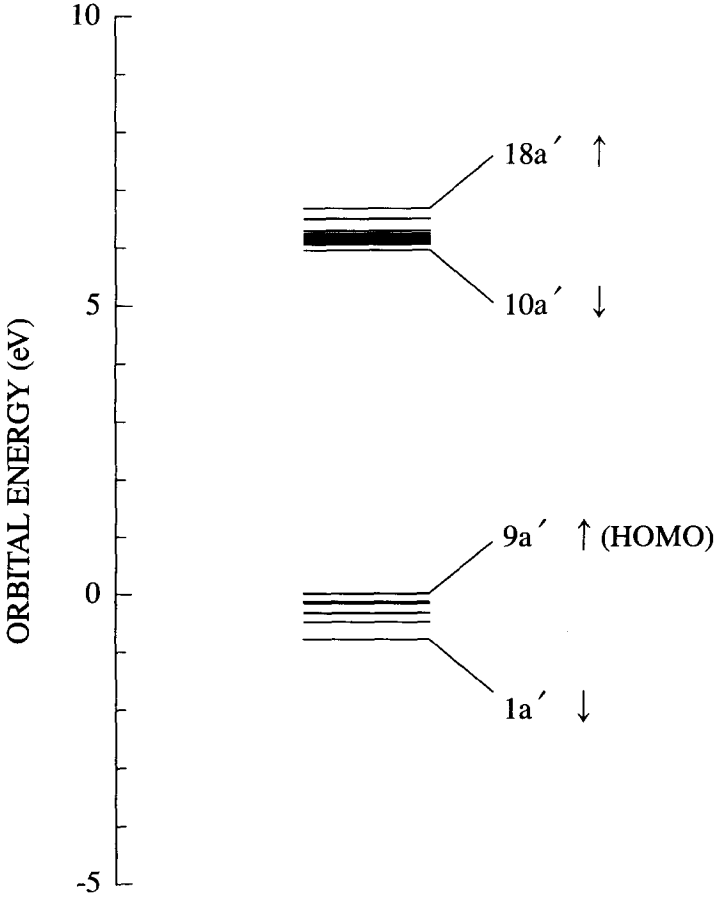

Fig. 9 Energy level diagram for the H_{18} cluster.

configurations. Figure 10 shows the energy gap between the top of the bonding states occupied by electrons (i.e., HOMO) and the bottom of the unoccupied antibonding states (i.e., LUMO). The energy gaps derived were 1.2, 0.4 and 0.3 eV for H_2, H_8 and H_{18}, respectively, suggesting that the spin-unpolarized calculation for an infinitely large system may result in a rather narrow gap. The energy gap between the HOMO and LUMO, as derived by the spin-polarized calculation were

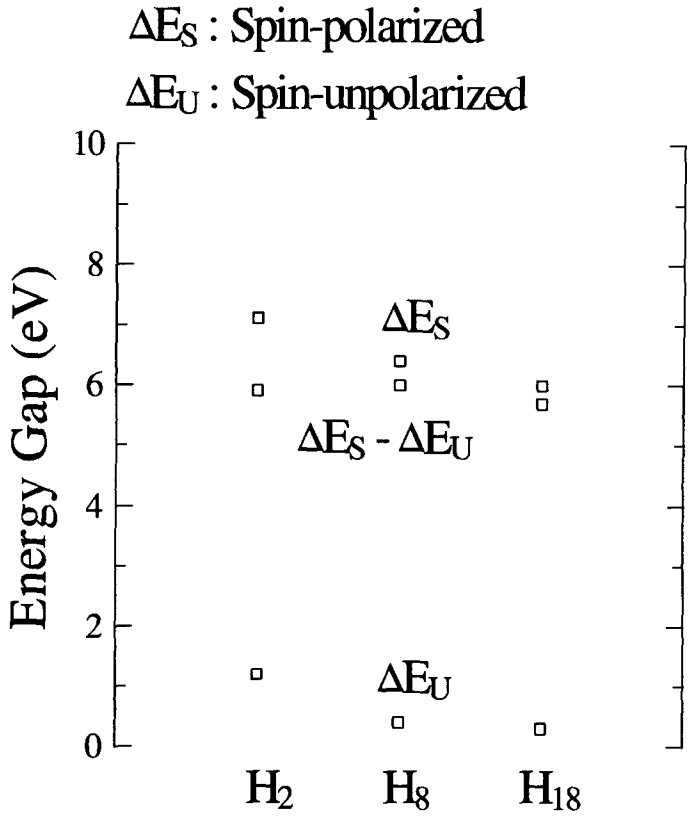

Fig. 10 Dependence of energy gap on cluster size.

7.1, 6.4 and 6.0 eV for H_2, H_8 and H_{18}, respectively. Thus, the differences in the energy gap between the spin-polarized and spin-unpolarized calculations were 5.9, 6.0 and 5.7 eV for H_2, H_8 and H_{18}, respectively. Half of this energy difference is attributable to the localization energy, which will probably remain finite for an infinitely large system. Figure 11 shows the calculated magnetic moments for the H clusters H_2, H_8 and H_{18}. It was found that the antiferromagnetic configuration attained between the nearest H atoms was stable for the cluster sizes mentioned.

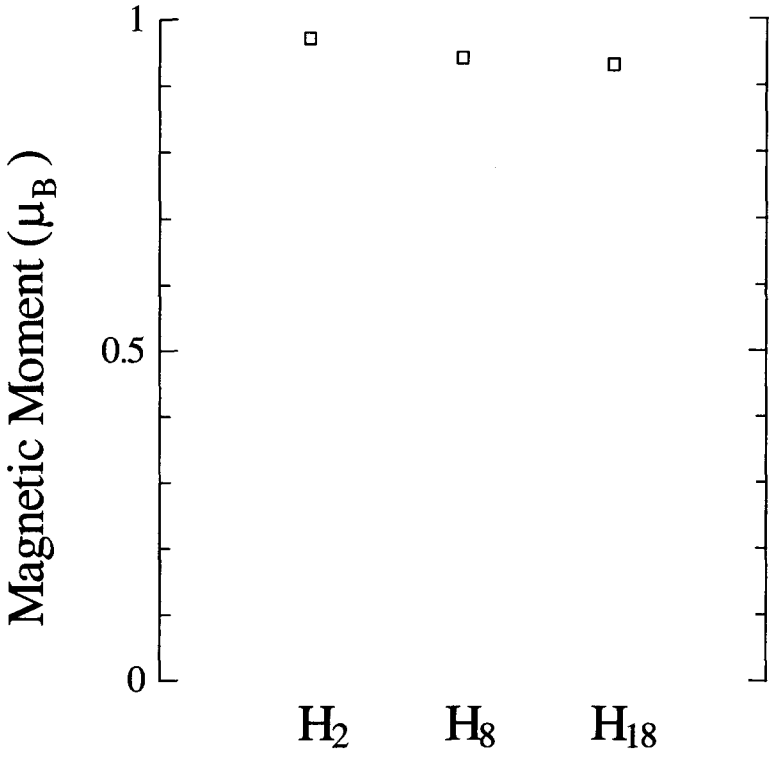

Fig. 11 Magnetic moment on the H atomic site as a function of cluster size.

The magnetic moments averaged on the H atom were 0.97, 0.94 and 0.93 μ_B for H_2, H_8 and H_{18}, respectively.

Given the above, one would expect the electronic structure to depend on the size and atomic configuration of H clusters. Electronic structures for an infinitely large system calculated based on the molecular orbital method agrees with band structure calculations at Γ point. It is noted that increased α and the mass enhancement (if it is renormalized before calculations), caused, for example, by an electron-phonon interaction, stabilize the antiferromagnetic state. In addition, this paper tried to assign α an unrealistic value greater than unity in each specific case.

We present the following as an addendum for solid hydrogen (the spin state is

not taken into account). In a hydrogen molecule (H_2), atomic orbitals form bonding and antibonding states with energy gaps in between. The H_2 molecule, with a reduced H-H interatomic distance, has an enlarged energy gap due to an enhanced covalent bond. We consider a solid composed of many H_2 molecules, the solid being compressed in some cases. In the molecular solid hydrogen, additional bonding and antibonding states are created between the molecular orbitals of H_2, which changes the energy gap of H_2. The solid hydrogen with a wide energy gap is insulating. When the energy gap closes, the system becomes metallic. Between these two phases, the system exhibits semiconducting and metallic characteristics, with a rather narrow energy gap. The existence of such a state for compressed solid hydrogen was suggested by the Hartree-Fock calculation [6]. In this system, charge fluctuations between the bonding and antibonding states may occur and result in the formation of a pair of electrons mediated by the charge fluctuations. In fact, there are references in the literature to a high-T_c superconducting state mediated by charge fluctuations [7].

In the case of the Cu oxide cluster Cu_2O_{11}, for $\alpha = 0.7$ and Type I basis function, the magnetic moment averaged on the Cu atomic site was 0.59 μ_B. The antiferromagnetic state also appeared in this case. It was found that the energy gap between LUMO and HOMO was 0.83 eV for $\alpha = 0.7$, and 1.2 times larger for $\alpha = 0.9$, i.e. 1.00 eV. For an increase in α, little change was observed in the magnetic moment on the Cu atomic site. When the Type II basis function was used, the magnetic moment averaged on the Cu atomic site was 0.98 μ_B for $\alpha = 0.9$. The antiferromagnetic state in this case became more stable than that for the Type I basis function. Figure 12 shows the energy levels near HOMO. The y-axis zero represents the HOMO energy. In the figure, the states occupied by electrons are the Cu 3*d* and O 2*p* atomic orbitals. The unoccupied states are antibonding states originating from the Cu 3*d* and O 2*p* orbitals (*d-p* mixing between nearest neighbors), as well as from Cu 3*d* orbitals (*d-d* mixing between next nearest neighbors). When α took on an unrealistic value of 1.4, the energy gap between LUMO and HOMO became 1.2 eV and the magnetic moment averaged on the Cu atom was 0.77 μ_B. (As for the H_2 cluster, the energy gap was 14.6 eV for $\alpha = 1.4$.)

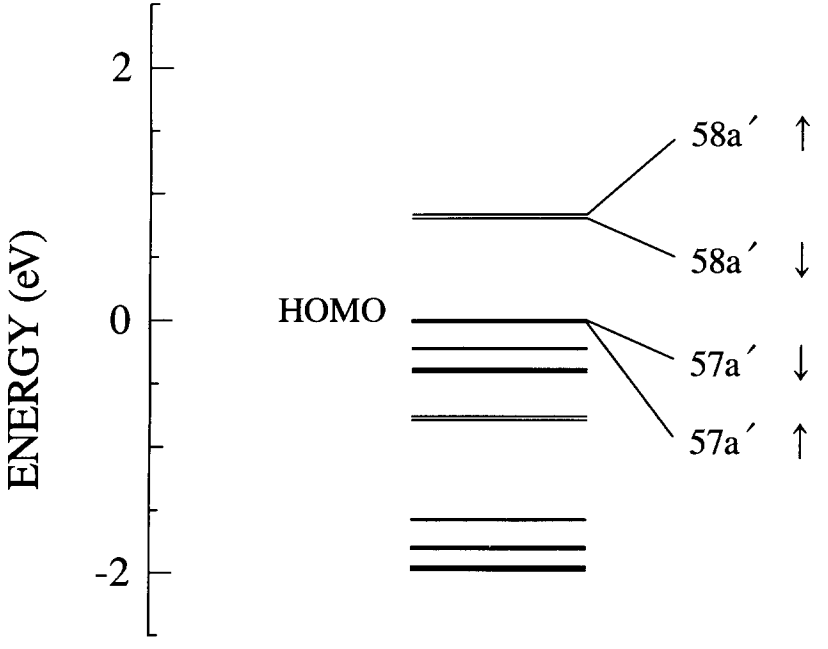

Fig. 12 Energy levels for the Cu_2O_{11} cluster.

4. CONCLUSIONS

The present study shows that a molecular orbital method that employs the conventional Xα method and localized atomic orbitals can accurately describe the antiferromagnetic state. In our calculations for hydrogen clusters with a rather long interatomic distance, we investigated the origin of the antiferromagnetic states, as well as the effect of cluster size on antiferromagnetic properties. More precise calculations of the O^{2-} state will be necessary for a more accurate representation of the antiferromagnetic state in Cu oxides. The basis function most suitable for describing the antiferromagnetic state of transition metal oxides will probably resemble the wave function of a free electron away from the nucleus.

REFERENCES

[1] C. G. Shull, W. A. Strauser and E. O. Wollan, Phys. Rev., 83, 333 (1951).
[2] J. Hubbard, Proc. Roy. Soc., A276, 238 (1963).
[3] A. Svane and O. Gunnarsson, Phys. Rev. Lett., 65, 1148 (1990).
[4] V. I. Anisimov, J. Zaanen and O. K. Andersen, Phys. Rev. B, 44, 943 (1991).
[5] M. Arai and T. Fujiwara, Phys. Rev. B, 51, 1477 (1995).
[6] D. E. Ramaker, L. Kumar and F. E. Harris, Phys. Rev. Lett., 34, 812 (1975).
[7] C. F. Richardson and N. W. Ashcroft, Phys. Rev. Lett., 78, 118 (1997).

New Pseudo-Binary Titanium Silicide Systems for Lowering Phase Transformation Temperature

K.Takai, M.Seike, K.Tanaka and Y.Hayafuji
School of Science, Kwansei Gakuin University
2-1 Gakuen, Sanda, Hyogo 669-1337, Japan
(e-mail: masa_seike@hotmail.com)

(Received January 11, 2002; in final form April 22, 2002)

Abstract

Ultra-large scale integration(ULSI) applications, where the critical dimensions of transistors are less than 0.15 μm, inevitably require annealing $TiSi_2$, serving as electrode material, at temperatures slightly higher than 900℃ for transformation from the metastable high-resistivity C49 $TiSi_2$ phase to the stable low-resistivity C54 $TiSi_2$ phase.

In the interest of avoiding agglomeration of $TiSi_2$ and thermal damage to transistors, annealing temperature is desirably kept below about 850℃, which is the phase transformation temperature of blanket $TiSi_2$. In the present study, we investigated ternary titanium silicide and pseudo-binary titanium disilicide systems for lowering C49 $TiSi_2$ to C54 $TiSi_2$ the phase transformation temperature. We drew new crystal structure maps using two electronic parameters, total bond order <Bo> and averaged d-orbital energy <Md> of metals, which were calculated by the Discrete Variational X α Molecular-Orbital cluster method. On the basis of these maps and a critical review of literature on reported experimental results in relation to the phase transformation temperature of ternary titanium silicide and pseudo-binary titanium disilicide, we predicted candidates for new pseudo-binary titanium disilicides with third elements added to binary $TiSi_2$ in order to enhance the phase transformation from C49 $TiSi_2$ to the C54 $TiSi_2$.

ADVANCES IN QUANTUM CHEMISTRY, VOLUME 42

0065-3276/03 $35.00

CONTENTS

1. INTRODUCTION

Owing to its low resistivity and high productivity, aluminum (Al), has been used as an electrode material for gates, contacts, and interconnections, since the middle 1960's, when the first metal-oxide-semiconductor-field-effect-transistors (MOSFETs) were fabricated. In the 1970's, gate electrodes were first made from doped poly-Si with $MoSi_2$ or WSi_2 thin film rather than from Al, by virtue of these compounds having good thermal stability and high resistance to oxygen and chemicals. In ULSI technology, where the critical dimensions of transistors are less than 0.25 μm, instead of $MoSi_2$ or WSi_2 which have a resistivity of 80-150 $\mu\Omega$-cm, $TiSi_2$, having a resistivity of only 15-20 $\mu\Omega$-cm, has been widely used, mainly in gate electrodes and contacts for sources and drains, by virtue of its low resistivity and high adhesion to an Si substrate with a small contact areas [1-3]. $TiSi_2$ can exist in two forms: a metastable C49 base-centered orthorhombic phase having a high resistivity of 60-70 $\mu\Omega$-cm and a stable C54 face-centered orthorhombic phase having a low resistivity of 15-20 $\mu\Omega$-cm [4,5]. Currently, a two-step rapid thermal annealing (RTA) process is widely applied for $TiSi_2$ formation through the silicidation of Ti on poly-Si gates and Si substrates. The C49 phase is the crystalline silicide formed first during a first low-temperature (550-700℃) RTA of blanket Ti films deposited on poly-Si gates and Si substrates. After chemical etching of the unreacted Ti for forming a self-aligned silicide (salicide), the C49 phase transforms to the C54 phase during a second high temperature (750-850℃) RTA [1]. The C54 $TiSi_2$ phase is clearly the target phase for ULSI applications requiring low resistivity electrodes and interconnects.

However, RTA below 850℃ very often involves incomplete phase transformation of a patterned C49 $TiSi_2$ with feature sizes below 0.15 μm [6]. The untransformed C49 phase is the cause of an increase in resistivity in sub-quarter-micron features. Thus, inevitably the patterned C49 $TiSi_2$ must be annealed at high temperature above 900℃ in order to transform the C49 $TiSi_2$ phase to the C54 $TiSi_2$ phase. The problem is RTA of the patterned C49 $TiSi_2$ above 900℃ leads to morphological instability such as agglomeration of $TiSi_2$ [7]. The C49-C54 phase transformation temperature is desirably lowered as much as possible in order to avoid silicide film agglomeration and dopant redistribution. Several attempts have been made to reduce the C49-C54 phase transformation temperature. Among these, addition of a third element to binary $TiSi_2$ has been shown to enhance the formation of C54 $TiSi_2$ and to lower the C49-C54 phase transformation temperature [8,9].

The object of this study is to build new crystal structure maps for the binary disilicide system, MSi_2, and the pseudo-binary titanium disilicide system, $M_xTi_{1-x}Si_2$, and then to examine new $M_xTi_{1-x}Si_2$ systems for lowering the C49 $TiSi_2$ to the C54 $TiSi_2$ phase transformation temperature. The basic concept underlying the present study is that the crystal structure of $TiSi_2$ remains unchanged even when the addition of a small amount of the third element is added to binary $TiSi_2$. As suggested by the Hume-Rothery rule, the metal M constituting $M_xTi_{1-x}Si_2$ occupies the Ti site to form a structure identical with that of the original $TiSi_2$. Another key concept underlying the present study is that new crystal structure maps for MSi_2 and $M_xTi_{1-x}Si_2$ can be drawn by use of two electronic parameters, total bond order <Bo> and averaged d-orbital energy <Md> of metals. These two parameters, <Bo> and <Md>, characterize the electronic states of the MSi_2 and $M_xTi_{1-x}Si_2$ systems, and can be calculated by utilizing the ab-initio Discrete Variational (DV)-X α Molecular-Orbital (MO) cluster method [10]. <Bo> is a measure of the covalent bond strength between atoms, and <Md> is closely related to the electronegativity and atomic radius of an element; therefore, these two parameters are very often used to classify crystal structure of a size-controlling alloy. Detailed explanations of numerical derivations for these two parameters and physical meanings of them are provided in other literature [11]. On the basis of the two concepts described above, we predicted new

pseudo-binary titanium silicides, $M_xTi_{1-x}Si_2$, having phase transformation temperatures lower than that of $TiSi_2$.

2. COMPUTATIONAL PROCEDURE

Two electronic parameters, <Bo> and <Md>, used to build crystal structure maps were derived from wave eigenfunctions and energy eigenvalues of the MSi_2 and $M_xTi_{1-x}Si_2$ systems. <Bo> is an index of the covalent bond strength between atoms, and <Md> is an index of the ionic interaction between atoms through interatomic charge transfer. The wave eigenfunctions and energy eigenvalues were obtained by real space electronic state calculations, which were carried out by use of a program code SCAT of the DV-X α MO cluster method with the Hartree-Fock-Slater approximation.

In the method, the exchange-correlation term Vxc in the one-electron Hamiltonian was expressed in terms of the statistical local potential (1),

$$Vxc(\mathbf{r}) = -3\,\alpha\,[(3/8\,\pi)\,\rho\,(\mathbf{r})]^{1/3} \qquad (1)$$

where $\rho\,(\mathbf{r})$ is the local electron density at $\mathbf{r}$, and α is the scaling parameter in the DV- X α MO method and throughout the present work is set to α=0.7. A random sampling method was used for calculating the matrix elements of the Hamiltonian and the overlap integrals. The basis functions for the MO calculations consisted of the atomic orbital wave eigenfunctions obtained in numerical form, including 1s-np (= 1s, 2s, 2p, ..., (n-1)s, (n-1)p, (n-1)d, ns, np) for transition metals and 1s-nd (= 1s, 2s, 2p, ..., ns, np, nd) for non-transition metals, where n is the principal quantum number of the valence shells.

Two kinds of cluster models were used in the electronic state calculations; these models are based on an extended C54 $TiSi_2$ orthorhombic structure having fifty-five atoms and constant lattice parameters a = 0.8236 nm, b = 0.4773 nm, and c = 0.8523 nm. Figure 1 shows the cluster models used for the MSi_2 and $M_xTi_{1-x}Si_2$ systems. For MSi_2 systems, the cluster model $M_{21}Si_{34}$, shown in Fig. 1(a), was used. In this model, all the Ti sites of the $TiSi_2$ structure are replaced by

a transition metal M of row 4 to row 6 of the periodic table other than the lanthanoid elements. For $M_xTi_{1-x}Si_2$ systems, the cluster model $MTi_{20}Si_{34}$, shown in Fig. 1(b), was used. In this model, only the central Ti atom of the model $M_{21}Si_{34}$ is replaced by a transition metal M. Electronic state calculations were carried out under the symmetry of D_2.

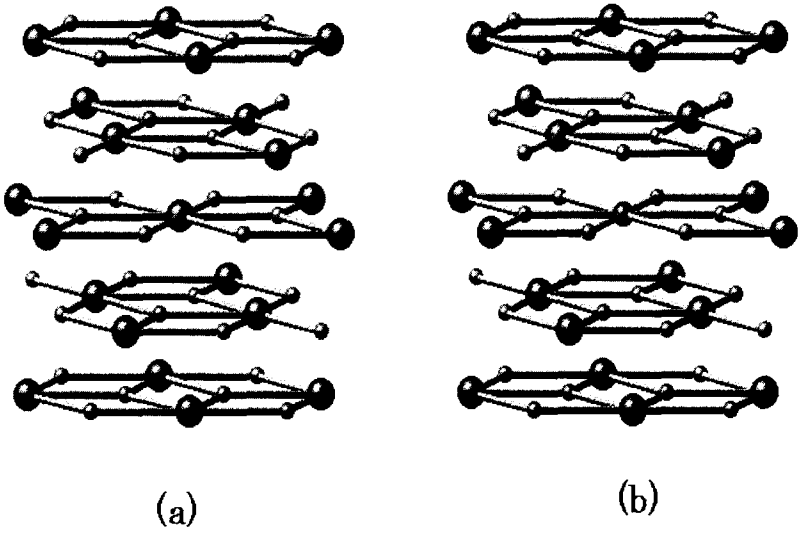

Fig. 1. Cluster models used for electronic state calculations: (a) $M_{21}Si_{34}$ for MSi_2 binary silicide systems, and (b) $MTi_{20}Si_{34}$ for $M_xTi_{1-x}Si_2$ pseudo-binary titanium silicide systems.

From wave eigenfunctions and energy eigenvalues obtained by the electronic state calculations, <Bo> and <Md> were derived in order to build crystal structure maps. <Bo> is defined as the integral of the overlap population, Bo, of electrons between atoms up to the Fermi energy. Thus, we calculated the overlap population between the transition metal M and the neighboring Si atoms in the cluster model $M_{21}Si_{34}$ for the MSi_2 systems, and the overlap population among the transition metals M and Ti and the neighboring Si atoms in the cluster model $MTi_{20}Si_{34}$ for the $M_xTi_{1-x}Si_2$ systems. To get an accurate derivation of <Bo> by means of

avoiding the effect of the atoms on the cluster surface, we integrated the overlap population between atoms for only the atoms inside the cluster, as shown in Fig. 2.

<Md> is defined as the weighted average of the d-orbital energies, Md, of metals. As such, we selected the molecular orbitals which contain the d-orbital of metals and calculated <Md> by using of a weighting factor of the (n-1)d component of transition metals in each molecular orbital, where n is the principal quantum number of the valence shells. In order to eliminate the surface effect, all results of <Md> are taken from only the five transition metal atoms inside the cluster, as shown in Fig. 2.

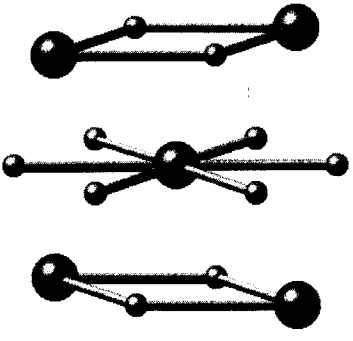

Fig. 2. Atomic configuration used for <Bo> and <Md> calculations.

3. RESULTS AND DISCUSSION

A. Crystal structure maps for metal silicides and pseudo-binary titanium disilicides

As a first step, in Fig.3 we show the components (hereafter, referred to as

the total orbital overlap population, TOOP) of the total bond order, <Bo>, which is the whole sum of TOOP. TOOP is defined as the sum of the orbital overlap population, OOP, calculated by the overlap integration between each of the Ti 1s-4p orbitals and each of the Si 1s-4s orbitals on all of the atomic combinations of Ti and Si atoms inside the cluster, but not on the cluster surface. For accuracy, Si 4s orbitals are added to the 1s-nd basis sets. As can be seen in Fig.3, the main components of <Bo> are the TOOP's between Ti 3d and Si 3s, 3p, or 3d; and those between Ti 4p and Si 3s, 3p, or 3d; and those between Ti 4s and Si 3p. The TOOP's are listed in detail in Table 1.

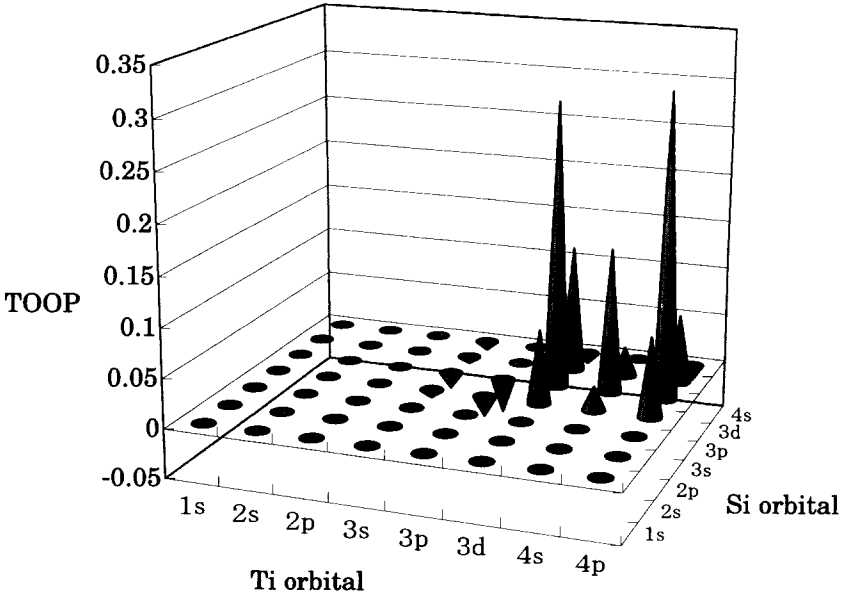

Fig. 3. Total orbital overlap population, TOOP, defined as the sum of the overlap integration of all combinations of Ti and Si orbitals.

Table 1. TOOP values used in Fig. 3

		Ti							
		1s	2s	2p	3s	3p	3d	4s	4p
Si	1s	0	0	0	0	0	0	0	0
	2s	0	0	0	0	0	-0.0011	-0.0002	-0.0009
	2p	0	0	0	0	0	-0.0011	-0.0004	-0.0006
	3s	0	0	0	-0.0078	-0.0198	0.0742	0.0241	0.0808
	3p	0	-0.0002	0	-0.0157	-0.0337	0.2873	0.1426	0.2993
	3d	0	-0.0002	0	-0.0068	0	0.1311	0.0303	0.0736
	4s	0	-0.0001	0	-0.0089	-0.0001	-0.0058	0.0016	-0.0071

For confirmation of the validity of the cluster size used in this paper, Fig. 4 and Table 2 show the OOP's between the 3d, 4s, and 4p orbitals of the central Ti atom and the 3s, 3p, and 3d orbitals of the nth nearest neighbor Si atoms. In Fig. 4, the n on the horizontal axis corresponds to the Si atom of the nth nearest neighbor. Fig. 4 shows that OOP tends to decrease with increasing distance between Ti and Si atoms. However, in a noteworthy exception, OOP between the central Ti atom and the 2nd nearest neighbor Si atom is smaller than that between the central Ti atom and the 3rd nearest neighbor Si atom. The OOP between the central Ti atom and any of the Si atoms beyond the 3rd nearest neighbor is less than one-tenth that between the central Ti atom and any of the Si atoms closer than the 4th nearest neighbor. Therefore, the interactions between the central Ti atom and the Si atoms beyond the 3rd nearest neighbor are negligible. Calculations have been carried out until the 9th nearest neighbor Si atom of the central Ti atom; therefore, the cluster size employed is valid for the present study.

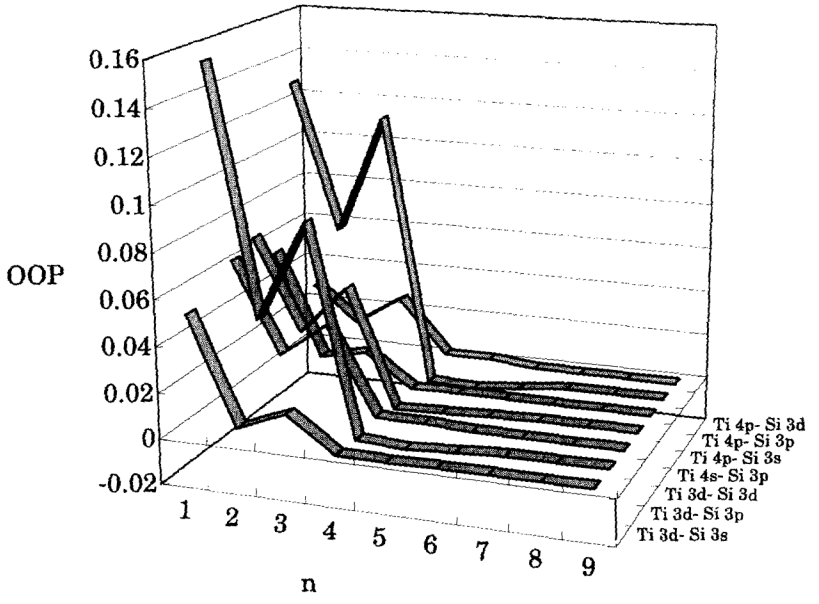

Fig. 4. OOP between the central Ti atom and the nth nearest neighbor Si atoms.

Table 2. OOP values between the central Ti atom and the nth nearest neighbor Si atoms, used in Fig. 4.

		Ti 3d - Si 3s	Ti 3d - Si 3p	Ti 3d - Si 3d	Ti 4s - Si 3p	Ti 4p - Si 3s	Ti 4p - Si 3p	Ti 4p - Si 3d
n	1	0.0531	0.1552	0.0642	0.0687	0.0559	0.1302	0.0292
	2	0.0064	0.0467	0.0244	0.0283	0.01	0.0635	0.0134
	3	0.0151	0.0904	0.0399	0.05	0.0144	0.1167	0.0265
	4	-0.0001	-0.0013	0.0013	-0.0021	-0.0001	-0.004	0.0021
	5	-0.0003	-0.0025	0.0012	-0.0016	0.0003	-0.0047	0.0022
	6	0	-0.0012	0.0001	-0.0007	0.0003	-0.0024	0.0002
	7	0	0	0	0	0	0	0
	8	0	0	0	0	0	0	0
	9	0	0	0	0	0	0	0

Next, in Fig. 5(a) we show one of the most important results of <Bo> and <Md> calculations for transition metal disilicides. The vertical axis of Fig. 5(a) corresponds to <Bo>, previously defined as total bond order, and the horizontal

axis corresponds to <Md>, previously defined as averaged d-orbital energy level. The solid curves and the dashed lines are provided as guides. The solid curves link data for disilicides with metal elements in the same row of the periodic table, and the dashed lines link elements in the same column of the periodic table. Three solid curves, corresponding to row 4 to row 6 of the period table, show similar trends in variation of <Bo> with <Md>; i.e., the three curves have similar shapes. Each of the three curves has a peak where <Md> is 0 to 5 eV, corresponding to the elements of columns VA to VIIA of the periodic table. The values of <Md> monotonously decrease with increasing atomic number of elements of the same row. For the elements Cr, Mo, and W, of column VIA, the value of <Bo> reaches a maximum and then drops rapidly with increasing atomic number. This behavior of <Bo> showing a maximum appears to be an important phenomenon in relation to phase transformation of binary metal disilicides, MSi_2. Figure 5(b) shows a crystal structure map for disilicides, MSi_2, which is drawn by use of the same data as used for Fig. 5(a). Disilicides, MSi_2, having the same crystal structure in a stable phase are grouped together by closed curves. We can see a meaningful separation of crystal structures. For example, both the C40 region and the C49 region are close to the C54 region of $TiSi_2$. According to a paper published in 2000 [12], $TiSi_2$ can exist not only in the stable C54 phase and in the metastable C49 phase, but also in the metastable C40 phase. Also, the C11b region for $MoSi_2$ is close to the C40 region, which appears in a metastable phase of $MoSi_2$. Indeed, the C54, C40, and C11b structures share the same atomic arrangement and similar geometrical dimensions in their stacking planes, but have different stacking sequences [13]. Disilicides that are not grouped in Fig. 5(b) have not been found in a stable phase in contact with Si at any particular temperature range from 600°C up to 1000°C. For convenience, Table 3 shows the resistivities and structural information of transition metal disilicides.

Figure 6 shows a diagram of <Bo> vs. <Md> for pseudo-binary titanium disilicides, $M_xTi_{1-x}Si_2$. This diagram is drawn in a manner similar to that for MSi_2 in Fig. 5(a), but with different scales for the axes. The considerable difference in scale between the diagrams is caused by a minute contribution of the small amount of the element, M, in the cluster model $MTi_{20}Si_{34}$ for pseudo-binary titanium disilicides, $M_xTi_{1-x}Si_2$. However, the solid curves and the dashed lines on

this diagram strongly resemble those shown in Fig. 5(a). Such a resemblance is thought to derive from an increase or decrease in <Bo> and <Md>, which are directly proportional to the amount of the element, M.

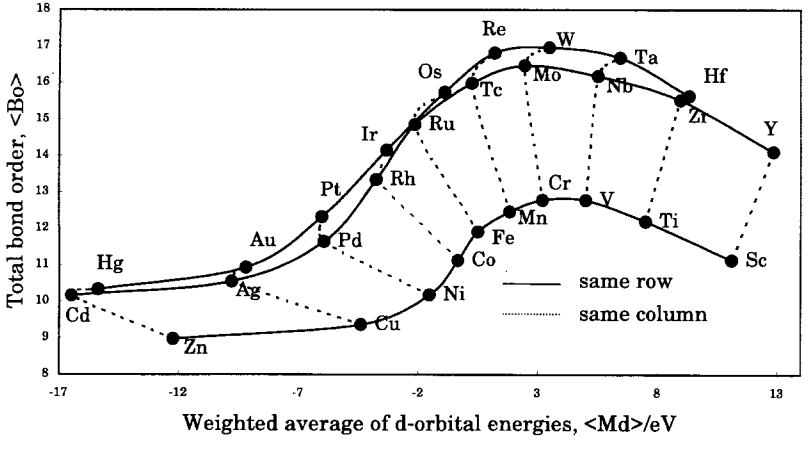

(a)

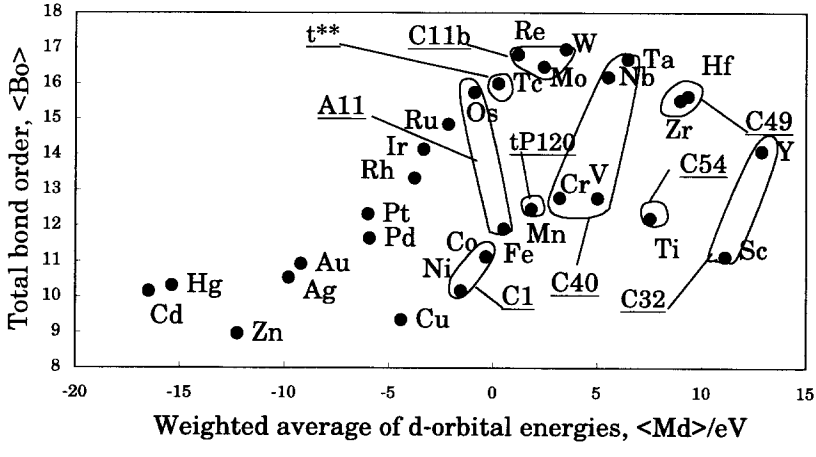

(b)

Fig. 5. Diagram of <Bo> vs. <Md> for transition metal disilicides, MSi_2; (a) variation of <Bo> vs. <Md> within rows and columns of the periodic table, and (b) crystal structure map for MSi_2.

Table 3. A relevant portion of the periodic table listing resistivity ($\mu\ \Omega$-cm) at room temperature and crystal structure of transition metal disilicides, MSi_2.

Sc 21	Ti 22	V 23	Cr 24	Mn 25	Fe(α) 26
	15-20	34-60	6000-9000		
hP3	oF24	hP9	hP9	tP120	oC48
P6/mmm	Fddd	$P6_222$	$P6_222$	P(-4)n2	Cmca
C32	C54	C40	C40		A11
Y 39	**Zr 40**	**Nb 41**	**Mo 42**	**Tc 43**	**Ru 44**
50	80-90	22-40	13-17		
hP3	oC12	hP9	tI6,hP9	t**	oP40
P6/mmm	Cmcm	$P6_422$	I4/mmm, $C6_222$		Pnca,Pbcn
C32	C49	C40	C11b,C40		
LA	**Hf 72**	**Ta 73**	**W 74**	**Re 75**	**Os 76**
	70	20-40	12-13	4000-18000	
	oC12	hP9	tI6	tI6	oC48
	Cmcm	P6222	I4/mmm	I4/mmm	Cmca
	C49	C40	C11b	C11b	A11

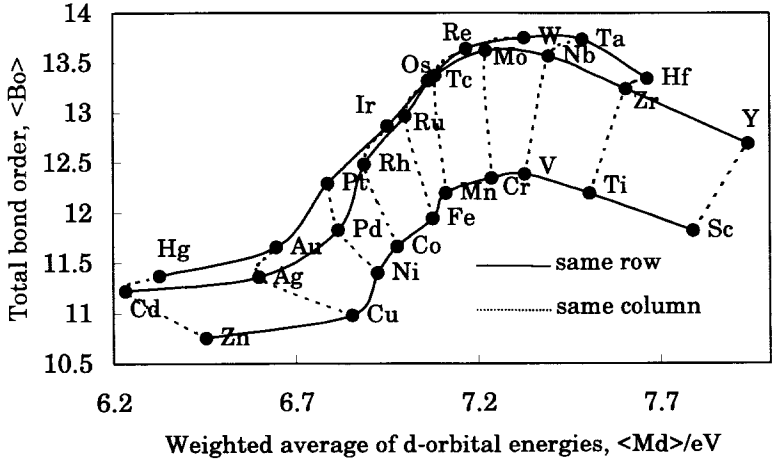

Fig. 6. Diagram of <Bo> vs. <Md> for pseudo-binary titanium disilicides, $M_xTi_{1-x}Si_2$, showing variation along rows and columns of the periodic table.

For careful comparison of <Bo> vs. <Md> between binary metal disilicides and pseudo-binary titanium disilicides, in Fig. 7 <Bo> vs. <Md> is plotted for both binary and pseudo-binary disilicides. As mentioned previously, in order to minimize the surface effect, <Md> and <Bo> have been calculated in consideration of major contributions of atoms until the 4th nearest neighbor around the center of the clusters. This manner of calculation is disadvantageous, in that it does not accurately reflect the atomic concentration of the third element on the contribution of the central atom to <Bo> and <Md>. Thus, the values of <Bo> and <Md> only for pseudo-binary titanium disilicides have been modified by use of adjustment parameters that vary with bonding number of each atom. The data for pseudo-binary titanium disilicides in Fig. 7 are heavily concentrated in a small area around the datum point of $TiSi_2$, reflecting the contribution of a small atomic concentration of the third element in the cluster model. Note that in Fig. 7 almost all the data on pseudo-binary titanium disilicides, $M_xTi_{1-x}Si_2$, are located on corresponding vectors originating from the datum point of $TiSi_2$ and passing through the respective datum points of binary metal silicides, MSi_2.

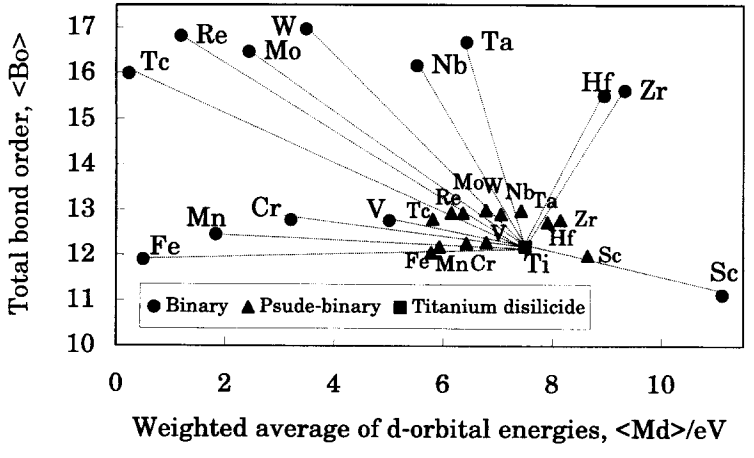

Fig. 7. Diagram of <Bo> vs. <Md> for binary and pseudo-binary disilicides. Solid circles represent data on binary metal disilicides, MTi_2, and solid triangles on pseudo-binary titanium disilicides, $M_xTi_{1-x}Si_2$. The solid square represents datum on $TiSi_2$.

Figure 8 shows a new structure map for binary metal disilicides, MSi_2, and pseudo-binary titanium disilicides, $M_xTi_{1-x}Si_2$. The new map has a C54 region wider than that shown in Fig. 5(b). In the map, the C54 region is marked by a solid closed curve, on the basis of experimental results concerning C54 phase formation temperature of pseudo-binary titanium disilicides, listed in Table 4 [14-19]. Table 4 shows substantial deviation of phase formation temperature of C54 $TiSi_2$ with the addition of a transition metal in relation to the case where pure C54 $TiSi_2$ phase is transformed from pure C49 $TiSi_2$ phase. The column "Atomic %" of Table 4 shows the desirable quantity of transition metal to be added. Under these conditions, the transition metal elements Mo, W, Nb, Ta, and Zr remain in the C54 phase when added to $TiSi_2$. Among these additives, only Zr stabilizes the C49 phase to increase transformation temperature.

The elements Re, Cr, V, and Hf, enclosed by a dotted line, are expected to remain in a C54 phase, because of their close proximity to the C54 region in the map. The element Sc, forming $ScSi_2$ of the C32 structure, retards the C49 $TiSi_2$ phase transformation [19]. The element Y, forming YSi_2 of the C32 structure, is thought to have a similar effect, retarding transformation.

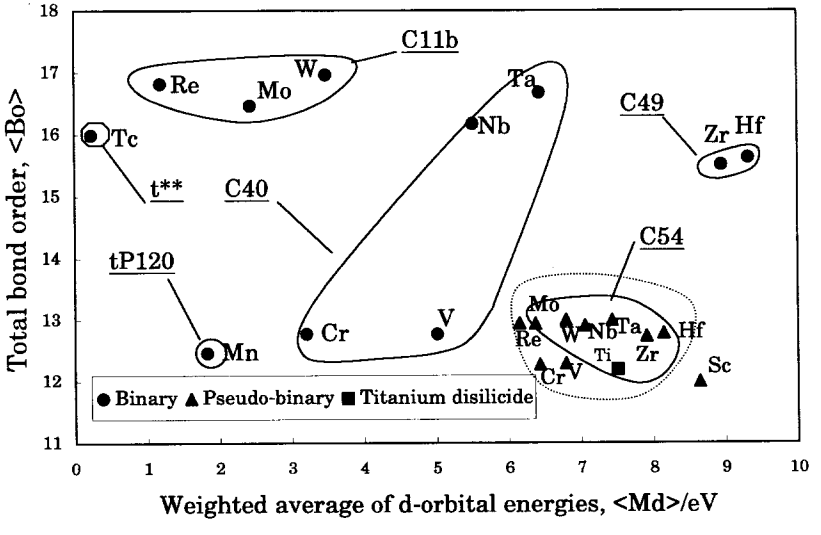

Fig. 8. Crystal structure map for binary metal disilicides, MSi_2, and pseudo-binary titanium disilicides, $M_xTi_{1-x}Si_2$.

Table 4. Deviation, in ℃, of C54 $M_xTi_{1-x}Si_2$ phase formation temperature from C49 $TiSi_2$ to C54 $TiSi_2$ phase formation temperature. Arrows pointing upward and downward represent increases and decreases of phase transformation temperatures, respectively.

Doped Element	Deviation of temperature	Atomic %
Mo	↓ 100	5
W	↓ 100	5
Nb	↓ 100	5
Ta	↓ 100	5
Zr	↑ 200	3

B. Ternary silicide systems for semiconductor industry

In this section, we explain that pseudo-binary titanium disilicide systems, $M_xTi_{1-x}Si_2$, could be solely responsible for the systems which lower the C49 $TiSi_2$ to C54 $TiSi_2$ phase transformation temperature.

A number of papers dealing with the thermal evolution of metal-metal reaction on Si can be found in the literature. In ternary systems for metal silicides, knowledge of important mechanisms such as nucleation of new phases, phase transformation, compound formation, solid solubility, diffusion processes, or moving species has been still growing. Experimental observations have been rigorously correlated with solid solubilities, electron affinities and atomic radii to derive a quantitative model describing crystallographic structures resulting from thin film reaction in ternary metal silicide systems for the current stage of semiconductor industry.

The evolution of metal M-Ti reaction on Si can be distinguished into three basic systems: ternary compounds, phase segregation without ternary compounds, and solid solutions.

In the first system, ternary silicide compounds, $Ti_xM_ySi_z$, the metal elements of a compound forming the system have greater affinity for each other than in other systems. Through electron transfer among the elements owing to their affinity, the system loses a good portion of free electrons, resulting in less-metallic properties. Resistivity of the compounds becomes higher than in two binary systems. The crystal structures of the compounds also different greatly from that of C54 $TiSi_2$. Ternary silicide compound systems are divided into three categories, according to Si concentration X(Si) [20-22]; specifically, (a) 0 % < X(Si) $\leq$ 30 at %, (b) 30 at % < X(Si) $\leq$ 50 at %, and (c) 50 at % $\leq$ X(Si). For case (a), 0 % < X(Si) $\leq$ 30 at %, one of the classes consists of the Laves phases, characterized by the formula $Ti(M_{1-x}Si_x)_2$. Another of the classes consists of the ordered phases of the formula $Ti_6M_{16}Si_7$, called G phases, with a Th_6Mn_{23} type structure, which has been reported for experiments with Co and Ni, but not for Fe. For compounds with intermediate Si concentrations of 30 at % < X(Si) $\leq$ 50 at %, two main phases are defined, as follows: V phase, $Ti_4M_4Si_7$, including $Ti_4M_4Si_8$, and E phase, TiMSi. Examples of compounds forming these phases are $Ti_4Fe_4Si_7$, $Ti_4Co_4Si_7$, $Ti_4Ni_4Si_7$, and $Ti_4Ni_4Si_8$ for V phase, and TiFeSi, TiCoSi, TiNiSi, TiCuSi, TiPtSi, and TiPdSi for E phase. For the last case, 50 at % $\leq$ X(Si), examples include $Ti_{0.75}Co_{0.25}Si_2$ and $Ti_7Al_5Si_{12}$. Mn has also been reported to form ternary compounds with Ti and Si. As mentioned above, the elements Mn, Fe, Co, Ni, and Cu of row 4 of the periodic table and the elements Ni, Pd, and Pt of column VIII can form ternary silicide compounds. For the elements of Tc, Ru, Rh, Ag, and Cd of row 5 and Os, Ir, Au, and Hg of row 6, we have no information on whether or not these transition metals form ternary silicide compounds. Three important parameters are proposed for evaluating the occurrence of a ternary compound: difference between the Zunger pseudo-potential radii sum and metallic radii sum, Δr; difference between the number of valence electrons, ΔVE; and the sum of the ratios of the melting temperatures, ΔTm [23]. By use of these parameters, compound formation has been shown to occur far from the three coordinate axes, Δr, ΔVE, and ΔTm, of the stability diagram. Extending this

idea, we can expect that the elements Tc, Ru, Rh, Ag, and Cd of row 5 and Os, Ir, Au, and Hg of row 6 can form ternary silicide compounds with Ti. Owing to higher resistivities and crystal structures of ternary titanium disilicide compounds that are considerably different from with that of $TiSi_2$, the elements forming ternary titanium disilicide compounds are considered inapplicable to searching for third elements for lowering the C49 $TiSi_2$ to C54 $TiSi_2$ phase transformation temperature.

In the second system, phase segregation without ternary compounds, phase segregation occurs when one of the constituents of the ternary alloy is released because of low solubility of the two silicides or low solubility of one metal in the growing layer. For ternary systems of silicides, phase segregation forms disilicide mixtures of M_1Si_2+M_2Si_2 [21,22]. Typical examples of phase segregation in ternary systems of titanium silicides are $TiSi_2$+Pd_2Si and $GdSi_2$+$TiSi_2$. One of the peculiar systems in this group is phase separation systems exhibiting distinct layers of M_1Si_2/M_2Si_2, where rejection of the refractory metal disilicide M_1Si_2 to the top of the product has been observed for various near-noble and refractory metal couples. For binary silicide separation, only one reference in the literature mentions that the phenomenon can occur during the annealing of Co-Ti-Si thin film to attain a final structure of $TiSi_2/CoSi_2$ [24]. Due to their formation of phases different from $TiSi_2$, the elements exhibiting phase segregation are also eliminated as candidates for third elements for lowering the C49 to C54 phase transformation temperature of $TiSi_2$.

For the third system, solid solutions, when a ternary silicide system is annealed at relatively high temperature where the species of diffusion; namely, the constituents of the alloy, can diffuse quickly, and the two silicides are isomorphous, the system can evolve into a solid solution [21,22]. We must, however, bear in mind that the isomorphism of two silicides does not imply complete solid solubility. Solubility of a third element added to a binary compound is influenced by the similarity between a solute element and the elements of the solvent compound. Three main parameters for determining the similarity of a solute element are the size of the substituting atom, its chemical potential or electron affinity, and the valency or lattice structure of the solvent compound. The limitation on solid solubility derives from the transfer of electron

needed to equilibrate the potentials in the binary compound causing an increase in the energy of the electrons in the compound as compared with the case of the solid phases of pure components. Solid solution systems for ternary titanium disilicides are categorized into two cases: complete solid solution, and pseudo-binary solid solution. Complete solid solution is represented by MSi_2+$TiSi_2$, which is slightly different from the formula for phase segregation, MSi_2+$TiSi_2$. Complete solid solution is not limited to disilicides, but is also applicable to monosilicides. To the best of our knowledge, however, the literature contains no reference describing complete solid solution of ternary titanium disilicide. Ternary disilicide systems without Ti, such as the V-Nb-Si, V-Ta-Si, and V-Cr-Si systems, show complete solid solubility [22]. Pseudo-binary solid solution with titanium disilicides is also not common, and is called continuous solid solution, represented by $M_xTi_{1-x}Si_2$, where the metal M and Ti statistically occupy the Ti site with a structure identical with that of the original $TiSi_2$. As indicated by the Hume-Rothery rule, their lattice parameters have to be within 15%. Several experiments have been reported for pseudo-binary solid solution for disilicides, such as a Ti-Zr-Si system with a 5 mol% solubility limit of $ZrSi_2$ in $TiSi_2$; a Ti-V-Si system with 5 mol% solubility limit of V in Si_2; a Ti-Nb-Si system with 3 mol% solubility limit of $NbSi_2$, and a Ti-Cr-Si system with a 7 mol% solubility limit of $CrSi_2$ [22]. Pseudo-binary solid solutions have been also reported for a Ti-Ta-Si system with minute solid solubility limit of $TaSi_2$ in $TiSi_2$, and for a Ti-W-Si system with a very large solid solubility limit of WSi_2 in $TiSi_2$. The Ti-Sc-Si, Ti-Mo-Si, and Ti-Re-Si systems also exhibit pseudo-binary solid solutions, but are not well documented. No solid solution in the Ti-Y-Si or Ti-Hf-Si system has been reported. Table 5 summarizes the system classification of ternary titanium disilicide [22].

The above discussion of ternary titanium disilicide compounds and phase segregation indicates that we can exclude the elements Mn, Fe, Co, Ni, Cu, and Zn of row 4, Tc, Ru, Rh, Pd, Ag, and Cd of row 5, and Os,Ir, Pt, Au, and Hg of row 6 as candidates for a third element to be added to $TiSi_2$ for forming ternary disilicide systems which lower the C49 $TiSi_2$ to C54 $TiSi_2$ phase transformation temperature. Therefore, we will discuss the role of the elements forming pseudo-binary solid solution with titanium disilicides, such as Sc, V, and Cr of row 4, Y, Zr, Nb, and Mo of row 5, and Hf, Ta, W, and Re of row 6.

Table 5. Brief summary of system classification of ternary titanium disilicide.

Sc 21	Ti 22	V 23	Cr 24	Mn 25	Fe 26	Co 27	Ni 28	Cu 29	Zn 30
p.b		p.b	p.b	t	t	p.s	t	t	u
Y 39	Zr 40	Nb 41	Mo 42	Tc 43	Ru 44	Rh 45	Pd 46	Ag 47	Cd 48
u	p.b	p.b	p.b	t	t	t	t	t	t
LA	Hf 72	Ta 73	W 74	Re 75	Os 76	Ir 77	Pt 78	Au 79	Hg 80
	u	p.b	p.b	p.b	t	t	t	t	t

p.b: psudo-binary, t: ternary compund, p.s: phase segregation, u: unknown

C. Prediction of the systems for lowering the transformation temperature of C49 $TiSi_2$ to C54 $TiSi_2$ phase

On the basis of the new crystal structure map shown in Fig. 8 and through the above discussion, we suggest a possible explanation of the mechanism of phase transformation from C49 $TiSi_2$ to C54 $TiSi_2$, and predict which systems would lower the phase transformation temperature. Figure 9 shows a magnified view of the C54 region shown in Fig. 8, and its surroundings. In Fig. 9, only the data of elements that form pseudo-binary titanium disilicide systems are plotted; i.e., the data for Sc and Y are not plotted. Figure 9 can be used as an area map for predicting systems for lowering the C49 $TiSi_2$ to C54 $TiSi_2$ phase transformation temperature. We divide the data in Fig. 9 into four regions by means of a vertical line and a horizontal line running through the datum point of $TiSi_2$. The two upper areas; namely, Area I and Area II, are of particular interest in the present discussion, because these areas encompass the elements that form pseudo-binary

titanium disilicide systems.

Recently, pseudo-binary titanium disilicides containing small amounts of Nb, Mo, Ta, and W, all from Area I, have been reported to greatly lower the C54 formation temperature through the first-forming template C40 phase, completely bypassing the C49 phase [14]. The supposed reason why the C40 to C54 phase transformation temperature is lower than the C49 to C54 phase transformation temperature is the extraordinary similarity in atomic configuration between the C40 and C54 phases. Fig. 10 shows the atomic configurations of extended crystal structures of the C54, C40, and C49 phases, along with that of the C11b phase [13]. The C54, C40, and C11b phases have similar basal hexagonal planes, which are stacked in the sequences ABCD, ABC, and AB, respectively. Their similar stacking patterns result in the easy transformation of the C40 or C11b phase to the C54 phase [25]. In contrast, the metastable C49 $TiSi_2$ phase has a crystal structure which is quite different from that of the C54 phase. The activation energy for C40-C54 transformation is much lower than that for C49-C54 transformation, because of the structural similarity between the C40 and C54 phases. Consequently, the C40 phase enhances the growth of the C54 $TiSi_2$ phase and hinders formation of the C49 phase. The presence of Mo, Nb, Ta, or W in $TiSi_2$ induces a shift in the values of <Bo> and <Md> of pure $TiSi_2$ close to the C40 region in the map shown in Fig. 8, at high-<Bo> and low-<Md>. This shift indicates that the C40 phase is to be the first-forming phase of $TiSi_2$ when these elements are added to binary $TiSi_2$. Therefore, elements in Area I are expected to promote the C40-C54 $TiSi_2$ transformation and lower the C54 formation temperature. The presence of Zr in $TiSi_2$ has been reported to stabilize C49 $TiSi_2$ phase and to raise the C54 formation temperature [18]. This is easily understandable, from the presence of Zr shifting the values of <Bo> and <Md> of pure $TiSi_2$ close to the C49 region, at high-<Bo> and high-<Md>. This means that the first-forming C49 $Zr_xTi_{1-x}Si_2$ in Area II becomes more stable than C49 $TiSi_2$. We can also reasonably presume that the first-forming C49 $Hf_xTi_{1-x}Si_2$ is more stable than C49 $TiSi_2$ and has a transformation temperature higher than that of C49 $TiSi_2$. Through this thoughtful discussion, we can safely predict that the elements V, Cr, and Re, forming new pseudo-binary $M_xTi_{1-x}Si_2$ systems, lower the C49 to C54 $TiSi_2$ phase transformation temperature.

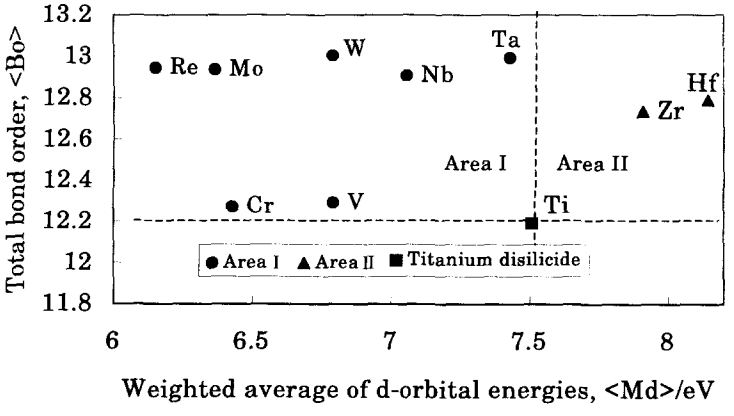

Fig. 9. Area map for prediction of the systems for lowering the temperature of the transformation of C49 $TiSi_2$ to C54 $TiSi_2$ phase.

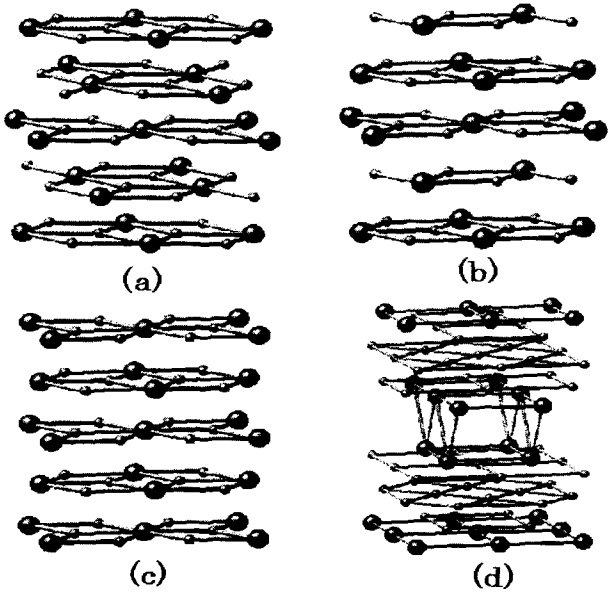

Fig. 10. Atomic configurations of (a) C54 $TiSi_2$ type structure, (b) C40 $CrSi_2$ type structure, (c) C11b $MoSi_2$ type structure, and (d) C49 $ZrSi_2$ type structure.

4. CONCLUSION

We examined ternary silicide and pseudo-binary titanium disilicide systems for lowering C49 to C54 $TiSi_2$ phase transformation temperature. We drew new crystal structure maps by use of two electronic parameters, total bond order, <Bo> and averaged d-orbital energy <Md> of metals, calculated by the Discrete Variational X α cluster method. From these maps and through thoughtful discussion about the phase transformation temperature of ternary and pseudo-binary titanium disilicides, we predicted candidates for new pseudo-binary titanium disilicides to be added as third elements to binary $TiSi_2$ in order to lower the C54 $TiSi_2$ formation temperature. From our results, we can reasonably predict that the elements V, Cr, and Re, which form new pseudo-binary $M_xTi_{1-x}Si_2$ systems, lower the C49 to C54 $TiSi_2$ phase transformation temperature.

The authors would like to thank Professor Hirohiko Adachi of Kyoto University, Professor Masahiko Morinaga of Nagoya University, and Dr. Akikazu Shibata, former general manager of Sony Corporation Research Center, for their valuable discussion and support. They also would express their thanks to Michael Lynn, Professor of Kwansei Gakuin University.

REFERENCES

[1] S. P. Murarka, J. Vac. Sci. Technol. **17**, 775 (1980).
[2] R. A. Haken, J. Vac. Sci. Technol. **B3**, 1657 (1985).
[3] K. Maex, Mater. Sci. Eng. **R11**, 53 (1993).
[4] F. Laves and H. J. Wallbaum, Z. Kristallogr. **101**, 78 (1979).
[5] R. Beyers and R. Sinclair, J. Appl. Phys. **57**, 5240 (1985).
[6] J. B.Lasky, J. S. Nakos, O. J. Cain, and P. J. Geiss, IEEE Trans.Electron Devices **ED-38**, 262 (1991).
[7] E. G. Colgan, J. P. Gambino, and Q. Z. Hong, Mater. Sci. Eng. **R16**, 43 (1996).
[8] A. Mouroux, S. L. Zhang, W. Kaplan, S. Nygren, M. Ostling, and C. S. Petersson, Appl. Phys. Lett. **69**, 975 (1996).

[9] C. Cabral, Jr., L. A. Clevenger, J. M. E. Harper, F. M. d'Heurle, R. A. Roy, K. L. Saenger, G. L. Miles, and R. W. Mann, J. Mater. Res. **12**, 304 (1997).

[10] H. Adachi, M. Tsukada, and C. Satoko, J. Phys. Soc. Japan, **45**, 874 (1978).

[11] Y. Harada, M. Morinaga, J. Saito, and Y. Takagi, J. Phys.:Condens. Mater. **9**, 8011 (1997).

[12] S. Y. Chea, Z. X. Shen, K. Li, A. K. See, and L. H. Chan, Appl. Phys. Lett. **77**, 4395 (2000).

[13] A. Kittl, M. A. Gribelyuk, and S. B. Samavedam, Appl. Phys. Lett. **73**, 900 (1998).

[14] C. Cabral, Jr., L. A. Clevenger, J. M. E. Harper, F. M. d'Heurle, R. A. Roy, K. L. Saenger, G. L. Miles, R. W. Mann, and J. S. Nakos, Appl. Phys. Lett. **71**, 3531 (1997).

[15] R. W. Mann, G. L. Miles, T. A. Knotts, D. W. Rakowski, L. A. Clevenger, J. M. E. Harper, F. M. D'Heurle, and C. Cabral,Jr. Appl. Phys. Lett. **67**, 3729 (1995).

[16] A. Mouroux, M. Roux, S. L. Zhang, F. M. d'Heurle, C, Cabral,Jr., C. Lavoie, and J. M. E. Harper, J. Appl. Phys. **86**, 2323 (1999).

[17] H. Jeon, B. Jumg, Y. D. Kim, W. Yang, and R. J. Nemanich, J. Appl. Phys. **88**, 2467 (2000).

[18] Y. Dao, A. M. Edwards, H. Ying, Y. L. Chen, D. E. Sayers, and R. J. Nemanich, Appl. Phys. Lett. **65**, 2413 (1994).

[19] O. Thomas, S. Delage and F. M. d'Heurle, in Extended Abstracts, Vol.88-1, Spring Meeting (Electrochemical Society, Pennington, NJ, 1988), p.209.

[20] H. Sprenger, J. Less-Common Met. **34**, 39 (1974).

[21] M. Setton and J. V. der Spiegel, Thin Solid Film, **156**, 351 (1988).

[22] M. Setton, in *Properties of Metal Silicides*, edited by K. Maex and M. V. Rossum (INSPEC, IMEC, Leuven, Belgium, 1995) p.129.

[23] P. Villars, J. Less-Common Met. **119**, 175 (1986).

[24] H. Yang and R. W. Bene, J. Appl. Phys. **59**, 1525 (1986).

[25] A. E. Carlsson and P. J. Meschter, J. Mater. Res. **6**, 1512 (1991).

Local Electronic Structures of Hydrogen and Phase Stability of Vanadium Hydride, V_2H

Hiroshi Yukawa*, Shigeyuki Ito, Daisuke Yamashita and Masahiko Morinaga

Department of Materials Science and Engineering, Graduate School of Engineering, Nagoya University, Furo-cho, Chikusa-ku, Nagoya 464-8603, Japan

(Received December 30, 2001; in final form March 2, 2002)

Abstract

The electronic structures of vanadium hydride, V_2H, have been calculated by the DV-Xα molecular orbital method. From a series of calculations, it is found that the subtle lattice distortion is introduced into pure vanadium by hydrogenation and the V_2H phase is formed so as to strengthen the metal-hydrogen chemical bond while keeping the metal-metal chemical bond nearly unchanged. Also, it is shown that the stability change of the V_2H phase by alloying is understood in terms of the metal-hydrogen chemical bond and its change with alloying elements. In fact, the measured plateau pressure at low hydrogen pressures for the alloyed V_2H phase changes in a similar way as does the calculated metal-hydrogen ionic interaction.

CONTENTS

Keywords: hydrogen storage alloys, vanadium hydride, alloying effects, hydride stability

*Corresponding Author, e-mail: hiroshi@numse.nagoya-u.ac.jp

ADVANCES IN QUANTUM CHEMISTRY, VOLUME 42

0065-3276/03 $35.00

1. INTRODUCTION

Vanadium metal with bcc crystal structure is one of the promising hydrogen storage materials with a high capacity. When vanadium metal react with hydrogen, the V_2H phase (β_1 phase) is formed first. As the hydrogenation proceeds, the first order phase transition from the β_1 phase to the β_2 phase (V_2H high-temperature phase or VH) takes place. Then, the VH_2 phase (γ phase) is formed when it is fully hydrogenated [1]. As a result, as shown in Fig.1, there exist two plateaus in the PCT (Pressure-Composition-Temperature) curve for the V-H system. Here, the first plateau appears due to the reaction between the α phase (hydrogen solid solution phase) and the V_2H phase, $2V(\alpha) + 1/2\ H_2 \rightleftarrows V_2H$. The second plateau appears due to the reaction between the VH phase (β_2 phase) and the VH_2 phase, $VH + 1/2\ H_2 \rightleftarrows VH_2$.

As the V_2H phase is so stable that the first plateau pressure for this hydride formation is as low as 0.1Pa at moderate temperatures [2]. Therefore, the hydrogen desorption reaction from the V_2H phase never occurs at moderate condition, for example at room temperature. On the other hand, the VH_2 phase is not so stable that its hydrogen absorption and desorption reaction can take place at moderate temperatures and pressures. For this reason, only about a half amount of hydrogen absorbed in vanadium metal can be used in the subsequent hydrogen absorption and desorption processes [1]. This amount is, however, not enough for practical applications, so it would be desirable to increase the usable hydrogen capacity by controlling the stability of the vanadium hydrides in some way. The alloying is one of the ways to modify the hydride stability.

The alloying effects have been studied on the VH_2 phase [1,3] and shown that its stability is modified largely by the addition of a small amount of alloying elements, M. In response to such modification, the second plateau pressure changes in a systematic way following the order of elements, M, in the periodic table. For example, the plateau pressure is high for the group 8 elements such as Fe, Ru and Os [3]. In addition, the electronic structures of the γ phase are calculated and the alloying effects have been studied in view of the chemical bond between atoms [4]. On the other hand, there has been very

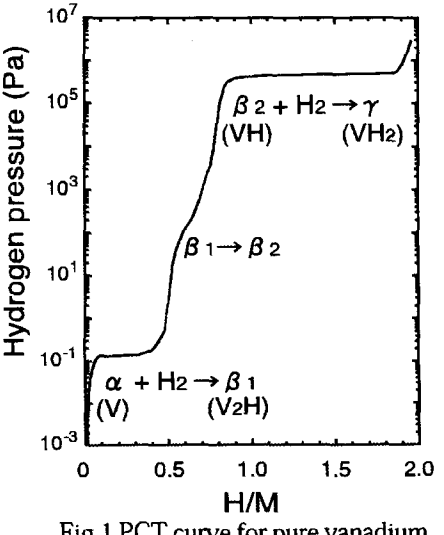

Fig.1 PCT curve for pure vanadium.

poor knowledge of the alloying effects on the hydriding properties of the β_1 phase. This is mainly due to the difficulties in measuring the PCT curves at low hydrogen pressures. Recently, we have developed a new electrochemical method for measuring the PCT curves at low hydrogen pressures [5]. Using this method, the alloying effects on the hydriding properties of vanadium at low hydrogen pressures have been investigated experimentally for the first time for binary V-M alloys, where M's are 3d transition metals. From such experiments, it is found that the first plateau pressure changes largely with alloying elements in vanadium metal. It changes monotonously following the order of elements, M, in the periodic table [5].

In this study, focusing our attention on the hydride stability, the electronic structures of the V_2H phase have been studied by the DV-Xα cluster method. The alloying effects on the electronic structures have been investigated in detail.

2. DV-Xα CLUSTER METHOD AND CLUSTER MODEL

The DV-Xα cluster method [6,7] is a molecular orbital method, assuming the Hartree-Fock-Slater (HFS) approximation. In this method, the exchange-correlation between electrons, V_{XC}, is given by Slater's Xα potential,

$$V_{XC} = -3\alpha\left[\frac{3}{8\pi}\rho(r)\right]^{1/3}, \qquad (1)$$

where $\rho(r)$ is the electron density at the position r, the parameter α is fixed at 0.7, and the self-consistent charge approximation is used in the calculation. The matrix elements of the Hamiltonian and the overlap integrals are calculated by a random sampling method. The molecular orbitals are constructed by a linear combination of numerically generated atomic orbitals (LCAO). The atomic orbitals used in the present calculation are 1s for hydrogen atom and 1s, 2s, 2p, 3s, 3p, 3d, 4s and 4p for V and other 3d transition metals.

The cluster model used in this study is shown in Fig.2. This is a $V_{40}H_{19}$ cluster model constructed on the basis of the crystal structure

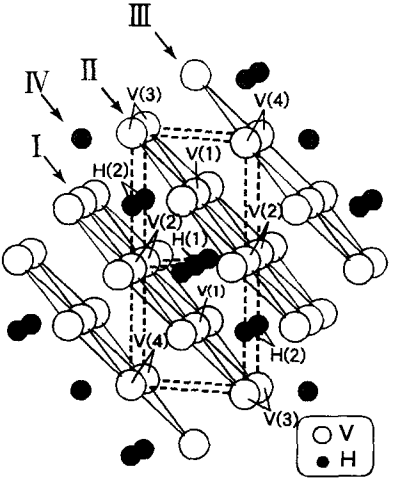

Fig.2 Cluster model used for the calculation of the V_2H phase.

of the V_2H phase [8]. For comparison, two other cluster models are also used in the calculation. One is a V_{40} cluster for pure vanadium with bcc crystal structure and the other is a hypothetical cluster, $V_{40}H_{19}$-hypo, in which hydrogen atoms are introduced into the octahedral interstitial site in pure vanadium lattice without any lattice distortion. In other words, the atomic arrangements are the same between the $V_{40}H_{19}$ and the $V_{40}H_{19}$-hypo clusters, but the difference lies at the lattice distortion between them.

In order to investigate the alloying effects on the electronic structures of V_2H phase, a series of calculations is conducted for alloyed V_2H. In this phase, the alloying elements, M, are supposed to occupy randomly the V sites because the hydride is formed from the disordered V-M alloys. In fact, according to our X-ray diffraction study, there is no evidence that new structure appears due to the ordered arrangements of V and M atoms in the alloyed V_2H. However, there is still the difficulty in the calculation involving random arrangements. For simplicity of the calculation, the alloying elements, M, are assumed to be substituted for the two V(1) atoms in the cluster shown in Fig.2. Therefore, the cluster model for alloyed V_2H phase is expressed as $V_{38}M_2H_{19}$. The lattice parameter used is the same as that of pure V_2H.

For a characterization of the electronic structure, the bond order which is a measure of the covalent bond strength between atoms is estimated following the Mulliken population analysis [9]. Also, the ionicities of each atom in the cluster are calculated in order to get information of the charge transfer between atoms. A detailed explanation of the calculation method is given elsewhere [10,11].

3 RESULTS

3.1 Change in the electronic structure of vanadium by hydrogenation

In Fig.3, the local atomic arrangement in V_2H is compared with that in pure vanadium. In V_2H, hydrogen atoms occupy the octahedral interstitial sites (Oz sites) of the bcc lattice and makes a layered structure parallel to the (011) atomic plane as shown in Fig.2. The vanadium atoms move away from the hydrogen atoms, so that the interlayer space between two (011) vanadium atomic planes (e.g., layer I and II shown

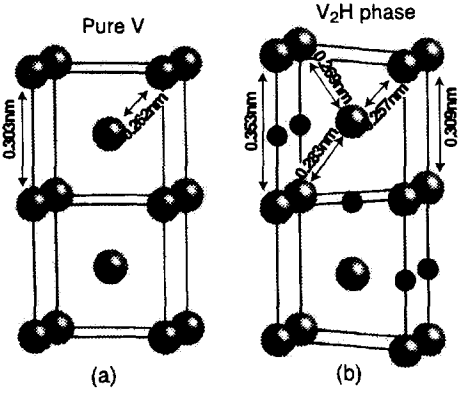

Fig.3 Comparison of the crystal structure between (a) pure vanadium and (b) V_2H phase.

in Fig.2) extends toward the [001] direction. Instead, the adjacent interlayer space between two vanadium layers (e.g., layer II and III) contracts to some extent. As a result, the bcc lattice of pure vanadium is distorted and a bct lattice is formed in V_2H [8].
In order to understand this lattice distortion by hydrogenation, the electronic structures are calculated for pure vanadium, V_2H and a hypothetical V_2H .

3.1.1 Bond order between atoms

The bond order between vanadium atoms, $Bo(V_{II}\text{-}V_{II})$, $Bo(V_{III}\text{-}V_{III})$, $Bo(V_{I}\text{-}V_{II})$ and $Bo(V_{II}\text{-}V_{III})$, are estimated from the calculation. Here, V_I, V_{II} and V_{III} are the vanadium atoms sitting on the layer I, II and III (see Fig.2), respectively. Therefore, for example, $Bo(V_{II}\text{-}V_{II})$ is the total bond order between vanadium atoms sitting on the same layers II. $Bo(V_{III}\text{-}V_{III})$ has the similar meaning. On the other hand, the $Bo(V_{I}\text{-}V_{II})$ is the bond order between two layers, I and II, where hydrogen atoms are intercalated. Also, the $Bo(V_{II}\text{-}V_{III})$ is the bond order between two layers, II and III, where hydrogen are not intercalated. In addition, the bond order between vanadium and hydrogen atoms, Bo $(V_{I}\text{-}H_{IV})$, is calculated. Here, H_{IV}'s are the hydrogen atoms in the layer IV, positioning at the first-nearest-neighbour sites from the vanadium atoms in the layer I.
The results of these bond orders are shown in Fig.4. Every bond order shown in this figure is the average value per atomic bond in the whole cluster. When hydrogen is introduced into vanadium, the bond order between V_I and H_{IV} atoms appears to be large in the $V_{40}H_{19}$-hype cluster, indicating that there exists covalent interaction operating between V_I and H_{IV} atoms. However, this bond order decreases remarkably by the introduction of the lattice distortion, as is seen in the $V_{40}H_{19}$ cluster for V_2H.

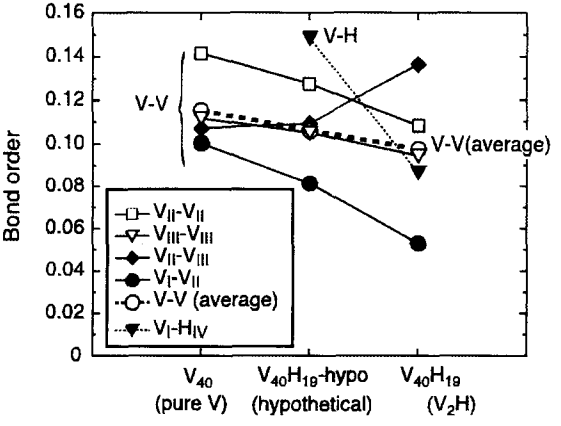

Fig.4 Changes in the bond order between atoms by the introduction of hydrogen and lattice distortion.

On the other hand, all the bond orders between vanadium atoms show large and positive values in pure vanadium, indicating that a strong covalent interaction is operating between vanadium atoms. When hydrogen is introduced, $Bo(V_{II}\text{-}V_{II})$, $Bo(V_{III}\text{-}V_{III})$ and $Bo(V_{I}\text{-}V_{II})$ all decrease. They further decrease when lattice distortion is introduced. On the other hand, the $Bo(V_{II}\text{-}V_{III})$ slightly increases by the introduction of hydrogen and largely increases by the lattice distortion. Such an increase in the bond order between V_{II} and V_{III} atoms is attributable mainly to the contraction of the interlayer distance between II and III. As a result, the average V-V bond order keeps nearly unchanged or less changed in the course of hydrogenation as is indicated by open circles in Fig.4.

3.1.2 Ionicities

The ionicity of each atom in the cluster is estimated according to the Mulliken population analysis. The results are shown in Fig.5 for the atoms in the central region of the cluster. As shown in Fig.5, the ionicities of vanadium atoms are almost neutral in pure vanadium. When hydrogen is introduced, the ionicities of vanadium atoms increase and show positive values. On the other hand, the ionicity of hydrogen atom is negative. It decreases largely from about -0.2 to about -0.4 when the lattice distortion is introduced. This makes the ionicities of vanadium atoms more positive. As a result, the ionicity difference between vanadium and hydrogen atoms increases considerably by the lattice distortion. Needless to say, the ionicity difference is a measure to show the transferred charges between atoms. Thus, it is found that the ionic interaction between vanadium and hydrogen atoms is strengthened by the lattice distortion.

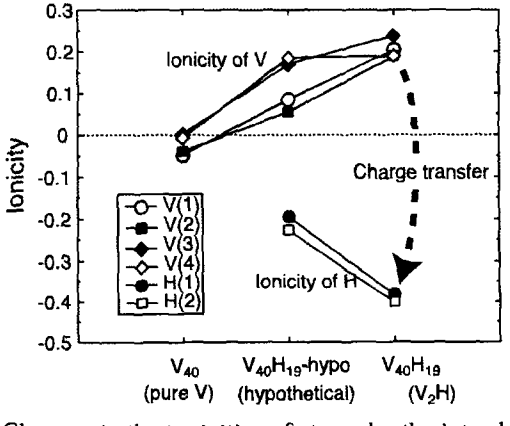

Fig.5 Changes in the ionicities of atoms by the introduction of hydrogen and lattice distortion.

3.2 Alloying effects on the electronic structure of V_2H phase

In order to examine alloying effects on the electronic structures, two central vanadium atoms in the cluster, V(1) shown in Fig.2, are replaced by various 3d transition metals, M, (M=Ti, Cr, Mn, Fe, Co, Ni, Cu). The changes in the bond order with alloying elements, M, are shown in Fig.6. Here, the Bo(V-V(M)) is the average bond order between metal atoms on the layer I, II and III. Also, the Bo(V(M) -H) is the average bond order between metal atom on the layer I and hydrogen atoms on the layer IV. As shown in Fig.6, both the Bo(V-V(M)) and the Bo(V(M) -H) decreases monotonously following the order of M in the periodic table. For example, the bond orders are large for the left side elements (e.g., Ti) but small for the right side elements (e.g., Cu). The changes in the ionicity of each atom with alloying elements are shown in Fig.7. As is evident form this figure, the ionicity of alloying element, M, changes largely. It decreases monotonously following the order of M in the periodic table. In response to this change in the ionicity of M, the ionicity of H(1) increases in a reverse way. As a result, the ionic interaction between M and H(1) atoms changes largely with M. All the other ionicities are scarcely changed by alloying.

4. DISCUSSION

4.1 Lattice distortion

Here, the lattice distortion during the hydrogenation of vanadium metal is discussed in view of the chemical bond between atoms. As shown in Figs. 4 and 5, both the covalent and the ionic interactions between metal and hydrogen atoms are operating

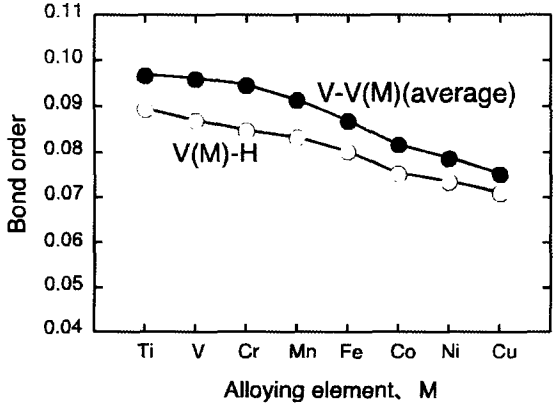

Fig.6 Changes in the bond order between atoms with alloying elements, M.

in the hypothetical cluster. However, when lattice distortion is introduced, the ionic interaction is enhanced, whereas the covalent interaction decreases largely between vanadium and hydrogen atoms. On the other hand, only the covalent interaction is operating between vanadium atoms in pure vanadium. As mentioned before, the average bond order between vanadium atoms keeps a high value even in the course of the hydrogenation, indicating that the average covalent interaction between vanadium atoms almost unchanged or less changed. From these results, it can be said that the lattice distortion takes place in the hydrogenated vanadium metal so as to enhance the ionic interaction between vanadium and hydrogen atoms while keeping the covalent interaction between vanadium atoms almost unchanged. The crystal structure of V_2H is settled in such a subtle lattice distortion.

4.2 Phase stability of V_2H phase in view of chemical bond between atoms

As mentioned before, the first plateau corresponds to the equilibrium of the α and the V_2H phases. According to the van't Hoff relation, the hydrogen pressure, P_{H2}, in this equilibrium can be written as follows,

$$\ln P_{H2} = \frac{\Delta H^\circ}{RT} - \frac{\Delta S^\circ}{R}, \qquad (2)$$

where ΔH° and ΔS° are the enthalpy change and the entropy change for the formation of the hydride, V_2H, respectively. Here, the entropy change, ΔS°, is approximately constant for most metal-hydrogen systems because it arises mainly from the entropy loss of gaseous hydrogen during the hydrogen uptake by the metal [12]. Therefore,

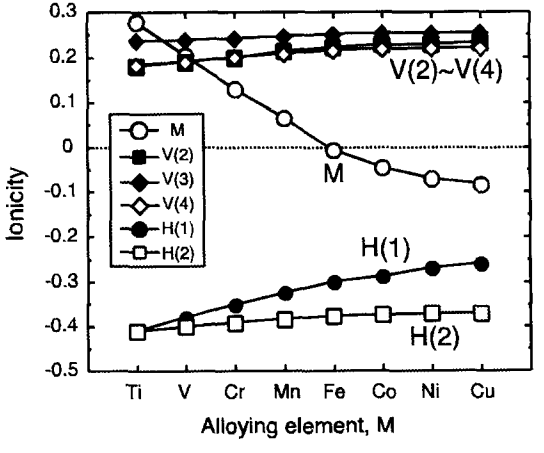

Fig.7 Changes in the ionicities of atoms in the cluster with alloying elements, M.

the heat of hydride formation, ΔH°, is proportional approximately to the logarithm of the equilibrium hydrogen pressure, P_{H2}, for a constant temperature. In other words, the change in the hydride stability correlates with the change in the plateau pressure of hydrogen.

For simplicity, instead of the heat of hydride formation, ΔH°, the alloying effects on the stability of the V_2H phase is discussed here in terms of the chemical bond between atoms. First, from the results of Figs.4 and 5, the chemical bonds between atoms expected to operate in alloyed V and alloyed V_2H phase are summarized in Fig.8. Needless to say, in pure vanadium, only the V-V bond is operating. When alloying element, M, is added into vanadium, the V-M bond appears and the metal-metal bonds are modified by the addition of M. However, such modification of the metal-metal bonds may also be expected in the alloyed V_2H phase. This is because that the metal-metal bond is little modified during the hydrogenation and keeps its original strength to some extent even in V_2H phase, as mentioned before.

On the other hand, a strong chemical bond is operating between metal and hydrogen atoms only in the V_2H phase. In this case, when alloying elements, M, is added into vanadium, the metal-hydrogen bond in V_2H is modified by alloying. Therefore, the alloying effects on the stability of the V_2H phase may be attributable mainly to the change in the M-H chemical bonds in the V_2H phase. If the metal-hydrogen interaction becomes strong, the V_2H phase probably become stable, and vice versa. It is noted here that the ionic interaction between metal and hydrogen atoms is considered to be mainly responsible for the phase stability of the V_2H phase rather than the covalent interaction. This is because that the lattice distortion takes place so as to enhance the ionic interaction, but not the covalent interaction between metal and hydrogen atoms, as shown in Figs.4 and 5.

For this reason, the difference in the ionicities between M and H(1), ΔIo, are calculated

Phase	V	V_2H
Chemical bond between atoms	Metal—Metal V — V V — M	Nearly unchanged Metal—Metal V — V V — M Metal—Hydrogen V — H M — H

Fig.8 Chemical bonds between atoms in alloyed V and alloyed V_2H phase.

and the result is shown in Fig.9. As shown in this figure, the metal-hydrogen ionic interaction is strongest in case of M=Ti, and it decreases monotonously following the order of M in the periodic table. Therefore, the stability of the V_2H phase is supposed to be highest in case of the Ti addition, and it would become unstable following the order of M in the periodic table. In fact, the change in the metal-hydrogen interactions in the alloyed V_2H phase correlates well with the changes in the measured plateau pressures of hydrogen shown in Fig.10 [5].

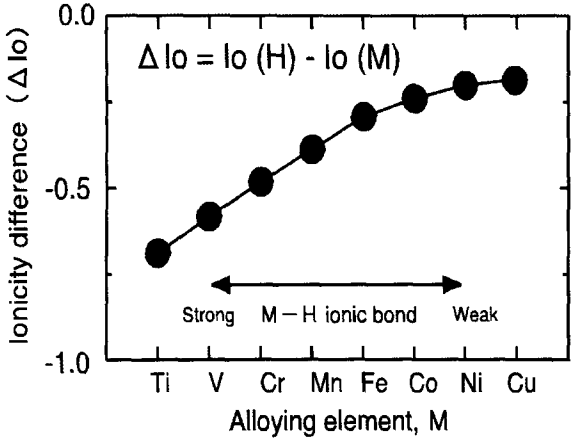

Fig.9 Change in the ionicity difference, ΔIo, with alloying elements, M.

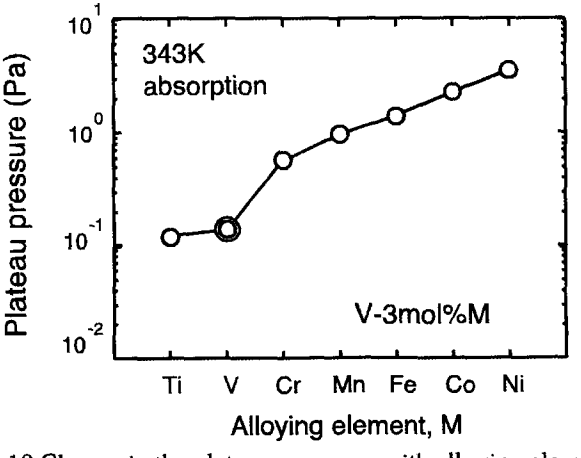

Fig.10 Change in the plateau pressures with alloying elements, M, for of V-3mol%M alloys.

5. CONCLUSION

The electronic structures of vanadium hydride, V_2H, have been calculated by the DV-Xα molecular orbital method. The physical meaning of the lattice distortion induced by hydrogenation is understood from a series of the electronic structure calculations. Also, the alloying effects on the electronic structures of the hydride, V_2H, are elucidated. Furthermore, it is shown that the stability of the V_2H phase can be understood in view of the chemical bond between atoms. In fact, the changes in the chemical bond strength between metal and hydrogen atoms correlate well with the changes in the measured plateau pressures of hydrogen.

ACKNOWLEDGMENTS

This research was supported by the Grant-in-Aid for Scientific Research from the Ministry of Education, Culture, Sports, Science and Technology of Japan, and from the Japan Society for the Promotion of Science.

REFERENCES

(1) J.J. Reilly, R.H.Wiswall, BNL Report 16546, Brookhaven National Lab. (1972).
(2) K.Fujita, Y.C.Huang, M.Tada, J. Jpn. Inst. Met. 43, 601 (1979).
(3) H.Yukawa, M.Takagi, A.Teshima and M.Morinaga, J. Alloys Comp., 330-332, 105 (2002).
(4) T.Matsumura, H.Yukawa and M.Morinaga, J. Alloys Comp., 284, 82 (1999).
(5) H.Yukawa, A.Teshima, D.Yamashita, S.Ito, S.Yamaguchi and M.Morinaga, J. Alloys Comp., in press.
(6) J.C. Slater, "Quantum Theory of Molecules and Solid vol. 4", Wiley, New York, (1974).
(7) F.W. Averill, D.E. Ellis, J. Chem. Phys., 59, 6413 (1973).
(8) Y.Noda, K.Masumoto, S.Koike, T.Suzuki and S.Sato, Acta Crystallographica B, 42, 529 (1986).
(9) R.C. Mulliken, J. Chem. Phys., 23, 1833, 1841, 2338, 2343 (1955).
(10) H. Adachi, M. Tsukada, C. Satoko, J. Phys. Soc. Jpn., 45, 874 (1978).
(11) M. Morinaga, N. Yukawa, H. Adachi, J. Phys. F, 15, 1971 (1985).
(12) Y.Fukai, "The Metal-Hydrogen System", Springer-Varlag, Berlin Heiderberg (1993).

Superconducting transition temperature of Laves phase V_2Zr compounds with alloyed magnetic elements

Wataru Takahara*, Hiroshi Maeda and Fumiyoshi Minami
Department of Manufacturing Science, Osaka University
2-1, Yamada-oka, Suita, Osaka 565-0871, Japan

(Received January 28, 2002; in final form May 28, 2002)

Abstract

The effects of alloyed 3d transition elements on the superconducting transition temperatures of C15 Laves phase compounds $(V_{1-x}M_x)_2Zr$ (M = Cr, Mn, Fe and Co) are investigated by the DV-Xα cluster method. The transition temperature T_c increases with concentration of magnetic elements and is found to correlate with the bond overlap population regardless of the presence of magnetic elements. Electron-phonon and/or magnetic interaction therefore appear not to be primary factors, and the orbital response itself may be the universal factor governing superconductivity.

CONTENTS

Keywords: Superconductivity, Laves phase, transition temperature, magnetic element, DV-Xα method, bond overlap population

*Corresponding Author: E-mail: takahara@mapse.eng.osaka-u.ac.jp

ADVANCES IN QUANTUM CHEMISTRY, VOLUME 42

0065-3276/03 $35.00

1. INTRODUCTION

It is generally thought that there are two types of typical superconductor, the conventional Bardeen-Cooper-Schrieffer (BCS) superconductor with electron-phonon paring mechanism, and superconductors in which the paring mechanism is unclear [1]. Although magnetic interaction is thought to be important, anomalous behavior has been observed in both BCS and non-BCS superconductors. For example, anomalous normal state electrical resistivity has been observed in both oxide and metallic superconductors [2, 3], iron exhibits superconductivity under high pressure [4], and UGe_2 [5] and C15 Laves phase Zn_2Zr [6] have been discovered to simultaneously act as both superconductors and normal ferromagnets. Add to this the observation of strong electron-phonon coupling in high-temperature oxide superconductors [7], and it becomes clear that the distinction between BCS and non-BCS is becoming less obvious.

In the present work, the effects of 3d transition elements on the superconducting transition temperature T_c were investigated by the DV-Xα cluster method using C15 Laves phase compounds $(V_{1-x}M_x)_2Zr$ with M = Cr, Mn, Fe and Co. It has been reported that the superconducting transition temperature increases with the addition of Cr [8, 9]. Elements with higher atomic numbers reduce T_c to M = Co in $(V_{0.9}M_{0.1})_2Zr$ [9]. In addition, T_c increases with the addition of a small amount of Fe in $(V_{0.98}Fe_{0.02})_2Zr$ despite the ferromagneticity [9]. Figures 1(a) and (b) show the variations in T_c reported by Roy [9]. In the BCS superconductor, a remarkable T_c decrease or even loss of superconductivity is expected with the addition of magnetic elements. The results in Fig. 1 indicate that the actual case is more complex for V_2Zr compounds.

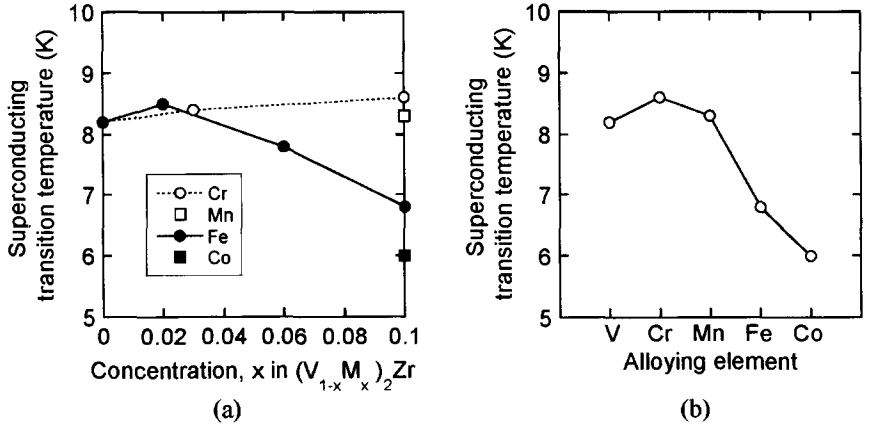

Fig. 1 Effects of alloyed 3d transition elements on T_c for C15 Laves phase compounds (a) $(V_{1-x}M_x)_2Zr$ and (b) $(V_{0.9}M_{0.1})_2Zr$.

2. COMPUTATIONAL METHOD

DV-Xα molecular calculation was carried out using the SCAT code developed by Adachi et al. [10]. Calculation was based on the Hartree-Fock-Slater approximation with exchange correlation between electrons including the Slater local exchange-correlation potential V_{xc} given by

$$V_{xc} = -3\alpha\left[\frac{3}{8\pi}\rho(r)\right]^{1/3} \tag{1}$$

where $\rho(r)$ is the local electron density at position r [10-12]. In this calculation, the parameter α is fixed at a constant value of 0.7 and the self-consistent charge approximation is employed. The molecular orbital wave function ϕ is expressed by a linear combination of atomic orbitals (LCAO) as

$$\phi_i = \sum_i C_{ii}\chi_i \tag{2}$$

where χ_i is a basis function. Numerical atomic orbitals are employed as the basis functions in the DV-Xα method [10-12].

Figure 2 shows the model clusters analyzed in the present work. Interatomic distance is determined by the lattice parameter data (a = 0.428 nm). The calculation is performed for three clusters, $(V_6M_1)Zr_6$, $(V_{18}M_1)Zr_6$ and $(V_{18}M_1)Zr_{14}$. The 3d transition metal atoms M are indicated by arrows in Fig. 2. The atomic basis functions used in the present calculations are 1s-5p for Zr, and 1s-4p for V, Cr, Mn, Fe and Co. The C_i point group is used to produce symmetry orbitals. Self-consistency within 0.001 electrons is obtained for the final orbital populations. Mulliken population analysis [13] is employed for evaluation of the net charge and the bond overlap population. Both the spin-polarized and non-spin-polarized cases

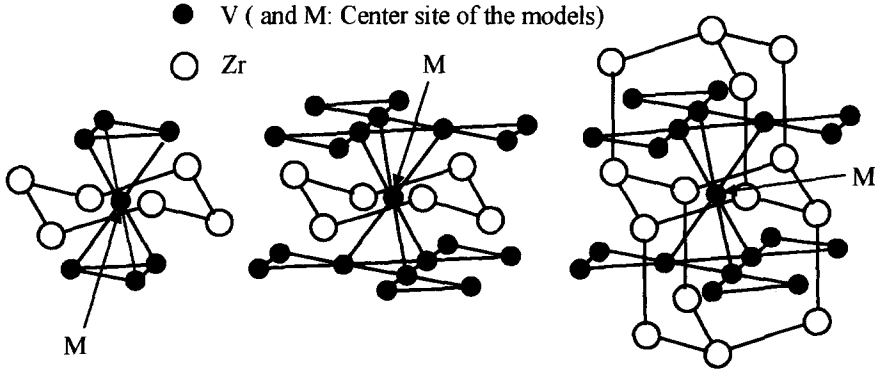

Fig. 2 Model clusters for $(V_{1-x}M_x)_2Zr$ (M = V, Cr, Mn, Fe, Co).

are considered in the molecular orbital calculations. In the spin-polarized cases, only the center atom M is polarized for the initial state in the calculation process.

3. RESULTS AND DISCUSSION

Figure 3 shows the net charge of the center atom M in clusters $(V_6M_1)Zr_6$, $(V_{18}M_1)Zr_6$ and $(V_{18}M_1)Zr_{14}$. In all clusters, the net charge decreases with addition of the alloying element in accordance with the periodic order. The net charge values of the $(V_{18}M_1)Zr_6$ and $(V_{18}M_1)Zr_{14}$ clusters are almost identical. Figure 4 shows the bond overlap population between the center atom M and neighboring V and Zr atoms in the cluster $(V_{18}M_1)Zr_6$. The bond overlap population increases with the addition of Cr and then decreases with increasing atomic number. Some difference between the spin-polarized and non-spin-polarized results were observed for $(V_{18}Fe_1)Zr_6$. The spin-polarized effects mainly become apparent in the 3d orbital populations of the center atom M in $(V_{18}M_1)Zr_6$ for M = Mn, Fe, Co. The difference between the 3d up-spin and down-spin orbital populations is about 1.1, 2.2 and 1.3 in Mn, Fe and Co, respectively. The relative large difference for Fe may affect the bond overlap population of $(V_{18}Fe_1)Zr_6$ in Fig. 4.

The superconducting transition temperature of $(V_{0.9}M_{0.1})_2Zr$ and the M-V bond overlap population of $(V_{18}M_1)Zr_6$ according to the spin-polarized calculation result in Fig. 4 are shown in Fig. 5. A good correlation can be seen between the bond overlap population and the superconducting transition temperature. Figure 6 shows the bond overlap population for the cluster $(V_{18}M_1)Zr_{14}$. The bond overlap

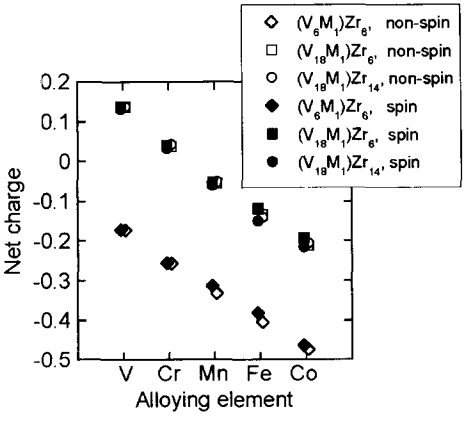

Fig. 3 Net charge with alloying elements M for $(V_6M_1)Zr_6$, $(V_{18}M_1)Zr_6$ and $(V_{18}M_1)Zr_{14}$ (M=V, Cr, Mn, Fe, Co).

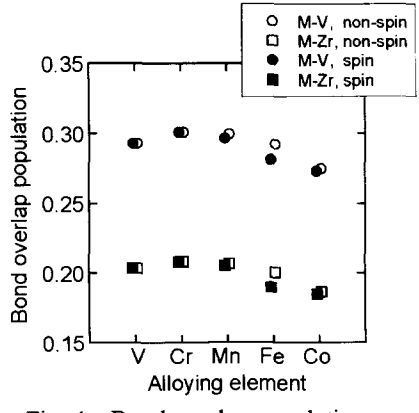

Fig. 4 Bond overlap population with alloying elements M for $(V_{18}M_1)Zr_6$. (M=V, Cr, Mn, Fe, Co).

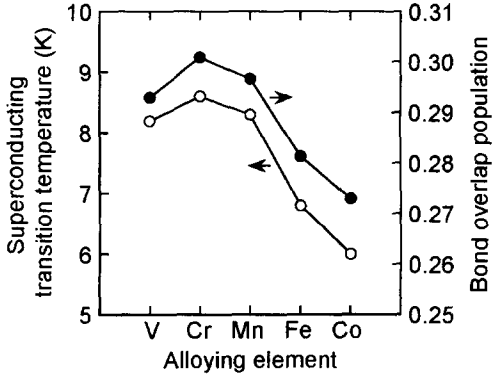

Fig. 5 Superconducting transition temperature for $(V_{0.9}M_{0.1})_2Zr$ [9] and the M-V bond overlap population with alloying element M for spin-polarized $(V_{18}M_1)Zr_6$ (M=V, Cr, Mn, Fe, Co).

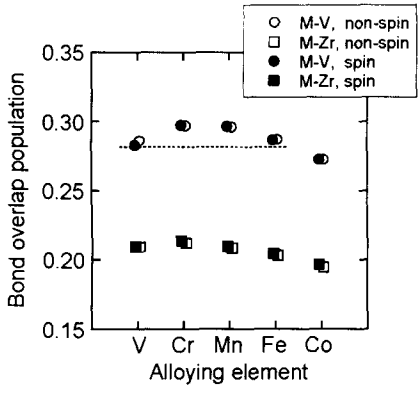

Fig. 6 Bond overlap population with alloying element M for $(V_{18}M_1)Zr_{14}$ (M=V, Cr, Mn, Fe, Co).

population increases with the addition of Cr and then decreases with increasing atomic number as in Fig. 4. It is notable that bond overlap population of $(V_{18}Fe_1)Zr_{14}$ is larger than that of $V_{19}Zr_{14}$. As the cluster increases in size, the ratio of the number of Fe atoms to the total number of atoms decreases. Consequently, the increase in superconducting transition temperature appears to be related to the change in the bond overlap population in the case of a small amount of Fe in V_2Zr. On the other hand, in the case of Cr, the change in the bond overlap population appears to have the opposite effect (Figs. 6 and 4), and the transition temperature of $(V_{0.9}Cr_{0.1})_2Zr$ is higher than that of $(V_{0.97}Cr_{0.03})_2Zr$. Although absolute quantitative evaluation of these concentration effects would be very difficult, the good correlation between bond overlap population and the superconducting transition temperature is a valuable result.

In the great majority of metallic superconductors, the conventional BCS mechanism is believed to be the origin of superconductivity. However, many unconventional superconductors have now been identified, including the C15 Laves phase compounds [1]. The present results for the C15 V_2Zr models containing magnetic elements demonstrate that the bond overlap population has an appreciable effect on the superconducting transition temperature even for magnetic element-doped compounds. The bond overlap population was derived from the DV-Xα orbitals in calculations considering only the Xα exchange correlation, without electron correlation. Although the finer details with respect to energy are rather sensitive to the way electron correlation is included, information concerning

the wave functions is insensitive to electron correlation and such DV-Xα calculations can be considered reliable [10-12, 14]. The DV-Xα orbitals appear to be directly related to the nature of superconductivity.

The mechanism of superconductivity in many compounds remains contentious. From the present results for V_2Zr, it appears that the key to understanding superconductivity is not in the analysis of electron-phonon and/or magnetic interaction. Rather, superconductivity appears to be strongly related to the behavior of molecular orbitals [15-17]. As superconductivity is frequently observed on the border of structural and/or magnetic transition, the present authors believe that electron-phonon and/or magnetic interaction are not primary factors as such and consider that the orbital response itself may be the universal factor governing the occurrence of superconductivity. Assuming that superconductivity is a chemical reaction phenomenon in a solid, it would be useful to focus on the changes of orbital mixing and orbital overlap with respect to atomic displacement in the search for new superconductors.

4. CONCLUSION

The effects of alloyed 3d transition elements on the superconducting transition temperature of C15 Laves phase V_2Zr were investigated based on the DV-Xα molecular orbital method. In $(V_{1-x}M_x)_2Zr$ compounds with M = Cr, Mn, Fe and Co, T_c increases with the addition of Cr and then decreasing with the addition of elements with higher atomic numbers, to M = Co in $(V_{0.9}M_{0.1})_2Zr$. Furthermore, the T_c increases with the addition of a small amount of Fe in $(V_{0.98}Fe_{0.02})_2Zr$ despite the ferromagneticity. A good correlation between bond overlap population and T_c was observed in the results of these calculations, and it appears that the key to understanding superconductivity may not be the analysis of electron-phonon and/or magnetic interaction. Rather, the orbital response itself may be a universal factor governing the occurrence of superconductivity.

5. REFERENCES

[1] J. F. Annett, Physica C, **317-318**, 1 (1999).
[2] C. C. Tsuei, Physica A, **168**, 238 (1990).
[3] W. Takahara, Y. Umakoshi and T. Yamane, Journal of Materials Science, **28**, 5070 (1993).
[4] K. Shimizu, T. Kimura, S. Furomoto, K. Takeda, K. Kontani, Y. Onuki and K. Amaya, Nature, **412**, 316 (2001).
[5] S. S. Saxena, P. Agarwal, K. Ahilan, F. M. Grosche, R. K. W. Haselwimmer, M. J. Steiner, E. Pugh, I. R. Walker, S. R. Julian, P. Monthoux, G. G. Lonzarich,

A. Huxley, I. Sheikin, D. Braithwaite and J. Flouquet, Nature, **406**, 587 (2000).
[6] C. Pfleiderer, M. Uhlarz, S. M. Hayden, R. Vollmer, H. v. Löhneysen, N. R. Bernhoeft and G. G. Lonzarich, Nature, **412**, 58 (2001).
[7] A. Lanzara, P. V. Bogdanov, X. J. Zhou, S. A. Kellar, D. L. Feng, E. D. Lu, T. Yoshida, H. Eisaki, A. Fujimori, K. Kishino, J.-I. Shimoyama, T. Noda, S. Uchida, Z. Hussain and Z.-X. Shen, Nature, **412**, 510 (2001).
[8] W. Takahara and T. Yamane, Journal of Materials Science Letters, **14**, 1193 (1995).
[9] S. B. Roy, Philosophical Magazine B, **65**, 1435 (1992).
[10] H. Adachi, M. Tsukada and C. Satoko, Journal of Physical Society of Japan, **45**, 875 (1978).
[11] H. Adachi, Advances in Quantum Chemistry, **29**, 49 (1997).
[12] H. Adachi, Materials Transactions, JIM, **38**, 485 (1997).
[13] R. S. Mulliken, Journal of Chemical Physics, **23**, 1833 (1955).
[14] M. Morinaga, S. Nasu, H. Adachi, J. Saito and N. Yukawa, Journal of Physics: Condensed Matter, **3**, 6817 (1991).
[15] H. Adachi and M. Takano, Physica C **157**, 169 (1989).
[16] R. Sekine, M. Kawai and H. Adachi, Physica C, **159**, 161 (1989).
[17] K. Fukushima and H. Adachi, Physica C, **207**, 119 (1993).

A New Approach to Electron Transition during Inner-Shell Ionization

Takeshi Mukoyama[†‡*] and Masayuki Uda[†]

[†]Department of Materials Science and Engineering,
Waseda University, Shinjuku, Tokyo, 169-8555 Japan
and
Laboratory for Materials Science and Technology,
Waseda University, Shinjuku, Tokyo, 169-0051 Japan
[‡]Kansai Gaidai University, Hirakata, Osaka, 573-1001 Japan

(Received January 10, 2002; in final form February 5, 2002)

Abstract

An alternative approach for calculation of the electron excitation probability accompanying inner-shell vacancy production is presented. The change in the central potential of atoms and molecules due to creation of inner-shell vacancy is estimated and only monopole term is found to be allowed in terms of electron charge density. Considering this change as the perturbation, the time-dependent Schrödinger equation is solved and the expression for the electron transition probabilities between two states is given. The relation between the present model, called Waseda Model, and the conventional shake model, which is due to the imperfect overlap between the initial- and final-state wave functions, is clarified. It is found that, although both models start from the same Hamiltonian, the different expressions for transition probabilities are obtained because of the different choice of the perturbation term. The calculated electron transition probabilities by the Waseda model are compared with those by the conventional shake model and with the experimental results following photoionization.

Keywords: Inner-shell ionization, Potential change, Time-dependent perturbation, Electron transition probability

*E-mail: mukoyama@kansaigaidai.ac.jp

ADVANCES IN QUANTUM CHEMISTRY, VOLUME 42

0065-3276/03 $35.00

1 Introduction

When an inner-shell vacancy is created in one of atoms in molecules, the remaining electrons experience sudden change in central potential due to core-hole creation. They have a small, but definite probability to be excited to a higher unoccupied state (shakeup) or ionized to the continuum (shakeoff) [1]. This shake process is caused by the sudden change in the central potential due to creation of an inner-shell vacancy. The shake process has been usually treated in the sudden approximation and its probability is expressed in terms of overlap integral between electron wave functions for initial and final states [2, 3].

Recently, we present an alternative approach to calculate the electron transition probability following inner-shell ionization process [4]. In this model, the change in the central potential of atoms and molecules due to creation of an inner-shell vacancy is estimated in terms of electron charge density. Considering this change as the perturbation, the time-dependent Schrödinger equation is solved and the electron transition probabilities between two states are calculated. When we use the two-state approximation, the problem becomes simple and the final expression is given by the well-known example in the standard textbook of quantum mechanics.

In the present work, the relation between the new model and the conventional shake model is clarified. Both models are based on the same total Hamiltonian. The difference consists in the choice of the perturbation term. As in the shake model, only the monopole transition is allowed in the present model, but the matrix element contains only wave functions for the initial state. This is different from the shake model, where the matrix element is an imperfect overlap integral between the initial- and final-state wave functions.

In order to test the validity of the present model, the numerical calculations for electron excitation probabilities after photoionization have been performed for Ne and Ar atoms. The calculated electron transition probabilities by the present model are compared with those by the conventional shake model and with the experimental results. Applications of this new model to various electron transition processes accompanying inner-shell ionization are discussed.

2 Electron Transition Probability

We consider an electron in atom and calculate its transition probability accompanying inner-shell ionization. Before inner-shell ionization process takes place, all the electrons are assumed to be in their ground state. The wave function of the electron, $\Psi(\boldsymbol{r}, t)$, satisfies the following time-dependent Schrödinger

equation:

$$\left(\boldsymbol{H}(\boldsymbol{r},t)-\frac{\partial}{\partial t}\right)\Psi(\boldsymbol{r},t)=0\ , \tag{1}$$

where $\boldsymbol{r}$ is the position vector of the electron. Atomic units are used throughout the present work.

We assume that the inner-shell ionization process takes place suddenly at time $t=0$. Then an atomic electron in the same atom experiences two effects simultaneously: disappearance of the inner-shell electron and appearance of the ionized electron. The Hamiltonian in Eq. (1) can be written by

$$\boldsymbol{H}(\boldsymbol{r},t)=\begin{cases}\boldsymbol{H}_0(\boldsymbol{r}), & t<0\\ \boldsymbol{H}_0(\boldsymbol{r})+U(\boldsymbol{r})+V(\boldsymbol{r},t) & t\geq 0\ ,\end{cases} \tag{2}$$

where $\boldsymbol{H}_0(\boldsymbol{r})$ is the Hamiltonian for the ground state before the ionization event, $U(\boldsymbol{r})$ is the change in the central potential due to creation of an inner-shell vacancy, and $V(\boldsymbol{r},t)$ represents the interaction between the ejected electron and the atomic electron.

When we use the perturbation theory to calculate the transition probability, there are two choices of the unperturbed Hamiltonian for $t>0$. In the first method, called Model I, we assume $\boldsymbol{H}_0(\boldsymbol{r})+U(\boldsymbol{r})$ as the unperturbed Hamiltonian and $V(\boldsymbol{r},t)$ is the perturbation term. On the other hand, in the second method, Model II, $\boldsymbol{H}_0(\boldsymbol{r})$ is the unperturbed part and the term $U(\boldsymbol{r})+V(\boldsymbol{r},t)$ is chosen as the perturbation.

2.1 Shake Model

In the Model I, the Hamiltonian changes from $\boldsymbol{H}_0(\boldsymbol{r})$ to $\boldsymbol{H}(\boldsymbol{r},t)$ suddenly at $t=0$. For $t>0$, we consider the time-independent part $\boldsymbol{H}_0'(\boldsymbol{r})=\boldsymbol{H}_0(\boldsymbol{r})+U(\boldsymbol{r})$ as the Hamiltonian in the final state and

$$V(\boldsymbol{r},t)=\frac{1}{|\boldsymbol{R}(t)-\boldsymbol{r}|}\ , \tag{3}$$

as a time-dependent perturbation. Here $\boldsymbol{R}(t)$ is the position vector of the electron ejected by the primary ionization event. Since $U(\boldsymbol{r})$ is included in the unperturbed Hamiltonian, its eigenstates correspond to those of a positive ion with inner-shell vacancy. The eigenfunction $\phi_n(\boldsymbol{r})$ and energy eigenvalue ϵ_n of $\boldsymbol{H}_0'(\boldsymbol{r})$ are expressed as

$$\boldsymbol{H}_0'(\boldsymbol{r})\phi_n(\boldsymbol{r})=\epsilon_n\,\phi_n(\boldsymbol{r})\ . \tag{4}$$

We expand the time-dependent wave functions in terms of these eigenfunctions:

$$\Psi(\boldsymbol{r},t)=\sum_n a_n(t)\,\phi_n(\boldsymbol{r})\,\mathrm{e}^{-i\,\epsilon_n\,t}\ . \tag{5}$$

Substituting Eq. (5) into Eq. (1), we obtain

$$i\,\dot{a}_m(t) = \sum_n a_n(t)\,V_{mn}(t)\,\mathrm{e}^{i\omega_{mn}t}\ , \tag{6}$$

where

$$V_{mn}(t) = \int \phi_m^*(\boldsymbol{r})\,V(\boldsymbol{r},t)\,\phi_n(\boldsymbol{r})\,d\boldsymbol{r}\ , \tag{7}$$

and $\omega_{mn} = \epsilon_m - \epsilon_n$. Integrating Eq. (6) with respect to time from 0 to t, we obtain

$$a_m(t) = a_m(0) - i\sum_n \int_0^t a_n(t')\,V_{mn}(t')\,\mathrm{e}^{i\omega_{mn}t'}\,dt'\ . \tag{8}$$

Before the inner-shell vacancy is produced, the atom stays in its ground state and the electron is found in one of the eigenstates of $\boldsymbol{H}_0(\boldsymbol{r})$:

$$\boldsymbol{H}_0(\boldsymbol{r})\,\phi_k^{(0)}(\boldsymbol{r}) = \epsilon_k^{(0)}\,\phi_k^{(0)}(\boldsymbol{r})\ . \tag{9}$$

For small values of t, we can assume that the wave function $\Psi(\boldsymbol{r},t)$ is written by

$$\Psi(\boldsymbol{r},t) \approx \phi_k^{(0)}(\boldsymbol{r})\,\mathrm{e}^{-i\epsilon_k^{(0)}t} = \sum_n a_n(t)\,\phi_n(\boldsymbol{r})\,\mathrm{e}^{-i\epsilon_n t}\ . \tag{10}$$

From this equation at $t = 0$, $a_m(0)$ is expressed as the overlap integral between $\phi_m(\boldsymbol{r})$ and $\phi_k^{(0)}(\boldsymbol{r})$:

$$a_m(0) = <\phi_m(\boldsymbol{r})|\phi_k^{(0)}(\boldsymbol{r})> = \int \phi_m^*(\boldsymbol{r})\,\phi_k^{(0)}(\boldsymbol{r})\,d\boldsymbol{r}\ . \tag{11}$$

Using Eqs. (8), (10), and (11), the electron transition amplitude at time t from the initial state k to the final state m as the result of inner-shell vacancy creation is expressed as

$$a_m(t) = <\phi_m(\boldsymbol{r})|\phi_k^{(0)}(\boldsymbol{r})> - i\int_0^t V'_{mk}(t')\,\mathrm{e}^{i\omega_{mk}t'}\,dt'\ . \tag{12}$$

where

$$V'_{mk}(t) = \int \phi_m^*(\boldsymbol{r})\,V(\boldsymbol{r},t)\,\phi_k^{(0)}(\boldsymbol{r})\,d\boldsymbol{r}\ , \tag{13}$$

and $\omega_{mk} = \epsilon_m - \epsilon_k^{(0)}$.

If we neglect the Coulomb interaction between the ejected electron and the atomic electrons and retain only the first term in Eq. (12), the final expression is simply given by the overlap integral:

$$a_m(t) \equiv a_m(0) = <\phi_m(\boldsymbol{r})|\phi_k^{(0)}(\boldsymbol{r})>\ . \tag{14}$$

This fact indicates that the Model I corresponds to the so-called *shake* model.

2.2 Waseda Model

In the case of the Model II, the unperturbed Hamiltonian is taken to be $\boldsymbol{H}_0(\boldsymbol{r})$ and the perturbation operator is defined as $U(\boldsymbol{r})+V(\boldsymbol{r},t)$. The time-dependent wave function is expanded in terms of the ground state wave functions:

$$\Psi(\boldsymbol{r},t) = \sum_n a_n(t)\,\phi_n^{(0)}(\boldsymbol{r})\,\mathrm{e}^{-i\,\epsilon_n^{(0)}\,t}\,, \tag{15}$$

where $\phi_n^{(0)}(\boldsymbol{r})$ is the eigenfunction of $\boldsymbol{H}_0(\boldsymbol{r})$ and $\epsilon_n^{(0)}$ is the corresponding energy eigenvalue, as given by Eq. (9).

Substituting Eq. (15) into Eq. (1) and following the similar method used for Eq. (8), we obtain

$$a_m(t) = a_m(0) - i\sum_n \int_0^t a_n(t')\,W_{mn}(t')\,\mathrm{e}^{i\,\omega_{mn}^{(0)}t'}\,dt'\,, \tag{16}$$

where

$$W_{mn}(t) = \int \phi_m^{(0)*}(\boldsymbol{r})\left(U(\boldsymbol{r}) + V(\boldsymbol{r},t)\right)\phi_n^{(0)}(\boldsymbol{r})\,d\boldsymbol{r}\,, \tag{17}$$

and $\omega_{mn}^{(0)} = \epsilon_m^{(0)} - \epsilon_n^{(0)}$.

When the electron is in the state k for $t < 0$, the first term in Eq. (16) is $a_m(0) = \delta_{mk}$. We have to solve the simultaneous equations, Eq. (16), with this initial condition. For simplicity, we shall introduce following two assumptions. First, as in the manner similar to Model I we neglect the electron-electron interaction term, $V(\boldsymbol{r},t)$, and retain only the electrostatic term, $U(\boldsymbol{r})$. It is important to note that in this case the perturbation potential is independent of time. Second, we use the two-state approximation. We consider that the electron in the state k makes a transition to the state m ($m \neq k$) and neglect contributions from all other states.

Then the simultaneous equations is decoupled and the problem becomes very simple one to calculate the electron transition probability between two states under the time-independent perturbation $U(\boldsymbol{r})$. When the perturbation is switched on at $t = 0$, the transition probability from the state k to the state m ($m \neq k$) at time t is found in the textbook of quantum mechanics [5]:

$$P_{km}(t) = \frac{4\,|W_{km}|^2}{\gamma^2 + 4\,|W_{km}|^2}\,\sin^2\beta\,t\,, \tag{18}$$

where

$$\begin{aligned}
\gamma &= W_{mm} - W_{kk} + \Delta E\,,\\
\beta &= \sqrt{\frac{1}{4}\gamma^2 + |W_{km}|^2}\,,\\
\Delta &= \epsilon_m^{(0)} - \epsilon_k^{(0)}\,,
\end{aligned}$$

and

$$W_{km} = \int_0^\infty \phi_k^{(0)*}(\boldsymbol{r})\, U(\boldsymbol{r})\, \phi_m^{(0)}(\boldsymbol{r})\, d\boldsymbol{r} \ . \tag{19}$$

However, it should be taken into account that the transition occurs only in the presence of the inner-shell vacancy, but the inner-shell hole is filled by radiative or nonradiative transitions. The probability that the vacancy survives until time t is proportional to $\mathrm{e}^{-\lambda t}$, where λ is the decay rate of the vacancy and corresponds to its level width. Taking into consideration this probability, the total electron transition probability can be obtained by integrating the differential probability, Eq. (18), with respect to time from 0 to ∞ with the weighting function $\mathrm{e}^{-\lambda t}$. The final expression for the transition probability is given by [6]

$$P_{km} = \frac{2\,\beta^2}{\lambda^2 + 4\,\beta^2} \frac{4\,|W_{km}|^2}{\gamma^2 + 4\,|W_{km}|^2} \ . \tag{20}$$

In general, $\beta \gg \lambda$ and we can use the expression

$$P_{km} \approx \frac{2\,|W_{km}|^2}{\gamma^2 + 4\,|W_{km}|^2} \ , \tag{21}$$

as a good approximation to Eq. (20).

The perturbation operator $U(\boldsymbol{r})$ is determined as follows. For the neutral atom with atomic number Z and N electrons, the central potential for its j-th electron in its ground state can be expressed as

$$U(\boldsymbol{r}_j) = -\frac{Z_{\mathrm{eff}}(r_j)}{r_j} = -\frac{Z}{r_j} + \int_0^\infty \sum_{i \neq j}^{N} |\psi_i(\boldsymbol{r}_i)|^2 \frac{1}{r_{ij}}\, d\boldsymbol{r}_i \ , \tag{22}$$

where $Z_{\mathrm{eff}}(r)$ is the effective nuclear charge, $\psi_i(\boldsymbol{r}_i)$ is the wave function of the i-th electron, $\boldsymbol{r}_i$ is the position vector of the i-th electron from the nucleus, $r_i \equiv |\boldsymbol{r}_i|$ is the radial distance, and $r_{ij} = |\boldsymbol{r}_i - \boldsymbol{r}_j|$ is the distance between two electrons i and j.

From Eq. (22), the potential for the j-th electron due to the presence of the i-th electron at $\boldsymbol{r}_i$ is given by

$$U_i(\boldsymbol{r}_j) = \int_0^\infty \frac{1}{r_{ij}} |\psi_i(\boldsymbol{r}_i)|^2\, d\boldsymbol{r}_i \ . \tag{23}$$

When an inner-shell vacancy is produced at the i-th state, this potential suddenly disappears from Eq. (22) and can be considered as the perturbation operator to the stationary state with the Hamiltonian $\boldsymbol{H}_0(\boldsymbol{r})$.

The wave function of an electron in the atom is expressed as

$$\psi_{nlm}(\boldsymbol{r}) = R_{nl}(r)\, Y_{lm}(\theta, \varphi) \ , \tag{24}$$

where $R_{nl}(r)$ is the radial part of the wave function and $Y_{lm}(\theta, \varphi)$ is the spherical harmonics, corresponding to its angular part. The subscripts, n, l, and m are the principal, orbital angular momentum, and magnetic quantum numbers, respectively. Substituting Eq. (24) into Eq. (23) and expanding r_{ij} in terms of multipoles, we can find that multipoles with even numbers are allowed from the selection rule of angular momenta and with some algebra only the monopole term remains. The change in the central potential due to creation of an inner-shell vacancy can be given by

$$U_i(r_j) = \frac{1}{r_j} \int_0^{r_j} |R_{nl}(r_i)|^2 r_i^2 \, dr_i + \int_{r_j}^{\infty} |R_{nl}(r_i)|^2 r_i \, dr_i \, . \tag{25}$$

Using Eq. (25) in Eq. (20), the electron transition probability accompanying an inner-shell vacancy production can be calculated. In this model, only the monopole transition is allowed. It should be noted, however, that Eq. (20) is different from the wave-function overlap in the shake model. There is another difference that in the shake model wave functions for two different potentials, for the initial neutral atom and the final positive ion with an inner-shell vacancy, are necessary, while only the wave functions for the ground state are used in the present model. These facts indicate that the present model is a new approach for the electron transition process following inner-shell ionization, alternative to the shake model. We shall refer this model as the *Waseda* model.

3 Potential Change due to Vacancy Creation

The change in the atomic potential due to the inner-shell vacancy production is calculated by Eq. (25). The numerical calculations have been performed with the Hartree-Fock-Slater (HFS) wave functions [7]. The potential change $rU(r)$ is plotted as a function of r in Fig. 1 for Ne and Ar atoms. As can be seen from Eq. (22), this quantity corresponds to the change in effective nuclear charge for outer-shell electrons. The solid curve is calculated for $1s$ vacancy in Ne with the HFS wave function. The similar results for Ar $1s$ and $2s$ vacancies are plotted in the figure for comparison. It can be seen that the change in effective nuclear charge is zero at the nucleus and approaches to unity for large r. The curve for $2s$ vacancy in Ar is more slowly increasing than the curve for the $1s$ vacancy. This fact reflects the difference in electron density distribution between $1s$ and $2s$ orbitals.

It is interesting to note that in the case of $1s$ vacancy the screened hydrogenic wave function gives a good approximation to the potential change with the HFS wave functions. By the use of the hydrogenic wave function for $1s$

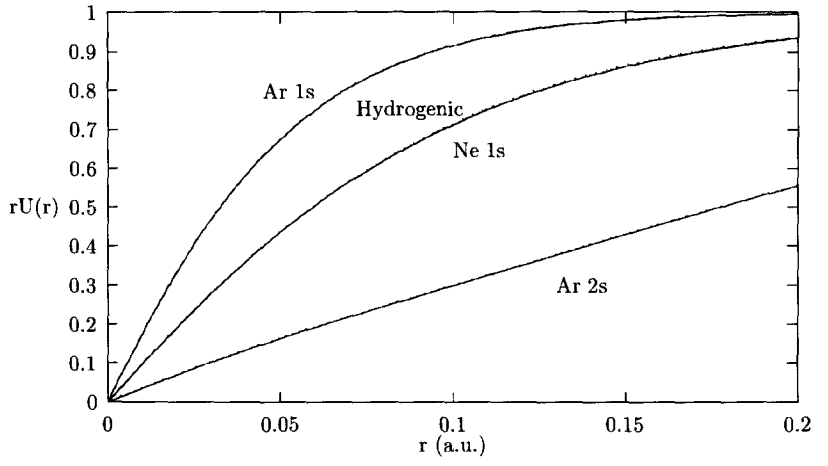

Figure 1: Change in the central potential due to inner-shell vacancy production. The solid curves are for Ne $1s$ vacancy, for Ar $1s$ vacancy, and for Ar $2s$ vacancy with the HFS wave functions, and the dotted curve for Ne $1s$ vacancy with the screened hydrogenic wave functions.

orbital, Eq. (25) can be expressed as

$$U_{1s}^{\rm hyd}(r) = \frac{1}{2r}\left[\gamma(3, 2Z_{1s}r) + 2Z_{1s}r\,\Gamma(2, 2Z_{1s}r)\right] , \tag{26}$$

where $\gamma(a,x)$ and $\Gamma(a,x)$ are the incomplete Gamma functions [8] and $Z_{1s} = Z - 0.3$ is the effective nuclear charge for the $1s$ orbital with the Slater's screening constant [9]. The calculated result for Ne $1s$ vacancy by Eq. (26) is also shown in Fig. 1 with the dotted curve. It is clear that the screened hydrogenic wave function gives almost same result as the HFS one for the $1s$ vacancy.

In the similar way, the approximate expressions of the potential change can be obtained for $2s$ and $2p$ vacancies with the screened hydrogenic wave functions. For the $2s$ orbital, Eq. (25) is given by

$$\begin{aligned} U_{2s}^{\rm hyd}(r) &= \frac{1}{2r}\Big\{\gamma(3, Z_2r) + Z_2r\,\Gamma(2, Z_2r) - \gamma(4, Z_2r) - Z_2r\,\Gamma(3, Z_2r) \\ &\quad + \frac{1}{4}\left[\gamma(5, Z_2r) + Z_2r\,\Gamma(4, Z_2r)\right]\Big\} , \end{aligned} \tag{27}$$

where the effective nuclear charge is defined with the Slater's screening constant to be $Z_2 = Z - 4.15$. In the case of the $2p$ orbital, the final expression is

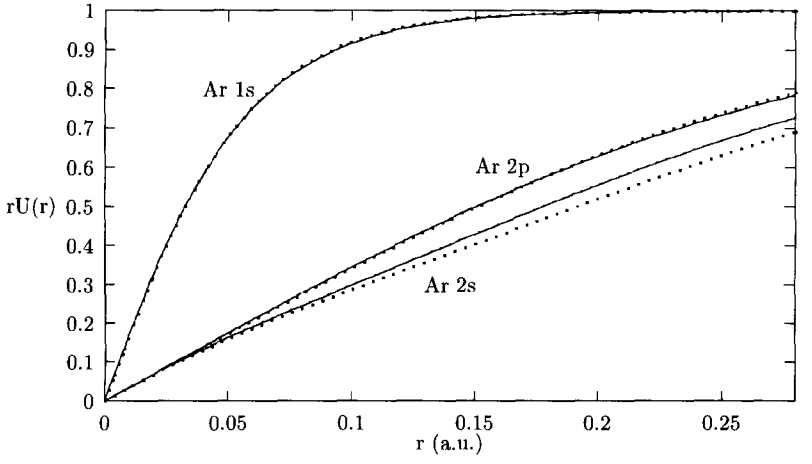

Figure 2: Change in the central potential due to the $1s$-, $2s$-, and $2p$-shell vacancy production for Ar. The solid curves are calculated with the HFS wave functions and the dotted curves with the screened hydrogenic wave functions.

written by

$$U_{2p}^{\mathrm{hyd}}(r) = \frac{1}{24r}\left[\gamma(5, Z_2 r) + Z_2 r\,\Gamma(4, Z_2 r)\right] . \tag{28}$$

In Fig. 2, the potential changes calculated with Eqs. (26)–(28) are plotted as a function of radial distance for the vacancy creation in the $1s$, $2s$, and $2p$ orbitals of Ar and compared with those by the HFS wave functions. It is clear that for the $1s$ orbital the screened hydrogenic model gives a good approximation to the HFS wave functions, as already shown above for Ne. In the case of the $2p$ vacancy, this approximation is still good, but worse than in the case of the $1s$ vacancy. However, for the $2s$ vacancy the screened hydrogenic model underestimates the results with the HFS wave functions. This can be ascribed to the fact that the same effective nuclear charge is used for the $2s$ and $2p$ orbitals, but the $2s$ electrons are not sufficiently screened by the $2p$ electrons.

4 Electron Excitation Probability

In oder to test the validity of the Waseda model, the calculations of electron excitation probabilities accompanying photoionization are performed with Eq. (20) and the obtained results are compared with the conventional shakeup

probabilities.

The transition probabilities have been calculated for $1s$ vacancy in Ne and $1s$, $2s$, and $2p$ vacancies in Ar with $W = -U_i(r)$ in Eq. (20). The values of the level width are taken from the table of Krause and Oliver [10]. We consider only the bound-bound transitions corresponding to the shakeup process. In Table I, the calculated results for Ne and Ar atoms are compared with the conventional values using the wave-function overlap. The latter values were obtained in the usual manner [11] as overlap integral between wave functions for the initial and final states. In both calculations the same wave functions were used because the final results are sensitive to small difference in wave functions. It should be noted, however, that in the calculations of overlap integrals two wave functions with different potentials, i.e. initial neutral atom and final positive ion with an inner-shell vacancy, are necessary, while in the present model only the wave functions for the initial ground-state potential are used. It is clear from the table that the present transition probabilities are in good agreement with the conventional shakeup values.

Most accurate experimental studies on the shakeup probabilities accompanying inner-shell vacancy production have been performed by observing the satellite peaks in x-ray photoelectron spectra. It is usual that the satellite intensities are given as relative ratios to the main peak without any additional electron transition. In order to compare the calculated results with these experimental data, the probabilities in Table 1 should be normalized so that the intensity of the main peak is 100. In the present model, the probability that the electron remains in its original state is given by $1 - P_{km}$ and the relative intensity for the electron transition is obtained as $P_{km}/(1 - P_{km})$.

The calculated results for the $1s$ vacancy in Ne are listed in Table 2 and compared with other theoretical values as well as the experimental ones. All other theoretical calculations were performed in the wave-function overlap approach with different choices of wave functions, i.e. the multi-configuration Hartree-Fock method with electron correlation [12], the optimized effective potential method [13], and the HFS method [11, 14]. It can be seen that for Ne the present values are in good agreement with the experimental ones and also with other theoretical calculations. In Table 3, similar comparison for Ar $2p$ vacancy is made. In this case, the present values are smaller than the experimental data, but agree well with the other theoretical calculations, except for the $3p \rightarrow 4p$ transition. However, the present probability for this transition is in fairly good agreement with the experimental value.

As can be seen from Tables 1–3, the present simple two-level model can give the electron transition probabilities in good agreement with the conventional shakeup probabilities by the use of imperfect wave function overlap and the relative satellite intensities also agree well with the experimental results. This

Table 1: Comparison of the calculated results for Ne and Ar with the conventional shakeup probability (%).

Element	Vacancy	Transition	Waseda[a]	Shake[b]
Ne	$1s$	$2s \rightarrow 3s$	1.07	0.65
		$2s \rightarrow 4s$	0.22	0.12
		$2p \rightarrow 3p$	5.62	7.98
		$2p \rightarrow 4p$	1.51	1.37
		$2p \rightarrow 5p$	0.63	0.50
		$2p \rightarrow 6p$	0.32	0.25
Ar	$1s$	$2s \rightarrow 4s$	0.018	0.013
		$2s \rightarrow 5s$	0.005	0.004
		$2p \rightarrow 4p$	0.062	0.062
		$2p \rightarrow 5p$	0.021	0.022
		$3s \rightarrow 4s$	1.44	0.95
		$3s \rightarrow 5s$	0.32	0.19
		$3p \rightarrow 4p$	7.24	8.68
		$3p \rightarrow 5p$	1.92	1.51
	$2s$	$3s \rightarrow 4s$	1.10	0.71
		$3s \rightarrow 5s$	0.24	0.14
		$3p \rightarrow 4p$	5.96	6.82
		$3p \rightarrow 5p$	1.54	1.15
	$2p$	$3s \rightarrow 4s$	0.61	0.74
		$3s \rightarrow 5s$	0.12	0.15
		$3p \rightarrow 4p$	4.27	7.05
		$3p \rightarrow 5p$	1.05	1.19

[a]Waseda model.

[b]Conventional shakeup calculation by overlap integral.

Table 2: Comparison of the calculated results for Ne with the experimental shakeup intensities for Ne $1s$ spectrum (relative to the main line in %).

Transition	Theoretical					Experimental				
	MS[a]	TBJ[b]	BTB[c]	MT[d]	Waseda[e]	G[f]	K[g]	M[h]	S[i]	A[j]
$2s \rightarrow 3s$		0.79		0.66	1.08	1.06		1.1	1.1	
$2s \rightarrow 4s$				0.12	0.22			0.3	0.3	
$2p \rightarrow 3p$	5.07	9.3	11.77	8.21	5.95	6.30	5.5[k]	6.42	6.42	5.0
$2p \rightarrow 4p$	2.18	1.5	1.50	1.41	1.53	2.98		3.1	3.2	0.9
$2p \rightarrow 5p$	0.54	0.54	0.47	0.52	0.63	0.59		0.9	0.9	
$2p \rightarrow 6p$	0.15		0.21	0.25	0.32	0.5		0.3	0.5	

[a]Ref. [12].
[b]Ref. [13].
[c]Ref. [14].
[d]Ref. [11].
[e]Waseda model.
[f]Ref. [15].
[g]Ref. [16].
[h]Ref. [17].
[i]Ref. [18].
[j]Ref. [19].
[k]Part of $2p \rightarrow 4p$ transition is included.

Table 3: Comparison of the calculated results for Ar with the experimental shakeup intensities for Ar $2p$ spectrum (relative to the main line in %).

Transition	Theoretical				Experimental
	TBJ[a]	BTB[b]	MT[c]	Waseda[d]	BTB[a]
$3s \rightarrow 4s$	1.02	1.12	0.75	0.61	2.1
$3s \rightarrow 5s$		0.17	0.15	0.12	1.0
$3p \rightarrow 4p$	8.63	10.91	7.21	4.46	6.0
$3p \rightarrow 5p$	1.24	1.34	1.22	1.07	4.2

[a]Ref. [13].
[b]Ref. [14].
[c]Ref. [11].
[d]Waseda model.

fact indicates that the present approach is useful to estimate the electron transition probability accompanying inner-shell ionization.

However, the present values are based on the simple two-level approximation, where each transition is independent of other transitions. This means that the probability for electron remaining in the same state depends on the transition concerned and is different for different transitions. In order to improve this situation, it is possible to extend the present approach to the case of multi-level atoms, but then we have to solve the coupled-states equation numerically and the result cannot be expressed in the analytical form as Eq. (20). Furthermore, we confine ourselves to the case of bound-bound transitions in the present work. It is also possible to calculate the probability for the bound-free transitions (shakeoff process) in the similar manner. Especially for outermost p electrons, the shakeoff probability is large [11] and the relative ratio of the satellite to the main peak is enhanced. If we use the shakeup-plus-shakeoff probability in Refs. [2] and [3] to estimate this ratio, the present theoretical values in Table 2 increase by about 10–20% for Ne $2p$ electrons and those in Table 3 about 15–20% for Ar $3p$ electrons. The values thus obtained are still in good agreement with the experimental results.

Finally, in the present work we considered the electron transition processes within the same atom. However, it is possible to apply the present model for calculations of electron transition probabilities from one atom to the other atom in the molecule by the use of molecular wave functions. Such transitions correspond to the charge-transfer process.

5 Conclusion

We have presented a new approach to calculate the electron transition probability accompanying inner-shell ionization. When the ionization process takes place, there are two possible methods to take into account the presence of the inner-shell vacancy. In the first method, the effect of the vacancy is included in the wave functions for the final state. Starting from the time-dependent Schrödinger equation, we have shown that this approach reduces to the conventional shake model, where the matrix element is expressed as the overlap of the wave functions between the initial and final states.

On the other hand, it is also possible to consider that the production of the inner-shell vacancy is equivalent to the change in the central potential of the atom. Treating this change as the perturbation to the atomic Hamiltonian, the time-dependent perturbation theory is used to calculate the electron transition probability. Although only the monopole transition is allowed, the matrix element is different from the overlap integral and only the initial-state wave

functions are involved.

This new approach, called the Waseda model, was tested for electron excitation following photoionization. The calculated probabilities are in good agreement with the shakeup probabilities from the shake model and with the experimental data. This fact indicates that the Waseda model is equivalent to the shake model.

In the present work, the calculations were made for bound-bound transitions in atoms accompanying photoionization. However, the present model is general and can be applied to any kinds of inner-shell ionization processes and to different electron transition modes. It is interesting to test the present model for various ionization mechanisms and electron transition processes. The calculations for bound-free transitions and for electron transitions between atoms in molecules with molecular wave functions (charge-transfer processes) are in progress. For the latter calculations, the molecular wave functions obtained with the DV-Xα method [20] are used.

References

[1] T. Mukoyama and Y. Ito, Nucl. Instr. and Meth. **B87**, 26 (1994) and references cited therein.

[2] T. A. Carlson and C. W. Nestor, Phys. Rev. A **8**, 2887 (1973).

[3] T. Mukoyama and K. Taniguchi, Phys. Rev. A **36**, 693 (1987).

[4] T. Mukoyama and M. Uda, Phys. Rev. A **61**, R030501 (2000).

[5] B. H. Bransden and C. J. Joachain, *Introduction to Quantum Mechanics* (Longman, London, 1983).

[6] I. S. Gradshteyn and I. M. Ryzhik, *Table of Integrals, Series, and Products* (Academic, New York, 1980).

[7] F. Herman and S. Skillman, *Atomic Structure Calculations* (Prentice-Hall, Englewood Cliffs, N.J., 1963).

[8] M. Abramowitz and I. A. Stegun, *Handbook of Mathematical Functions with Formulas, Graphs, and Mathematical Tables* (Dover, New York, 1965).

[9] J. C. Slater, Phys. Rev. **36**, 57 (1930).

[10] M. O. Krause and J. H. Oliver, J. Phys. Chem. Ref. Data **8**, 329 (1979).

[11] T. Mukoyama and K. Taniguchi, Bull. Inst. Chem. Res., Kyoto Univ. **70**, 1 (1992).

[12] R. L. Martin and D. A. Shirley, Phys. Rev. A **13**, 1475 (1978).

[13] J. D. Talman, G. M. Bancroft, and D. D. Johnston, Phys. Rev. A **24**, 669 (1981).

[14] D. Bristow, J. S. Tse, and G. M. Bancroft, Phys. Rev. A **25**, 1 (1982).

[15] U. Gelius, J. Electron Spectrosc. Relat. Phenom. **5**, 985 (1974).

[16] P. H. Kobrin, S. Southworth, C. M. Trusdale, D. W. Lindle, U. Becker, and D. A. Shirley, Phys. Rev. A **29**, 194 (1984).

[17] N. Mårtensson, S. Svensson, and U. Gelius, J. Phys. B **20**, 6243 (1987).

[18] S. Svensson, B. Eriksson, N. Mårtensson, G. Wendin, and U. Gelius, J. Electron Spectrosc. Relat. Phenom. **47**, 327 (1988).

[19] L. Avaldi, G. Dawber, R. Camilloni, G. C. King, M. Roper, M. R. F. Siggel, G. Stefani, M. Zitnik, A. Lisini, and P. Decleva, Phys. Rev. A **51**, 5025 (1995).

[20] H. Adachi, M. Tsukada, and C. Satoko, J. Phys. Soc. Jpn **45**, 875 (1978).

Density functional theory calculations of quantum electron transport: carbon nanotubes-gold contacts

José Luis Mozos[†], Pablo Ordejón[†], Mads Brandbyge[‡], Jeremy Taylor[‡] and Kurt Stokbro[‡]

[†] *Instituto de Ciencia de Materiales de Barcelona - CSIC, 08193 Bellaterra, Barcelona, Spain*

[‡] *Mikroelektronik Centret (MIC), Technical University of Denmark, Bldg. 345E, DK-2800 Lyngby, Denmark*

(Received December 22, 2001; in final form June 14, 2002)

We present a first principles method to study electronic transport through atomic-scale systems under non-equilibrium conditions. The method is based on density functional theory, and allows the calculation of the response of the system to an applied finite potential difference. The potential drop profile, induced electronic current, nonlinear current-voltage characteristics, and the resulting forces on the atoms are obtained from first principles. The method allows us to take explicitly into account the atomic structure of both the contact region and the semiinfinite electrodes through which the potential is applied. Non-equilibrium Green's functions techniques are used to calculate the quantum conductance. Here we apply the method to the study of the electronic transport in finite carbon nanotubes in contact to gold electrodes.

ADVANCES IN QUANTUM CHEMISTRY, VOLUME 42

0065-3276/03 $35.00

I. INTRODUCTION

The development of electronic devices at the atomic scale now constitutes one of the most active fields of research in nanotechnology. It is possible to fabricate devices such as transistors or diodes where the active zone is as small as a single molecule or a carbon nanotube. This poses new challenges to theoretical analysis, as the transport properties, *e.g.* current-voltage characteristics, depend strongly on the atomic arrangements of a few atoms. The device characteristics cannot be rationalized by the effective models commonly applied in solid state electronics. The simulation of transport processes at the atomic scale must take into account the quantum-mechanical nature of the electrons. Electronic structure methods constitute today a highly developed tool for investigating the physics and chemistry of new molecules and materials.[1] An important factor for the success of these techniques is the development of first principles methods that reliably model a wide range of systems without introducing system dependent parameters. Most methods are, however, limited in two aspects: (1) the geometry is restricted to either finite or periodic systems, and (2) the electronic system must be in equilibrium. In order to address theoretically the situation where an atomic/molecular-scale system (contact) is connected to bulk electrodes, a method capable of treating an infinite and non-periodic system is required. Also, if a finite voltage bias is applied to the electrodes, a current is driven through the contact, and the electronic subsystem is not in thermal equilibrium. The model must be able to describe this nonequilibrium situation.

In the present work we describe our first principles nonequilibrium electronic structure method for modeling a nanostructure coupled to external electrodes

with different electrochemical potentials. We treat the whole system (contact and electrodes) on the same footing, describing the atomic and electronic structure of both at the same level. Our method is based on Density Functional Theory (DFT).[2–5] We use the standard local density (LDA) or generalized gradient approximation (GGA) to describe the exchange-correlation terms. The starting point for our implementation is the SIESTA electronic structure approach.[6] In this method the effect of the core electrons is described by soft norm-conserving pseudopotentials[7] and the electronic structure of the valence electrons is expanded in a basis set of numerical atomic orbitals with finite range.[8,9] The quality of the basis set can be improved at will by using multiple-ζ orbitals, polarization functions, etc.,[9] allowing one to achieve convergence of the results to the desired level of accuracy. SIESTA has been tested in a wide variety of systems, with excellent results.[10,11] The great advantage of using orbitals with finite range (besides the numerical efficiency[6]), is that the Hamiltonian interactions are strictly zero beyond some distance, which allows us to partition the system unambiguously. Furthermore, the Hamiltonian takes the same form as in empirical tight-binding calculations, and therefore techniques developed in this context can be straightforwardly applied.

We have extended the SIESTA computational scheme to nonequilibrium systems by calculating the density matrix with a nonequilibrium Green's functions technique.[12–15] We have named this nonequilibrium electronic structure code TRANSIESTA. Here we give an brief overview of the technical implementation. A full description is given elsewhere[16] and we will here highlight the main differences as compared to equilibrium methods. We will conclude by presenting results for the transport properties of different contact geometries between finite

carbon nanotubes and gold electrodes.

II. METHODOLOGY

The system setup we are considering in our calculations is depicted in Fig. 1a. It consists of two semiinfinite metallic electrodes (L) and (R), and a contact region (C). A voltage bias is applied between the electrodes and an electron current is flowing through the system (along the z direction in the figure). This contact region is defined such that it contains the portion of the physical electrodes where all the screening effects are taking place. Then, the electronic charge distributions in the electrodes, L and R, correspond to the bulk phases of the same material to a prescribed numerical accuracy. It also means that the selfconsistent potentials in those regions may be shifted rigidly relative to each other by an external potential bias V.

In that case, we can make use of the Greens functions formalism to map our infinite system into a finite one (Fig. 1b), amenable to computer simulations. The Greens function of the system, $\mathbf{G}$, is then evaluated by inverting the finite matrix:

$$\begin{pmatrix} \mathbf{H}_L + \mathbf{\Sigma}_L & \mathbf{V}_L & 0 \\ \mathbf{V}_L^\dagger & \mathbf{H}_C & \mathbf{V}_R \\ 0 & \mathbf{V}_R^\dagger & \mathbf{H}_R + \mathbf{\Sigma}_R \end{pmatrix}, \tag{1}$$

$\mathbf{H}_L$, $\mathbf{H}_R$ and $\mathbf{H}_C$ are the Hamiltonian matrices in the L, R and C regions, respectively, and $\mathbf{V}_L$ ($\mathbf{V}_R$) is the interaction between the L (R) and C regions. The coupling of L and R to the remaining part of the semi-infinite electrodes is fully taken into account by the self-energies, $\mathbf{\Sigma}_L$ and $\mathbf{\Sigma}_R$, that are extracted from separate calculations of the corresponding bulk phases of the electrodes.

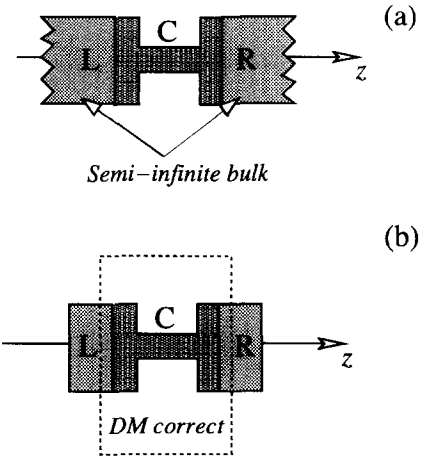

FIG. 1. (a) We model the *Contact* (C) region coupled to two semi-infinite *Left* (L) and *Right* (R) electrodes. The direction of transport is denoted by z. (b) We only describe a finite section of the infinite system: Inside the L and R parts the Hamiltonian matrix elements have bulk electrode values.

Once the Greens function is known, all the observables of the system can be computed. In particular the density matrix, $\mathbf{D}_{\mu\nu}$, is given by,

$$\mathbf{D}_{\mu\nu} = \int_{-\infty}^{\infty} d\varepsilon \left\{ \rho^{L}_{\mu\nu}(\varepsilon) n_F(\varepsilon - \mu_L) + \rho^{R}_{\mu\nu}(\varepsilon) n_F(\varepsilon - \mu_R) \right\}, \tag{2}$$

where μ_L and μ_R are the electrochemical potentials of each electrode, i.e., $\mu_L - \mu_R = V$. The spectral density matrix, $\rho^{L}(\varepsilon)$, is calculated as

$$\rho^{L}_{\mu\nu}(\varepsilon) = \frac{1}{\pi} \left(\mathbf{G}(\varepsilon) \mathrm{Im}\mathbf{\Sigma}_{\mathrm{L}}(\varepsilon) \mathbf{G}^{\dagger}(\varepsilon) \right)_{\mu\nu} \tag{3}$$

with an analogous expression for ρ^{R}.

Then the electron density

$$n(\vec{r}) = \sum_{\mu,\nu} \phi_{\mu}(\vec{r}) \mathbf{D}_{\mu\nu} \phi_{\nu}(\vec{r}), \tag{4}$$

with ϕ being the numerical basis orbitals of SIESTA, allows us to compute, by standard methods, the DFT hamiltionian elements $\mathbf{H}$, in Eq. 1. Equations 1-4 are then iterated until selfconsistency is achieved.

In addition, the nonlinear current intensity through the contact, I, is obtained as,[12–14]

$$I(V) = G_0 \int_{-\infty}^{\infty} d\epsilon \, (n_F(\epsilon - \mu_L) - n_F(\epsilon - \mu_R)) \times \\ \mathrm{Tr}\left[\mathrm{Im}\mathbf{\Sigma}_{\mathrm{L}}(\epsilon)\mathbf{G}^{\dagger}(\epsilon)\mathrm{Im}\mathbf{\Sigma}_{\mathrm{R}}(\epsilon)\mathbf{G}(\epsilon)\right] , \tag{5}$$

where $G_0 = 2e^2/h$. By comparison to the Landauer-Büttiker formula[17], we can readily identify the (left-to-right) transmission amplitude matrix $\mathbf{t}$ as,[18]

$$\mathbf{t}(\epsilon) = (\mathrm{Im}\mathbf{\Sigma}_{\mathrm{R}}(\epsilon))^{1/2} \, \mathbf{G}(\epsilon) \, (\mathrm{Im}\mathbf{\Sigma}_{\mathrm{L}}(\epsilon))^{1/2} , \tag{6}$$

Finally, we can also decompose the quantum transmission into eigenchannels with corresponding eigenvalues τ_n, by diagonalizing the transmission matrix $\mathbf{t}$ as,[19,20]

$$\mathbf{t} = \mathbf{U}_R \, \mathrm{diag}\{|\tau_n|\} \, \mathbf{U}_L^{\dagger} . \tag{7}$$

This decomposition will be instrumental in the interpretation of the mechanisms of transport.[21,18,12]

III. CONDUCTANCE IN CARBON NANOTUBE-GOLD CONTACTS

We have applied our approach to the calculation of conductance of nanotubes brought in contact with gold leads. In particular, we have considered the atomic configurations depicted in Figs. 2. The systems consist of a finite (5,5) armchair nanotube (150 atoms), and Au(100) leads (from 162 to 300 atoms, depending

on the configuration). The nanotube has open ends in the structure shown in Fig 2(a) and is capped otherwise. The cap resembles "half" a C_{60} fullerene molecule as seen from a five-fold symmetry axis[22]. The nanotube is then closed by the presence of 6 five-atom rings at the tips. The ions were allowed to relax completely in the structure in Fig. 2(a). In the other structures the nanotubes and the gold leads were relaxed separately and then the equilibrium separation distance between them was determined.

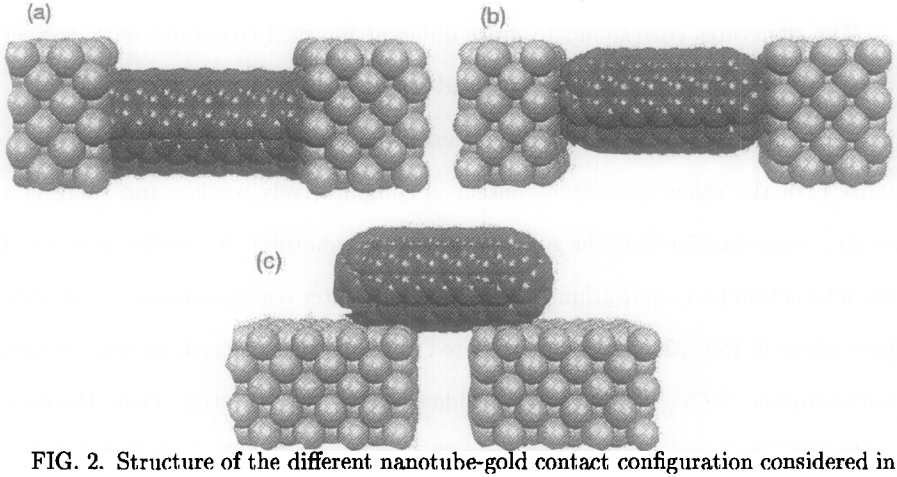

FIG. 2. Structure of the different nanotube-gold contact configuration considered in the text: (a) open nanotube normal to surface (CBC); (b) capped nanotube normal (NC) and (c) side (SC) contacted to the gold electrodes. Carbon and gold atoms are in dark and light grey color, respectively

Current is propagating along the nanotube axis. The system is periodic in the transversal directions. The lateral dimensions are large enough such that the interaction of the nanotube with its periodic images is negligible. In all the cases, the separation between Au leads is such that the contribution to the current of

the direct tunneling through the vacuum between them is negligible. Thus, the electrons flow though the nanotube and the resistance is due to the limited number of channels of the nanotube as well as the gold-nanotube contact resistance. In our calculations, we have used a single-ζ plus polarization basis set of 9 orbitals corresponding to the $5d$ and $6(s,p)$ of gold and a single-ζ representation of the $2s$ and $2p$ orbitals of carbon. We have found this basis set to provide a faithful description of the system as compared to tests done with a double-ζ representation.

The structures correspond to quite different physical situations with respect to the interaction between the surface and the nanotube, and the electronic transport behaviour. In case of Fig. 2(a) there is a strong covalent bonding contact (CBC). In the other cases, the contact is comparatively weaker and there is a small charge transfer from the gold surface to the nanotube. A detailed account of the interaction and equilibrium properties of the later configurations has already been given in Ref. 23. We have considered here two situations: a normal contact to the surface (NC) , Fig. 2(b), and a side contact (SC) structure where the nanotube lies sideways on top of the Au surface (Fig. 2(c)). The last configuration is usually encountered in present electronic device applications.

A perfect *infinite* (5,5) nanotube has a metallic character. Up to 1 eV around the Fermi level, two conduction channels, of character π and π^*, contribute each with a quantum of conductance, $G_0 = \frac{2e^2}{h}$. In a perfect contact, the resistance is thus expected to be of the order of a few $k\Omega$. This is the case when the nanotube is dipped in liquid Hg[24]. However, the reported experimental measurements on nanotube electronic devices reach values for the resistance of up to $M\Omega$[25–27]. The nanotube-metal contact is then far form ideal. Finally, it has been found that

the contact resistance could be reduced by orders of magnitude by exposing the contact areas to an electron beam in a scanning electron microscope[28].

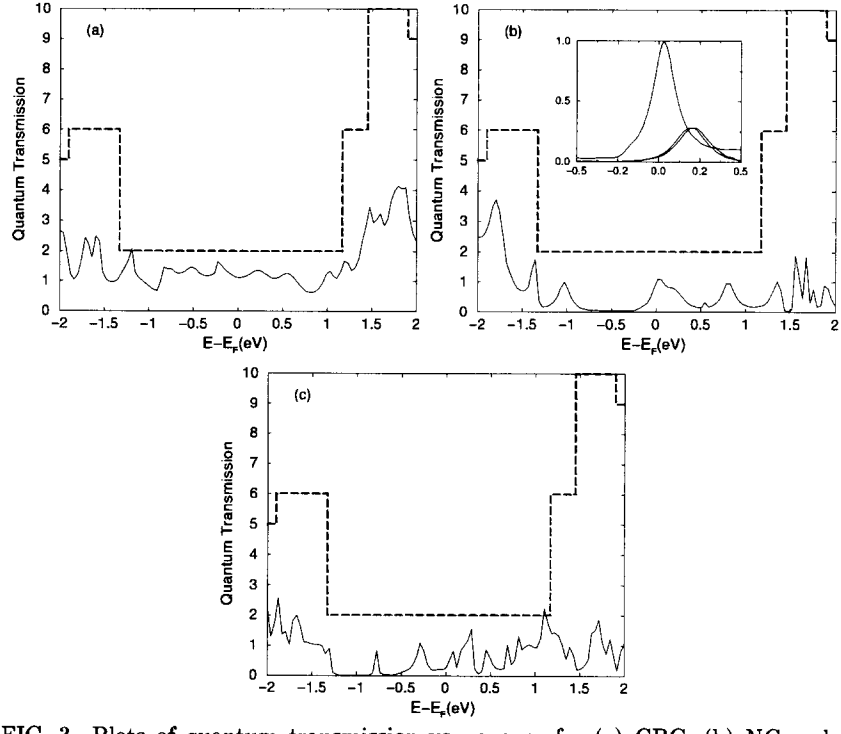

FIG. 3. Plots of quantum transmission vs. energy for (a) CBC, (b) NC and (c) SC geometries (see text). For reference, the transmission of a perfect infinite (5,5) is also plotted in dashed lines. Inset in (b): decomposition of the transmission into eigenchannels.

In both the NC and SC, a tunnel barrier against conduction is anticipated. However, for an *infinite* nanotube-gold lead, in the NC configuration, the tunnel barrier is perpendicular to the propagation direction and the electron's large momentum will allow it to overcome the barrier. In the SC, the evanescent character

of the wavefunction in the tunneling direction will lead to smaller transmission[29]. In the *finite* configurations considered here, this translational invariance is broken and the differences between the contacts will be less dramatic.

In Figs. 3 we present our results for the quantum transmission as a function of the electron energy in equilibrium. These were calculated applying our formalism to the simpler case of zero bias ($\mu_L = \mu_R$), in particular Eqs. 5 –7.

For the CBC geometry, Fig. 3(a), the calculated conductance around the Fermi level does not deviate very much from an average value of 1 G_0. This is expected from a strong chemical bonding and thus strong overlap between the nanotube and the surface states, which facilitates the electron propagation from one lead to the other. The nanotube is finite and thus has a discrete spectrum. The molecular levels turn into resonances due to the interaction with the surface. After an eigenchannel analysis, we have found that the resonances widen significantly (of the order of tenths of eV) yielding an overall constant transmission. Our result resembles previous calculations of nanotubes immersed in a jellium slab intended to simulate the experiments of nanotube dipping in mercury[30]. There, it was argued that only the π^* channel is responsible for the electron transport at E_F, after the π channel is pushed down below the Fermi level.

Regarding the NC, the quantum transmission, Fig. 3(b), presents a series of discrete peaks, most of them of transmission equal to one. In the inset we present the eigenchannel decomposition for energies close to the Fermi level, E_F. The main contribution to the conductance at E_F comes from a resonance of a maximum transmission equal to 1 at $E = E_F + 0.027\ eV$ and two features of lower transmission. The peak shape of the main feature are fit almost perfectly by Lorentzian shapes with half width of $\sim 0.08\ eV$. This indicates a relatively

weak interaction between the states at the nanotube and the electrodes and corresponds to a regime of resonant tunneling. Other peaks are present with the same half width indicating that nanotube states interact mainly with broad bands of *sp* character in the gold surface. The separation of the peaks is related to the size of the nanotube as indicated in tight binding calculations of similar structures[31]. An estimation with a 1D particle-in-a-box model reproduces well our calculated average energy separation between the peaks. The nature of the resonant states in finite nanotubes were reported in Ref. 23. For instance, in Fig. 4 we plot the local density of transmitted states at one of the resonance peaks which reproduces closely one of the states reported there.

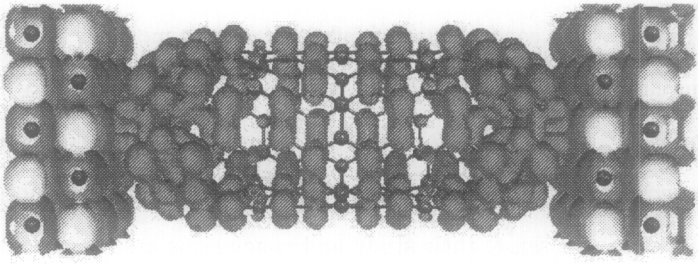

FIG. 4. Isosurface of the local density of states at the resonance energy, $E = E_F + 0.027\ eV$, for the NC configuration.

In the SC, Fig. 3(c), the behaviour is qualitatively similar to the NC. Nevertheless, the transmission shows more resonant features in this case. The spatial distribution of the states in the nanotube is analogous to the NC. In fact, the nanotube states do not have a prefect transmission and similar half-width in contrast to the previous case. The half-width is larger than previous estimates using non-self consistent simplified models[32]. The peak distribution is more irregular and the resistance at the Fermi level is larger. As mentioned above, the electrons have

a low momentum in the tunneling direction. This makes the nanotube-surface scattering more sensitive to the precise details of carbon-gold interface structure such as disorder, roughness, defects and dependent on the contact length. This observation readily connects with the observation of reduction of contact resistance by electron irradiation[28]. In particular, the microscopic details of the relationship between the creation of defects or disorder and resistance still remain unclear. Whether a large disorder is required or the creation of defects in the nanotube and/or electrodes strengthens the bonding and thus reduces the tunneling barriers are still open questions. These issues are beyond the illustrative scope of this paper, and we are currently investigating them.

Finally, it has come to our knowledge that Bernholc and coworkers[33] have recently analyzed the conductance of infinite carbon nanotubes in contact with aluminum electrodes. They considered side contacts of different nature. However, Bernholc et al. investigate the effect of the metallic electrodes on the intratube conductance, while in this study we consider the metal-nanotube-metal conductance. In this sense, their study and conclusions are consistent with and complementary to ours.

IV. CONCLUSIONS

We have presented our method for the calculation of nonequilibrium electron transport properties in nanostructures based on Density Functional Theory. The method treats the atomic and electronic degrees of freedom on the same level of accuracy and detail as an analogous equilibrium total energy calculation. It yields information of quantities such as current intensity distributions as well as voltage drops across the system both in the linear and nonlinear transport regimes. In

particular, we have applied our formalism to the analysis of the contacts between metallic carbon nanotubes and gold electrodes. We have considered different geometries which give an overview of different transport modes involved in this system.

ACKNOWLEDGMENTS

We thank Profs. Hans Skriver, J.M. Soler and A.-P. Jauho for fruitful discussions. This work has benefited from the collaboration within, and was partially funded by, the ESF Programme on "Electronic Structure Calculations for Elucidating the Complex Atomistic Behaviour of Solids and Surfaces". We acknowledge support from the Danish Research Councils (M.B. and K.S.), and the Natural Sciences and Engineering Research Council of Canada (NSERC) (J.T.). M.B. has benefited from the European Community - Access to Research Infrastructure action of the Improving Human Potential Programme for a research visit to the ICMAB and CEPBA (Centro Europeo de Paralelismo de Barcelona). J.L.M. and P.O. acknowledge support from the European Union (SATURN IST-1999-10593), the Generalitat de Catalunya (1999 SGR 207), Spain's DGI (BFM2000-1312-C02) and Spain's Fundación Ramón Areces. Part of the calculations were done using the computational facilities of CESCA and CEPBA, coordinated by C^4.

REFERENCES

[1] P. Fulde, *Electron Correlations in Molecules and Solids* (Springer, Berlin Heidelberg, 1995).

[2] P. Hohenberg and W. Kohn, Phys. Rev. **136**, B864 (1964).

[3] W. Kohn and L. J. Sham, Phys. Rev. **140**, A1133 (1965).

[4] W. Kohn, A. D. Becke, and R. G. Parr, J. Phys. Chem. **100**, 12974 (1996).

[5] R. G. Parr and W. Yang, *Density-Functional Theory of Atoms and Molecules* (Oxford University Press, New York, 1989).

[6] D. Sánchez-Portal, P. Ordejón, E. Artacho, and J. M. Soler, Int. Journ. of Quant. Chem. **65**, 453 (1999). J. M. Soler, E. Artacho, J. D. Gale, A. García, J. Junquera, P. Ordejón and D. Sánchez-Portal, J. Phys.: Cond. Mat. **14**, 2745 (2002).

[7] N. Troullier and J. L. Martins, Phys. Rev. B **43**, 1993 (1991).

[8] O. F. Sankey and D. J. Niklewski, Phys. Rev. B **40**, 3979 (1989).

[9] E. Artacho, D. Sánchez-Portal, P. Ordejón, A. García and J. M. Soler, Phys. Stat. Sol. (b) **215**, 809 (1999).

[10] P. Ordejón, Phys. Stat. Sol. (b) **217**, 335 (2000).

[11] P. Ordejón, E. Artacho, R. Cachau, J. Gale, A. García, J. Junquera, J. Kohanoff, M. Machado, D. Sánchez-Portal, J. M. Soler and R. Weht, in *MRS Proc.* (MRS, San Francisco, 2001), Vol. 677, p. AA9.6.1.

[12] M. Brandbyge, N. Kobayashi, and M. Tsukada, Phys. Rev. B **60**, 17064 (1999).

[13] H. Haug and A.-P. Jauho, *Quantum kinetics in transport and optics of semiconductors* (Springer-Verlag, Berlin, 1996).

[14] S. Datta, in *Electronic Transport in Mesoscopic Systems*, edited by H. Ahmed, M. Pepper, and A. Broers (Cambridge University Press, Cambridge, UK, 1995).

[15] J. Taylor, H. Guo, and J. Wang, Phys. Rev. B **63**, 245407 (2001).

[16] M. Brandbyge, J. L. Mozos, P. Ordejón, J. Taylor and K. Stokbro, Phys. Rev. B **65**, 165401 (2002)

[17] M. Büttiker, Y. Imry, R. Landauer, and S. Pinhas, Phys. Rev. B **31**, 6207 (1985).

[18] J. C. Cuevas, A. L. Yeyati, and A. Martín-Rodero, Phys. Rev. Lett. **80**, 1066 (1998).

[19] M. Büttiker, IBM J. Res. Dev. **32**, 63 (1988).

[20] T. Martin and R. Landauer, Phys. Rev. B **45**, 1742 (1992).

[21] M. Brandbyge, M. R. Sørensen, and K. W. Jacobsen, Phys. Rev. B **56**, 14956 (1997).

[22] M. S. Dresselhaus, G. Dresselhaus, and P. C. Eklund, *Science of Fullerenes and Carbon Nanotubes* (Academic Press Inc., San Diego, 1996).

[23] A. Rubio, D. Sánchez-Portal, E. Artacho, P. Ordejón , and J. M. Soler, Phys. Rev. Lett. **82**, 3520 (1999).

[24] S. Frank, P. Poncharal, Z. L. Wang, and W. A. de Heer, Science **280**, 1744 (1998).

[25] S. Tans, M. H. Devoret, H. Dai, A. Thess, R.E. Smalley, L. Georliga and C. Dekker, Nature **386**, 6624 (1997).

[26] S. Tans, R. M. Verschueren and C. Dekker, Nature **393**, 49 (1998).

[27] R. Martel, T. Schmidt, H. Shea, and P. Avouris, Appl. Phys. Lett. **73**, 2447 (1998).

[28] A. Bachtold, M. Henny, C. Terrier, C. Strunk, C. Schonenberger, J.-P. Salvetat, J.-M. Bonard, and L. Forró, Appl. Phys. Lett. **73**, 274 (1998).

[29] J. Tersoff, Appl. Phys. Lett. **74**, 2122 (1999).

[30] H. J. Choi, J. Ihm, Y.-G. Yoon and S. G. Louie, Phys. Rev. B **60**, R14009 (1999).

[31] D. Orlikowski, H. Mehrez, J. Taylor , H. Guo, J. Wang, and C. Roland, Phys. Rev. B **63**, 155412 (2001).

[32] M. Anantram, S. Datta, and Y. Xue, Phys. Rev. B **61**, 14219 (2000).

[33] M. Buongiorno Nardelli, J.-L. Fattebert and J. Bernholc, Phys. Rev. B **64**, 245423 (2001)

Energetics and Chemical Bonding of Lithium Absorbed Carbon Nanotubes

Yi Liu*, Hiroshi Yukawa, and Masahiko Morinaga
Department of Materials Science and Engineering, Graduate School of Engineering, Nagoya University, Nagoya 464-8603, Japan
(Received; December 31, 2001; in final form May 8, 2002)

Abstract

The lithium absorption energy of carbon nanotubes and the nature of local Li-C and C-C chemical bondings have been investigated using first-principles molecular orbital methods. The Li absorption energy was found to be larger outside the nanotube than inside the nanotube when the nanotube diameter is small. However, the Li outside-absorption energy decreases with the nanotube diameter, whereas the Li inside-absorption energy increases. When the nanotube diameter increases beyond approximately 0.824 nm, the Li outside-absorption energy tends to reach a value similar to the Li inside-absorption energy. The absorption of Li both inside and outside carbon nanotubes remains energetically favorable. In addition, the present study reveals the distinctive chemical interactions between Li and C atoms and between C atoms due to the curvature of carbon sheet in Li absorbed carbon nanotubes, which is obviously different from that of Li absorption into graphite.

CONTENTS

Keywords: carbon nanotube; lithium absorption; electronic structure; chemical bonding; molecular orbital method.

* Corresponding author. E-mail address: y.liu@fz-juelich.de

ADVANCES IN QUANTUM CHEMISTRY, VOLUME 42

0065-3276/03 $35.00

1. INTRODUCTION

Various carbonaceous materials, which can be reversibly intercalated with lithium, have been used as the anode for secondary lithium-ion batteries. Graphite is one of these materials because graphite can be intercalated up to one lithium per six carbon atoms to form the so-called first stage graphite intercalation compound (GIC), LiC_6 [1]. However, the theoretical specific capacity of LiC_6 (372 mAh/g) is unsatisfactory to meet the demand for increasingly high-capacity anode materials. For example, cellular phones currently on the market use secondary batteries that have a capacity of approximately 600 mAh/g as a power source. Recently, the ability of single-walled carbon nanotubes (SWNT) to be reversibly intercalated with lithium up to $Li_{1.7}C_6$ (632 mAh/g) has been reported [2]. Moreover, this reversible saturation of Li composition increases to $Li_{2.7}C_6$ (1004 mAh/g) by applying a suitable ball-milling treatment to purified SWNTs [3]. The absorption property of carbon nanotubes is thus of great interest due to their potential energy storage applications.

The mechanism for lithium absorption in carbonaceous materials is known to depend on the carbon type [4]. The absorption sites of lithium are found to be very different among various kinds of carbon. These are schematically illustrated in Fig. 1 and are summarized briefly as follows: the second nearest-neighbor Li sites between every pair of carbon sheets in LiC_6 or graphitic carbon (site A) [4]; the nearest-neighbor Li sites to form covalent Li_2 molecules in disordered carbon (site B) [5]; the Li sites absorbed on both sides of carbon layers to form lithium metallic clusters in materials that are formed predominantly of single

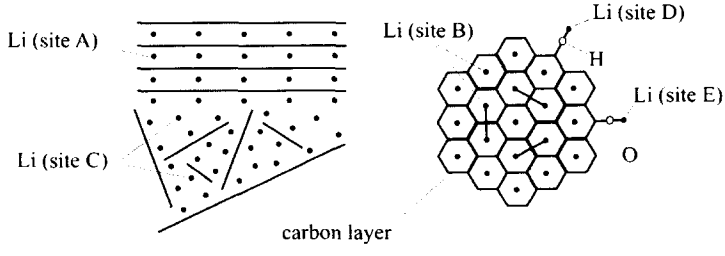

Fig 1. Schematic diagram of possible Li absorption sites in carbonaceous materials as proposed in Ref. 4-7 [4-7].

carbon layers and micropores (site C) [4, 6]; the Li sites in the vicinity of the H atoms in the hydrogen-containing carbon (site D) [4]; and the Li sites in the vicinity of the O atoms in the oxygen-containing carbon (site E) [7]. In general, the extra Li absorption sites need to be clarified in order to account for the excess Li storage capacity beyond LiC_6.

At present, the mechanism for high Li storage capacity in SWNTs is not clear. This mechanism may arise from a combination of several of the absorption sites described above. The intercalation of lithium into the inner cores of carbon nanotubes has been proposed [2]. However, this hypothesis is difficult to prove directly from experiments. In the present paper, we investigate primarily the possibility of lithium absorption in both sides of the single carbon sheet in SWNTs in terms of the Li absorption energy. The effect of diameter on the Li absorption energy has been investigated by calculating SWNT (3, 3)-(6, 6) armchair nanotubes having diameters ranging from 0.426 nm to 0.824 nm. Moreover, the characteristics of local chemical bondings between lithium and carbon and between carbon atoms have been investigated in the lithium absorbed carbon nanotubes and graphite. The fundamental difference between the lithium absorption into carbon nanotubes and that into graphite has been discussed by comparing these bonding characteristics with that of lithium intercalated graphite [8, 9].

2. CLUSTER MODELS

A series of cluster models for finite length carbon nanotubes terminated by hydrogen atoms, as shown in Fig. 2, are constructed in order to investigate the electronic structures of pure (3, 3), (4, 4), (5, 5) and (6, 6) SWNT and Li-absorbed nanotubes. The pure nanotube cluster models are shown in Figs. 2 (a)-(d) and (o). In the Li-absorption models, limited numbers of lithium atoms are placed outside, inside and on both sides of the nanotubes in various assumed configurations. For example, in the case of the Li absorbed (6, 6) nanotube clusters, as shown in Figs. 2 (h), (l), (m), (n) and (p), six or twelve Li atoms are placed outside, inside or on both sides of the nanotube. In addition, these Li atoms are assumed to be located above or below the centers of six-membered carbon rings, and to form a circuit around the middle of the nanotube clusters. Such Li arrangements are presumed based on

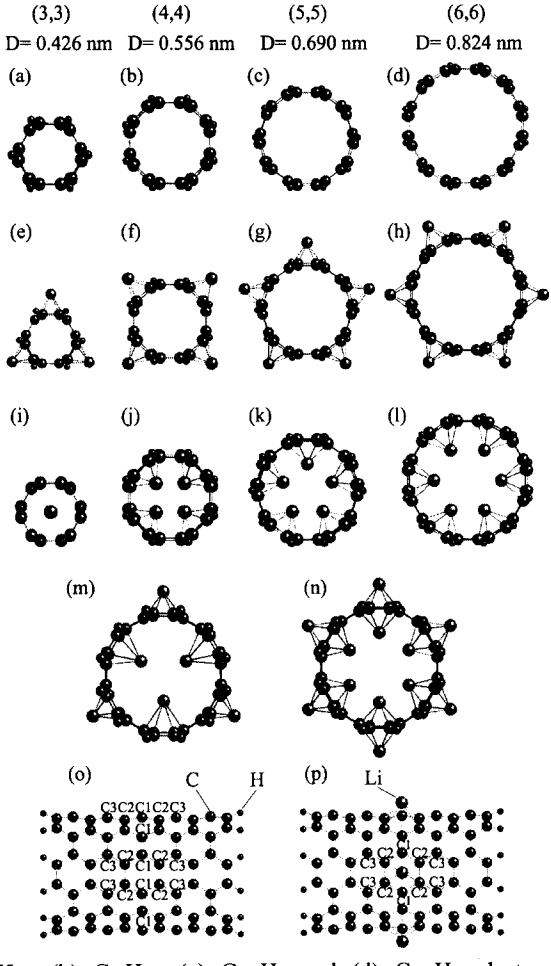

Fig 2. (a) $C_{66}H_{12}$, (b) $C_{88}H_{16}$, (c) $C_{110}H_{20}$ and (d) $C_{132}H_{24}$ cluster models used for calculations of pure (3, 3), (4,4), (5, 5) and (6, 6) SWNTs; (e) $Li_3C_{66}H_{12}$, (f) $Li_4C_{88}H_{16}$, (g) $Li_5C_{110}H_{20}$ and (h) $Li_6C_{132}H_{24}$ cluster models used for Li outside-absorption; (i) $LiC_{66}H_{12}$, (j) $Li_4C_{88}H_{16}$, (k) $Li_5C_{110}H_{20}$ and (l) $Li_6C_{132}H_{24}$ cluster models used for Li inside-absorption; (m) $Li_6C_{132}H_{24}$, (n) $Li_{12}C_{132}H_{24}$ cluster models used for Li inside/outside-absorption in the (6, 6) nanotube. Figures 2 (a)-(n) are top views from the mouth of the nanotube. Figures 2 (o) and (p) are side views for the pure and Li outside-absorbed (6, 6) nanotubes. Three kinds of carbon atoms, denoted by C1, C2 and C3, are shown in these figures.

the lithium occupancy sites in the first stage GIC, LiC_6 [1]. As in the case of the Li absorbed (6, 6) nanotube cluster, three, four or five Li atoms are placed outside the (3, 3), (4, 4) and (5, 5) nanotubes, respectively, as shown in Figs. 2 (e)-(g). In addition, one, four or five Li atoms are inserted inside these nanotubes, as shown in Figs. 2 (i)-(k). The diameter, D, of these nanotubes varies from 0.426 nm to 0.824 nm, and the length of each model nanotube is approximately 1.23 nm. The effect of hydrogen termination in the nanotube mouth is negligible because the optimized nanotube diameter is almost constant at the center. The assumption of hydrogen termination does not affect the later discussion based on the comparison of Li absorption energy inside and outside of nanotubes. In addition, only the local electronic structure of the central atoms in nanotubes is analyzed in present study.

The geometries of the carbon skeletons as well as the positions of absorbed Li atoms are relaxed under D_{nh} (n=3, 4, 5 and 6) symmetry, and their binding energies are obtained by employing the DMol optimization calculation based on the density functional theory (DFT) [10]. The local electronic structure and chemical bonding of these relaxed clusters have been investigated using the DV-X_α molecular orbital method [11]. We selected the DV-X_α method because this method provides faster calculation of bond order. The numerical atomic orbitals of 1s-2p for C and Li and 1s for H are used as the basis functions for these calculations. The bond orders between atoms and the ionicities of constituent elements are calculated following the Mulliken population analyses.

3. CALCULATED RESULTS

3.1 Li absorption energy

The diameter dependence of the binding energy of the carbon nanotube is shown in Fig. 3 (a). The binding energy is set to zero at the pure (3, 3) SWNT, which provides a reference in this figure. The binding energies of both the pure and the Li absorbed nanotubes increases with diameter. The present results for the pure nanotubes agree well with those calculated using the continuum elastic model [12]. According to the continuum elastic model, the binding energy of the pure nanotube is proportional to the square of the

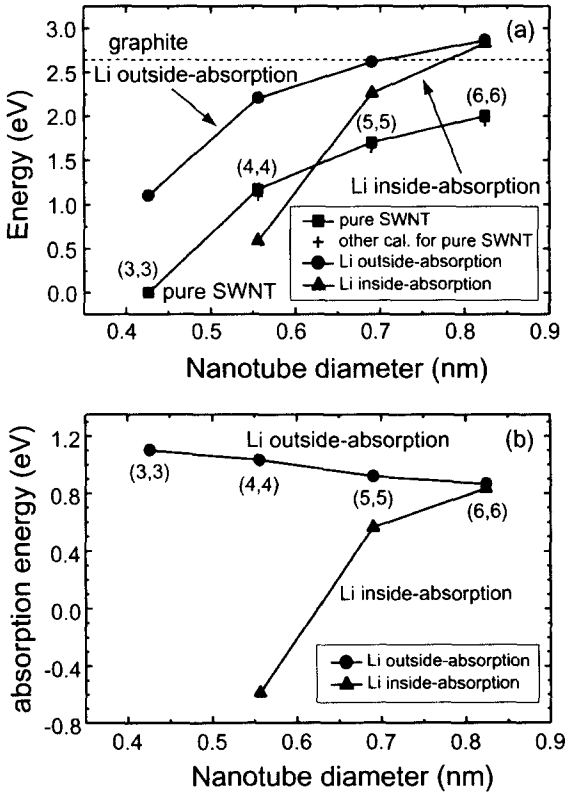

Fig 3. Dependence of (a) binding energies of carbon nanotubes (before and after Li absorption) and (b) Li absorption energy on nanotube diameter. For convenience, the binding energy of the (3, 3) SWNT is set to zero in (a).

nanotube diameter. The present results show that the binding energy of the Li outside-absorbed nanotube increases with diameter in a manner similar to that of the pure nanotube. On the other hand, the binding energy in the Li inside-absorption case increases very abruptly with the diameter. In all of the present calculations, except for the (6, 6) SWNT, the binding energy of the nanotube is larger in the Li outside-absorption case than in the Li inside-absorption case. As the diameter increases, the binding energy converges to the value of graphite in the case of pure nanotubes and converges to the value of LiC_6 in the

case of Li absorbed nanotubes.

The Li absorption energy is defined as the change in total energy due to the Li absorption, which is a measure of the tendency for Li absorption to occur in the carbon nanotube, and is obtained as follows:

$$\begin{aligned} E_{absorption} &= E_{total}(Li_n@C_xH_y) - nE_{total}(Li) - E_{total}(C_xH_y) \\ &= [E_{total}(Li_n@C_xH_y) - nE_{total}(Li) - xE_{total}(C) - yE_{total}(H)] - \\ &\quad [E_{total}(C_xH_y) - xE_{total}(C) - yE_{total}(H)] \\ &= E_{binding}(Li_n@C_xH_y) - E_{binding}(C_xH_y) \end{aligned}$$

Here, $E_{total}(C_xH_y)$, $E_{total}(Li_n@C_xH_y)$, $E_{total}(Li)$, $E_{total}(C)$ and $E_{total}(H)$ are the total energies of the pure nanotubes, the Li absorbed nanotubes and each of the three isolated atom shown, as shown in parentheses, respectively. $E_{binding}(C_xH_y)$ and $E_{binding}(Li_n@C_xH_y)$ are the binding energies of the pure and the Li absorbed nanotubes, respectively. The Li absorption energy is then calculated from the difference in binding energies between the pure and the Li absorbed nanotubes.

As shown in Fig. 3 (b), the Li outside-absorption energy decreases with nanotube diameter, whereas the Li inside-absorption energy increases. The Li outside-absorption energy is larger than the Li inside-absorption energy so long as the nanotube diameter is less than approximately 0.8 nm. However, the difference between these absorption energies decreases as the nanotube diameter increases. Both of the Li absorption energies tend toward a similar value for the (6, 6) SWNT having a diameter of 0.824 nm. As shown in Table 1, the Li outside-absorption energy in the (6, 6) nanotube is 0.87 eV, only 0.04 eV larger than the Li inside-absorption energy. Carbon nanotubes having diameters of approximately 0.8 nm (or larger) are abundantly found in experimentally synthesized nanotubes. The energetic tendencies of the Li outside-absorption and the Li inside-absorption were assumed to be very similar for the larger nanotubes. In addition, Li absorption may not occur inside the (4, 4) SWNT having a diameter of 0.556 nm due to the negative binding energy.

In the case of the inside/outside-absorption I model for the (6, 6) nanotube shown in Fig. 2 (m), three Li atoms are placed separately on both sides of the nanotube. The total number of Li atoms is six, the same as that in the outside-absorption model shown in Fig. 2 (h) and in the inside-absorption model shown in Fig. 2 (l). The absorption energy of the

Table 1. Li absorption energy for various Li absorption models in the (6, 6) nanotube.

	Li absorption model	Li absorption energy (eV/Li atom)
(6,6)	Li inside-absorption	0.83
	Li outside-absorption	0.87
	Li inside/outside-absorption I	1.04
	Li inside/outside-absorption II	0.69

inside/outside-absorption I model shown in Fig. 2 (m) is 1.04 eV, as shown in Table 1, indicating that the Li atom will more preferably locate at either side, rather than exclusively on the inside or outside if the number of absorbed Li atoms does not change. On the other hand, in case of the inside/outside-absorption II model for the (6, 6) nanotube shown in Fig. 2 (n), six Li atoms are located separately on both the sides of the nanotube. The absorption energy is 0.69 eV, which is approximately 0.14 eV less than the Li inside-absorption energy. Thus, when a large number of Li atoms occupy both sides of the nanotube, the absorption energy per Li atom decreases. This may occur due to the repulsive coulomb interaction between Li atoms at high concentration. This result is in agreement with the results of the experiment in which the Li electrochemical potential decreases during Li intercalation into SWNT [2].

3.2 Li-C chemical bonding

The changes in the effective charges of Li and C atoms and the Li-C bond lengths with respect to nanotube diameter are shown in Figs. 4 (a) and (b), respectively. These results are obtained for the Li outside-absorption case. The Li-C bonds have two lengths, which are denoted as long Li-C1 and short Li-C2 in the insert of Fig. 4, due to the curvature of the carbon sheet in the nanotubes. The calculated bond orders between Li and C atoms are nearly zero, which indicates that little covalent interaction occurs between these atoms. Most of the 2s electrons of the lithium atom move to the carbon atom, thus the ionic chemical interaction operates primarily between Li and C atoms. The nearer C2 atoms were observed to have fairly large negative charges, whereas the farther C1 atoms have small negative charges, which indicates that the ionic interaction is much stronger between Li and

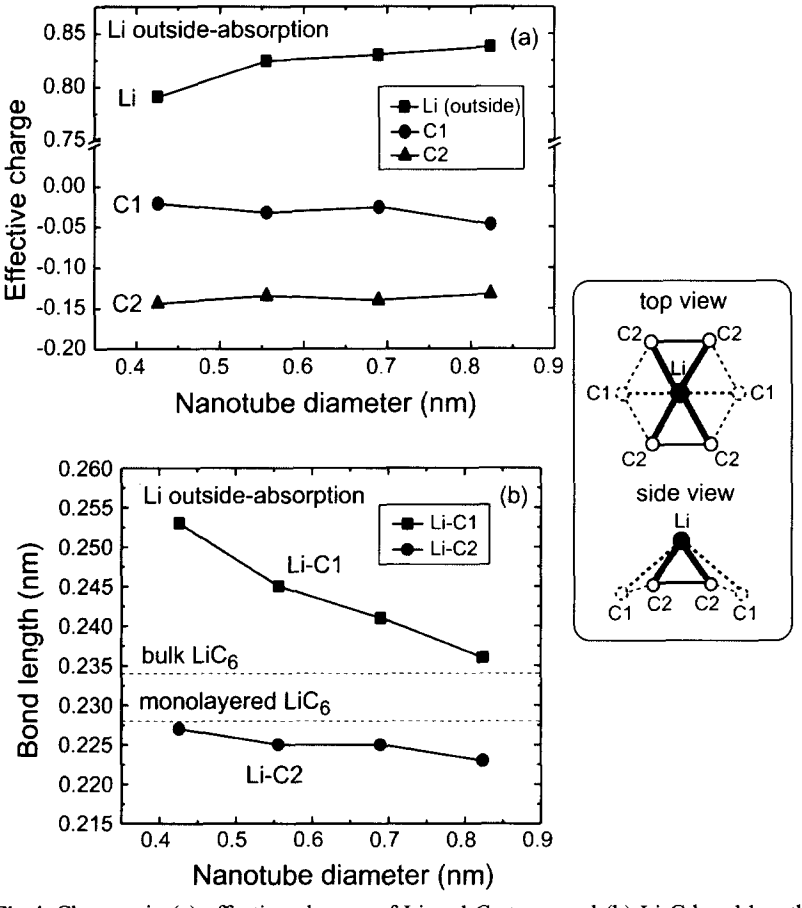

Fig 4. Changes in (a) effective charges of Li and C atoms and (b) Li-C bond lengths with respect to nanotube diameter. The insert illustrates the positions of Li, C1 and C2 atoms, which are also given in Fig 2.

C2 atoms than between Li and C1 atoms. On the other hand, all of the Li-C bond lengths in Li intercalated graphite, LiC_6, are identical due to the flat carbon sheet in graphite. Thus all of the carbon atoms should have identical negative charges and identical ionic interactions with lithium in the LiC_6.

As shown in Fig. 4 (b), the Li-C2 bonds in nanotubes maintain a length similar to that of the Li-C bond in the flat monolayered LiC_6. Here, the flat monolayered LiC_6 is a hypothetical model having one flat carbon sheet above (or below) which Li atoms are arranged following the structure of LiC_6 [1]. The Li-C1 bond is longer than the Li-C2 bond, but its length decreases with the nanotube diameter and may converge to the Li-C bond length in the flat monolayered LiC_6. Moreover, as shown in Fig. 4 (a), the effective charge of Li increases slightly with the nanotube diameter. Therefore, the Li-C ionic interaction probably becomes stronger when Li is absorbed into larger nanotubes.

3.3 C-C chemical bonding

The change in the bond order and the bond length between carbon atoms with respect to the nanotube diameter are shown in Figs. 5 (a) and (b), respectively. The results denoted by open symbols are those for pure nanotubes and the results denoted by solid symbols are those for the Li outside-absorbed nanotubes. Both the C1-C2 and C2-C2 bond lengths are elongated, and hence their bond strengths are weakened due to the Li outside-absorption into the nanotubes. However, the C1-C1 bond length is shortened, and the bond strength is enhanced by the Li absorption. In addition, the bond orders between carbon atoms increase with the nanotube diameter.

For comparison, we investigated the Li absorption into the hypothetical monolayered graphite. The results of this investigation show that the bond order of the nearest neighbor C1-C2 bond in graphite decreases from 1.00 to 0.59 due to the Li absorption. In addition, the bond order of the second nearest neighbor C1-C1 bond (or the C2-C3 bond) decreases from 0.86 to 0.54 after the Li absorption. That is to say, all of the C-C bonds in graphite are elongated and weakened due to the Li absorption, which is in contrast with the result for single-walled nanotubes.

3.4 Charge density

The contour maps of charge density in the central section are shown in Figs. 6 (a)-(e) for pure and Li-absorbed (6, 6) carbon nanotubes. The charge densities between C atoms are fairly large, but the charge densities between Li and C1 atoms are rather small. This indicates again that the C-C bonding has a covalent nature, whereas the Li-C bonding has

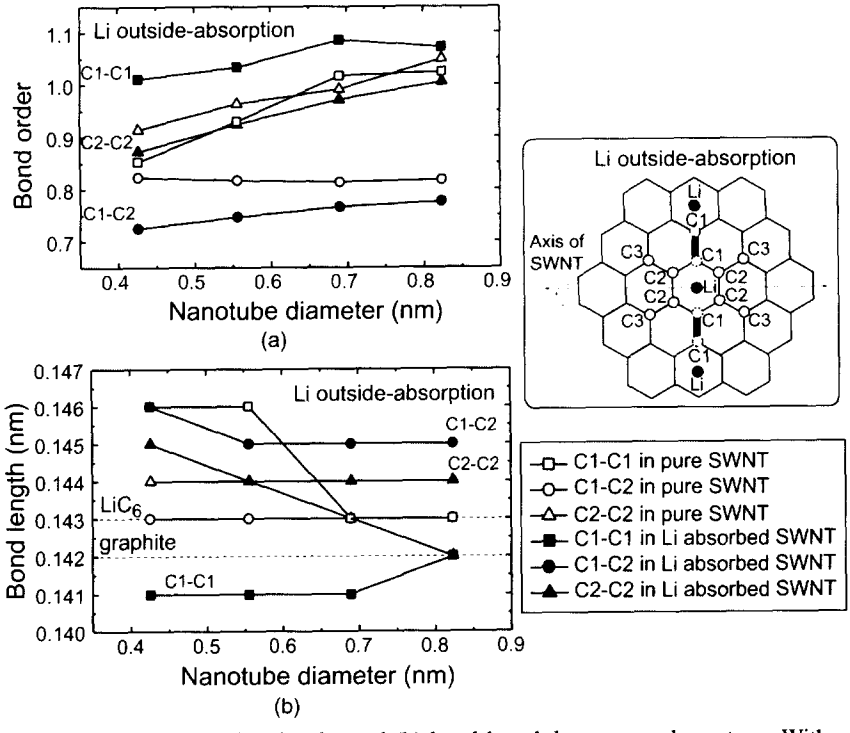

Fig 5. Changes in (a) bond order and (b) bond length between carbon atoms With respect to nanotube diameters. The insert illustrates the positions of Li, C1, C2 and C3 atoms, which are also given in Fig 2.

an ionic nature. Moreover, the charge densities between Li and C1 atoms are larger in the Li inside-absorption case than in the Li outside-absorption case. A similar result is obtained for the Li inside/outside-absorption II model. This may occur since the Li-C1 bond length is shorter in the Li inside-absorption case than in the Li outside-absorption case due to the curvature of the carbon sheet in the nanotube. This infers that the Li-C1 ionic interaction is stronger outside the nanotubes than inside the nanotubes. In the Li inside/outside-absorption I model, the charge density between Li and C1 atoms is less inside the nanotube than outside the nanotube. This may be related to the less repulsive coulomb interaction due to the low Li concentration inside the nanotube in this model.

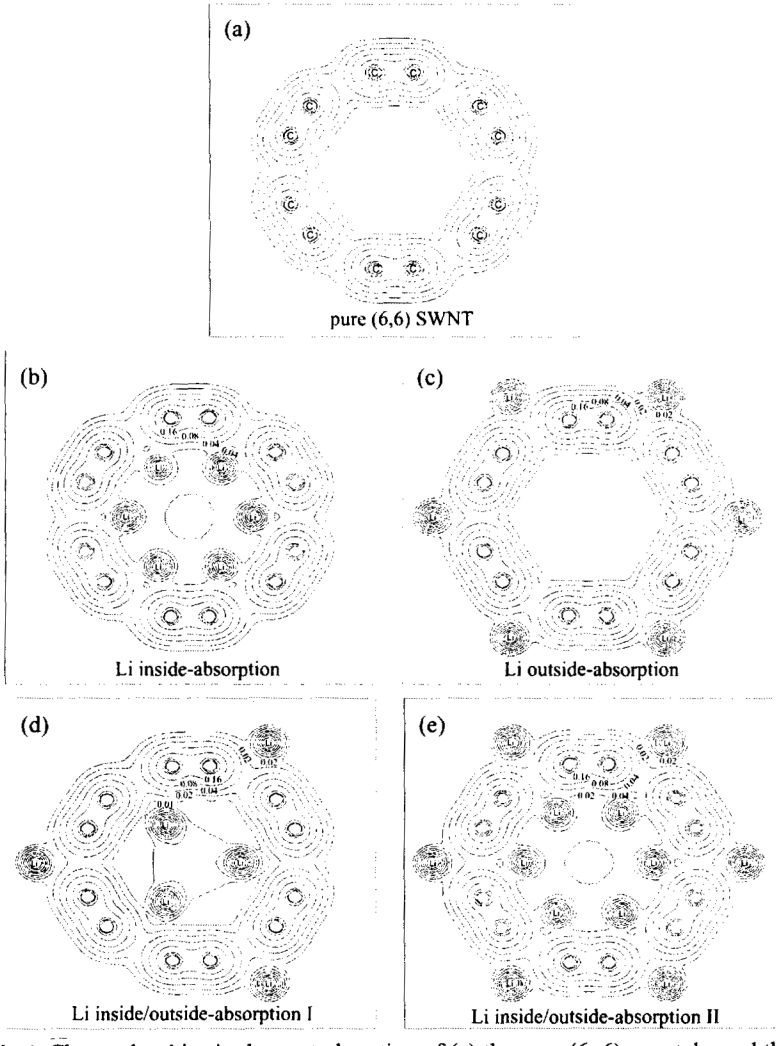

Fig 6. Charge densities in the central section of (a) the pure (6, 6) nanotube and the Li absorbed (6, 6) nanotubes for (b) the Li inside-absorption model; (c) the Li outside-absorption model; (d) the Li inside/outside-absorption I model; and (e) the Li inside/outside-absorption II model. The charge densities increase gradually in steps of 0.01, 0.02, 0.04, 0.08, 0.16, 0.32, 0.64, 1.28 e/(a.u.)^3.

4. DISCUSSION

Based on chemical bonding analyses, both the Li-C ionic interaction and the C-C covalent interaction become stronger with increasing nanotube diameter. This is helpful in understanding why the binding energies of the pure and the Li absorbed nanotubes increase with nanotube diameter. However, the result that the Li outside-absorption energy is large in the small nanotube, despite the Li-C ionic interaction being weak, is unexpected. Thus, the change in the C-C covalent interaction due to Li absorption should be considered. In fact, as described earlier, the positive contribution from the strengthening C1-C1 bonds is fairly large in small nanotubes, which may result in the large Li absorption energy. Such a contribution to the Li outside-absorption energy decreases with the nanotube diameter. In graphite, since no strengthening C-C bonds exist, the Li absorption energy of graphite is expected to be lower than that of carbon nanotube. On the other hand, in small nanotubes, the Li inside-absorption appears to be more difficult than the Li outside-absorption, and even becomes energetically unfavorable in nanotubes smaller than the (4, 4) nanotube having a diameter of 0.556 nm. Since the lithium absorption is a kinetic process, the lithium diffusion path should also be considered in order to fully understand the Li absorption process, although this is not the aim of the present study.

The changes in the Li-C and C-C chemical bondings due to the Li absorption into graphite and carbon nanotubes are illustrated schematically in Fig. 7. In these figures, the strengthening bonds and the weakening bonds due to the Li absorption are illustrated using solid lines and dotted lines, respectively. Figure 7 (a) shows that the same Li-C ionic interactions occur during the Li absorption into graphite because of non-difference in the bond length between Li-C1 and Li-C2. In addition, the Li absorption into graphite weakens all bonds between carbon atoms. However, this is not the case in the carbon nanotube. For example, when lithium is absorbed outside the armchair carbon nanotube (Fig. 7(b)), the C1-C1 bonds which bridge the two neighboring six-membered carbon rings onto which Li is absorbed, become stronger due to the shortened bond length. The strength of the C1-C2 and C2-C3 bonds, however, becomes weaker due to the bond elongation, as is the case for graphite. The distribution and the number of these strengthening C-C bonds vary with the carbon nanotube structure (e.g., (n, n) armchair type, (n, m) zigzag type, etc.) and Li

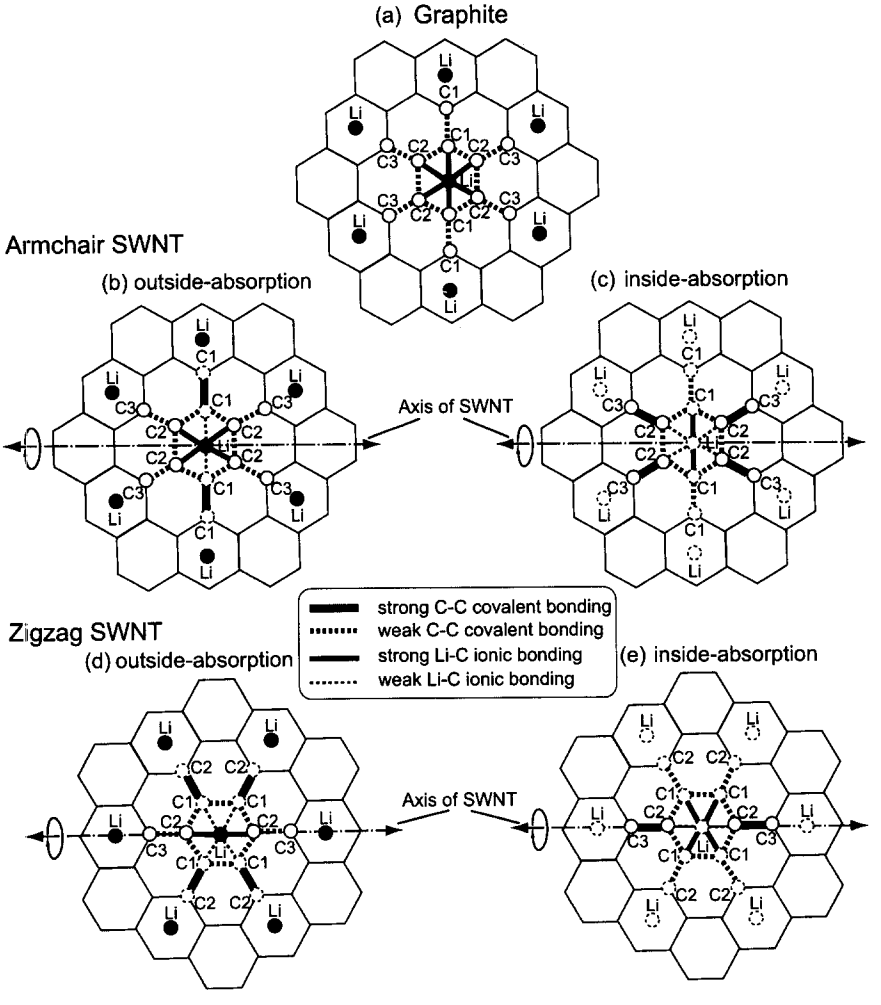

Fig 7. Schematic illustration of showing changes in the Li-C and C-C chemical bondings due to (a) Li absorption into graphite; (b) Li outside-absorption into the armchair nanotube; (c) Li inside-absorption into the armchair nanotube; (d) Li outside-absorption into the zigzag nanotube; and (e) Li inside-absorption into the zigzag nanotube.

absorption sites (outside or inside). Several possible patterns of the Li-C and C-C chemical bondings in Li absorbed carbon nanotubes are proposed based on the calculation results. These are illustrated in Figs. 7 (b)-(e).

5. CONCLUSION

The dependencies of the Li absorption energy on both the diameter of the carbon nanotube and the Li absorption site (outside or inside nanotubes) was investigated by combining first-principles DMol and DV-X techniques. The Li outside-absorption energy was found to decrease with the nanotube diameter, whereas the Li inside-absorption energy was found to increase with the nanotube diameter. The Li outside-absorption is energetically more favorable than the Li inside-absorption in small carbon nanotubes. However, the Li outside-absorption tends to have a Li absorption energy similar to that of the Li inside-absorption when the nanotube diameter increases beyond approximately 0.824 nm. The Li absorption both inside and outside of nanotubes were proven to remain energetically favorable, although the absorption tendency is weak compared to that of single-side Li absorption.

The unique adjustment of both weakening and strengthening C-C bonds is characteristic of the Li absorption into carbon nanotubes. The arrangement of the strengthening C-C bonds depends on the structure of nanotubes and the Li absorption sites. The strengthening effect of the C-C bond adjustment contributes to the high Li absorption energy in nanotubes and is more prominent in small nanotubes. Graphite, however, in that every C-C bond is weakened evenly by the Li absorption into graphite, as observed in LiC_6. A fundamental understanding of the Li absorption into carbon nanotubes is beneficial in the search for more advanced carbon materials which can be used as anodes for secondary Li-ion batteries.

ACKNOWLEDGEMENTS

The authors would like thank the Computer Center of the Institute for Molecular Science, at the Okazaki National Institute, for the use of their supercomputer and Venture Business Laboratory, at Nagoya University, for the use of their DMol code. This research was supported in part by a grant-in-aid for Scientific Research from Ministry of Education, Culture, Sports, Science and Technology of Japan. One of the authors (Yi Liu) would like to thank the Japan Society for the Promotion of Science (JSPS) for its generous financial support of this study.

REFERENCES

(1) D. Guerard and A. Herold, Carbon, 13, 337 (1975).
(2) B. Gao, A. Kleinhammes, X. P. Tang, C. Bower, L. Fleming, Y. Wu and O. Zhou, Chemical Physics Letters, 307, 153 (1999).
(3) B. Gao, C. Bower, J. D. Lorentzen, L. Fleming, A. Kleinhammes, X. P. Tang, L. E. McNeil, Y. Wu and O. Zhou, Chemical Physics Letters, 327, 69 (2000).
(4) J. R. Dahn, T. Zheng, Y. Liu and J. S. Xue, Science, 270, 590 (1995).
(5) K. Sato, M. Noguchi, A. Demachi, N. Oki and M. Endo, Science, 264, 556 (1994).
(6) M. Ishikawa, N. Sonobe, H. Chuman and T. Iwasaki, *35th Battery Symposium in Japan*, p.49, Nagoya, Japan, Nov. 14-16, (1994).
(7) E. Frackowiak, S. Gautier, H. Gaucher, S. Bonnamy and F. Beguin, Carbon, 37, 61 (1999).
(8) Y. Liu, H. Yukawa and M. Morinaga, *International Symposium on Nanocarbons 2001*, p. 149, Nagano, Japan, Nov. 14-16, (2001).
(9) Y. Liu, H. Yukawa and M. Morinaga, *XI Workshop on Computational Materials Science (CMS2001)*, p. 23, Villasimius, Italy, Sep. 17-23, (2001).
(10) DMol 96.0/4.0.0 User guide, San Diego: Molecular Simulations (1996).
(11) H. Adachi, M. Tsukada and C. Satoko, J. Phys. Soc. Jpn., 45, 875 (1978).
(12) D. H. Robertson, D. W. Brenner, and J. W. Mintmire, Phys. Rev. B, 45, 12592 (1992).

Interpreting Auger spectra in cluster approximation

László Kövér

Institute of Nuclear Research of the Hungarian Academy of Sciences
P.O. Box 51, H-4001 Debrecen, Hungary

(Received: June 7, 2002; in final form June 22, 2002)

Abstract

Following a brief review of the Auger process including effects of molecular and solid environment on Auger spectra, the Auger decay from excited (multihole) states is discussed. Illustrating applications and possibilities for interpreting Auger spectra by the help of cluster models, case studies are presented involving determination of charge transfer in binary alloys, sampling unoccupied density of electronic states from Auger satellite analysis and from resonant Auger spectra, and describing multiplet structure of deep core transitions.

CONTENTS

1. INTRODUCTION

In a solid environment, the creation of a vacancy in the atomic core induces a response of the system resulting in changes in the core potential, in the valence charge and in the distribution outside of the atom with the core hole [1]. The decay of the core hole can proceed either via an emission of an X-ray photon or through an emission of an Auger electron. In the case of photoionization, the initial state of the process includes the exciting photon and the neutral atom inside the solid, while the final state includes the photoelectron emitted upon photoionization, the doubly ionized atom with two vacancies in its outer shell and the Auger electron emitted during the decay of the core hole. The final state holes in solids can appear in the valence and conduction bands as well and they can be delocalized or localized around the initial core hole. By the two electron nature of the Auger process, Auger spectra carry information on electron correlation and on

ADVANCES IN QUANTUM CHEMISTRY, VOLUME 42

0065-3276/03 $35.00

the electronic structure surrounding the atom (with the initial core hole) of a given element – in a particular position or chemical state – in a solid material. This local electronic structure is determining for the mechanical, electronic, magnetic, optical and chemical character of the given material. Information on the local electronic structure is crucial in designing materials with novel properties. In the innovation of new materials, the Localized Quantum Structure, i.e. the electronic states and chemical bonding at special locations in solids (e.g. grain boundary, impurity, atom vacancy) has been proved to be a key concept [2], leading to a rapid progress in materials science and nanotechnology.

X-ray induced Auger and core photoelectron spectra, emitted from surface and interface layers of solids, provide rich and unique details on the local electronic structure. Recent developments of electron spectroscopy and theoretical models describing materials have led to a leap in understanding the effects of atomic environment on processes and structures reflected in the electron spectra [3,4].

Studies of deep core transitions offer a number of advantages:

- The core potential model is assumed to be valid in the deep core region, i.e. due to changes in the valence charge similar shifts of the electron binding energies are expected, the validity of the core potential model is important in estimating charge transfer from environmentally induced shifts in Auger parameters (in differences of the kinetic energies of core Auger lines and of the respective photoelectron lines) in the case of binary alloys [4].
- Various effects due to the solid environment are amplified (e.g. resulting in larger energy separations between structures – environmentally shifted Auger peaks and satellites – in the spectra).
- Easier interpretation of the less complex spectra at near threshold excitation (e.g. the intensity of the satellites appearing as a consequence of initial state – shake – excitations becomes small or vanish).

2. THE AUGER PROCESS: FROM ATOMIC VIEW TO EFFECTS OF MOLECULAR AND SOLID ENVIRONMENT

Types of Auger process

Fig. 1 shows the main types of the Auger transitions, including Auger decay of excited states. It should be added, that final state angular momentum coupling has an important role in the Auger process, e.g. validity of the coupling models (indicating the dominance of either the electrostatic or the relativistic interaction) can determine the number of the peaks in the KLL Auger spectra [5].

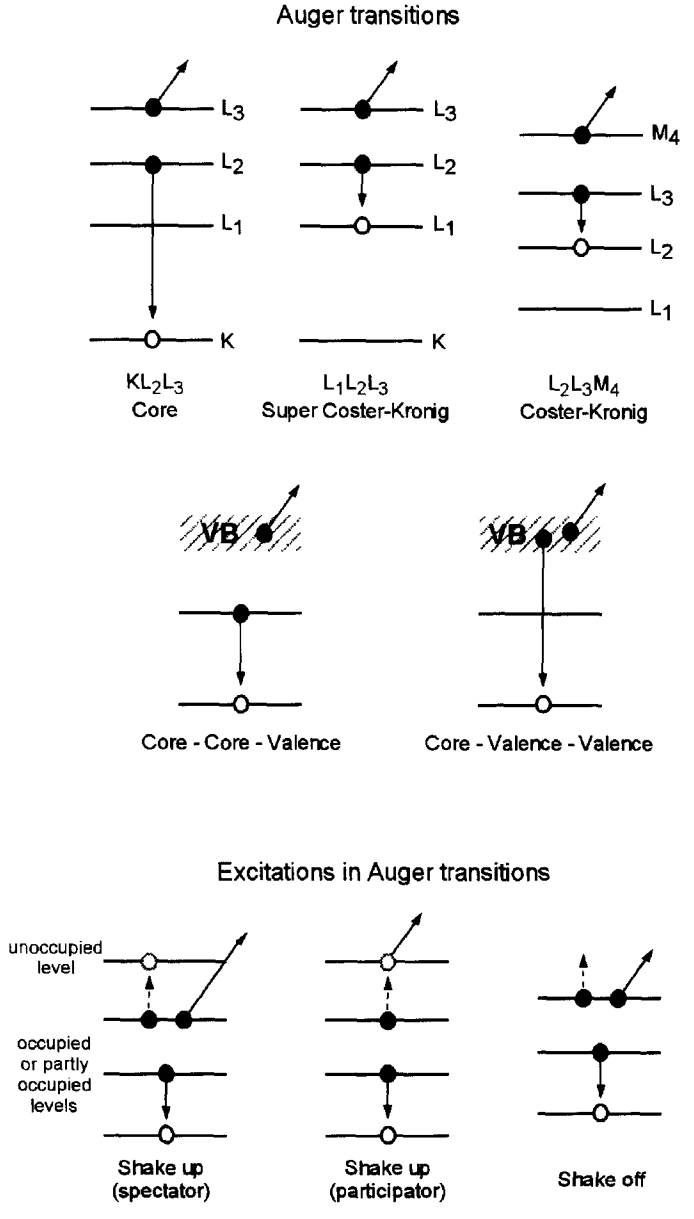

Fig. 1 The main types of the Auger decay of the initial core hole including core and core-valence transitions (upper and middle part) as well as excitations (lower part) during the Auger process.

Auger transition energy and probability

The transition energy $E_{i,j,k}$ of the atomic core Auger process involving the levels i (with the initial vacancy) j and k (with the final state vacancies) can be approximated by:

$$E_{i,j,k} = E_i - E_j - E_k - U_{jk} \quad (1)$$

where E_i, E_j, and E_k are the electron binding energies of the respective electrons in the atom (ground state) and U_{jk} denotes the Coulomb repulsion or correlation energy between the final state holes. For a more correct approximation, further terms accounting for intra-atomic and extra-atomic relaxation effects, should be added to the right side of eq. (1).

For valence shells, the binding energy shifts induced by the atomic environment, can differ noticeable from that observable for core levels. Theoretical values for $E_{i,j,k}$ can be obtained from the difference in total energies of the initial and final states calculated using ab initio methods. The convergence of the total energy calculations in the case of clusters, however, often difficult to be achieved [6]. Applying the so called Slater's transition method [7] (Fig. 2) for Auger decay [8], correlation effects can also be accounted for and in many cases a good approximation is provided. Estimating Auger transition energies accurately, multiplet structures should also be considered [5,9].

The probability of the *ijk* Auger transition in the simplest, frozen core independent particle approximation with the Wentzel Ansatz approach is expressed as [6]:

$$I_{ijk} = \left| < \Psi_f(i\varepsilon) \left| e^2 / r_{12} \right| \Psi_i(jk) > \right|^2 \quad (2)$$

where ε is the energy of the ejected Auger electron, e^2/r_{12} is the Coulomb interaction between the two electrons involved in the transition, $\Psi_i(jk)$ and $\Psi_f(i\varepsilon)$ are the wave functions of the initial and final states, respectively. This simple picture reflects the highly local character of the Auger process. Different hybridizations between the initial state with the core hole and the Auger final state can result in a satellite structure of the Auger spectra which is dependent on the atomic environment.

Core Auger parameters

From the differences in the measured Auger kinetic energies and the related binding energies between two atomic environments surrounding the atom with the initial state core hole, the Auger parameter shifts can be obtained using the definition [10]:

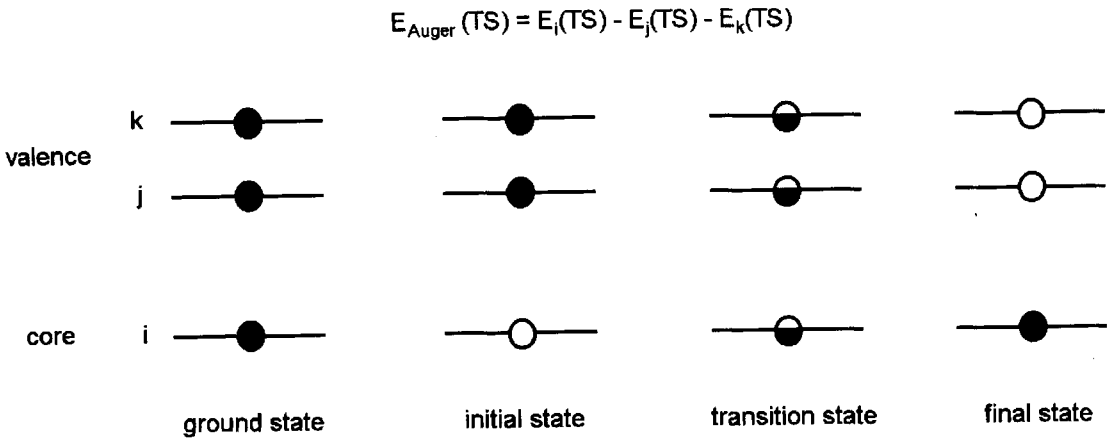

Fig. 2. The transition state (TS) concept for the Auger process

(E_{Auger} (TS), E_i (TS), E_j (TS), E_k(TS) are the Auger kinetic energy and the binding energies of the i,j,k atomic levels involved in the Auger transition, calculated in the transition state.)

$$\Delta\xi(j) = \Delta E_k(ijj) - \Delta E_b(i) + 2\Delta E_b(j) \tag{3}$$

where $\Delta E_k(ijj)$ is the environmentally induced shift in the kinetic energy of an Auger transition involving the i and j core levels and ΔE_b is the difference in the binding energy of a core level between two atomic environments. If ΔE_b is similar for all core levels (1) corresponds to the conventional definition of the modified Auger parameter shift $\Delta\alpha' = \Delta E_k(ijk) + \Delta E_b(core)$ [11]. In this case $\Delta\xi \cong \Delta\alpha' \cong 2\Delta R^{ea}$ is the environmentally induced change in the final state extra-atomic relaxation energy, R^{ea}. Therefore ξ is called "final state Auger parameter". A different definition for Auger parameter is:

$$\Delta\beta(j) = \Delta E_k(ijj) + \Delta E_b(i) + 2\Delta E_b(j) \approx 2\Delta V \tag{4}$$

where ΔV is the change in the core potential as a consequence of changes in the valence charge. β is called "initial state Auger parameter" reflecting changes in the core potential. For interpreting $\Delta\xi$ using a model based on atomic structure parameters [10]:

$$\Delta\xi = \Delta\left[q(dk/dN) + (k - 2dk/dN)(dq/dN) + (dU/dN)\right] \tag{5}$$

where q is the valence charge, k is the change in the potential in the core when a valence electron is removed, N is the occupancy of the core orbitals and U is the contribution from the atomic environment. Assume k and q depend linearly on N. For two conductors, the efficient screening yields $\Delta(dU/dN) = 0$ and the on-site core hole screening $(dq/dN) = 1$, therefore $\Delta(dq/dN) = 0$, leading to

$$\Delta\xi = \Delta q(dk/dN) \tag{6}$$

for the case when the valence electrons belong to a single band. The parameter dk/dN can be obtained from the results of atomic structure calculations for free atoms [12]. From (6) the charge Δq transferred between two components of a binary alloy, can be derived. Charge transfer among constituent atoms of crystals is very important from the point of view of mechanical and chemical stability and of alloying and surface catalytic processes. This Auger parameter analysis is expected to improve when deep core levels are involved in the Auger transition. Using cluster molecular orbital models, local charges and the ground state local density of electron states (LDOS) can be independently estimated. The transferred charges derived from the Auger parameter analysis can be compared to the charge distribution obtained using cluster MO calculations.

For non-local screening of the core hole the electronic polarizability of the atomic environment determines the relaxation mechanism and the charge transfer process involves spatially extended orbitals. In this case the extra atomic polarization energies and the Auger parameter shifts can be estimated using the electrostatic model of Moretti [13] i.e. interpreting the final state polarization in terms of the electric field generated by the core hole as well as by the induced dipoles.

Assuming same ligands with the same distance R from the core ionised atom and high symmetry, this model gives [14]:

$$\Delta\alpha' = 14.4\, n\alpha / \left(R^4 + RD\alpha\right) \tag{7}$$

where α is the electronic polarizability of the ligand, n is the number of the first neighbours and D is a geometric factor. The generalized electrostatic model [15] uses the matrix representation, leading to:

$$[F_{Li}]\,[D_{ij}] = [F_j] \tag{8}$$

where the $[F_{Li}]$ matrix represents the total electrostatic field $\vec{F}_{Li}$ on ligands i and $[F_j]$ the electrostatic field due to the core hole and $[D_{ij}]$ contains the geometrical parameters and ligand polarizabilities. Solving the corresponding system of linear equations, the total relaxation energy or the final state Auger parameter shift can be derived.

Auger parameter shifts are often utilized in studies of electronic parameters of metal particles deposited on oxides. A recent work introduces a new concept, the "chemical state vector" for systematizing the variation of the Auger parameters determined at metal-oxide interfaces and for describing the changes in the electronic parameters of these systems [16].

Effects of atomic environment on Auger transition probabilities and Auger lineshapes

Core-valence relative Auger intensities can be strongly influenced by a preceding Coster-Kronig transition, the probability of which is strongly dependent on the localization of the valence electron involved [17].

Using atomic Auger transition matrix elements and the model proposed by Ramaker [3] on the basis of the Final State Rule, neglecting configuration mixing, localization and shake, the lineshapes of core-valence Auger spectra of solids can

be described in terms of the local density of electron states (LDOS). When the main components of the valence band are *s* and *p* orbitals, the experimental lineshape *A(E)* for the core-core-valence (CCV) and for the core-valence-valence (CVV) Auger processes can be approached as [3]:

$$A_{ccv}(E) = C_s \rho'_s(E) + C_p \rho'_p(E) \tag{9}$$

and

$$A_{cvv}(E) = C_{ss} R_s^2 \rho_s(E) \otimes \rho_s(E) + C_{sp} R_s R_p \rho_s(E) \otimes \rho_p(E) + C_{pp} R_p^2 \rho_p(E) \otimes \rho_p(E) \tag{10}$$

where $\otimes$ denotes convolution integral, ρ_l (ρ'_l) is the LDOS (screened LDOS) of the final state without (with) the core hole, C_i, C_{ij} denote atomic Auger transition matrix elements normalized per filled shell, and the R_l factors provide the ratio of local charges in the screened initial state to that in the unscreened final state of the CVV process.

In the case of on site final state hole-hole interaction and completely filled bands, correlation effects on CVV Auger lineshapes can be described by the Cini-Sawatzky theory [18]:

$$A_{cvv}(E) \sim \frac{\rho \otimes \rho'(E)}{\left[1 - \Delta U I(E)\right]^2 + \left[\Delta U \pi \rho \otimes \rho'(E)\right]^2} \tag{11}$$

where $I(E) = \int (\rho \otimes \rho(E)/(E-\varepsilon)) d\varepsilon$, and ΔU is the effective hole-hole correlation parameter.

For calculating the respective LDOS distributions for Al (O_h symmetry, a cluster of 19 atoms) and Al-Ni alloys (14 atom cluster, cubic O_h symmetry for $AlNi_3$; 16 atom cluster, orthorombic DO_{20} structure for Al_3Ni) using the DV-Xα cluster molecular orbital model, a good agreement with the experiment was obtained [19, 20].

3. AUGER TRANSITIONS WITH EXCITATIONS IN SOLIDS

Due to the creation of the core hole "intrinsic" excitations (Fig. 1) can take place, as:

- "shake up", where the initial state is a core hole plus an outer shell electron excited into an unoccupied state with the same angular

momentum, then the excited electron either participates ("participator") or doesn't ("spectator") in the Auger process
- "shake off", where the initial state is a core hole plus an outer shell hole plus an electron ejected from the atom
- plasmon(s) can also be excited in certain solids, in this case the initial state is a core hole plus excited plasmon(s)

It should be noted, that in all of the cases listed above, these excitations result in the appearance of satellite lines in the Auger spectra, separated from the main (diagram) Auger lines at their low kinetic energy side. Only in the case of the "participator" type transitions, where the excited electron with excess energy is involved, however, the satellite appear at the higher kinetic energy side. An analogue is the "plasmon gain" satellite, where the energy of the excited plasmon is transferred to the emitted Auger electron, proving the intrinsic nature of the process. For estimating the magnitude of the excitations upon creation of the core hole atomic calculations were performed, showing a change in the share of excitations within the subshell photoionization cross section between 10-20 % [21]. The Manne-Åberg sum rule ensures that in the case of having a high intensity satellite the remaining ones all should have low intensities [22].

Similar ("final state") excitations can occur as a result of the appearance of the second hole in the final state.

In addition, further satellites can be induced in the Auger spectra as a result of "extrinsic" inelastic energy loss processes (plasmon(s) excitations, interband transitions, atomic excitations, ionization) induced by the Auger electron on its way escaping from the surface of the solid.

4. CASE STUDIES

Charge transfer in Cu-noble metal alloys

Table 1 demonstrates the accuracy achieved determining charge transfer in Cu Pd alloy from deep core Auger parameter shifts [23]. The very small charge transfer from the Pd to the Cu site is confirmed by the DV-Xα cluster MO calculations using a cluster of 15 atoms, O_h symmetry and a near minimal basis set.

Table 1.
CuPd Auger parameter shifts (eV) and transferred charges Δq [23]

		Δq(Cu)	Δq(Pd)
Δξ(Cu)	0.03	-0.01	
Δβ(Cu)	-1.30	-0.05 (0.08*; -0.23^{+})	
Δβ(Pd)	0.70		0.05
DV-Xα cluster			
MO theory (g.s.)		-0.03^{++}	0.03^{++}

dk^{Cu}/dN=-3.30* est. err. < | 0.10 | eV k^{Pd}(average)=11*

* R.J. Cole and P. Weightman, in Metallic Alloys: Experimental and Theoretical Perspectives, eds. J.S. Faulkner and R.G. Jordan (Kluwer, 1994)

$^{+}$ R.J. Cole, N.J. Brooks, P. Weightman, S.M. Francis and M. Bowker, Surf. Rev. Lett. **3,** 1763 (1996).

$^{++}$ I. Cserny, private communication

Screening of the core hole in 3d metals Cu and Ni

Figs 3 and 4 show the X-ray excited high resolution KLL Auger spectra obtained from thin (~10 nm thickness) metallic layers of Cu and Ni [24] as measured (a) and following corrections for contribution from electrons scattered inelastically in the sample (b).

Near the main diagram ($^1D_2$) line in the spectra an intense satellite (satellite 2) can be observed in the spectra, its localized intrinsic excitation origin has been indicated earlier [25]. In Table 2 the experimental shake up satellite – main line energy separations are compared to those obtained from atomic and Discrete Variational Xα cluster molecular orbital calculations (using fcc lattice and clusters of 13(43) atoms with lattice constants of 0.361 nm (Cu) and 0.352 nm (Ni), and near minimal basis sets) [26]. As it can be seen from the data, the difference in the energy separations for Cu and Ni can be attributed to different screening of the core hole in the two metals and it is correctly interpreted by the MO calculations using large clusters.

The estimations based on atomic models and the sudden approximation fail to explain the high intensity of the satellites [5], confirming the presence of strong solid state effects.

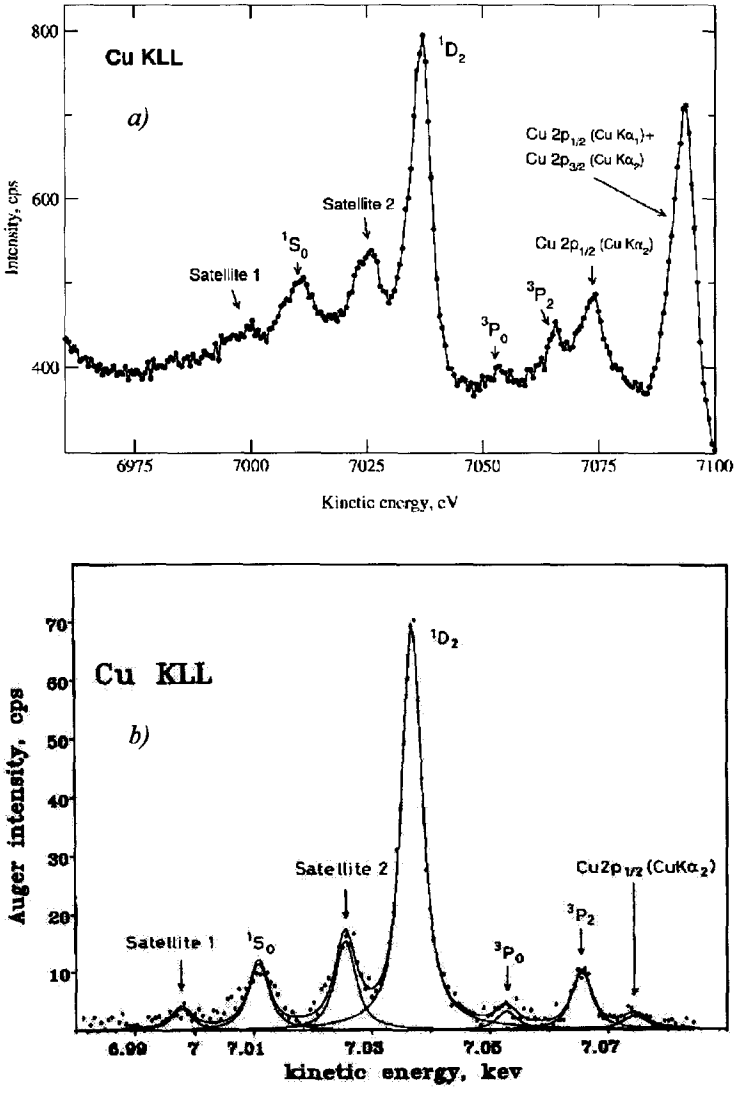

Fig. 3 Experimental Cu KLL spectrum of a metallic Cu layer of ~10 nm thickness, excited by X-rays (a) and the decomposition of the spectrum corrected for inelastic background (b) [24].

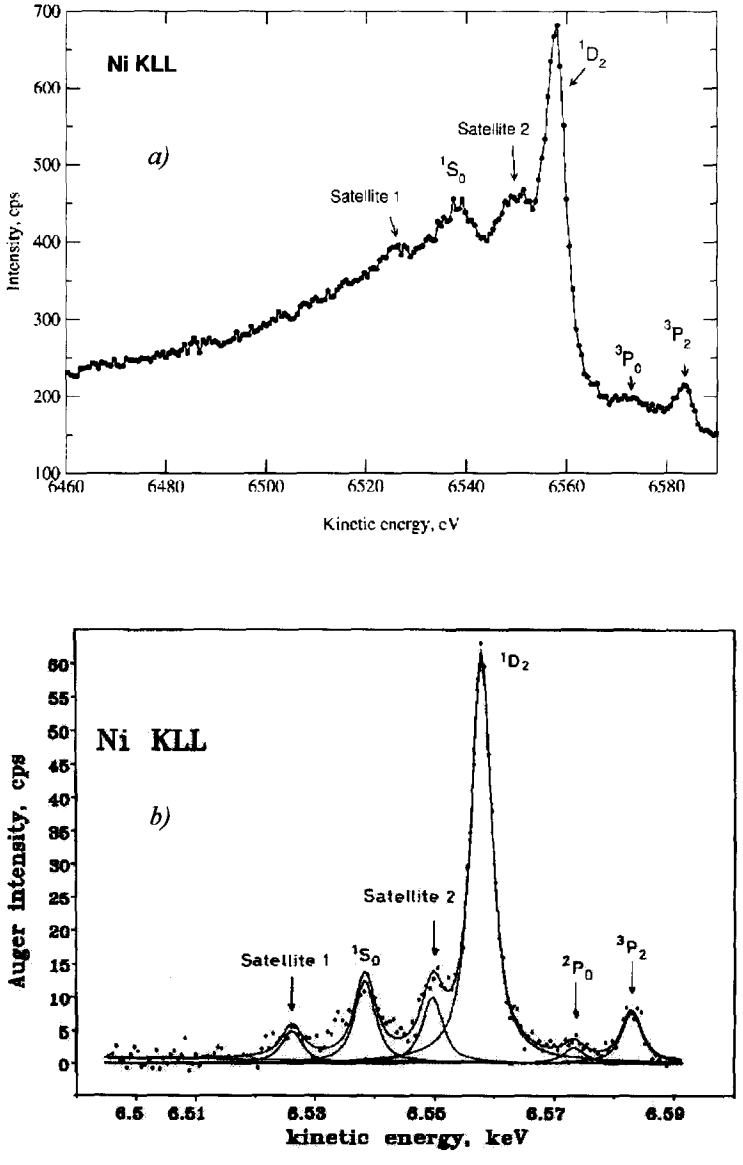

Fig. 4 Experimental Ni KLL spectrum of a metallic Ni layer of ~10 nm thickness, excited by X-rays (a) and the decomposition of the spectrum corrected for inelastic background (b) [24].

Table 2

Energy separation between the satellite 2 and the main Cu and Ni KLL Auger line (eV) [26]

		Atomic Dirac-Fock-Slater model			DV-Xα MO cluster model		
Sample	Exp.	Transition	Unscreened	Screened	Transition	Uncompensated	Compensated
Cu	11.9	$3d_{5/2} \rightarrow 4d_{5/2}$	15.8	10.5	$8e_g \rightarrow 15e_g$	10.9*	10.2
					$8t_{2g} \rightarrow 16t_{2g}$		10.6
Ni	6.4	$3d_{5/2} \rightarrow 4d_{5/2}$	15.4	6.9	$8e_g \rightarrow 15e_g$	5.9*	5.7
					$8t_{2g} \rightarrow 16t_{2g}$		6.4

*22 $e_g \rightarrow 42\ e_g$ excitation, calculated for cluster of 43 atoms

Localization of unoccupied electron states in fluorides

In Fig. 5 the F KLL Auger spectra excited by Cu Lα X-rays from rutile-type fluorides are shown [27]. The satellite denoted by M was earlier identified as a result of a resonant transition between the highest occupied molecular orbital in the ground state and the lowest unoccupied molecular orbital in the K-shell ionized state [28]. Multiplet structure (DV-ME) calculations for the case of polycrystalline KF using a K_6F cluster in octahedral symmetry confirm that multiplet splitting can be excluded as a possible origin of the M satellite [27]. As it can be seen from Figs 5 and 6, the energy broadening of the satellite is strongly dependent on the chemical environment of the fluorine atom [27], while the energy broadenings of the main (diagram) lines are similar. This indicates considerable changes in the density of the unoccupied electronic states and in their localization.

Local excitation of collective electron states in Ge

During the Auger process in a solid collective electron states can be excited as well. In the case of free electron gas materials, the induced plasma oscillations in the bulk are characterized by the plasmon frequency and satellites appear in the core Auger spectra at the energy loss corresponding to the bulk plasmon energy. Surface plasmon satellites can also appear at a somewhat smaller energy loss as a result of collective excitations which are restricted in their spatial extension to the uppermost atomic layer. The plasmon loss features in the photoinduced electron spectra are dependent on the surface nanostructure as well [29].

Fig. 7 shows the high energy resolution Ge KLL spectra excited from amorphous Ge by Cu bremsstrahlung [30], including a very intense satellite near the main ($^1D_2$) Auger line, at the same energy loss as the bulk plasmon energy (the "excited atom" model [31] gives a smaller energy separation for an initial state shake up excitation). Our preliminary results indicate that this plasmon satellite includes a substantial contribution from intrinsic excitation as a consequence of the appearance of the core hole(s).

Core polarization in MnO

In the Mn KLL Auger spectra of MnO an intense "extra peak" was observed earlier with an energy separation of 7.9 eV [32] from the main ($^1D_2$) Auger line, which "extra peak" is missing in the KLL spectra of the metallic Mn sample. Earlier studies reported an exchange energy splitting of ~6 eV for the Mn 3s photoelectron peak in the case of MnO, due to the coupling of the spin of the photoinduced core hole to the spin of the valence orbital [33]. Preliminary calculations using a multiplet structure cluster model [34] confirm that the "extra peak" in the Mn KLL Auger spectra of MnO can probably be attributed to a similar multiplet splitting [35].

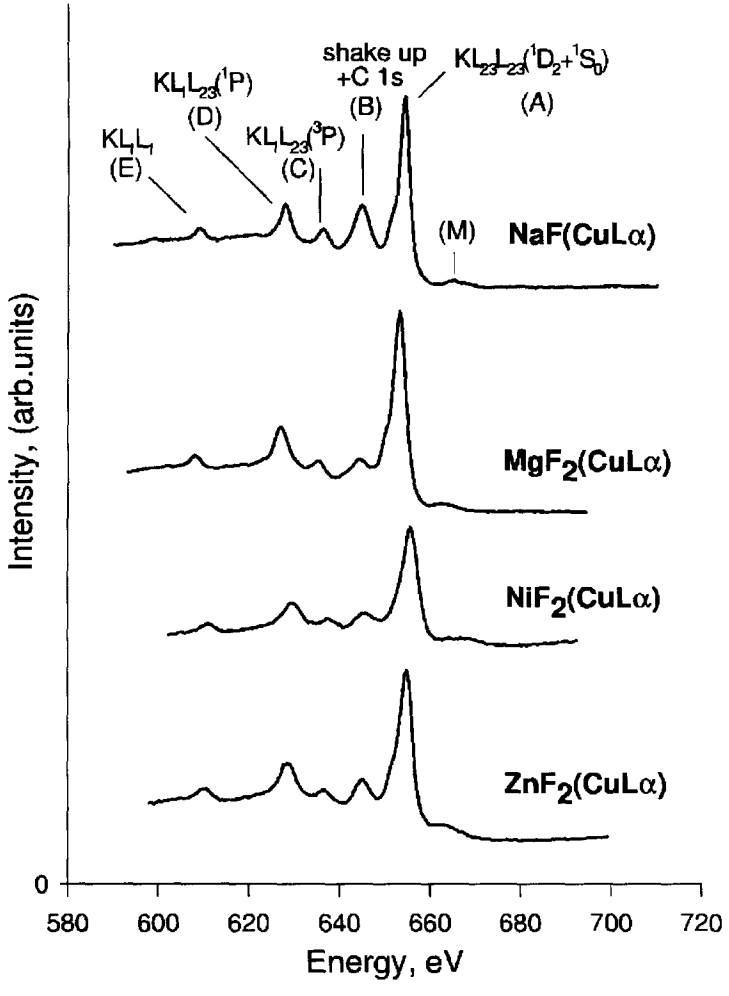

Fig. 5 F KLL Auger spectra excited by Cu Lα X-rays from NaF and rutile type fluorides [27]

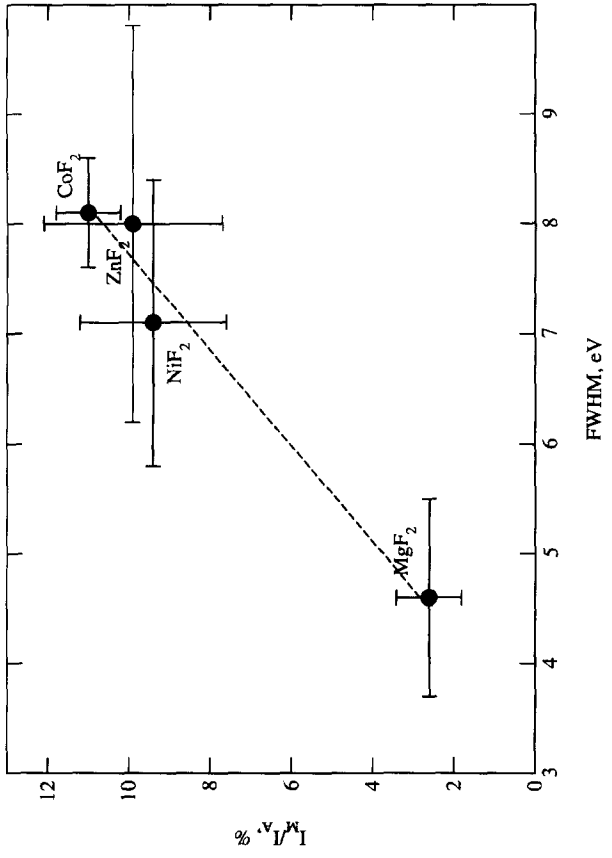

Fig. 6 Intensities of the *M* satellite peaks related to that of the main diagram peak *A* as a function of the energy widths (FWHM) of the satellites in the case of the F KLL spectra of rutile type fluorides [27].

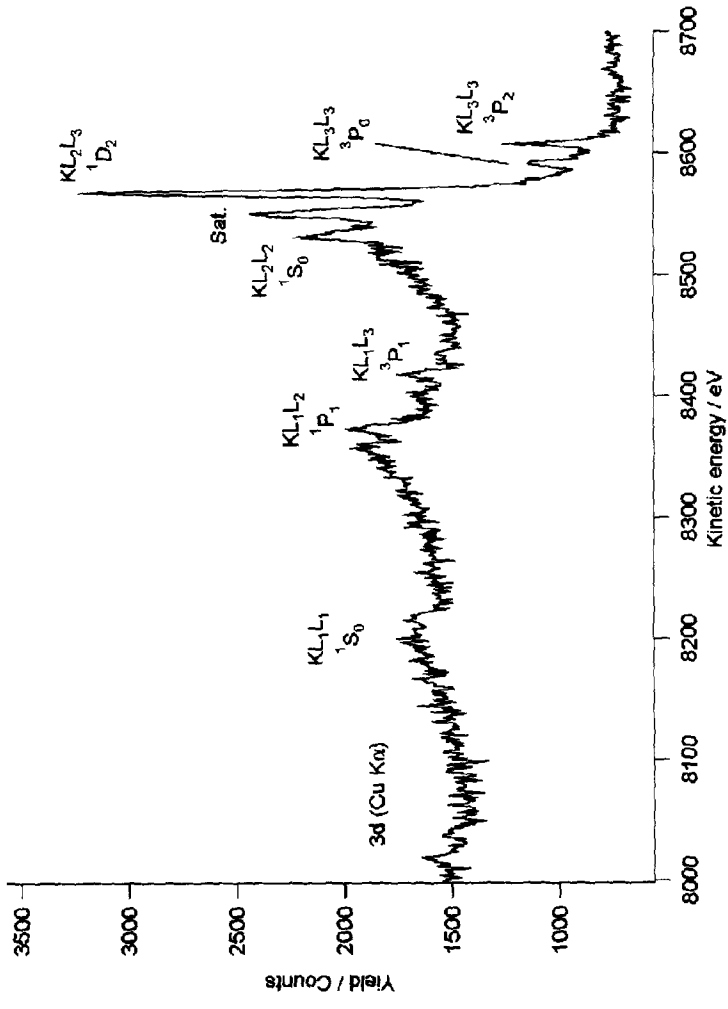

Fig. 7 Ge KLL spectra excited from a Ge layer of 100 nm thickness by Cu X-rays [30].

Resonant excitations in KLL Auger spectra of solids

Using synchrotron radiation, it is possible to set the energy of monochromatic X-rays near to the ionization threshold of a deep core level resonantly exciting an electron from this shell to unoccupied bound states. This resonant photon absorption process can be followed by a resonant Auger emission showing the characteristics of the Auger resonant Raman effect below threshold (a linear dispersion of the Auger peak position with changing photon energy and only partial contributions of the lifetime broadenings to the Auger lineshape) [36]. When the core electron is photoexcited to an unoccupied state, the shape of the Auger peak will be influenced by the density of the unoccupied electron states [37].

Fig. 8 shows the evolution of the Cu KLL spectra photoexcited from metallic Cu using photon energies below the ionization threshold.

The energy distribution $i(\varepsilon_A)$ of the KLL main line ($^1D_2$) Auger electrons ε_A for $\hbar\omega$ exciting photon energy at near threshold energy is from resonant scattering theory [36,37]:

$$i(\varepsilon_A,\hbar\omega)=C\int_0^\infty\int_0^\infty \frac{\rho(\varepsilon)N_{ph}(\hbar\omega-\hbar\omega')d\varepsilon\, d\hbar\omega'}{\left[(\hbar\omega'-\varepsilon-E_K)^2+\Gamma_K^2/4\right]\left[(\hbar\omega'-\varepsilon-\varepsilon_A-E_{L_2L_3})^2+\Gamma_{L_2L_3}/4\right]} \quad (12)$$

where N_{ph} is the photon energy distribution, E_K the K edge position, Γ the lifetime width, ε the photoelectron energy, $\rho(\varepsilon)$ the partial density of the unoccupied states and C is a constant. For the final state, $E_{L_2L_3}$ is obtained from the energy position E_A of the $^1D_2$ line at exciting photon energies well above the threshold since $E_A=E_K-E_{L_2L_3}$. The final state width, $\Gamma_{L_2L_3}$ is obtained from the corresponding single hole lifetime widths.

From (12) it can be seen that the resonant Auger lineshape contains unique information on the local density of the unoccupied electron states around the initial core hole. At the same time the evolution of the shape and intensity of the satellite lines as a function of excitation energy can be very helpful in clarifying their origin.

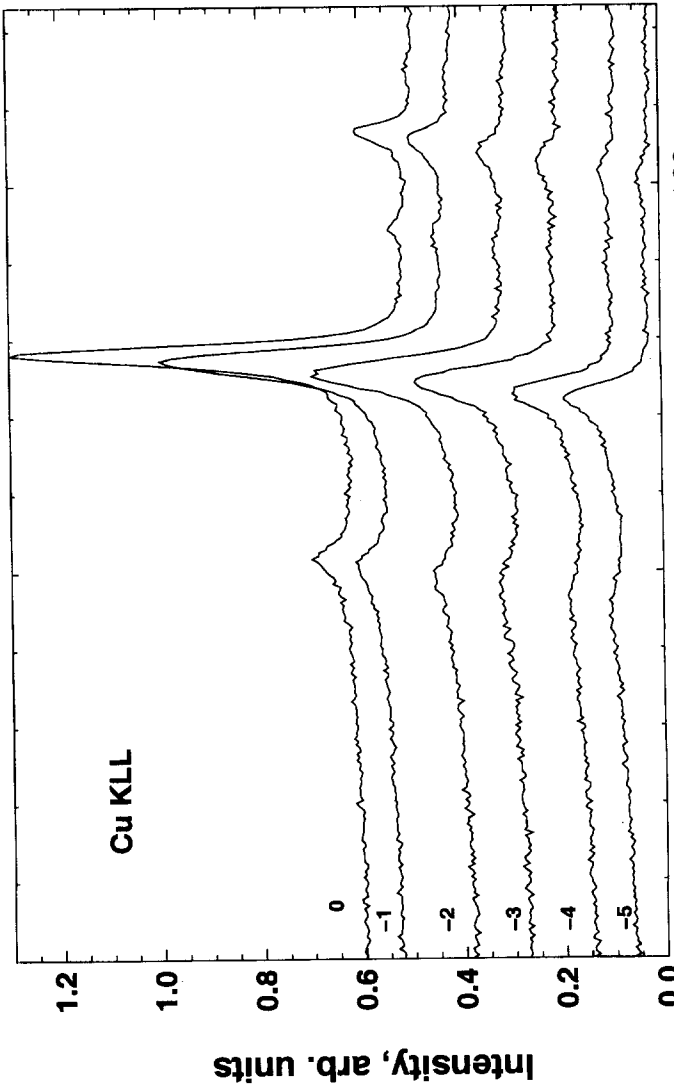

Fig. 8. The evolution of the Cu KLL spectra photoexcited from metallic Cu using photon energies below the ionization threshold (indicated in eV).

5. SUMMARY

Cluster molecular orbital models have been proved to be very useful for interpreting chemical and solid state effects in Auger spectra, providing good estimates on transferred charge in binary alloys, density of occupied and unoccupied electron states local to the core hole, multiplet structure and resonance phenomena. The DV-Xα MO cluster calculations present a promising performance in treatment of core holes and excitations. Some possibilities for further relevant improvements and challenging problems concerning the interpretation of Auger spectra are:

- the use of an accurate description of the exchange correlation potential [39].
- calculation of Auger transition probabilities for a given atomic environment
- calculation of shake up/off excitation probabilities for different atomic surroundings
- estimation of environmentally induced Auger parameter shifts.

Acknowledgements

This work was supported by the projects OTKA T 038016 and MTA-JSPS 59/2001.

6. REFERENCES

1. C.S. Fadley, in C.R. Brundle and A.D. Baker (Eds): Electron Spectroscopy, Theory, Technique and Applications, Vol. 2, Acad. Press, New York, 1978, p. 84.
2. H. Adachi, this volume
3. D.E. Ramaker, *Crit. Rev. in Solid State Mater Sci.* **17,** 211 (1991).
4. P. Weightman, *J. Electron Spectrosc. Rel. Phenom.* **68,** 127 (1994).
5. M. Thompson, M.D. Baker, A. Christie and J.F. Tyson, Auger Electron Spectroscopy (in the series "Chemical Analysis", vol. 74, serial editors P.J. Elving, J.D. Winefordner and I.M. Kolthoff), J. Wiley and Sons, New York, 1985. p. 21.
6. F. P. Larkins, *J. Electron Spectrosc. Relat. Phenom.* **51,** 115 (1990).
7. J. C. Slater, Quantum Theory of Molecules and Solids, McGraw-Hill, New York, 1974, Vol. 4.

8. Á. Nagy, *J. Molecular Structure (Theochem)*, **165,** 205 (1988); H. Adachi and T. Tanabe, *Hyoumen (Surface)*, **14,** 595 (1976). In Japanese.
9. K. Ogasawara, T. Iwata, Y. Koyama, T. Ishii, I. Tanaka and H. Adachi, *Phys. Rev.* **B 64,** 115413 (2001).
10. 10.P. Weightman, *J. Electron Spectrosc. Relat. Phenom.* **68,** 127 (1994).
11. C. D. Wagner, L. H. Gale and R. H. Raymond, *Anal. Chem.* **51,** 466 (1979).
12. 12.D. A. C. Gregory, A. D. Laine, P. S. Fowles, A. Takahashi and P. Weightman, *J. Phys.* **C5,** 3843 (1993).
13. G. Moretti, *J. Electron Spectrosc. Relat. Phenom.* **47,** 283 (1998).
14. G. Moretti, *Surf. Interface Anal.* **16,** 159 (1990); **17,** 352 (1991).
15. Zs. Kovács, L. Kövér, F. Filippone, G. Moretti and J. Pálinkás, Proc. of the 7th European Conference on Applications of Surface and Interface Analysis, Göteborg, June 16-20, 1997 (ECASIA '97), Eds: I. Olefjord, L. Nyborg and D. Briggs, John Wiley and Sons, 1997, p. 848.
16. A. Barranco, F. Yubero, J. P. Espinós and R. González-Elipe, *Surf. Interface Anal.* **31,** 761 (2001).
17. L. Kövér, I. Cserny, V. Brabec, M. Fišer, O. Dragoun and J. Novák, *Phys. Rev.* **B42,** 643 (1990).
18. M. Cini, Solid State Commun. **20,** 655 (1976); G. A. Sawatzky, *Phys. Rev. Lett.* **39,** 504 (1977).
19. Zs. Kovács, L. Kövér, P. Weightman, D. Varga, R. Sanjinés, J. Pálinkás and H. Adachi, *J. Electron Spectrosc. Relat. Phenom.* **72,** 157 (1995).
20. Zs. Kovács, L. Kövér, P. Weightman, D. Varga, R. Sanjinés, J. Pálinkás, G. Margaritondo and H. Adachi, *Phys. Rev.* **B54,** 8501 (1996).
21. V. G. Yarzhemsky, V. I. Nefedov, M. B. Trzhaskovskaya, I.M. Band and R. Szargan, *J. Electron Spectrosc. Relat. Phenom.* **123,** 1 (2002).
22. R. Manne and T. Åberg, *Chem. Phys. Lett.* **7,** 282 (1970); T. Åberg, in: Photoionization and Other Probes of Many-Electron Interactions, Ed.: F. J. Wuilleumier, New York, Plenum, 1976, pp. 273, 49.
23. L. Kövér, Zs. Kovács, P. Weightman, R. Sanjinés, D. Varga, G. Margaritondo, J. Pálinkás and M. Abon, Proc. of the 7th European Conference on Applications of Surface and Interface Analysis, Göteborg, June 16-20, 1997 (ECASIA '97), Eds: I. Olefjord, L. Nyborg and D. Briggs, John Wiley and Sons, 1997, p. 185.
24. L. Kövér, I. Cserny, J. Tóth, D. Varga and T. Mukoyama, *J. Electron Spectrosc. Rel. Phenom.* **114-116,** 55 (2001).
25. L. Kövér, Zs. Kovács, J. Tóth, I. Cserny, D. Varga, P. Weightman and S. Thurgate, *Surface Sci.* **433-435,** 833 (1999).
26. I. Cserny, L. Kövér, H. Nakamatsu and T. Mukoyama, *Surf. Interface Anal.* **30,** 199 (2000).
27. L. Kövér, M. Uda, I. Cserny, J. Tóth, J. Végh, D. Varga, K. Ogasawara and H. Adachi, *J. Vac. Sci. Technol.* **A 19,** 1143 (2001).

28. M. Uda, T. Yamamoto and Takenaga, *Adv. Quantum Chem.* **29,** 389 (1997).
29. S. Sato, S. Nozaki and H. Morisaki, *Thin Solid Films,* **343-344,** 481 (1999).
30. L. Kövér, Z. Berényi, J. Tóth, I. Cserny, D. Varga, IUVSTA 15th Int. Vacuum Congr. and AVS 48th Int. Symp., San Francisco, Oct. 28-Nov. 2, 2001, AS-MoA1, to be published
31. G.G. Kleiman, S.G.C. de Castro and R. Landers, *Phys. Rev.* **B 49,** 2573 (1994).
32. A. Némethy, L. Kövér, I. Cserny, D. Varga and P.B. Barna, *J. Electron Spectrosc. Rel. Phenom.* **70,** 183 (1995).
33. Fig. 2.23 in: S. Hüfner, "Photoelectron Spectroscopy", Springer-Verlag, Berlin, Heidelberg, 1995. p. 57
34. K. Ogasawara, T. Ishii, I. Tanaka and H. Adachi, *Phys. Rev.* **B 61,** 143 (2000).
35. T. Ishii and H. Adachi, personal communication
36. T. Åberg and B. Crasemann, in Resonant Anomalous X-ray Scattering: Theory and Applications, Eds: G. Materlik, C. Sparks and K. Fisher (Elsevier, Amsterdam, 1994), p. 431.
37. W. Drube, R. Treusch and G. Materlik, *Phys. Rev. Lett.* **74,** 42 (1995).
38. L. Kövér, W. Drube, Z. Berényi, I Cserny, to be published.
39. Á. Nagy, this volume.

Theoretically Predicted Soft X-ray Emission and Absorption Spectra of Graphitic-Structured BC_2N

Yasuji Muramatsu
Kansai Research Establishment, Japan Atomic Energy Research Institute (JAERI)
1-1-1 Kouto, Mikazuki, Sayo-gun, Hyogo 679-5148, Japan
E-mail: murama@spring8.or.jp

(Received September 6, 2001; in final form March 26, 2002)

Abstract

Theoretical B *K*, C *K* and N *K* x-ray emission/absorption spectra of three possible graphitic-structured BC_2N clusters are predicted based on the B2p-, C2p-, and N2p- density-of-states (DOS) calculated by discrete variational (DV)-Xα molecular orbital calculations. Several prominent differences in DOS spectral features among BC_2Ns, *h*-BN, and graphite are confirmed from comparison of calculated B2p-, C2p-, and N2p-DOS spectra. These variations in the spectra allow BC_2N structures to be positively identified by high-resolution x-ray emission/absorption spectroscopy in the B *K*, C *K*, and N *K* regions.

Keywords

BC_2N, soft x-ray spectra, x-ray emission, x-ray absorption, molecular orbital calculations, electronic structure, density of states

1. INTRODUCTION

In the search for advanced materials with novel physical and chemical properties, boron/carbon/nitrogen materials are attractive targets. A new and particularly exciting area for such BCN materials is the synthesis and characterization of graphitic-structured BC_2N [1]. The graphitic network structure of BC_2N should be similar to graphite and hexagonal boron nitride (*h*-BN), yet should exhibit very different physical and chemical properties. It is well known that graphite and *h*-BN have contrasting properties; for example, graphite is a semimetal and excellent host material while *h*-BN is an insulator and generally

ADVANCES IN QUANTUM CHEMISTRY, VOLUME 42

0065-3276/03 $35.00

does not form intercalation materials. Thus, graphitic-structured BC_2N may exhibit novel semiconducting and intercalation properties that could prove useful in many applications including light-emitting materials, thermoelectric conversion materials, lightweight electrical conductors, electrode material for batteries, high-temperature lubricants, and coating materials.

In the synthesis of graphitic-structured BC_2N materials, structural characterization is important because various structural isomers are possible and the properties of each exhibit strong structural dependence. For the characterization of composite materials consisting solely of light elements, high-resolution soft x-ray emission and absorption spectroscopy using synchrotron radiation is a powerful tool that reveals detailed information regarding the electronic and chemical structure [2]. Spectroscopic analysis of these x-ray spectra can best be achieved using discrete variational (DV) Xα molecular orbital (MO) calculations [3], which approximately reproduce the x-ray spectral features from the calculated density-of-states (DOS) spectra [4 - 6]. The present author has successfully characterized several carbon nitride films as covalent C_3N_4 materials using soft x-ray spectroscopy and DV-Xα MO calculations, demonstrating the power of this method in the characterization of light-element composite materials [7].

Characterizing graphitic-structured BC_2N materials using soft x-ray emission and absorption spectroscopy requires theoretically calculated x-ray spectra in order to identify the x-ray spectral features of the various structural isomers. Here, the author reports theoretically predicted x-ray emission and absorption spectra calculated from the occupied and unoccupied DOS for the possible structural isomers of BC_2N using DV-Xα MO calculations.

2. DV-Xα MO CALCULATIONS

2.1. CONFIRMATION OF DV-Xα MO CALCULATIONS FOR GRAPHITE AND *h*-BN CLUSTER MODELS

To confirm the validity of DV-Xα MO calculations for graphitic-structured BC_2N materials, the x-ray emission/absorption spectra of graphite and *h*-BN are compared to the corresponding DOS spectra obtained by DV-Xα MO calculations. Cluster models of graphite ($C_{96}H_{24}$) and *h*-BN ($B_{48}N_{48}H_{24}$) used in the DV- Xα MO calculations are illustrated in Figure 1. These structures were optimized using molecular mechanics (MM2) [8] with commercially available Chem3D Plus software. DV-Xα MO calculations for these cluster models were conducted on the electronic structure of the ground states with a basis set of 1s, 2s, and 2p orbitals for B, C, and N atoms. Calculations were performed using the SCAT program [3] as part of commercially available DV-Xα software running on a DOS/V computer.

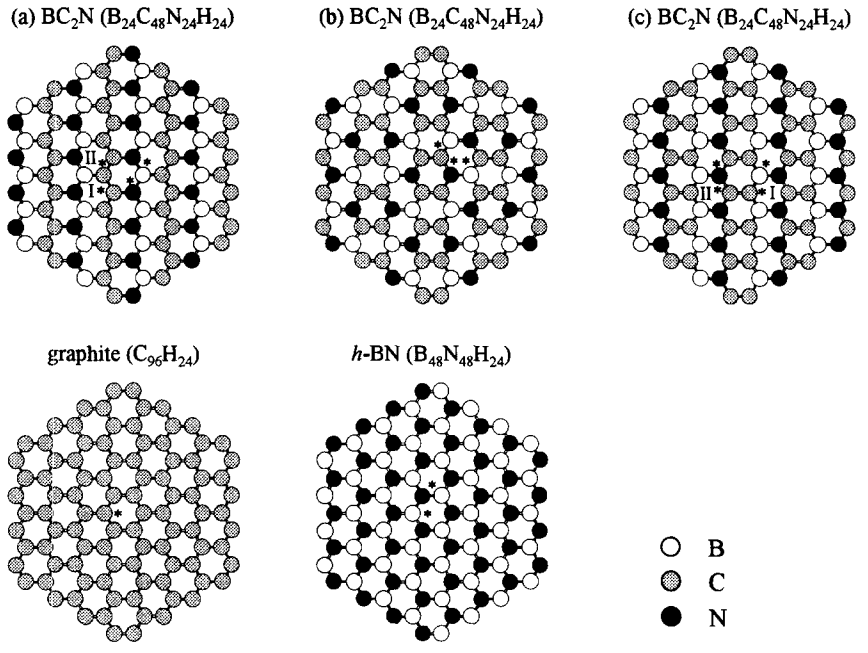

Fig. 1. Cluster models of three possible structural isomers of graphitic-structured BC_2N ($B_{24}C_{48}N_{24}H_{24}$) with references *h*-BN ($B_{48}N_{48}H_{24}$) and graphite ($C_{96}H_{24}$). Hydrogen atoms terminating the edge atoms in the cluster models are not shown in the figure.

X-ray spectral measurements of graphite and *h*-BN powders were carried out using high-brilliance synchrotron radiation at the Advanced Light Source (ALS; Berkeley, USA). High-resolution x-ray emission spectra in the B *K*, C *K*, and N *K* regions were obtained using a grating x-ray spectrometer installed on beamline 8.0 [9], and absorption spectra were obtained using beamline 6.3.2 [10] by the total-electron-yield method. The resolving power (E/ΔE) was estimated to be approximately 270 for emission measurements and 1600 for absorption in the C *K* region.

Measured x-ray emission/absorption spectra in the B *K* and N *K* regions of *h*-BN and those in the C *K* region of graphite are shown in Figure 2. Superimposed upon these measured spectra are the individual DOS spectra for centered atoms (denoted by asterisks) of B2p and N2p in *h*-BN and C2p in graphite. The calculated spectra are obtained by broadening individual DOS with 0.5 eV-wide Lorentzian functions. The occupied B2p-, C2p-, and N2p-DOS spectra well reproduce measured x-ray emission spectra. This suggests that the generation of DOS spectra from DV-Xα MO calculations is an appropriate method for

simulating x-ray emission spectra. However, the calculated unoccupied DOS spectral features do not exactly agree with the experimental absorption spectra at the B *K*, C *K*, and N *K* threshold. This is reasonable in that the final state relaxation effects, which should be considered in exact calculations of core photoabsorption spectroscopy, were not taken into account. However, outline features such as π^* and σ^* peaks in the x-ray absorption spectra were roughly reproduced by the calculated DOS spectra. These results confirm that DV-Xα MO calculations on monolayer models composed of nearly 100 atoms reproduce x-ray emission spectra with good accuracy [12] and may also be useful in assigning the absorption spectral features for graphitic-structured BC_2N materials.

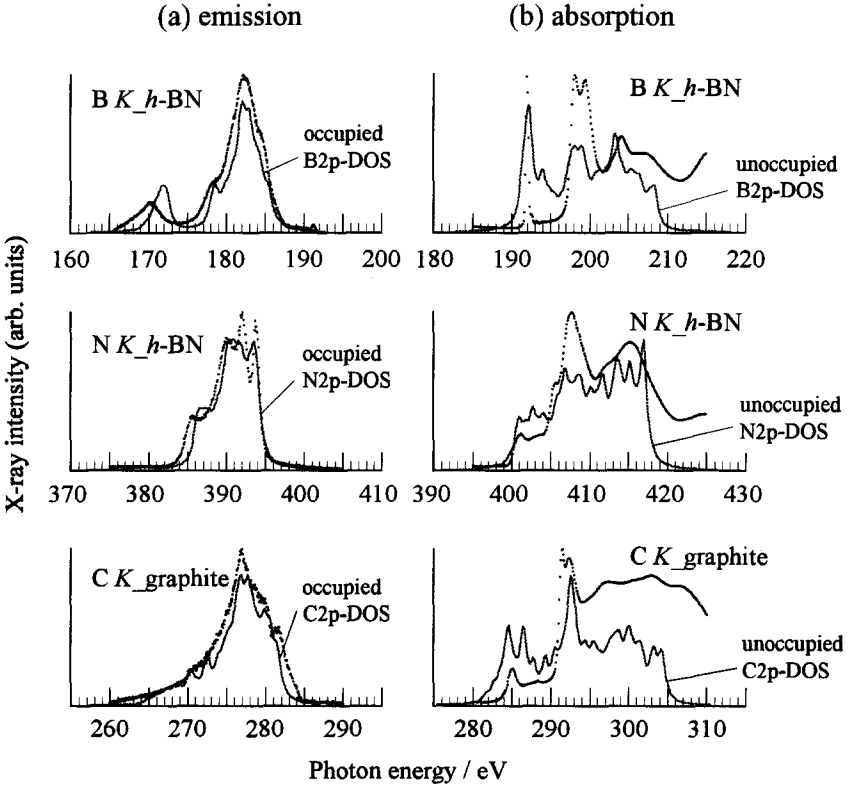

Fig. 2. Soft x-ray emission spectra (a) and absorption spectra (b) in the B *K* and N *K* regions of *h*-BN and those in the C *K* region of graphite. Corresponding occupied and unoccupied C2p-DOS spectra of the *h*-BN and graphite cluster models calculated with DV-Xα MO calculations are superimposed on the x-ray emission and absorption spectra.

2.2. DV-Xα MO CALCULATIONS FOR BC_2N CLUSTER MODELS

Three possible structures of BC_2N were predicted by Liu et al. [11] as shown in Fig. 1. Carbon atoms in model (a) form poly-acetylene-like structures. Each carbon atom in model (b) is bound to carbon, boron, and nitrogen atoms. There are two kinds of carbon atoms in model (c): one carbon atom is bound to one carbon atom and two boron atoms, while the other is bound to one carbon atom and two nitrogen atoms. Based on these structures, DV-Xα MO calculations were performed for the three cluster models of $B_{24}C_{48}N_{24}H_{24}$. Atoms on the edges of the clusters are terminated by hydrogen atoms. The geometries of these model structures were initially optimized by the MM2 method. DV-Xα MO calculations of these cluster models were performed on the electronic ground states with a basis set of 1s, 2s, and 2p orbitals for B, C, and N atoms. DOS spectra were obtained by broadening the calculated individual DOS of the centered atoms (denoted by asterisks in Fig. 1) using 0.5 eV-wide Lorentzian functions.

3. RESULTS AND DISCUSSION

Figure 3 shows the occupied and unoccupied DOS spectra of 2s- and 2p-orbitals in B, C, and N atoms of the three BC_2N cluster models. DOS spectra for B and N atoms in *h*-BN and for C in graphite are also shown as references. In these DOS spectra, the energy levels of the highest occupied molecular orbitals (HOMOs) are defined as zero eV on the MO energy scale.

The occupied DOS spectra of B atoms for all three BC_2N models exhibit a low-energy tail feature in B2p-DOS, which hybridizes with the B2s orbital. However, the low-energy peak observed in *h*-BN is not observed in the BC_2N. This low-energy peak feature therefore represents an index for distinguishing BC_2N from *h*-BN. The high-energy features differ among the three BC_2N models: model (a) has small shoulder peaks, model (b) has a sharp peak, and model (c) exhibits no high-energy fine structures. These differences in high-energy features will provide useful indices for identifying BC_2N structures in B *K* x-ray emission spectra. In the occupied DOS spectra of N atoms, the N2p-DOS spectrum of *h*-BN is the main peak feature with a high-energy peak and a low-energy step-like shoulder. However, such fine structure is not observed in the BC_2N models. This difference in N2p-DOS spectra between BC_2N and *h*-BN is another clear index for distinguishing BC_2N from *h*-BN. In the BC_2N models, the main peak feature in model (c) is slightly sharper than that of models (a) and (b). However, there is little significant difference in the N2p-DOS spectra among the three BC_2N models.

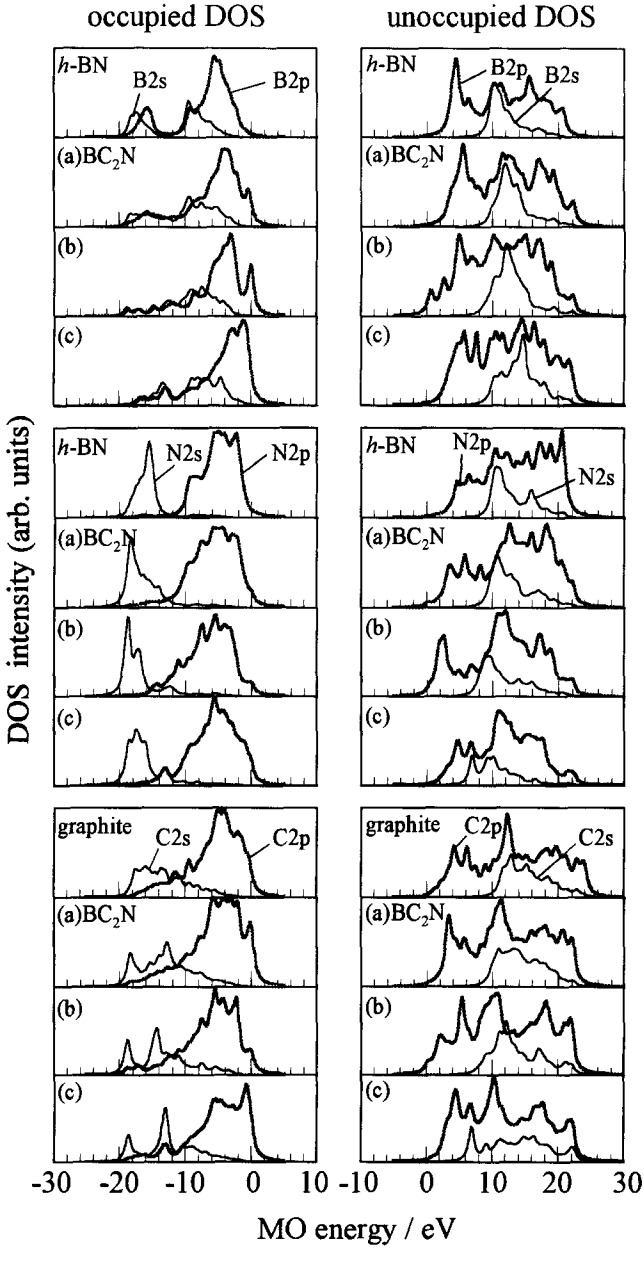

Fig. 3. Occupied and unoccupied DOS spectra of 2s- and 2p-orbitals in B, C and N atoms of the three BC_2N cluster models. Molecular structures of the BC_2N models (a – c) are shown in Fig. 1.

It therefore appears difficult to distinguish between the three BC_2N structures based solely on N *K* x-ray emission spectra. In the occupied DOS spectra of C atoms, there are clear differences in C2p-DOS spectral features of the main peak and high-energy shoulder/peak between the BC_2N models and graphite. These main-peak and high-energy-shoulder/peak features can therefore be used to distinguish BC_2N from graphite. In the BC_2N models, there are clear differences among the three models: a broad main peak with a high-energy peak in model (a), a main peak with a small high-energy peak in (b), and a broad main peak with a prominent high-energy peak in (c). Spectral features of the main peak and high-energy peak in C *K* x-ray emission can also be used as indices for identifying BC_2N structures.

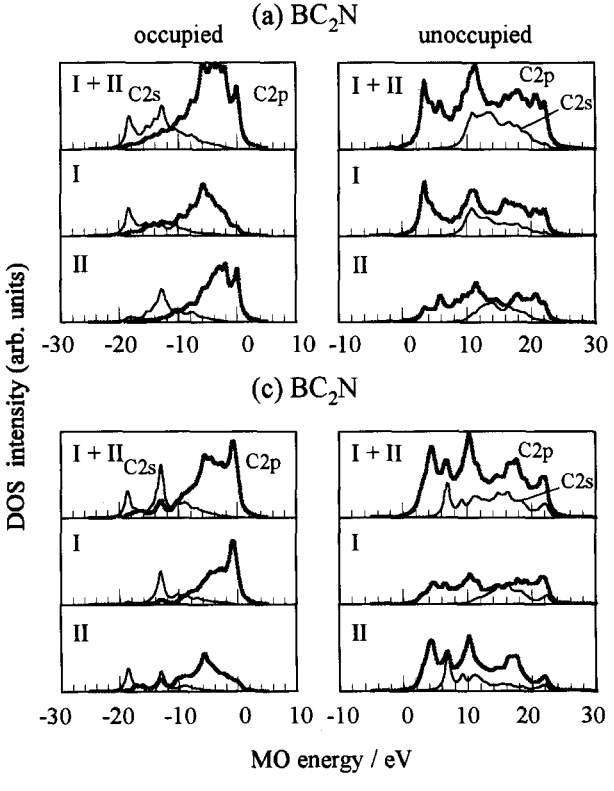

Fig. 4. Occupied and unoccupied C2p-DOS spectra drawn by separating the components of C(I) and C(II) atoms in BC_2N cluster models (a) and (c). Molecular structures of (a) and (c) models are shown in Fig. 1.

In the unoccupied DOS spectra, there are distinctive differences in B2p-, N2p-, and C2p-DOS among the three BC_2N models and the reference *h*-BN and graphite in the fine threshold structures. This demonstrates that BC_2N structures can be identified from high-resolution x-ray absorption spectra at the B *K*, C *K*, and N *K* thresholds, in addition to identification using the above-mentioned x-ray emission spectra.

There are two kinds of C atoms in BC_2N models (a) and (c). In model (a), one C atom (denoted by I in Fig. 1) is bound to two C atoms and one N atom, while C (II) is bound to two C atoms and a single B atom. In model (c), one C (I) is bound to a single C atom and two B atoms, while C (II) is bound to one C atom and two N atoms. The clear difference in the C2p-DOS spectra between (a) and (c) results from these variations in chemical bonding. Figure 4 shows the occupied and unoccupied C2p-DOS spectra after separation of the components of C (I) and C (II) atoms in (a) and (c). In the occupied spectra, high-energy peak features are assigned primarily to hybridization with B atoms. Consequently, the prominent high-energy peak in (c) can be well explained by strong hybridization with two B atoms of the C (I) atom. In the unoccupied spectra, the prominent low-energy peaks in (a) and (c) are due to hybridization with N atoms.

4. CONCLUSIONS

The author has obtained B2p-, C2p-, and N2p-DOS spectra for the three possible graphitic-structured BC_2N models ($B_{24}C_{48}N_{24}H_{24}$) based on DV-Xα MO calculations in order to predict the B *K*, C *K* and N *K* x-ray emission/absorption spectra. From a comparison of the occupied/unoccupied DOS spectra of BC_2N models with graphite ($C_{96}H_{24}$) and *h*-BN ($B_{48}N_{48}H_{24}$) references, clear differences in the individual DOS spectra of the BC_2N and reference models were identified. In addition, clear variations in both occupied and unoccupied DOS spectra were discovered, with the exception of occupied N2p-DOS, among the three BC_2N models. Thus, the author demonstrated that high-resolution soft x-ray emission and absorption spectral measurements in the B *K*, C *K*, and N *K* regions for graphitic-structured BC_2N compounds are a useful tool for structure identification.

5. ACKNOWLEDGMENTS

The author would like to thank Dr. Rupert C. C. Perera, Dr. Jonathan Denlinger, and Eric M. Gullikson (Lawrence Berkeley National Laboratories) for their support in x-ray spectral measurements of the reference compounds at the Advanced Light Source. Gratitude is also extended to Dr. Muneyuki Motoyama (Hyogo Prefectural Institute for Industrial Research) and Dr. Wataru Utsumi (Japan Atomic Energy Research Institute) for valuable discussions. This work was supported by the Hyogo Science and Technology Association and by the US

Department of Energy under contract No. DE-AC03-76SF00098.

6. REFERENCES

[1] M. Kawaguchi, Adv. Mater. 9, 615 (1997).
[2] *for example*, T. A. Callcott, "Vacuum Ultraviolet Spectroscopy II" ed. by J. A. R. Samson and D. L. Ederer (Academic Press, 2000) pp.279.
[3] C. Satoko, M. Tsukada, and H. Adachi, J. Phys. Soc. Jpn., 45, 1333 (1978).
[4] J. Kawai, I. Tanaka, and H. Adachi, Bunseki Kagaku, 44, 251 (1995).
[5] R. Manne, J. Chem. Phys., 52, 5733 (1970).
[6] D. S. Urch, J. Phys., C3, 1275 (1970).
[7] Y. Muramatsu, Y. Tani, Y. Aoi, E. Kamijo, T. Kaneyoshi, M. Motoyama, J. J. Delaunay, T. Hayashi, M. M. Grush, T. A. Callcott, D. L. Ederer, C. Heske, J. H. Underwood, and R. C. C. Perera, Jpn. J. Appl. Phys., 38, 5143 (1999).
[8] U. Bunkert and N. L. Allinger, "Molecular Mechanics" (ACS, 1995).
[9] J. J. Jia, T. A. Callcott, J. Yurkas, A. W. Ellis, F. J. Himpsel, M. G. Samant, J .Stohr, D. L. Ederer, J. A. Carlisle, E. A. Hudson, L. J. Terminello, D. K. Shuh, and R. C. C. Perera, Rev. Sci. Instrum., 66, 1394 (1995).
[10] J. H. Underwood, E. M. Gullikson, M. Koike, P. J. Batson, P. E. Denham, K. D. Franck, R. E. Tachaberry, and W. F. Steele, Rev. Sci. Instrum., 67, 1 (1996).
[11] A. Y. Liu, R. M. Wentzcovitch, and M. L. Cohen, Phys. Rev. B 39, 1760 (1989).
[12] Y. Muramatsu and T. Hayashi, Advances in X-Ray Chemical Analysis, Japan, 30, 41 (1999).

Theories for excited states

Á. Nagy
Department of Theoretical Physics
University of Debrecen
H–4010 Debrecen, Hungary

(Received November 20, 2001; in final form February 14, 2002)

Abstract
Ensemble theory of excited states is reviewed. A recently proposed generalization of the optimized potential method is discussed. A non-variational theory based on Kato's theorem and valid for Coulomb systems and a variational density functional theory of a single excited state are reviewed.

Contents

1 Introduction

Recently, there has been a growing interest in studying excited states in the density functional theory [1]. Nowadays there exist excited state theories in both the time-independent [2, 3] and the time-dependent [4] density functional theory.

ADVANCES IN QUANTUM CHEMISTRY, VOLUME 42

0065-3276/03 $35.00

The first rigorous generalization of time-independent density functional theory for excited states was given by Theophilou [5]. His theory was enlarged into the theory of ensembles of excited states by Gross, Oliveira and Kohn [6]. The relativistic generalization of this formalism was also done [7]. A perturbation theory of excited states was presented by Görling[8, 9]. Kohn [10] proposed a quasi-local-density approximation and exitation energies of He atom were calculated using this method [6]. Excitation energies of several atoms [11, 12, 13, 2] were determined using the ensemble theory and several ground-state approximate functionals have been tested [14]. The coordinate scaling for the density matrix of ensembles was explored [15]. The adiabatic connection formula was extended to the ensemble exchange-correlation energy and a simple local ensemble exchange potential was presented [16]. (For reviews of excited-state theories see [2, 3].)

Unfortunately, the exchange-correlation part of the ensemble Kohn-Sham potential is not known exactly. The optimized potential method (OPM) that turned to be very succesful in treating exchange exactly in the ground-state theory [17-20] was generalized for ensembles of excited states. The first generalization was based on the ensemble Hartree-Fock method [21]. Recently, ghost-interaction correction to this scheme has been proposed [22]. A new, more appropriate OPM has recently been proposed [23]. In the next section this new OPM method for ensembles is discussed.

Recently, time-independent theories for a single excited state have also been proposed [24-27] A non-variational theory [24, 25] based on Kato's theorem is reviewed in Section 3. Görling developed a stationary theory of excited states [28]. Section 4 summarizes the variational density functional theory of a single excited state [26, 27].

2 Optimalized potential method in the ensemble theory of excited states

The eigenvalue problem of the Hamiltonian $\hat{H}$ can be given by

$$\hat{H}\Psi_k = E_k\Psi_k \qquad (k = 1, ..., M)\,. \tag{1}$$

From the energy eigenvalues

$$E_1 \leq E_2 \leq ... \tag{2}$$

the ensemble energy

$$\mathcal{E} = \sum_{k=1}^{M} w_k E_k \tag{3}$$

can be constructed, where $w_1 \geq w_2 \geq \ldots \geq w_M \geq 0$. The generalized Rayleigh-Ritz variational principle is valid [6] for the ensemble energy. Therefore the generalized Hohenberg–Kohn-theorems can be derived. (i) The external potential $v(r)$ is determined within a trivial additive constant, by the ensemble density n defined as

$$n = \sum_{k=1}^{M} w_k n_k \,. \tag{4}$$

(ii) For a trial ensemble density $n'(r)$ such that

$$n'(r) \geq 0 \tag{5}$$

and

$$\int n'(\mathbf{r}) d\mathbf{r} = N \tag{6}$$

$$\mathcal{E}[n] \leq \mathcal{E}[n'] \,, \tag{7}$$

i.e. the ensemble functional $\mathcal{E}$ takes its minimum at the correct ensemble density n.

Kohn-Sham equations can also be derived for the ensemble:

$$\left[-\frac{1}{2}\nabla^2 + v_{\text{KS}}\right] \phi_i(\mathbf{r}) = \epsilon_i \phi_i(\mathbf{r}) \,. \tag{8}$$

The ensemble Kohn-Sham potential

$$v_{\text{KS}}(\mathbf{r}; w, n_w) = v(\mathbf{r}) + V_c(\mathbf{r}; w, n_w) + V_{xc}(\mathbf{r}; w, n_w) \,, \tag{9}$$

is a sum of the external, the ensemble Coulomb and the ensemble exchange-correlation potentials. These equations have exactly the same form as the ground-state equations. However, because of Eq. (4) there are non-integer occupation numbers, too.

The optimized potential method developed for the ground state [17-20,29] was generalized for ensembles [21, 23]. Here the most recent version is discussed [23]. In the optimized potential method the total ensemble energy $\mathcal{E}$ should be known as a functional of the ensemble Kohn-Sham orbitals

$$\mathcal{E}[\phi_j] = T_s + \int n(\mathbf{r})v(\mathbf{r}) + E_c + E_{xc} \,, \tag{10}$$

where T_s, E_c and E_{xc} are the non-interacting kinetic energy, the Coulomb energy and the exchange-correlation energy, respectively. These quantities can be expressed with the following sums:

$$T_s = \sum_k w_k T_s^k \tag{11}$$

and

$$E_c = \sum_k w_k E_c^k \,, \tag{12}$$

where

$$T_s^k = -\frac{1}{2} \sum_j \lambda_j^k \int \phi_j^* \nabla^2 \phi_j d\mathbf{r} \,, \tag{13}$$

$$E_c^k = \frac{1}{2} \int \frac{n_k(\mathbf{r}) n_k(\mathbf{r}')}{|\mathbf{r} - \mathbf{r}'|} d\mathbf{r} d\mathbf{r}' \tag{14}$$

and

$$n_k = \sum_j \lambda_j^k |\phi_j|^2 \tag{15}$$

are the kinetic energy, the Coulomb energy and the density corresponding to the eigenvalue k, respectively. The exchange-correlation term E_{xc} is defined by Eq. (10). As the total ensemble energy can be written as a sum

$$\mathcal{E}[\phi_j] = \sum_{k=1}^{M} w_k E_k \,, \tag{16}$$

where

$$E_k = T_s^k + \int n_k(\mathbf{r})v(\mathbf{r}) + E_c^k + E_{xc}^k \,, \tag{17}$$

the exchange-correlation term E_{xc} can also be partitioned as

$$E_{xc} = \sum_k w_k E_{xc}^k \,. \tag{18}$$

Introducing the ensemble occupation numbers

$$\alpha_j = \sum_k w_k \lambda_j^k \tag{19}$$

we arrive at the following expression of the kinetic energy

$$T_s = -\frac{1}{2} \sum_j \alpha_j \int \phi_j^* \nabla^2 \phi_j d\mathbf{r} \,. \tag{20}$$

Now, the optimized potential is defined in the usual way: the local effective optimized potential $V(\mathbf{r})$ minimizes the the total ensemble energy $\mathcal{E}$

$$\frac{\delta \mathcal{E}}{\delta V} = \sum_j \int \frac{\delta \mathcal{E}}{\delta \phi_j^*(\mathbf{r}')} \frac{\delta \phi_j^*(\mathbf{r}')}{\delta V(\mathbf{r})} d\mathbf{r}' + c.c. = 0 \,. \tag{21}$$

The functional derivative of the one-electron orbitals ϕ_j with respect to the local effective potential V can be calculated with the help of the Green's function

$$\frac{\delta \phi_j^*(\mathbf{r}')}{\delta V(\mathbf{r})} = -G_j(\mathbf{r}', \mathbf{r}) \phi_j(\mathbf{r}) \,, \tag{22}$$

and an integral equation for V can be derived:

$$0 = \sum_j \alpha_j \int \left[V_j(\mathbf{r}') - V_c(\mathbf{r}') - V_{xc}(\mathbf{r}') \right] G_j(\mathbf{r}', \mathbf{r}) \phi_j^*(\mathbf{r}') \phi_j(\mathbf{r}) + cc. \,, \tag{23}$$

where

$$V_j(\mathbf{r}) = \frac{1}{\alpha_j \phi_j^*(\mathbf{r})} \frac{\delta (E_c + E_{xc})}{\delta \phi_j(\mathbf{r})} \tag{24}$$

and $V(\mathbf{r})$ is written as a sum of the external, the classical Coulomb and exchange-correlation potential:

$$V(\mathbf{r}) = v(\mathbf{r}) + V_c(\mathbf{r}) + V_{xc}(\mathbf{r}) \,. \tag{25}$$

It is very difficult to calculate the effective potential V because of vast numerical problems. Consequently, the ensemble analogue of the Krieger-Li-Iafrate (KLI) [20] approach has been introduced [23]. The generalized ensemble KLI potential is a sum of the external potential v and the KLI-like expression for the sum of the Coulomb and exchange-correlation potentials V_{cxc}:

$$V(\mathbf{r}) = v(\mathbf{r}) + V_{cxc}(\mathbf{r}) \,, \tag{26}$$

where

$$V_{cxc} = V_S + \sum_j \alpha_j \frac{|\phi_j|^2}{n} \langle \phi_j | V_{cxc} - V^j_{cxc} | \phi_j \rangle \,. \tag{27}$$

The Slater potential

$$V_S = V_S^c + V_S^{xc} \tag{28}$$

has both Coulomb and exchange-correlation part:

$$V_S^c = \sum_k w_k \frac{n_k}{n} v_c^k \tag{29}$$

$$V_S^{xc} = \sum_k w_k \frac{n_k}{n} v_{xc}^k \,. \tag{30}$$

These are the ensemble averages of the Coulomb and exchange-correlation potentials weighted with the densities. The orbital dependent ensemble Coulomb and exchange-correlation potentials are

$$v_c^k = \int \frac{n_k(\mathbf{r}')}{|\mathbf{r} - \mathbf{r}'|} \, d\mathbf{r}' \tag{31}$$

and

$$v_{xc}^k = \frac{1}{n_k} \sum_j \alpha_j \phi_j v_{xcj}^k \phi_j \,, \tag{32}$$

where

$$v_{xcj}^k = \frac{1}{\lambda_j} \frac{\delta E_{xc}^k[\phi_j]}{\delta \phi_j^*} \,. \tag{33}$$

Notice that these ensemble Coulomb and exchange-correlation potentials are different for different orbitals. The orbital dependent potential in Eq. (27) has the form

$$V_{cxc}^{j} = V_{c}^{j} + V_{xc}^{j} , \tag{34}$$

where

$$V_{c}^{j} = \frac{\sum_k w_k \lambda_j^k v_c^k}{\sum_k w_k \lambda_j^k} \tag{35}$$

and

$$V_{xc}^{j} = \frac{\sum_k w_k \lambda_j^k v_{xcj}^k}{\sum_k w_k \lambda_j^k} . \tag{36}$$

In the exchange-only case the exchange energy E_x^k is given by

$$E_x^k = -\frac{1}{2} \sum_i \sum_j \lambda_i^k \lambda_j^k \int \frac{\phi_i^*(\mathbf{r}) \phi_j^*(\mathbf{r}') \phi_j(\mathbf{r}) \phi_i(\mathbf{r}')}{|\mathbf{r} - \mathbf{r}'|} d\mathbf{r} d\mathbf{r}' . \tag{37}$$

It is important to emphasize that the ensemble exchange-correlation energy defined in the present approach is different from the one in the original paper of Gross, Oliveira and Kohn [6]. The original definition was

$$\tilde{E}_{xc} = \mathcal{E} - T_s - \int n(\mathbf{r}) v(\mathbf{r}) - \frac{1}{2} \int \frac{n(\mathbf{r}) n(\mathbf{r}')}{|\mathbf{r} - \mathbf{r}'|} d\mathbf{r} d\mathbf{r}' , \tag{38}$$

while the present definition is

$$E_{xc} = \mathcal{E} - T_s - \int n(\mathbf{r}) v(\mathbf{r}) - \frac{1}{2} \sum_{k=1}^{M} w_k \int \frac{n_k(\mathbf{r}) n_k(\mathbf{r}')}{|\mathbf{r} - \mathbf{r}'|} d\mathbf{r} d\mathbf{r}' . \tag{39}$$

That is the Coulomb terms are different. In Eq. (39) only the true Coulomb energies of the ground and excited states are added. On the other hand, Eq. (38) contains non-physical 'self-Coulomb' terms between the different excited states [22, 23]. Both definitions are correct. However, if the original definition (Eq. (38)) is used the exchange-correlation energy ($\tilde{E}_{xc}$) will contain 'self-exchange' terms to eliminate the 'self-Coulomb' terms mentioned

above. Consequently, approximate expressions of $\tilde{E}_{xc}$ should also include 'self-interaction' terms to obtain at least a partial elimination of the 'self-Coulomb' terms. In the present approach (Eq. (39)) there is no need of such 'self-interaction' terms.

As an illustration excitation energies of the He atom and Li^+, Be^{++} and B^{+++} ions are presented. The ensemble energy (3) depends on the weighting factors w_k. The excitation energies, however, are independent on w_k provided that the exact ensemble Kohn-Sham potential is used. In the exchange only case, however, there is slight dependence on the weighting factors w_k. It has been shown that the dependence of the excitation energies on the weighting factors is of second or higher order. Table 1 presents the triplet and singlet excitation energies separately. The following averages were calculated:

$$\mathcal{E}_1 = \frac{1}{4}E_{1^1S} + \frac{3}{4}E_{2^3S} \,, \tag{40}$$

$$\mathcal{E}_2 = \frac{3}{8}E_{1^1S} + \frac{15}{32}E_{2^3S} + \frac{5}{32}E_{2^1S} \,, \tag{41}$$

$$\mathcal{E}_3 = \frac{3}{8}E_{1^1S} + \frac{15}{104}E_{2^3S} + \frac{5}{104}E_{2^1S} + \frac{45}{104}E_{1^3P} \,, \tag{42}$$

and

$$\mathcal{E}_4 = \frac{1}{2}E_{1^1S} + \frac{3}{32}E_{2^3S} + \frac{1}{32}E_{2^1S} + \frac{9}{32}E_{1^3P} + \frac{3}{32}E_{1^1P} \,. \tag{43}$$

These weighting factors lead to very good excitation energies. For comparison the experimental data [30] are also pesented.

Table 1

Excitation energies for the He atom and the Li^+, Be^{++} and B^{+++} ions calculated with the ensemble KLI method (in Ry). Experimental values, where available (taken from Moore's tables [30]), are shown for comparison.

Transition		He	LI^+	Be^{++}	B^{+++}
	^3S KLI	1.4562	4.3541	8.7519	14.6495
	exp	1.4567	4.3381	8.7162	14.5940
$1s^2 \rightarrow 1s2s$					
	^1S KLI	1.4989	4.3959	8.7936	14.6931
	exp	1.5152	4.6559		
	^3P KLI	1.5433	4.5160	8.9862	14.9558
	exp	1.5408	4.5041	8.9609	14.9166
$1s^2 \rightarrow 1s2p$					
	^1P KLI	1.5875	4.5604	9.0307	15.0004
	exp	1.5594	4.5729	9.0896	15.1090

3 Theory for a single excited state

According to the Hohenberg-Kohn theorem of the density functional theory the ground state electron density determines in principle all molecular properties. About fifty years ago Kato proved the following theorem [31]

$$Z_\beta = -\frac{1}{2\bar{n}(r)} \left.\frac{\partial \bar{n}(r)}{\partial r}\right|_{r=R_\beta}, \tag{44}$$

where the partial derivatives are taken at the nuclei β. $\bar{n}$ denotes the angular average of the density n. It was Bright Wilson [33] who noticed that it follows from Kato's theorem [31, 33] that the electron density determines the Hamiltonian for a Coulomb system. From Eq. (44) the cusps of the density tell us where the nuclei are (R_β) and what the atomic numbers Z_β are and

the integral of the density gives us the number of electrons:

$$N = \int n(\mathbf{r}) d\mathbf{r} \,. \tag{45}$$

Thus from the density the Hamiltonian can be readily obtained from which every property of the system can be determined. One has to emphasize, however, that this argument holds only for Coulomb systems, while the density functional theory is valid for any external potential.

Kato's theorem is valid not only for the ground state but also for the excited states. Consequently, if the density n_i of the i-th excited state is known, the Hamiltonian $\hat{H}$ is also in principle known and its eigenvalue problem

$$\hat{H}\Psi_k = E_k \Psi_k \qquad (k = 0, 1, ..., i, ...) \tag{46}$$

can be solved, where

$$\hat{H} = \hat{T} + \hat{V} + \hat{V}_{ee} \,. \tag{47}$$

$$\hat{T} = \sum_{j=1}^{N} (-\frac{1}{2} \nabla_j^2) \,, \tag{48}$$

$$\hat{V}_{ee} = \sum_{k=1}^{N-1} \sum_{j=i+1}^{N} \frac{1}{|\mathbf{r}_k - \mathbf{r}_j|} \,, \tag{49}$$

and

$$\hat{V} = \sum_{k=1}^{N} \sum_{J=1}^{M} -Z_J / |\mathbf{r}_k - \mathbf{R}_J| \tag{50}$$

are the kinetic energy, the electron-electron energy and the electron-nucleon operators, respectively.

There are certain special cases, however, where Eq. (44) does not provide the atomic number. The simplest example is the $2p$ orbital of the hydrogen atom. In this case the spherical average of the derivative of the wave function is zero and the value of the wave function is also zero at the nucleus.

$$n_{2p}(r) = cr^2 e^{-Zr} \tag{51}$$

It means, that though Kato's theorem (44) is valid in this case, too, it does not give us the desired information, that is the atomic number. Similar cases occur in those highly excited atoms, ions or molecules, for which the spherical average of the derivative of the wave function is zero at a nucleus, that is where we have no s-electrons.

Pack and Brown [34] derived cusp relations for the wave functions of these systems. There are several works concerning the cusp of the density [35-44]. Recently, the corresponding cusp relations have been derived for the density [45]. Let us now define

$$\eta_l(\mathbf{r}) = \frac{n(\mathbf{r})}{r^{2l}} , \tag{52}$$

where l is the smallest integer for which η_l is not zero at the nucleus. The new cusp relations for the density

$$\left.\frac{\partial \bar{\eta}^l(\mathbf{r})}{\partial r}\right|_{r=0} = -\frac{2Z}{l+1}\eta^l(0) . \tag{53}$$

In the present example Eq. (52) leads to

$$\eta_{2p}(r) = \frac{n_{2p}}{r^{2l}} = ce^{-Zr} \tag{54}$$

and the new cusp relation has the form:

$$-2Z\eta_{2p}(0) = 2\eta'_{2p}(0) . \tag{55}$$

So we can again readily obtain the atomic number from the electron density. Other useful cusp relations have also been derived [46, 47].

Using the concept [48, 49] of adiabatic connection Kohn-Sham-like equations can be derived. We suppose the existence of a continuous path between the interacting and the non-interacting systems. The density n_i of the i-th electron state is the same along the path.

$$\hat{H}_i^\alpha \Psi_k^\alpha = E_k^\alpha \Psi_k^\alpha , \tag{56}$$

where

$$\hat{H}_i^\alpha = \hat{T} + \alpha \hat{V}_{ee} + \hat{V}_i^\alpha . \tag{57}$$

The subscript i denotes that the density of the given excited state is supposed to be the same for any value of the coupling constant α. $\alpha = 1$ corresponds to the fully interacting case, while $\alpha = 0$ gives the non-interacting system:

$$\hat{H}_i^0 \Psi_k^0 = E_k^0 \Psi_k^0 \,, \tag{58}$$

For $\alpha = 1$ the Hamiltonian $\hat{H}_i^\alpha$ is independent of i. For any other values of α the 'adiabatic' Hamiltonian depends on i and we have different Hamiltonian for different excited states. Thus the non-interacting Hamiltonian($\alpha = 0$) is different for different excited states.

The optimized potential method [18] can be generalized for a single excited state, too. It was shown [24] that from the fact that the energy is stationary at the true wave function follows that the energy is stationary at the true potential. It is well-known that considering the energy as a functional of the wave function $E[\Psi]$, the eigenvalues of the Hamiltonian are stationary points of E

$$\frac{\delta E}{\delta \Psi_k} = 0 \qquad (k = 1, ..., i, ...) \,, \tag{59}$$

and only the eigenvalues are stationary points.

From the density of a given excited state n_i, one can obtain the Hamiltonian, the eigenvalues and eigenfunctions and through adiabatic connection the non-interacting effective potential $V_i^{\alpha=0}$ and certainly the solution of equations of the non-interacting system leads to the density n_i:

Thus, we can consider the total energy as a functional of the non-interacting effective potential:

$$E[\Psi_i] = E[\Psi_i[V_i^0]] \,. \tag{60}$$

Making use of Eq. (59) we obtain

$$\frac{\delta E}{\delta V_i^0} = \int \frac{\delta E}{\delta \Psi_i} \frac{\delta \Psi_i}{\delta V_i^0} + c.c. = 0 \,. \tag{61}$$

So an optimized effective potential can be found for the given excited state. The KLI approximation to the optimized effective potential can also be derived straighforwardly [24]. The generalized KLI exchange potential for the ith excited state reads [24]

$$v_x^i = v_S^i + \sum_j \frac{|\phi_j|^2}{n_i} (\bar{v}_{xj}^i - \bar{v}_{xj}^{i,HF}) \,, \tag{62}$$

where $\bar{v}^i_{xj}$ and $\bar{v}^{HF}_{xj}$ are the expectation values of the exchange potential v^i_x (62) and the Hartree-Fock exchange potentials $v^{i,HF}_{xj}$ (defined in the usual way) with respect to orbital ϕ_j.

$$v^i_S(\mathbf{r}) = -\frac{1}{2}\int d\mathbf{r}' \frac{|\sum_j \phi^{i*}_j(\mathbf{r}')\phi^i_j(\mathbf{r})|^2}{n_i(\mathbf{r}')|\mathbf{r}-\mathbf{r}'|} \,. \tag{63}$$

is the Slater potential.

4 Variational theory for a single excited state

The theory discussed in the previous section is a non-variational one. It has recently been shown, however, that there exists a variational Kohn-Sham density-functional theory, with a minimum principle, for the self-consistent determination of an individual excited-state energy and density [26]. The functionals in this variational theory are bifunctionals, that is, they are functionals of not only the given excited state density n_i, but of the ground-state density n_0 as well. The variational principle is written in the form of a constraint search

$$E_i = \min_n \min_{\substack{\Psi\to n \\ \Psi\perp\Psi_0,\ldots,\Psi_{i-1}}} \langle\Psi|\hat{H}|\Psi\rangle \,. \tag{64}$$

The minimization process is done in two steps: first, for all wave functions giving n_i and being orthogonal to the first $i-1$ states of $\hat{H}$, then for the density. It can also be written as

$$E_i = \min_{n_i}\left\{\int v(\mathbf{r})n_i(\mathbf{r})d\mathbf{r} + F_i[n,n_0]\right\} = \int v(\mathbf{r})n_i(\mathbf{r})d\mathbf{r} + F_i[n_i,n_0] \,, \tag{65}$$

where the universal functional $F_i[n,n']$ is given by

$$F_i[n,n'] = \min_{\Psi\to n}\langle\Psi|\hat{T}+\hat{V}_{ee}|\Psi\rangle = \langle\Psi[n,n']|\hat{T}+\hat{V}_{ee}|\Psi[n,n']\rangle \,. \tag{66}$$

Now define the non-interacting kinetic energy $T_i[n_i,n_0]$ by

$$T_i[n_i,n_0] = \min_{\substack{\Phi\to n \\ \Phi\perp\Phi_0,\ldots,\Phi_{m-1} \\ \int(n^i_0-n_0)^2\ min}} \langle\Phi|\hat{T}|\Phi\rangle = \langle\Phi[n,n_0]|\hat{T}|\Phi[n,n_0]\rangle \,, \tag{67}$$

where each Φ is orthogonal to the first $m-1$ states of the non-interacting Hamiltonian $\hat{H}_w^i$ if n_i is the density of the mth state of the non-interacting system $\hat{H}_w^i$. It then follows that $\Phi[n_i, n_0]$ is that non-interacting excited state wavefunction of $\hat{H}_w^i$ whose density is n_i. Moreover, we have the minimum principle

$$\begin{aligned} T_i[n_i, n_0] &+ \int w_i([n_i, n_0]; \mathbf{r}) n_i(\mathbf{r}) d\mathbf{r} \\ &= \min_n \left\{ T_i[n, n_0] + \int w_i([n, n_0]; \mathbf{r}) n(\mathbf{r}) d\mathbf{r} \right\} , \end{aligned} \tag{68}$$

where the non-interacting Hamiltonian is defined

$$\hat{H}_w^i = \hat{T} + \sum_{i=k}^{N} w_i([n_i, n_0]; \mathbf{r}_k) . \tag{69}$$

$\hat{H}_w^i$ is identified as the one whose ground-state density resembles n_0 most closely. This means that from all those non-interacting excited states (if there are more than one) for which the excited state density is n_i we select the one for which $\int (n_0^i - n_0)^2$ is minimum. n_0^i is the ground-state density of the non-interacting Hamiltonian $\hat{H}_w^i$.

The Kohn-Sham equations have the form

$$\left[-\frac{1}{2}\nabla^2 + w_i([n_i, n_0]; \mathbf{r}) \right] \phi_j^i(\mathbf{r}) = \epsilon_j^i \phi_j^i(\mathbf{r}) , \tag{70}$$

where the orbitals are occupied as necesarry, so that

$$n_i = \sum_{k=1} \lambda_k^i |\phi_k^i|^2 . \tag{71}$$

The occupation numbers λ_k^i will be 0,1 or 2 for a non-degenerate system. Since n_i is an excited-state density of $\hat{H}_w^i$, at least one of the λ_k^i will be zero. As in the usual Kohn-Sham scheme, w_i here is obtained by first approximating it with a starting guess for n_i in the Kohn-Sham potential, and then the Kohn-Sham equations are solved in a self-consistent manner. The total excited-state energy is

$$E_i = \int v(\mathbf{r}) n_i(\mathbf{r}) d(\mathbf{r}) - \frac{1}{2} \sum_j \lambda_j^i \langle \phi_j^i | \nabla^2 | \phi_j^i | \rangle + G_i[n, n_0] , \tag{72}$$

where

$$G_i[n, n_0] = F_i[n, n_0] - T_i[n, n_0] \tag{73}$$

is the sum of the Coulomb and exchange-correlation energy. For practical calculations G must be approximated. The optimized potential method and the KLI approximation mentioned above can also be generalized to approximate G and the Kohn-Sham potential w. It is convenient to partition $G_i[n, n_0]$ into

$$G_i[n, n_0] = Q_i[n, n_0] - E_c^k[n, n_0] \,, \tag{74}$$

where Q_i is the Coulomb plus exchange component and E_c^i is the correlation component of G_i. A crucial constraint for approximating Q_i and $\frac{\delta Q_i}{\delta n}$ is

$$\begin{aligned} \langle \Phi[n_i, n_0] | \hat{V}_{ee} | \Phi[n_i, n_0] \rangle \;\; &- \;\; \langle \Phi^{N-1}[n_i, n_0] | \hat{V}_{ee} | \Phi^{N-1}[n_i, n_0] \rangle \\ = \int d(\mathbf{r}) [n_i(\mathbf{r}) \;\; &- \;\; n_i^{N-1}(\mathbf{r})] \left. \frac{\delta Q_i[n, n_0]}{\delta n} \right|_{n=n_i} \,, \end{aligned} \tag{75}$$

where Φ^{N-1} is the ground-state of H_w^i in Eq. (69), but with $N-1$ electrons, and n_i^{N-1} is the density of Φ^{N-1}. Also, it is understood that both w_i and $\frac{\delta Q_i}{\delta n}$ vanish as $|r| \to \infty$. Eq. (75) is analogous to the ground-state exchange-only Koopmans relation that has been previously obtained for finite systems [20, 50] and for infinite systems [51]. Other useful constraints can also be derived [26].

5 Discussion

One can apply the theories discussed in this review in a large variety of calculations. In a ground-state calculation one needs only one exchange-correlation functional. In excited state calculations, on the other hand, we have different exchange-correlation functionals for the different excited states or for the different ensembles. It is believed that these functionals can be constructed as orbital dependent functionals, that is the difference between excited state functionals is revealed in the exchange-correlation functional only through the occupation numbers (i.e. the electron configuration). This can be realized by the optimized potential method. This method can be

applied not only for exchange-only calculations. The inclusion of correlation is straightforward in principle. One only needs a correlation functional as a functional of the orbitals and then the way of the derivation and calculation is exactly same. Unfortunatelly, we do not have ensemble or excited state correlation functionals. In the ground-state theory it is also a fundamental problem to find an appropriate correlation functional, i.e. a correlation functional that performs well together with the KLI exchange. In the existing approximating functionals exchange and correlation are treated together and if we change only the exchange part (into KLI) the balance between the exchange and correlation is ruined and we might receive worse results than in the exchange-only case. Gross and coworkers [52] found that among the existing correlation functional the Colle-Salvetti correlation functional is the best. In a lot of cases KLI + Colle-Salvetti gives results better than any other existing functional. The study of correlation in excited state calculation is a challenge of future research.

We can emphasize that ensemble calculations or calculations on a single excited state are only slightly more complicated than the ground-state calculation. So these calculations can be routinly done just like the ground-state calculations. They can be regarded as competitive with the powerful time-dependent density functional approach for the calculation of excitation energies. The practical troubles one has to face in dealing with bigger systems are exactly the same as in the ground state. (For a recent review of ground-state OPM and KLI calculations see [52].)

Acknowledgements

The grant 'Széchenyi' from the Hungarian Ministry of Education is gratefully acknowledged. This work was supported by the grants OTKA No. T 029469.

References

1. P. Hohenberg and W. Kohn Phys. Rev. **136**, B864 (1864).
2. Á. Nagy, Adv. Quant. Chem. **29**, 159 (1997).
3. R. Singh and B. D. Deb, Phys. Reports **311**, 47(1999).

4. E. K. U. Gross, J. F. Dobson and M. Petersilka, in *Density Functional Theory*, Ed. R. Nalewajski, Topics in Current Chemistry (Springer-Verlag, Heidelberg, 1996) vol. 181. p 81.
5. A. K. Theophilou, J. Phys. **C 12**, 5419 (1978).
6. E. K. U. Gross, L. N. Oliveira and W. Kohn, Phys. Rev. A **37**, 2805, 2809, 2821 (1988)
7. Á. Nagy Phys. Rev. **A 49**, 3074 (1994).
8. A. Görling, Phys. Rev. A **54**, 3912 (1996).
9. A. Görling and M. Levy, Int. J. Quantum. Chem.S. **29** 93 (1995); Phys. Rev. B **47**, 13105 (1993).
10. W. Kohn Phys. Rev. A **34,** 737 (1986).
11. Á. Nagy, Phys. Rev. **A 42**, 4388 (1990).
12. Á. Nagy, J. Phys. B **24**, 4691 (1991).
13. Á. Nagy Int. J. Quantum. Chem.S. **29**, 297 (1995).
14. Á. Nagy and I. Andrejkovics, J. Phys. B **27**, 233 (1994).
15. Á. Nagy, Int. J. Quantum. Chem. **56,** 225 (1995).
16. Á. Nagy, J. Phys. **B 29**, 389 (1996).
17. R. T. Sharp and G. K. Horton, Phys. Rev. **30,** 317 (1953).
18. J. D. Talman and W. F. Shadwick, Phys. Rev. A **14**, 36 (1976).
19. K. Aashamar, T. M. Luke and J. D. Talman, At. Data Nucl. Data Tables **22** 443 (1978).
20. J. B. Krieger, Y. Li and G. J. Iafrate, Phys. Rev. A **45**, 101 (1992); Phys. Rev. A **46**, 5453 (1992).
21. Á. Nagy, Int. J. Quantum. Chem. **69**, 247 (1998).
22. N. I. Gidpoulos, P. Papakonstantinou and E. K. U. Gross, Phy. Rev. Lett. (in press).
23. Á. Nagy, J. Phys. B **34**, 2363 (2001).
24. Á. Nagy, Int. J. Quantum. Chem. **70**, 681 (1998).
25. Á. Nagy, in *Electron Correlations and Materials Properties* Eds. A. Gonis, N. Kioussis and M. Ciftan (Kluwer, New York,1999) p. 451.

26. M. Levy and Á. Nagy, Phys. Rev. Lett. **83**, 4631 (1999).
27. Á. Nagy and M. Levy, Phys. Rev. A **63**, 2502 (2001).
28. A. Görling, Phys. Rev. A **59,** 3359 (1999).
29. Á. Nagy, Phys. Rev. A **55**, 3465 (1997).
30. C. E. Moore, Atomic Energy Levels, Circular 467, National Bureau 0f Standards, vol. 1 (1949).
31. T. Kato, Commun. Pure Appl. Math. **10**, 151 (1957).
32. E. Steiner, J. Chem. Phys. **39**, 2365(1963); N. H. March, Self-consistent fields in atoms (Pergamon, Oxford, 1975).
33. N. C. Handy, in *Quantum Mechanical Simulation Methods for Studying Biological Systems* Eds. D. Bicout and M. Field (Springer–Verlag, Heidelberg,1996) p.1.
34. R. T. Pack and W. B. Brown, J. Chem. Phys. **45**, 556 (1966).
35. F. J. Gálvez, J. Porras, J. C. Angulo and J. S. Dehesa, J. Phys. B. **21**, L271 (1988).
36. J. C. Angulo, J. S. Dehesa and F. J. Gálvez, Phys. Rev. A **42**, 641 (1990); erratum Phys. Rev. A **43**, 4069 (1991).
37. J. C. Angulo and J. S. Dehesa, Phys. Rev. A **44**, 1516 (1991).
38. F. J. Gálvez and J. Porras, Phys. Rev. A **44**, 144 (1991).
39. J. Porras and F. J. Gálvez, Phys. Rev. A **46**, 105 (1992).
40. R. O. Esquivel, J. Chen, M. J. Stott, R. P. Sagar and V. H. Smith, Jr., Phys. Rev. A **47**, 936 (1993).
41. R. O. Esquivel, R. P. Sagar, V. H. Smith, Jr., J. Chen and M. J. Stott, Phys. Rev. A **47**, 4735 (1993).
42. J. S. Dehesa, T. Koga and E. Romera, Phys. Rev. A **49**, 4255 (1994).
43. T. Koga, Theor. Chim. Acta **95**, 113 (1997); T. Koga and H. Matsuyama, Theor. Chim. Acta **98**, 129 (1997)
44. J. C. Angulo, T. Koga, E. Romera and J. S. Dehesa, THEOCHEM **501-502**, 177 (2000).
45. Á Nagy and K. D. Sen, J. Phys. B **33**, 1745 (2000).

46. Á Nagy and K. D. Sen, Chem. Phys. Lett. **332**, 154 (2000).

47. Á Nagy and K. D. Sen, J. Chem. Phys. **115**, 6300 (2001).

48. O. Gunnarsson and B.I. Lundqvist, Phys. Rev. **B 13**,4274(1976); O. Gunnarsson, M. Jonson and B.I. Lundqvist, Phys. Rev. **B 20**,3136(1979).

49. J. Harris and R. O. Jones, J. Phys. F **4**,1170 (1974); J. Harris, Phys. Rev. A **29**,1648 (1984).

50. M. Levy and A. Görling, Phys. Rev. A **53**, 3140 (1996).

51. J. P. Perdew, in *Density Functional Methods in Physics* Eds. by R. M. Dreizler and J. da Providencia (Plenum, New York, 1985).

52. T. Grabo, T. Kreibich, S. Kurth and E. K. U. Gross, in *Strong Coulomb Correlations in Electronic Structure, Beyond the Local Density Approximation* Eds. V. I. Anisimov (Gordon & Breach, Tokyo,1999).

New Perspectives in Theoretical Chemical Physics

Erkki J. Brändas
Department of Quantum Chemistry, Uppsala University
Box 518, S-751 20 Uppsala, Sweden

(Received February 11, 2002; accepted April 22, 2002)

Abstract

We discuss some new aspects and related open problems in theoretical chemical physics. These include the fundamental issue of the system-environment partition, the problem of entanglement versus dissipation and the approach to the classical limit via coherence-decoherence mechanisms. In these applications resonances act as an intermediary and it can be proven that microscopic selforganisation emerges as a consequence of the approach towards a higher order complexity level. Present methods and applications act as an edge-boundary for the quantum-classical and/or micro-macro (meso-)situation.

CONTENTS

1. INTRODUCTION

In the present report we discuss and review some open problems related to the interaction between a quantum system and its environment particularly the transition from a pure quantum state to the classical limit. The principal issue is the fundamental conflict between a quantum system and its classical environment [1]. The problem is usually conjectured in terms of concepts like entanglement and quantum dissipation or phrased differently on the notions and mechanisms of coherence-decoherence.

ADVANCES IN QUANTUM CHEMISTRY, VOLUME 42

0065-3276/03 $35.00

A different approach to this question is to invoke general quantum statistical methods to attend the open boundary regions of seemingly random correlations and fluctuations. It is proposed that in this vanguard territory stochastic resonances will act as an intermediate instrumentation of information. As a result, the well-known measurement problem is extended to deal concurrently with the effects of entanglement and dissipation.

This alternative viewpoint brings in the density matrix as the fundamental unit [2], particularly the reduced density operators and their representability properties [3,4,5]. To paint the coherent-dissipative portrait it is thus necessary to describe the emergence (or loss) of off-diagonal long-range order, *ODLRO* [3]. The production of quantum correlations contributing to the coming out of a macroscopically large eigenvalue in the appropriately reduced density matrix - a manifestation of *ODLRO* - is already a well-known element in most theories of super-conductivity and -fluidity, see e.g. [6]. The theory is however less developed and understood in connection with general properties of open, dissipative complex systems.

As the tools of modern physics extend into many new areas which leads to technical progress and new industrial applications the present viewpoint is far from academic. As examples we mention the initiation of the new Uppsala Research Graduate School *Advanced Instrumentation and Measurements* [7]. On the microscopic level e.g. a novel type of quantum technology is becoming essential for miniaturised objects and for advanced computer and data communications. We end this review by enclosing a table of Quantum Technology, techniques and mechanisms.

2. SYSTEM-ENVIRONMENT

In a statistical framework random-, thermal-, and quantum fluctuations compete in the process of structural formation and break up. The theoretical formulation, in terms of Liouville like master equations, must therefore be properly generalised to incorporate thermal correlations. This is usually carried out by means of appropriate thermalisations and/or inclusions of non-Hamiltonian terms in the evolution dynamics [8]. In this enlarged setting the thermalized Liouville equation, see e.g. [9], extends the dynamical environment and brings forth a possible framework for microscopic self-organization.

To complete the picture of integrating a rigorous resonance representation in the present formulation we stress the following well-known results. First, complex resonance states necessitate, in general, a nonhermitean extension of quantum mechanics [10] and support moreover classical entities within a nonlinear stochastic setting. The latter has recently attracted attention in various complexity situations under the name of Stochastic Resonances [11]. The generic interpretation is coupled to quantum-and classical scattering processes including signal processing technology.

The mathematical formulations are formally linked through the solutions of the associated Helmholtz equation for the scattering process or the related finite Fourier transform for the bandlimited signal [12]. Ellipsoidal co-ordinates in general and prolate spheroidal wave functions in particular are here of fundamental and technological importance in arriving at attainable solutions [13].

The progress in quantum technology, see the introduction above, has also been paralleled by strong developments in the understanding of non-linear dynamical systems operating in a noisy environment. These considerations include general cooperative phenomena with characteristic deterministic and stochastic time scales, which sometimes are collected under the name of a new complexity paradigm [11]. This in turn brings forward several unorthodox questions. For instance what are the supposed boundaries as regards appropriate phenomenological levels of organisation and description, e. g. the ordering into various micro-, meso-, and macroscopic distributions, and most interestingly, the conflict in bridging the gap of understanding between classical and quantum physics. This is also related to the well-known inconsistency of irreversibility on a higher order phenomenological level and the fundamental time reversible dynamics of Schrödinger´s and Newton´s equations [14], see also the discussions at the Nobel 90-year Jubilee [15]. The situation is further perplexing in that the interpretation and understanding of quantum mechanics even today defeats a general feeling of agreement or consensus.

We support the indirect measurement philosophy in Quantum Mechanics, see e.g. [16]. In this formulation [17] the initial step rules that the quantum system and the measuring device and/or environment entangle through objectively defined quantum correlations uniquely given by the mirror theorem [18]. The fundamental step of the measurement is then a resonance forming and decaying process, which connects the phenomenon with a relevant time scale. These correlations lead us to an objective description that will guide our physical intuition towards an adequate comprehension and inclusion of general quantum phenomena. The formulation, now referring to the Liouville level, also contains stochastic components, c.f. recent studies of stochastic like resonances in driven nonlinear dynamical systems with possible relations to quantum aspects of chaos via the actuality of nonlocal hidden variables [17].

The present trend involves several theoretical and technical advances. We will first mention the application of the mirror theorem that states that the product of two noncommuting mappings (with non-zero eigenvalues) have the same classical canonical forms irrespective of the order of the product. This leads to several consequences in the formulation of quantum aspects of atomic and molecular systems. It also leads to the definition of so-called natural expansions and a general definition of entanglement, see [9] and references therein.

Next we refer to well-known extensions of quantum theory to incorporate the resonance picture of unstable states. These are often supported via so-called dilation analytic techniques [10] or through precise semigroup constructions, see e.g. [19]. It

depends on the physical situation, which one is to be preferred. We will not say more on this except pointing out that the analytic approach may appear more convenient in applications in quantum chemistry and chemical physics.

The Liouville picture, finally, has here several advantages over the standard Schrödinger-Heisenberg picture. It allows a direct comparison between quantum-classical behaviour. More directly it permits the simultaneous incorporation of all kinds of general correlations irrespective of their quantum- and/or thermal origin.

We have recently discussed many of these aspects in quite some detail [20]. In the next section we will show how thermal behaviour are brought together in the density matrix through a simple relation between phenomenological relaxation times and the absolute temperature of the environment and the consequences of this condition.

3. DENSITY MATRICES AND EXTREME STATES

In quantum statistics it is convenient to focus on the density operator ρ and to use the Liouville equation

$$i\frac{\partial \rho}{\partial t} = \hat{\mathrm{L}}\rho \tag{1}$$

Husimi [2] first realised that the exact energy of a system of identical particles can be expressed by the second order reduced density matrix. Important theorems regarding fermionic behaviour was developed by Yang [3], Coleman [4] and Sasaki [5], for a recent review on reduced density matrices and the famous N-representability problem, see Coleman and Yukalov [21].

The N particle (and its p-reduced companions) representable density matrix $\Gamma^{(p)}$ can be defined as follows

$$\Gamma^{(p)}(x_1 \ldots x_p | x_1' \ldots x_p') = \binom{N}{p} \int \Psi^*(x_1 \ldots x_p, x_{p+1} \ldots x_N) \Psi(x_1' \ldots x_p', x_{p+1} \ldots x_N) dx_{p+1} \ldots dx_N . \tag{2}$$

where the (normalised) wave function $\Psi(x_1 \ldots x_N)$ represents a many-body quantum mechanical system. Traditionally one ususally consider two types of particles, bosons and fermion, but since quantum chemical applications concern the electronic structure of atoms and molecules it is common practice to focus on the characteristics of fermion reduced density density matrices, particularly with p=2.

Note that the definition (2) normalises $\rho = \Gamma^{(p)}$ to the number of pairings of N fermions [2]. Other normalisations [3,4] also exits

$$\begin{aligned} &\text{Löwdin: } \Gamma^{(p)};\ \mathrm{Tr}\{\Gamma^{(p)}\} = \binom{N}{p} \\ &\text{Coleman: } D^{(p)};\ \mathrm{Tr}\{D^{(p)}\} = 1 \\ &\text{Yang: } \rho^{(p)};\ \mathrm{Tr}\{\rho^{(p)}\} = p!\binom{N}{p}. \end{aligned} \tag{3}$$

The Löwdin normalisation is often used in quantum chemistry, but other choices are also frequently used depending somewhat on the circumstances.

It was first believed that the eigenvalues (in the Löwdin normalisation) of $\Gamma^{(2)}$, like in the one matrix case, were bounded between zero and one. This was however wrong and this realisation led in fact to a very important and interesting development. The possible limits that the two-matrix eigenvalues may obtain correspond to every conceivable correlated arrangement from the independent particle model to a fully pair coherent condensate. The principal concept of off-diagonal long-range order, *ODLRO*, was introduced by Yang [3] in connection with his proof of the largest bound for $\Gamma^{(2)}$.

The manifestation of a macroscopically large eigenvalue $\lambda_L^{(2)}$ in the reduced density matrix showed a very strong physical organisation in the system. The emergence of *ODLRO* through $\lambda_L^{(2)} = N/2$ in the Löwdin normalisation, leads to many interesting consequences, see e.g. [22]. Note that in the Yang and Coleman normalisations $\lambda_L^{(2)} = N$ and $\lambda_L^{(2)} = 1/N\text{-}1$.

Although the concept of an extreme state, Coleman [4, 21] is quite well-known in quantum chemistry and chemical physics, the concept is not fully acknowledged in general since the custom seems to be that one refers more or less unconsciously to the thermodynamic limit. Nevertheless *ODLRO* has been of central importance in super- conductivity/fluidity and it will also play a central role below. In connection with this development Coleman [2] identified the precise condition for the so-called extreme state which in certain cases could develop *ODLRO*. The observation that a simple AGP-function gave the largest possible eigenvalues of the 2-matrix was given by Sasaki [5] in a report that unfortunately was delayed through a misplacement by the publisher [21]. The clue to describe a convenient representation for open systems will be obtained via the extreme state as follows:

Starting from a set of m localised pair functions or geminals $\mathbf{h} = (h_1, h_2, \ldots h_m)$ obtained from appropriate pairing of one particle basis spin functions, we will build the following transformations, the motive to be explained further below,

$$\mathbf{B} = \frac{1}{\sqrt{m}} \begin{pmatrix} 1 & \omega & \omega^2 & . & \omega^{m-1} \\ 1 & \omega^3 & \omega^6 & . & \omega^{3(m-1)} \\ . & . & . & . & . \\ . & . & . & . & . \\ 1 & \omega^{2m-1} & \omega^{2(2m-1)} & . & \omega^{(m-1)(2m-1)} \end{pmatrix} \quad \omega = e^{\frac{i\pi}{m}} \tag{3}$$

The scenario is usually obtained from discussions of total wavefunctions constructed as an Antisymmetrised Geminal Power, AGP, where the units (geminals) are obtained from two-particle determinants of suitable spin orbitals. More general quantum statistical settings are also possible [23].

To proceed we introduce a coherent and a correlated basis $\mathbf{g}$ and $\mathbf{f}$ respectively through

$$\begin{aligned} |\mathbf{h}\rangle\mathbf{B} &= |\mathbf{g}\rangle = |g_1, g_2, \ldots g_m\rangle \\ |\mathbf{h}\rangle\mathbf{B}^{-1} &= |\mathbf{f}\rangle = |f_1, f_2, \ldots f_m\rangle \end{aligned} \tag{4}$$

At present we do not appreciate the significance of either $\mathbf{g}$ or $\mathbf{f}$, except noting that the functions in $\mathbf{g}$ are completely delocalised over the region of sites defined by the localised (may be chosen real) basis $\mathbf{h}$. The differences between the g_i's are simply that of different phases at every numbered h_k, where for each consecutive number of sites there seem to follow a certain oddity-rule. The $\mathbf{f}$-basis contains all possible phase shifted contributions from each site in accordance with Eq.(4) above.

There are several inter-connections to be mentioned here. The first one concerns Coleman's extreme state. If $\mathbf{h}$ is the set of two particle determinants and the AGP wave function is constructed from g_1, see Coleman [4] for the exact condition for the extreme state, the two-particle reduced density matrix (not explicitly writing the "tail contribution" which results from the remaining pair configurations) can be expressed as

$$\Gamma^{(2)} = \Gamma_{\mathrm{L}}^{(2)} + \Gamma_{\mathrm{S}}^{(2)} = \lambda_{\mathrm{L}} |g_1\rangle\langle g_1| + \lambda_{\mathrm{S}} \sum_{k=2}^{m} |g_k\rangle\langle g_k| \tag{5}$$

with the (possibly) large eigenvalue λ_L and the degenerate one λ_S given by

$$\lambda_L = \frac{N}{2} - (m-1)\lambda_S;\ \lambda_S = \frac{N(N-2)}{4m(m-1)} \tag{6}$$

Note that we have m basis pairfunctions or geminals and $2m$ spin orbitals. The number of fermion pairings and pair configurations are therefore

$$\binom{N}{2};\binom{2m}{2}$$

respectively. The dimension of the "box contribution" defined in Eq. (5) is m and consequently the dimension of the missing "tail contribution", not explicitly written out above is $2m(m-1)$.

To summarise the situation we add the fact that one can prove that the eigenvalue associated with the missing "tail" is the same as λ_S [4]. We thus have for the extreme state one possible large eigenvalue λ_L and an $(m-1)(2m+1)$ degenerate eigenvalue λ_S. The physical significance of the extreme state follows by noting that λ_L may under specific circumstances grow to be macroscopically large, i.e. approach the macroscopic number $N/2$ (in the Löwdin normalization) thereby developing *ODLRO*. However, rather than focusing only at the latter transition we will also consider the precursor level of the extreme state and the importance played by the basis $\mathbf{g}$.

As we have mentioned above analogous equations can be derived [23] in a statistical framework both for the case of localised fermions in a specific pairing mode and/or bosons subject to a quantum transport environment. The relevance of the basis $\mathbf{f}$ will be demonstrated in the following section

4. THE ROLE OF TEMPERATURE

To complete the picture including a theoretical formulation of random-, thermal- and quantum fluctuations the temperature must somehow be incorporated. This is fundamentally a difficult problem as we are dealing with systems out of equilibrium. We have also stated that we do not apply the thermodynamic limit. Still we will show that it is possible to incorporate the temperature in a quasi-equilibrium context and then to demonstrate the constructive interaction between the thermal input from the environment and the open quantum system.

It is a very well-known trick to make time imaginary by formally including

temperature in the formulation through the relation

$$t \rightarrow t - i\beta;\ \beta = \frac{1}{kT} \tag{7}$$

where k is Boltzmann's constant and T the absolute temperature in Kelvin. In the extended dynamical picture to be presented below this analogy does no longer hold. To rigorously comprehend the temperature we can as usual resort to the Bloch equation via

$$-\frac{\partial \rho}{\partial \beta} = \hat{\mathrm{L}}_{\mathrm{B}}\rho \tag{8}$$

where $\hat{\mathrm{L}}_{\mathrm{B}}$ is the energy super operator appropriately extended to a biorthogonal complex representation [24].

$$\hat{\mathrm{L}}_{\mathrm{B}} = \frac{1}{2}\{H| \rangle\langle *| + | \rangle\langle *|H\} \tag{9}$$

Note the complex conjugate in the bra-position compared to the extended Liouville time generator

$$\hat{\mathrm{L}} = H| \rangle\langle | - | \rangle\langle |H^{\dagger} \tag{10}$$

where we instead admit the hermitean conjugate in the commutator above. For more on this, see e.g. Ref. [9]. Applying now Eqs. (8-9) to

$$\Gamma_{\mathrm{S}}^{(2)} = \lambda_{\mathrm{S}} \sum_{k=2}^{m} |g_k\rangle\langle g_k| = \lambda_{\mathrm{S}} \sum_{k=1}^{m}\sum_{l=1}^{m} |h_k\rangle(\delta_{kl} - \frac{1}{m})\langle h_l| \tag{11}$$

we obtain, with E the real part of the energy,

$$e^{-\beta\hat{\mathrm{L}}_{\mathrm{B}}}\tilde{\Gamma}_{\mathrm{S}}^{(2)} = \lambda_{\mathrm{S}} e^{-\beta E} \sum_{k=1}^{m}\sum_{l=1}^{m} |h_k\rangle e^{i\beta\frac{1}{2}(\varepsilon_k+\varepsilon_l)}(\delta_{kl} - \frac{1}{m})\langle h_l *| \tag{12}$$

where ε_k is the imaginary part of the energy, which is related to the life time as ($\hbar$ is Planck's constant divided by 2π)

$$\varepsilon_k = \frac{\Gamma_k}{2} = \frac{\hbar}{2\tau_k} \tag{13}$$

The tilde over the two matrix indicates an extended complex biorthogonal representation according to the analyticity requirements [10] given by the resonance formulation.

To appreciate the formulas (11) and (12) we remind the reader of the result quoted in Ref. [25], i.e.

$$\mathbf{Q} = \mathbf{B}^{-1}\mathbf{J}\mathbf{B} \tag{14}$$

where the unitary matrix $\mathbf{B}$ connects the standard Jordan form $\mathbf{J}$

$$\mathbf{J} = \begin{pmatrix} 0 & 1 & 0 & . & 0 \\ 0 & 0 & 1 & . & . \\ . & . & . & . & 0 \\ . & . & . & . & 1 \\ 0 & . & . & . & 0 \end{pmatrix} \tag{15}$$

with the symmetric representation $\mathbf{Q}$ defined by

$$\mathbf{Q}_{kl} = (\delta_{kl} - \frac{1}{m}) e^{i\frac{\pi}{m}(k+l-2)}; \; k,l = 1,2,..m \tag{16}$$

Hence, if we can find a relation between ε_k, β with the dimension $r = m$, so that the transformed density operator in Eq. (12) assumes a Jordan block form (i.e. proportional to $\mathbf{Q}$ or $\mathbf{J}$) one of the consequences for the related dynamics is the emergence of a dramatically increased lifetime [9]. Hence if

$$\beta\varepsilon_l = 2\pi\frac{l}{r}; \; l = 1,2,...r \tag{17}$$

we find that the thermalised density matrix in Eq. (12) becomes proportional to $\mathbf{Q}$. A similar analysis with $m = 2$ obtains for $\Gamma_L^{(2)}$. Using (7), (8) and (17) one finds that the longest relaxation time τ_{rel} - obtained for $l = 1$ - compatible with the smallest

dimension or "size" $r_{\min}$ is given by

$$\beta\varepsilon_l = \frac{\hbar}{2kT\tau_{\rm rel}} = \frac{2\pi}{r_{\min}} \tag{18}$$

Thus the sought after relation between the absolute temperature, the relaxation time and the "minimal size" of our dissipative system is

$$\hbar\tau_{\rm rel}^{-1} = \frac{4\pi kT}{r_{\min}} \tag{19}$$

where the relaxation time is given by

$$\tau_{\rm rel} = r_{\min}\tau_{\rm lim};\ \tau_{\rm lim} = \frac{\hbar}{4\pi kT} \tag{20}$$

Note that $\tau_{\rm lim}$ is the shortest time commensurate with the uncertainty relation.

The relevance of the $\mathbf{f}$-basis is now clear. It appears through Eq. (14) and the unitarity property of $\mathbf{B}$, noting that (12) and (17) connects $\Gamma^{(2)}$ with

$$\hat{\mathrm{J}} = |\mathbf{h}\rangle\mathbf{Q}\langle\mathbf{h}| = |\mathbf{h}\rangle\mathbf{B}^{-1}\mathbf{J}\mathbf{B}\langle\mathbf{h}| = |\mathbf{f}\rangle\mathbf{J}\langle\mathbf{f}| = \sum_{k=1}^{r-1}|f_k\rangle\langle f_{k+1}| \tag{21}$$

The vectors of $\mathbf{B}^{\dagger}$ express $\mathbf{f}$ in the original basis $\mathbf{h}$, see Eqs. (3-4), while producing the natural basis for the thermalized density matrix. Thus a quantum system with *ODLRO* emerging through a dominant macroscopic eigenvalue in the appropriately reduced density matrix may decay through characteristic life times τ.

It is, however, easy to prove that the operator $\hat{\mathrm{T}} = \dfrac{\hat{\mathrm{J}}}{\tau}$ generates the evolution

$$e^{-i\frac{\hat{\mathrm{J}}t}{\tau}} = \sum_{k=0}^{m-1}\left(\frac{-it}{\tau}\right)^k \frac{1}{k!}\hat{\mathrm{J}}^{\mathrm{k}} \tag{22}$$

Since Eq.(22) is multiplied with $e^{-\frac{t}{\tau}}$ we find that the general decay rule associated with the time dependent probability *N(t)* to find our system at time *t* in its initial configuration given by

$$dN = -\frac{1}{\tau} N(t)dt \tag{23}$$

is modified to, assigning the highest power in the polynomial to $m=r$,

$$N(t) \propto t^{r-1} e^{-\frac{t}{\tau}} \tag{24}$$

and

$$dN = t^{r-2}\left(r - 1 - \frac{t}{\tau}\right)N(t)dt \tag{25}$$

While we find $dN(t) < 0$ for all times in (23), the law deduced in (24) and (25) yields

$$dN(t) > 0;\ t < (r-1)\tau. \tag{26}$$

Hence, instead of the usual disintegration law for the initial state, we find that Eq.(23) leads to increasing (self)-organization during a finite number of life times τ. It is in this context that we can speak of microscopic selforganization at the microscopic level.

We have here been very careful to refer to precise constructions and theorems in density matrix theory and resonance formation. It is clear, however, that the present development can be generalised to other more general processes in non-equilibrium quantum statistics, where the two natural basis partners **g** and **f** refer to density matrices and/or transition matrices [9].

The theory above has been applied in a variety of realistic situations. The range includes ionic conductance in aqueous solutions and molten alkali chlorides, damped spin-wave behaviour in paramagnetic systems, stimulated emission of adiation in masers, the fractional quantum Hall effect and quantum correlations in high-T_C cuprates and other non-BCS superconductors [6, 9, 22, 23, 26].

5. QUANTUM COMPLEX SYSTEMS: CONCLUSIONS

We will end this review by introducing the popular concept of *Complex Systems* particularly with the focus on *Quantum Complex Systems.*

Complex systems share the feature of exhibiting a variety of behaviours. The fundamental mechanism behind this is instability principally manifested in bifurcations towards a multiplicity of states and deterministic chaos. It confers to the underlying

system a sensitivity to the unavoidable perturbations of intrinsic or environmental origin present in the world around us [27]. The most common evidence of complexity comes from phenomena at the macroscopic level, where emphasis is placed on the origin of collective behavior in multi-unit systems giving rise to new emergent properties absent at the level of the constituting units.

There is, however, an increasing awareness that complexity appears also at the microscopic level. For instance the very origin of irreversibility is intimately related to the intrinsic complexity generated by the interactions and correlations between the elementary particles constituting the macroscopic system [15]. A variety of systems operate on an intermediate scale between the micro- and microscopic ones. Such mesoscopic systems exhibit a growing importance in the new quantum technology domain [28].

The tools of modern physics extend into many new areas with the developments focused on a new level of description never before believed to be possible. The complexity paradigm emphasises the appropriate level of formulation as well as the supposed boundary between classical and quantum physics. Recent developments in quantum technology involve basic quantum phenomena [28], stochastic resonances and information theoretic analysis [29], ellipsoidal wavefunctions for scattering and signal processing [30], coherence-decoherence in dissipative systems [9] including the phenomenon of high temperature cuprate super conductors [6].

It may be useful to make a more systematic arrangement of *Quantum Complex Systems* by stressing the techniques and mechanisms of *Quantum Technology* subjects involved in the present research programme. It will be specified below, for more details see reference [28]:

QUANTUM TECHNOLOGY

Application Area	**Mechanism/Technique**
Quantum information	**Nonclassical**
Quantum computers	Q-bits
Cryptography	Superposition
Quantum memory	Spins, squids
Teleportation	Entanglement
Quantum optics	Interference
Quantum Nondemolition QND	Uncertainty relation
Condensed matter	**Broken symmetry**
Superconductivity SC	ODLRO
Quantum Hall effect	Topology
High temperature SC	Quantum Statistics
Superfluidity	Gauge symmetry
SQUID	Josephson effect

Ultracold matter
Traps
Laser cooling
Ultracold molecules
Atom laser
Micro maser
Electron holography

Interferometry
Photons
Electrons
Muons
Neutrons
Atoms

Coherent dissipative systems
Aqueous solutions
Proton transfer
Polar molecules
Molten salts
Protons and muons in metals
Polymers, organic molecules

Stochastic non-linear dynamical systems
Complex Systems
Cellular systems
Image processing
Signal processing
Antenna synthesis
Resonances in atoms and molecules
Signal-to-noise

Dissipation-dispersion
Doppler dispersive forces
Anti-Stokes Raman process
Intermolecular forces
Bose-Einstein condensation
Mode selection
Aharonov-Bohm effect

Coherence-decoherence
Entanglement
Vortex dynamics
Spin resonance
Spinor symmetry
Cavity QED

Quantum-thermal correlations
Grotthus type
Self-dissociation
FIR
Ionic conductance
Coherent tunneling
Quantum diffusion

Stochastic Resonances

Semigroups, dilations
Self-organisation
Aliasing
Prolate spheroidals
Finite Fourier transform
Complex potentials
Stochastic differential equations

ACKNOWLEDGEMENTS

It is a great pleasure for me to acknowledge financial support as well as assistance in every way of the Chairpersons of the DVXα-Symposium, namely Professor Hirohiko Adachi, Professor Masayuki Uda and Professor Hisanobu Wakita. I am further indebted to Professor Rika Sekine for practical help and assistance during my visit and for the detailed work of editing this volume.

6. REFERENCES

1. E. B. Karlsson and E. Brändas, Phys. Scripta, **T76,** 7 (1998).
2. K. Husimi, Proc. Phys. Math. Society Japan, **22,** 264 (1940); see also P. O. Löwdin, Phys Rev. **97,** 1474 (1955); *ibid.* 1490 (1955); 1509 (1955).
3. C. N. Yang, Rev. Mod. Phys. **34,** 694 (1962).
4. A. J. Coleman, Rev. Mod. Phys. **35,** 668 (1963).
5. F. Sasaki, Technical Report **77,** Uppsala Quantum Chemistry Group (1962); Phys. Rev. **138B,** 1338 (1965).
6. L. J. Dunne and E. J. Brändas, *D-wave Bipolaronic Condensate with Short Range Repulsive Electronic Correlations in an Extended Hubbard Model of HighTc Cuprate Superconductors,* Advan. Quant. Chem. **40,** 225-248 (2001).
7. Rolf Boström, Erkki Brändas and Sven Kullander: *Promoting University – Industry Links by a New Type of PhD Education: The AIM Graduate School.* Conference Proceedings, Vienna, 4-6 November 1998 **ESA 432** – Academic and Industrial Cooperation in Space Research, p. 181 (1998).
8. G. Lindblad, Commun. Math. Phys. **40,** 119 (1976).
9. E. Brändas, in *Dynamics during Spectroscopic Transitions,* eds. E. Lippert and J. D. Macomber, Springer Verlag, Berlin, p. 148 (1995).
10. E. Balslev and J. M. Combes, Commun. Math. Phys. **22,** 280 (1971); C. van Winter, J. Math. Anal. **47,** 633 (1974).
11. A. R. Bulsara and L. Gammaitoni, Phys. Today **49**, (1996).
12. B. Larsson, T. Levitina and E. J. Brändas, Int. J. Quant. Chem. **85,** 392 (2001).
13. T. Levitina and E. J. Brändas: *Angle Dependent Total Cross Sections and the Optical Theorem,* Computers and Chemistry, **25**, 55-67 (2001).
14. I. Prigogine, *From Being To Becoming* W. H. Freeman and Company, San Francisco, (1980).
15. *Fundamentals, Logical Structure, and Unification of Natural Sciences*, Nobel Jubilee Meeting 1901-1991, Eds. E. Brändas and C. A. Chatzidimitriou-Dreismann, Int. J. Quant. Chem., **53** (1995).
16. V. B.Braginski and F. Ya. Khalili, *Quantum Measurement*, (Cambridge University Press, Cambridge, 1992); see also M. B. Mensky, *Continuous Quantum Measurements and Path Integrals,* Institute of Physics, Publishing Ltd,Techno House, Redcliffe Way, (Bristol and Philadelphia, 1993).
17. E. Brändas and B. Hessmo, Lecture Notes in Physics **504,** 359 (1998).
18. E. Schmidt, Math Ann. {\bf 63,} 433 (1907); B. C. Carlson and J. M. Keller, Phys. Rev. **121**, 659 (1961); P.-O. Löwdin, Int. J. Quant. Chem. **21**, 269 (1982); Isr. J. Chem. **31,** 297 (1991).
19. A. Bohm and M. Gadella, *Dirac Kets, Gamow vectors and Gel'fand Triplets,* Springer Verlag, Berlin, (1989).
20. E. Brändas, *Dissipative Systems and Microscopic Selforganization,* a tribute to Per-Olov Löwdin, Advan. Quant. Chem. in press (2002).
21. A. J. Coleman and V. I. Yukalov, *Reduced Density Matrices Coulson's Challenge,* Lecture Notes in Chemistry, **72,** Springer-Verlag, Berlin (2000).

22. E. J. Brändas, Ber. Bunsenges. Phys. Chem. **96,** 49 (1992).
23. E. J. Brändas and C. A. Chatzidimitriou-Dreismann, *On the Connection between Certain Properties of the Second-Order Reduced Density Matrix and the Occurrence of Coherent-Dissipative Structures in Disordered Condensed Matter.* Int. J. Quant. Chem. **40,** 649 (1991).
24. E. Brändas, N. Elander, Eds. *Resonances, The Unifying Route Towards the Formulation of Dynamical Processes, Foundations and Applications in Nuclear, Atomic and Molecular Physics,* Lecture Notes in Physics **325,** 1-564 (1989).
25. C. E. Reid and E. J. Brändas, Lecture Notes in Physics, **325,** 475 (1989).
26. E. J. Brändas in *Dynamics of Transport in Plasmas and Charged Beams,* eds. G. Maino and M. Ottaviani, World Scientific Publ. Comp., 160 (1996).
27. G. Nicolis och I. Prigogine, *Exploring Complexity*, W.H. Freeman, (1989).
28. *Modern studies of basic quantum concepts and phenomen*a, Nobelsymposium nr 104, Eds. E. Karlsson and E. Brändas, Physica Scripta, **T76** (1998).
29. J. W. C. Robinson, J. Rung A. Bulsara and M.E. Inchiosa, *General Measures for Signal-Noise Separation in Nonlinear Dynamical Systems,* Phys. Rev. **E. 63,** 1, (2001).
30. T. Levitina and E. Brändas, *On the Schrödinger equation in ellipsoidal coordinates,* Comp. Phys. Comm. **126,** 107-113 (2000).

Near Edge Structures of Mg-, Co-, Cu- and Zn-Tetraphenylporphyrins Measured by PESA and Calculated with DV-Xα

Y. Nakajima [a], M. Hoshino [b], D. Yamashita [d] and M. Uda [c,d]

a) Riken Keiki Co., Ltd., Research Department
2-7-6, Azusawa, Itabashi-ku, Tokyo 174-8744, Japan
b) The Institute of Physical and Chemical Research
2-1, Hirosawa, Wako, Saitama 351-0198, Japan
c) Laboratory for Materials Science and Technology, Waseda University
2-8-26 Nishiwaseda, Shinjuku-ku, Tokyo 169-0051, Japan
d) Department of Materials Science and Engineering, Waseda University
3-4-1 Ohkubo, Shinjuku-ku, Tokyo 169-8555, Japan
(Received January 23, 2002; in final form March 15, 2002)

Abstract

The near-edge electronic structures of several tetraphenylporphyrins (TPPs), modified by substituting the central metal atoms (M), were measured using photoelectron spectroscopy in air (PESA), and were estimated using the DV-Xα molecular orbital calculation method. The metal atoms used were Mg, Co, Cu and Zn. The ionization thresholds and the photoelectron emission yields of these TPPs changed significantly from compound to compound. The thresholds for ionization or photoemission can be divided into two groups, i.e. 1) less than 5.26 eV for Mg^{II}TPP and Zn^{II}TPP, and 2) more than 5.38 eV for Co^{II}TPP and Cu^{II}TPP.

DV-Xα calculations demonstrated that the upper valence band primarily consists of C2p in Mg^{II}TPP and Zn^{II}TPP, M3d in Co^{II}TPP, and M3d and N2p in Cu^{II}TPP. Such valence band components can be used to explain the difference in observed photoemission threshold energies and to elucidate the change in photoemission yields for electrons with low kinetic energy.

Keywords: TPP, PESA, DV-Xα, DOS,

Corresponding Author: Yoshiyuki Nakajima: y-nakajima@rikenkeiki.co.jp

ADVANCES IN QUANTUM CHEMISTRY, VOLUME 42

0065-3276/03 $35.00

1. INTRODUCTION

Extensive studies have been conducted on porphyrin-complexes because the skeleton structure of these compounds is similar to those of "*in vivo* functional materials" such as chlorophyll and hemoglobin. Recent reports indicate that ZnTPP [1] and PtOEP [2] are potentially useful as red organic light-emitting diodes (OLEDs). Therefore, theoretical and experimental studies of the near-edge electronic structures of porphyrin complexes are necessary to further understand the functions of these materials.

An OLED is an electronic device in which a thin film of organic emissive material is sandwiched between a transparent anode and metal cathode. The emissive layer emits light as a result of the recombination of electrons injected from the cathode and holes injected from the anode. The injection barrier height at the interface between the emissive layer and the anode or cathode can be experimentally estimated from the difference in photoemission threshold energies at the interfaces, as measured by photoelectron spectroscopy in air (PESA). Although photoemissions from the emissive layer, anode or cathode cannot be measured directly at the interface by PESA, the photoemission or ionization threshold energy can be theoretically estimated from the energy difference between the vacuum level and the highest occupied molecular orbital (HOMO).

We observed photoelectrons emitted from the near-edge structures of some tetraphenylporphyrins (TPPs) by PESA. Such "in air" measurements are very effective for studying materials used in air. However, the surface of some materials becomes oxidized when exposed to air during measurements, leading to ambiguity of the near-edge structures. The DV-Xα molecular orbital calculation method can be used to estimate the near-edge electronic structures and also to confirm whether the surface of the material investigated is oxidized after photoelectron measurements. Although the absolute binding energies of molecular orbitals cannot be determined using the DV-Xα method, these energies can be estimated from PESA experiments. Therefore, the complementary use of PESA and DV-Xα is required to fully understand the near-edge electronic structures of TPPs used in air.

2. EXPERIMENT

Pulverized $Mg^{II}TPP$, $Co^{II}TPP$, $Cu^{II}TPP$, and $Zn^{II}TPP$ were prepared according to literature [3-6]. Fine crystals of TPPs purified by recrystallization were used as the samples for the photoemission measurements. Photoemission measurements were conducted at room temperature in air (temperature 23-25 °C, humidity 43-50%Rh and pressure 1014-1015 hPa). Photons from a deuterium lamp were monochromatized by a grating spectrometer (Japan Spectroscopic,

CT-10) and focused on a sample. Generated electrons from the sample were measured using PESA with a 0.05-eV photon energy step. An open counter (AC-2, Riken Keiki) [7-10] was employed as a detector of generated electrons. The number of incident electrons per second into the counter N_{in} was then estimated with the aid of the following equation.

$$N_{in}=N_{em}f=\frac{N_{obs}}{1-\tau N_{obs}} \quad (1)$$

Here N_{em} is the number of emitted electrons per second, f is the fraction of electrons incident at the counter, τ is the dead time, and N_{obs} is the number of observed electrons per second. The photoelectric quantum yield Y is derived by dividing N_{in} by the number of incident photons, which was estimated using a photodiode (S1220-1010BQ, Hamamatsu Photonics), placed in the sample position [9].

3. CALCULATION

The DV-Xα method [11] was employed to calculate molecular orbitals. Convolution of the squares of molecular orbital amplitudes to plot a partial density of states (PDOS) curve was carried out adopting a line width of 0.5 eV. The model used for calculations is shown in Fig. 1. The geometries of Zn^{II}TPP are based on X-ray data [12]. Molecular orbitals of Mg^{II}-, Co^{II}-, and Cu^{II}-TPP were calculated employing the same geometries as those of Zn^{II}TPP where a central metal is substituted with one of the metal atoms mentioned above.

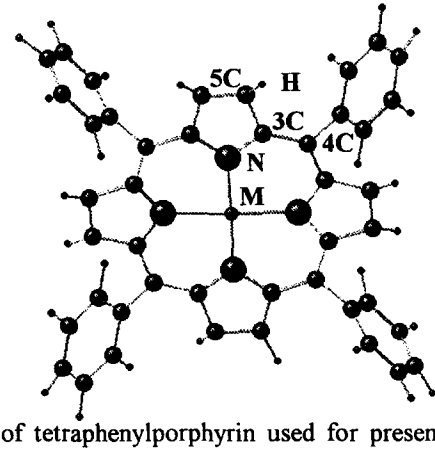

Fig.1. Geometry of tetraphenylporphyrin used for present calculations, where a central metal atom M is substituted with Mg, Co, Cu or Zn.

Calculating conditions were as follows: basis sets of 1s-3p for N, 1s-3p for C, 1s for H, 1s-3d for Mg, and 1s-4p for Co, Cu and Zn; potential well of 2.5 atomic units in width and –2.0 Hartrees in depth; and 38500 sampling points for all TPPs.

4. RESULTS AND DISCUSSION

The density of states (DOS) was estimated by differentiating photoemission yield (Y) with incident photon energy (E). Square roots of photoemission yields against incident photon energies for Zn^{II}TPP are shown in Fig. 2. The threshold energy for photoemission was deduced from the intersection point of $Y^{1/2}$ and background (listed in Table 1 for the TPPs).

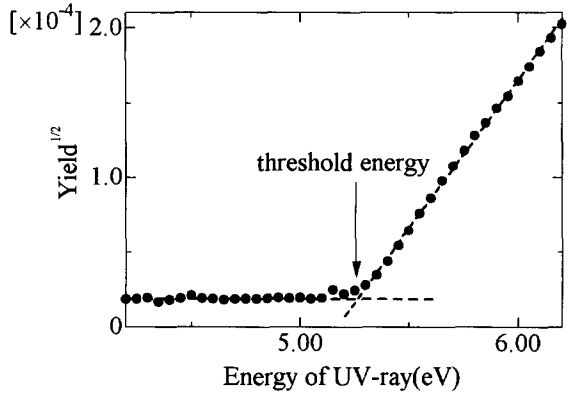

Fig.2 Relationship between energy of incident UV-rays and square root of photoelectric yield (Y) for Zn^{II}-TPP.

Observed threshold energies were divided into two groups; 1) Mg^{II}- and Zn^{II}-TPP with low threshold energies of less than 5.26 eV and include non-transition elements as central atoms, and 2) Co^{II}- and Cu^{II}-TPP with high threshold energies of 5.38 eV or greater and include 3d elements. DOS values estimated from photoelectron spectra are shown in Fig. 3. The abscissa and ordinate indicate energy of UV-rays and DOS values, respectively.

Table 1. Threshold energies for photoemissions from TPPs

Sample	Threshold energy (eV)
$Mg^{II}TPP$	5.24
$Co^{II}TPP$	5.38
$Cu^{II}TPP$	5.64
$Zn^{II}TPP$	5.26

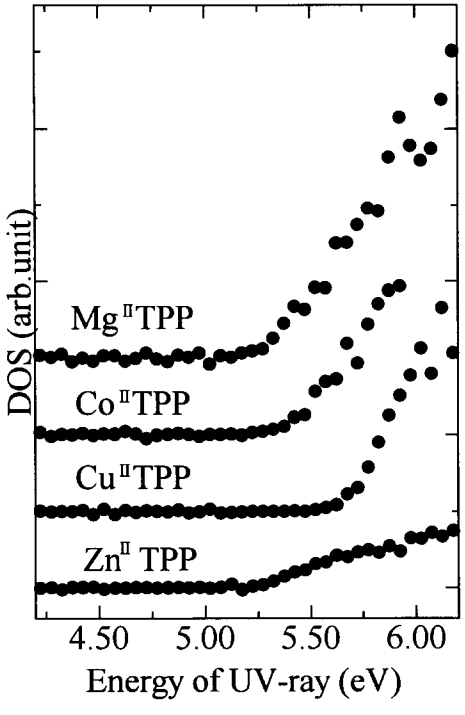

Fig.3. Density of states (DOS) estimated from observed photoelectron spectra.

Relative binding energies and major orbital components of the HOMOs of Mg^{II}-, Co^{II}-, Cu^{II}- and Zn^{II}-TPP are shown in Table 2. The major HOMO components of the TPPs consist of 4C 2p and N2p for Mg^{II}- and Zn^{II}-TPP, forming the basis of first classification from observed photoemission threshold energies. The major HOMO components consist of M 3d for Co^{II}-TPP, and consist of M 3d and N 2p for $Cu^{II}TPP$, forming the second group. Such classification

based on calculated orbital components for the HOMOs appears to be consistent with classification based on observed photoemission threshold energies. Furthermore, calculated relative binding energies for Mg^{II}- and Zn^{II}-TPP are smaller than those for Co^{II}- and Cu^{II}-TPP, and this grouping is consistent with that based on observed photoemission threshold energies.

Table 2. Binding energies and orbital components of HOMOs in TPPs

Complex	Energy (eV)	Components Rate (%)					
		M[1] 3d	N 2s	N 2p	3C 2p	4C 2p	5C 2p
Mg^{II}TPP	-1.035	0	0	28	3	53	5
Co^{II}TPP	-0.573	82	0	2	6	0	8
Cu^{II}TPP	0.115	49	9	28	4	2	5
Zn^{II}TPP	-1.066	0	0	25	4	52	7

1) M=Mg, Co, Cu or Zn

A linear relationship does not exist, however, between the observed threshold energies for photoemissions and the calculated HOMO binding energies of the TPPs. This is because the molecular geometries of the TPPs, with the exception of Zn^{II}-TPP, are hypothetical, and not experimentally determined. Furthermore, the calculated binding energies are relative, not absolute. The relationship between observed photoemission yields for near-edge structures and calculated DOS values remains a subject of future study as the photoemission yields are expected to be expressed as the product of the DOS and the photoemission probabilities for near-edge molecular orbitals, both of which have yet to be studied.

5. CONCLUSION

The photoemission threshold energies of TPPs were measured using the PESA method. The TPPs examined here can be divided into two groups, i.e. 1) Mg^{II}-and Zn^{II}-TPP with low threshold energies of less than 5.26 eV, and 2) Co^{II}- and Cu^{II}-TPP with high threshold energies of more than 5.38 eV.

DV-Xα calculations revealed that the HOMOs of the TPPs consisted primarily of 4C 2p and N2p in Mg^{II}TPP and Zn^{II}TPP, M 3d in Co^{II}TPP, and M 3d and N 2p in Cu^{II}TPP. These calculated results helped to explain observed photoemission threshold energies and emission yields.

For quantitative explanation of observed photoemission threshold energies, DOS and partial density of states (PDOS) at the HOMOs of tetraphenylporphyrins, it is necessary to know the exact geometries of the TPPs as well as the photoelectron emission probability for molecular orbitals, rather than

that for atomic orbitals.

REFERENCES

[1] Y. Hamada, IEEE Trans. Electron Devices, 44, 1208 (1997)
[2] M. A. Baldo, D. F. O'Brien, Y. You, A. Shoustikov, S. Sibley, M. E. Thompson, S. R. Forrest, Nature, 395, 151 (1998)
[3] J. W. Buchler, In The Porphyrins ed. D. Dolphin, Academic press New York, 1979; Vol. 1, Chapter 10.
[4] D. Dorough, J. R. Miller, and F. M. Fuennekens, J. Am. Chem. Soc., 73, 4315 (1951)
[5] T. Sakurai, K. Yamamoto, H. Naito, and N. Nakamoto, Bull. Chem. Soc. Jpn., 49, 3042 (1976).
[6] A. D. Alder, F. R. Longo. F. Kampas, J. Kim. J. Inorg. Nucl. Chem., 32, 2443 (1970).
[7] H. Kirihata, M. Uda, Rev. Sci. Instr 52, 68 (1981).
[8] M.Uda, Jpn. J. Appl. Phys. 24, 284 (1985).
[9] T. Noguchi, S. Nagashima, M. Uda, Nucl. Instr. Meth. A342, 521 (1994).
[10] S. Nagashima, T. Tsunekawa, N, Shiroguchi, H. Zenba, M. Uda, Nucl. Instr. Meth. A373, 148 (1996).
[11] H. Adach, M. Tsukada, C. Satoko, J. Phys. Soc. Jpn. 49, 875 (1978).
[12] P. Dastidar and I. Goldbarg, Acta Cryst. C52, 1976 (1996)

Theoretical Analysis of XANES for Aqueous Aluminum Salt Solutions

Shuji Matsuo[†], Kaori Shirozu[‡], Yuichi Tateishi[‡], and Hisanobu Wakita[†‡]*
[†]*Advanced Materials Institute, and* [‡]*Department of Chemistry, Faculty of Science, Fukuoka University, Nanakuma, Jonan-ku, Fukuoka 814-0180, Japan*

Takushi Yokoyama
Department of Chemistry, Faculty of Science, Kyushu University, Ropponmatsu, Chuo-ku, Fukuoka 810-8560, Japan

(Received June 3, 2002; in final form June 22, 2002)

Abstract
In order to understand the coordination behavior of Al(III) ions in hydrosphere, discrete variational Xα molecular orbital calculations were performed to analyze Al K-edge XANES spectra for the aqueous solutions of $Al(NO_3)_3 \cdot 9H_2O$ and Al-EDTA (EDTA = ethylenediaminetetraacetate) complex. As to $Al(NO_3)_3 \cdot 9H_2O$, the hydrate structure was presumed to be rather an asymmetric hexahydrated structure than an high-symmetric structure. As to Al-EDTA, the 5-fold coordinated Al-EDTA was concluded to be the coexistence of the pyramidal and trigonal bipyramidal structures in proportion of 4 to 6.

Contents

KEYWORDS: Al(III) complex, aqueous solution, XANES analysis, DV-Xα MO method, theoretical electron transition

*Corresponding author, e-mail: wakita@fukuoka-u.ac.jp

ADVANCES IN QUANTUM CHEMISTRY, VOLUME 42

0065-3276/03 $35.00

1. INTRODUCTION

Recently, Al(III) ions in soil and/or rocks dissolving in hydrosphere due to acid rain exhibit toxic effects against living thing, especially plants (1,2). The toxicity of Al(III) ions appears strongly in the hydrated Al(III) ion and its hydrolytic products. The Al(III)-toxicity is, however, suppressed by the complexation of Al(III) ion and organic ligands, especially the ligands with carboxylate groups(1-3). Therefore, it is important on environmental science to understand the coordination behavior of Al(III) ions in hydrosphere.

For Al(III)-EDTA complex (EDTA = ethylenediaminetetraacetate), we have studied the coordinated structure to the aluminum(III) ion in the aqueous solution from NMR measurements. As a result, it has been proposed that the Al(III)-EDTA complex in aqueous solution is the dynamic 5-fold coordinated structure with one O atom of a H_2O molecule, two N atoms of EDTA, and two O atoms which alternatively exchange by two atoms of four CH_2COO groups of EDTA, as seen in Fig. 1 (4). The coordination structure is, however, insufficiently revealed in the steric structure from NMR measurements.

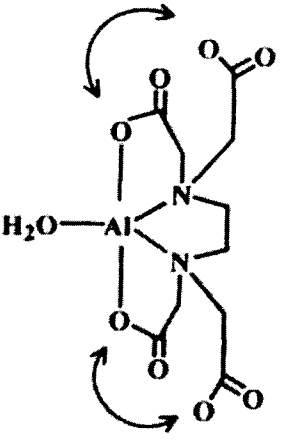

Fig 1. Structure of Al-EDTA presumed by NMR measurements.

X-ray absorption near-edge structure (XANES) spectra, which give us the information on the electronic state and steric structure of absorbing atoms (5), for light atoms in solid compound have been also measured popularly using soft X-ray and analyzed in combination with a discrete variational Xα (DV-Xα) molecular orbital (MO) method (6-11). However, few studies for light atom species in solution have been carried out by XANES until we develop a liquid cell system for soft X-ray (rightly by transmission mode) (12).

Using the liquid cell system, Al K-edge XANES spectral measurements were made for aluminum nitrate nanohydrate ($Al(NO_3)_3 \cdot 9H_2O$), as model of harmful chemical species in soil, and Al-EDTA in aqueous solution (13). Figure 2 shows the XANES spectra together with that in powder measured by use of a total electron yield mode. The XANES spectrum of $Al(NO_3)_3 \cdot 9H_2O$ in aqueous solution was little different in the spectral feature and peak position from that in powder, though the peak width in the powder was slightly broader than that in the aqueous solution. This suggested that the structure around the Al(III) ions in aqueous solution becomes hexahydrate structure the same as that in powder. On

the other hand, the XANES spectrum of Al-EDTA in aqueous solution was outstandingly different in peak position from that in powder, though the peak position for the powder sample of Al-EDTA was the same as that of powder sample of $Al(NO_3)_3 \cdot 9H_2O$. This suggested that six coordination sites of Al(III) ion in Al-EDTA powder are occupied only by EDTA which is a hexadentate ligand, while the coordination structure of Al-EDTA in aqueous solution is different from that in powder. From the results of NMR for Al-EDTA in aqueous solution, the chemical shift of XANES spectrum is expected to derive from the 5-fold coordinated structure as shown in Fig. 1. However, it is hard to argue it from only the comparison of the spectral feature and peak position for the observed XANES spectra whether the steric structure of the coordination of six H_2O molecules to Al(III) ions in aqueous solution of $Al(NO_3)_3 \cdot 9H_2O$ is similar to that in powder or not, and whether the chemical shift occurs by the change of the coordination number for Al(III) ions or not.

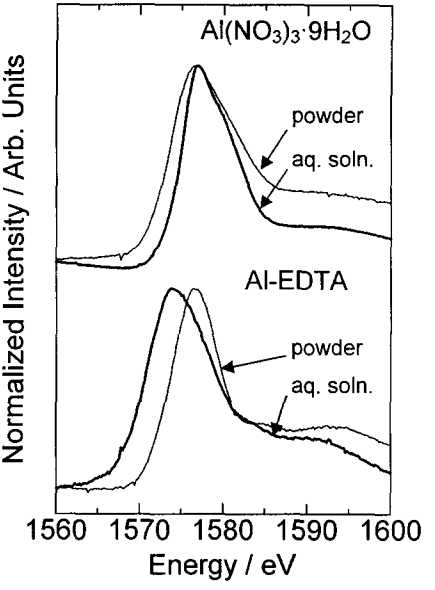

Fig 2. Observed XANES spectra of powder (thin) and aqueous solution (bold) of each of $Al(NO_3)_3 \cdot 9H_2O$ and Al-EDTA.

In this study, our aim is to examine theoretically the influence of the steric structure around Al(III) ions on the XANES spectra from the DV-Xα calculations and to discuss the hydrated structure of Al(III) ions and the chemical shift of Al-EDTA in aqueous solution.

2. COMPUTATIONAL METHOD

For $Al(NO_3)_3 \cdot 9H_2O$, model I is an asymmetrical structure with six different Al-O bond lengths, 1.80, 1.90, 1.91, 1.97, 2.03, and 2.03 Å, which is based on the crystal structure (14), and model II is an octahedral structure with six same Al-O bond lengths, 1.88 Å, which is O_h symmetry on the basis of the structure in aqueous solution (15) (see in Fig. 3). Basis sets used are 1s, 2s, 2p, 3s, 3p, and 3d

for Al, 1s, 2s, and 2p for O, and 1s for H. Charges of models I and II both became 3. Sample points used in the numerical integration were taken up to 20000 for each calculation. Convergence point of self-consistent-field iterations for all models was set 0.001 electrons in difference of electron before and after the iterations. The calculations were made for both the ground state and Slater's transition state (16) with non-symmetry.

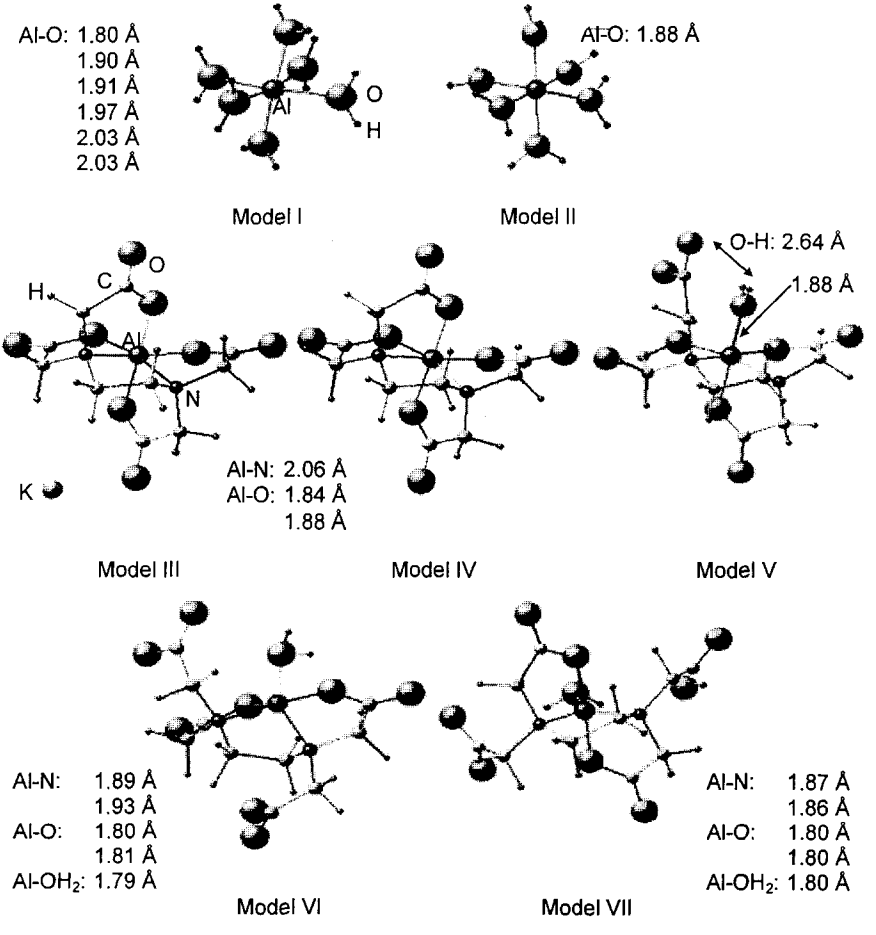

Fig 3. Models of $Al(NO_3)_3 \cdot 9H_2O$ and Al-EDTA used for DV-Xα calculations.

For Al-EDTA, model III is 6-fold coordinated Al(III) ion only by EDTA (see in Fig. 3). This model was constructed by referring to the single-crystal structure of $K[Al(EDTA)]\cdot 2H_2O$ (17). Model IV is that K(I) ion is removed from model III, and model V is that one CH_2COO group coordinated at the axial positions to Al(III) ion in model IV is replaced with one H_2O molecule (see in Fig. 3). Then, the free CH_2COO group is arranged that two O atoms little interact with the Al(III) ion. Models IV and V were used to investigate the influence of the complex ion and coordinated H_2O molecule on the chemical shift of the XANES for the aqueous solution of Al-EDTA, respectively, compared with 5-fold coordinated models. Models VI and VII were constructed as pyramidal and trigonal structures, respectively (see in Fig. 3), and are based on the results of NMR experiments as mentioned above. Note that only one of two CH_2COO groups bonded to each N atom can coordinate to the Al(III) ion. In addition, the geometry optimizations for the two models were performed with the Cerius^2 ver.3.5 (Accelrys Inc.) programs (18). Basis sets used are 1s, 2s, 2p, 3s, 3p, and 3d for Al, 1s, 2s, and 2p for C, N, and O, and 1s for H. Charges became zero for model III and 1- for other models. Sample points used in the numerical integration were taken up 1000 points per atom for each calculation. Convergence point of self-consistent-field iterations for all models was set 0.001 electrons in difference of electron before and after the iterations. The calculations were made for both the ground state and Slater's transition state with non-symmetry.

The DV-Xα calculations were made for the models mentioned above and transition peaks were subsequently calculated by the suite of programs (19,20). The transition peaks that appear above lowest unoccupied orbitals should be only utilized to analyzed observed XANES spectra because their shapes are based on the theory that an electron is excited from an inner orbital to an unoccupied orbital by an electric dipole transition and the details of procedure can be seen in Ref. 21.

3. THE PRESUPPOSITION OF XANES SPECTRAL FEATURE FOR HEXAHYDRATED Al(III) ION

The calculated transition peaks (bars) for models I and II are shown in Fig. 4 with the observed XANES spectrum (solid line) of $Al(NO_3)_3\cdot 9H_2O$ in aqueous solution. The calculated transition peaks are convoluted by a Gaussian function (broken line) of 1.2 eV full width at half maximum (FWHM). The energy scale was calibrated by adding 7.8 eV to the calculated energy (eV) for model I, because it was in good agreement with the observed XANES spectrum of $Al(NO_3)_3\cdot 9H_2O$ powder. This 7.8 eV was also added to the calculated energy (eV) for model II.

The transition peaks for model II, which is constructed as a structure in aqueous solution, show mainly two bunches of them. Bunch **e** in lower energy side is assigned by the transition to the MO's composed of Al 3p and O 2s orbitals, Bunch **f** in higher energy side is assigned by the transition to the MO's composed of Al 3p and O 2p orbitals. The appearance of bunches such these is due to high symmetry of model II, and that is reason why the transition peaks for model II are not in well agreement with the feature of the observed spectrum in aqueous solution, though the high-symmetrical $Al^{3+}(H_2O)_6$ structure calculated by a molecular dynamics simulations in water (max. 1728 water molecules) has well agreed with the experimental result of Al-O length (22). If the structure of $Al^{3+}(H_2O)_6$ keeps high symmetry in aqueous solution, the observed XANES spectrum would indicate two outstanding peaks. On the other hand, the transition peaks for model I, which is constructed as a structure in powder, are separated due to asymmetry. Consequently, this is well correspondent with the feature of the observed spectrum in aqueous solution as well as in powder. These results predict, therefore, that the steric structure around Al(III) ions in aqueous solution of $Al(NO_3)_3{\cdot}9H_2O$ is a hexahydrated structure with an asymmetric Al-O bond manner rather than O_h symmetry.

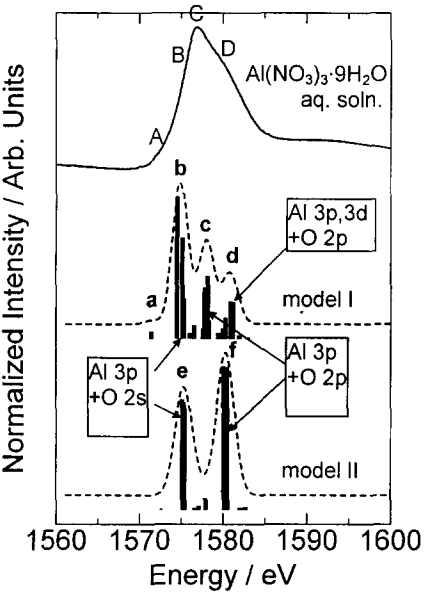

Fig 4. Calculated transition peaks (vertical bars) and curves (broken) for the models I and II. The observed XANES spectrum (solid) for aqueous solution of $Al(NO_3)_3{\cdot}9H_2O$. is given for reference with the prominent features A-E. The main atomic orbitals composing significant MO's are shown.

4. THE CHEMICAL SHIFTS OF XANES SPECTRA FOR Al-EDTA COMPLEX

Figures 5 and 6 show the results for 6-fold coordinated and 5-fold coordinated Al-EDTA models, respectively, with the observed XANES spectra

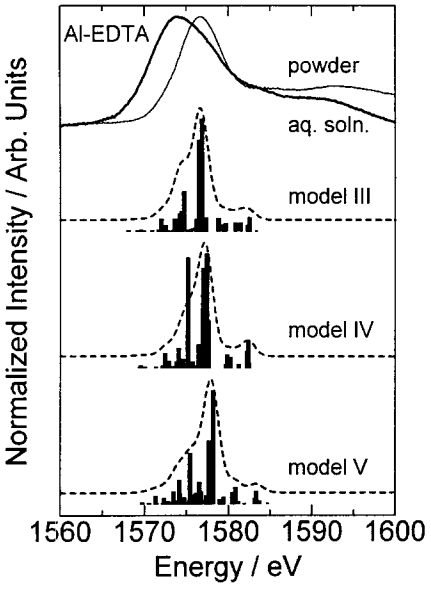

Fig 5. The chemical shifts of 6-fold coordinated Al-EDTA complex species for the models III-V. The vertical bars and broken lines are the calculated transition peaks and curves, respectively. The solid lines are the observed XANES spectra for the powder (thin) and aqueous solution (bold) of Al-EDTA complex, which are given for references.

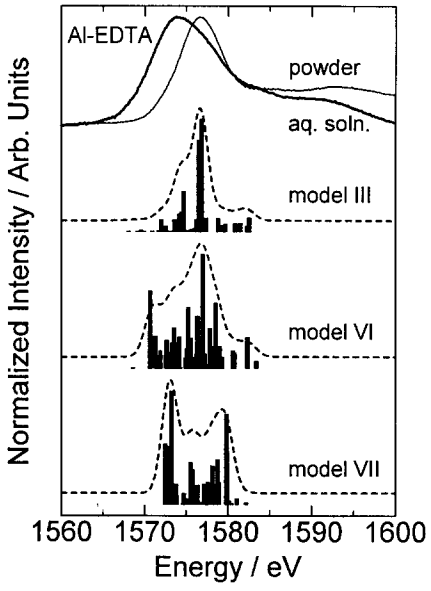

Fig 6. The chemical shifts of 5-fold coordinated Al-EDTA complex species for the models VI and VII, as compared with model III. The vertical bars and broken lines are the calculated transition peaks and curves, respectively. The solid lines are the observed XANES spectra for the powder (thin) and aqueous solution (bold) of Al-EDTA complex, which are given for references.

for powder and aqueous solution of Al-EDTA. The calculated transition peaks are convoluted by a Gaussian function of 1.0 eV full width at half maximum (FWHM). The energy scale was calibrated by adding 2.25 eV to the calculated energy (eV) for model III, because it was in good agreement with the observed XANES spectrum of Al-EDTA powder. This 2.25 eV was also added to the calculated energy (eV) for models IV-VII.

In Fig. 5, the positions of the calculated main transition peak for both models IV and V are less different from that of model III. These results would show for 6-fold coordinated Al-EDTA complex that both the ionization and

hydration structure replaced one CH_2COO group coordinated to Al(III) ion with one H_2O molecule are little relation to the chemical shifts of the Al K-edge XANES spectra for Al-EDTA.

On the other hand, the prominent peaks of the calculated transition peak for both models VI and VII appear at low energy of 5-7 eV, compared with that of model III, as can be seen in Fig. 6. These results would show that the chemical shifts of the K-edge XANES spectra for Al-EDTA mainly depend upon the difference in the coordination structure between 5-fold and 6-fold coordinates. Similar chemical shifts have been also obtained for that of aluminosilicate minerals including 4-fold, 5-fold, and 6-fold coordination structures. The chemical shifts depending on the coordination number of Al-EDTA further support the results of NMR experiments (4).

However, the steric structure of 5-fold coordinated Al-EDTA in aqueous solution cannot be concluded by either pyramidal or trigonal bipyramidal structures such as models VI and VII, respectively, since both the calculated results for models VI and VII show the calculated transition peaks illustrating the features characteristic of the Al K-edge XANES for aqueous solution of Al-EDTA. Therefore, the authors propose two steric structures as follows: the coexistence of the pyramidal and trigonal bipyramidal structures in a certain proportion, and the intermediate structure of them.

The former idea may be interpreted in Fig. 7, which shows the mixed peaks that the transition peaks calculated for models VI and VII are mixed in the proportions of 5 to 5, 4 to 6, and 3 to 7. The atomic orbitals, particularly the Al atom and the surrounding N and O atoms, constituting the MO's of the prominent peaks, **a-f**, and their proportions per one atom for each

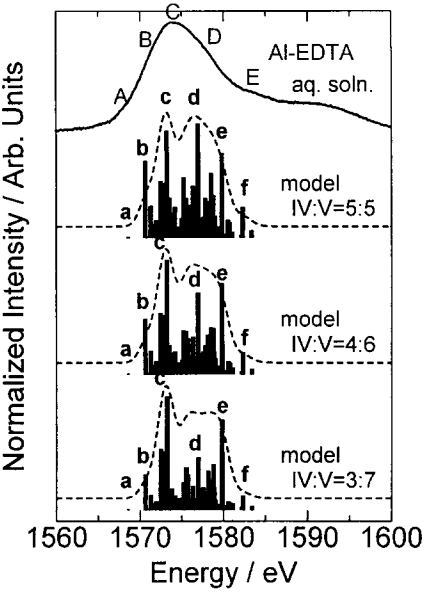

Fig 7. The consideration of the mixed structure of the pyramidal and trigonal bipyramidal structures by the use of models VI and VII. The appropriate proportions of model VI to model VII are shown in. The vertical bars and broken lines are the calculated transition peaks and curves, respectively. The solid line is the observed XANES spectrum for the aqueous solution of Al-EDTA complex, which is given for reference.

atomic species are shown in Table 1. Peaks **a**, **c** and **e** are of model VII, and peak **b**, **d**, and **f** are of model VI. The N atom orbitals equivalently contribute to peaks **b-e**, that is, it would show to be independent of the geometry. However, the O atom orbitals of H_2O molecule contribute to peaks **b** and **d** more than that of COO groups, i.e., peaks of model VI, while that of COO groups contribute to peaks **c** and **e** more than that of H_2O molecule, i.e., peaks of model VII. Thus, these results suggest that the characteristic on the steric structure may appear on the observed XANES spectrum. By mixing the transition peaks characteristic of each model, the mixed peaks obtained is in better agreement with the prominent features of the observed XANES spectrum than the peaks obtained for each model. For instance, feature B, C, and D in the observed spectrum can be assigned to the peak **b** of model VI, the peak **c** of model VII, and both of the peak **d** of model VI and the peak **e** of model VII. In particular, the transition peaks mixed in proportion of 4 to 6 are well correspondent with the feature D in the observed spectrum, though there is no direct evidence for this consideration. However, the pyramidal and trigonal bipyramidal structures are likely to exist easily in the equilibrium that two O atoms which exchange alternatively among four CH_2COO groups of EDTA occupy the remaining two coordination sites of Al (III) ion in aqueous solution, as seen in Fig. 1. Therefore, the 5-fold coordinated Al-EDTA in aqueous solution is suggested to form the pyramidal and trigonal bipyramidal structures such as models VI and VII, respectively, in proportion of 4 to 6.

Table 1. The atomic orbitals constituting the MO's of the prominent peaks, **a-f** in Fig. 7, and their proportions

	Atomic orbital and its proportion[a] (%)								
Peak	Al 3s	Al 3p	Al 3d	O^b 2s	O^b 2p	O^c 2s	O^c 2p	N 2s	N 2p
a	0.0	0.3	1.2	0.2	9.7	0.1	0.2	0.1	0.2
b	14.8	25.7	13.9	0.1	1.1	9.1	7.0	2.0	2.2
c	0.0	41.7	20.4	0.2	1.6	0.1	1.2	0.5	4.5
d	1.8	39.5	11.0	0.7	2.7	<0.1	2.5	2.2	3.8
e	0.0	29.2	7.8	0.6	2.5	0.1	0.3	0.1	11.0
f	0.2	9.5	22.9	1.8	9.4	0.1	0.3	0.1	1.8

[a]Proportion per one atom for each atomic species. [b]The O atom coordinated to Al(III) ion in COO group. [c]The O atom in H_2O molecule.

In the case of the latter, the DV-Xα method may be limited because it is hard to construct the model structure for the intermediate. In the molecular dynamics simulations of $Al^{+3}(H_2O)_5$ in water, the geometry converged at pyramidal- or trigonal bipyramidal-like structure, which is due to basis set (22,23). In the case of geometry optimizations for our Al-EDTA models, nothing converged at the structure except for models VI and VII, but not in water.

However, if the molecular dynamics simulation of Al-EDTA in water is performed, intermediate structure may be obtained. This matter will be improved in future.

5. CONCLUSION

The Al K-edge XANES spectra for the aqueous solutions of $Al(NO_3)_3 \cdot 9H_2O$ and Al-EDTA complex were analyzed by the DV-Xα calculations to investigate the steric structure around Al(III) ions. As to $Al(NO_3)_3 \cdot 9H_2O$, the hydrate structure was presumed to be rather an asymmetric hexahydrated structure than an high-symmetric structure. As to Al-EDTA, the 5-fold coordinated Al-EDTA was concluded to be the coexistence of the pyramidal and trigonal bipyramidal structures in proportion of 4 to 6. By the use of the combination of the Al K-edge XANES spectra and DV-Xα method, it will be expected to understand the coordination behavior of Al(III) ions in hydrosphere.

6. ACKNOWLEDGEMENTS

The authors thank KOBELCO Research Institute Inc. in Japan for the use of a Cerius^2 suite of programs. This work is supported by the Advanced Materials Institute of Fukuoka University.

7. REFERENCES

(1) L. V. Kochian, *Annu. Rev. Plant Physiol. Plant Mol. Biol.*, **46**, 237 (1995).
(2) J. F. Ma, *Plant Cell Physiol.*, **41**, 383 (2000).
(3) P. R. Ryan, E. Delhaize, and D. L. Jones, *Annu. Rev. Plant Physiol. Plant Mol. Biol.*, **52**, 527 (2001).
(4) T. Yokoyama, K. Shirozu, and H. Wakita, in preparation, and presented at the IUPAC International Congress on Analytical Sciences 2001, Tokyo, Japan, (2001).
(5) D. C. Konigsberger and R. Prins, (Eds.), "X-Ray Absorption: Principles, Applications, and Techniques of EXAFS, SEXAFS and XANES", John Wiley & Sons, New York, (1988).
(6) H. Nakamatsu, T. Mukoyama, and H. Adachi, *J. Chem. Phys.*, **95**, 3167 (1991).
(7) I. Tanaka, J. Kawai, and H. Adachi, *Phys. Rev. B*, **52**,11733 (1995).
(8) I. Tanaka and H. Adachi, *Phys. Rev. B*, **54**, 4604 (1996).
(9) H. Ichihashi, T. Kurisaki, T. Yamaguchi, T. Yokoyama, and H. Wakita, *Jpn.*

J. Appl. Phys., Part 1, **38**(*suppl.*), 101 (1999).
(10) Y. Muramatsu, T. Hayashi, and R. C. C. Perera, *J. Electron Spectrosc. Relat. Phenom.*, **104**, 155 (1999).
(11) J. Tsuji, K. Kojima, S. Ikeda, H. Nakamatsu, T. Mukoyama, and K. Taniguchi, *J. Synchrotron Radiat.*, **8**, 554 (2001).
(12) R. C. C. Perera and H. Wakita, in preparation, and presented at the IUPAC International Congress on Analytical Sciences 2001, Tokyo, Japan, (2001).
(13) H. Wakita, S. Matsuo, and R. C. C. Perera, in preparation, and presented at the IUPAC International Congress on Analytical Sciences 2001, Tokyo, Japan, (2001).
(14) P. Herpin and K. Sudarsanan, *Bull. Soc. Franç. Minér. Crist.*, **88**, 595 (1965).
(15) R. Caminiti and T. Radnai, *Z. Naturforsch.*, **A35**, 1368 (1980).
(16) J. C. Slater, "Quantum Theory of Molecules and Solids, vol. 4", McGraw-Hill, New York (1974).
(17) T. N. Polynova, L. A. Zasurskaya, and A. B. Iiyukhin, *Kristallografiya*, **42**, 168 (1997).
(18) http://www.accelrys.com/cerius2/index.html
(19) H. Adachi, M. Tsukada, and C. Satoko, *J. Phys. Soc. Jpn.*, **45**, 875 (1978).
(20) H. Adachi and K. Taniguchi, *J. Phys. Soc. Jpn.*, **49**, 1944(1980).
(21) S. Matsuo and H. Wakita, *J. Struct. Chem.*, to be submitted.
(22) E. Wasserman, J. R. Rustad, and S. S. Xantheas, *J. Chem. Phys.*, **106**, 9769 (1997).
(23) M. I. Lubin, E. J. Bylaska, and J. H. Weare, *Chem. Phys. Lett.*, **322**, 447 (2000).

Self-absorption Correction for Mn, Fe and Cu L X-ray Spectra Based on MO Calculations

D. Yamashita[a], Y. Nakajima[c], H. Nakamatsu[d] and M. Uda[a,b]

[a] *Department of Materials Science and Engineering, Waseda University, 3-4-1, Ohkubo, Shinjuku-ku, Tokyo 169-8555, Japan*
[b] *Laboratory for Materials Science and Technology, Waseda University, 2-8-26, Nishiwaseda, Shinjuku-ku, Tokyo 169-0051, Japan*
[c] *Riken Keiki Co, Ltd, Research Department, 2-7-6, Azusawa, Itabashi-ku, Tokyo 174-8744, Japan*
[d] *Institute for Chemical Research, Kyoto University, Gokasho, Uji, Kyoto 611-0011, Japan*

(Received January 21, 2002; in final form March 18, 2002)

Lα X-ray fluorescence (XRF) spectra emitted from some typical transition metals and their compounds showed different shapes characteristic of their chemical environments, which were Mn, MnO and MnO_2, Fe, α-Fe_2O_3, Fe_3O_4 and $FeSO_4$ and Cu, Cu_2O, CuO and CuCl. Such change in spectral shapes was successfully explained, except for CuO and CuCl, in view of the self-absorption scheme, where the DV-Xα molecular orbital calculation method was employed to estimate occupied and unoccupied density of states (DOS) responsible for X-ray emission and absorption.

The Lα X-rays resulted from electron transition between an M 2p electron vacancy and occupied molecular orbitals including, at least in part, M 3d orbitals of the atom of interest were theoretically explained to be absorbed by neighboring M atoms, where M means the same kind of transition elements, i.e. Mn, Fe and Cu. Here a part of the emitted Lα X-rays must be used to excite M 2p electrons to unoccupied molecular orbitals composed, at least in part, of M 3d.

Keywords: L X-ray, DV-Xα, X-ray absorption, unoccupied molecular orbital
Corresponding Author: M. Uda : muda@mn.waseda.ac.jp

ADVANCES IN QUANTUM CHEMISTRY, VOLUME 42

0065-3276/03 $35.00

1. Introduction

Lα X-rays emitted from chemical compounds including transition elements embedded in different chemical environments show significant difference in shape [1-6]. The shape of the L X-ray spectra has been explained qualitatively to be much altered by change in the near edge structures composed of occupied and unoccupied molecular orbitals. However, enough explanation had not yet been given in view of the quantum chemical scheme [1, 2].

Recently, the present authors succeeded to explain shape-difference in Fe Lα spectra emitted from Fe, α-Fe_2O_3, Fe_3O_4 and $FeSO_4$ quantum-chemically [7]. Such difference was quantitatively explained by introducing an assumption that a part of X-rays emitted through electron transition between the Fe 2p and 3d orbitals of Fe atom of interest is absorbed by another Fe atom with partially unfilled 3d orbitals, i.e. self-absorption, which is situated on the neighborhood of the X-ray emitting Fe atom.

The same explanation must be done for all the other chemical compounds composed of transition elements. As typical examples of transition element compounds, Mn, MnO and MnO_2 and Cu, Cu_2O, CuO and CuCl were selected and their observed and calculated Lα spectra were compared with those of the Fe Lα. For molecular orbital calculation the DV-Xα method [8] was employed.

2. Experiment and calculation

X-ray fluorescence (XRF) spectra emitted from Mn-, Fe- and Cu-containing compounds were recorded using Phillips PW 1480 spectrometer. The anode of the X-ray tube is made of molybdenum coated with a scandium thin layer. The accelerating voltage and the electric current on the anode were kept at 60 kV and 50 mA during experiments. Emitted X-rays were analyzed with the aid of a thallium acid phthalate (TLAP(001) 2d=25.75 Å) single crystal. The pellets of pulverized Mn (FURUUCHI CHEMICAL, 99.9%), MnO (RARE METALLIC, 99.9%), MnO_2 (RARE METALLIC, 99.9%), Fe (WAKO PURE CHEMICAL INDUSTRIES), α-Fe_2O_3 (RARE METALLIC, 99.9%), Fe_3O_4 (SOEKAWA CHEMICALS, 99%), $FeSO_4$ (SOEKAWA CHEMICALS, 99.9%), Cu (SOEKAWA CHEMICALS, 99.9%), CuO (SOEKAWA CHEMICALS, 99.99%),

Cu_2O (RARE METALLIC, 99.9%) and CuCl (Junsei Chemical, 99%), were used for the experiments.

The DV-Xα method [8] was employed for calculating the partial density of states (PDOS). The calculating conditions were as follows; 1) basis sets used for, Mn, Fe and Cu: 1s-4p, for O: 1s-2p, for S: 1s-3p and for Cl: 1s-3d; 2) clusters used for 2-1) Mn: Mn_{17} with T_d symmetry and with 8500 discrete sample points (DSP), for 2-2) MnO: MnO_6^{10-} with O_h and 3500 DSP, for 2-3) MnO_2: MnO_6^{8-} with D_{2h} and 3500 DSP, for 2-4) Fe: Fe_{15} with O_h and 7500 DSP, for 2-5) α-Fe_2O_3: FeO_6^{9-} with C_3 and 3500 DSP, for 2-6) Fe_3O_4: FeO_4^{5-} with T_d and 4500 DSP and $FeO_6^{9.5-}$ with C_i and 3500 DSP, for 2-7) $FeSO_4$: $FeS_6O_{24}^{10-}$ with C_i and 15500 DSP, for 2-8) Cu: Cu_{13} with O_h and 6500 DSP, for 2-9) Cu_2O: $Cu_7O_2^{3+}$ with C_3 and 4500 DSP, for 2-10) CuO: $Cu_{11}O_4^{14+}$ with C_i and 7500 DSP, and for 2-11) CuCl: $Cu_{13}Cl_4^{9+}$ with T_d and 8500 DSP. The size of a potential well used for all the clusters is 7.0 atomic units in width and -0.5 Hartrees in depth.

3. Results and discussion

Mn Lα spectra emitted from Mn, MnO and MnO_2 were of one peak but their shapes were much different each other, as shown in Fig. 1. Fe Lα spectra emitted from Fe, α-Fe_2O_3, Fe_3O_4 and $FeSO_4$ split into two and their shapes were characteristic of these compounds, as shown in Fig. 2. Cu Lα spectra emitted from CuO and CuCl, as shown in Fig.3, had a shoulder at the higher energy side of main peaks but those from Cu and Cu_2O had not.

The occupied and unoccupied M 3d PDOS (M=Mn, Fe and Cu) calculated here are shown in Fig. 4 for Mn, Fig. 5 for Fe and Fig. 6 for Cu, respectively. Here convolution of the PDOS was carried out adopting the line width of 4eV. As can be seen in Figs. 4-6, difference in the peak-top energies and in relative intensities of the occupied and unoccupied M 3d PDOS is remarkable. This suggests that the Lα X-rays emitted from these compounds must experience different degrees in self-absorption due to electron transition from the 2p orbital of the M atom of interest to the unoccupied molecular orbitals. This must give different and characteristic spectral shapes for these compounds mentioned above.

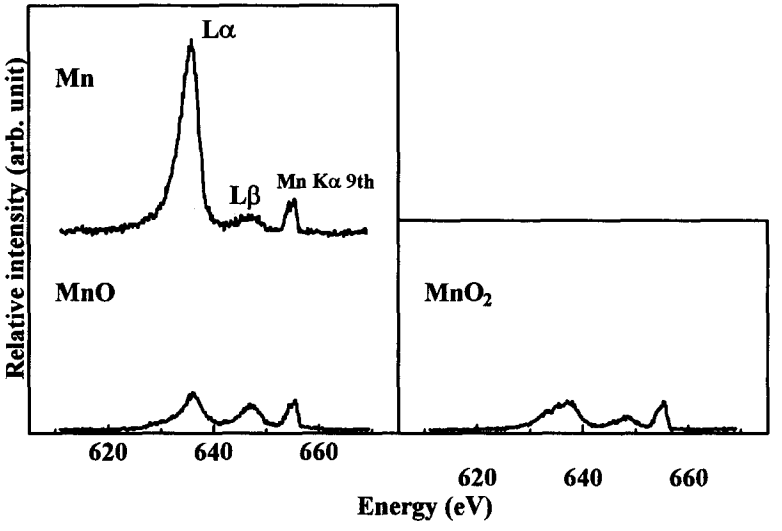

Fig. 1. Observed Mn Lα and Lβ XRF spectra emitted from Mn, MnO and MnO_2.

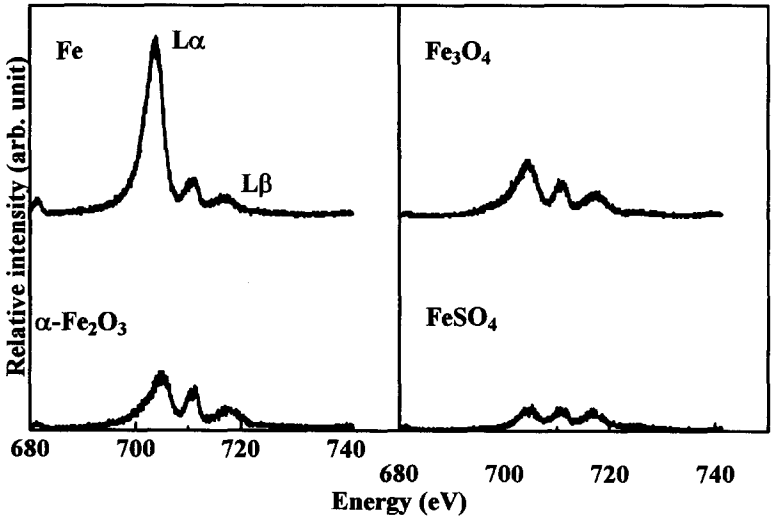

Fig. 2. Observed Fe Lα and Lβ XRF spectra emitted from Fe, α-Fe_2O_3, Fe_3O_4 and $FeSO_4$.

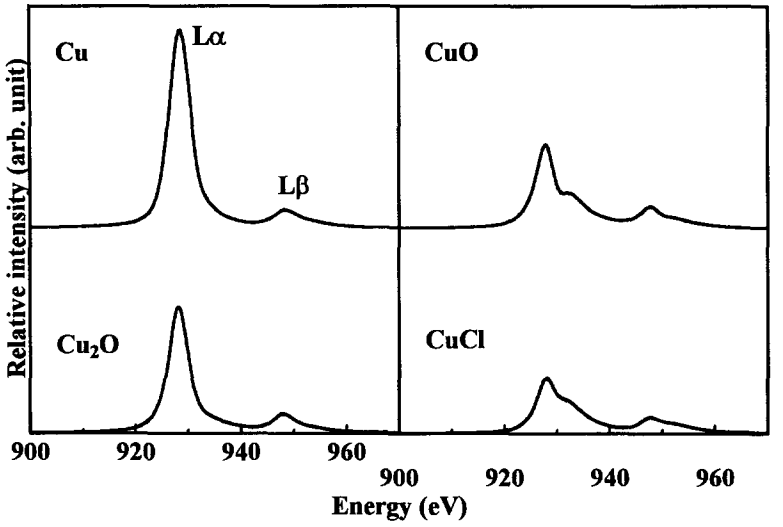

Fig. 3. Observed Cu Lα and Lβ XRF spectra emitted from Cu, Cu_2O, CuO and CuCl.

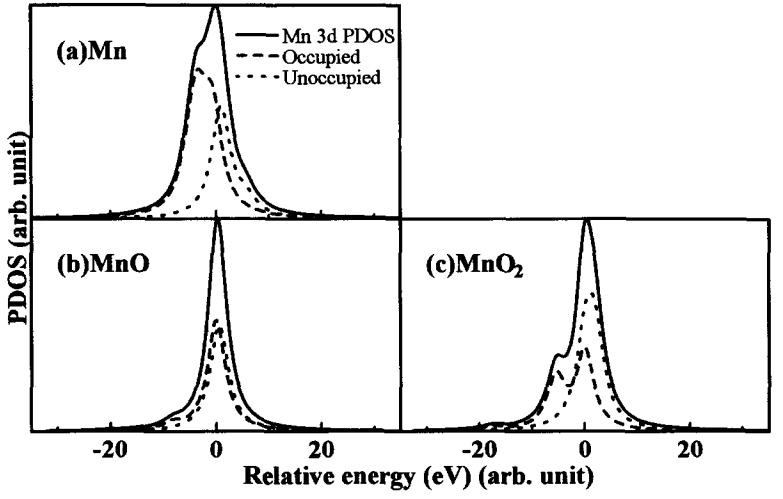

Fig. 4. Calculated occupied and unoccupied Mn 3d PDOS for (a) metallic Mn, (b) MnO and (c) MnO_2, respectively.

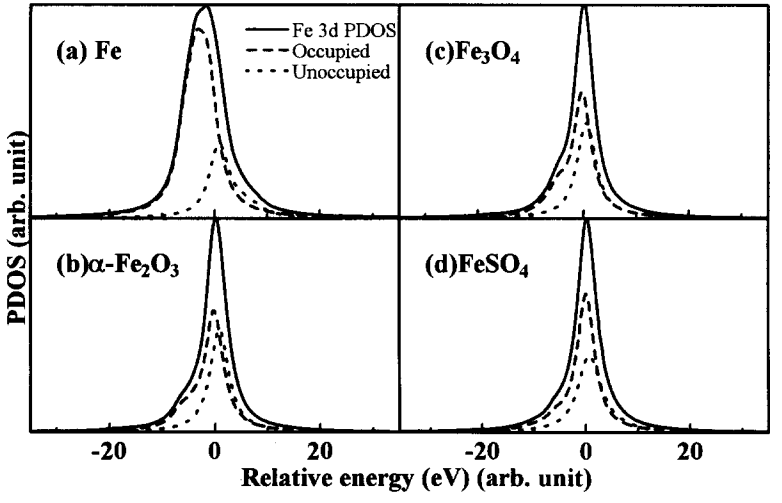

Fig. 5. Calculated occupied and unoccupied Fe 3d PDOS for (a) metallic Fe, (b) α-Fe_2O_3, (c) Fe_3O_4 and (d) $FeSO_4$, respectively.

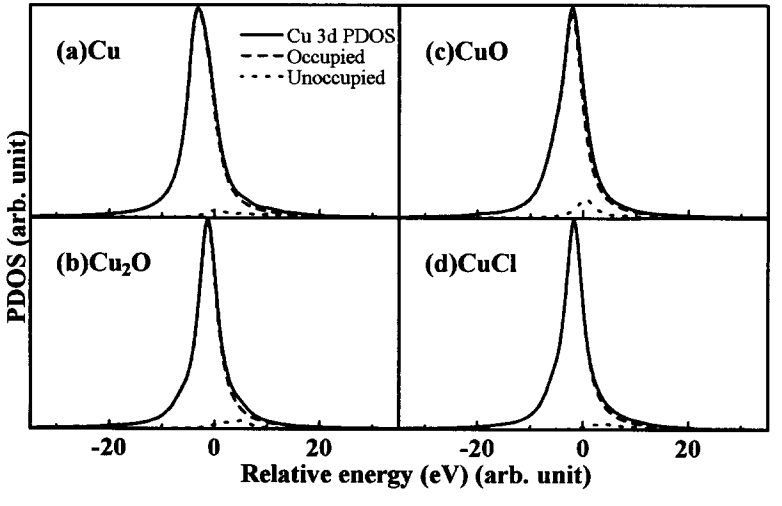

Fig. 6. Calculated occupied and unoccupied Cu 3d PDOS for (a) metallic Cu, (b) Cu_2O, (c) CuO and (d) CuCl, respectively.

Comparison between observed and calculated M Lα spectra is given in Fig. 7 for Mn, MnO, MnO_2, in Fig. 8 for Fe, α-Fe_2O_3, Fe_3O_4 and $FeSO_4$, and in Fig. 9 for Cu, Cu_2O, CuO and CuCl, respectively. Here for better understanding, Lβ spectra and contributions from the 9th order diffraction of Fe Kα at 710 eV and of Mn Kα at 655 eV were reduced from observed spectra. The extent of contributions from the 9th order diffraction of Kα was estimated by multiplying the intensity of the 9th order diffraction of Kβ with the intensity ratios of Kα/Kβ. On the other hand, the calculated Lα spectra were prepared by multiplying the occupied PDOS shown in Figs. 4, 5 and 6 with $(1-\eta D_U)$, where D_U means the PDOS of the M 3d unoccupied orbitals and η is a coefficient, i.e. 0-1. In our experiments, η is selected to be 1 because the samples used were thick enough and then absorb emitted M L X-rays in proportion to the numbers of 3d electron deficiencies in the M atom.

Coincidence between observed and calculated Lα spectra is satisfactory for all the Mn- and Fe-containing compounds, and Cu and Cu_2O, but is insufficient for CuO and CuCl. This suggests that a further correction, such as the multiple ionization correction is necessary for the latter.

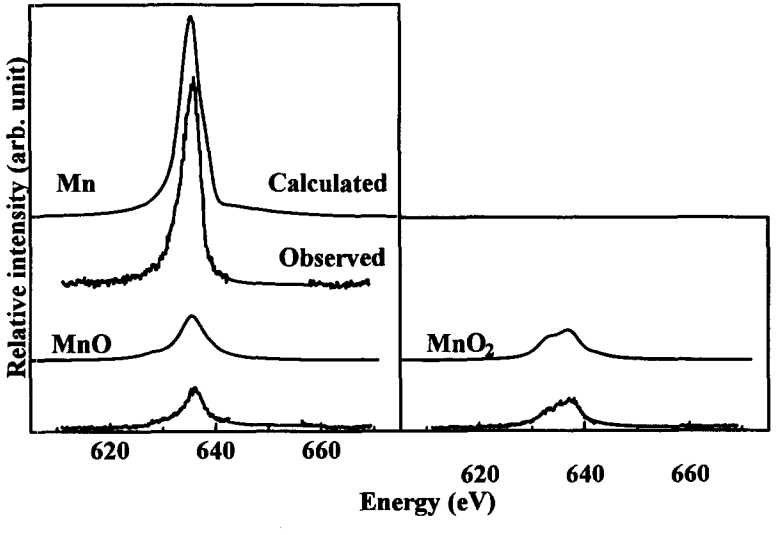

Fig. 7. Comparison between calculated and observed Mn Lα spectra, where Lβ spectra and contributions from the 9th order diffraction of Mn Kα were reduced from the observed spectra.

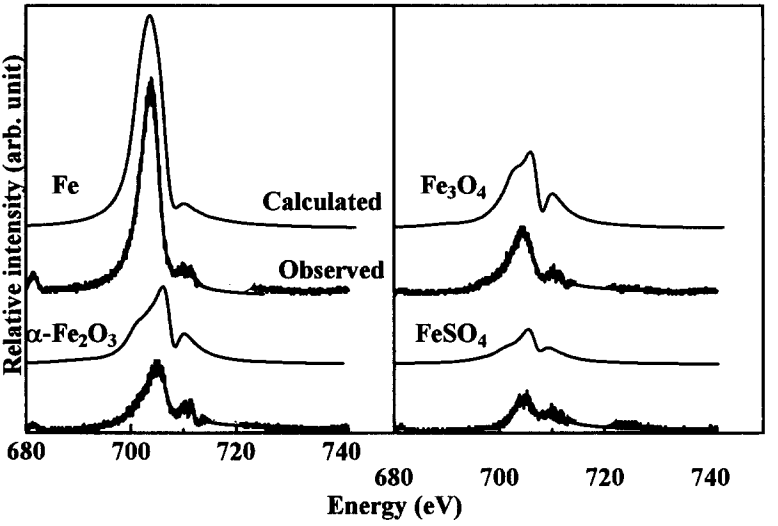

Fig. 8. Comparison between calculated and observed Fe Lα spectra, where Lβ spectra and contributions from the 9th order diffraction of Fe Kα were reduced from the observed spectra.

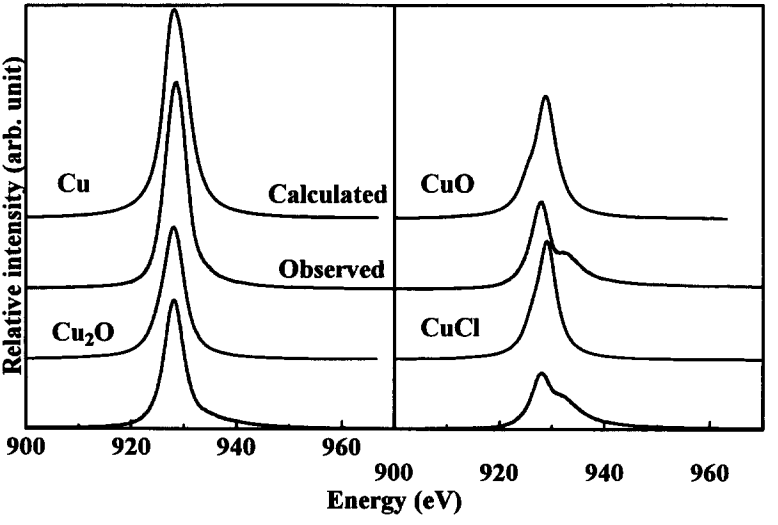

Fig. 9. Comparison between calculated and observed Cu Lα spectra, where Lβ spectra were reduced from the observed spectra.

4. Conclusion

Simulation to reproduce fine structures of Lα X-ray spectra emitted from some 3d transition elements is performed. Observed Mn Lα spectra emitted from Mn, MnO and MnO_2 were of one peak but their shapes were much different each other. Fe Lα spectra emitted from Fe, α-Fe_2O_3, Fe_3O_4 and $FeSO_4$ were of well separated two peaks. Cu Lα spectra emitted from CuO and CuCl had a shoulder at the higher energy side of main peaks but those from Cu and Cu_2O had not. These features were theoretically reproduced in view of the self-absorption scheme using the DV-Xα molecular orbital calculation.

Difference in the shapes of the observed spectra emitted from Mn, MnO and MnO_2, Fe, α-Fe_2O_3, Fe_3O_4 and $FeSO_4$, and Cu and Cu_2O was well reproduced by introducing unoccupied DOS of 3d elements, which are responsible for X-ray self-absorption. However, Cu Lα spectra emitted from CuO and CuCl were not well reproduced only by considering the self-absorption, suggesting that the satellite peak originated from the multiple ionization is not negligible in intensity for these compounds.

5. References

1. T. Kendelewicz, P. Lie, C. S. Doyle, G. E. Brown, Jr. E. J. Nelson, S. A. Chamber, Surface Sci. 429 (1999) 219
2. D. W. Fisher, J. Appl. Phys. 36 (1965) 2048
3. A. S. Koster, Molecular Phys. 26 (1973) 625
4. T. Robert, G. Offergeld, phys. stat. sol. (a), 14 (1972) 277
5. Brahm Dev, H. Brinkman, Physica 57 (1972) 616
6. T. J. Ribble, phys. Stat. sol. (a), 6 (1971) 473
7. M. Uda, D. Yamashita, Y. Nakajima and H. Nakamatsu, Intern. Conf. PIXE, 2001 June 8-12 in Guelph, Canada
8. H. Adachi, M. Tsukada, C. Satoko, J. Phys. Soc. Jpn. 45 (1978) 875

First-Principles Analysis of Tunneling Spectra for Rutile $TiO_2(110)$ Surface with Oxygen Vacancies

Yoshiyuki Sakai

Department of Industrial Education, Ashiya University
13-22, Rokurokuso-cho, Ashiya, Hyogo, Japan

(Received January 23, 2002; in final form April 8, 2002)

Abstract

Tunneling spectra in $TiO_2(110)$ surface observed by scanning tunneling spectroscopy are identified using the spin-polarized Discrete Variational (DV)-Xα molecular orbital calculation. The features in the tunneling conductance spectra obtained at each ionic site are assigned on comparison with calculated spectra. The results clearly indicate that a paramagnetic Ti^{3+} is produced due to an oxygen vacancy immediately below the fivefold-coordinated titanium ions rather than a bridging oxygen vacancy.

CONTENTS

Keywords: scanning tunneling spectroscopy, tunneling conductance, first -principle analysis, DV-Xα molecular orbital calculation, $TiO_2(110)$ surface, oxygen vacancy.

E-mail address: sakai@ashiya-u.ac.jp/

ADVANCES IN QUANTUM CHEMISTRY, VOLUME 42

0065-3276/03 $35.00

1. INTRODUCTION

Titanium dioxide has recently attracted considerable attention since it is known to have strong activity as a photocatalyst that decomposes a large number of undesirable chemical pollutants upon irradiation of ultraviolet rays. The oxygen vacancies in this surface are considered to play important roles in the photocatalytic reaction [1-3]. However, it is still not clear exactly which features of the oxygen-deficient TiO2 surface are responsible for the surface chemical reaction [3]. It is considered that the electronic and geometric information at oxygen vacancies in the surface is important for understanding the mechanism underlying the surface chemical reaction.

Scanning tunneling microscopy/spectroscopy (STM/STS) is a powerful tool to provide such information in real space with atomic resolution on various material surfaces of metal, semiconductor, and molecules [4,5]. In STS measurements, the tunneling current (I) versus sample voltage (V_s) spectrum as well as its differential spectrum (dI/dV_s vs V_s) or a vibrational spectrum ($d^2I/d\,V_s^2$ vs V_s) can be obtained at each atomic site [5,6]. Its local density of states (LDOS) is estimated from tunneling conductance (dI/V_s) spectra [7] which is in good agreement with those by Photo-Emission Spectroscopy (PES) [8]. Recently, this technique has been applied to oxide surfaces such as $SrTiO_3$,[9,10] MO_3[11], MgO,[12] ZnO[13], VO_2[14], V_2O_5[15,16], Fe_3O_4[17], TiO_2 [18-23].

The electronic structures around oxygen vacancies in $TiO_2(110)$-(1×1) surface is rather complicated: the unoccupied defect states due to a bridging oxygen vacancy were observed by STS [23][24] while occupied defect states in this surface were often observed by non-imaging techniques of PES [25-27] or Electron- Energy- Loss Spectroscopy (EELS) [25,28]. As those experimental facts were found, first-principles calculations have been performed to investigate the detailed geometric or electronic structure in this non-stoichiometric $TiO_2(110)$ surface [29-34].

In this study, a variety of electronic structures are theoretically reinterpreted for the consistency with experimental facts [23] of STS measurements. The spin- polarized DV-X α molecular orbital method is used to calculate local density of states (LDOS) in rutile $TiO_2(110)$ surface with oxygen vacancies. Theoretical dI/dV_s spectra at each ionic site are also calculated to assign peaks of experimental spectra in comparison with the calculated spectra.

2. OBSERVATION OF CURRENT IMAGES AND TUNNELING SPECTRA IN $TiO_2(110)$ SURFACE BY SCANNING TUNNELING SPECTROSCOPY [23]

Electrons are tunneling between a tip and a sample surface at some 10 Å distance from each other as illustrated in Fig.1. By scanning a metal tip over a surface keeping tunneling current to be constant, corrugation of atomic size in the surface can be imaged in real space [35]. The I-V_s spectra and their differential conductance (dI/dV_s) are measured at each of the 64×64 pixels in a topographic image. All the experiments in this study were carried out in an ultrahigh-vacuum (UHV) chamber at a pressure of 1×10^{-10} Torr. Experimental set up was

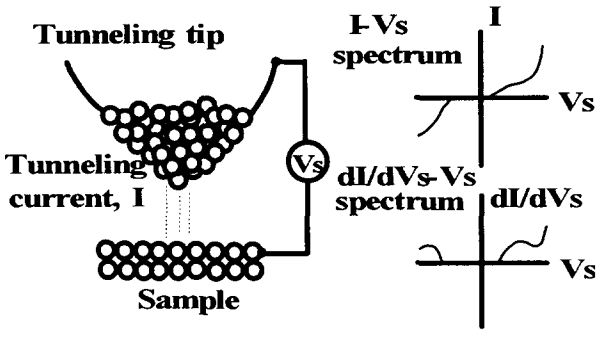

Fig.1 Principle of scanning tunneling spectroscopy

carefully arranged to avoid tip-surface interaction causing the deterioration of reliability of STS measurements: The bias voltage V_s was swept from -1 V to 2.5 V in STS measurements so that atom transfer between a tip and a sample might not occur due to strong electric field [36,37]. One step in voltage sweeping was 1/50 of the full voltage range. Therefore, features of tunneling spectra were determined within 0.1 eV in accuracy. Also, Pt-Ir tip apex was annealed by electron bombardment in UHV to eliminate the contamination on tip apex. A rutile TiO_2 crystal with a mechanically polished surface was cleaned by cycles of Ar^+ ion bombardment and annealing up about 1000 K in UHV .

Figure 2(a) shows the unoccupied state image of the rutile TiO_2(110) surface. It is well established that the bright rows along the (001) direction correspond to rows of fivefold-coordinated Ti ions [19, 20].

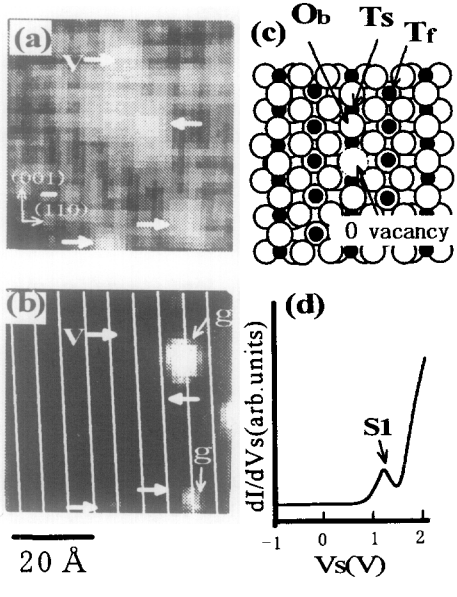

Fig.2 (a) STM image of TiO_2(110) and (b)simultaneously obtained tunneling current image at V_s=-1 V. White lines in (b) indicate the positions of fivefold-coordinated Ti rows. Arrows V and g indicate bridging O vacancies and trapped electron charge, respectively.

(c) Schematic structure of TiO_2(110)-(1×1) surface with a bridging O vacancy. A bridging O ion, a fivefold-coordinated Ti ion and a sixfold-coordinated Ti ion are labeled as "Ob", "Tf" and "Ts", respectively.

(d) Typical example of the *dI/dVs* spectrum obtained at a bridging O vacancy. The arrow S1 indicates the unoccupied defect state.

Several bright spots are observed between Ti ion rows at around 1.5V. It is known that these spots correspond to bridging O vacancies as illustrated in Fig. 2 (c) [19, 23] and they disappear at lower bias voltage less than 1 V [23].

When a bridging O is removed as a neutral atom, two electrons are left at two neighboring Ti ions to maintain charge neutrality so that an occupied defect state is produced in the surface band gap. It is believed that one electron is trapped at a Ti^{4+} adjacent to a bridging O vacancy to create a Vo-Ti^{3+} paramagnetic defect complex [25] (Vo: oxygen vacancy). Such a state due to the oxygen vacancy was observed within 1 eV below the Fermi level (E_f) by PES [25-27] on both an ion- bombarded surface and an annealed surface of TiO_2(110).

However, the defect state (marked as S1 in Fig.2(d)) due to a bridging O vacancy is found to be unoccupied in this experiment and moreover, any occupied state of a trapped electron is not found at this site within 1 eV below E_f. As shown in Fig.2(b), a trapped electron is found only on the fivefold-coordinated Ti ion row as a conductive spot in the current image simultaneously obtained at Vs of -1 V. The dark area in the image results from the electrically insulating property at negative Vs. These conductive spots in Fig.2(b) begin to appear below –0.8 eV.

These results are contrary to the idea that a Vo-Ti^{3+} defect complex is produced at a bridging O vacancy. It is considered that trapped electrons at the bridging O defect sites are easily driven to the conduction band by large surface band bending of 1.7 eV [25] in a nearly perfect TiO_2(110). The other type of oxygen defect is possible to be created at the trapped electron site: it is created immediately below a fivefold-coordinated Ti ion in the surface during the heat treatment in UHV, and a Vo-Ti^{3+} defect complex is formed in the subsurface layer (see Sec. 4).

3. COMPUTATIONAL METHOD OF TUNNELING CONDUCTANCE

Variations of tunneling current between the STM tip and each constituent ion in an oxide surface can be calculated by the simple equation [38, 39] depending on V_s as

$$I \propto \int_0^{eV_s} \rho(E) T(eV_S, E)\, dE \quad , \qquad (1)$$

where $\rho(E)$ is the LDOS at the energy E (eV) relative to E_f and $T(eV_s,E)$ is tunneling probability [38] which is expressed as

$$T(eV_S, E) = \exp\left(-1.02r \sqrt{\frac{\phi_s + \phi_t}{2} + \frac{eV_s}{2} - E} \right) , \qquad (2)$$

where r is the distance (Å) between the sample surface and the tip apex and ϕ_s and ϕ_t are the work functions (eV) of the sample and tip, respectively. In equation (1), the density of states of tip apex is assumed to be constant.

Tunneling conductance dI/dV_s is derived from eq. (1) as

$$\frac{dI}{dV_s} \propto \rho(eV_s)T(eV_s, eV_s) + \int_0^{eV_s} \rho(E)\frac{\partial}{\partial E'}T(E', E)\Big|_{E'=eV_s} \quad (3)$$

When the voltage V_s is small, the first term in eq. (3) is dominant and, therefore, dI/dV_s is proportional to the LDOS in the surface at energy of eV_s. The LDOS $\rho(E)$ in the above equations is estimated by the spin-polarized DV-X α molecular orbital calculation using the surface cluster of TiO_2(110). The computer program SCAT [40] is used for this calculation. Figure 3 shows the stoichiometric (110) surface cluster (Ti_4O_{16}) used for the calculation.

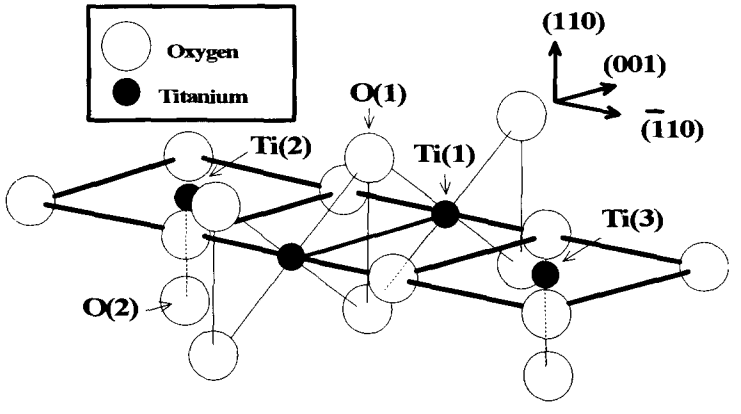

Fig. 3 Structure of the cluster model used for DV-Xα molecular orbital calculation.

The Madelung potential was taken into account in the calculation. There are two types of titanium ions in the surface as illustrated in the figure: a fivefold coordinated Ti ion which is surrounded by five oxygen ions and a sixfold coordinated Ti ions surrounded by six oxygen ions. The population of Ti3d character in the molecular state is the important factor to evaluate the LDOS at each Ti ion site. In the calculation, $\rho(E)$ is approximated by the sum of Gaussian distributions as

$$\rho(E) = \sum_i \frac{f_i}{\sqrt{2\pi}\sigma} \exp\left\{\frac{-1}{2}\left(\frac{E - E_i}{\sigma}\right)^2\right\}, \quad (4)$$

where f_i is the population of the atomic orbital component of the i_{th} electronic state at the energy of E_i and σ is the half-width of the Gaussian distribution. The value of ρ can be estimated using value of f_i mentioned above. Substituting $\rho(E)$ into eq. (3), the differential conductance (dI/dVs) is evaluated.

4. RESULTS AND DISCUSSIONS

Figures 4(a) shows the partial densities of states (PDOS) of the Ti3d character at fivefold- and sixfold-coordinated Ti ions in the stoichiometric $TiO_2(110)$ surface, using the cluster model Ti_4O_{16} of Fig.3.

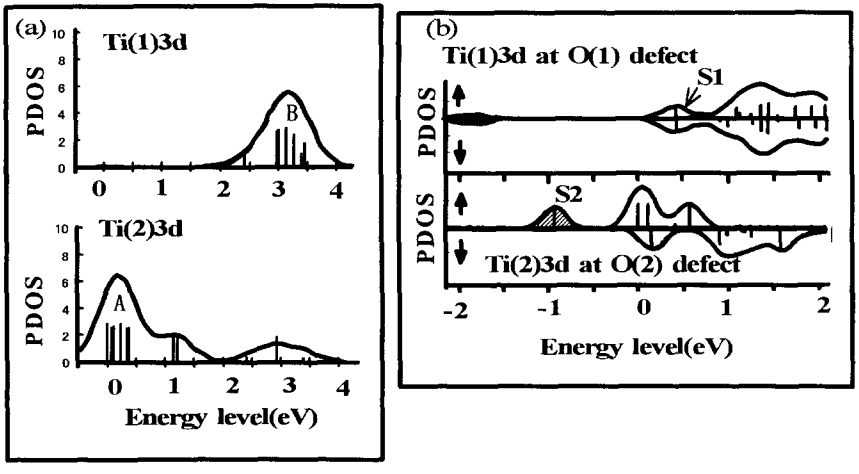

Fig.4 Partial densities of states (PDOS) in $TiO_2(110)$ surface calculated by DV-Xα method using the cluster model. (a) PDOS at sixfold- and fivefold- coordinated Ti ion sites in a stoichiometric surface (at Ti(1) and Ti(2) in Fig.3)and (b) PDOS at Ti(1) and Ti(2) where O(1) and O(2) are removed, respectively. Arrows S1 and S2 indicate corresponding two types of defect states.

Atomic orbitals used in the calculation are 1s~4p in Ti atom and 1s~2p in O atom. For the states spreading over the energy region of -1 eV~2 eV, the Ti3d character is predominant. In this case, results of PDOS of upspin orbital are shown in the figure (PDOS of downspin orbital is the same as that in the upspin case). The PDOS profile is obtained by the overlap of the Gaussians of eq.(4) with the width of 0.5 eV centered on each cluster level . Zero level is set on the level E_L of the lowest unoccupied molecular orbital (LUMO).

At fivefold-coordinated Ti site, the broad peak *A* is an intrinsic surface state. On the other hand, at sixfold-coordinated Ti ion site, the peak *B* of t_{2g} like level appears at 3 eV from E_L .

Figure 4(b) shows the PDOS of the Ti3d character at two types of oxygen vacancies (a bridging O vacancy and an O vacancy immediately below the fivefold-coordinated Ti ion). The cluster model used is derived from Ti_4O_{16} by removing O(1) and O(2) ions. In this case, it is assumed that no electron is trapped at Ti(1) site (adjacent to a bridging O vacancy) and one electron is trapped at Ti(2) site (adjacent to an O vacancy just under a Ti(2) ion) based on the above argument in Sec. 2. Therefore, the charge state of the cluster is

assumed to be $(Ti_4O_{14})^{13-}$, the charge of which is determined from the sum of the formal charge of each constituent ion(Ti^{4+},O^{2-}) and one electron added to the cluster. As shown in the figure, the separation between the levels of upspin and downspin occurs in the Ti(2) 3d states. One electron is trapped in the spin-polarized state *S2*, which is the origin of a paramagnetic defect state. The energy difference between the *S2* level and E_L is about 1 eV. On the other hand, the defect state *S1* due to a bridging O vacancy is unoccupied. Albaret *et al.* [30] pointed out by using density functional theory that an excess electron in $Ti_nO_m^x$ cluster generally rests on an inequivalent titianium ion with a lowest coordination number in the weakest Madelung potential. The situation is similar in this case of $(Ti_4O_{14})^{13-}$ cluster with two types of oxygen vacancies mentioned above (*i.e.*, the fivefold-coordinated Ti(1) at bridging O vacancy and the fourfold-coordinated Ti(2) at O vacancy immediately below Ti(2)). This is the probable reason why an excess electron is trapped not at the Ti(1) ion site but at the Ti(2) ion site. The PDOS is also calculated for the cases of two or more electrons added to the cluster(not shown in the figure). In those cases, the *S2* state level is raised by the mutual Coulomb repulsion so that the energy difference between the *S2* level and E_L becomes as small as less than 0.1 eV, which is much smaller than the experimentally obtained value (~1.4 eV)[23]. Therefore, it is reasonable that one electron is trapped at the O(2) defect site forming a Vo-Ti^{3+} paramagnetic defect complex.

As shown in Fig.5(a), the unoccupied *S1* orbital appears around the Ti(1) site at 0.5 eV above E_L (It does not appear at lower energy), which is consistent with voltage dependent STM image of bridging O vacancies.

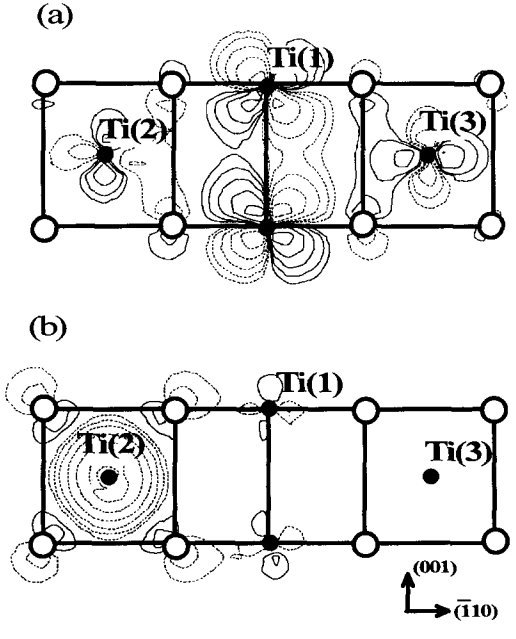

Fig.5 Calculated molecular orbitals of (a) the unoccupied defect state *S1* and (b) the defect state *S2* at -1 eV below LUMO level when O(1) and O(2)ions are removed from the cluster of Fig.3 and one electron is left to the cluster.

On the other hand, a trapped electron at *S2* state is localized around the Ti(2) site as shown in Fig.5(b) in agreement with the trapped electron image in Fig.2(b). In this case, the trapped electron charge at Ti(2) site occupies 82 % of a total population of the *S2* state while that at Ti(1) site is very small to be less than 1 %.

The conductance spectra (dI/dV_s) are calculated by substituting the calculated ρ (E) of Fig.4 into eq. (3) as shown in Fig.6 where the experimental spectra are also shown for the comparison. It is difficult to theoretically estimate what energy E_f takes from E_L since its level often varies due to the band bending effect depending on amount of surface oxygen vacancies[41]. The Fermi level E_f is determined empirically to be 0.8 eV below E_L so that the calculated *S1* level coincides with the experimental *S1*.

The features of the calculated spectra agree well with experimental results as shown in Fig.6.

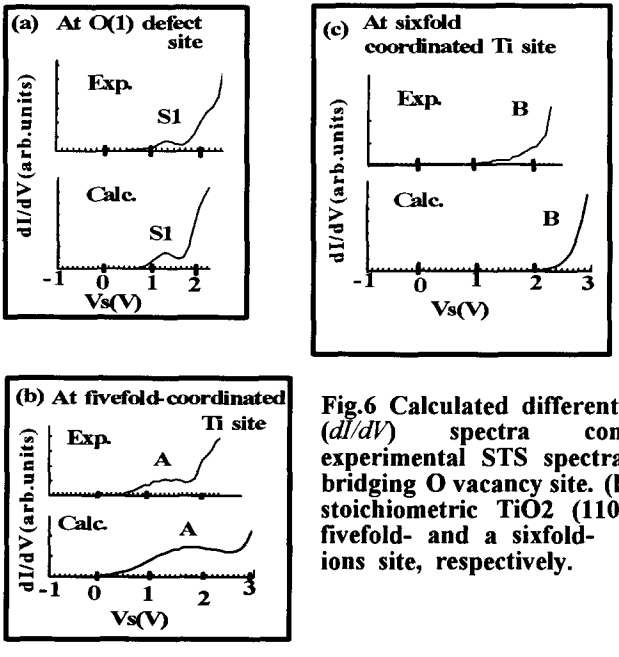

Fig.6 Calculated differential conductance (dI/dV) spectra compared with experimental STS spectra. Spectra at a bridging O vacancy site. (b),(c) Spectra in stoichiometric TiO2 (110) surface at a fivefold- and a sixfold- coordinated Ti ions site, respectively.

Experimental peaks (*S1, A*) and the curve *B* can be assigned to those of calculated spectra in Fig.6(a)-(c): The peak *S1* belongs to the defect state due to the bridging O vacancy. The peak *A* and the curve *B* in the spectra obtained in the stoichiometric surface belong to the intrinsic surface state of Ti(2)3d orbital and the t2g like level of Ti(1)3d orbital, respectively.

In the above calculations, the position of each constituent ion in the surface was determined from the bulk structure. To achieve more accurate quantitative calculations, the relaxation effect in the surface should be taken into account.

According to the first principle calculations for the relaxed (110) surface

structure, Ti and O ions are usually displaced normal to the surface[31,32]: In a stoichiometric (110) surface, sixfold-coordinated Ti ions move away from the bulk with respect to the unrelaxed positions while fivefold-coordinated Ti ions move toward the bulk by the amount of more than 0.1 Å. Jung *et al.*[42] theoretically confirmed optimum displacement of each Ti ion in the surface for the consistency with the STM images using the extended Hückel tight binding method. They pointed out that displacement of each Ti in a stoichiometric surface is small (-0.05 Å). Therefore, the relaxation effect is considered to be smaller than expected. This is one of the reasons why the calculated spectra by using unrelaxed surface structure are in fairy good agreement with STS measurements. On the other hand, it is also pointed out that two Ti ions adjacent to a bridging O vacancy move largely inward due to strong Ti-O bond, assuming that two electrons are trapped at these sites to produce Ti^{3+} ions. This assumption is however not the case in the STS measurements as mentioned in Sec.2. Therefore, the calculation for the relaxed structure at a bridging O vacancy site should be performed with no trapped electrons to discuss quantitatively with more accuracy.

5. CONCLUSIONS

The STS spectra in TiO_2(110) surface are identified by first-principles calculation using the spin-polarized DV-X α method. The results presented in this paper clearly indicate that a Vo-Ti^{3+} paramagnetic defect complex is produced at the O vacancy site immediately below the fivefold-coordinated Ti ion rather than at a bridging O vacancy site. The features of STS spectra in TiO_2(110) surface are found to originate from the d-orbital levels of Ti ions at defect and non-defect sites by comparison with the calculated dI/dV_s spectra. A variety of voltage dependent STM images of oxygen-deficient TiO_2(110) surface can be explained by DV-X α molecular orbital calculation using the cluster model with the fitting number of electron charges.

REFERENCES

(1) W. J. Lo, Y. W. Chung and G. A. Somorjai, Surf. Sci., **71**, 199 (1978).
(2) J. G. Mavroides, D. I. Tchernev, J. A. Kafalas and D. F. Kolesar, Mater. Res.Bull., **10**, 1023 (1975).
(3) V. E. Henrich and P. A. Cox, "The Surface Science of Metal Oxide", Cambridge University Press, Cambridge, pp.317-324 (1994).
(4) Y.Kuk and P.J.Silverman, Rev.Sci.Instum. **60**,165(1989).
(5) R.M.Feenstra "Scanning Tunneling Microscopy and Related Method",eds. R.J.Behm, N.Garucia and H.Rohre, Kluwer Academic Publishers, Netherland, pp. 211-240(1990).
(6) D.P.E.Smith, M.D.Kirk and C.F.Quate, J. Chem. Phys. **86**, 6034(1987).
(7) J. Tersoff and D. R. Hamann, Phys. Rev. Lett., **50**, 1998 (1983).
(8) R.J.Hamers, R.M.Tromp and J.E.Demuth, Phys. Rev. Lett. **56**,1972(1986).
(9) H.Tanaka, T. Matsumoto, T. Kawai and S.Kawai, Jpn. J. Appl. Phys. **32**,

1405, (1993).
(10) Y. Liang, D. A. Bonnell , Surf. Sci. **285**, L510-516(1993).
(11) R.L. Smith and G.S. Rohrer, J. Catalysis, **180,** 270-278 (1998).
(12) S.Schintke,S.Messerli,M.Pivetta,F.Patthey,L.Libioulle,M.StengelA.D.Vita and W.D.Schneider, Phys. Rev. Lett. **87**,276801-1(2001).
(13) G. S. Rohrer, D. A. Bonnell , Surf. Sci.. , **247** ,L195-L200 (1991).
(14) T.Oshio, Y. Sakai and S.Ehara, Ultramicroscopy, **42-44**, 744-748 (1992).
(15) R. L. Smith, G. S. Rohrer, K. S. Lee, D.-K. Seo and M.-H. Whangbo, Surf. Sci., **367**, 87 (1996).
(16) Y.Sakai and S. Ehara, Jpn. J. Appl. Phys. **38**,2944(1999).
(17) Y.Joseph, C.Kuhrs, W.Ranke,M.Ritter and W.Weiss, Chem. Phys. Lett. **314**, 195 (1999).
(18) G.S.Rohrer, V.Henrich and D.A.Bonnell, Science, **250**,1230(1991).
(19) U. Diebold, J. F. Anderson, K.-O. Ng and D. Vanderbilt: Phys. Rev. Lett. 77 (1996)1322.
(20) H. Onishi, K. Fukui and Y. Iwasawa: Bull. Chem. Soc. Jpn. **68**, 151 (1995).
(21) H. Onishi and Y. Iwasawa: Phys. Rev. Lett. **76** ,791(1996).
(22) Y. Sakai and S. Ehara, Jpn. J. appl. Phys., **39**, 3789 (2000).
(23) Y. Sakai and S. Ehara, Jpn. J. appl. Phys., **40**, L773 (2001).
(24) G. S. Rohrer, V. E. Henrich and D. A. Bonnell: Mater. Res. Soc. Symp. Proc. **209**, 611 (1991).
(25) Y. W. Chung, W. J. Lo and G. A. Somorjai, Surf. Sci. **64**, 588 (1977)
(26) R. Heise and R. Courths, "Adsorption on Ordered Surfaces of Ionic Solids & Thin Films", eds. E. Umbach and H. J. Freund, Springer Series of in Surface Sciences, Berlin, Vol. 33, p. 91(1993).
(27) W. J. Lo, Y. W. Chung and G. A. Somorjai: Surf. Sci., **71**, 199 (1978).
(28) G. Rocker, J. A. Schaefer and W. Gopel, Phys. Rev. B, **30**, 3704 (1984).
(29) M.Tsukada, C. Satoko and H.Adachi, J. Phys. Soc. Jpn., **47**, 1610 (1979).
(30) T.Albaret, F.Finocchi and C.Noguera, Faraday Discuss.,**114**,285(1999).
(31) M.Ramamoorthy, R.D.King-Smith and D. Vanderbilt, Phys. Rev. B, **49**, 7709 (1994).
(32) M.Ramamoorthy and D. Vanderbilt, Phys. Rev. B, **49**, 16721 (1994).
(33) S.Munnix and M.Schmeis, Phys. Rev. B, **30**, 2202 (1984).
(34) S.Munnix and M.Schmeis, Phys. Rev. B, **28**, 7342 (1983).
(35) G. Binnig, H. Rohrer, Ch. Gerber and E. Weibel, Phys. Rev. Lett., **40**, 178 (1982).
(36) S.Ciraci, A.Baratoff and I.P.Batra, Phys. Rev.B, **41**,2763(1990).
(37) M.Tomitori, K.Sugata,G.Okuyama and H.Kimata, Surf. Sci. **355**,127(1996).
(38) J.A.Strocio, R.M.Feestra, D.M.Newns and A.P.Fein, J. Vac. Sci. Technol. A, **6**, 499 (1988).
(39) E.L.Wolf, " Principles of Electron Tunneling Spectroscopy", Oxford University Press, New York , p.46 (1985).
(40) H. Adachi, M. Tsukada and C. Satoko, J. Phys. Soc. Jpn., **45**, 875 (1978).
(41) W.Göpel, G.Rocker and R.Feierabend, Phys. Rev. B, 28, 3427(1983).
(42) D.Jung, H.-J.Koo, D.Dai and M.-H.Whangbo, Surf. Sci. **473**,193(2001).

Electronic Structures of Silicon Clusters with Vacancies

Noboru Esashi, Yasuhiko Ohama and Yoshinori Hayafuji
School of Science, Kwansei Gakuin University
2-1 Gakuen, Sanda, Hyogo 669-1337, Japan

(Received January 16, 2002; in final form March 14, 2002)

Abstract

The electronic structures of silicon clusters with a mono-vacancy and a di-vacancy are calculated with use of the discrete variational (DV)-X α molecular orbital method. The results show that deep energy levels are produced in the middle of the energy gap in cooperation with dangling bonds due to vacancy introduction. We propose a new mechanism of eliminating the deep energy levels by substituting vacancies with atoms or a pair of atoms for applications in Si ultra-large scaled integrated circuits. One of the best candidates as a substitute of the vacancy is a pair of combined interstitial boron atoms.

Keywords: silicon cluster, point defect, vacancy, DV-X α cluster method

CONTENTS

e-mail:nobo_@hotmail.com

ADVANCES IN QUANTUM CHEMISTRY, VOLUME 42

0065-3276/03 $35.00

1. INTRODUCTION

Although silicon (Si) is widely used to fabricate devices as the original Si has few defects, numerous point defects such as vacancies, self-interstitials and impurities, and their aggregates are unintentionally introduced in the fabrication process of devices. 200 or more spectra originating from defects have been reported in electron spin resonance (ESR) experiments.[1]-[6] Unsaturated bonds (hereafter, we refer to as "dangling bonds") originating from vacancies cause deep levels in the energy gap between the highest occupied molecular orbital (HOMO) and the lowest unoccupied molecular orbital (LUMO) levels.[7],[8] The deep level acts as traps of carriers. These traps become positively or negatively charged. The positive charge attracts an electron, and the electron recombines with a closely localized hole and emits some light (photon) or nonradiative lattice energy (phonon). The positive charge also scatters a hole and an electron. Since the primary mechanism for current fluctuation in a Si device is the trapping of carriers, the control of vacancy introduction is a principal issue in the Si technology. It is one of the serious problems as the current fluctuation causes a fault of pixel image on a display.[9]

An extensive study of point defects including vacancies and interstitials has been carried out with the purpose to improve performance of deep sub-micrometer and nano-micrometer scaled devices. Ballistic ion processes which occur during plasma treatment and implantation into Si lattice lead directly to local excess vacancies at depths up to about half of projected ion range and excess interstitials at deeper depths close to the ion range.[10] During annealing after ion processes the vacancies diffuse rapidly through the crystal and interact with themselves, self-interstitials and impurities.[7],[11] The recent studies using the Au decoration method of so called $R_p/2$ defects for MeV implants is entirely convincing the presence of vacancy clusters.[12],[13] On the theoretical point of view, there is considerable interest as to the stability of such defects and their evolution during annealing. Self-consistent molecular dynamics calculations based on the density-functional theory and the local density approximation have shown that stable forms of multi-vacancy clusters are V_6, V_{10}, ... etc.[11],[14],[15] The number of vacancies forming multi-vacancy clusters is called a "magic

number". It has been also found that a H-decorated multi-vacancy is capable of containing an additional H_2 molecule.[16] Although there is much effort to eliminate deep energy levels caused by dangling bonds due to introduction of vacancies and their aggregates, it is surprising that no detailed information on the elimination mechanism of the deep energy levels due to the dangling bonds is publicly known. Two traditional mechanisms to eliminate the deep energy levels have been reported: first, termination of dangling bonds by hydrogen atoms, and second, replacement of vacancies by group IV elements, C, Ge, Sn, or Pb.[16]

The purpose of the present paper is to propose new elimination mechanisms of the deep energy levels generated by dangling bonds due to vacancy introduction. We have tried to eliminate the deep energy levels by replacing a mono-vacancy by a pair of atoms, and by replacing a di-vacancy by a transition metal atom. In group III elements such as B, Al, Ga, In, and Tl, an atomic valence configuration is ns^2np at the atomic core. The number n labels the principal quantum number of the atomic orbital. The basic idea is that a combined boron pair with the valence configuration of $ns^2np{=}npns^2$ may be expected to have four orbital bondings with four dangling bonds with the mono-vacancy. The combined boron pair has the <100> split boron pair structure, $B_2^{<100>}$, in Si , which is supposed to be stable.[17] The second idea is that a transition metal atom forming co-ordination compounds sometimes has a co-ordination number of six. The orbitals of such a transition metal atom may successfully combine with six dangling bonds due to the di-vacancy in the elimination of the deep energy levels. The analysis shows that the <100> split boron pair structure, $B_2^{<100>}$, in Si is electrically inactive and eliminates the deep energy levels.

2. CALCULATION DETAILS AND CLUSTER MODELS

The electronic structures of silicon clusters were calculated using the discrete variational (DV)-X α molecular orbital (MO) method with a linear combination of atomic orbitals (LCAO) expansion of molecular orbitals.[18] In this method the exchange-correlation potentials are approximated by the simple Slater form,[19]

$$V_{Xc\uparrow}(r) = -3\alpha\left\{\frac{3}{4\pi}\rho_{\uparrow}(r)\right\}^{\frac{1}{3}}$$

where the coefficient α is a scaling parameter and is fixed at 0.7 throughout the present work. ρ (**r**) is the local electron density at a position **r**. Using the simple form for the potentials, high-speed calculations have been realized using a personal computer. Calculations were iterated until ρ (**r**) reached to a constant value by the self-consistent-charge method. The basis functions for the MO calculations were constituted of the atomic orbital wave eigenfunctions obtained in the numerical form, which included 1s-3d for Si and P atoms, 1s-2p for B atoms, and 1s for H atoms. Mulliken overlap population analysis[20] was used in order to discuss the bonding natures, which gave the net charge of atoms and the bond overlap population between each pair of atoms in the cluster.

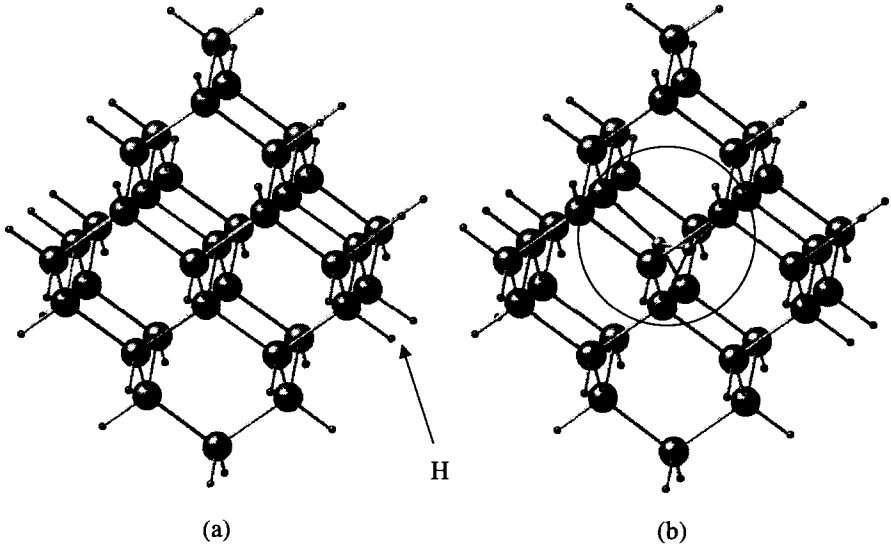

Fig. 1. Cluster models for: (a) $Si_{35}H_{36}$, extracted from a regular Si without a defect, and (b) III_2-$Si_{34}H_{36}$, with a <100> split atom pair such as group III element pair.

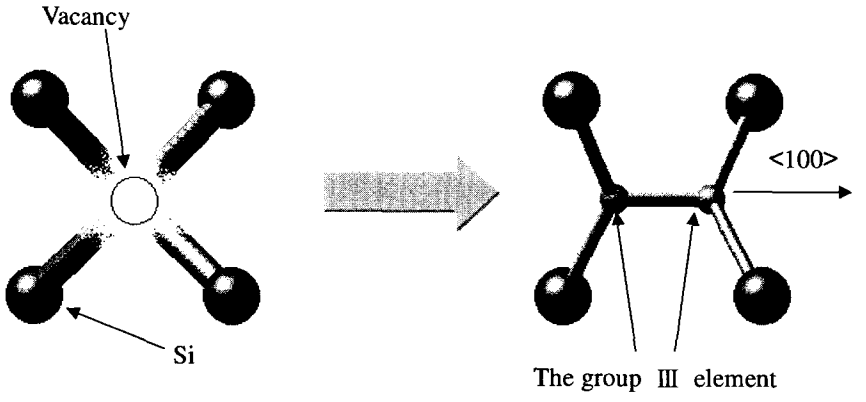

Fig. 2. Magnified view of the portion surrounded with the circle in Fig. 1(b)

The cluster model, $Si_{35}H_{36}$, shown in Fig. 1(a) was extracted from a regular Si crystal without a defect within the cluster. To calculate the electronic structure of the cluster with a mono-vacancy, the cluster model, V-$Si_{34}H_{36}$, was employed by introducing a mono-vacancy at the center of the cluster model, $Si_{35}H_{36}$, by removing the central Si atom.

Figure 1(b) shows the cluster model, III_2-$Si_{34}H_{36}$, with the <100> split atom pair such as a group III element pair instead of a mono-vacancy. Many researchers believe the <100> split interstitial atom configuration as the most stable interstitial configuration in Si.[21] In this cluster model, the distance $d_{III-III}$ between the <100> split atom pair is set to $d_{III-III} = 0.25a$ Å, where a is 5.431 Å, the lattice parameter of Si crystal. This model was used to examine the effect of replacing a mono-vacancy by an group III element pair on elimination of the deep energy levels of dangling bonds due to the mono-vacancy.

Figure 2 is a magnified view of the portion surrounded with the circle in Fig. 1(b). This figure clearly shows that the mono-vacancy is replaced by a group III element pair in the <100> direction. A consensus has already emerged that lattice reconstruction occurs in the interior of Si. In all the calculations, however, we have not considered the effects of lattice relaxation.

The cluster model shown in Fig. 3(b) was used to examine the effect of replacing a di-vacancy by a transition metal atom on elimination of the deep energy levels of dangling bonds due to the di-vacancy. This model, having a transition metal atom at the center of two vacancies, was made from the cluster model, $Si_{44}H_{42}$, shown in Fig. 3(a), which was extracted from the regular Si crystal without a defect. The dangling bonds of Si atoms on the cluster surface were terminated with H atoms to eliminate the deep energy level in the energy gap. The Si-Si bond length was fixed to 2.35 Å and the Si-H bond length was fixed to 1.48 Å.

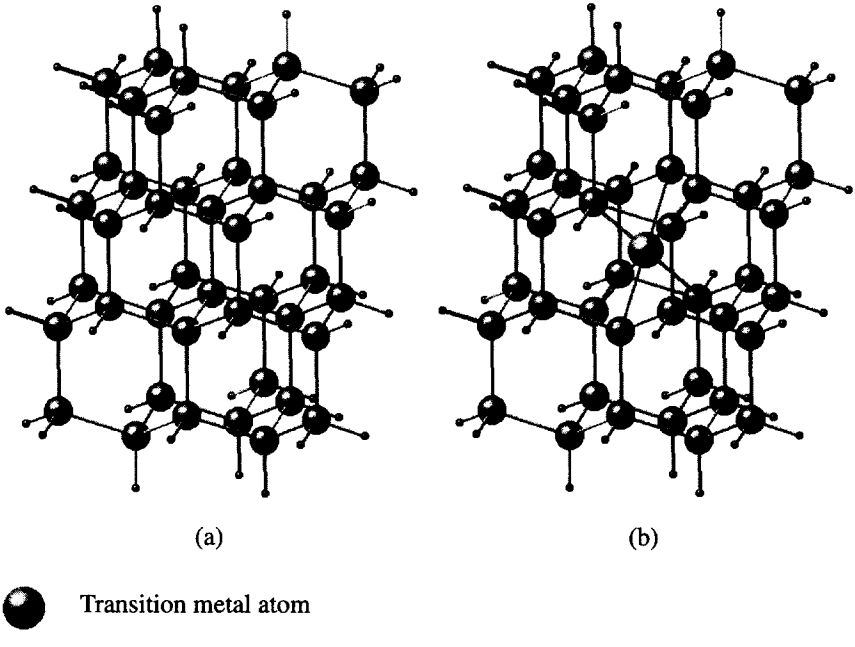

Fig. 3. Cluster models for examining the effect of replacing a di-vacancy by a transition metal atom on eliminating the deep energy levels: (a) $Si_{44}H_{42}$, and (b) TM-$Si_{42}H_{42}$. TM represents a transition metal atom.

3. RESULTS AND DISCUSSION

Figure 4 shows seven diagrams of energy levels obtained for the $Si_{35}H_{36}$, V-$Si_{34}H_{36}$ and III_2-$Si_{34}H_{36}$ cluster models, where III represents the group III element, B, Al, Ga, In, or Tl. The vertical axis shows the level energy in eV.

The solid lines in each diagram are occupied energy levels, and the broken lines are unoccupied ones. The gap between the highest occupied molecular orbital (HOMO) and the lowest unoccupied molecular orbital (LUMO) corresponds to the energy gap of the cluster. The gap energy of each of the clusters is about 4.0 eV, which is much larger than 1.1 eV of crystalline silicc The big difference of the gap energy comes from the difference of tl confinement of electron movement whether it is inside of a small cluster or ov the infinitely extended crystal. The details of the effect of the electron confinement on gap energy has been reported in the previous paper.[8]

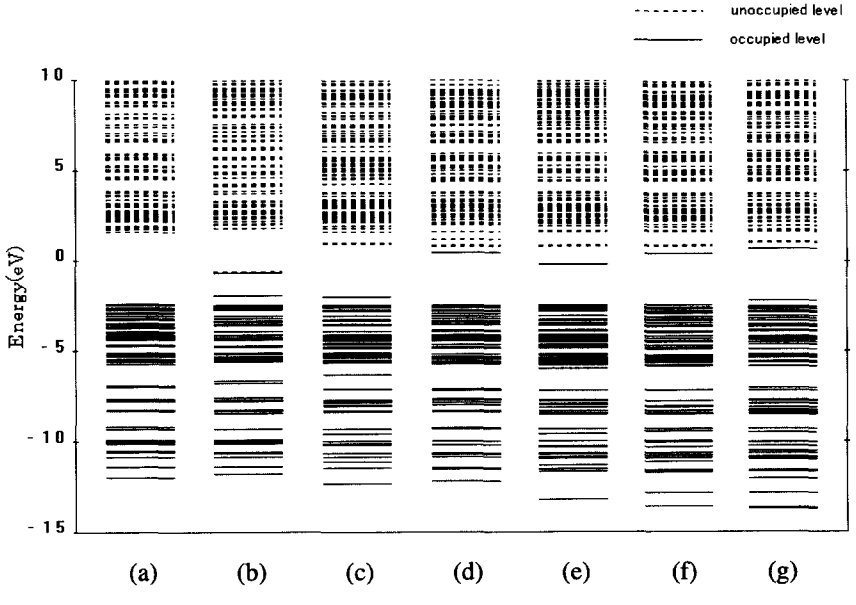

Fig. 4. Diagrams of energy levels obtained for (a) $Si_{35}H_{36}$, (b) V-$Si_{34}H_{36}$ and III_2-$Si_{34}H_{36}$ clusters. III represents group III element of (c) B, (d) Al, (e) Ga, (f) In, and (g) Tl.

In Fig. 4(a) for the $Si_{35}H_{36}$ cluster without a defect, we can see no energy level in the energy gap, whereas in the diagrams for the V-$Si_{34}H_{36}$ and III$_2$-$Si_{34}H_{36}$ except B_2-$Si_{34}H_{36}$ clusters, energy levels can be seen in the middle or in the upper half of the energy gap. Figure 4(b) shows that the mono-vacancy in the V-$Si_{34}H_{36}$ cluster causes generation of deep energy levels in the gap. The levels associated with mono-vacancies consist of four levels: two are occupied levels and the other two are unoccupied levels. Such deep energy levels act as traps and generation-recombination centers, and disturb the carrier transport. Five figures, Fig. 4(c)-(g), show the energy diagrams for the III$_2$-$Si_{34}H_{36}$ cluster. These diagrams give two notable features on the configuration of energy levels in the gap: first, a pair of B atoms at the vacancy site eliminates deep energy levels and generates shallow occupied and unoccupied levels. These levels mainly consist of B 2p, Si 3p, and Si 3d orbitals. This means that Si atoms combine with a pair of boron atoms. The transition of deep energy levels to shallow energy levels is considered to be due to the interactions of deep energy levels of the dangling bonds with that of a pair of B atoms. Although the energy gap of the B_2-$Si_{34}H_{36}$ cluster becomes narrower by about 25 % than that of the $Si_{35}H_{36}$ cluster, the effect of elimination of a deep energy level on carrier transport should improve the performance of Si devices. Second, a pair of Al, Ga, In, or Tl atoms at a mono-vacancy site introduces shallow donor levels near LUMO. These donor levels emit electrons to compensate acceptor levels originated from single group III atoms. The occurrence of compensation decreases the number of acceptors, and then degrades the electrical characteristics of devices. The finding of the introduction of shallow donor levels by a pair of group III atoms suggests a novel and important approach to solve some problematical phenomena appearing when the concentration of group III atoms in Si is very high.

In the following, we will focus on the narrowing of the energy gap in the B_2-$Si_{34}H_{36}$ cluster. To develop further the analysis of the narrowing of the energy gap, we investigated the dependence of the gap energy on the B-B distance $d_{B\text{-}B}$ of a pair of B atoms.

Figure 5 shows five diagrams of energy levels obtained for the $Si_{35}H_{36}$, V-$Si_{34}H_{36}$ and B_2-$Si_{34}H_{36}$ cluster models. For the B_2-$Si_{34}H_{36}$ cluster, we varied $d_{B\text{-}B}$ from 1.10 Å to 1.70 Å. The gap energies were obtained to be 2.2 eV, 3.0 eV,

and 2.9 eV for d_{B-B} = 1.70 Å, 1.36 Å, and 1.10 Å, respectively. The variation of the gap energy has an energy maximum of 3.0 eV at d_{B-B} of 1.36 Å. The value of d_{B-B} = 1.36 Å is a quarter of the lattice parameter of Si crystal. Although d_{B-B} calculated from the rationalized tetrahedral radius of B atom is 1.71 Å, a pair of substitutional B atoms has a structure with a strong B-B bond of a length of 1.6 Å in Si crystal.[22] Hence it appears that atomic configuration which gives a gap energy maximum of 3.0 eV at d_{B-B} of 1.36 Å occurs caused by pairing of interstitial B atoms.

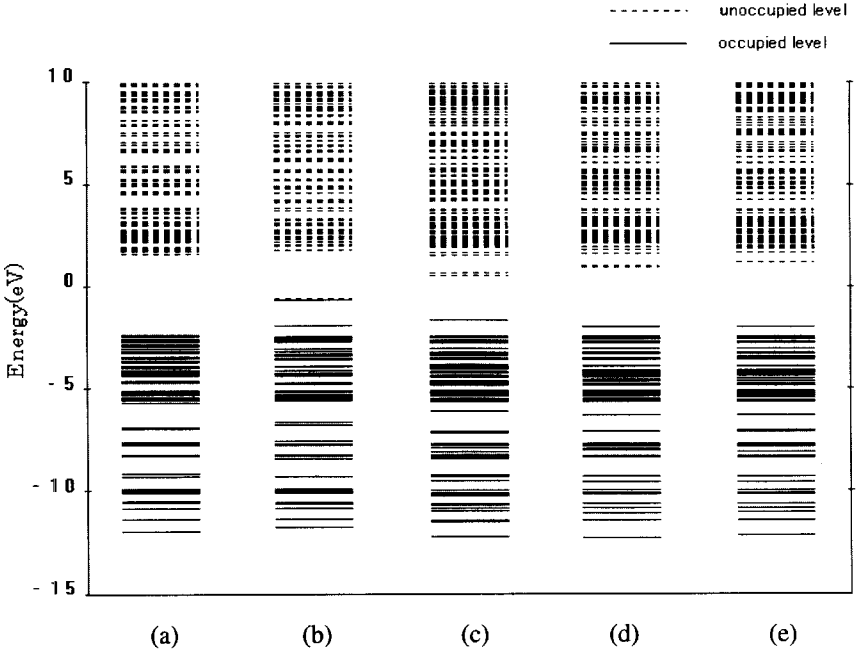

Fig. 5. Diagrams of energy levels obtained for (a) $Si_{35}H_{36}$, (b) V-$Si_{34}H_{36}$ and (c)-(e) B_2-$Si_{34}H_{36}$ clusters. The distances between B atoms in pairs are (c) 1.70 Å, (d) 1.36 Å, and (e) 1.10 Å.

Figure 6 shows diagrams of energy levels obtained for the $Si_{44}H_{42}$, V_2-$Si_{42}H_{42}$ and TM-$Si_{42}H_{42}$ cluster models, where TM are transition metal atoms, Sc, Ti, Y, or Zr. This model was used to eliminate the deep energy levels by replacing a di-vacancy by a transition metal atom. The di-vacancy in the V_2-$Si_{42}H_{42}$ cluster is the origin of the deep energy levels in the middle of the energy gap, as shown in Fig. 6(b). This attempt is not successful in eliminating the energy levels in the middle of the energy gap by use of a transition metal atom. Replacing a di-vacancy by a Zr atom, however, results in a considerably shallower occupied level in the energy gap than by other transition metal atoms, as shown in Fig. 6(f).

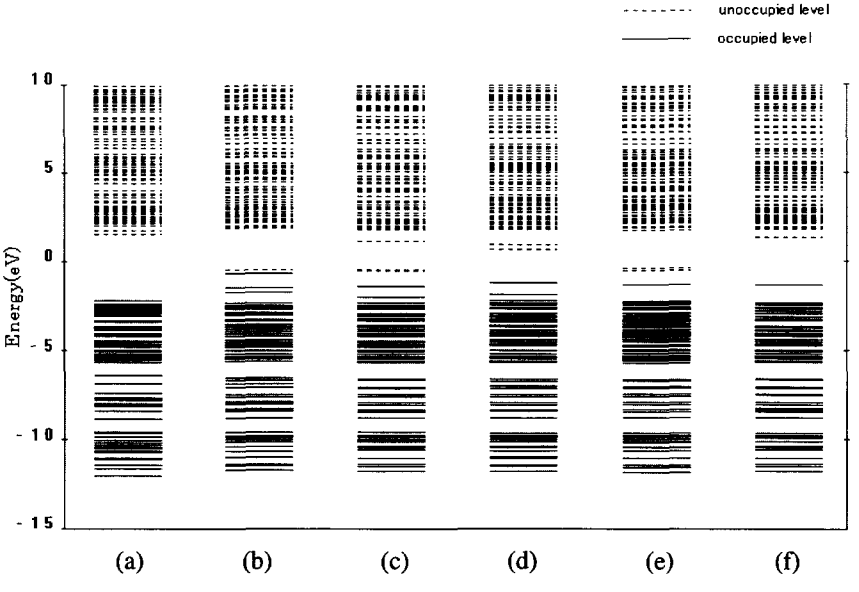

Fig. 6. Diagrams of energy levels obtained for (a) $Si_{44}H_{42}$, (b) V_2-$Si_{42}H_{42}$, (c) Sc-$Si_{42}H_{42}$, (d) Ti-$Si_{44}H_{42}$, (e) Y-$Si_{42}H_{42}$, and (f) Zr-$Si_{42}H_{42}$.

This result encourages us to find other transition metal atoms for eliminating the energy levels in the energy gap.
The basic idea for finding such transition metal atoms is as follows: first, such atoms have to have a co-ordination number of six, because the number of dangling bonds originating from a di-vacancy is six. Second, the radius of a di-vacancy is approximately 2.35 Å. The atoms having such a large atomic radius never exit. Thus, we have to choose the atoms having an atomic radius as large as possible.

4. CONCLUSIONS

The electronic structures of Si clusters with a mono-vacancy and a di-vacancy are calculated with use of the DV-X α MO method. The results show that deep energy levels are generated in the middle of the energy gap of Si in cooperation with dangling bonds due to introduction of the mono-vacancy and the di-vacancy. We propose a new mechanism to eliminate the deep energy levels by substituting a mono-vacancy with a molecule-like pair of atoms. One of the best candidates for this process may be a pair of combined interstitial boron atoms, especially a <100> split boron pair. On the other hand, an attempt is not successful to eliminate the energy levels caused by the di-vacancy using a transition metal atoms. Replacing a di-vacancy by a Zr atom results in a considerably shallower occupied level in the energy gap than by other transition metal atoms. It seems that the elimination of the deep energy levels by incorporating a transition metal atom having an atomic radius as large as possible with a co-ordination number of six is promising.

The authors would like to thank Professor Hirohiko Adachi of Kyoto University and Dr. Akikazu Shibata of former general manager of SONY Corporation Research Center for valuable discussion and support.

5. REFERENCES

(1) J. Isotani, Oyo-Butsuri. **61**, 788 (1992) (in Japanese).
(2) G. D. Watkins and J. W. Corbett, Phys. Rev. **134**, A1359 (1964).
(3) G. D. Watkins and J. W. Corbett, Phys. Rev. **138**, A543 (1965).
(4) J. W. Corbett and G. D. Watkins, Phys. Rev. **138**, A555 (1965).
(5) A. O. Evwaraye and E. Sun, J. Appl. Phys. **47**, 3776 (1976).
(6) B. G. Svensson and M. Willander, J. Appl. Phys. **62**, 2758 (1987).
(7) G. D. Watkins, Mat. Res. Soc. Symp. Proc. **469**, 139 (1997).
(8) H. Kimura, S. Imanaga, Y. Hayafuji, and H.Adachi, Jpn. J. Appl. Phys. 62, 2663 (1993).
(9) Y. Hayafuji, T. Shimada, and S. Kawado, *Semiconductor Silicon 1977* (The Electrochemical Society, Princeton, New Jersey 1977) p.750.
(10) A. M. Mazzone, Phys. Status Solidi **A95**, 149 (1986).
(11) S. K. Estreicher, J. L. Hastings, and P. A. Fedders, Appl. Phys. Lett. **70**, 432 (1997).
(12) V. C. Venezia, D. J. Eaglesham, T. E. Haynes, A. A.garwal, D. C. Jacobson, H-J.Gossmann, and F.H.Baumann, Appl. Phys. Lett. **73**, 2980 (1998).
(13) R. Kalyanaraman, T. E. Haynes, V. C. Venezia. D. C. Jacobson, H-J. Gossmann, and C. S. Rafferty, Appl. Phys. Lett. 76, 3379 (2000).
(14) T. Akiyama, A. Oshiyama, and, O. Sugino, J. Phys. Soc. Jpn. **67**, 4110 (1998).
(15) T. Akiyama, Y. Okamoto, M. Saito, and A. Oshiyama, Jpn. J. Appl. Phys. **38**, 1365 (1999).
(16) T. Akiyama, Y. Okamoto, M. Saito, and A. Oshiyama, Jpn. J. Appl. Phys. **38**, L1363 (1999).
(17) M. Okamoto, K. Takayanagi, and S. Takeda, Mat. Res. Soc. Symp. Proc. **510**, 343 (1998).
(18) H. Adachi, M. Tsukada, and C. Satoko, J. Phys. Soc. Japan, **45**, 874 (1978).

(19) J. C. Slater, Phys. Rev. **81**, 385 (1951).

(20) R. S. Mulliken, J. Chem. Phys. **23**, 1841 (1955).

(21) N. Arai, S. Takeda, and M. Kohyama, Phys. Rev. Lett. **78**, 4265 (1997).

(22) J. Zhu, T. D. de la Rubia, L. H. Yang, C. Mailhiot, and G. H. Gilmer, Phys. Rev. B54, 4741 (1996).

Density of States of Cu with Stacking Faults

Yoko Uchida[a], Tomoko Jimbo[b], D. Yamashita[c], and M. Uda[c]

[a]Hitachi, Ltd., Semiconductor & Integrated Circuits,
16-3, Shinmachi 6-chome, Ome-shi, Tokyo 198-8512, Japan
[b]Hitachi, Ltd., Device Development Center,
16-3, Shinmachi 6-chome, Ome-shi, Tokyo 198-8512, Japan
[c]Department of Materials Science and Engineering, Waseda University,
3-4-1 Ohkubo, Shinjuku-ku, Tokyo 169-8555, Japan

(Received January 31, 2002; in final form June 10, 2002)

The density of states (DOSs) of Cu with stacking faults was calculated using the DV-Xα method employing 13-atom fcc and hcp clusters. A fcc sequence was contaminated with a hcp sequence when stacking faults were introduced in the former. The calculated DOSs near Fermi edge were characterized with closely separated two peaks in the case of the fcc. On the other hand, separation of the peaks became larger (0.21 eV) and the energy level of lower energy peak became shallow in the case of the hcp, where non-negligible amounts of 4p component were found at the lower peak.

These results suggested that the valence structure of the fcc on a Cu thin film changed by introducing stacking faults.

Keywords : Cu, stacking fault, DV-Xα , DOS, fcc, hcp

Corresponding Author: Yoko Uchida : uhcida@epl-aset-unet.ocn.ne.jp

ADVANCES IN QUANTUM CHEMISTRY, VOLUME 42

0065-3276/03 $35.00

1. Introduction

Lately, Cu has been employed as a new interconnect material in place of conventional Al alloys for integrated circuits (ICs) due to high conductivity and good reliability [1]. A rolled Cu has a fcc (face - centered cubic structure) and is oriented in the direction of <001>. However, as evaporated or electro-deposited thin films used for ICs are mostly oriented in the direction for <111>, the structure is easy to distort along a <111> direction. Therefore, introducing faults with sliding along the {111} planes (ex. stacking faults) changes the stacking sequence of close-packed atomic planes from the fcc sequences into the other sequences (ex. hcp (hexagonal closest packed structure))[2].

It is important to figure out its electrical properties for application of electron devices. In this study to understand the properties of the valence structure of the Cu thin films, the discrete variational X α potential (DV-X α) method [3-7] was employed by which molecular orbitals located near Fermi edge or of the valence band were calculated. As cluster models, the structures with the fcc sequences and the hcp sequences were used in consideration of stacking faults [8,9].

2. Calculation

The discrete variational X α potential (DV-X α) method was employed to understand the properties of the valence electron for Cu thin films with <111> orientation and the valence density of states (DOS) was calculated out. Here it was assumed that the Cu thin film with stacking faults had a partial structure of a hcp, which had the stacking sequence of ABABAB, in a fundamental fcc structure, which had the stacking sequence of ABCABC. Therefore, in this calculation two cluster models of 13 Cu atoms were used with the fcc and hcp sequences as shown in Fig. 1 and DOSs for the fcc and hcp sequences were compared for Cu films without and with stacking faults, respectively.

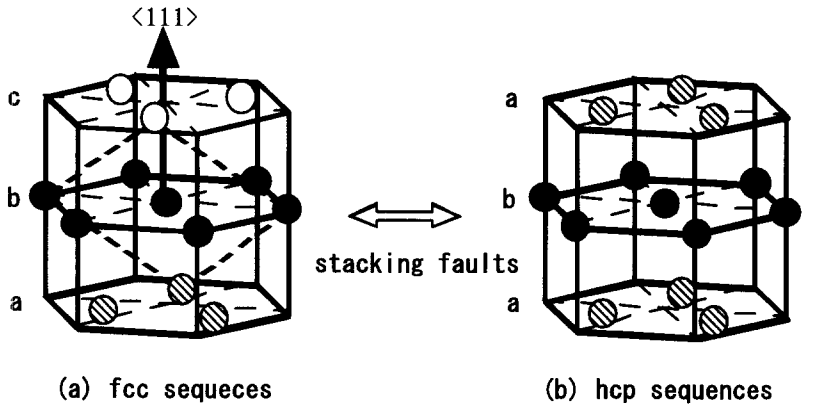

Fig.1. Model clusters for 13 Cu-atoms aggregates.
(a) fcc sequences and (b) hcp sequences

The calculations were performed under the following conditions: basis sets 1s - 4p orbitals of Cu, well potential width 5 a.u. (1.03 x a), where a was distance between the nearest neighbor atoms, well potential depth -2.0 Hr, discrete sampling points 6500, and symmetry C3v. In the DV-Xα method, numerical integration is used for a molecular orbital calculation and calculation time is decreased as the result. The wave function and potential are calculated at the sampling points that are generated at random around each atom and summed up. The calculation domain is often made into at least an atomic radius. Since well potential width corresponds to the area in calculating a wave function, it must be considered that calculation results differ depending on a spread of the orbit of the radius direction for a composition atom. Then, in the cases of well potential widths, 4 a.u. (0.83 x a) and 2.5 a.u. (0.52 x a), the calculations were also done here. The DOS and PDOS (partial density of states) spectra were made by convoluting squares of coefficients of molecular orbital wave functions with Gaussian function of 0.2 eV width.

3. Results and Discussion

A valence structure of Cu with the hcp sequences is compared with that with the fcc sequences. Figure 2 shows DOS spectra of occupied levels for the Cu with 13-atoms fcc and hcp sequences as a function of well potential width, respectively. The abscissa axis is shown by an eigen-energy of a molecular orbital. In order to make it legible, the spectra in well potential widths 4.0 a.u. and 2.5 a.u. are shifted in the direction of a vertical axis +1 (1/eV) and +2 (1/eV), respectively.

When well potential width becomes larger, the eigen-energies of valence orbitals shift to lager but components of DOS seem not to change remarkably. Then a microscopic valence structure near Fermi level is studied at 5 a.u. of well potential width. The DOS spectra of Cu with the fcc (dashed line) and the hcp (solid line) sequences near Fermi edge are shown in Fig. 3, respectively. In this energy region (-3 ~ -4.5 eV), both spectra are composed of two energy levels for both sequences, which are represented by inset bars in the figure. In the fcc sequence, two levels (-3.93 eV and -3.95 eV) are overlapped each other. In the hcp sequence, two levels are of -3.80 eV and -4.01 eV, whose energy difference is 0.21 eV.

A main orbital component is of 3d for both sequences as shown in Fig. 4. As a minor component, 4p orbital appears in the hcp sequence, which is overlapped with the 3d orbital at -3.80 eV, but contributions from other orbitals are negligible within calculation error limits as shown in Fig. 5.

These calculated results show that when the fcc structure is contaminated with the hcp structure, two overlapped levels for the fcc structure near Fermi edge separate into two levels, i.e. shallower and deeper energy levels. It suggests that if the hcp sequence is introduced into the fcc sequence by forming stacking faults, change in the valence structure must be found. In other words, there is possibility that the existence of stacking faults is to be detected by observing the valence structure.

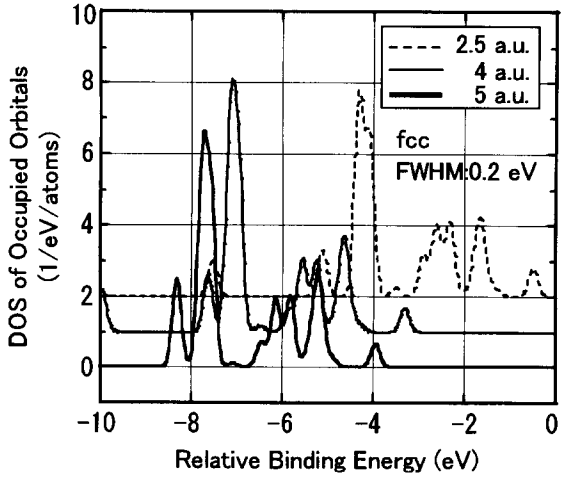

(a)

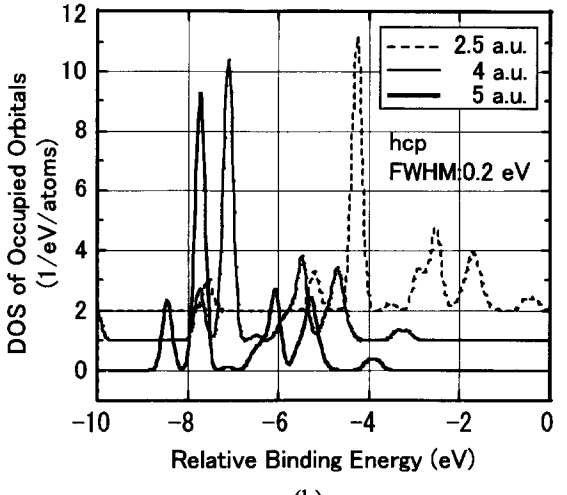

(b)

Fig. 2 The calculated density of states of the valence bands for 13 Cu atoms cluster. (a)fcc sequences and (b) hcp sequences

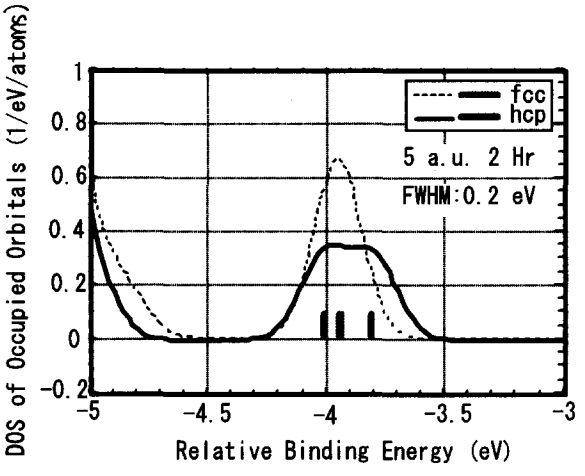

Fig. 3 The DOS spectra of Cu near Fermi edge for fcc sequences and hcp sequences.

It is difficult to observe the splitting of 0.2 eV in DOS spectra near Fermi edge by common electron spectroscopy. However, it is possible to detect such a small energy separation by using the photoemission yield spectroscopy, whose energy resolution is order of 0.01 eV. In addition, as non-negligible amounts of 4p orbital component exit only for hcp sequence, the observation of the dipole transition related to 4p but not to 3d orbital is expected to detect stacking faults. These facts suggest that calculated results in this study might be confirmed experimentally in near future.

Cluster size dependence of the metallic electronic structure resulting from Cu-4sp orbitals was also examined using a 43-atoms cluster model, which included even the 3rd neighbor atoms. Compared with a 13-atoms cluster only in consideration of the nearest neighbor atoms the levels near Fermi level increased in a 43-atoms cluster. However, they consisted of levels mainly originated in 3d orbital, and it turned out that the rate of the levels resulting from 4sp was not dependent on a cluster size. Then, the cluster model of 13 atoms with easy deforming was discussed here.

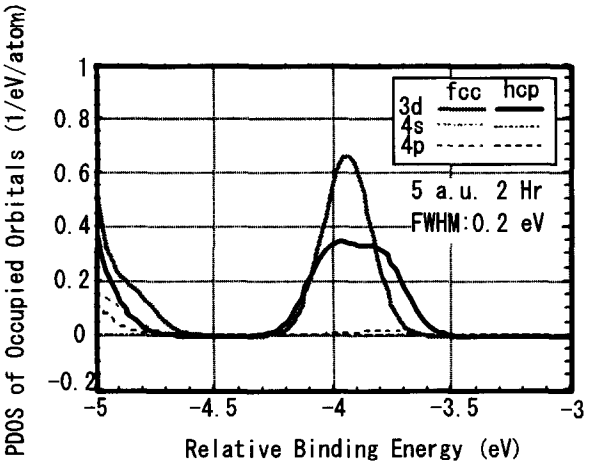

Fig. 4 The PDOS spectra of Cu near Fermi edge for fcc sequences and hcp sequences.

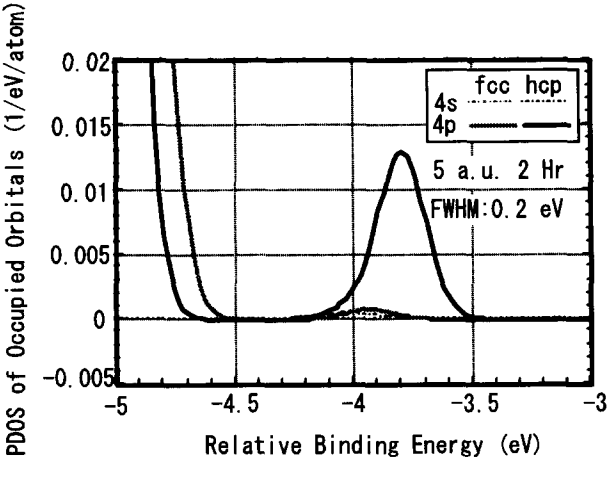

Fig.5 The 4s and 4p components in PDOS spectra of Cu near Fermi edge for fcc sequences and hcp sequences at 5 a.u. of well potential width.

4. Conclusion

The valence structure for Cu thin films with <111> orientation was studied by using the DV-Xα method. When the fcc sequence of Cu atoms was contaminated with the hcp sequence, i.e. stacking faults, the DOS spectra near Fermi edge changed with accompanied by the split of two overlapped energy levels. This result suggested that the observation of the valence structure was expected to show the difference in electronic near edge structures for Cu thin films with and without stacking faults.

5. References

(1) See for example, special volume of Thin Solid Films 262, 1 (1995) and MRS Bull. 19, 23 (1994)

(2) L. G. Wang and M. Sob, Phys. Rev., B60, 844 (1999)

(3) H.Adachi, M.Tshukada, and C.Satoko, J.Phys.Soc.Jpn. 45,875(1978)

(4) C.Satoko, M.Tshukada and H.Adachi, J.Phys.Soc.Jpn. 45,1333(1978)

(5) H.Adachi, M.Tshukada, and C.Satoko, J.Phys.Soc.Jpn. 47,1528(1979)

(6) H.Adachi, M.Tshukada, and C.Satoko, J.Phys.Soc.Jpn. 49,1994(1980)

(7) H.Adachi, Advances in Quantum Chemistry, 29,179(1997)

(8) M. Uda, A. Nakamura, T. Yamamoto, and Y. Fujimoto, J. Electron Spectrosc. relat. Phenom. 88-91, 643 (1998)

(9) Y. Fujimoto and M. Uda, Advances in Quantum Chemistory 37, 229 (1998)

Appendix

The dependence of well potential width on calculated results is also studied. Figures A-1 and A-2 show the DOS and PDOS spectra derived from Cu with 4 a.u. and 2.5

a.u. of well potential width, respectively, which are corresponding, to Figs. 3 and 5 in the case of 5 a.u. When the fcc sequences change over to the hcp sequences, two overlapped energy levels are separated at the interval of ~0.2 eV. The main component of the levels is 3d orbital for both sequences, and 4p orbital exists only for the hcp sequences as a minor component. These results, which characterize the change of valence structure related to stacking faults on Cu thin films, are the same in the case of 5 a.u. of well potential width. Therefore the calculated results in this study are available for the description of the valence structure of Cu thin films.

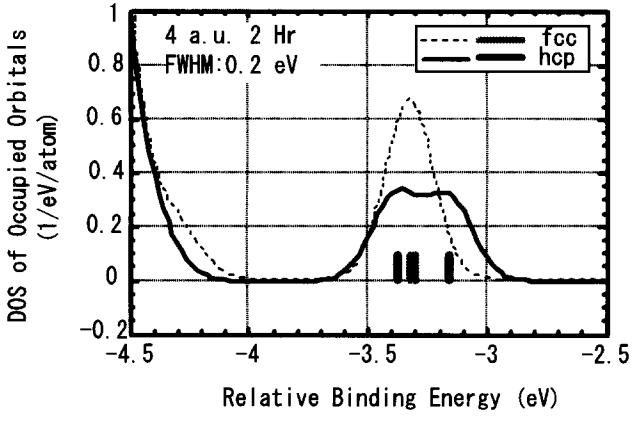

(a)

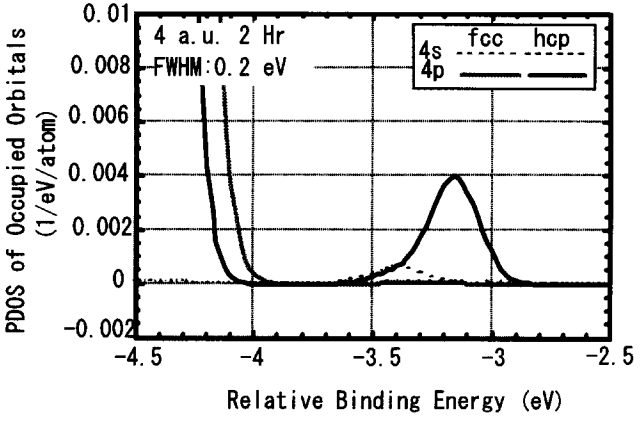

(b)

Fig. A-1 The DOS spectra (a) and the 4s and 4p components in PDOS spectra (b) of Cu near Fermi edge for fcc sequences and hcp sequences at 4 a.u. of well potential width

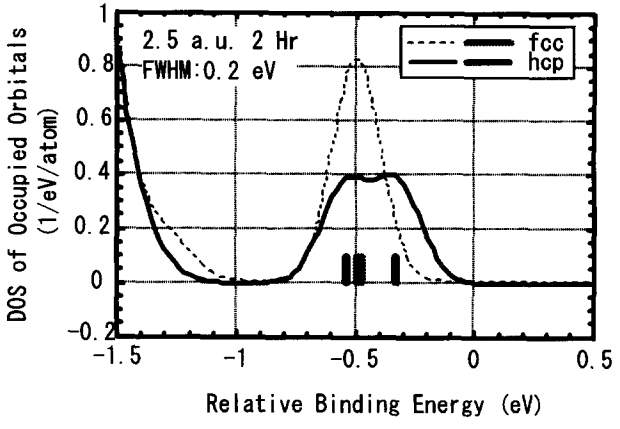

(a)

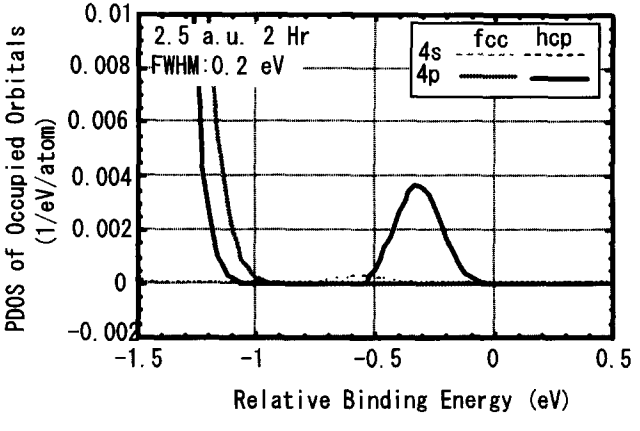

(b)

Fig. A-2 The DOS spectra (a) and the 4s and 4p components in PDOS spectra (b) of Cu near Fermi edge for fcc sequences and hcp sequences at 2.5 a.u. of well potential width

Analysis of Wetting Property of Electrode Metal on AlN at Their Interface Using Discrete Variational-Xα

Sunao Sugihara, Masahiro Yamamoto, Takamasa Isobe and Yukio Yutoh
Shonan Institute of Technology, Tsujido nishikaigan, Fujisawa, Japan

(Received February 23, 2002; in final form August 5, 2002)

Abstract

Electronic structures between electrode metals and AlN, which is comparable to oxides such as ZnO and TiO_2 were investigated in relation to wetting property by use of Discrete Variational Xα. The electrode metals employed were Ag, Cu and Al. The results suggest that the movement of electrons between the substrate and electrode metal related to the wetting mechanism are closer to covalence than ionicity. Therefore, we can estimate macroscopic wettability of metal on a substrate from the nature of microscopic bonding in the electronic structures at the interfaces. We proposed the wetting mechanism through the function of the oxygen and bonding natures between electrode metal, and AlN, or oxide.

Key words: wetting property, bond order, effective charge, electrode metal, AlN ceramic

CONTENTS

e-mail: sugihara@mate.shonan-it.ac.jp

ADVANCES IN QUANTUM CHEMISTRY, VOLUME 42

0065-3276/03 $35.00

1. INTRODUCTION

Wetting property of an electrode metal on a substrate is a very important parameter for electronic ceramic function. In integrated circuits, oxides are popularly employed as capacitors, varistors or substrates, and in addition to oxides, AlN also can be used in electrodes mounted on ceramics, in order to make best use of the electrical properties for the ceramics. Therefore, the electrode metal should wet the ceramics. Usually, wetting property has been discussed in terms of thermodynamics or surface tension on macroscopic scale, and experiments have been conducted by changing oxygen partial pressure, temperature, and other parameters [1,2]. Wetting property is usually evaluated by measuring contact angle. Selection of appropriate metal for joining has been based mainly on practical experience in industry; few basic studies on wetting property have been carried out. We have studied the experimental results of wetting property of electrode metals on oxides since 1990, and have reported electronic structures for wetting of $BaTiO_3$ with electrode metal [3] as determined by DV-Xα and compared these with experimental results. We found that charge transfer occurs between a metal atom and Ti; specifically, the effective charge of Ti drops as a result of electron transfer from metal to Ti. This result was suggested to relate to wettability. Furthermore, as has been determined experimentally, Ag and Cu exhibit improved wettability on oxide in comparison with than Al and Sn. We discussed the wetting property of TiO_2 ceramic with electrode metal, in which the covalent bonding nature of Ti with Ag or Cu is greater than that of Al or Sn [4]. The wetting tendencies of these metals were posited to relate to the covalent bonding nature of Ti with the electrode metal.

After the oxide ceramic Al_2O_3, AlN is most commonly used substrate material, and is well known for its good thermal conductivity of 100~170 $W/m \cdot K$ and relative permittivity of 8.8 at room temperature and 1MHz, which is close to that Al_2O_3. In the present study, we discuss another AlN electronic ceramic in terms of wetting property with electrode metals, and study oxides in terms of electronic structures. The experimental results show that the nitride exhibits low wettability with an electrode metal [5]. ZnO, which is another electronic ceramic, and AlN have the same wurtzite crystal structure. Oba et al. [6] analyze and discuss the electronic structures in terms of the varistor property of ZnO of the wurtzite structure. However, no analyses have been conducted on the electronic structures for AlN for connecting macroscopic property of wetting tendency with the electronic structures by DV-Xα although band structure was calculated by a pseudo-potential method [7]. Therefore, in the present study we analyzed the interfacial problems in the electronic structures between AlN and ZnO, and the metals in relation to wetting property.

2. CALCULATION AND EXPERIMENTS

AlN has a wurtzite structure having lattice parameters; a = 3.11 Å, c=4.982 Å (at 298K). Figure 1 shows the cluster model, and calculation was based on C_{3v} symmetry [8]. The wurtzite structure of ZnO, has lattice parameters; a= 3.250 Å and c= 5.207 Å. The space group is P6 $_{3mc}$ in atomic coordinates; Al or Zn (1/3, 2/3, 1/2) and N (1/3, 2/3, 1/2+Z, Z=0.3821)[9] or O (1/3, 2/3, 1/2+Z, Z=~0.382) [9], and for both ceramics the cluster was assumed to be electrically neutral as a whole [8].

Although the wetting experiment is not described in detail here, the bulk metal was put on the ceramics, then the metal was melted in a vacuum (~10^{-3} Pa), and the contact angle was measured in photographs taken with a camera. The substrates were AlN and ZnO, and the electrode metals were Ag, Cu, and Al. Calculation was also carried out on ZnO assumed to have the cluster shown in Fig.1.

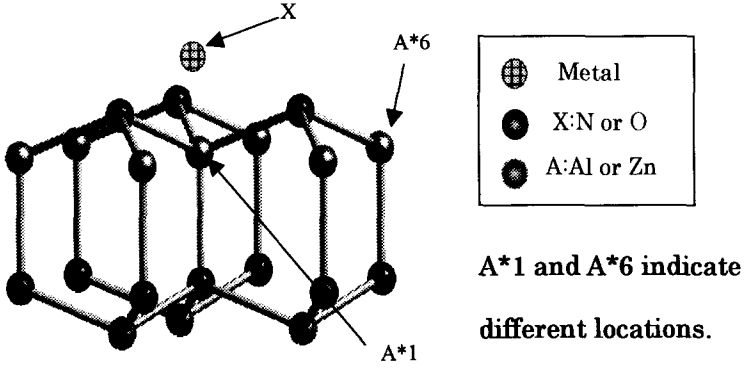

Fig.1 Cluster model of AlN and ZnO

3. RESULTS AND DISCUSSION

3.1 Experimental aspects

Contact angle is defined as shown in the left side of Fig.2; an acute angle (less than 90°) indicates wetting and an angle of more than 90° indicates lack of wetting [10]. Microscopic discussions of wetting property are difficult, in that,

whereas contact angle serves as a macroscopic parameter for wettability, no microscopic parameter for wettability is known to exist. Surface thermodynamic energy and surface tension are also macroscopic figures. Intermediate phenomena towards the final stage of wetting are important for understanding wettability. Discussions of the electronic structures between a metal and ceramic may facilitate understanding of electron transfers at the interfaces that lead to the macroscopic thermodynamic results. The parameters employed are effective charge, bond order, energy gap and bond overlap population diagram analyzed by DV-Xα.

Figure 2 illustrates the wetting behaviors of Ag on various oxide substrates and an AlN substrate. PLZT denotes $(Pb,La)(Zr,Ti)O_3$, which is a typical transparent ferroelectric ceramic of perovskite structure, and Mn-Zn is an oxide-ferrite of spinel structure. According to these experimental results, oxide is usually not wetted by a metal. Ag on $BaTiO_3$ presents the lowest contact angle (90°) thereby showing the most wetted behavior. Almost the same contact angle is obtained in the case of Cu on $BaTiO_3$. According to our previous report [4], the contact angles of Ag and Sn on TiO_2 are 90°and 140°, respectively, and AlN shows the highest angle. Sn forms a more thermodynamically stable oxide (heat of formation of around –300 kJ/mol) at the interfaces or on the surface of the metal; in comparison, heat of formation of Ag-oxide is around –0.3 kJ/mol.

From our previous experimental findings, we propose the following microscopic wetting mechanisms: Ag_2O is not stable, although Ag can easily form an oxide. The oxidation phenomena are supposed to relate to wetting of metal on the ceramics: that is, formation of the metal oxide is important for lowering surface energy at the interfaces [2]. The physical meaning of surface oxidation is dynamical electron-movement or electron-transfer between a metal and an element in the substrate. Herein lies a big difference between the chemical adsorption on the surface of a substrate and wetting behavior; chemical adsorption is merely formation a product (such as oxide) on the surface or at the interface. Whereas, wetting property is thought to relate to a dynamical process wherein the product is formed and immediately dissociated and the process is repeated to lower surface energy, resulting in the achievement of equilibrated contact angle, regardless of whether or not wetting occurs.

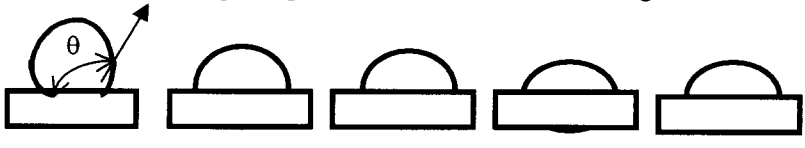

Fig. 2 Wetting behaviors of Ag on AlN and oxides (contact angle, θ)

In the first stage of the wetting process, the oxide is formed, and is immediately dissociated if the oxide is an unstable species. Through this process, the new surface of a metal can be generated, wetting of a metal proceeds, and these processes continue until the achievement of equilibrium conditions, leading to the macroscopic contact angle at the final stage. Previously we reported [5] that after melting at 973K Al, shows a contact angle of 140° on the oxide PLZT, and when temperature is raised to 1273K the contact angle drops to 120°. This finding suggests that the oxides (Al_2O_3 film) on Al metal were partially eliminated, and then a new surface appeared, thereby leading to wetting. Therefore, a metal surface can no longer appear if a stable product such as oxide film completely covers on the metal. Electron transfer between the metal and substrate seems to be a key factor. This is a different view from chemical or physical adsorption. That is to say, wetting property is a more dynamical issue at the interfaces.

Electron transfer seems to require microscopic discussion of wetting property, including interfacial electronic structures. In the present study, we discuss the metal/ZnO system as another oxide. Therefore, we can compare the wetting properties of different electrode metals on a nitride or oxide substrate, in terms of both experimental results and calculation.

3.2 Calculated aspects

3.2.1 Effective charges

Table 1 shows effective charges in AlN were shown when a metal was placed on AlN, where the initial valence of a metal is assumed to be 0. First of all, Al(1) in AlN shows a valence of 1.68, obtaining 1.32 electrons in the valence of +3 of Al, and N(1) releases 1.53 electrons, leading to the valence of −1.47, and 0.76 electrons of Al placed on AlN are transferred to the adjacent ions in the AlN substrate. When Ag is placed on the AlN substrate, Al(1) is located at the nearest position to the metal. If Al is ionized (+3) in AlN, Al obtains 1.28 electrons, leading to the valence of 1.72. Ag releases only 0.24 electrons. In contrast, N(1) gives 1.64 electrons to its neighbors, acquiring valence of −1.36. Furthermore, in the case of Cu on the AlN, Al(1) takes 1.28 electrons, and whereby the effective charge becomes to 1.72, and only 0.32 electrons of Cu are transferred to the neighbors in the substrate, while N (1) releases 1.63 electrons, acquiring valence of resulting in −1.37.

When placed on AlN, Al showed a change in the number of electron from 13 to 12.263, indicating movement of 0.76 electrons. Ag also shows a change in the number of electrons (47 electrons to 46.76, indicating movement of 0.24 electrons), as does Cu (29 to 28.68 electrons, indicating movement of 0.32 electrons). More electrons move in Al than in Cu and Ag, suggesting that Al electrode metal has lower wettability of Al.

When the substrate is ZnO, Al metal placed thereon shows a charge of 0.64,

whereas Ag shows a charge of 0.30 and Cu a charge of 0.4. In contrast, oxygen in the substrate receives more electrons, showing a charge of -0.92 in the case of Al, as compared with -0.89 for both Ag and Cu, indicating more polarization in Al on the substrate. These results of oxide substrate show the same tendency as that of the AlN substrate described above.

Table 1 Effective charges of a placed- metal and constituent elements in the substrate of AlN.

Metal/AlN	Element	Effective charge
Al	N(1)	-1.47
	Al (1)	1.68
	Placed-Al	0.76
Ag	N(1)	-1.36
	Al(1)	1.72
	Placed-Ag	0.24
Cu	N(1)	-1.37
	Al(1)	1.72
	Placed-Cu	0.32

The placed-metal is neutral upon placement. N(1) and Al(1) designate the nearest element to the placed metal on the AlN substrate.

3.2.2 Coulomb force

Table 2 shows Coulomb force which represents the ionicity of metal on AlN, where Coulomb force is computed by the following equation;

$$E = \frac{q_1 q_2}{4\pi\varepsilon_0 r^2} \quad (\text{nN=N}\times 10^{-9}) \tag{1}$$

where q_1 and q_2 indicate charges of the ions (C), $\varepsilon_0 = 8.854\times 10^{-12}$ $C^2/N\cdot m^2$,and r is the distance between ions.

Ag and Cu show -0.96nN and -1.36nN, respectively, which are greater than that of Al, -3.06nN. Therefore, electrons seem to be easily polarized on Al/AlN as compared with Ag/AlN and Cu/AlN, indicating slightly less electron transfer between a metal and AlN. Namely, Ag and Cu are considered to be covalent. This coincides with the results of effective charge shown in Table 1.

Table 2 Coulomb interaction of metal /AlN system ($\times 10^{-9}$)

Top metal	Metal-N(1)	Metal-Al(1)	N-Al(1)
Al	3.06	3.59	15.89
Ag	0.96	1.26	15.02
Cu	1.36	1.81	15.24

N(1) and Al(1) have the same meanings as in Table 1.

Table 3 Coulomb interaction of metal/ZnO($\times 10^{-9}$)

Top metal	Metal-O(1)	Metal-Zn(1)	O-Zn(1)
Al	1.72	1.96	5.29
Ag	0.78	0.94	5.28
Cu	1.18	1.44	5.06

When the substrate is ZnO, Al shows greater ionicity than Ag or Cu. This suggests that electrons around Al are apt to be polarized, leading to more stable oxide and Al showing less wettability as compared with Ag or Cu.

3.2.3 Bond overlap population

The bond overlap population per atom serves as an index of covalent bonding tendency. Table 4 lists the bond overlap populations for a metal/AlN systems and metal/ZnO systems. A positive value indicates covalent bonding rather than ionic bonding. As seen in Table 4, Ag (0.127) and Cu (0.123) on the AlN substrate show more covalence than does Al (0.045) in metal/N and metal/Al. This trend is also seen in the ZnO substrate; namely, the bonding natures of metal-O and metal-Zn are 0.056 and 0.103, respectively, and these values are smaller than those of Ag and Cu. For both substrates, we can expect that electron transfers are more active in Ag and Cu than in Al. We see similar results in the wetting behaviors of $BaTiO_3$ with Ag and Al [3]; Ti in the substrate of the Ag/ $BaTiO_3$ system shows a bond overlap population of 0.08 and –0.01 for the Al/ $BaTiO_3$ system, which indicates that the former shows more covalence the latter.

Furthermore, we defined the ratio (W_a) of covalence/ionicity according to the values of Coulomb interaction and bond overlap population; the values are thought to predict the interfacial interactions between a metal and the substrate, associated with the tendency of wettability. Note that the interfacial interaction does not necessarily mean the chemical reaction between a metal and a substrate in the sense of wetting behavior. Table 5 lists value of the ratio.

Table 4 Bond overlap population of metal /AlN systems and /ZnO systems (per bond).

Metal	Metal/ AlN		Metal	Metal/ ZnO	
	Metal-N	Metal-Al(1)		Metal-O	Metal-Zn(1)
Al	0.045	0.046	Al	0.056	0.103
Ag	0.127	0.055	Ag	0.075	0.110
Cu	0.123	0.074	Cu	0.085	0.148

Table 5 Ratio of bond overlap population to Coulomb interaction.

	Al/	Ag/	Cu/AlN	Al/	Ag/	Cu/ZnO
W_a = (bond overlap population) / (Coulomb interaction)	0.015	0.13	0.09	0.033	0.096	0.072

As seen in Table 5, larger values of W_a suggest that electrons move around at the interfaces between the electrode metal (Ag and Cu as compared to Al) and a substrate; hereafter an electron is considered to be localized on neither a placed-metal nor a substrate element, resulting in instantaneous formation of an oxide or non-strong interaction with AlN or ZnO, after which the oxide is expected to be promptly dissociated, leading to a new surface of a placed-metal, and these processes continue until the achievement of an equilibrium contact angle of a metal on the substrate. In the case of Al, the electrons are apt to be localized as seen in larger effective charge, such as 0.76(Table 1) and smaller W_a (0.015 and 0.033 in Table 5). Ag and Cu showed larger values of W_a (0.13 and 0.09 for Ag/ and Cu/AlN, respectively). Furthermore, in the case where a ZnO substrate is employed values of 0.096 and 0.072 are obtained for Ag/ and Cu/ZnO, respectively. For both substrates, W_a is expected to somehow show a tendency leading to larger covalence, which as discussed here, would indicate better wettability. These computed results suggest that Ag and Cu possess more wettability than Al, which agrees with contact angles obtained in wetting

experiments results. Therefore, electron-movement is a microscopic key factor for wettability of an electrode metal on a ceramic substrate.

In the oxide, when Ag was placed on TiO_2, the bond of upper-oxygen and Ag showed greater covalence (0.557) than did Al (0.292). Furthermore, Cu also exhibited a grater value (0.456) than did Al. The parameter of bond overlap population in TiO_2 provides relative electron-transfer between a metal and the element in the substrate, which is in connection with another substrate of ZnO as well as AlN. Note that the value of bond overlap population is not an absolute value among metals on a substrate, but even relative values of W_a are useful for forecasting the tendency of wetting nature.

As discussed previously, the electron-transfer suggesting covalent bonding nature is expected to serve as a microscopic monitoring parameter for wetting. Figure 3 schematically shows interfaces between the substrate and metal (Ag or Al), while focusing on only bond overlap population. Ag showed higher bond order between metal and anion in both substrates, indicating more wetting than Al.

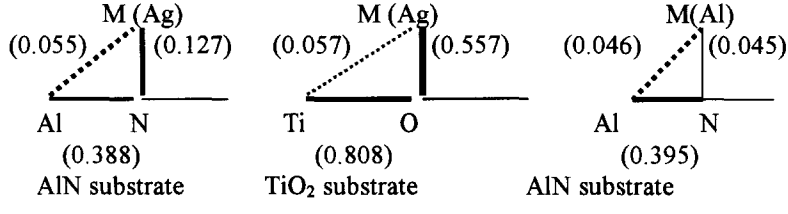

Fig.3 Example illustrations for bond order; AlN or TiO_2 substrate and metal (Ag or Al) placed thereon.

4. CONCLUSION

We investigated wetting tendency through electronic structures of a metal/AlN system and compared the results with those for a metal/oxide substrate (ZnO), and as well as the wetting mechanism at the interfaces between the electronic ceramic and the electrode metal. The DV-Xα method revealed that the electron-transfer between the substrate and electrode metal suggested the tendency of wettability showing grater covalence than ionicity between an electrode metal and AlN or any other oxide such as ZnO or TiO_2 and $BaTiO_3$. Therefore, we can estimate relative wettability of a metal in the macroscopic sense from the microscopic bonding natures in electronic structures among ceramic substrates.

ACKNOWLEDGEMENT

The authors wish to express their sincere gratitude to Professors T. Mizuno of Osaka University and R. Sekine of Shizuoka University, for their fruitful discussion. They would also like to express their gratitude to Toshiba Ceramic Engineering Company for providing AlN substrates and to Fuji titanium industry for providing $BaTiO_3$ powder.

REFERENCES

[1] K. Nagesh, A. P. Tomsia and J. A. Pask, J. of Mater. Sci., **18**, 2173(1986).
[2] N. Takiuchi, T. Taniguchi, N. Shinozuka and K. Muraki, J. of Jpn. Inst. of Met. **55**, 180(1991)[in Japanese].
[3] S. Sugihara, I. Yonekura N. Asaba and R. Sekine, J. of Korean Phys. Soc., **32**, S1119 (1998).
[4] S. Sugihara, H. Katanahara and T. Isobe, Bull. of the Soc. for DV-Xα, **13**, 80 (2000).
[5] S. Sugihara and Y. Hirose, J. of Ceramic Society of Japan, **102**, 217 (1994).
[6] F. Oba, H. Adachi and I. Tanaka, Bulletin of the Society for Discrete Variational Xα, **11**, 36 (1998).
[7] D. Jones and A. H. Lettington, Solid State Commun., **11**, 701 (1972).
[8] F. S. Galasso, *Structure and Properties of Inorganic Solids*, Pergamon Press, Ltd., London, translated by M. Katoh and K. Uematsu, Agune Gijyutsu Center [in Japanese].
[9] H. Schulz and K. H. Thiemann, Solid State Commun.**23**, 815(1977).
[10] S. Sugihara , K. Okazaki, J. of Ceramic Society of Japan, **101**, 129(1993).
[11] N. Takiuchi, T. Taniguchi, N. Shinozaki and K. Mukai, J. Jpn. Inst. Met., **55**, 44 (1991)[in Japanese].

Subject Index